



Leble, Vladimir (2016) *Integrated simulation of off-shore wind turbine*. PhD thesis.

<http://theses.gla.ac.uk/7865/>

Copyright and moral rights for this work are retained by the author

A copy can be downloaded for personal non-commercial research or study, without prior permission or charge

This work cannot be reproduced or quoted extensively from without first obtaining permission in writing from the author

The content must not be changed in any way or sold commercially in any format or medium without the formal permission of the author

When referring to this work, full bibliographic details including the author, title, awarding institution and date of the thesis must be given

Glasgow Theses Service

<http://theses.gla.ac.uk/>

theses@ gla.ac.uk



University
of Glasgow

**Integrated Simulation of Off-shore Wind
Turbine**
by
Vladimir Leble MSC

A thesis submitted in partial
fulfillment of the requirements for
the degree of Doctor of Philosophy
University of Glasgow
School of Engineering
October 2016

© 2016
Vladimir Leble

Declaration

I hereby declare that this dissertation is a record of work carried out in the School of Engineering at the University of Liverpool during the period from March 2013 to August 2016, and at the University of Glasgow during the period from January 2016 to October 2016. The dissertation is original in content except where otherwise indicated.

October 2016

.....

(Vladimir Leble)

Abstract

This thesis presents coupled model for the floating off-shore wind turbines, using a 10-MW machine as an example. The idea put forward is to employ high fidelity Navier-Stokes solvers for air and water. For this reason, the Helicopter Multi-Block solver was used for air, and the Smoothed Particles Hydrodynamic method was used for water. A multi-body solver was implemented to solve for the wind turbine dynamics. All solvers were validated before coupling, and results are presented in this thesis. The employed, loosely coupled, algorithm is described in detail, and the importance of coupling is assessed. Additional aerodynamic cases were studied to form the foundation for further model development.

The study started from the aerodynamic analysis of a 10-MW wind turbine. Straight and pre-bent configurations of the blade were investigated under the assumption of uniform inflow. Next, the effects of the atmospheric boundary inflow and atmospheric turbulence were studied. For this, the power law wind speed profile was employed, and atmospheric turbulence was introduced using Mann's model.

The aero-elasticity of the 10-MW rotor was studied next. The structural model was constructed using *NASTRAN*, and the natural frequencies and modes were compared to published results, showing good agreement. This model was then used for steady and unsteady aero-elastic computations.

The effects of employing deformable trailing and leading edge flaps on a 10-MW wind turbine were also investigated. The results showed that the trailing edge flap can be used to control flap-wise bending of the blade, whilst the leading edge flap can be used to counter additional pitching moment created by the trailing edge flap.

A floating 10-MW rotor was considered next, as well as forced yaw and pitch oscillations of the machine. The results showed large variations in thrust and power as the wind turbine pitched about a point located $119m$ below the rotor. The vortex ring state was also encountered when the wind turbine was forced to a pitching motion with amplitude of 5° and period of $8.8s$.

A coupled method for the analysis of the dynamics of floating off-shore wind turbines was finally described, along with the test cases and numerical parameters. The results of decoupled and coupled computations are presented and analysed. The results showed that the employed floating turbine under studied conditions did not enter a vortex ring state. A turbulent wake state was encountered, but only at the initial pitching phase. The gyroscopic effects were also small for studied system, and did not cause significant rotations due to large inertia of the employed floater.

Publications

In Journals

V. Leble and G. Barakos, "Demonstration of a coupled floating offshore wind turbine analysis with high-fidelity methods", *Journal of Fluids and Structures*, Volume 62, pp. 272–293, April 2016, ISSN 0889-9746, DOI:10.1016/j.jfluidstructs.2016.02.001.

V. Leble and G. Barakos, "Rigid actuation of the wind turbine", submitted to the *Journal of Solar Energy Engineering*

V. Leble and G. Barakos, "A coupled floating offshore wind turbine analysis with high-fidelity methods", *Energy Procedia*, Volume 94, September 2016, Pages 523-530, ISSN 1876-6102, DOI:10.1016/j.egypro.2016.09.229

S. Colonia, V. Leble, R. Steijl and G. Barakos, "Assessment and Calibration of the γ -Equation Transition Model for a Wide Range of Reynolds Numbers at Low Mach", submitted to the *AIAA Journal*

V. Leble and G. Barakos, "Forced pitch motion of wind turbines", *The Science of Making Torque from Wind (TORQUE 2016)*, *Journal of Physics: Conference Series* 753 (2016), DOI:10.1088/1742-6596/753/2/022042

S. Colonia, V. Leble, R. Steijl and G. Barakos, "Calibration of the γ -Equation Transition Model for High Reynolds Flows at Low Mach", *The Science of Making Torque from Wind (TORQUE 2016)*, *Journal of Physics: Conference Series* 753 (2016), DOI:10.1088/1742-6596/753/8/082027

Chapters in Books

V. Leble and G. Barakos, "Trailing and leading edge flaps for load alleviation and structure control", W. Ostachowicz, M. McGugan, J.U. Schröder-Hinrichs, M. Luczak (eds.), "MARE-WINT, New Materials and Reliability in Offshore Wind Turbine Technology", pp. 103–114, Springer, ISBN 978-3-319-39095-6

V. Leble and G. Barakos, "CFD investigation of a complete floating offshore wind turbine", W. Ostachowicz, M. McGugan, J.U. Schröder-Hinrichs, M. Luczak (eds.), "MARE-WINT, New Materials and Reliability in Offshore Wind Turbine Technology", pp. 227–308, Springer, ISBN 978-3-319-39095-6

In Conference Proceedings

V. Leble and G. Barakos, Coupled NS/SPH Analysis of Off-Shore Wind Turbine, In proceedings of 71 American Helicopter Society Annual Forum & Technology Display, Virginia Beach, VA USA, May 2015

V. Leble, Y. Wang and G. Barakos, CFD analysis of 10-MW wind turbines, In proceedings of DEWEK 2015, Bremen, Germany, May 2015

Y. Wang, V. Leble, M. White and G. Barakos, Wake Characteristics of Large-scale Wind Turbines, In proceedings of 2015 European Rotorcraft Forum, Munich, Germany, September 2015

V. Leble, Y. Wang and G. Barakos, Detailed Simulation of Offshore Wind Turbine, In proceedings of EWEA Conference 2015, Paris, France, November 2015

V. Leble and G. Barakos, Numerical Simulation of Oscillating Wind Turbines, In proceedings of 72 American Helicopter Society Annual Forum & Technology Display, West Palm Beach, Florida, USA, May 2016

In Conferences without Proceedings

V. Leble and G. Barakos, Static and dynamic aero-elastic calculations for 10-MW wind turbines, MARE-WINT side event, EWEA Offshore 2015, Copenhagen, Denmark, March 2015

V. Leble and G. Barakos, Dynamic analysis of Off-Shore Wind Turbines, poster presentation at EPSRC Supergen Wind Hub General Assembly, Loughborough, UK, April 2015

Technical Notes

V. Leble, Computations of Wind Turbine Cases with Flaps in HMB, Technical Note TN14-009

V. Leble, MBDM - Multi-Body Dynamics Module, Technical Note TN16-004

V. Leble, Using HMB with Mann Box turbulence inflow, Technical Note TN16-006

Reports for the MARE-WINT Initial Training Network

"1st Progress Report - University of Liverpool contribution to MARE-WINT", October 2013

"Mid-Term Report - University of Liverpool contribution to MARE-WINT", April 2014

"2nd Progress Report - University of Liverpool contribution to MARE-WINT", November 2014

"3rd Progress Report - University of Glasgow contribution to MARE-WINT", November 2015

Acknowledgements

Firstly, I would like to thank my supervisor Prof. George Barakos for his guidance and constant support throughout the PhD. His technical knowledge and advise was crucial for this work and his contagious enthusiasm was a source of motivation. I am also very grateful to Dr. Rene Stejil, Dr. Mark Woodgate, and Dr. Massimo Biava for sharing their expertise in numerical methods and providing me with valuable advise. Many thanks have to be granted to Dr. Marcin Luczak from the Institute of Fluid-Flow Machinery of Polish Academy of Sciences, whose efforts were essential to success of the MARE-WINT project.

The financial support of the Marie Curie Host Fellowships Program: FP7-PEOPLE-2012-ITN-309395 - New Materials And Reliability In Offshore Wind Turbines Technology "MARE-WINT" is gratefully acknowledged. Moreover, I would like to highlight the significance of European Initial Training Networks, and thank all the fellows who worked with me and exchanged a lot of ideas to complete MARE-WINT project successfully.

Results were partially obtained using the EPSRC funded ARCHIE-WeSt High Performance Computer (www.archie-west.ac.uk). EPSRC grant no. EP/K000586/1. The University of Liverpool is gratefully acknowledged for providing access to the N8 HPC facility Polaris, and the Chadwick system.

Also, I would like to extend my gratitude to all past and present members of the CFD Lab, for creating a stimulating work environment and making me feel at home. The time spent with Dr. Nick Tantaroudas, Dr. George Zografakis, Dr. Vasilis Pastrokakis, Dr. Simone Colonia, Dr. Mikolaj Jarkowski, Dr. Yaxing Wang, Antonio Jimenez Garcia, and many others, is of great value.

Last but not least, I would like to thank my family and friends, whose unconditional support and understanding gave me the strength to keep going.

Contents

1	Introduction	1
1.1	Motivation	1
1.2	Literature Survey	4
1.2.1	Aerodynamic modelling	6
	Algebraic models	6
	Blade Element Momentum method	6
	Lifting-line and Vortex-wake methods	7
1.2.2	Hydrodynamic modelling	9
	Morison’s representation	9
	Potential theory	10
1.2.3	Support structures and mooring lines	13
	Force-displacement representation	16
	Quasi-static representation	17
	Dynamic modelling	17
1.2.4	Structural modelling	18
1.2.5	Modelling approaches for FOWTs	19
1.2.6	Coupling schemes	20
	Definitions	22
	Explicit coupling	23
	Implicit coupling	26
1.2.7	Experimental data for FOWTs	28
1.2.8	Active rotor blades	29
1.2.9	Atmospheric turbulence	31
	Sandia model	32
	Mann’s model	32
1.3	Summary of findings	33
1.4	Outline of the thesis	34
2	Hydrodynamic simulation method	36
2.1	Concept and formulation	36
2.2	Smoothing functions	39
2.3	SPH formulation of Navier-Stokes equations	41
2.3.1	Continuity equation	42
2.3.2	Momentum equation	42
	Artificial viscosity	43
	Laminar viscosity	44
2.3.3	Equation of state	44
2.4	SPH implementation	44

2.4.1	Moving particles	44
2.4.2	Time marching schemes	45
	Verlet scheme	45
	Symplectic scheme	46
2.4.3	Solid boundary particles	47
	Dalrymple boundary condition	47
	Repulsive force boundary condition	48
2.4.4	Computational efficiency and method overview	49
3	Aerodynamic simulation method	51
3.1	CFD Solver	51
3.1.1	Upwind schemes	54
	Roe's flux-splitting scheme	55
	Osher's scheme	55
	MUSCL scheme	55
3.1.2	Parallel method	56
3.1.3	Turbulence modelling	56
3.2	Reynolds Averaging	56
3.2.1	Time Averaging	57
3.3	Boussinesq-Based Models	58
3.4	Viscosity-Dependent Parameters	58
3.5	Two-Equation Models	59
3.5.1	Model Equations: Linear $k - \omega$ Model	61
3.6	CSD solver	63
3.6.1	Blade structural model	63
3.6.2	Grid deformation method	65
	Constant Volume Tetrahedron	65
	Spring Analogy Method	66
	Trans-Finite Interpolation	67
	Summary and efficiency	68
3.6.3	Steady FSI method	69
3.6.4	Unsteady FSI method	70
4	Multi-body simulation method	72
4.1	Concept and essential formulation	72
4.1.1	Joint definition frames	74
4.1.2	Basic kinematic constraints	75
4.1.3	Absolute constraints on a body	77
4.1.4	Constraints between pairs of bodies	78
	Distance constraint	78
	Spherical joint	79
	Revolute joint	79
	Revolute-cylindrical composite joint	80
	Translational joint	81
	Relative rotational driving constraint	82
4.1.5	Euler parameter normalisation constraint	84
4.2	Kinematic analysis	84
4.2.1	Position analysis	85
4.2.2	Velocity analysis	85

4.2.3	Acceleration analysis	86
4.2.4	Derivatives of basic constraints	86
4.3	Dynamic analysis	88
4.3.1	Equations of motion of a rigid body	88
4.3.2	Equations of motion with a centroidal body-fixed reference frame	90
4.3.3	Equations of motion for constrained system	91
4.4	Coordinate partitioning method	94
4.4.1	Example of automatic partitioning	97
4.5	Translational springs and dampers	99
5	Conceptual model of coupling	102
5.1	Importance of strong coupling	102
5.2	Communication between solvers	103
5.2.1	MPI communication	105
	MPI communication with HMB	106
	MPI communication with SPH	107
5.3	Generation of regular waves	114
6	Validation of SPH	119
7	Validation of CFD	125
7.1	NREL Annex XX experiment	125
7.1.1	Grid and computational parameters	126
7.1.2	Results of validation	128
7.2	MEXICO project experiment	130
7.2.1	Grid and computational parameters	130
7.2.2	Results of validation	132
8	Validation of the Multi-Body Dynamic Module	136
8.1	2D slider-crank mechanism	136
8.1.1	Kinematic analysis of the 2D slider-crank mechanism	137
8.1.2	Dynamic analysis of the 2D slider-crank mechanism	139
8.2	3D slider-crank mechanism	141
8.3	Gyroscopic wheel	144
9	DTU 10-MW Reference Wind Turbine	146
9.1	Overview of the design	146
9.2	Computational parameters	149
9.3	Grid convergence study	150
9.4	Rigid blade cases with uniform inflow	157
9.4.1	Straight blade	157
9.4.2	Blade with pre-bend and pre-cone	168
9.5	Atmospheric boundary inflow and atmospheric turbulence	173
9.5.1	Atmospheric boundary inflow	173
9.5.2	Mann turbulence model	173
	Computational procedure	175
9.5.3	Computational grids and parameters	177
9.5.4	Results	179

10 Elastic computations for DTU 10-MW RWT	187
10.1 Elastic eigenvalue analysis	187
10.2 Static aero-elastic calculations	195
10.2.1 Grids and computational parameters	195
10.2.2 Results for the straight blade	196
10.2.3 Results for the blade with pre-bend and pre-cone	199
10.3 Dynamic aero-elastic calculations	202
10.3.1 Grids and computational parameters	202
10.3.2 Results	204
10.4 Complete assembly of DTU 10MW RWT	207
10.4.1 Grids and computational parameters	207
10.4.2 Results	208
11 Trailing and leading edge flaps for DTU 10-MW RWT	213
11.1 Flap deflection algorithm	213
11.2 Definition of the flaps	214
11.3 Computational grid and flow conditions	217
11.4 Results and discussion	217
11.4.1 Results for the TE flap	217
11.4.2 Results for the LE flap	223
11.4.3 Comparison of the performance	228
12 Forced oscillations of DTU 10-MW Reference Wind Turbine	230
12.1 Test cases	231
12.1.1 NREL Phase VI wind turbine	232
Grid and computational parameters	232
12.1.2 DTU 10MW reference wind turbine	234
Grid and computational parameters	234
12.2 Results and discussion	235
12.2.1 NREL Phase VI wind turbine	235
12.2.2 Static and dynamic yawing of DTU 10MW reference wind turbine	237
12.2.3 Dynamic pitching of DTU 10MW reference wind turbine	240
13 Coupled computation of floating off-shore wind turbine	244
13.1 Coupling scheme	245
13.2 Test case description	246
13.2.1 CFD mesh	247
13.2.2 SPH setup and resolution	248
13.2.3 Initial conditions	250
13.2.4 Demonstration cases	250
13.3 Results and Discussion	251
13.3.1 Decoupled cases - constant and time-varying thrust	251
13.3.2 Coupled case	256
13.3.3 Computational performance	263
14 Conclusions and future work	265
14.1 Conclusions	265
14.2 Future work	267
References	268

A	Structural models for DTU 10MW RWT blade	282
A.1	Straight DTU 10MW RWT blade	282
A.2	DTU 10MW RWT blade with pre-bend and pre-cone	292
B	Simplified hydrodynamic model in MBDM	302
B.1	Cylinder in calm water	302
B.1.1	Buoyancy force and moment	302
B.1.2	Validation of the model	304
C	Convection of the Mann’s turbulence field into Cartesian grids	309

List of Figures

1.1	Size evolution of wind turbines over time with corresponding rated capacity ^[55]	1
1.2	Prototypes of the floating off-shore wind turbines: decommissioned (a), operating (b-f).	3
1.3	Vortex filament methods: Lifting-line model (a) and Free-Vortex Method (b).	8
1.4	Superposition of radiation and diffraction loads ^[94]	10
1.5	Panels employed for quarter of the spar support (left) and quarter of the free surface (right) to account for the second-order wave loads ^[96]	13
1.6	Floating platform concepts for off-shore wind turbines ^[181]	14
1.7	Mooring line systems – catenary (a), taut leg (b), and tension leg (c).	15
1.8	Schematic representation of the coupled domains.	22
1.9	Generic cycles of some explicit algorithms. Letters A and H denote aerodynamic and hydrodynamic solver, respectively.	25
1.10	Different approaches to achieve desired thrust of scaled FOWTs: drag disc approach (a) and thrust-matched blade design (b).	29
1.11	Active wind turbine rotor: conceptual layout of a smart blade (a), and trailing edge flaps concept (b). Adapted from ^[14]	30
2.1	The SPH particle approximation in a two-dimensional problem domain Ω bounded by a surface S . W is the smoothing function that is used to approximate field variables at particle i by using particles j within the support domain.	38
2.2	The Gaussian smoothing function and its first derivative.	40
2.3	The cubic spline smoothing function and its first derivative.	40
2.4	Two different lattice types for a square floating object.	47
2.5	SPH method key steps - a) represent the problem domain by a set of particles b) use particle approximation and iteratively choose particle c) find all the particles close to the current particle d) flag the interaction particles e) solve the NS equations using all the particles within the support domain f) update the particle to its new position. Dashed lines represent data splitting into bins for efficient parallel computing.	50
3.1	<i>CBEAM</i> -type element of <i>NASTRAN</i> , with <i>PBEAM</i> properties. Adapted from <i>NASTRAN</i> user’s guide ^[6]	64
3.2	The DTU 10MW RWT blade with the structural model consisting of beams, bars, and triangular elements.	65
3.3	Projection of the fluid grid on the structural model through Constant Volume Tetrahedron (CVT) method.	66
3.4	Spring Analogy Method (SAM) to obtain the updated block vertex positions. Dashed lines represent springs on the block faces.	67
3.5	Notation of a block face for Transfinite Interpolation (TFI) for full mesh generation.	68
3.6	Cell volume ration (a), and skewness ratio (b) between deformed and undeformed grids at the tip of the DTU 10MW RWT blade. Tip displacement 8.5m.	69

3.7	Diagram of the static (a), and dynamic (b) aero-elastic coupling method employed in the HMB solver.	70
4.1	Translation and rotation of a reference frame.	73
4.2	Construction of a joint definition frame.	74
4.3	Position vectors \mathbf{r}_i and \mathbf{r}_j , vector between bodies \mathbf{d}_{ij} , and body fixed vectors \mathbf{a}_i and \mathbf{a}_j	75
4.4	Parallel vectors on and between adjacent bodies.	77
4.5	Distance constraint.	78
4.6	Spherical joint.	79
4.7	Revolute joint.	80
4.8	Revolute-cylindrical joint.	80
4.9	Translational joint.	81
4.10	Parallel vectors on and between adjacent bodies.	82
4.11	Forces acting on a rigid body in space.	89
4.12	Simple pendulum.	98
4.13	Body with translational spring fixed at one point.	100
5.1	"Campbell"-like diagram for the investigated FOWT showing frequencies of the rotor and the waves as function of sea state and wind speed.	103
5.2	Schematic of the solvers employed in the floating off-shore wind turbine model.	103
5.3	Flow chart of the MPI implementation and data exchange for coupled model.	105
5.4	Meshes around the TL190-82 aerofoil used in 2D computations to validate communication protocol.	106
5.5	Coefficients of lift, drag and moment $c/4$ as functions of time for pure HMB3 and HMB3 with communication, where grid motion is applied at each time step.	108
5.6	Position of the TL190-82 aerofoil and pressure coefficient distribution at time $t = 3s$. Comparison between computations using pure HMB3 and HMB3 with communication.	109
5.7	Schematic geometry of the test case, not in scale. Floating body is a cube with mass $m = 0.216kg$	109
5.8	Initial particles distribution for all validation test cases. Spacing between particles $d = 0.01m$	110
5.9	Lateral dynamics of the cube during the drop into calm water. Comparison between four test cases - Pure SPH, SPH with simple communication, SPH with calculation and SPH with calculations using MBDM. See Table 5.3 for the description.	111
5.10	Rotational dynamics of the cube during the drop into calm water. Comparison between four test cases - Pure SPH, SPH with simple communication, SPH with calculation and SPH with calculations using MBDM. See Table 5.3 for the description.	112
5.11	Comparison between the real shape of the body (red lines) and the particles used to represent the body. Last layer of particles in x direction is missing.	113
5.12	Comparison between the position of the corner particle in MBDM and in SPH that is governed by the MBDM dynamic equations. Initial position of the particle was $[1.0, 0.34, 0.26]m$	114
5.13	Two dimensional water basin for regular waves generation test cases. Not to scale. Wave height is measured around $150m$ from the paddle.	115
5.14	Results for sea state 4 - definition of the wave height (a), and calculated wave height as function of paddle amplitude (b).	116
5.15	Span-shots of the pressure distribution and surface elevation for the sea state 4 for various amplitudes of paddle motion. Period of paddle motion $T = 8.8s$. Time of the solution $t = 60.0s$	117
5.16	Wave height and paddle amplitude as function of sea state.	117
6.1	Schematic of the SPH validation setup: a) isometric view b) side view.	119

6.2	Depth of penetration of a cylinder of density 500 kg/m^3 : SPH results for different viscosity parameters α and constant number of particles. Experimental data of Greenhow and Lin ^[66] is shown for comparison.	121
6.3	Depth of penetration of a cylinder of density 500 kg/m^3 : SPH results for different distance between particles (d) and experimental results of Greenhow and Lin ^[66]	122
6.4	Depth of penetration of a cylinder of density 500 kg/m^3 : Comparison between current SPH method and results of Vandamme <i>et al.</i> ^[199] and Skillen <i>et al.</i> ^[185] , and experimental results of Greenhow and Lin ^[66]	122
6.5	Surface deformation during water entry of a cylinder for time $t = 0.32s$ from the beginning of the fall. Comparison between different distances d and experimental results by Greenhow and Lin ^[66]	124
6.6	Comparison between velocity and acceleration curves over time for different initial particle distance d . CoG - centre of gravity of the cylinder.	124
7.1	NREL Phase VI blade – twist distribution (a), geometry (b), and NACA S809 aerofoil (c).	126
7.2	Grid employed for the NREL Phase VI wind turbine. Slice through the volume close to the blade surface (a), surface mesh (b), and computational domain (c).	127
7.3	Thrust and torque over the fifth revolution for the rigid NREL blade.	128
7.4	Comparison of C_p distribution at three blade stations, for blade azimuth positions of 0 and 180 degrees (rigid blade), at the fifth revolution.	129
7.5	MEXICO project blade – twist distribution (a), chord distribution (b), and blade geometry (c).	131
7.6	Grid employed for the MEXICO wind turbine. Slice through the volume close to the blade surface (a), surface mesh (b), and computational domain (c).	132
7.7	Velocity profiles extracted at a straight line crossing the first vortex for wind speed $15m/s$: axial velocity (a) and radial velocity (b). Wake behind the MEXICO Project rotor visualised with iso-surfaces of $\lambda_2 = -0.01$ (c). Adapted from ^[29]	134
7.8	Contours of vorticity of the tip vortex for two wind speeds: $10m/s$ and $15m/s$. Comparison between CFD results (a-b), and experimental data (c-d). Adapted from ^[29]	135
8.1	Schematic representation of slider-crank mechanism.	137
8.2	Solution of the kinematic analysis of 2D slider-crank mechanism compared to the results of Haug ^[73]	138
8.3	Slider in a compression chamber, as used in the dynamic analysis of the 2D slider-crank mechanism.	139
8.4	Gas force versus slider position.	140
8.5	Results of the dynamic analysis of 2D slider-crank compression mechanism compared to the results of Haug ^[73]	140
8.6	Schematic of the 3D slider-crank mechanism.	141
8.7	Results of the kinematic analysis of 3D slider-crank mechanism compared to the results of Haug ^[73]	143
8.8	Schematic of the MBDM gyroscopic set-up. System shown in the initial condition.	144
8.9	Computed rate of precession compared to the analytical value.	145
9.1	FFA-W3 aerofoils with relative thickness between 24.1% and 36%.	147
9.2	DTU 10MW reference blade.	148
9.3	The Gurney flap applied to the DTU 10MW RWT blade: aerofoil section with the flap (a), and isometric view of the blade root showing the flap (b). Adapted from ^[11]	149
9.4	The pre-bent shape of the DTU 10MW RWT blade. Not in scale.	149
9.5	DTU 10MW reference wind turbine design. Not in scale.	150

9.6	Computational domain for mesh convergence study with employed boundary conditions. Part of the domain is removed to expose the blade.	151
9.7	Slices through the volume mesh at $75\%R$ and close to the blade surface for various grids employed for the grid convergence study. Colour contours show cell volumes.	152
9.8	Convergence history of thrust and power, and corresponding coefficients for $7.0M$ cells grid.	153
9.9	Thrust fore and mechanical power as function of computational grid density.	154
9.10	Distribution of the thrust and driving forces, and pitching moment along the blade span. Comparison between solutions obtained with grids of different density.	155
9.11	Pressure coefficient distribution around the aerofoil section for different radial positions along the blade.	156
9.12	Two grids employed for straight and rigid blade cases – $7.0M$ and $9.2M$ cells grids. Slices through mesh in the vicinity of the surface of the blade (a-b); and surface grids (c-d). Distances in maximum chords, c	158
9.13	Shape of the DTU 10MW RWT blade with simplified nacelle as employed for the $9.2M$ cells mesh.	158
9.14	Thrust and power as functions of wind speed for straight, rigid blade. Comparison between results obtained by present CFD computations and Bak <i>et al.</i> ^[11]	159
9.15	Distribution of the thrust and driving forces, and pitching moment along the blade span. Comparison between solutions obtained for different wind speeds using $9.2M$ cells grid.	160
9.16	Distribution of the surface pressure coefficient (C_p) on the pressure side of the blade for the $9.2M$ cells grid at various wind speeds.	161
9.17	Distribution of the surface pressure coefficient (C_p) on the suction side of the blade for the $9.2M$ cells grid at various wind speeds.	162
9.18	Streamlines showing recirculation on the pressure side, and separation on the suction side for DTU 10MW wind turbine at $11m/s$ wind speed.	163
9.19	Pressure coefficient distribution around the aerofoil section for different radial positions along the blade and for different wind speeds.	164
9.20	Distribution of the skin friction coefficient (C_f) over the pressure side of the blade for the $9.2M$ cell grid at various wind speeds.	165
9.21	Distribution of the skin friction coefficient (C_f) over the suction side of the blade for the $9.2M$ cell grid at various wind speeds.	166
9.22	Skin friction coefficient distribution around the aerofoil section for different radial positions along the blade and for different wind speeds.	167
9.23	Grid employed for the DTU 10MW blade with pre-bend and pre-cone.	168
9.24	Domain decomposition methods: (a) sliding, and (b) overset methods. Adapted from ^[98]	169
9.25	Distribution of the loads for straight blade, and with pre-cone and pre-bend.	170
9.26	Distribution of the surface pressure coefficient (C_p) over the pressure side (a), and suction side (b). Comparison between straight and pre-coned blades.	171
9.27	Pressure coefficient distributions at different radial positions along the blade.	172
9.28	Distributions of the wind speed, pressure and density obtained with the power law profile by setting $U_{hub} = 11m/s$, $z_{hub} = 119.0m$, and $\beta = 7$. Logarithmic law profile was computed using $U(z) = U_{hub} \ln(\frac{z}{z_0}) / \ln(\frac{z_{hub}}{z_0})$, where $z_0 = 0.03m$ is the roughness length of a flat terrain. Quantities are normalised to the values at the hub-height.	174
9.29	The Mann turbulence field obtained with parameters from Table 9.6.	176
9.30	The Mann box turbulence field with extracted planes used to interpolate onto the HMB3 inflow plane.	177
9.31	Computational grids employed in this section.	179
9.32	Comparison between two employed grids G1 and G2 – (a-b) slice through the rotor grid, (b-c) rotor surface mesh.	180

9.33	Comparison between employed grids for the atmospheric boundary inflow. Grid points are skipped for clarity (2 for grid G1, and 4 for grid G2).	181
9.34	Thrust as function of revolution shown for each blade.	182
9.35	Power as function of revolution shown for each blade.	183
9.36	Fast Fourier transforms of the thrust and power time series for the blade number 1. The harmonics correspond to multiples of the blade-passing frequency $f_n = n \cdot f_1$, where $f_1 = 0.147Hz$	183
9.37	Thrust force and mechanical power as function of revolution. Comparison between the cases of atmospheric inflow with and without the turbulence, and uniform inflow of $11m/s$	184
9.38	Fast Fourier transforms of the total thrust and power. The harmonics correspond to multiples of the blade-passing frequency $f_n = n \cdot f_1$, where $f_1 = 0.441Hz$	185
9.39	Vortical structures represented by iso-surface of Q criterion for cases with and without wind turbulence. Contours of non-dimensional axial velocity W are shown in the middle of domain.	185
10.1	The DTU 10MW RWT blade surface with the structural model consisting of beams and bars.	188
10.2	DTU 10-MW RWT blade properties along span-wise direction employed in the NASTRAN model.	189
10.3	Campbell diagram for DTU 10-MW blade.	190
10.4	Frequencies and corresponding shapes of the first 4 modes for the straight blade.	191
10.5	Frequencies and corresponding shapes of the modes from 5 through 8 for the straight blade.	192
10.6	Frequencies and corresponding shapes of the first 5 modes for the blade with pre-cone and pre-bend.	193
10.7	Frequencies and corresponding shapes of the modes from 6 through 8 for the blade with pre-cone and pre-bend.	194
10.8	Details of the grids employed for the static aero-elastic analysis of the DTU 10MW RWT. Mesh close to the blade surface (a, c), and blocking (b, d).	195
10.9	Convergence history of the loads for the static aero-elastic computation for straight DTU 10MW RWT blade.	197
10.10	Resulting deformations of the initially straight blade from static aero-elastic computations. Shape of the blade for consecutive iteration (a); tip displacement for consecutive iteration (b); and final displacement at the tip in flap-wise (b) and edge-wise (c) directions.	198
10.11	Pressure coefficient distribution around the aerofoil section at $0.75R$ for rigid and elastic blade. Straight configuration of the blade.	199
10.12	Convergence history of the loads for the static aero-elastic computation for the DTU 10MW RWT blade with pre-bend and pre-cone.	200
10.13	Deformations of the blade with pre-bend and pre-cone for static aero-elastic analysis. Shape of the blade for consecutive iteration (a); tip displacement for consecutive iteration (b); and final displacement at the tip in flap-wise (b) and edge-wise (c) directions.	201
10.14	Pressure coefficient distribution around the aerofoil section at $0.75R$ for rigid and elastic blade. Pre-bent and pre-coned configuration of the blade.	202
10.15	Grid employed for the dynamic aero-elastic case of DTU 10MW RWT rotor without the tower - (a) slice through the volume, (b) surface mesh, and (c) computational domain.	203
10.16	Time histories of loads and the tip displacements for unsteady aero-elastic case of DTU 10MW RWT rotor without tower.	204
10.17	Deformation of the DTU 10MW RWT blades after 2 revolutions.	204
10.18	Distributions of the loads for the aero-elastic computations for the DTU 10MW RWT blade with pre-bend and pre-cone.	205
10.19	Comparison of the blade shapes from static and dynamic aero-elastic computations.	206

10.20	Grid employed for the DTU 10MW RWT - (a) slice through the rotor grid, (b) blade surface mesh, (c) slice through the tower grid, and (d) computational domain.	207
10.21	Thrust force and mechanical power as functions of revolution for the DTU 10MW RWT. Comparison between the rigid and elastic blades.	209
10.22	Thrust force and mechanical power as functions of azimuth angle for the first 120° of the 4th revolution. Comparison between the rigid and elastic blades.	209
10.23	Displacement of the tip as function of revolution (a), comparison between the shapes of rigid and elastic blades (b), and shape of the blade for different azimuth angles Ψ (c).	210
10.24	The wake of the DTU 10MW RWT visualised with the iso-surface of $Q = 0.007$ criterion: (a) rigid and (b) elastic blades.	212
10.25	Contours of velocity component W in meters per second: (a) rigid and (b) elastic blades. . .	212
11.1	Schematic of the trailing edge flap, showing mean and maximum negative deflections, and real and interpolated length of the flap during motion.	214
11.2	Cell volume ratio (a), and skewness ratio (b) between deformed and undeformed grids for the leading edge flap deflected 10° towards the pressure side.	214
11.3	The location and dimensions of the trailing and leading edge flaps.	215
11.4	Definition conditions for the LE (a) and TE (b) flap deformation.	216
11.5	Definition of the positive and negative deflection for the LE (a) and TE (b) flap.	217
11.6	Pressure coefficient distribution around the aerofoil section in the middle of the TE flap for different angles of deflection β	219
11.7	Pressure coefficient distribution around the blade with the TE flap for different angles of deflection β - pressure side (a), and suction side (b).	220
11.8	Instantaneous vortices visualised with the iso-surfaces of $Q = 0.02$ criterion. The TE flap case with $\beta = 10^\circ$	221
11.9	Span-wise distribution of thrust force (a), driving force (b) and pitching moment (c) for DTU 10-MW blade equipped with TE flap. Flap motion frequency $f = 0.96Hz$ (6 times per revolution).	222
11.10	Pressure coefficient distribution around the aerofoil section in the middle of the LE flap for different angles of deflection β	224
11.11	Pressure coefficient distribution around the blade with the LE flap for different angles of deflection β - pressure side (a), and suction side (b).	225
11.12	Instantaneous vortices visualised with the iso-surfaces of $Q = 0.02$ criterion. The LE flap case with $\beta = 10^\circ$	226
11.13	Span-wise distribution of thrust force (a), driving force (b) and pitching moment (c) for DTU 10-MW blade equipped with LE flap. Flap motion frequency $f = 0.96Hz$ (6 times per revolution).	227
11.14	Definition of the normal force, tangential force and pitching moment. Quantities shown in the directions defined as positive.	228
11.15	Comparison of the performance of TE and LE flaps based on the non-dimensional coefficients as function of flap deflection angle β	229
12.1	Hypothetical flow states of FOWT during pitching motion. From left to right: windmill state, turbulent wake state, vortex ring state and propeller state. Adapted from ^[196]	230
12.2	Grid employed for the NREL Phase VI rotor without the tower - (a) slice through the volume and (b) surface mesh, and (c) computational domain.	233
12.3	Grid employed for the DTU 10MW RWT rotor without the tower - (a) slice through the volume, (b) surface mesh, (c) computational domain.	234

12.4	Regions of instrumentation and tower influence on measured pressure. Definitions of positive yaw and azimuth angles are also included. Figures adapted from [70].	236
12.5	Comparison between experimental data and C_p values at various span-wise station for aligned case.	236
12.6	Comparison between experimental data and C_p values at various span-wise station for 10° yaw misalignment.	237
12.7	Comparison between experimental data and C_p values at various span-wise station for 30° yaw misalignment.	237
12.8	Fixed yaw test cases: employed notation for yaw angles (a), and thrust and power as function of the rotor revolution (b).	238
12.9	Power as function of time (a) and yawing amplitude (b).	239
12.10	Instantaneous vortices visualised with the iso-surfaces of $Q = 0.05$ criterion coloured by the pressure coefficient C_p . Yawing amplitude 3° , and yawing period $8.8s$	239
12.11	Yaw angle and yaw angular velocity as function of time.	240
12.12	Thrust and power as function of time (a) and pitching amplitude (b).	241
12.13	Instantaneous vortices visualised with the iso-surfaces of $Q = 0.05$ criterion coloured by the pressure coefficient C_p . Pitching period $8.8s$, pitching amplitude 3° (a-d), and 5° (e-h).	242
12.14	Sinusoidal pitch test cases. Definition of the employed notation for pitch angles (a), and (b) the pitch angle and pitch angular velocity as function of time for pitching amplitude 3°	243
12.15	Estimated ratio of induced velocity as function of inflow velocity ratio (a), and ratio of inflow velocity as function of time (b) for pitching wind turbines with pitching amplitude of 3° and 5°	243
13.1	The parallel conventional staggered method employed in present work.	245
13.2	Schematic of the employed model of FOWT (a), and dimensions of the semi-submersible support and tower (b). FOWT model consists of three mooring lines and two rigid bodies: the rotor (blue) and combined body representing nacelle, tower and support (red).	246
13.3	The FOWT model placed in a shallow tank. Mooring lines are shown with dashed lines.	248
13.4	$8M$ mesh used to solve for aerodynamic loads. Surface mesh (a), and slice through the volume close to the blade surface (b).	249
13.5	Thrust as function of azimuth angle of the rotor. Two test cases are shown: with constant thrust and estimated time varying thrust.	251
13.6	Comparison of lateral and rotational dynamics of the support for two test cases: constant thrust (Case 1) and time varying thrust (Case 2).	252
13.7	Comparison of last 20 seconds of lateral and rotational accelerations of the support for two test cases: constant thrust (solid line) and time varying thrust (dashed line). Solid line represents time varying thrust, as applied in the second test case.	253
13.8	Forces and moments acting at CoG of the support for constant thrust case.	255
13.9	Forces and moments acting at CoG of the support for time varying thrust case.	257
13.10	Lateral and rotational dynamics of the support platform for coupled test case.	258
13.11	Forces acting on the rotor and velocity of centre of gravity of the rotor as function of time for coupled computation.	259
13.12	Forces and moments acting at CoG of the support for the coupled test case.	260
13.13	Estimated ratio of induced velocity as function of inflow velocity ratio (a), and ratio of inflow velocity as function of time (b) for coupled computation.	261
13.14	Position and orientation of the FOWT at times $t = 0s$ and $t = 12s$ during coupled computation. Contours on the rotor correspond to pressure coefficient C_p , contours on the water surface correspond to surface elevation z in meters.	262

B.1	Configuration of the cylinder in calm water with arbitrary rotation and position.	303
B.2	Schematics of the floating platform. Not in scale. Only one mooring line is presented for simplicity.	305
B.3	Lateral dynamics of a cylinder in calm water. Cylinder placed in equilibrium position and cylinder with offset from equilibrium by 15° about y axis. Results with and without mooring lines.	306
B.4	Rotational dynamics of a cylinder in calm water. Cylinder placed in equilibrium position and cylinder with offset from equilibrium by 15° about y axis. Results with and without mooring lines.	307
B.5	Schematics of the floating platform rotated by 15°	308
C.1	Comparison of the computational grids employed in this chapter.	310
C.2	Comparison of the solutions obtained with different methods for the Grid M1. Contours of the non-dimensional velocity component W in the middle of the domain.	311
C.3	Comparison of the solutions obtained with different methods for the Grid M1. Iso-surface of non-dimensional $Q = 0.0001$ criterion.	311
C.4	Comparison of the solutions obtained with different methods for Grids M2 and M3. Contours of the non-dimensional velocity component W in the middle of the domain.	312
C.5	Comparison of the solutions obtained with different methods for Grid M2 and M3. Iso-surface of non-dimensional $Q = 0.0001$ criterion.	312
C.6	Comparison of the solutions obtained with the 2nd order MUSCL scheme using fine Grid M2, and with the 4th order MUSCL scheme using coarse Grid M1.	313

List of Tables

1.1	List of floating off-shore wind turbine prototypes built to date.	2
1.2	Keywords entered into databases, including the number of relevant papers found.	4
1.3	Support platform design parameters and tradeoffs ^[26] . Key: + – relative advantage; - – relative disadvantage.	15
1.4	Characteristics of different models for mooring lines.	18
1.5	Works relevant for the complete FOWT models.	20
1.6	Advantages and disadvantages of different coupling strategies.	21
3.1	Different types of two-equation turbulence models and the corresponding second variable used	59
3.2	Different types of linear $k - \omega$ turbulence models	61
3.3	Values of constants used in linear $k - \omega$ models (continued)	62
3.4	Values of constants used in linear $k - \omega$ models (concluded)	62
4.1	Partial derivatives of constraint functions	87
5.1	Coupling test case conditions for 2D simulations of TL190-82 aerofoil.	107
5.2	Computational parameters of SPH communication test cases.	107
5.3	Test cases to validate communication protocol between SPH and master.	110
5.4	Annual sea occurrences in the North Atlantic ^[51]	115
5.5	Computational parameters of SPH for wave generation test cases.	116
5.6	Amplitude and period of paddle motion to generate regular waves corresponding to characteristic waves in sea states from 3 to 6.	118
6.1	Computational parameters of SPH for validation test cases.	120
6.2	Validation test cases for the SPH method.	121
7.1	Conditions and numerical parameters employed for the validation case against NREL Annex XX experiment.	128
7.2	Conditions and numerical parameters employed for the validation case against MEXICO project experiment.	133
8.1	Summary of the joints employed to represent the 2D slider-crank mechanism.	137
8.2	Properties of the bodies employed to represent the 2D slider-crank mechanism for kinematic analysis.	138
8.3	Summary of the joints employed to represent the 3D slider-crank mechanism.	141
8.4	Properties of the bodies employed to represent the 3D slider-crank mechanism for kinematic analysis.	142
8.5	Properties of the bodies employed to model the gyroscopic effect.	145
9.1	Conditions for the grid convergence study.	151

9.2	Comparison between thrust and power coefficients and corresponding thrust and power obtained by present CFD computations and by Bak ^[11]	154
9.3	Operational parameters for the DTU 10-MW RWT rotor ^[11] . The pitch is defined positive nose down.	157
9.4	Results for straight and rigid blade for two grids in terms of thrust and power.	159
9.5	Comparison between thrust and power for straight and pre-coned blades.	170
9.6	Parameters used in the Mann box generator.	175
9.7	Details of computational grids employed in this section.	178
10.1	Comparison between natural frequencies for the isolated blade obtained with NASTRAN and results of Bak ^[11] and Horcas ^[77]	190
10.2	Computational grids employed for static aero-elastic analysis.	196
10.3	Comparison between thrust and power for undeformed and deformed blades. Straight blade case.	199
10.4	Comparison between thrust and power for undeformed and deformed blade. Pre-bent and pre-coned configuration of the blade.	202
10.5	Structural damping coefficients used in the aero-elastic computation for the complete DTU 10MW RWT.	208
12.1	Description of presented test cases.	232
13.1	Mechanical properties of the employed bodies and mooring lines.	247
13.2	Test cases investigating the influence of the domain width and particle spacing on the forces acting on the support structure.	250
13.3	Computational performance of the coupling algorithm for various coupling time steps.	264
B.1	Properties of the cylinder and mooring cables representing moored floating platform.	304
C.1	Computational grids employed in this chapter.	309

Nomenclature

Latin symbols

A	Area, Amplitude
\mathbf{A}	Rotational matrix
A_{ij}	Added-mass matrix
b	Spring damping coefficient
B	Damping matrix
B_{ij}	Hydrodynamic damping matrix
c	Chord, speed of sound
C	Restoring matrix
C_a	Added mass coefficient
C_d	Drag coefficient
C_l	Lift coefficient
C_m	Inertia coefficient
C_p	Pressure coefficient
C_P	Power coefficient
C_T	Thrust coefficient
C_f	Skin friction coefficient
CM	Pitching moment coefficient
CN	Normal force coefficient
CT	Tangential force coefficient
d	Initial particle spacing
\mathbf{d}_{ij}	Distance vector
D_i	Time derivative of density for particle i
e	Specific internal energy
E	Energy
f	Frequency
F	Force
F_C	Gas force in compressor
g	Gravitational acceleration
h	Smoothing length, thickness distribution
\mathbf{I}	Identity matrix
J	Torsional stiffness
\mathbf{J}	Moment of inertia matrix
k	Heat transfer coefficient, specific kinetic energy of fluctuations, spring stiffness
K_{ij}	Wave-radiation-retardation kernel
l	Turbulence length scale
L	Length, angular momentum of the wheel
m	Mass
M	Mach number
M_{ij}	Mass matrix

n	Moment due to external forces, vector normal to a surface
<i>p</i>	Pressure
p	Euler parameters (quaternion)
<i>P</i>	Power
P	Momentum flux
q	State vector, displacement vector, heat flux vector
<i>Q</i>	Cell centre values of conservative variables
<i>r</i>	distance, radial position along the blade
r	Position vector
<i>R</i>	Radius, non-dimensional distance between particles
R	Residual vector
<i>R_g</i>	Radius of gyration
<i>Re</i>	Reynolds number
<i>s'</i>	Vector in the local coordinate system
<i>S</i>	Area, wave spectrum function, cell skewness
<i>t</i>	Time
<i>T</i>	Temperature, period, thrust force
<i>Ti</i>	Turbulence intensity
u	Vector of dependent coordinates
<i>U</i>	Velocity
v	Vector of independent coordinates
<i>V</i>	Volume
<i>V_c</i>	Inflow velocity normal to the rotor plane
<i>v_h</i>	Induced velocity in hover
<i>v_i</i>	Induced velocity
<i>W</i>	Smoothing function
W	Vector of conserved variables
x	Displacement vector, solution vector, position vector
<i>X</i>	Wave excitation function
<i>y⁺</i>	Non-dimensional wall distance
<i>z</i>	Elevation above the ground

Greek symbols

α	Artificial viscosity parameter, weighting parameter, angle, Kolmogorov constant
β	Angle, wind profile power coefficient
γ	Adiabatic index
Γ	Domain boundary, stretching parameter
δ_{ij}	Kronecker delta function
$\delta(x - x_i)$	Dirac delta function
δ	Node displacement vector
ε	Rate of viscous dissipation
λ	Tip speed ratio
λ	Lagrange multiplier vector
μ	Molecular viscosity
μ_t	Dynamic eddy-viscosity
ν	Kinematic viscosity
π_{ij}	Artificial viscosity term in SPH method
ρ	Density
τ	Time, viscous stress tensor, dissipation rate, torque
ϕ	Eigenvector

Φ	Constrain function
χ	Angular displacement
ω	Frequency, relaxation factor
$\boldsymbol{\omega}$	Rotational velocity
ω_p	Precession rate
Ω	Volume

Subscripts, superscripts and brackets

\bar{C}	Average value of C
f_i	Value of f for body i , value of f in direction i
f^i	Value of f at time level i
f_∞	Free stream value of f
$\langle f \rangle$	Particle approximation of f
$\hat{\mathbf{R}}$	Approximation of \mathbf{R}
$\tilde{\mathbf{s}}$	Skew-symmetric matrix of vector \mathbf{s} , intermediate value of \mathbf{s}
\mathbf{s}'	Vector \mathbf{s} in a local coordinate system
\dot{x}	First derivative of x with respect to time
\ddot{x}	Second derivative of x with respect to time

Acronyms

ALE	Arbitrary Lagrangian-Eulerian
BEM	Blade Element Momentum method
BILU	Block Incomplete Lower-Upper factorisation method
CFD	Computational Fluid Dynamics
CFL	Courant-Friedrichs-Lewy number
CoG	Centre of Gravity
CSD	Computational Structural Dynamics
CVT	Constant volume tetrahedron method
DOF	Degree of freedom
FFT	Fast Fourier Transform
FOWT	Floating Off-shore Wind Turbine
FVM	Free Vortex method
GCG	Generalised Conjugate Gradient method
GCS	Global coordinate system
GDW	Generalised Dynamic Wake model
HMB3	Helicopter Multi-Block solver version 3
HPC	High Performance Computer
IDW	Inverse Distance Weighting method
ISA	International Standard Atmosphere
ISPH	Incompressible SPH method
LE	Leading edge
MGIV	Modified Givens Method
MPI	Message Passing Interface
MPMD	Multiple Program, Multiple Data (MPI paradigm)
NREL	National Renewable Energy Laboratory
OC3	Offshore Code Comparison Collaboration
PIV	Particle Image Velocimetry
PSD	Power Spectral Density
RAM	Random Access Memory
RANS	Reynolds-Averaged Navier-Stokes method

RAO	Response Amplitude Operator
RDT	Rapid Distortion Theory
RHS	Right-hand side
RMS	Root Mean Square
ROM	Reduced Order Model
rpm	Revolutions per minute
RSM	Reynolds Stress Model
RWT	Reference Wind Turbine
SAM	Spring analogy method
SAS	Scale Adaptive Simulation model
SPH	Smoothed Particle Hydrodynamics method
SPMD	Single Program, Multiple Data (MPI paradigm)
SST	Shear Stress Transport turbulence model
SWL	Still Water Level
TE	Trailing edge
TFI	Trans-finite interpolation method
URANS	Unsteady Reynolds-Averaged Navier-Stokes method
WCSPH	Weakly compressible SPH method
WT	Wind Turbine

Chapter 1

Introduction

1.1 Motivation

Wind is a substantial renewable energy source that is free, environmentally friendly, and cost effective. Historical trends presented in Figure 1.1 show the large development of the on-shore wind turbine (WT)

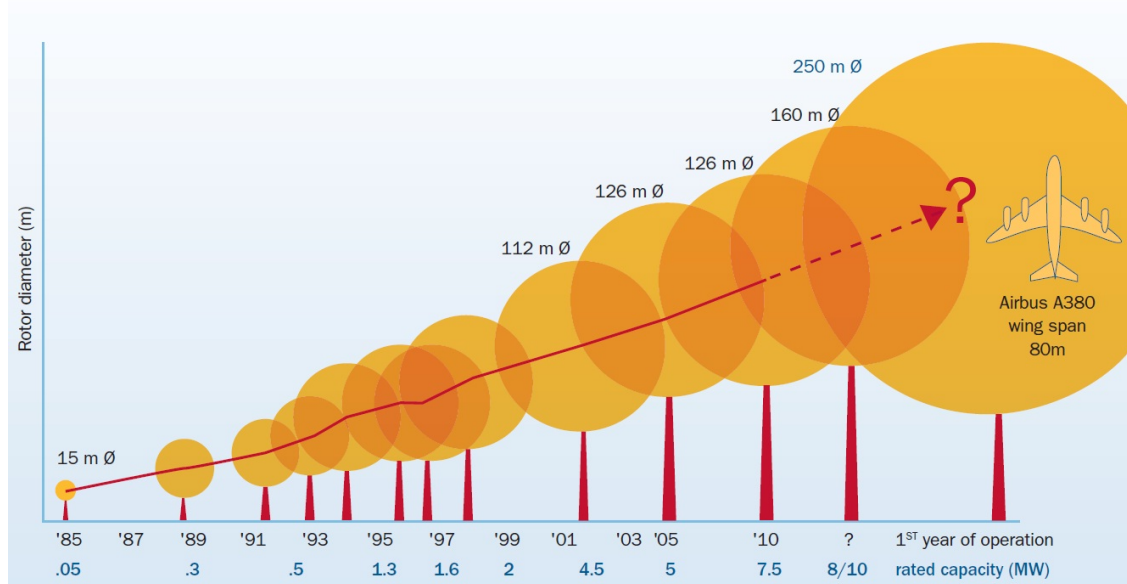


Figure 1.1: Size evolution of wind turbines over time with corresponding rated capacity^[55].

size and power capacity over the last three decades. However, many high potential sites on land are already occupied, and others are hard to utilise due to e.g. difficult access, high altitude, costly transportation and

on-site assembly. Also, majority of worldwide power demand comes from the coastal areas. Therefore, a growing trend is to exploit the off-shore wind potential and take advantage of the available space and steady winds. According to the European Wind Energy Association (EWEA), new off-shore seabed-fixed wind turbines have been installed in Europe, continuously since 2000. At the end of 2012 there were 1,662 turbines giving 5GW of installed, off-shore, wind capacity^[35, 75]. However, in 2015 alone, Europe fully connected to its grid 3GW of off-shore wind capacity. Further, the annual on-shore market decreased in Europe in 2015 by 7.8%, and off-shore installations more than doubled as compared to 2014^[33]. This illustrates the growing trend in off-shore wind energy. As of today, off-shore wind represents 23.7% of the annual wind energy installations across Europe^[33]. Estimates for the year 2030 predict up to 11.3% coverage of total European electricity demand by off-shore wind^[34]. Similar trends are seen in the US, where on-shore and off-shore wind energy is projected to provide up to 20% of the US electricity by 2030^[58].

Over the years, off-shore wind farms moved further from the shore and into deeper waters. At the end of 2014, the average water depth of grid connected wind farms was 22.4m and the average distance to shore 32.9km. Projects under construction, consented and planned, confirm that average water depths and distances to shore are likely to increase^[9]. Shallow water regions suitable for constructing seabed-fixed, off-shore wind turbines are limited, and for sea depths exceeding 30 – 60m, floating structures become more economic. Hence, emphasis is placed on the development of floating off-shore wind turbines (FOWTs) with several prototypes already operational across the world^[9]. Table 1.1 presents the list of existing prototypes, while Figure 1.2 shows their designs with clear differences in size and the support structure. The first commercial floating wind farm of 5 machines with total capacity of 30MW is planned to be constructed 25km off-shore Scotland, UK. The design is based on the Hywind prototype, and the production is expected to start in late 2017.

Table 1.1: List of floating off-shore wind turbine prototypes built to date.

Prototype name	Year	Location	Rated power	Support platform
Blue H	2007	Italy	80kW	Tension leg
Hywind	2009	Norway	2.3MW	Spar buoy
WindFloat	2011	Portugal	2MW	Semi-submersible
VolturnUS 1:8	2013	USA	20kW	Semi-submersible
Fukushima Mirai	2013	Japan	2MW	Semi-submersible
Fukushima Shimpuu	2015	Japan	7MW	Semi-submersible

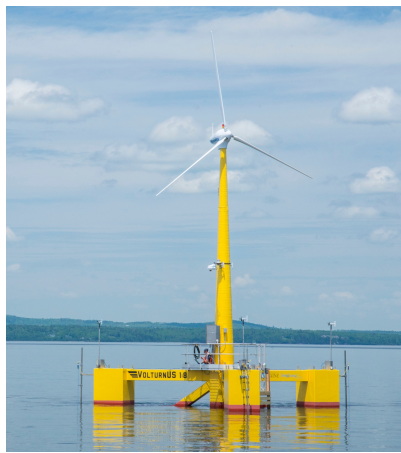
(a) Blue H¹.(b) Hywind².(c) WindFloat³.(d) VolturnUS 1:8⁴.(e) Fukushima Mirai⁵.(f) Fukushima Shimpuu⁵.

Figure 1.2: Prototypes of the floating off-shore wind turbines: decommissioned (a), operating (b-f).

Unlike on-shore machines, the FOWT is a highly dynamic system since it is simultaneously subjected to the wind and wave loads, and only constrained by a mooring system. Further, the rotor frequency is low due to the large size of the blades, and wave frequencies may come close or coincide with the rotational frequency of the rotor. Also, the FOWT may be subjected to large amplitude pitching motions, and therefore, operate in various aerodynamic flow states, including windmill, propeller and transient states too. Finally, aero-elasticity becomes more important due to the large size of the off-shore WT blades, and tall towers. Taking above into account, it is important to develop a method for the analysis of this air-structure-water system, that can simultaneously model the effects of waves, aerodynamic forces, and platform and mooring

¹ Photo: Blue H Engineering (www.bluehengineering.com)

² Photo: Statoil (www.statoil.com)

³ Photo: Principle Power (www.principlepowerinc.com)

⁴ Photo: University of Maine (www.umaine.edu)

⁵ Photo: Fukushima Forward (www.fukushima-forward.jp)

response.

The motivation behind the present PhD thesis is to develop such a model for floating off-shore wind turbines by employing high-fidelity CFD methods for air and water, and representing the wind turbine with a multi-body dynamic model. This coupled model should accurately incorporate important physical phenomena, and should be capable of analysing the complexity of proposed FOWT systems and the variety of their configurations. Ultimately, this type of model should provide a better understanding of the FOWTs performance.

1.2 Literature Survey

The literature survey was conducted using the databases available at the University of Glasgow, namely Science Direct, Aerospace Research Central, Scopus and Web of Knowledge. Lists of the explored keywords with corresponding number of relevant papers found from each database are presented in Table 1.2. Science Direct was the first database to search as it was found to contain the larger amount of relevant papers. Then all other databases were searched according to Table 1.2.

Table 1.2: Keywords entered into databases, including the number of relevant papers found.

Keywords	Science Di- rect	Aerospace Research Central	Scopus	Web of Knowledge
Active blades offshore wind turbine	1,072	170	45	15
Atmospheric turbulence	26,713	11,689	17,629	10,468
CFD solver wind turbine	838	1,684	189	92
Coupling schemes	382,554	27,621	21,175	36,540
Cylinder impact Greenhow	38	2	-	-

Continued on next page

Table 1.2 – continued from previous page

Keywords	Science Di- rect	Aerospace Research Central	Scopus	Web of Knowledge
Floating body SPH	343	20	31	26
Mann turbulence wind turbine	108	135	16	13
Mooring line forces	8,224	185	568	394
Morison equation	1,313	72	560	346
Off-shore floating structures	9,686	76	153	13
Off-shore support structures	55,787	403	184	34
Off-shore wind turbine	7,338	158	677	145
Partially submerged bodies	9,566	663	82	62
Wind turbine	31,227	5,811	39,451	21,752
Wind turbine flaps	1,000	1,614	432	245

Firstly, the aerodynamic and hydrodynamic modelling approaches are presented in Sections 1.2.1 and 1.2.2, respectively. This is followed by the description of different designs for the support structure, and mooring cable models in Section 1.2.3. Then, the structural modelling of the wind turbine components and overall system is introduced in Section 1.2.4. The approaches to model FOWT dynamics as a combination of those methods are discussed in Section 1.2.5. More general overview of the coupling schemes is presented in Section 1.2.6. This is followed by the description of experimental campaigns for FOWTs in Section 1.2.7. Active rotor blades and atmospheric turbulence modelling are addressed in Sections 1.2.8 and 1.2.9, respectively. Finally, conclusions are drawn in Section 1.3 and the outline of the thesis is provided in Section 1.4.

1.2.1 Aerodynamic modelling

This section covers the aerodynamic modelling of off-shore wind turbines. An overview of general wind turbine aerodynamics and its modelling is given by Vermeer *et al.* [204] and Sanderse *et al.* [171]. The common approach for modelling FOWTs is to combine simplified tools into a hybrid model to predict wind turbine responses under wind and wave loads. The reduced order methods known as *Engineering Models* are traditionally employed in the wind energy industry, due to the small computational cost and time they require. Among others, these include the Blade Element Momentum (BEM), lifting-line, and vortex-wake models. In the following, descriptions of these methods are provided.

Algebraic models

The first FOWT models employed simplified methods for aerodynamic modelling. The thrust force F_t on the turbine in these methods is computed from:

$$F_t = \frac{1}{2} \rho A U_{rel}^2 C_T(U_{rel}), \quad (1.1)$$

where ρ is the density of air, A is the area of the rotor plane, U_{rel} is the relative velocity between the incoming wind and the wind turbine hub. The thrust force coefficient C_T is a function of relative velocity. It depends on the control strategy for the wind turbine (pitch/stall controlled), and should be provided as an input to the model. The algebraic aerodynamic model was employed in works of Nielsen *et al.* [152], Roddier *et al.* [168], and Karimirad and Moan [97].

Blade Element Momentum method

The Blade Element Momentum (BEM) method is the most popular model for aerodynamics of floating wind turbines. It is assumed in this method that the forces on a blade element can be calculated by means of two-dimensional aerofoil characteristics using an angle of attack determined from the incident resultant velocity in the cross-sectional plane of the element. The velocity component in the span-wise direction is ignored, as well as three-dimensional effects.

The velocity components at a radial position on the blade expressed in terms of the wind speed, the inflow velocity and the rotational speed of the rotor will determine the angle of attack. Having information

about the aerofoil characteristic coefficients C_l and C_d and their variation with the angle of attack, the forces on the blade element for given values of induced velocity can be determined. Hence, the method consists of dividing the blade into small elements along its radius. For each element lift and drag can be obtained using two-dimensional tabulated aerofoil data. The forces are then integrated along the entire blade and over one rotor revolution in order to obtain the total thrust and power. One of the key difficulties lies in modelling the induced velocity on the rotor disk. For this reason the blade element theory is combined with the momentum theory to provide additional relationships necessary to describe the induced velocity on the rotor disk.

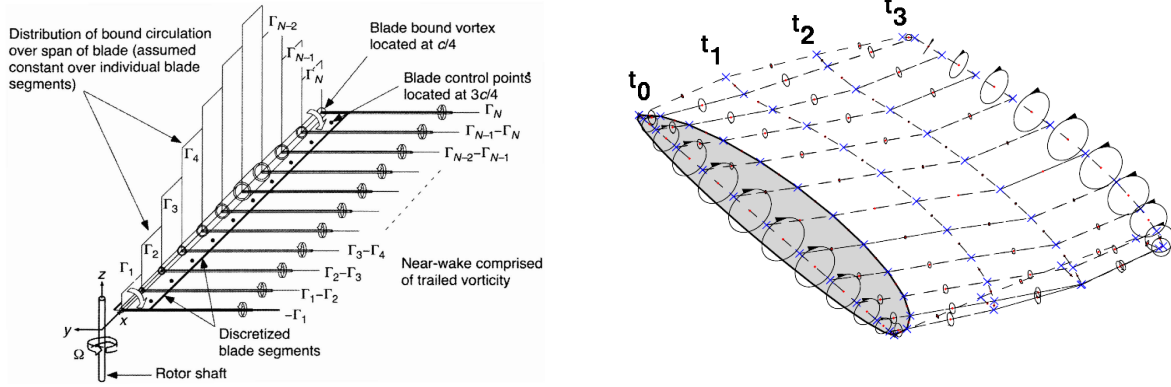
There are a number of corrections commonly applied in conjunction with the BEM model to account for the detailed aerodynamics experienced by a wind turbine rotor. This includes the tip loss correction (Prandtl's tip loss factor), dynamic stall, yaw misalignment, turbulent wake, unsteadiness of the inflow and rotational effects^[171]. However, the BEM method has still several limitations like momentum balance assumption. Hence, it is hard to model atmospheric turbulence, wind shear due to ground effect, deep stall, and the effect of neighbouring turbines. In addition to this, the theory is still not validated for rotors operating in large yaw angles or experiencing large pitching motion. The extensions listed above can be applied to improve the accuracy of prediction in turbulent flow, but these corrections do not fully capture all the unsteady flow effects.

The BEM method for FOWTs application was adopted by many authors including Larsen *et al.* ^[109], Skaare *et al.* ^[184], Jonkman *et al.* ^[90, 92], Bae *et al.* ^[10], Lackner *et al.* ^[106], Karimirad *et al.* ^[96], and Philippe *et al.* ^[159].

Lifting-line and Vortex-wake methods

Both Lifting-line and Vortex-wake methods assume that the flow is potential i.e. inviscid, incompressible and irrotational; and are used to obtain the velocity induced by vortex lines (filaments). The Lifting-line model represents the wind turbine blades by bound vortex lines, as shown in Figure 1.3(a). The strength or circulation (Γ) of the vortex filament depends on the lift coefficient, which is extracted from a tabulated data. Assuming the vorticity is concentrated onto a curve, as is the case for a vortex filament, the Biot-Savart may be used to link induced velocity and strength or circulation. The mathematical approach to calculate the actual lift on a blade element due to the induced velocities is given by the Kutta-Joukowski equation. The

major limitation of the lifting-line model for FOWT application is the assumption of steady state, although extensions to unsteady flow are possible^[178].



(a) Lifting-line diagram for a rotor blade, illustrating trailing vorticity^[118]. (b) Vortex lattice wake structure, illustrating wake evolution between time steps^[180].

Figure 1.3: Vortex filament methods: Lifting-line model (a) and Free-Vortex Method (b).

The vortex-wake methods assumes variation of the circulation with space and time, allowing for unsteady wake development. Multiple filaments may be combined to form a closed vortex lattice that grows with each time step, thereby modelling the complex and unsteady flow field associated with a wake, see Figure 1.3(b). In the Free-Vortex Method (FVM), the vortex filaments are advected with the velocity \mathbf{U} , given by Sebastian and Lackner^[180] as

$$\mathbf{U} = \mathbf{U}_{wind} + \mathbf{U}_{induced} + \mathbf{U}_{platform}, \quad (1.2)$$

where \mathbf{U}_{wind} is the wind speed, $\mathbf{U}_{induced}$ is the induced velocity due to the influence of vortex filaments, and $\mathbf{U}_{platform}$ is the velocity due to FOWT platform motion. The Biot-Savart law is used to compute the induced velocity at a point in space from the strength or circulation. When approaching the vortex line itself for an evaluation point, the Bio-Savart law behaves singularly. This is circumvented with the introduction of a vortex core model^[180, 74]. After advecting the vortex filaments, the distribution of the lift coefficient can be obtained from tabulated data and induced velocity. Then, the new strength or circulation is computed from the Kutta-Joukowski equation.

Unlike BEM methods, vortex-wake models do not rely on global momentum balance, hence, can be used in unsteady conditions and with yaw misalignment. Also, a non-uniform axial induction over the

azimuth angle within the rotor plane is considered more accurate with the lifting-line free vortex wake approach as compared to BEM^[74]. The FVM model was employed by Sebastian and Lackner^[179] to model FOWT aerodynamics.

1.2.2 Hydrodynamic modelling

Similarly to the aerodynamic modelling, the reduced order methods for hydrodynamics are often employed for the FOWT dynamic analysis. This includes Morison's equation^[144] and potential theory assuming inviscid, incompressible and irrotational flow. Those two models are described in detail below.

Morison's representation

The Morison's equation^[144] is commonly used to simulate hydrodynamic loads on slender cylindrical structures, and is also widely used in the analysis of bottom-fixed offshore wind turbines^[157]. Similarly to the BEM aerodynamic method, the structure is split into a number of elements or strips, where two-dimensional properties are used to determine the overall three-dimensional loading on the structure. The total hydrodynamic force F is computed by integrating over the length of the structure the loads acting on each strip dF . As was first proposed by Morison^[144], and then extended to include platform motion, the lateral force on each strip can be represented by the following equation

$$dF = \left[C_m \rho S \dot{u}_n - C_a \rho S \ddot{x}_n + \frac{1}{2} \rho L C_d (u_n - \dot{x}_n) |u_n - \dot{x}_n| \right] dz, \quad (1.3)$$

where C_a is the added mass coefficient, C_m is the inertia coefficient, and C_d is the drag coefficient. The quantities \dot{u}_n and u_n are the acceleration and velocity of the fluid normal to the body, and \ddot{x}_n and \dot{x}_n are the acceleration and velocity of the floating body in the normal direction, respectively. The density of the fluid is denoted by ρ , and S and L represent the cross sectional area and cross sectional length, such that displaced volume by the strip is $S \cdot dz$, and projected area is $L \cdot dz$.

The drag C_d and added mass C_a coefficients involved in Morison's equation are often determined based on experiments. Since they depend on many factors, including the Reynolds number, geometry, and the presence of a free surface and a free end of a body, the experimental data is not always directly applicable. The drag coefficient can be obtained from a CFD computation for given support platform and then applied

to Morison's equation improving the results as was shown by Benitz *et al.* [20]. Nevertheless, Morison's equation can not capture time varying loads, which occur due to vortex shedding. Other limitations of this method include the assumption of undisturbed velocity field by the presence of the body, therefore neglecting the diffraction. This makes it applicable only for slender structures, like spar support, see Section 1.2.3 for description of support platforms. Further, this model assumes that viscous drag dominates the damping such that wave-radiation damping can be ignored^[92]. Due to the above, the Morison's representation is rarely used alone. Often, this model is used in conjunction with potential theory, as explained in the following section. However, Morison's representation for FOWT application was adopted by Savenije *et al.* [173] and Huang *et al.* [78].

Potential theory

The hydrodynamic loads on the support structure of FOWTs are often modelled with a linear potential theory, also known as Airy wave theory^[51, 90, 168, 96]. The hydrodynamics problem can be then split into three separate and simpler problems: radiation, diffraction, and hydrostatics. The total hydrodynamic force is obtained by using a linear superposition of the loads due to each of those problems, see Figure 1.4 for illustration.

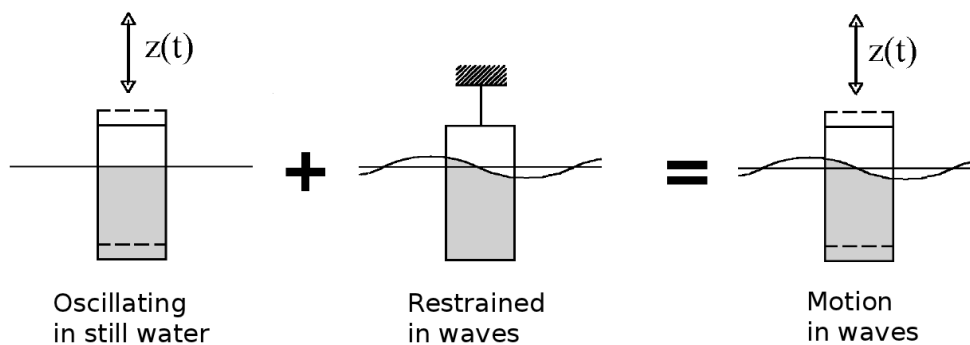


Figure 1.4: Superposition of radiation and diffraction loads^[94].

The radiation problem seeks to find the loads on a floating platform when the body is forced to oscillate with the wave excitation frequency in any rigid-body motion mode. There are no incident waves in this case, and the resulting radiation loads are the effect of the generated outgoing waves. This includes contributions from added mass, and from wave-radiation damping. The diffraction problem seeks to find

the loads on a support platform when the structure is restrained from oscillating (fixed) and incident surface waves are present and scattered by the body. Those hydrodynamic loads are called wave excitation loads and compose the so-called Froude-Kriloff (due to undisturbed pressure field) and diffraction forces and moments due to wave scattering. The hydrostatics problem is based on the Archimedes' principle, and sometimes included in the radiation problem as restoring forces^[51]. The derivation of a simple hydrostatic model can be found in Appendix B.

Given the above description, the hydrodynamic loads are computed by the following expression^[40] for each degree of freedom $i = 1, \dots, 6$ corresponding to surge, sway, heave, roll, pitch, and yaw

$$F_i^{hydrodynamic} = F_i^{waves} + \rho g V_0 \delta_{i3} - C_{ij}^{hydrostatic} q_j - \int_0^t K_{ij}(t - \tau) \dot{q}(\tau) d\tau, \quad (1.4)$$

where F_i^{waves} represents the total excitation load on the support platform from incident waves, ρ is the density of water, g is the gravitational acceleration, V_0 is the submerged volume at equilibrium, q_i is the displacement from equilibrium in i -th degree of freedom, matrix $C_{ij}^{hydrostatic}$ relates the hydrostatic force to the displacement vector, and K_{ij} is the wave-radiation-retardation kernel. The last term is the convolution integral in the radiation problem, where integration is over a dummy variable τ indicating past times. This way the memory effects are taken into account, since the wave-radiation loads depend on the history of motion for the support platform. In other words, if the support platform experiences a succession of impulses, the response at any time is assumed to be the sum of the responses to the individual impulses, each response being calculated with an appropriate time lag from the instant of the corresponding impulse^[40, 154].

The added-mass matrix A_{ij} resulting from radiation problem should be added to the mass matrix M_{ij} of the platform in the dynamic equation of motion. Writing this explicitly, the following ordinary differential equation (ODE) is solved at each time step

$$M_{ij} \ddot{q}_j = -A_{ij} \ddot{q}_j + F_i^{hydrodynamic}(q_j, \dot{q}_j) + F_i^{mooring}(q_j, \dot{q}_j), \quad (1.5)$$

where, $F_i^{hydrodynamic}$ are the hydrodynamic loads given by Equation 1.4, and $F_i^{mooring}$ is the force due to the mooring system that can be obtained by means of various models presented in Section 1.2.3.

The solution approach adopted by many researchers reduces then to finding functions $F_i^{waves}(t)$, $K_{ij}(t)$ and the added-mass matrix A_{ij} . The excitation load from incident waves F_i^{waves} is a function of

the wave spectrum $S(\omega)$, and the incident wave excitation $X_i(\omega)$, where ω is the frequency of the waves. Commonly used wave spectra include the Pierson-Moskowitz^[160], and the Joint North Sea Wave Project (JONSWAP)^[72] spectrum. $X_i(\omega)$ is a complex-valued array that represents the wave excitation force on the support platform normalised per unit wave amplitude, where the imaginary components permit the force to be out of phase with the wave elevation^[90]. The wave-radiation-retardation kernel K_{ij} is a function of the hydrodynamic damping matrix $B_{ij}(\omega)$, and the added-mass matrix A_{ij} is often assumed frequency independent^[92].

These unknown parameters ($X_i(\omega)$, $B_{ij}(\omega)$, and A_{ij}) are usually obtained from the frequency-domain analysis, where a specific solver is employed as a pre-processor. Detailed derivation of the frequency-domain representation of potential hydrodynamics can be found in Faltinsen^[51] and Newman^[149]. Here, only the main ideas and computational procedure are outlined for brevity, and detailed description of the approach can be found in Jonkman^[90, 92].

Since the equations are linear, the non-linear hydrodynamic viscous drag is included from Morison's equation^[144] using strip theory, see previous section for details. Linearisation of the hydrodynamic problem implies that the translational displacements of the support platform are small relative to the size of the body, and that amplitudes of the incident waves are much smaller than their wavelengths *i.e.* steep or breaking waves can not be modelled. The first-order potential theory for FOWT application was employed by Kvittem *et al.* ^[105], Jonkman^[90, 92], Karimirad and Moan^[97], Roddier *et al.* ^[168] Nielsen *et al.* ^[152] (neglecting radiation damping), Lackner and Rotea^[106, 107], Skaare *et al.* ^[184], Zhao *et al.* ^[216], and Philippe *et al.* ^[159].

Some extensions to the second-order potential flow was performed *e.g.* by Newman^[150], Marino *et al.* ^[131] and Roald *et al.* ^[167]. The second order velocity potential (like the first order) is the sum of incoming potential, diffraction potential and radiation potentials associated with the rigid body motions^[150, 151]. To calculate the second-order sum and difference frequency forces a free surface should be modelled, as shown in Figure 1.5. A panel method is then employed to solve the diffraction/radiation problem using the quadratic transfer functions^[96, 10].

The second-order potential theory for FOWT application was employed by Bae *et al.* ^[10], Karimirad^[96], and Roald *et al.* ^[167]. Even with second-order hydrodynamic terms included, however, the potential hydro-

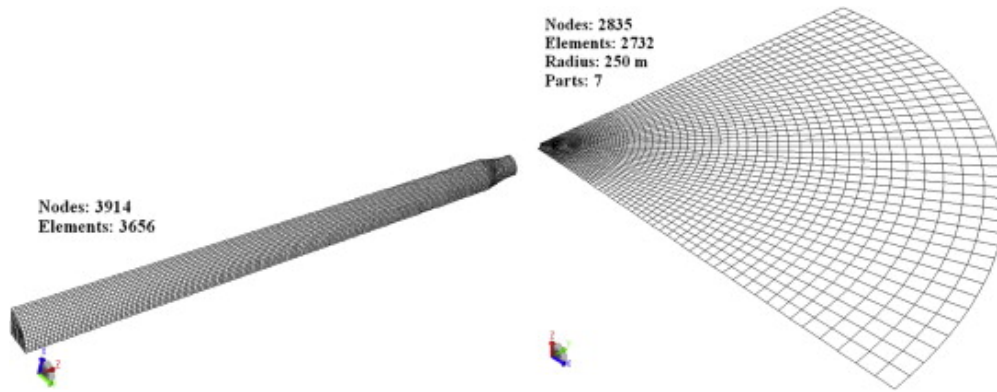


Figure 1.5: Panels employed for quarter of the spar support (left) and quarter of the free surface (right) to account for the second-order wave loads^[96].

dynamic theory might not completely apply to floating wind turbine platforms due to the large displacements encountered^[134].

1.2.3 Support structures and mooring lines

As already mentioned in the motivation section, the support platform configurations vary. Typically, the overall architecture of a floating platform will be determined by a first-order static stability analysis, although there are many other critical factors that will determine the size and features of the final design^[26] e.g. site location and water depth, mooring system, economic feasibility etc. A classification system was developed that divides all platforms into three general categories based on the physical principle that is used to achieve static stability, as shown in Figure 1.6. The first type is the tension leg platform (TLP), used for early prototypes due to experience from the floating oil and gas industry platforms. The stability is provided through the use of mooring tension lines, where the balance between the buoyancy force and mooring lines tension creates a righting moment. This type possess good stability characteristics, and have a small footprint, but high vertical anchors forces require complex and costly anchors with limited anchoring options^[146]. The second type are ballast stabilised platforms, like spar-buoy support structures. In this case the stability is achieved by using ballast weights attached below the centre of buoyancy, which creates a righting moment and high inertial resistance to pitch and roll^[26]. This is, of course, a tradeoff between the stability and the cost of the structure, where long structures are more stable, but also more expensive. Also, the centre of mass for FOWT with this type of support and without the ballast is usually above the

centre of buoyancy. Consequently, significant ballast must be added below the centre of buoyancy, or the buoyancy must be widely distributed to provide stability^[146]. The last type of the support structure employs distributed buoyancy, and relies on a weighted water plane areas to create righting moments. Due to the working principle, this type is classified as the buoyancy stabilised floating platform. The advantage is that it can support heavy wind turbines and is largely independent of the sea depth. However, this comes with the cost of increased wave sensitivity^[26]. Recently, the semi-submersible platforms have become the most popular for off-shore wind turbines, see Table 1.1 and Figure 1.2 . This structure employs a mix of buoyancy and ballast stabilised platforms to achieve stability. Typically, multiple floaters are used (often three) that are interconnected by a frame. Table 1.3 summarises design parameters that would impact the performance and cost of a floating wind turbine system^[26].

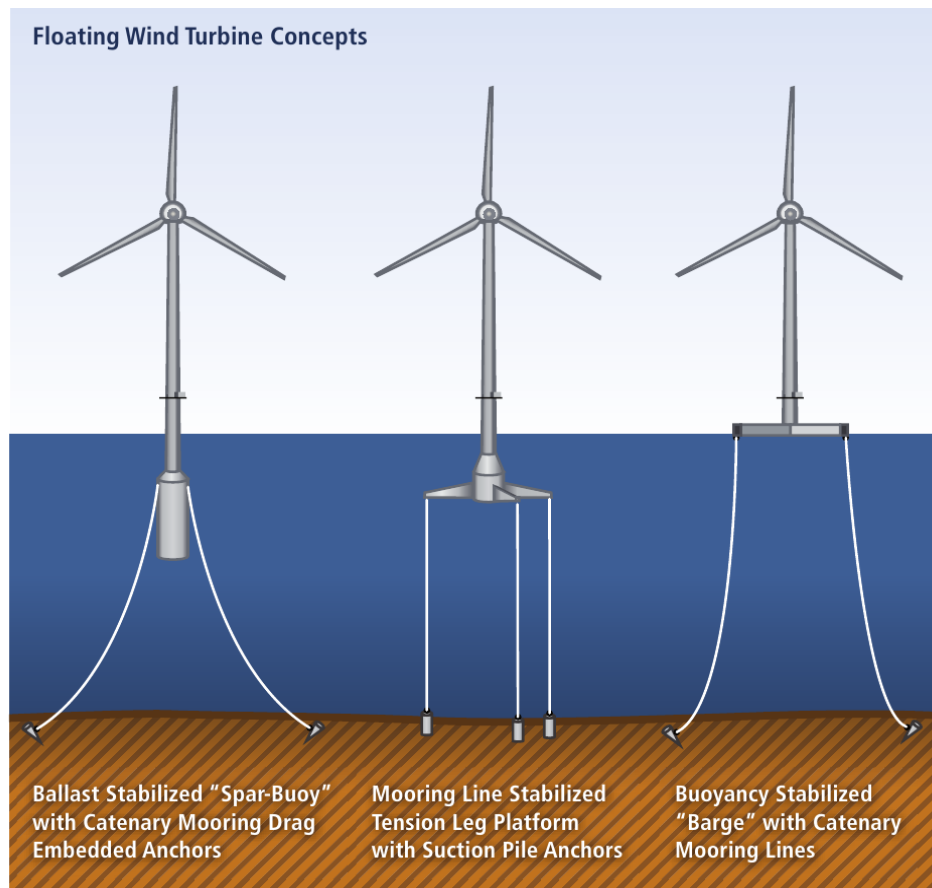


Figure 1.6: Floating platform concepts for off-shore wind turbines^[181].

The ballast-stabilised, buoyancy-stabilised, and semi-submersible platform concepts achieve hydrodynamic stability without relying on the mooring system, which is mainly required for station keeping. The

Table 1.3: Support platform design parameters and tradeoffs^[26]. Key: + – relative advantage; - – relative disadvantage.

Platform Design Parameter	Platform Stability Classification		
	Mooring Line (TLP)	Ballast	Buoyancy
Design Tools and Methods	+	-	-
Floater Cost/Complexity	+	-	-
Mooring Line System Cost/Complexity	+	-	-
Anchors Cost/Complexity	-	+	+
On-site Installation Simplicity	-	+	+
Decommissioning & Maintainability	-	+	+
Corrosion Resistance	+	+	-
Depth Independence	-	-	+
Sensitivity to Bottom Condition	-	+	+
Minimum Footprint	+	-	-
Wave Sensitivity	+	+	-
Turbine Weight	-	-	+

catenary mooring system is the most popular for this application, and the literature review is focused primarily on this type. Other mooring systems are the taut leg, and the tension leg moorings, as shown in Figure 1.7.

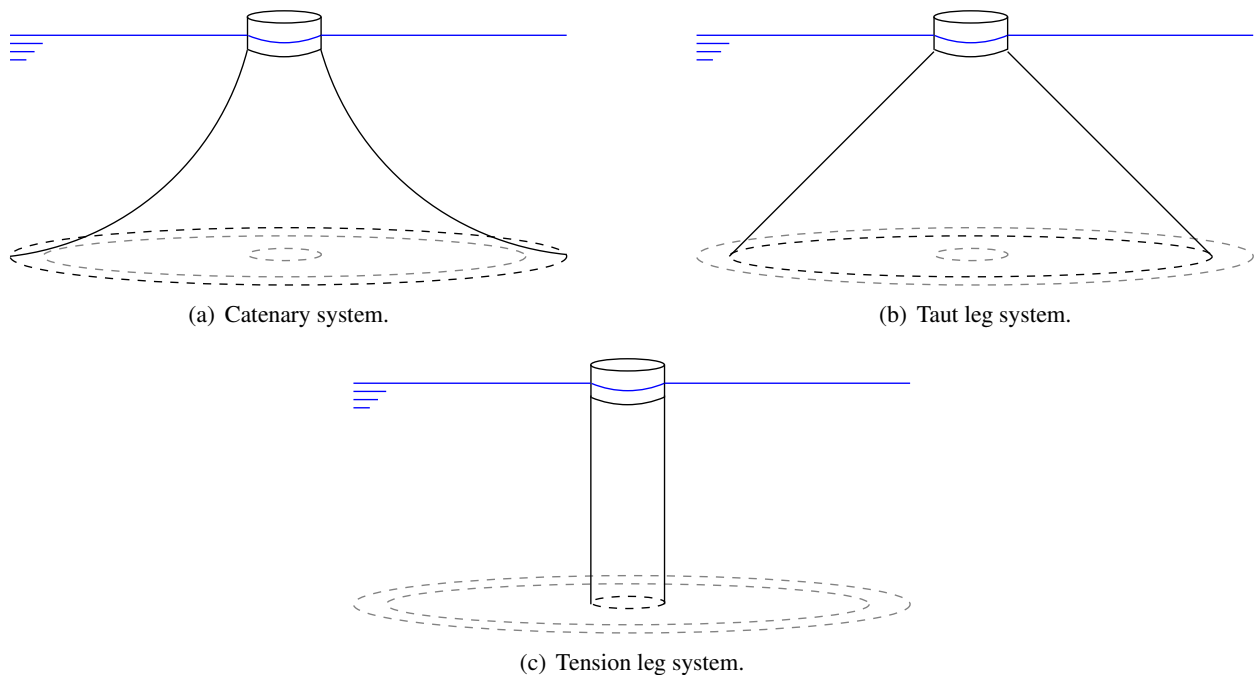


Figure 1.7: Mooring line systems – catenary (a), taut leg (b), and tension leg (c).

A mooring system is made up of a number of cables that are attached to the floating support platform

at fairlead connections, with the opposite ends anchored to the seabed. Cables can be made up of steel rope, steel chain, or synthetic fibers. Due to their different properties it is common to combine different materials to achieve the most suitable system. The mooring tension at the fairlead depends on a number of parameters, including the buoyancy of the support platform, the cable weight in water, the elasticity of the cable or its components, the geometrical layout of the mooring system, and the viscous flow separation around the platform and mooring system. Clearly, many effects should be taken into account to accurately model the mooring cable dynamics. Hence, simplified engineering methods are usually employed.

Force-displacement representation

A common method for modelling the foundations of fixed-bottom off-shore wind turbines is the P-Y method^[126] in which springs are employed to represent the relationship between force and displacement in the soil. This method can be extended to the modelling of mooring lines for floating wind turbines by applying linear or non-linear spring stiffnesses for all six degrees of freedom at the fairlead position (surge, sway, heave, roll, pitch, and yaw). A damping matrix may also be included to account for the mooring line drag. If mooring inertia and the hydrodynamic forces are ignored, the total load on the support platform from the contribution of all mooring lines can be expressed as:

$$\mathbf{F}(t) = \mathbf{F}_0 - C\mathbf{q}(t) - B\dot{\mathbf{q}}(t), \quad (1.6)$$

where \mathbf{F}_0 is the total mooring system load, acting on the support platform in its initial position i.e. pre-tension; \mathbf{q} is the displacement vector from the initial position; $\dot{\mathbf{q}}$ is the time derivative of the displacement vector; C is the the restoring matrix from all mooring lines; and B is the damping matrix. If matrices C and B do not depend on the displacement vector \mathbf{q} , the relation 1.6 is linear. This model is not the most accurate, but it can be used in the analysis of moored floating structures since it adequately represents the mooring system characteristics for the global motions of FOWTs^[24]. On the other hand, if the relation is not linearised, the relevant force-displacement characteristics ($C(\mathbf{q}(t))$ and $B(\mathbf{q}(t))$) of the mooring system must be calculated separately and added as inputs to the model. The advantage of using a single stiffness matrix is its simplicity and ease of implementation. However, in most cases, this method is limited due to the fact that the loads are generally not specified as functions of displacement in all six degrees of freedom. Often,

the restoring forces are specified as independent functions of each platform displacement, and important couplings can be missed. Modelling a spring at each mooring line attachment can minimise this loss of accuracy^[37]. This type of model was employed by Huang *et al.* ^[78] and Savenije *et al.* ^[173], where mooring lines were represented by springs. A precomputed nonlinear force-displacement relationship for FOWT application was employed by Karimirad and Maon^[97, 96], and Matha *et al.* ^[134].

Quasi-static representation

An alternative method for representing the non-linear mooring line restoring forces is the quasi-static approach. The assumption for this type of method is that the mooring lines are in static equilibrium at any instant in time. Hence, the tensions in the mooring lines are computed from the equations of static equilibrium for the mooring line suspended between given anchor and fairlead points. For this reason, this method cannot account for the drag force and inertia of the lines. Neglecting the mooring line damping can lead to inaccuracies since the dynamics of the mooring lines is significantly affected by the drag loading due to hydrodynamics^[16]. Neglecting mooring line inertia is justified in ^[92], where for the studied system it represented a small percentage of the overall inertia of the system (around 2%). The advantage of using the quasi-static model is that it allows properties of the mooring lines to be provided directly. Those properties include length, diameter, mass and extensional stiffness. The quasi-static representation for FOWT application was employed by Jonkman^[90, 92], Matha *et al.* ^[134], Coulling *et al.* ^[38] and Hall *et al.* ^[68, 69].

Dynamic modelling

The dynamic modelling approach gives an accurate representation of the drag and inertia of mooring lines and their effect on the floating platform. These effects can be significant, especially in very deep water where the mooring line is unable to take up its catenary shape instantly. Therefore, a quasi-static analysis is incapable of accurately predicting the line tensions^[37], and the dynamic approach is required. Further, dynamic modelling allows for dynamic interaction between the mooring line and the sea-bed. One of the limitations of this method is that due to its complexity, the model requires much more computational time than the alternatives. This is especially pronounced for off-shore wind turbine design calculations, in which a large number of simulations is required to fulfil the design criteria. Following the dynamic approach, the

mooring lines are usually modelled by finite-element or multi-body methods. The latter is considered a simplification of the former, since the model excludes torsional stiffness, and sometimes bending stiffness too, as in [69]. The finite element model for mooring lines was employed by Skaare *et al.* [184], Bae *et al.* [10], Jeon *et al.* [82], Koo *et al.* [101], and Hall *et al.* [68], where the mooring cable is considered a contiguous set of higher-order segments, or elements, often cubic. The multi-body formulation, also known as lumped-mass method, was first proposed by Nakajima *et al.* [147], and then extended by Kreuzer and Wilke [102]. In this method, the mooring line is represented by a chain of rigid bodies, interconnected by spring/damper elements. The interaction with the sea-bed can be included by employing additional spring/damper elements that are activated when some of the nodes are below certain depth. The dynamic model of the mooring lines for the FOWT application in form of multi-body method was adopted by Matha *et al.* [134], Hall *et al.* [69], and Bae *et al.* [10]. Table 1.4 provides a brief overview of the capabilities of the models outlined above.

Table 1.4: Characteristics of different models for mooring lines.

	Force-displacement	Quasi-static	Dynamic
Evaluation of static forces	Yes	Yes	Yes
Line inertia	No	No	Yes
Line damping	Yes	No	Yes
Line-seabed interaction	No	Yes (static)	Yes
Line bending stiffness	No	No	Yes
Line torsional stiffness	No	No	Yes

1.2.4 Structural modelling

The structure of the FOWT is usually split onto components, representing floating support, tower, nacelle, and blades. These components are then assembled using a multi-body representation, similar to the one employed in this work, see Chapter 4 for details. In most of the cases floating platform is assumed rigid, therefore hydro-elastic effects are neglected. This is justified for many support structures, where the floater is very stiff as compared to the blades and the tower^[92]. However, hydro-elasticity can be included in the potential method using beam elements^[96], but this is not very common.

If aero-elasticity is considered, it is often included in the BEM method. Following a multi-body formulation, the wind turbine structures are subdivided into a number of bodies, and each body consists of an assembly of Timoshenko beam elements^[108]. Another approach is to characterise flexible bodies using

linear modal representation, which usually assumes small deflections^[93]. Typically, two flap-wise bending modes and one edge-wise bending mode per blade, along with two fore-aft and two side-to-side bending modes for the tower are considered^[36]. This requires an additional solver as a pre-cursor step to calculate the mode shapes of the blades and the tower. A similar technique is employed in this work for the dynamic aero-elastic computations, where NASTRAN is used to compute the modes, as explained in Section 3.6.4 of Chapter 3,

1.2.5 Modelling approaches for FOWTs

The most common approach for modelling FOWT dynamics is by combining simplified tools into one hybrid model. The BEM method is frequently adopted for the aerodynamic loads, and the linear potential theory for hydrodynamic loads. In this case, frequency-dependent hydrodynamic-added-mass and hydrodynamic-damping matrices, along with wave-excitation force vector are precomputed for a given problem, and serve as input to the coupled model. At the beginning of the computation, the wave-radiation-retardation kernel is obtained by integrating user-supplied added-mass or damping coefficients^[90]. This way external computer routines can be linked to the aerodynamic solver as a function that employs convolution integrals and returns hydrodynamic loads at given instances evaluated from current position and velocity of the floater, see Section 1.2.2 for details. Hence, due to the underlying assumptions, the coupling between solvers is not of concern. In view of the coupling schemes described in Section 1.2.6, this approach would be classified as monolithic. Similar procedure is applied for the second-order potential model, where the difference- and sum-frequency quadratic transfer functions are required^[96] additionally to the frequency dependent matrices from the linear theory.

However, sometimes solvers are coupled directly by input/output in a staggered manner without relying on frequency dependent parameters and convolution integrals in the aerodynamic solver, as in Bae *et al.*^[10]. In this case what is referred to as "fully coupled" is in fact adaptation of the loosely coupled Conventional Sequential Staggered scheme, see Section 1.2.6 for details.

Some of the works in the field of FOWT modelling are summarised in Table 1.5. These were chosen, because they represent different combination of models, or different coupling strategies.

Table 1.5: Works relevant for the complete FOWT models.

Author(s)	Aerodynamic method	Hydrodynamic method	Mooring model
Jonkman ^[90]	BEM	Linear potential	Quasi-static
Roddier <i>et al.</i> ^[168]	Algebraic	Linear potential	Dynamic
Huang <i>et al.</i> ^[78]	Algebraic	Morison's equation	Force-displacement
Sebastian and Lackner ^[179]	FVM	Linear potential	Force-displacement
Bae <i>et al.</i> ^[10]	BEM	Second-order potential	Dynamic
Karimirad ^[96]	BEM	Second-order potential	Quasi-static
Hall <i>et al.</i> ^[69]	BEM	Second-order potential	Dynamic

1.2.6 Coupling schemes

Coupling algorithms have been studied extensively for the past three decades^[217], since they are needed in many multi-physics problems, like fluid-structure interaction (FSI), or problems that benefit from domain decomposition, where each sub-domain employs a different discretisation method, or it is solved with a different solution approach. Multi-physics problems with adjacent domains can be simulated in a monolithic or in a partitioned way. The former refers to the case where flow, and structural equations are solved simultaneously, while the latter means that they are solved separately. The monolithic approach requires a specific solver for each particular combination of physical problems, whereas the partitioned approach allows for solver modularity. Moreover, the partitioned approach allows for solution of the governing equations with different techniques developed specifically for the corresponding domains; air and water in the case of FOWT. Further, this approach reduces the computational complexity per time-step, simplifies mixed explicit/implicit treatment of sub-domains, facilitates sub-cycling in the data exchange between solvers, and eases code updates when better mathematical models and methods emerge. On the other hand, the partitioned simulation requires a special treatment to account for the interaction between the involved domains. Hence, the computational efficiency over a monolithic approach is not necessarily guaranteed^[53]. The advantages and disadvantages of different coupling strategies are summarised in Table 1.6. Considering that two available and validated solvers (HMB3 and SPH) can be used in this work, the emphasis is placed on partitioned algorithms.

Partitioned coupling can be weak or strong. Explicit algorithms are weak (or loose) as the solvers exchange information once per time step, and the coupled equations are not exactly satisfied due to explicit

Table 1.6: Advantages and disadvantages of different coupling strategies.

Coupling strategy	Advantages	Disadvantages
Weak/Loose	<ul style="list-style-type: none"> – Modular. – Fast explicit schemes. – Easy implementation. – Computationally inexpensive. 	<ul style="list-style-type: none"> – Less accurate. – Possibly unstable.
Strong/Tight	<ul style="list-style-type: none"> – Modular. – Accurate. 	<ul style="list-style-type: none"> – Harder to implement. – Slow convergence for simple schemes. – Requires Jacobians for faster Newton’s methods. – Computationally expensive.
Monolithic	<ul style="list-style-type: none"> – Most accurate. – Computationally inexpensive. 	<ul style="list-style-type: none"> – Not modular. – Requires solver for specific problem. – Does not recognise the differences between the mathematical properties of the subsystems.

treatment. Depending on the formulation, one side of the coupling boundary conditions is usually lagging behind another. This can be improved with staggering or extrapolation techniques, but the scheme remains weak, and coupling errors may be introduced for large time steps. However, loosely coupled algorithms are attractive, since among all solution methods, they are the simplest to implement for realistic applications, and the most computationally inexpensive per time step.

Implicit algorithms are strong (or tight), and enforce exactly the coupling conditions at each time level. This is obtained by conducting iterations until the boundary equations are satisfied to a certain, prescribed accuracy. The coupling problem can be formulated either as fixed-point or root-finding problem. For the former, fixed-point Jacobi or Gauss-Seidel methods can be employed. Although easy to implement, those methods converge slowly if at all. Under-relaxation techniques can be used to improve convergence of the fixed-point iterations. Methods like fixed under-relaxation, adaptive Aitken’s under-relaxation or steepest descent relaxation are some of the possible choices^[104, 43]. The Newton’s method can also be used. This requires Jacobians relating the solutions of both solvers that are usually not known. This can be circumvented by employing approximation of Jacobians or Jacobian-vector products. Those types of coupling methods are called Quasi-Newton^[43].

Three next sections describe in detail the partitioned coupling schemes.

Definitions

In this section, a general abstract formulation for coupled systems is presented. Consider two fluids - water and air - defined on separate domains connected by an interface as shown in Figure 1.8. The coupling problem consists of the aerodynamic fluid on the domain $\Omega_a(t) \subset \mathbb{R}^3$ with the boundary $\Gamma_a(t)$, and the hydrodynamic fluid on the domain $\Omega_h(t) \subset \mathbb{R}^3$ with the boundary $\Gamma_h(t)$. The two domains are connected by the interface $\Gamma_I(t) = \Omega_a(t) \cap \Omega_h(t)$. At each coupling cycle, two interface boundary conditions correspond-

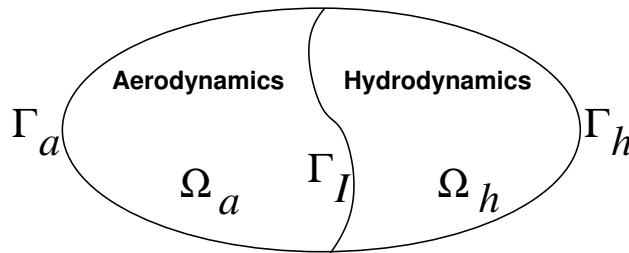


Figure 1.8: Schematic representation of the coupled domains.

ing to the continuity of the momentum flux and velocities must be satisfied along the common interface boundary Γ_I . Those can be viewed as Neumann or Dirichlet conditions, respectively. Let \mathbf{P}_a and \mathbf{x}_a denote the aerodynamic momentum flux and displacement field along the interface Γ_a , while \mathbf{P}_h and \mathbf{x}_h denote the hydrodynamic momentum flux and displacement field along the interface Γ_h , respectively. The equilibrium of momentum and compatibility of velocity field can be expressed as

$$\mathbf{P}_a = \mathbf{P}_h \quad (1.7a)$$

$$\frac{\partial \mathbf{x}_a}{\partial t} = \frac{\partial \mathbf{x}_h}{\partial t} \Rightarrow \mathbf{v}_a = \mathbf{v}_h \quad (1.7b)$$

on boundary Γ_I , where $\mathbf{P}_a = p_a \mathbf{n}_a - \boldsymbol{\sigma}_a \mathbf{n}_a$ and $\mathbf{P}_h = p_h \mathbf{n}_h - \boldsymbol{\sigma}_h \mathbf{n}_h$. Here, p_a and p_h are the aerodynamic and hydrodynamic pressures; $\boldsymbol{\sigma}_a$ and $\boldsymbol{\sigma}_h$ are the aerodynamic and hydrodynamic viscous tensors; and \mathbf{n}_a and \mathbf{n}_h are the local, unit outward normals along the interface, respectively, with $\mathbf{n}_a = -\mathbf{n}_h$ for matched interfaces. Equation 1.7b in strong formulation also ensures the coincidence of the positions at time $t > t_0$ [135]. The coupling scheme aims to satisfy the compatibility conditions 1.7 at every instant of time.

We shall formulate the coupling problem using the following definitions. Consider the aerodynamic solver \mathbb{A} that takes as an input position at the interface \mathbf{x}_h , and returns momentum flux or force distribution

\mathbf{P}_a :

$$\mathbf{P}_a = \mathbb{A}(\mathbf{x}_h). \quad (1.8)$$

Similarly, the hydrodynamic solver \mathbb{H} takes as an input momentum flux \mathbf{P}_a , and computes the new interface position \mathbf{x}_h :

$$\mathbf{x}_h = \mathbb{H}(\mathbf{P}_a). \quad (1.9)$$

The system of equations to be solved thus become

$$\begin{cases} \mathbf{P}_a = \mathbb{A}(\mathbf{x}_h) \\ \mathbf{x}_h = \mathbb{H}(\mathbf{P}_a) \end{cases} \quad (1.10)$$

for each instant of time.

It is assumed in the following sections, for the sake of simplicity, that both subsystems have the same time step Δt . Otherwise, one subsystem may be sub-cycling. In this case what is referred to as one step for this system is indeed a number of steps, and the Δt is the interval between synchronisation points.

Explicit coupling

Assuming that both subsystems in Equation 1.10 have been discretized in space and time with some appropriate methods, and denoting the discrete approximation to the solution of governing equations at step n by x_j^n , where $j = a, h$, the explicit integration algorithms for the two subsystems may be expressed as:

$$x_a^n = \phi_a(x_a^{n-1}, y_h), \quad (1.11a)$$

$$x_h^n = \phi_h(x_h^{n-1}, y_a), \quad (1.11b)$$

where the two functions $y_h(t)$ and $y_a(t)$ are assumed given and represent the variables of the other subsystem in the time interval $\Delta t = t_n - t_{n-1}$.

The simplest coupling procedure is the *Conventional Sequential Staggered* (CSS) scheme^[53, 135, 52] presented in Figure 1.9(a). The basic steps of the CSS cycle are described in Algorithm 1, where α is a weightening parameter to interpolate the interface solutions from the hydrodynamic to the aerodynamic solver between time levels n and $n + 1$. In fact, the CSS algorithm in its most popular form is obtained with $\alpha = 0$. In the case of $\alpha = 1$, the hydrodynamic solution at time step $n + 1$ is omitted, and the previous solution

at time level n is used instead. This method is often referred to as *Conventional Parallel Staggered*^[153, 135] method (CPS), where Steps 1 and 3 in Figure 1.9(a) can be carried out concurrently. The resulting cycle of the CPS scheme is shown in Figure 1.9(b). It should be noted, that this way, one of the solvers is always one step behind the other. In general, the sequential staggered solution procedure is at most first-order, energy accurate in time on the boundary Γ_I when predictors are not employed^[135], even though the individual sub-domains may be higher order accurate. It is typical for fluid solvers to employ second order time accurate schemes, as in the case of HMB3.

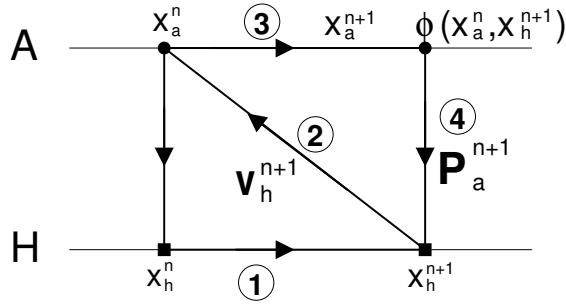
Algorithm 1 Conventional Sequential/Parallel Staggered scheme

1. Start from known solutions of interface momentum flux \mathbf{P}_I^n and velocity field \mathbf{v}_I^n
 2. For each coupling cycle between time $t \in [t^n, t^{n+1}]$
 - (a) Solve the hydrodynamic system for the motion of the interface boundary \mathbf{v}_h^{n+1} using known aerodynamic forcing at the interface
 - (b) Apply Dirichlet velocity continuity condition
 $\mathbf{v}_a^{n+1} = (1 - \alpha)\mathbf{v}_h^{n+1} + \alpha\mathbf{v}_h^n$ on Γ_I , where $\alpha \in [0, 1]$
 - (c) Update aerodynamic mesh and advance the aerodynamic subsystem to the next time level
 - (d) Extract new interface momentum flux \mathbf{P}_a^{n+1} and apply Neumann condition
 $\mathbf{P}_h^{n+1} = \mathbf{P}_a^{n+1}$ on Γ_I
-

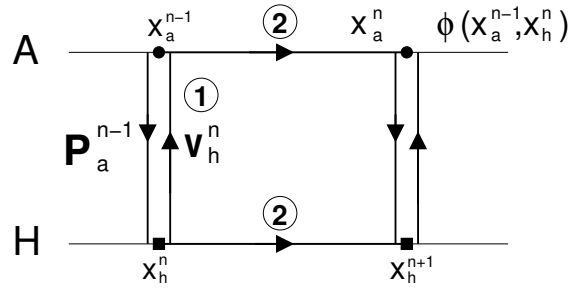
Algorithm 2 Improved Sequential Staggered scheme

1. Start from known solutions of predicted velocity field \mathbf{v}_{IP}^n and corrected momentum flux \mathbf{P}_{IC}^n
 2. For each coupling cycle between time $t \in [t^n, t^{n+1}]$
 - (a) Predict interface velocity for time level t^{n+1}
 $\mathbf{v}_{aP}^{n+1} = \mathbf{v}_h^n + \Delta t(\alpha_0\dot{\mathbf{v}}_h^n - \alpha_1\dot{\mathbf{v}}_h^{n-1})$, where $\alpha_0, \alpha_1 \in [0, 1]$
 - (b) Update aerodynamic mesh and advance the aerodynamic subsystem to the next time level
 - (c) Compute corrected interface momentum flux
 $\mathbf{P}_{hC}^{n+1} = (1 - \beta)\mathbf{P}_a^{n+1} + \beta\mathbf{P}_a^n$ on Γ_I
 - (d) Solve the hydrodynamic system for the motion of the interface boundary \mathbf{v}_h^{n+1} using corrected interface momentum flux \mathbf{P}_{hC}^{n+1}
-

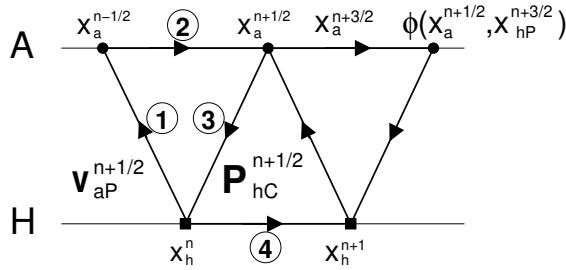
As proposed by Lesoinne and Farhat^[119], the temporal accuracy of the staggered partitioned scheme can be improved by applying the prediction of the boundary motion based on higher order interface velocity extrapolation and momentum flux correction. Several variants were proposed for the selection of extrapolation and correction based on the discrete energy arguments^[162, 161, 52]. One variant is the *Improved Sequential Staggered* (ISS) scheme^[135], also sometimes called *Generalized Serial Staggered* (GSS) procedure^[52], with the generic cycle described in Algorithm 2. Constant real coefficients α_0 , α_1 and β are chosen to increase the accuracy of the method. For instance the settings $\alpha_0 = 1$, $\alpha_1 = 0$ yield a first-order time ac-



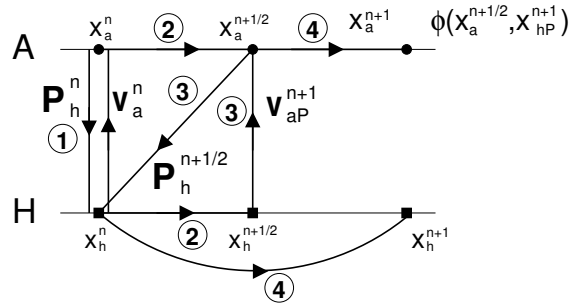
(a) Conventional Sequential Staggered (CSS) scheme.



(b) Conventional Parallel Staggered (CPS) scheme.



(c) Improved Sequential Staggered (ISS) algorithm with an offset of half time-step between fluid integrations.



(d) Improved CPS algorithm.

Figure 1.9: Generic cycles of some explicit algorithms. Letters A and H denote aerodynamic and hydrodynamic solver, respectively.

curate predictor, and a second time accurate if $\alpha_0 = 3/2$, $\alpha_1 = 1/2$. The best choice of the last coefficient is $\beta = 1/2$ [161], and correction step can be viewed as momentum flux averaging. These formulations are shown to preserve second order accuracy of the coupled simulations using Taylor series expansion [52]. The prediction based algorithm can be constructed in a leap-frog non-collocated fashion [53, 52], where one of the fluids is solved at time level t^n , and another at time level $t^{n+1/2}$, as presented in Figure 1.9(c).

The improved CPS method was proposed by Piperno *et al.* [162]. The algorithm employs an estimate of the interface velocity for the next time-step from a half time-step solution, as shown in Figure 1.9(d). At the same time, the aerodynamic solver computes the half time-step momentum flux. In the second half of the time-step, the aerodynamic subsystem is solved using estimated interface velocity, and the hydrodynamic solver is recomputed in parallel using the newly received pressure distribution.

In this work, the Conventional Parallel Staggered scheme is employed. Details of implementation are presented in Chapter 5, where importance of implicit coupling is assessed for studied wind turbine and sea conditions. The algorithm is described in detail in Chapter 13, along the obtained results.

Implicit coupling

Due to availability of several implicit coupling schemes in the literature, only a brief overview of main ideas is presented in this section. More elaborate review of strongly coupled algorithms can be found in Matthies *et al.* [135] and Degroote *et al.* [43].

The goal of the coupled scheme is to ensure that the system of equations 1.10 is satisfied at each time-step. This can be formulated using the composition of functions. In this case the coupling problem is the solution to one of the following equations:

$$\mathbf{x}_h = \mathbb{H} \circ \mathbb{A}(\mathbf{x}_h), \quad (1.12a)$$

$$\mathbf{R}(\mathbf{x}_h) = \mathbb{H} \circ \mathbb{A}(\mathbf{x}_h) - \mathbf{x}_h = \mathbf{0}, \quad (1.12b)$$

where \mathbf{R} is a residual vector. The first is a fixed-point formulation, and the other is a root-finding formulation. Depending on the chosen approach, different convergence strategy can be adopted. All implicit methods are iterative, and in the following, the subscripts are dropped for clarity, and superscripts indicate the coupling iteration.

One of the popular fixed-point methods is the Aitken's adaptive relaxation technique^[104]. This method determines a dynamically varying scalar relaxation factor ω^k for the fixed-point iterations within a time step. The next input for function composition $\mathbb{H} \circ \mathbb{A}$ is thus a linear combination of the last output and the previous input. The value of ω^k is obtained as

$$\omega^k = \frac{(\mathbf{r}^{k-1})^T (\mathbf{r}^k - \mathbf{r}^{k-1})}{(\mathbf{r}^k - \mathbf{r}^{k-1})^T (\mathbf{r}^k - \mathbf{r}^{k-1})}, \quad (1.13)$$

where \mathbf{r}^k is the residual based on the solution at current iteration (\mathbf{x}^k) and the result of evaluation of the composition of functions using this solution ($\tilde{\mathbf{x}}^{k+1} = \mathbb{H} \circ \mathbb{A}(\mathbf{x}^k)$), such that $\mathbf{r}^k = \tilde{\mathbf{x}}^{k+1} - \mathbf{x}^k$. At the next iteration, the updated solution is obtained as $\mathbf{x}^{k+1} = \mathbf{x}^k + \omega^k \mathbf{r}^k$. The procedure is repeated until the norm of the residual vector is below a prescribed threshold.

This type of relaxation techniques was shown to be 2 – 4 times slower^[43, 54] as compared to Quasi-Newton methods, for instance the Interface Quasi-Newton algorithm that uses an approximation for the inverse of the Jacobian from a Least-Squares model (IQN-ILS), as proposed by Vierendeels *et al.* [205]. The idea behind the Quasi-Newton methods is to approximate unknown Jacobians or Jacobian-vector products

by taking into account some limited number of previous inputs and solutions obtained from the solvers using those inputs. The approach is based on the root-finding formulation, where the solution must satisfy a set of nonlinear equations

$$\mathbf{R}(\mathbf{x}) = \mathbf{0}. \quad (1.14)$$

This can be obtained by means of Newton-Raphson iterations as

$$\left. \frac{d\mathbf{R}}{d\mathbf{x}} \right|_{\mathbf{x}^k} \Delta\mathbf{x}^k = -\mathbf{r}^k, \quad (1.15a)$$

$$\mathbf{x}^{k+1} = \mathbf{x}^k + \Delta\mathbf{x}^k, \quad (1.15b)$$

where the residual \mathbf{r}^k is defined the same way as for Aitken's relaxation method. The Jacobian $d\mathbf{R}/d\mathbf{x}$ is often not known, and must be approximated. It is sometimes advantageous to approximate the inverse of the Jacobian, and write the quasi-Newton iterations as^[43]

$$\mathbf{x}^{k+1} = \mathbf{x}^k + \left(\left. \widehat{\frac{d\mathbf{R}}{d\mathbf{x}}} \right|_{\mathbf{x}^k} \right)^{-1} (-\mathbf{r}^k), \quad (1.16)$$

where the hat symbol ($\widehat{}$) indicates approximation. The procedure is to store a set of known residual vectors $\mathbf{r}^k, \mathbf{r}^{k-1}, \dots, \mathbf{r}^1, \mathbf{r}^0$ and the corresponding set of intermediate solution vectors $\tilde{\mathbf{x}}^{k+1}, \tilde{\mathbf{x}}^k, \dots, \tilde{\mathbf{x}}^2, \tilde{\mathbf{x}}^1$. This allows to construct a set of $\Delta\mathbf{r}/\Delta\tilde{\mathbf{x}}$ vectors to approximate the Jacobian or its' inverse, as in Vierendeels *et al.*^[205], where the least-square fit and QR-decomposition was employed to approximate the inverse of the Jacobian. Better estimates of the Jacobian are obtained with each Newton step, and the procedure is repeated until the norm of the residual vector is sufficiently small.

Regarding the performance, Fernandez *et al.*^[54] reformulated FSI as a non-linear problem in the state of the structure, and employed the Newton-Raphson method using an exact Jacobian. The performance of this algorithm was compared with the performance of the Aitken relaxation and Quasi-Newton Generalised Minimal Residual (GMRES) methods, for the inviscid flow in an elastic tube. Results showed that Aitken's relaxation was twice as slow as the Quasi-Newton and the exact Jacobian methods, and required almost 40 times more iterations. Further, for time steps of $\Delta t = 10^{-4}s$, both latter algorithms showed similar behaviour in convergence. However, for time steps of $\Delta t = 10^{-3}s$, the fixed-point and Quasi-Newton algorithms failed to converge. This implies sensitivity of the methods to the employed Jacobian.

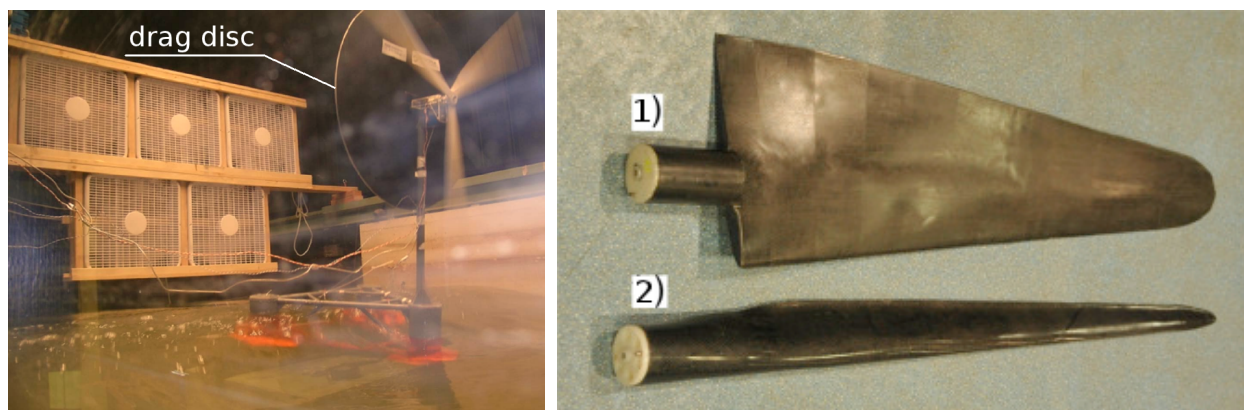
1.2.7 Experimental data for FOWTs

The experimental campaigns for the full-scale FOWTs are expensive due to the cost of the turbine, floating support and system deployment (overall cost around \$60 million^[4]). As was shown in Section 1.1, however, several prototypes were constructed and tested. Perhaps the most studied design is the Hywind prototype owned by Statoil^[4]. The design was towed out to sea in the middle of 2009 for a two-year test campaign. The turbine was operated for at least two more years after the initial testing, and by 2014 it had generated over 32GWh of electrical energy^[4]. However, the collected data is a property of Statoil, and as such is not publicly available. This restriction applies to all installed full-scale FOWT prototypes, to date.

Model testing in wave basins have been also carried out. In 2006, a 1/47 scale model test of the NREL 5-MW^[89] wind turbine with a spar-buoy floating support was conducted at Marintek's Ocean Basin Laboratory^[152]. In 2008 and 2009, 1/105 and 1/67 scale models of the WindFloat design were tested at University of California towing tank before full-scale deployment in 2011^[168, 31]. In 2010, the DeepCwind Consortium tested three 1/50 scale floating platforms to support the NREL 5-MW wind turbine at the Maritime Research Institute (MARIN). The platforms were the Offshore Code Comparison Collaboration (OC3) project spar-buoy, a semi-submersible and a TLP foundations^[133]. In 2013, several concepts including the GustoMSC Tri-Floater, GICON[®]-TLP and PelaStar tension leg platforms were tested in the basin of MARIN^[8, 79, 206]. Unfortunately, similar proprietary restrictions as for full-scale experiments apply to model-scale test data. The publicly presented results are in form of the Response Amplitude Operators (RAOs), which are defined as the square root of the ratio between power spectral densities of the response and input. Hence, measured physical quantities are not directly provided for comparison.

It is worth mentioning here that the above basin tests employed Froude scaling and geometric similarity to the full-size hydrodynamic loads, gravity, and inertia. Under such conditions the Reynolds number of the air flow in the model is much lower than that in the reference system, making the aerodynamic properties of the model far different from those of the reference turbine. As a result, the rotor thrust of the model wind turbine is much lower than the target rotor thrust^[136]. This is usually circumvented by installing a drag disc in place of the rotor, as shown in Figure 1.10(a). Recent experiments addressed this issue by designing a thrust-matched blade, as in Duan *et al.*^[48] and McTavish *et al.*^[136]. This results, however, in geometrically

different shape, with different structural and inertia properties, as shown in Figure 1.10(b).



(a) WindFloat model with drag disc during testing in water basin^[168]. (b) Comparison between thrust-matched blade (1), and geometry-matched blade (2)^[48].

Figure 1.10: Different approaches to achieve desired thrust of scaled FOWTs: drag disc approach (a) and thrust-matched blade design (b).

1.2.8 Active rotor blades

Substantial research interest in development of so called *smart rotor controls* and *active blades* can be observed in the open literature. These concepts involve distributed actuators, and sensors, and one or more microprocessors that analyse the response from the sensors and change the local aerodynamic characteristics of the blade to alter its response. The aerodynamic loads and structural vibrations are of main interest for control or reduction. Different aerodynamic control solutions were proposed in the open literature including plasma actuators^[208], synthetic jets^[194], micro tabs^[12, 86, 198], active vortex generators^[182], and flaps^[15, 30, 57, 115]. A good overview of the concepts, concerns, and efficiency is given by Barlas and van Kuik^[14]. As reported there, the flaps are considered as a concept of high potential. The general idea is to employ small movable control surfaces to directly control lift on a blade, see Figure 1.11(a). By increasing (deployment towards the pressure side) or decreasing (deployment towards the suction side) the camber of the airfoil, trailing edge flaps can generate substantial change in the lift coefficient of the airfoil section^[7]. This affects the maximum lift, lift curve slope and zero-lift angle of attack. Other advantages include good structural and safety features, possibility of high frequency control, and substantially smaller power requirements than full- or part-span pitch controls^[14].

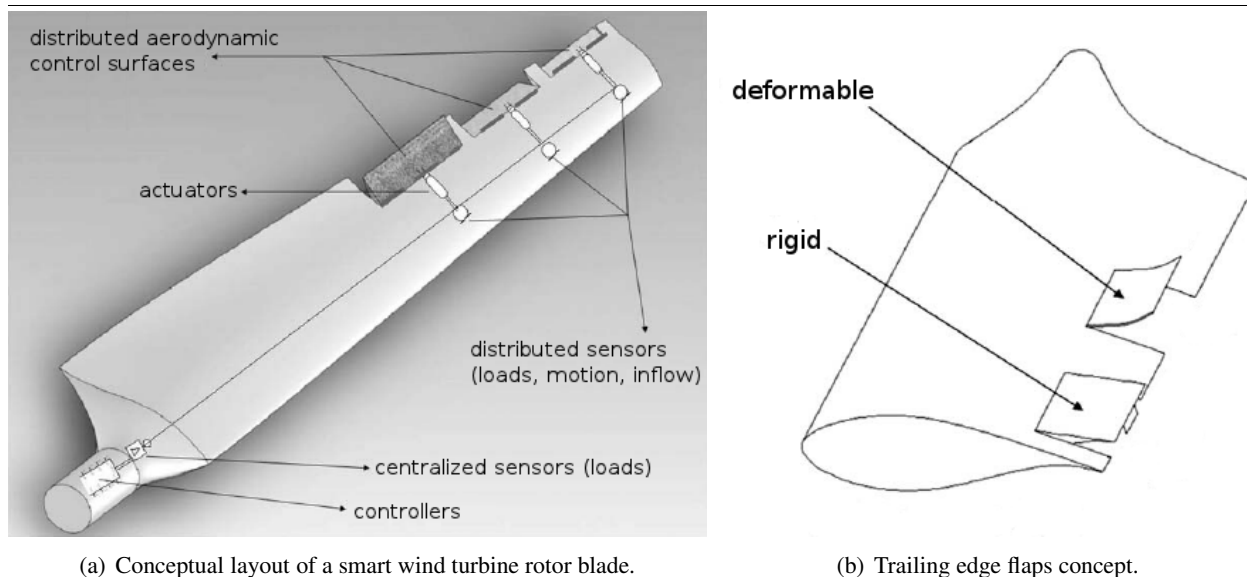


Figure 1.11: Active wind turbine rotor: conceptual layout of a smart blade (a), and trailing edge flaps concept (b). Adapted from ^[14].

Trailing edge flaps can be employed in two manners: either as discrete flaps, or as continuous deformable trailing edge, see Figure 1.11(b) for illustration. Discrete flaps are mounted on the blade and require a moment over the hinge to achieve the required deflection. These kinds of flaps are generally easy to construct, but pose certain disadvantages. They do not comprise an integrated design solution, and all the necessary structural components are subject to wear and corrosion, and the aerodynamic performance is reduced due to the sharp change in the camber^[14]. Furthermore, surface discontinuity can trigger stall and cause noise issues. A continuous deformable trailing edge has a smooth change in shape, which increases its effectiveness^[7]. However, to be actuated, a bending moment must be applied on the trailing edge. Further, this kind of control has to work against the structural rigidity of the trailing edge, and its skin is subject to fatigue. This type of the trailing edge flap was designed by Madsen *et al.* ^[127] using rubber with reinforced voids within the elastic flap that are pressurised to achieve deflection. Experimental studies showed feasibility of such approach, and measured change in the lift coefficient C_L was about 0.2 for applied pressure of 8bar.

Other research activities related to the actuated flaps and active blades include work of Frederick *et al.* ^[57], where the application of a small (4% chord), rapidly actuated, actively controlled trailing-edge flap was experimentally tested. Measurements were conducted in water using NACA 0012 aerofoil.

Results showed, that the root-mean-square loading can be reduced by up to 79% with the proportional-integral-derivative controller. Castaignet *et al.* ^[30] performed a full-scale experiments on Vestas V27 wind turbine (225kW rated power, and 27m diameter) equipped with one active 70cm long rigid trailing edge flap. The results showed consistent flap-wise blade root load reduction with the trailing edge flap controlled by frequency-weighted model predictive controller. An average of 14% load reduction, and 20% reduction of the amplitude of the one-per-revolution loads were reported. Barlas *et al.* ^[15] conducted wind tunnel tests on two-bladed, small-scale (1.8m diameter) wind turbine equipped with two flexible trailing edge flaps per blade. The length of each flap was 50% of the local chord, and flaps were composed of piezo-ceramic bender actuators. A series of H_∞ controllers were designed to minimise different regions of the loads spectrum. The best performing controller managed to considerably reduce load fluctuations. The standard deviation of the flap-wise strains was reduced up to 58.12% for 0° yaw misalignment case. Results also showed the reduction of 50.5% in the flap-wise moment fatigue equivalent loads. Numerical investigations (BEM method) of Markou *et al.* ^[132] for the NREL 5-MW wind turbine showed up to 73% flap-wise load reduction for employed trailing-edge flaps. It was concluded that in general, the flap with larger maximum deflection performs better. Similar method was adopted by Barlas *et al.* ^[13] for the same wind turbine. As was reported, the flap-wise blade root moment was reduced by up to 27.3%.

To summarise, the results for the trailing edge flap applications showed reduction in flap-wise loads up to 58% for wind tunnel experiments^[15], average reduction of 14% for field tests^[30], and up to 73% for aerodynamic method based on BEM theory^[132]. These results confirm a high potential of trailing edge flap concepts for load alleviation. For this reason, the continuous deformable leading and trailing edge flaps were studied in Chapter 11.

1.2.9 Atmospheric turbulence

Wind turbines are often exposed to complex wind conditions in which atmospheric wind turbulence dominates, causing large blade deformations and fatigue loadings. Hence, a realistic transient turbulent wind field modelling is important for large wind turbine simulations.

The most accurate approach to simulate the turbulent field is to solve the Navier-Stokes equations using Direct Numerical Simulations (DNS) to resolve the turbulent fluctuations. However, the computational

cost is very high and this approach is not currently feasible for engineering applications due to the large span of turbulent scales. Another accurate but less expensive method is Large Eddy Simulation (LES), which is an approximate solution to the Navier-Stokes equations where the smallest scales are not resolved but modelled^[17, 99, 114, 186]. This approach was adopted for instance by Sim *et al.*^[183], Lavelly *et al.*^[110], and Lee *et al.*^[114] for on-shore wind turbines. Nevertheless, the LES method still requires large computational resources.

Currently, the most widely adopted models for wind turbulence simulations are based on the construction of spectral tensors such as the Sandia method^[200] (also known as Veers model) and the Mann's^[129, 130] model. Descriptions of these methods are provided in the next paragraphs.

Sandia model

The basic approach of the Sandia method is to simulate wind speed time series at several points located on a plane perpendicular to the mean wind direction. By using Taylor's frozen turbulence hypothesis^[200], those time series are propagated in the mean wind direction. Hence, this method provides a three-dimensional block of space with a grid of instantaneous wind speeds. Analysis is performed initially in the frequency domain, and the time series are obtained by means of inverse Fourier transforms. The required input to the model includes the single point power spectral densities (PSDs) for all points, and the coherence functions, which describe how turbulence is correlated as a function of spatial separation, mean wind speed, and frequency^[200]. In the original model, the coherence is assumed to be isotropic in the cross-wind plane, and the cross spectral densities are assumed to be real-valued. Possible choices of PSDs include Frost^[59], Kaimal^[95] and von Kármán^[207] spectra. The Sandia model was calibrated and validated against measurements obtained by Pacific Northwest Laboratories.

Mann's model

Jakob Mann^[129, 130] proposed and developed an efficient wind turbulence model based on the construction of a spectral tensor for atmospheric surface layer turbulence. The model is capable of simulating three-dimensional fields of the wind velocity fluctuations, and has the same second-order statistics as in the real atmosphere, e.g. variances and cross spectra. Similar to Sandia method, the Mann's model adopts Taylor's

frozen turbulence hypothesis to relate the spatial wind fluctuations with time, which interprets time series as "space series". Also, starting from the basis of the isotropic von Kármán spectrum, Mann's model linearises the Navier-Stokes equation to estimate the effect of the shear on the turbulence by assuming the mean wind field can be represented by a uniform shear with the flow in the prevailing wind direction. The Rapid Distortion Theory (RDT) is used to model the response of turbulence to shear, such that the wind turbulence is anisotropic. Two atmospheric experiments designed to investigate the spatial structure of turbulence were used to calibrate and validate the model.

The advantage of the Mann's model over Sandia method is that it takes into account more physical properties e.g. boundary layer shear, and eddy life time. It also produces incompressible velocity field i.e. the generated velocity field is divergence-free. For this reason this model was employed in Chapter 9 of this work. Similar approach to the one presented here was used in work of Li *et al.* ^[121].

1.3 Summary of findings

The literature review showed that extensive research interest is placed on the development of floating offshore wind turbines. The FOWTs are very complex systems that are simultaneously subjected to sea and wind loads, and constrained solely by the mooring system. The common approach in FOWTs modelling is to combine simplified tools into a hybrid model to predict wind turbine responses. Due to underlying assumptions, the monolithic coupling between the aerodynamic and hydrodynamic models is usually possible. These assumptions, however, reduce the applicable range of those models. For instance, wave run-up against semi-submersible columns, and viscous flow separation on the floaters cannot be fully captured by the potential-based approach. Also, as was indicated by Matha *et al.* ^[134], the potential hydrodynamic theory might not completely apply to floating wind turbine platforms due to the encountered large displacements. Additional limitations come from the chosen support design, where some models are only applicable for slender structures, like Morison's model^[144]. Further, the assumptions of BEM and GDW aerodynamic models are violated when the wind turbine undergoes large pitching motion^[179, 195]. Mooring line models are also important, since they directly influence the FOWT motion.

Due to mentioned above limitations of engineering models, only two very recent works employed

CFD solvers based on Navier-Stokes equations^[164, 197]. Tran and Kim^[197] in 2016 employed the incompressible volume of fluid (VOF) method to solve for the hydrodynamic and aerodynamic loads. The 6-DOF solver was used to compute dynamic motion of FOWT, where the rotation of the rotor was included by a superimposed rotation technique, which superimposes a fixed body rotation in addition to the floating motion. This way the gyroscopic effect was excluded from the model. The quasi-static mooring line model was employed, and the coupling between the CFD and 6-DOF solvers was not addressed in this work.

Qualen *et al.*^[164] in 2014 employed incompressible finite-difference solver. The one-sided coupling between two phases was achieved through the free surface interface, which is subject only to the conditions of the denser phase (water), and the air is then constrained by the calculated free surface. The FOWT dynamics was modelled with the 6-DOF solver. The coupling between structural and CFD solvers was obtained by means of predictor-corrector scheme, where the aero-hydrodynamic solver is solved twice per time-step, leading to prediction, and then correction for the 6-DOF solver. The dynamic and quasi-static mooring line models were adapted in this work.

In this thesis, the weakly-compressible Smoothed Particle Hydrodynamics (SPH) method was coupled to the finite volume, compressible CFD solver (HMB3). This is in contrast to two works mentioned above, where incompressible solvers were employed. Further, in current method, the motion of the FOWT is computed using the multi-body formulation, allowing naturally for the gyroscopic motion. Again, this is more accurate representation of the FOWT dynamics, whilst other works employed a simple 6-DOF solver. Also, the linear force-displacement model was used for the mooring lines in this work, and authors above employed a quasi-static and dynamic models. Finally, the coupling is addressed in this thesis, and the employed scheme is described in detail, which is not very common for research articles published to date.

1.4 Outline of the thesis

The present PhD thesis is divided as follows.

Chapter 1 introduces the motivation behind the present work and provides the state-of-the-art on FOWTs simulation methods, as well as the challenges it involves. The objectives of the thesis are also presented.

Chapters 2-4 provide theoretical background of the employed numerical methods. In particular, Chapter 2 is focused on the hydrodynamic method SPH, Chapter 3 is devoted to the finite volume aerodynamic solver HMB3, and Chapter 4 presents the multi-body method, with derivation of the Newton-Euler equations of motion and employed method of solving mixed differential-algebraic system of equations.

Chapter 5 presents the coupling scheme employed in this work. The validation of communication between the solvers is also included in this chapter. Definitions of the sea states are given at the end, and parameters to obtain a particular sea state using SPH method are provided.

Chapters 6-8 are the validation chapters for each solver. Chapter 6 presents the validation test cases for the employed SPH method. Chapter 7 shows the validation of the HMB3 solver. This includes the NREL Annex XX ^[70] and the MEXICO project ^[176, 177] experiments, where the pressure and PIV data have been used for validation. Finally, Chapter 8 presents the validation of the multi-body solver.

Chapter 9 describes the 10-MW wind turbine employed in this work. It contains the computational parameters, grid convergence study, and the results of rigid blade cases. The effects of the atmospheric boundary layer inflow and turbulence are also investigated in this chapter.

Chapter 10 considers elasticity of the blades. It provides information of the structural model, obtained natural frequencies and mode shapes. This structural model is then employed to conduct aero-elastic computations with and without the tower.

Chapter 11 considers the application of deformable trailing and leading edge flaps for the 10-MW wind turbine. Work presented in this chapter can be viewed as a ground for future research, where the FOWT rotor will be equipped with flaps.

Chapter 12 is devoted to aerodynamic performance of the 10-MW rotor undergoing prescribed yawing and pitching motions. The possibility of a wind turbine entering vortex ring state during pitching oscillations is also assessed in this chapter.

Finally, the results of coupled computations of the FOWT are presented in Chapter 13. This includes analyses of decoupled and coupled results, as well as the computational performance of employed scheme.

Conclusions extracted from the different subjects covered in this work are provided at the end of the thesis. Ideas and recommendations for future work are also given.

Chapter 2

Hydrodynamic simulation method

All hydrodynamic computations were performed using the Smoothed Particle Hydrodynamics (SPH) flow solver. Instead of starting from scratch, an open source version of the SPH solver^[60, 62, 63, 214] was adopted, and then improved at the University of Glasgow.

2.1 Concept and formulation

The SPH is a mesh-free method where the state of a system is represented by a set of particles. Each particle carries individual material properties like mass, density, position and velocity. The particles move according to the governing conservation equations, where the SPH method employs weighted interpolation which approximates values and derivatives of continuous variables by using a set of discrete points.

The first step in the SPH method is an *integral function representation* of field functions. The concept of integral representation of a function $f(\mathbf{x})$ starts from the following identity.

$$f(\mathbf{x}) = \int_{\Omega} f(\mathbf{x}') \delta(\mathbf{x} - \mathbf{x}') d\mathbf{x}' \quad (2.1)$$

where f is a function of position vector \mathbf{x} , Ω is a volume containing \mathbf{x} , and $\delta(\mathbf{x} - \mathbf{x}')$ is the Dirac delta function given by

$$\delta(\mathbf{x} - \mathbf{x}') = \begin{cases} 1 & \text{if } \mathbf{x} = \mathbf{x}' \\ 0 & \text{otherwise} \end{cases} \quad (2.2)$$

If the Dirac delta function is replaced by a smoothing function $W(\mathbf{x} - \mathbf{x}', h)$, the integral representation becomes the so-called *kernel approximation* of a function $f(\mathbf{x})$ and is marked by $\langle \rangle$

$$\langle f(\mathbf{x}) \rangle = \int_{\Omega} f(\mathbf{x}') W(\mathbf{x} - \mathbf{x}', h) d\mathbf{x}' \quad (2.3)$$

where h is a smoothing length defining the influence area of the smoothing function W . Note that as long as W is not the Dirac delta function, the kernel approximation can only be an approximation of the integral representation.

The smoothing function W must satisfy a number of conditions:

$$\int_{\Omega} W(\mathbf{x} - \mathbf{x}', h) d\mathbf{x}' = 1, \quad \text{Normalisation} \quad (2.4a)$$

$$\lim_{h \rightarrow 0} W(\mathbf{x} - \mathbf{x}', h) = \delta(\mathbf{x} - \mathbf{x}'), \quad \text{Delta function} \quad (2.4b)$$

$$W(\mathbf{x} - \mathbf{x}', h) = 0 \text{ when } |\mathbf{x} - \mathbf{x}'| > \kappa h, \quad \text{Compactness} \quad (2.4c)$$

The first one is the *normalisation condition*, which means that the integral of smoothing function over the support domain equals unity. The second one is the *Delta function property* and ensures that the smoothing function becomes the Delta function when the smoothing length approaches zero. The third is the *compactness condition* where κ is a constant and defines the effective area of the smoothing function. Apart from the above, the smoothing function must also be monotonically decreasing with the increase of the distance $|\mathbf{x} - \mathbf{x}'|$. Two more important properties of the smoothing function include

$$W(\mathbf{x} - \mathbf{x}', h) \geq 0, \quad \text{Positivity} \quad (2.5a)$$

$$\int_{\Omega} (\mathbf{x} - \mathbf{x}') W(\mathbf{x} - \mathbf{x}', h) d\mathbf{x}' = 0, \quad \text{Symmetry} \quad (2.5b)$$

where the first one is the *positivity property* that ensures physically meaningful representation of the physical phenomena. The second one is the *symmetric property*, which combined with condition (2.4a) ensures the first order consistency of kernel approximation ^[124].

The approximation for the derivative $\nabla \cdot f(\mathbf{x})$ is obtained simply by substituting $f(\mathbf{x})$ with $\nabla \cdot f(\mathbf{x})$ in Equation 2.3. The following equation is obtained by applying Gauss-Ostrogradsky theorem, some divergence properties and assuming that the support domain is located within the problem domain such that the surface integral becomes zero.

$$\langle \nabla f(\mathbf{x}) \rangle = - \int_{\Omega} f(\mathbf{x}') \nabla W(\mathbf{x} - \mathbf{x}', h) d\mathbf{x}' \quad (2.6)$$

If the support domain overlaps with the problem domain, the smoothing function W is truncated by the problem boundary and the surface integral is no longer zero.

The next component of the SPH method is the *particle approximation*. Since in the SPH the entire system is described by a finite number of particles, the continuous kernel approximation (Equation 2.3) is converted to a discrete summation over all the particles in the support domain^[140]. This is made by replacing the infinitesimal volume $d\mathbf{x}'$ at the location of the particle j by the finite volume of the particle ΔV_j that is related to the mass m_j of the particle by

$$\Delta V_j = \frac{m_j}{\rho_j} \quad (2.7)$$

where ρ_j is the density of the particle j . The continuous SPH integral from Equation 2.3 can then be written in the following discretized form for particle i

$$\langle f(\mathbf{x}_i) \rangle = \sum_{j=1}^N \Delta V_j f(\mathbf{x}_j) \cdot W_{ij} = \sum_{j=1}^N \frac{m_j}{\rho_j} f(\mathbf{x}_j) \cdot W_{ij}, \quad (2.8)$$

where summation is over total number of particles N , and

$$W_{ij} = W(\mathbf{x}_i - \mathbf{x}_j, h) = W(|\mathbf{x}_i - \mathbf{x}_j|, h) \quad (2.9)$$

is the smoothing function evaluated at distance $|\mathbf{x}_i - \mathbf{x}_j|$ between particles. In this way the continuous integral is converted to the weighted summation of the neighbouring particles to given particle i . See Figure 2.1 for illustration in a two-dimensional domain.

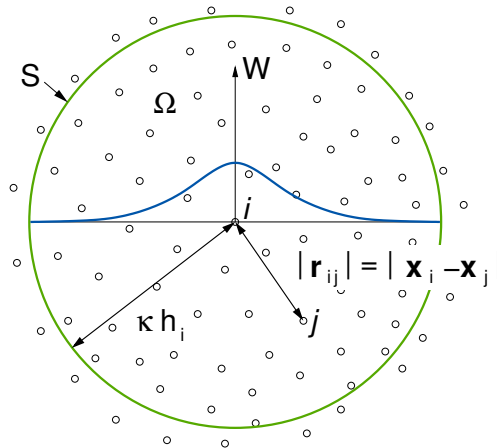


Figure 2.1: The SPH particle approximation in a two-dimensional problem domain Ω bounded by a surface S . W is the smoothing function that is used to approximate field variables at particle i by using particles j within the support domain.

Following the same procedure, the particle approximation for the derivative of the function is

$$\langle \nabla \cdot f(\mathbf{x}_i) \rangle = \sum_{j=1}^N \frac{m_j}{\rho_j} f(\mathbf{x}_j) \cdot \nabla_i W_{ij} \quad (2.10)$$

where the gradient $\nabla_i W_{ij}$ is taken with respect to particle i

$$\nabla_i W_{ij} = \frac{\mathbf{x}_i - \mathbf{x}_j}{r_{ij}} \frac{\partial W_{ij}}{\partial r_{ij}} = \frac{\mathbf{x}_{ij}}{r_{ij}} \frac{\partial W_{ij}}{\partial r_{ij}} \quad (2.11)$$

Equation 2.10 states that the value of the gradient of a function at a particle can be approximated by the summation of those values of the function at all the particles in the support domain weighted by the gradient of the kernel function. The smoothing kernel is usually known beforehand, simplifying evaluation of the gradients of field variables. However, for improved approximation accuracy, the smoothing function can be reconstructed for each particle at every time step ^[123, 124].

There are also other possible ways to represent the divergence of the function at particle i by substituting gradient operator identities

$$\nabla \cdot f(\mathbf{x}) = \frac{1}{\rho} [\nabla \cdot (\rho f(\mathbf{x})) - f(\mathbf{x}) \cdot \nabla \rho] \quad (2.12a)$$

$$\nabla \cdot f(\mathbf{x}) = \rho \left[\nabla \cdot \left(\frac{f(\mathbf{x})}{\rho} \right) + \frac{f(\mathbf{x})}{\rho^2} \cdot \nabla \rho \right] \quad (2.12b)$$

into the integral equation of the form of Equation 2.6. Following the same procedure as previously, new approximations of the divergence are obtained as:

$$\langle \nabla \cdot f(\mathbf{x}_i) \rangle = \frac{1}{\rho_i} \left[\sum_{j=1}^N m_j [f(\mathbf{x}_j) - f(\mathbf{x}_i)] \cdot \nabla_i W_{ij} \right], \quad (2.13)$$

$$\langle \nabla \cdot f(\mathbf{x}_i) \rangle = \rho_i \left[\sum_{j=1}^N m_j \left[\frac{f(\mathbf{x}_j)}{\rho_j^2} + \frac{f(\mathbf{x}_i)}{\rho_i^2} \right] \cdot \nabla_i W_{ij} \right]. \quad (2.14)$$

2.2 Smoothing functions

The smoothing function of the SPH method determines the pattern of approximation of the flow field, the dimensions of the support domain of particles, and accuracy and consistency of particle approximation. Different smoothing functions can be used in the SPH method. Below are presented some of most frequently

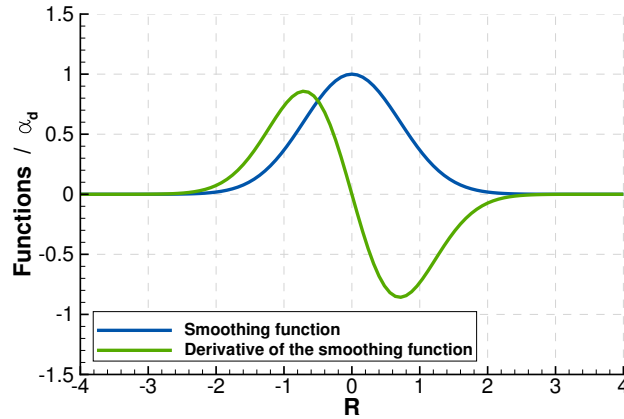


Figure 2.2: The Gaussian smoothing function and its first derivative.

used versions. Kernels are expressed as a function of the dimensionless distances between particles given by $R = \frac{r}{h} = \frac{|\mathbf{x}-\mathbf{x}'|}{h}$, where r is a distance between two particles.

The Gaussian kernel is sufficiently smooth even for high order of derivatives. It is, however, not really compact, as it never goes to zero theoretically, unless R approaches to infinity. Because it approaches to zero very fast numerically, it is practically compact. The Gaussian kernel and its first derivative are shown in Figure 2.2. The equation is

$$W(R, h) = \alpha_d e^{-R^2} \quad (2.15)$$

where α_d is a parameter introduced so that the unity condition can be satisfied and is dependent on the dimensions of the space. For two-dimensional space $\alpha_d = 1/\pi h^2$, and $\alpha_d = 1/\pi^{3/2} h^3$ for three-dimensional space.

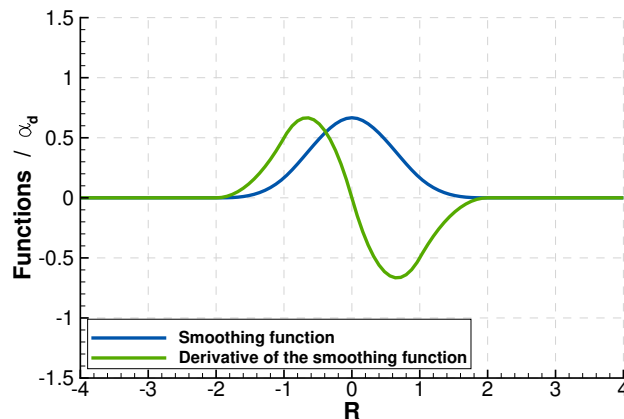


Figure 2.3: The cubic spline smoothing function and its first derivative.

The cubic spline function was devised by Monaghan^[143] and resembles a Gaussian function while

it has a narrower compact support. However, the second derivative of the cubic spline is piecewise linear function. The cubic kernel and its first derivative are shown in Figure 2.3. The equation describing this kernel has the following form

$$W(R, h) = \alpha_d \times \begin{cases} \frac{2}{3} - R^2 + \frac{1}{2}R^3 & 0 \leq R < 1 \\ \frac{1}{6}(2 - R)^3 & 1 \leq R < 2 \\ 0 & R \geq 2 \end{cases} \quad (2.16)$$

where $\alpha_d = 15/7\pi h^2$ for two-dimensional space, and $\alpha_d = 3/2\pi h^3$ for three-dimensional space.

It should be noted that the support radius h from a smoothing kernel is crucial for a stable and robust fluid simulation. If smoothing length is too large, the result from an SPH approximation is inaccurate due to large averaging radius. On the other hand, if smoothing length is too small, the results are imprecise due to small number of particles that are included in the weighting by the smoothing kernel. It is common to employ smoothing length h in range $1.0 - 3.0d$, where d is initial particle spacing^[19, 39], although it is possible to choose an adaptive length based on local particle density^[163, 170]. However, the adaptive smoothing length methods are implicit, requiring additional iterations for each particle. Hence, the constant smoothing length of $1.5d$ was employed in this work.

2.3 SPH formulation of Navier-Stokes equations

The basic governing equations of fluid dynamics are based on the following three physical laws of conservation:

- conservation of mass
- conservation of momentum
- conservation of energy

The governing equations in Lagrangian form will be employed in this section. The derivation of the SPH formulation of conservation equations is based on a direct application of the particle approximation concept to the nabla operator. Angle brackets $\langle \rangle$ indicating particle approximation are dropped for convenience.

2.3.1 Continuity equation

The continuity equation in Lagrangian form is

$$\frac{D\rho}{Dt} = -\rho \nabla \cdot \mathbf{U}, \quad (2.17)$$

where ρ is the density and \mathbf{U} is the velocity vector. As was shown before, different representations of derivatives exist for the SPH method. Therefore, different forms of the conservation equations can be found.

By substituting Equation 2.13 into Equation 2.17 the most frequently used form of the continuity equation is obtained as^[123]

$$\frac{D\rho_i}{Dt} = \sum_{j=1}^N m_j \mathbf{U}_{ij} \nabla_i W_{ij}, \quad (2.18)$$

where $\mathbf{U}_{ij} = \mathbf{U}_i - \mathbf{U}_j$ is the difference in velocity of the neighbouring particles. $\frac{D}{Dt}$ is the substantial derivative, which is the time rate of change of some flow-field variable following a moving fluid particle. The substantial derivative of variable H in vector notation is

$$\frac{DH}{Dt} = \frac{\partial H}{\partial t} + (\mathbf{U} \cdot \nabla)H, \quad (2.19)$$

where \mathbf{U} is the velocity of the fluid. The use of Equation 2.13 instead of Equation 2.14 to represent the derivative operator serves to symmetrise final equation, which reduces the errors arising from particle inconsistencies. Particle inconsistencies are created when the smoothing function satisfies the normalisation condition (Equation 2.4a) and the symmetry property (Equation 2.5b) for the continuous approximation, but particle approximation does not (due to the distribution of particles). Then the following equations do not hold:

$$\sum_{j=1}^N W(\mathbf{x} - \mathbf{x}_j, h) \Delta \mathbf{x}_j = 1, \quad (2.20a)$$

$$\sum_{j=1}^N (\mathbf{x} - \mathbf{x}_j) W(\mathbf{x} - \mathbf{x}_j, h) \Delta \mathbf{x}_j = 0, \quad (2.20b)$$

where the summation is over the all particles N in the support domain.

2.3.2 Momentum equation

The momentum conservation equation in Lagrangian form is

$$\frac{D\mathbf{U}}{Dt} = -\frac{1}{\rho} \nabla p + \mathbf{g} + \Gamma, \quad (2.21)$$

where Γ contains dissipative terms, p is the pressure, ρ is the density, and \mathbf{g} is the gravitational acceleration. Again, this equation may take different forms. The artificial compressibility considers that every theoretically incompressible fluid is actually compressible. Therefore, in order to symmetrise the approximation, Equation 2.14 is usually employed to represent the nabla (∇) operator. Also, different representations of viscosity are possible and described below.

Artificial viscosity

The artificial viscosity proposed by Monaghan^[140] is the most widely used in SPH methods^[123]. It provides the correct amount of viscosity to convert kinetic energy into heat at shocks and also helps to prevent unphysical penetration when two particles become close. Applying Equation 2.14 to the pressure part of the right-hand-side of the Equation 2.21 and introducing Monaghan's dissipation term leads to following symmetrised particle momentum equation:

$$\frac{D\mathbf{U}_i}{Dt} = - \sum_{j=1}^N m_j \left[\frac{p_j}{\rho_j^2} + \frac{p_i}{\rho_i^2} + \Pi_{ij} \right] \nabla_i W_{ij} + \mathbf{g}. \quad (2.22)$$

The viscosity term is given by

$$\Pi_{ij} = \begin{cases} \frac{-\alpha \overline{c_{ij}} \phi_{ij}}{\overline{\rho_{ij}}} & , \quad \mathbf{U}_{ij} \cdot \mathbf{r}_{ij} < 0 \\ 0 & , \quad \mathbf{U}_{ij} \cdot \mathbf{r}_{ij} > 0 \end{cases} \quad (2.23)$$

where

$$\phi_{ij} = \frac{h \mathbf{U}_{ij} \cdot \mathbf{r}_{ij}}{|\mathbf{r}_{ij}|^2 + \varphi^2}, \quad (2.24a)$$

$$\overline{c_{ij}} = \frac{1}{2} (c_i + c_j), \quad (2.24b)$$

$$\overline{\rho_{ij}} = \frac{1}{2} (\rho_i + \rho_j), \quad (2.24c)$$

$$\mathbf{U}_{ij} = \mathbf{U}_i - \mathbf{U}_j, \quad \mathbf{r}_{ij} = \mathbf{r}_i - \mathbf{r}_j. \quad (2.24d)$$

In the above equations c is the speed of sound of the medium assumed (see Section 2.3.3 for weak compressibility), $\varphi = 0.1h$ is a factor inserted to prevent numerical divergence when two particles are approaching each other, and α is a free constant depending on the problem typically set around 1.0^[123].

Laminar viscosity

Alternatively, the viscous stresses in the momentum equation can be expressed as^[125]

$$(\nu_0 \nabla^2 \mathbf{U})_i = \sum_{j=1}^N m_j \left(\frac{4\nu_0 \mathbf{r}_{ij} \cdot \nabla_i W_{ij}}{(\rho_i + \rho_j)(r_{ij}^2 + \phi^2)} \right) \mathbf{U}_{ij} \quad (2.25)$$

where $\nu_0 = 10^{-6} m^2/s$ is a kinematic viscosity. By introducing the above equation into the momentum conservation equation (2.21) the following expression is obtained:

$$\frac{D\mathbf{U}}{Dt} = - \sum_{j=1}^N m_j \left[\frac{p_j}{\rho_j^2} + \frac{p_i}{\rho_i^2} \right] \nabla_i W_{ij} + \mathbf{g} + \sum_{j=1}^N m_j \left(\frac{4\nu_0 \mathbf{r}_{ij} \cdot \nabla_i W_{ij}}{(\rho_i + \rho_j)(r_{ij}^2 + \phi^2)} \right) \mathbf{U}_{ij}. \quad (2.26)$$

2.3.3 Equation of state

The fact that a theoretically incompressible flow is practically compressible leads to a concept of artificial compressibility. Therefore, it is feasible to use a quasi-incompressible equation of state to model the incompressible flow. The compressibility is adjusted to slow the speed of sound so that the time step in the model is reasonable. Another limit imposed on the compressibility is to restrict the speed of sound to be at least 10 times faster than the maximum fluid velocity, thereby keeping density fluctuations within 1%. Following Monaghan^[141], the relationship between pressure and density is expressed as

$$p = B \left[\left(\frac{\rho}{\rho_0} \right)^\gamma - 1 \right] \quad (2.27)$$

where γ is the constant representing adiabatic index, $\rho_0 = 1000 kg m^{-3}$ is the reference density, and B is a problem-dependent parameter, which sets a limit for the maximum change of the density, and determines the speed of sound. In most circumstances $\gamma = 7$, and $B = c_0^2 \rho_0 / \gamma$, where $c_0 = c(\rho_0) = \sqrt{\partial p / \partial \rho} \Big|_{\rho_0}$ is the speed of sound at the reference density.

2.4 SPH implementation

2.4.1 Moving particles

The particles are updated using the XSPH variant according to Monaghan^[139] which was introduced to stop SPH particles passing through each other. The idea Monaghan used was that each particle is moved with

an average of the velocities of its neighbours. This approach significantly reduces the number of particles passing through each other. The method is non-dissipative and conserves linear and angular momentum ^[139].

The velocity of each particle is computed by

$$\frac{d\mathbf{r}_i}{dt} = \mathbf{U}_i + \varepsilon \sum_{j=1}^N m_j \frac{2}{\rho_i + \rho_j} \mathbf{U}_{ji} W_{ij}, \quad (2.28)$$

where $\mathbf{U}_{ji} = \mathbf{U}_j - \mathbf{U}_i$, and ε is a user defined parameter usually taken to be 0.5.

2.4.2 Time marching schemes

To run the simulation forward in time each particle is updated using a global fixed time step Δt . For clarity consider the following system of equation for density, position, and momentum:

$$\frac{d\rho_i}{dt} = D_i, \quad (2.29a)$$

$$\frac{d\mathbf{r}_i}{dt} = \mathbf{V}_i, \quad (2.29b)$$

$$\frac{d\mathbf{U}_i}{dt} = \mathbf{F}_i, \quad (2.29c)$$

where D_i is the time derivative of density given by Equation 2.18, and \mathbf{V}_i is the velocity of the particle. If XSPH correction is used, then \mathbf{V}_i is computed by Equation 2.28, otherwise $\mathbf{V}_i = \mathbf{U}_i$. Following sections give a brief overview of the most common integration schemes of the SPH method.

Verlet scheme

Verlet integration ^[202, 203] is a common time integration scheme used to calculate trajectories of particles in molecular dynamics. The basic idea is to expand two Taylor series for the position \mathbf{r}_i one forward, and one backward in time, and then add both equations.

$$\mathbf{r}_i^{n+1} = \mathbf{r}_i^n + \mathbf{U}_i^n \Delta t + \frac{1}{2} \mathbf{F}_i^n \Delta t^2 + \frac{1}{6} \mathbf{s}_i^n \Delta t^3 + O(\Delta t^4), \quad (2.30a)$$

$$\mathbf{r}_i^{n-1} = \mathbf{r}_i^n - \mathbf{U}_i^n \Delta t + \frac{1}{2} \mathbf{F}_i^n \Delta t^2 - \frac{1}{6} \mathbf{s}_i^n \Delta t^3 + O(\Delta t^4), \quad (2.30b)$$

where \mathbf{r} is the position, \mathbf{U} is the velocity, \mathbf{F} is acceleration, and \mathbf{s} is the second time derivative of velocity.

The current scheme is split into two parts. Normally the variables are calculated using

$$\mathbf{U}_i^{n+1} = \mathbf{U}_i^{n-1} + 2\mathbf{F}_i^n \Delta t, \quad (2.31a)$$

$$\mathbf{r}_i^{n+1} = \mathbf{r}_i^n + \mathbf{U}_i^n \Delta t + \frac{1}{2} \mathbf{F}_i^n \Delta t^2, \quad (2.31b)$$

$$\rho_i^{n+1} = \rho_i^{n-1} + 2D_i^n \Delta t, \quad (2.31c)$$

where n is a current time step. Since these equations are not coupled, every few iterations (usually 10 to 40 steps) the variables are calculated using the explicit Euler scheme as:

$$\mathbf{U}_i^{n+1} = \mathbf{U}_i^n + \mathbf{F}_i^n \Delta t, \quad (2.32a)$$

$$\mathbf{r}_i^{n+1} = \mathbf{r}_i^n + \mathbf{U}_i^n \Delta t + \frac{1}{2} \mathbf{F}_i^n \Delta t^2, \quad (2.32b)$$

$$\rho_i^{n+1} = \rho_i^n + D_i^n \Delta t. \quad (2.32c)$$

Symplectic scheme

The symplectic time integration algorithms are designed for the numerical solution of Hamilton's equations and since these conserve the Hamiltonian, are widely applied in molecular dynamics where a long term evolution is required. These schemes are also reversible in the absence of frictional or viscous forces ^[117], and hence represent a very attractive option for mesh-less particle schemes. First, the values of density, velocity, and position are calculated at the middle of the time step as:

$$\rho_i^{n+1/2} = \rho_i^n + \frac{1}{2} \Delta t D_i^n, \quad (2.33a)$$

$$\mathbf{U}_i^{n+1/2} = \mathbf{U}_i^n + \frac{1}{2} \Delta t \mathbf{F}_i^n, \quad (2.33b)$$

$$\mathbf{r}_i^{n+1/2} = \mathbf{r}_i^n + \frac{1}{2} \Delta t \mathbf{U}_i^n. \quad (2.33c)$$

The pressure at the half time-step $p_i^{n+1/2}$ is obtained from the equation of state. The SPH equations are then solved for new time derivatives at step $(n + 1/2)$, and in the second stage the following equations are used:

$$\rho_i^{n+1} = \rho_i^n \frac{\left(2\rho_i^{n+1/2} + D_i^{n+1/2} \Delta t\right)}{\left(2\rho_i^{n+1/2} - D_i^{n+1/2} \Delta t\right)}, \quad (2.34a)$$

$$\mathbf{U}_i^{n+1} = \mathbf{U}_i^n + \mathbf{F}_i^{n+1/2} \Delta t, \quad (2.34b)$$

$$\mathbf{r}_i^{n+1} = \mathbf{r}_i^n + \frac{\Delta t}{2} (\mathbf{U}_i^n + \mathbf{U}_i^{n+1}). \quad (2.34c)$$

Again, the pressure at the end of the time-step is obtained from the equation of state.

2.4.3 Solid boundary particles

The SPH code has two different lattice types for boundary particles, as shown in Figure 2.4. The type one lattice has a single layer of particles representing solid surface, while the type two lattice has a double layer of particles. For a given mass of the solid, the type two lattice particles have half the mass of lattice one particles. The reason for the second approach is to reduce penetration of fluid particles through the solid boundaries, especially for the Dalrymple ^[41] boundary condition. The two types of solid boundary conditions are described in the next paragraphs.

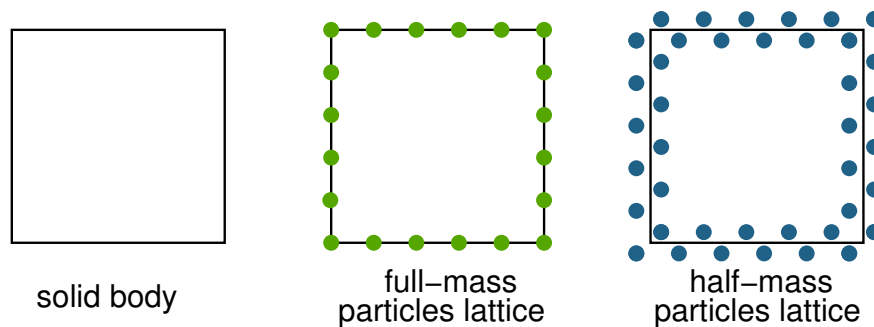


Figure 2.4: Two different lattice types for a square floating object.

Dalrymple boundary condition

This type of boundary condition was first proposed by Dalrymple ^[41]. In this method, boundary particles are forced to satisfy the same equations as fluid particles. However, they do not move according to Equation 2.28. Instead, the floating body particles are grouped, and together follow six degrees of freedom rigid

body motion. When a fluid particle approaches a solid boundary the density of the boundary particles is increased according to Equation 2.18. In return, the pressure is increased following the equation of state (Equation 2.27). Therefore, the force exerted on the fluid particle increases due to the pressure term p/ρ^2 in momentum equation (Equation 2.22 or 2.26). The force and moment about the centre of gravity of the floating body are obtained from the pressure. These are then used to solve for new velocity and position of the floating body and associated particles.

Repulsive force boundary condition

This boundary condition was developed by Monaghan ^[141] to ensure that a water particle can never cross a solid boundary. In this method, the force per unit mass between the fluid and solid particles has the form similar to the Lennard-Jones potential. In the original form ^[141], this boundary condition produces radial forces with bumps, making fluid particles bounce over each boundary particle. Modified formulation was proposed by Monaghan and Kos ^[142] to address this issue. The boundary particles are assigned a position and a local unit normal vector \mathbf{n} that points from the boundary into the fluid. The force per unit mass \mathbf{f} is then computed using the components of particles separation along the normal (denoted here by y) and along the tangent (denoted by x). The distances x and y are taken as positive, and the force is computed as

$$\mathbf{f} = \mathbf{n}R(y)P(x), \quad (2.35)$$

where $R(y)$ is designed to fall to zero as the spacing normal to the wall y is increased, and $P(x)$ is to ensure the constant force as the fluid particle moves parallel to the boundary. As proposed in ^[142]:

$$R(y) = \begin{cases} A \frac{1}{\sqrt{\frac{y}{2d}}} \left(1 - \frac{y}{2d}\right) & \text{if } \frac{y}{2d} < 1 \\ 0 & \text{otherwise} \end{cases} \quad (2.36)$$

where d is the initial particle spacing, and A is the parameter with dimensions of an acceleration. If fluid particle is denoted by i and boundary particle by j , then A is chosen as ^[142]:

$$A = \frac{1}{h} (0.01c^2 + c\mathbf{U}_{ij} \cdot \mathbf{n}_j). \quad (2.37)$$

Finally, the function $P(x)$ is given by

$$P(x) = \begin{cases} \frac{1}{2}(1 + \cos(\pi x/d)) & \text{if } x < d \\ 0 & \text{otherwise} \end{cases} \quad (2.38)$$

The advantage of the repulsive force boundary condition over the Dalrymple boundary condition is that the former reduces fluctuations of the forces acting on the floating object ^[213]. However, this comes with the increased computational cost. Also, the normal vector \mathbf{n} should be obtained for each boundary particle, which is often not trivial for complex geometries.

2.4.4 Computational efficiency and method overview

The outline of the SPH steps is shown in Figure 2.5. First, particles are distributed in the volume, where each particle has associated physical properties like mass, density, position and velocity. Next, a neighbour list is constructed to find the adjacent particles. This is done by splitting the computational domain into boxes of size κh , see Figure 2.5 for illustration. A list is then built of all the particles which are in each box. Since the kernel function limits the number of interacting particles, the interaction takes place only between the particles in adjacent boxes. In this way the number of calculations per time step and, therefore, the computational effort is reduced, from N^2 operations to $N \log N$, N being the total number of particles. Each particle is then visited once, and neighbouring particles within the range of the kernel are then chosen. Finally, the particles interaction is calculated and obtained field variables are used to update the physical properties of each particle.

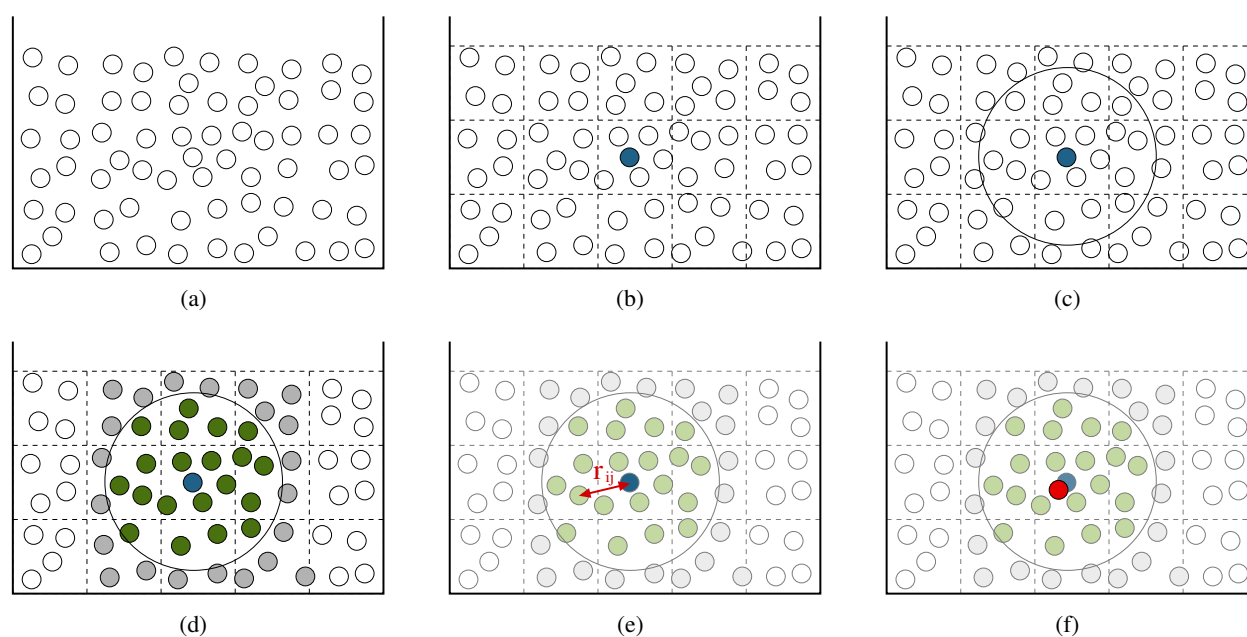


Figure 2.5: SPH method key steps - a) represent the problem domain by a set of particles b) use particle approximation and iteratively choose particle c) find all the particles close to the current particle d) flag the interaction particles e) solve the NS equations using all the particles within the support domain f) update the particle to its new position. Dashed lines represent data splitting into bins for efficient parallel computing.

Chapter 3

Aerodynamic simulation method

All aerodynamic computations were performed using the HMB3 flow solver developed at the University of Glasgow. The flow solver has been revised and updated over a number of years and has been successfully applied to a variety of problems including cavity flows, delta wing flows, flutter, maneuvering helicopters, and wind turbines amongst others.

3.1 CFD Solver

The HMB3 code is a 3D multi-block structured solver for the compressible Navier-Stokes equations using a Cartesian frame of reference. The Navier-Stokes equations consist of Partial Differential Equations (PDEs) describing the laws of conservation for:

- Mass (continuity equation).
- Momentum (Newton's 2nd Law).
- Energy (1st Law of Thermodynamics).

The continuity equation states that the mass is conserved, and in Cartesian coordinates, x_i , is written as:

$$\frac{\partial \rho}{\partial t} + \frac{\partial (\rho u_i)}{\partial x_i} = 0, \quad (3.1)$$

where ρ is the density of the fluid, t is the time and u_i is the velocity vector. In the above, Einstein's notation is used, which implies summation for repeated indices.

The second conservation principle states that momentum is conserved, and is written in Cartesian coordinates as:

$$\frac{\partial (\rho u_i)}{\partial t} + \frac{\partial (\rho u_i u_j)}{\partial x_j} = \rho f_i - \frac{\partial p}{\partial x_i} + \frac{\partial \tau_{ij}}{\partial x_j}, \quad (3.2)$$

where f_i represents the body forces, p the pressure and τ_{ij} the viscous stress tensor, which is defined as:

$$\tau_{ij} = \mu \left[\left(\frac{\partial u_i}{\partial x_j} + \frac{\partial u_j}{\partial x_i} \right) - \frac{2}{3} \delta_{ij} \frac{\partial u_k}{\partial x_k} \right], \quad (3.3)$$

where μ is the molecular viscosity and δ_{ij} represents the Kronecker delta, defined as:

$$\delta_{ij} = \begin{cases} 1, & \text{if } i=j \\ 0, & \text{otherwise.} \end{cases} \quad (3.4)$$

The third conservation principle can be written in Cartesian coordinates as

$$\frac{\partial \rho E}{\partial t} + \frac{\partial}{\partial x_j} [u_i (\rho E + p)] - \frac{\partial}{\partial x_j} (u_i \tau_{ij} - q_j) = 0, \quad (3.5)$$

where E is the total energy of the fluid, defined as

$$E = \left[e + \frac{1}{2} u_i u_i \right] \quad (3.6)$$

and e is the specific internal energy with $u_i u_i$ representing the kinetic energy.

The heat flux vector, q_i , is calculated using Fourier's Law

$$q_i = -k \frac{\partial T}{\partial x_i} \quad (3.7)$$

where k is the heat transfer coefficient and T is the temperature of the fluid.

These three laws of conservation can be combined and written in the equation shown below, which is referred to as the Navier-Stokes equation for viscous flow. For brevity, vector notation is used:

$$\frac{\partial \mathbf{W}}{\partial t} + \frac{\partial (\mathbf{F}^i + \mathbf{F}^v)}{\partial x} + \frac{\partial (\mathbf{G}^i + \mathbf{G}^v)}{\partial y} + \frac{\partial (\mathbf{H}^i + \mathbf{H}^v)}{\partial z} = S, \quad (3.8)$$

where \mathbf{W} is the vector of conserved variables and is defined by

$$\mathbf{W} = (\rho, \rho u, \rho v, \rho w, \rho E)^T, \quad (3.9)$$

with the variables ρ , u , v , w , p and E having their usual meaning of density, the three components of velocity, pressure and total energy, respectively. The superscripts i and v in Equation 3.8 denote the inviscid and viscous components of the flux vectors \mathbf{F} (in the x-direction), \mathbf{G} (in the y-direction) and \mathbf{H} (in the z-direction). The inviscid flux vectors, \mathbf{F}^i , \mathbf{G}^i and \mathbf{H}^i , are given by

$$\begin{aligned}\mathbf{F}^i &= (\rho u, \rho u^2 + p, \rho uv, \rho uw, u(\rho E + p))^T, \\ \mathbf{G}^i &= (\rho v, \rho uv, \rho v^2 + p, \rho vw, v(\rho E + p))^T, \\ \mathbf{H}^i &= (\rho w, \rho uw, \rho vw, \rho w^2 + p, w(\rho E + p))^T.\end{aligned}\tag{3.10}$$

while the viscous flux vectors, \mathbf{F}^v , \mathbf{G}^v and \mathbf{H}^v , contain terms for the heat flux and viscous forces exerted on the body and can be represented by

$$\begin{aligned}\mathbf{F}^v &= \frac{1}{\text{Re}} (0, \tau_{xx}, \tau_{xy}, \tau_{xz}, u\tau_{xx} + v\tau_{xy} + w\tau_{xz} + q_x)^T, \\ \mathbf{G}^v &= \frac{1}{\text{Re}} (0, \tau_{xy}, \tau_{yy}, \tau_{yz}, u\tau_{xy} + v\tau_{yy} + w\tau_{yz} + q_y)^T, \\ \mathbf{H}^v &= \frac{1}{\text{Re}} (0, \tau_{xz}, \tau_{yz}, \tau_{zz}, u\tau_{xz} + v\tau_{yz} + w\tau_{zz} + q_z)^T.\end{aligned}\tag{3.11}$$

where the term τ_{ij} represents the viscous stress tensor and q_i the heat flux vector.

S is the source term in Equation 3.8. For most calculations this term is set to 0, however, for hovering rotors, a fixed grid approach is used and a source term is then added. It is defined as:

$$S = [0, -\rho \boldsymbol{\omega} \times \mathbf{u}_h, 0]^T,\tag{3.12}$$

where \mathbf{u}_h is the local velocity field in the rotor-fixed frame of reference.

Although the Navier-Stokes equations completely describe turbulent flows, the large number of temporal and spatial turbulent scales associated with high Reynolds numbers make it difficult to resolve all the turbulent scales computationally. In such circumstances, the number of turbulent scales are reduced by time averaging the Navier-Stokes equations to give the Reynolds-Averaged Navier-Stokes equations (RANS). This results in additional unknowns (called Reynolds stresses) which must be modelled. The viscous stress tensor mentioned in Equation 3.11 is then approximated by the Boussinesq hypothesis, more description of which is provided in the following sections.

The HMB3 solver uses a cell-centred finite volume approach combined with an implicit dual-time method. In this manner, the solution marches in pseudo-time for each real time-step to achieve fast con-

vergence. According to the finite volume method, the RANS equations can be discretized for each cell by

$$\frac{d}{dt} (\mathbf{W}_{i,j,k} V_{i,j,k}) + \mathbf{R}_{i,j,k} = 0. \quad (3.13)$$

where $V_{i,j,k}$ denotes the cell volume and $\mathbf{R}_{i,j,k}$ represents the flux residual.

The implicit dual-time method proposed by Jameson^[80] is used for time-accurate calculations. The residual is redefined to obtain a steady state equation which can be solved using acceleration techniques.

The following system of equations are solved in the implicit scheme during the time integration process

$$\frac{\Delta V \mathbf{W}_{i,j,k}^{m+1} - \Delta V \mathbf{W}_{i,j,k}^m}{\Delta V \Delta \tau} \frac{\Delta V \mathbf{W}_{i,j,k}^{n+1} - \Delta V \mathbf{W}_{i,j,k}^n}{\Delta V \Delta t} = \mathbf{R}_{i,j,k}^{n+1} \quad (3.14)$$

where ΔV is the change in cell volume, $\Delta \tau$ is the pseudo time-step increment and Δt is the real time-step increment. The flux residual $\mathbf{R}_{i,j,k}^{n+1}$ is approximately defined by

$$\mathbf{R}_{i,j,k}^{n+1} \approx \mathbf{R}_{i,j,k}^n + \frac{\partial \mathbf{R}_{i,j,k}^n}{\partial \mathbf{W}_{i,j,k}^n} (\mathbf{W}_{i,j,k}^{n+1} - \mathbf{W}_{i,j,k}^n) \quad (3.15)$$

By substituting Equation 3.15 into Equation 3.14, the linear system can be approximated to

$$\left(\frac{1}{\Delta t} + \left(\frac{\partial \mathbf{R}}{\partial \mathbf{W}} \right)^n \right) \Delta \mathbf{W} = -\mathbf{R}^n \quad (3.16)$$

where the subscripts i, j, k have been dropped for clarity and ΔW is used for $(\mathbf{W}_{i,j,k}^{n+1} - \mathbf{W}_{i,j,k}^n)$.

3.1.1 Upwind schemes

Osher's upwind scheme^[156] is used to resolve the convective fluxes. Roe's flux-splitting scheme^[169] is also available. The MUSCL variable extrapolation method is employed in conjunction to formally provide third-order spacial accuracy. The van Albada limiter is also applied to remove any spurious oscillations across shock waves. The central differencing spatial discretisation method is used to solve the viscous terms. The non-linear system of equations resulting from the linearisation is then solved by integration in pseudo-time using a first-order backward difference. A Generalised Conjugate Gradient (GCG) method is then used in conjunction with a Block Incomplete Lower-Upper (BILU) factorisation as a pre-conditioner to solve the linear system of equations, which is obtained from a linearisation in pseudo-time.

Roe's flux-splitting scheme

Its popularity is due to its capability in resolving both shock waves and shear layers accurately in the Navier-Stokes solutions.

The flux-splitting method consists of splitting the flux F into a forward and backward flux, as $F(Q) = F^+(Q) + F^-(Q)$ where $\frac{\delta F^+}{\delta Q}$ has the positive eigenvalues and $\frac{\delta F^-}{\delta Q}$ has the negative ones.

The approximate Riemann solver is then, $\tilde{F}_{i+1/2} = F^+(Q_i) + F^-(Q_{i+1})$

The Euler equations, therefore, are replaced by the following linearised equation:

$$\frac{\delta Q}{\delta t} + \tilde{A}(Q_L, Q_R) \frac{\delta Q}{\delta x} = 0 \quad (3.17)$$

where $\tilde{A}(Q_L, Q_R)$ is a constant numerical Jacobian matrix, which is a function of the constant data states Q_L and Q_R in the local Riemann problem. The determinant of this matrix is obtained by using the Roe averages $\tilde{\rho}$, \tilde{u} , \tilde{h} and \tilde{a} , from the conserved variables at the right and left states.

Osher's scheme

This scheme is considered as a refinement of the flux splitting method; since it also excludes the expansion shock and the solver is continuously differentiable, which provides the possibility of using Newton-like methods of convergence.

The Osher's approximate Riemann solver is defined as

$$\tilde{F}^{OS}(Q_L, Q_R) = \frac{1}{2}(F(Q_L) + F(Q_R)) + \int_{Q_L}^{Q_R} |A|(Q) dQ \quad (3.18)$$

MUSCL scheme

It is based on a linear or quadratic distribution of $Q(x)$ in each cell. The formulas are given for the interface values as:

$$\begin{aligned}
Q_{i+1/2}^L &= Q_i + \frac{1}{4}(1-k)(Q_i - Q_{i-1}) + \frac{1}{4}(1+k)(Q_{i+1} - Q_i) \\
Q_{i+1/2}^R &= Q_{i+1} - \frac{1}{4}(1+k)(Q_{i+1} - Q_i) - \frac{1}{4}(1-k)(Q_{i+2} - Q_{i+1})
\end{aligned} \tag{3.19}$$

The first term on the right-hand side corresponds to the first order scheme; the additional terms include a dependence on the adjacent points, hence, a high order accuracy in space. In order to have a second-order accuracy, k should be different from $1/3$.

3.1.2 Parallel method

The flow solver can be used in serial or parallel mode. To obtain an efficient parallel method based on domain decomposition, different methods are applied to the flow solver ^[212]. An approximate form of the flux Jacobian resulting from the linearisation in pseudo-time is used which reduces the overall size of the linear system by reducing the number of non-zero entries. Between the blocks of the grid, the BILU factorisation is also decoupled thereby reducing the communication between processors. Each processor is also allocated a vector that contains all the halo cells for all the blocks in the grid. Message Passing Interface (MPI) is used for the communication between the processors in parallel.

3.1.3 Turbulence modelling

A number of linear and non-linear statistical turbulence models have been implemented into HMB3, including several one- and two- equation models. Turbulence simulation is also possible using either the Large-Eddy or the Detached-Eddy simulation approach ^[189, 188]. Some of these turbulence models and indeed the simulation techniques are described in greater detail in the following sections.

3.2 Reynolds Averaging

In this work the averaged Navier-Stokes equations were used. In a turbulent flow, the fields of pressure, velocity, temperature and density vary randomly in time. Reynold's approach involves separating the flow quantities into stationary and random parts. The quantities are then presented as a sum of the mean flow

value and the fluctuating part

$$\phi = \bar{\phi} + \phi' \quad (3.20)$$

This formulation is then inserted into the conservation equations and a process known as **Reynolds averaging** is performed. Three averaging methods are possible:

- Time averaging.
- Spatial averaging.
- Ensemble averaging.

Time averaging is used in this work.

3.2.1 Time Averaging

Time averaging is the most common averaging method. It can be used only for statistically stationary turbulent flows, i.e. flows not varying with time on the average. For such flows, the mean flow value is defined as

$$\bar{u}_i = \lim_{T \rightarrow \infty} \frac{1}{T} \int_i^{i+T} u_i(t) dt \quad (3.21)$$

In the above, $T \rightarrow \infty$ means that the integration time T needs to be long enough relative to the maximum period of the assumed fluctuations. In practice, it is assumed that the average value may be established in a relatively short time, a few seconds or perhaps a few milliseconds depending upon the flow. Therefore, for flows that exhibit a non-stationary character, provided that over the minimum necessary averaging time the change in average velocity is small, then an ensemble average may be used. This means that the time step should be chosen large enough for the average of turbulent fluctuations to be zero, and small enough to resolve unsteadiness of the mean flow. For wind turbine applications, the time step is often chosen as a time that is required for a rotor to cover an azimuth angle of $0.25 - 1^\circ$ ^[28, 29, 64]. This range is also used throughout this work.

3.3 Boussinesq-Based Models

The Boussinesq approximation is based on an analogy between viscous and Reynolds stresses and expresses the Reynolds stresses as a product of the eddy viscosity (μ_t) and the velocity gradient. The Boussinesq's eddy viscosity hypothesis states that

$$-\rho \overline{u'_i u'_j} = \mu_t \left[\left(\frac{\partial u_i}{\partial x_j} + \frac{\partial u_j}{\partial x_i} \right) - \frac{2}{3} \delta_{ij} \frac{\partial u_k}{\partial x_k} \right] - \frac{2}{3} \rho \delta_{ij} k \quad (3.22)$$

where k represents the specific kinetic energy of the fluctuations and is given by

$$k \equiv \frac{u'_i u'_i}{2} \quad (3.23)$$

The key idea behind Boussinesq's hypothesis is that the Reynolds stresses can be calculated as a product of the dynamic eddy-viscosity, μ_t , and the strain-rate tensor of the mean flow, i.e.

$$-\rho \overline{u'_i u'_j} = 2\mu_t S_{ij} - \frac{2}{3} \delta_{ij} k \quad (3.24)$$

where

$$S_{ij} = \frac{1}{2} \left(\frac{\partial u_i}{\partial x_j} + \frac{\partial u_j}{\partial x_i} - \frac{2}{3} \delta_{ij} \frac{\partial u_k}{\partial x_k} \right) \quad (3.25)$$

Eddy viscosity, μ_t , is a scalar and consequently the Reynolds stress components are linearly proportional to the mean strain-rate tensor. What is implied here is that compressibility plays a secondary role in the development of the turbulent flow-field. According to Morkovin's hypothesis ^[145], compressibility affects turbulence only at hypersonic speeds. To compute μ_t , the most popular models belong to the two-equation family.

3.4 Viscosity-Dependent Parameters

Non-dimensionalised wall distances for turbulent flow, y^* , and non-turbulent flow, y^+ , are defined by the following

$$y^* \equiv \frac{y_n k^{1/2}}{\nu}, \quad y^+ \equiv \frac{y_n u_\tau}{\nu}, \quad (3.26)$$

where y_n is the distance from the nearest wall, $u_\tau \equiv \sqrt{\tau_w/\rho}$ is the frictional velocity and τ_w represents the dynamic wall shear stress. Turbulent Reynolds numbers for the $k - \varepsilon$ model (denoted by Re_t) and for the

$k - \omega$ model (denoted by Re_ω) are given by the following equation

$$Re_t \equiv \frac{k^2}{\nu \varepsilon}, \quad Re_\omega \equiv \frac{k}{\nu \omega}. \quad (3.27)$$

3.5 Two-Equation Models

By far the most popular type of turbulence model used is of the two-equation type. Two-equation models are ‘complete’, i.e. can be used to predict properties of a given flow with no prior knowledge of the turbulence structure or flow geometry. Two transport equations are used for the calculation of the turbulent kinetic energy, k , and turbulence length scale, l , or a function of it. The choice of the 2nd variable is arbitrary and many proposals have been presented. The most popular involve using:

- ε — dissipation rate of turbulence.
- ω — k -specific dissipation rate.
- τ — turbulent time-scale.

A description of the different types of two-equation models is provided in Table 3.1 below. As well as indicating the variable used for the second transport equation, Table 3.1 includes the equation used to calculate the eddy viscosity.

Table 3.1: Different types of two-equation turbulence models and the corresponding second variable used

Two-Equation Model	Equation	2nd Variable Used
Kolmogorov (c. 1942) ^[100]	$k^{1/2}l^{-1}$	ω (Frequency Length Scale)
Rotta (c. 1950)	l	
Harlow-Nakayama (1968) ^[71]	$k^{3/2}l^{-1}$	ε (Energy Dissipation Rate)
Spalding (1969) ^[190]	kl^{-2}	ω^2 (Vorticity fluctuations squared)
Speziale (1992) ^[191]	$lk^{-1/2}$	τ (Time-Scale)
Nee	kl	kl (k times length scale)
Harlow-Nakayama	$lk^{-1/2}$	ν_t (Eddy viscosity)

One of the most widely used two-equation turbulence models is the $k - \varepsilon$ model. One of the original versions of this model was developed by Jones and Launder ^[87] in 1972. The turbulent scale in the $k - \varepsilon$

model is calculated using a second transport equation for the turbulent dissipation rate, ε . The eddy viscosity for the $k - \varepsilon$ model is typically derived from

$$\mu_T = C_\mu \rho \frac{k^2}{\varepsilon} \quad (3.28)$$

where C_μ is the model coefficient. The advantage of the $k - \varepsilon$ model is that it performs well for attached flows with thin shear layers and jets but fails to predict the correct flow behaviour in many flows with adverse pressure gradients, extended separated flow regions, swirl, buoyancy, curvature secondary flows and unsteady flows.

The other class of two-equation turbulence models that is widely used is the $k - \omega$ model. In 1988, Wilcox^[209] developed the famous $k - \omega$ model originally conceived by Kolmogorov. The $k - \omega$ model is similar to the $k - \varepsilon$ model but instead uses the k -specific dissipation rate as a second variable to compute the turbulent length scale. The eddy viscosity is obtained by

$$\mu_T = \rho \frac{k}{\omega} \quad (3.29)$$

Although the $k - \omega$ model provides better performance in adverse pressure gradient flows, it suffers largely from the same problems as the $k - \varepsilon$ model. Hybrid versions of the $k - \omega$ and $k - \varepsilon$ models called the Baseline $k - \omega$ and Shear Stress Transport (SST) models were later introduced by Menter^[137]. These, in particular the SST version, perform well in separated flows. The idea behind the Baseline $k - \omega$ model is to exploit the robust and accurate formulation of the $k - \omega$ model near the wall but to also take advantage of the lack of sensitivity to free-stream values of the $k - \varepsilon$ model away from the wall. Menter^[137] achieved this by transforming the $k - \varepsilon$ model into the same format as the $k - \omega$ formulation. This process generated an additional cross-diffusion parameter in the ω transport equation. For the SST model^[137], the idea was to improve the Baseline $k - \omega$ model by including terms to account for the transport of the principal shear stress. This term is incorporated in Reynolds Stress Models (RSM) and was also applied in the Johnson-King model^[85]. Its importance was realised based on the significantly improved results for adverse pressure gradient flows^[137]. For this reason, the $k - \omega$ SST model^[137] was employed in the simulations presented in this work, unless otherwise stated.

3.5.1 Model Equations: Linear $k - \omega$ Model

Mathematical formulations of the different types of the linear $k - \omega$ two-equation turbulence models discussed in the previous sections are described here. More information on the $k - \varepsilon$ and $k - g$ models can be obtained from Ref. ^[148].

Since the introduction of the linear $k - \omega$ model by Wilcox in 1988^[209], the other notable modification to the $k - \omega$ model came from Menter in 1994^[137] who proposed the hybridisation of the $k - \omega$ model with the $k - \varepsilon$ model, as described previously. Table 3.2 lists the four notable versions of the $k - \omega$ models and further describes if they include parameters to compute the low Reynolds number properties.

Table 3.2: Different types of linear $k - \omega$ turbulence models

Type of Model	Low-Re
Wilcox (1988) ^[209]	Yes
Wilcox (1994) ^[210]	Yes
Menter (1994) ^[137] — (i) Baseline Model	Yes
Menter (1994) ^[137] — (ii) SST Model	Yes

Turbulence transport equations used in the formulation of the $k - \omega$ models are given by the following.

$$\frac{\partial}{\partial t}(\rho k) + \frac{\partial}{\partial x_j}(\rho U_j k) = \frac{\partial}{\partial x_j} \left[\left(\mu + \frac{\mu_t}{\sigma_k} \right) \frac{\partial k}{\partial x_j} \right] + \rho (P - \beta^* \omega k) \quad (3.30)$$

$$\frac{\partial}{\partial t}(\rho \omega) + \frac{\partial}{\partial x_j}(\rho U_j \omega) = \frac{\partial}{\partial x_j} \left[\left(\mu + \frac{\mu_t}{\sigma_\omega} \right) \frac{\partial \omega}{\partial x_j} \right] + \rho \left(\frac{\alpha}{\nu_t} P - \frac{\beta}{\beta^* \omega^2} \right) + \rho S_l \quad (3.31)$$

In the transport equation for k and ω above, the production of turbulence, P , and the dissipation rate specific to k , P_ω , is defined by

$$P_k = \tau_{ij}^R \frac{\partial u_i}{\partial x_j}, \quad P_\omega = \rho \frac{\alpha}{\nu_t} P_k. \quad (3.32)$$

Values for the coefficients used in all the four types of linear $k - \omega$ models discussed here are given in the Tables 3.3 and 3.4.

Menter's models ^[137] are constructed as a 'blend' of the $k - \omega$ and $k - \varepsilon$ models. Here the $k - \varepsilon$ model is phrased in the same form as the $k - \omega$ model so as to exploit its independence of free-stream

Table 3.3: Values of constants used in linear $k - \omega$ models (continued)

Type of Model	α^*	β^*	α	β
Wilcox (1988) ^[209]	1	$\frac{9}{100}$	$\frac{5}{9}$	$\frac{3}{40}$
Wilcox (1994) ^[210]	$\frac{1}{40} + \frac{R\omega}{6}$	$\frac{9}{100} \frac{5}{18} + \left(\frac{R\omega}{8}\right)^4$	$\frac{5}{9} \frac{1}{10} + \frac{R\omega}{2.7}$	$\frac{3}{40}$
Menter (1994) ^[137] (<i>Baseline</i>) ¹	1	0.09	$B \begin{pmatrix} 0.553 \\ 0.440 \end{pmatrix}$	$B \begin{pmatrix} 0.075 \\ 0.083 \end{pmatrix}$
Menter (1994) ^[137] (<i>SST</i>) ²	$\min \left(1, \frac{0.31}{F_2} \frac{\omega}{w} \right)$	0.09	$B \begin{pmatrix} 0.553 \\ 0.440 \end{pmatrix}$	$B \begin{pmatrix} 0.075 \\ 0.083 \end{pmatrix}$

Table 3.4: Values of constants used in linear $k - \omega$ models (concluded)

Type of Model	σ_k	σ_ω	S_1
Wilcox (1988) ^[209]	2	2	0
Wilcox (1994) ^[210]	2	2	0
Menter (1994) ^[137] (<i>Baseline</i>) ¹	$B \begin{pmatrix} 1 \\ 0.5 \\ 1.0 \end{pmatrix}$	$B \begin{pmatrix} 1 \\ 0.5 \\ 0.856 \end{pmatrix}$	$B \begin{pmatrix} 0 \\ \frac{1.71}{\omega} \nabla k \cdot \nabla \omega \end{pmatrix}$
Menter (1994) ^[137] (<i>SST</i>) ²	$B \begin{pmatrix} 1 \\ 0.85 \\ 1.0 \end{pmatrix}$	$B \begin{pmatrix} 1 \\ 0.5 \\ 0.856 \end{pmatrix}$	$B \begin{pmatrix} 0 \\ \frac{1.71}{\omega} \nabla k \cdot \nabla \omega \end{pmatrix}$

values. Blending of the $k - \varepsilon$ and $k - \omega$ model values for α , β , σ_k^{-1} and σ_ω^{-1} is (in this notation) given by the following equation

$$B \begin{pmatrix} a \\ b \end{pmatrix} \equiv F_1 a + (1 - F_1) b. \quad (3.33)$$

The blending function is defined by

$$F_1 = \tanh(\arg_1^4), \quad (3.34)$$

where

$$\arg_1 = \min \left[\max \left(\frac{k^{1/2}}{\beta^* \omega y}, \frac{500\nu}{y_n^2 \omega} \right), \frac{2k\omega}{y_n^2 \max(\nabla k \cdot \nabla \omega, 0.0)} \right]. \quad (3.35)$$

The SST model places an additional vorticity-dependent limiter on the shear stress

$$F_2 = \tanh(\arg_2^2), \quad \arg_2 = \max \left(\frac{2k^{1/2}}{\beta^* \omega y}, \frac{500\nu}{y^2 \omega} \right). \quad (3.36)$$

Note that this model also uses a slightly different value of σ_k .

For low-Reynolds number versions of the $k - \omega$ model and Menter's Baseline $k - \omega$ and SST models, the following boundary conditions are assumed for a direct integration to the wall

$$\text{For } k: \quad k_w = 0, \quad flux(k)_w = 0. \quad (3.37)$$

$$\text{For } \omega: \quad \omega = 0, \quad flux(\omega)_w = -\nu \nabla \omega. \quad (3.38)$$

where the subscript w denotes the value *at* the wall.

3.6 CSD solver

This section presents the employed Computational Structural Dynamics (CSD) solver, and the fluid structure interaction (FSI) approach. First, the structural model of the blade is described along with the structure-fluid mapping and the grid deformation techniques. Then, the numerical procedures for steady and unsteady cases are described.

3.6.1 Blade structural model

Under the assumption that the blade structural properties are mainly distributed in the span-wise direction and that the span is much longer than the chord, and the aerofoil thickness, a WT blade can be modelled as a beam. For this reason, the structure of the blade is represented by a set of tapered beam elements (*CBEAM*-type) using *NASTRAN*^[6], as shown in Figure 3.1. Each beam contains *PBEAM* structural properties. Typically, the following properties are included in the blade's structural model:

- area of the beam cross section (A),
- chord-wise (or edge-wise) and flap-wise area moment of inertia (I_1, I_2),
- torsional stiffness (J),
- linear mass distribution (dm),
- location of the shear centre relative to the actual node location (\vec{w}_a, \vec{w}_b) to allow for the shear centre off-set,

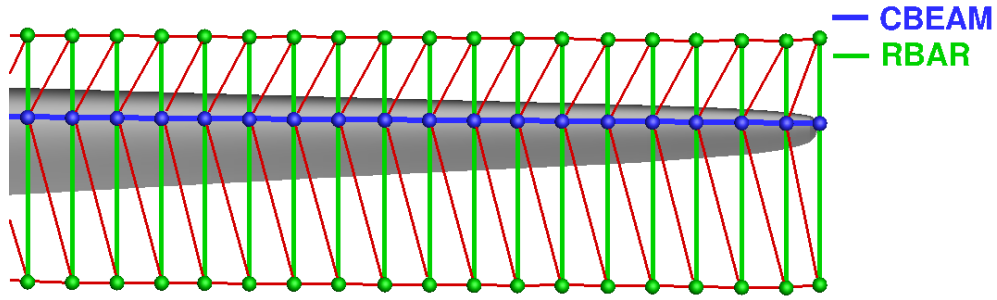


Figure 3.2: The DTU 10MW RWT blade with the structural model consisting of beams, bars, and triangular elements.

3.6.2 Grid deformation method

The structural model of the blade contains fewer elements than the blade surface on the fluid mesh. Therefore, the structural solution has to be interpolated on the blade surface. The deformation of the fluid mesh is done in three main steps, as described in greater detail by Dehaeze *et al.* [47]. Firstly, the constant volume tetrahedron (CVT) method is used to interpolate the deformed shape of the blade surface. Secondly, the block vertices are moved accordingly to the spring analogy method (SAM). Finally, the full mesh is regenerated with a trans-finite interpolation (TFI). The TFI first interpolates the block edges and faces from their new vertex positions and then interpolates the full mesh from the surfaces. This method uses the properties of multi-block meshes and maintains efficiency as the number of blocks increases. The use of spring analogy on the block vertices only allows for efficient calculation, large deformations of the blade and good mesh quality. Alternatively to the TFI method, the Inverse Distance Weighting (IDW) method can be used.

Constant Volume Tetrahedron

The Constant Volume Tetrahedron (CVT) method was first developed by Goura^[65]. This method projects each fluid node to the nearest structural triangular element and moves it linearly with the element. The first step for calculating the transformation is finding the nearest triangular element (S_1, S_2, S_3) to each fluid point (F) as shown in Figure 3.3. Then, the location of the fluid element can be expressed as follows:

$$\mathbf{c} = \alpha\mathbf{a} + \beta\mathbf{b} + \gamma\mathbf{d} \quad (3.39)$$

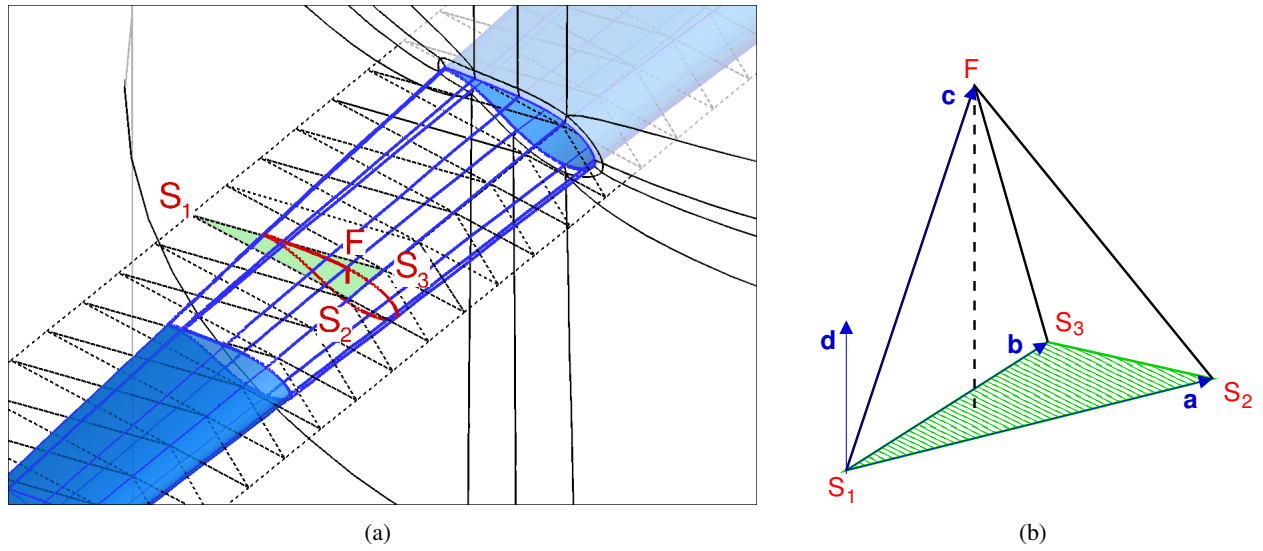


Figure 3.3: Projection of the fluid grid on the structural model through Constant Volume Tetrahedron (CVT) method.

where $\mathbf{a} = \overrightarrow{S_1 S_2}$, $\mathbf{b} = \overrightarrow{S_1 S_3}$, $\mathbf{c} = \overrightarrow{S_1 F}$, and $\mathbf{d} = \mathbf{a} \times \mathbf{b}$ are known. The coefficients α , β and γ can then be expressed as functions of vectors \mathbf{a} , \mathbf{b} , \mathbf{c} and \mathbf{d} as:

$$\alpha = \frac{(\mathbf{a} \cdot \mathbf{c}) \|\mathbf{b}\|^2 - (\mathbf{a} \cdot \mathbf{b})(\mathbf{b} \cdot \mathbf{c})}{\|\mathbf{a}\|^2 \|\mathbf{b}\|^2 - (\mathbf{a} \cdot \mathbf{b})^2}, \quad (3.40a)$$

$$\beta = \frac{(\mathbf{b} \cdot \mathbf{c}) \|\mathbf{a}\|^2 - (\mathbf{a} \cdot \mathbf{b})(\mathbf{a} \cdot \mathbf{c})}{\|\mathbf{a}\|^2 \|\mathbf{b}\|^2 - (\mathbf{a} \cdot \mathbf{b})^2}, \quad (3.40b)$$

$$\gamma = \frac{(\mathbf{c} \cdot \mathbf{d})}{\|\mathbf{a}\|^2 \|\mathbf{b}\|^2 - (\mathbf{a} \cdot \mathbf{b})^2}. \quad (3.40c)$$

The new position of the deformed blade fluid point is obtained by:

$$\mathbf{c}' = \alpha \mathbf{a}' + \beta \mathbf{b}' + \gamma \mathbf{d}' \quad (3.41)$$

where \mathbf{a}' , \mathbf{b}' and \mathbf{d}' are the same vectors after the structural deformation.

Spring Analogy Method

The spring Analogy Method (SAM)^[23] consists of adding springs on each surface side and diagonal of the mesh blocks, see Figure 3.4. The springs along the sides of the surfaces tend to avoid large compression or dilatation of the block surfaces and the ones on the diagonals tend to limit block skewness.

The strength of the springs is set as the inverse of their length and the springs in contact with the blade are usually made stiffer in order to make the blocks close to the blade surface extremely rigid. The

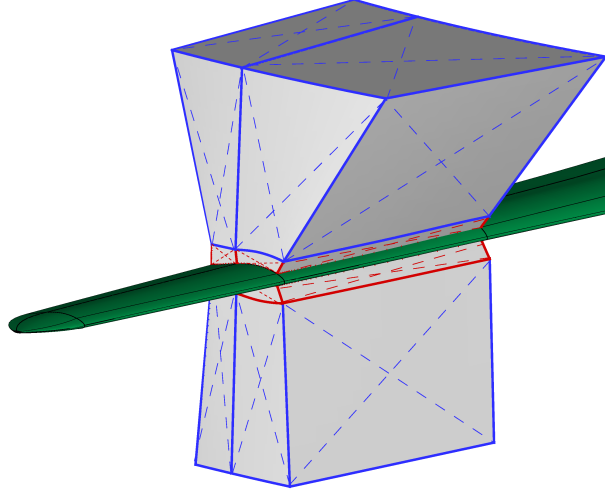


Figure 3.4: Spring Analogy Method (SAM) to obtain the updated block vertex positions. Dashed lines represent springs on the block faces.

force on each vertex is calculated as the sum of the forces due to the neighbouring springs:

$$\mathbf{F}_i = \sum_{j=1}^{n_i} k_{ij} (\boldsymbol{\delta}_j - \boldsymbol{\delta}_i), \quad (3.42)$$

where k_{ij} is the stiffness of the spring between i -th and j -th nodes, $\boldsymbol{\delta}_i$ is the displacement vector of the i -th node, and n_i is the number of vertices linked by springs to the i -th node. The displacement of the nodes on the blade surface is obtained from the CVT method. Then, the nodes on the blade and the far-field are fixed, and the new equilibrium position of the interior nodes is obtained by solving for each node the equation:

$$\sum_{j=1}^{n_i} \mathbf{F}_{ij} = \mathbf{0}, \quad (3.43)$$

where \mathbf{F}_{ij} is the force exerted on the i -th node by the spring between the i -th and j -th nodes and is defined by $\mathbf{F}_{ij} = k_{ij}(\boldsymbol{\delta}_j - \boldsymbol{\delta}_i)$. The iterative process is employed to solve for equilibrium vertices position and is initialised with the vertices located in the original grid except for vertices on the blade surface which are moved to the deformed position.

Trans-Finite Interpolation

The Trans-Finite Interpolation (TFI), described by Dubuc *et al.* ^[49], is used for interpolating the deformed mesh. For this, the face deformations are interpolated from the edge deformations, and then the full block

deformation from the deformation of the block faces. The mesh deformation uses a weighted approach to interpolate a face/block from the boundary vertices/surfaces respectively. The weight depends on the curvilinear coordinate divided by the length of the curve, whose notation is shown in Figure 3.5. Following this notation, the generation of the mesh on a block face, x_1 , x_2 , x_3 and x_4 , can be expressed as:

$$dx(\xi, \eta) = f_1(\xi, \eta) + \phi_1^0(\eta)[dx_1(\xi) - f_1(\xi, 0)] + \phi_2^0(\eta)[dx_3(\xi) - f_1(\xi, 1)], \quad (3.44)$$

where, f_1 is defined as,

$$f_1(\xi, \eta) = \psi_1^0(\xi)dx_4(\eta) + \psi_2^0(\xi)dx_2(\eta) \quad (3.45)$$

with dx_1 , dx_2 , dx_3 and dx_4 , representing the displacements of the four corners of a face and ϕ and ψ the blending functions in the η and ξ directions.

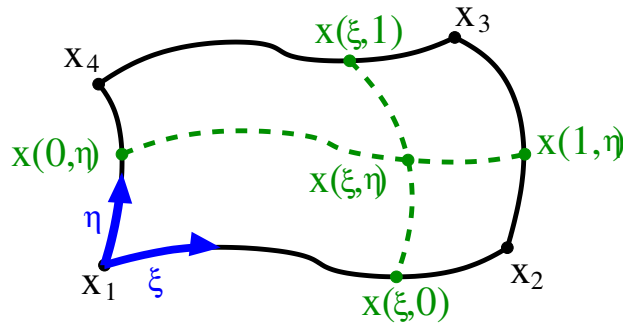


Figure 3.5: Notation of a block face for Transfinite Interpolation (TFI) for full mesh generation.

A more detailed description can be found in reference ^[49]. The method uses the properties of multi-block meshes to maintain its efficiency as the number of blocks increases, particularly in the span-wise blade direction. It provides flexibility, and allows for complex multi-block topologies to be used with good control over the distribution of mesh deformation all over the computational domain.

Summary and efficiency

This three-step grid deformation method preserves the quality of the mesh, avoiding high cell skewness and drastic change of cell volumes. Figure 3.6 shows the changes on the cell volumes and skewness of the grid for the DTU 10MW wind turbine^[11] with 8.5m displacement at the tip. The cell volume and skewness ratios

were computed as:

$$r_V = \frac{V_{deformed}}{V_{undeformed}}, \quad (3.46a)$$

$$r_S = \frac{S_{deformed}}{S_{undeformed}}, \quad (3.46b)$$

where V is the cell volume, and S is the cell skewness, chosen as the maximum norm of the scalar product of the vectors normal to the cell face.

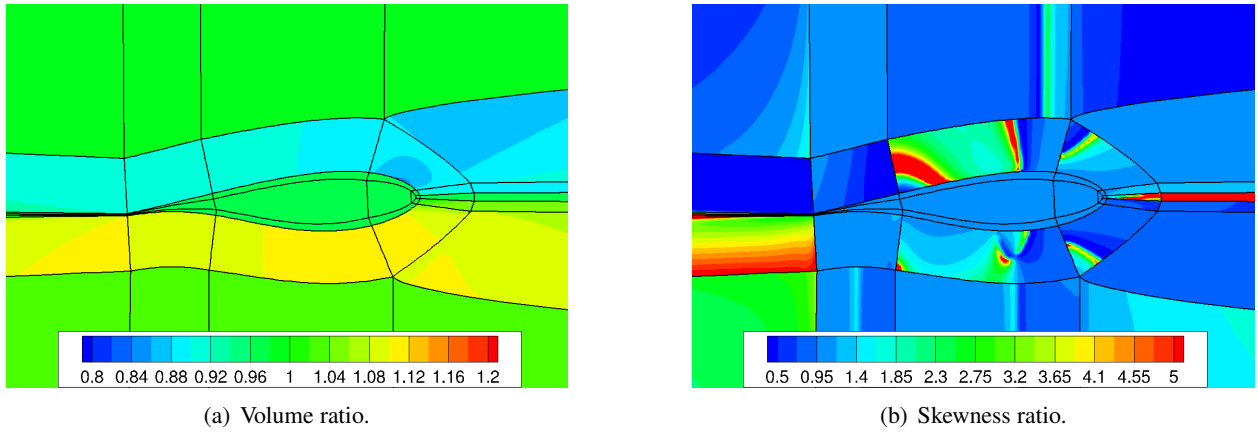
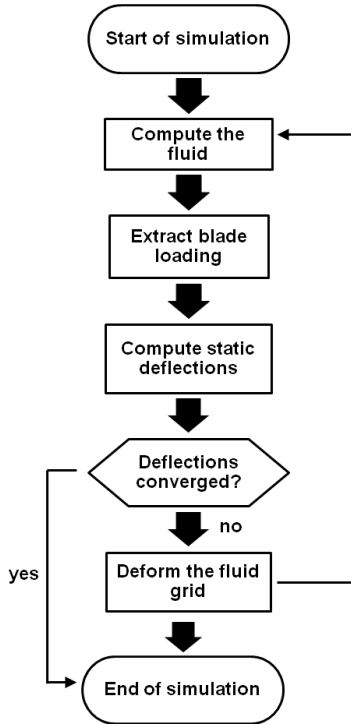


Figure 3.6: Cell volume ration (a), and skewness ratio (b) between deformed and undeformed grids at the tip of the DTU 10MW RWT blade. Tip displacement $8.5m$.

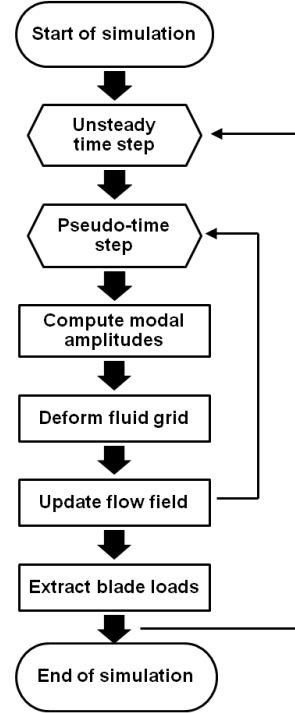
3.6.3 Steady FSI method

Steady aero-elastic coupling is realised using an iterative method, shown in Figure 3.7(a). *NASTRAN*^[6] is used as the structural solver, using the non-linear solution sequence *SOL106* to solve for the blade shape. The eigenvectors are extracted with the modified GIVens (MGIV) method^[44]. This is followed by an iterative process allowing for the large displacements to be taken into account while recomputing the forces due to the aerodynamic and centrifugal forces at each step. For CFD/CSD exchange, the aerodynamic loading is first extracted from the fluid grid, using a sectional pressure integration. *NASTRAN* is then used to compute the deformed shape of the blade with the loads introduced as *PLOAD* elements (linear loading between both ends of the beam). This new shape is applied to the fluid grid using the mesh deformation method described in Section 3.6.2. The process is repeated until the shape of the blade and the aerodynamic loads converge to a final value, as described in reference ^[45]. Figure 3.7(a) shows a diagram of this process. The advantage of

this method is that a non-linear structural solution is always performed.



(a) Aero-elastic coupling strategy for steady case.



(b) Strong (implicit) fluid-structure coupling scheme for unsteady aero-elasticity.

Figure 3.7: Diagram of the static (a), and dynamic (b) aero-elastic coupling method employed in the HMB solver.

3.6.4 Unsteady FSI method

For unsteady aero-elastic coupling, the modal approach is used to lower the cost of computing the blade deformations. It expresses the blade deformation as a function of the blade eigenmodes. The blade shape is then described as a sum of eigenvectors ϕ_i representing the blade displacements for each eigenmode multiplied by the coefficient α_i :

$$\phi = \phi_0 + \sum_{i=1}^{n_m} \alpha_i \phi_i, \quad (3.47)$$

where ϕ_0 is the undeformed eigenvector, and n_m is the number of modes. The problems is then reduced to solving for the coefficients α_i . Following the modal approach, those coefficients can be obtained by solving the second order differential equation

$$\frac{\partial^2 \alpha_i}{\partial t^2} + 2\zeta_i \omega_i \frac{\partial \alpha_i}{\partial t} + \omega_i^2 \alpha_i = \mathbf{f} \phi_i, \quad (3.48)$$

whose derivatives are discretized as follows:

$$\left[\frac{\partial \alpha_i}{\partial t} \right]_t = \frac{3[\alpha_i]_t - 4[\alpha_i]_{t-1} + [\alpha_i]_{t-2}}{2\Delta t}, \quad (3.49a)$$

$$\left[\frac{\partial^2 \alpha_i}{\partial t^2} \right]_t = \frac{3 \left[\frac{\partial \alpha_i}{\partial t} \right]_t - 4 \left[\frac{\partial \alpha_i}{\partial t} \right]_{t-1} + \left[\frac{\partial \alpha_i}{\partial t} \right]_{t-2}}{2\Delta t}, \quad (3.49b)$$

where \mathbf{f} is the vector of external forces applied to the blade projected at each structural node, ω_i is the eigenfrequency and ζ_i is the structural damping coefficient, which tends to be small. For stability purposes, the analysis is usually starting with strong damping of $\zeta_i = 0.7$ for each mode, to damp the oscillations created by the sudden change in the forcing applied to the system. Once the blade reaches a level of deformation of 80 – 90%, often after a half of revolution, the damping is reduced to smaller values (e.g. $\zeta_i = 0.03$) [44]. At each pseudo-time step of the employed dual time-step method, the modal amplitudes are computed by solving the discretized Equation (3.48), which results in Equation (3.50),

$$\begin{bmatrix} 2\zeta_i \omega_i + \frac{3}{2\Delta t} & \omega^2 \\ -1 & \frac{3}{2\Delta t} \end{bmatrix} \begin{pmatrix} \left[\frac{\partial \alpha_i}{\partial t} \right]_t \\ (\alpha_i)_t \end{pmatrix} = \begin{pmatrix} [f_i^s]_t + \frac{4 \left[\frac{\partial \alpha_i}{\partial t} \right]_{t-1} - \left[\frac{\partial \alpha_i}{\partial t} \right]_{t-2}}{2\Delta t} \\ \frac{4[\alpha_i]_{t-1} - [\alpha_i]_{t-2}}{2\Delta t} \end{pmatrix}, \quad (3.50)$$

the CFD grid is deformed using the method described in Section 3.6.2 and the flow field updated by solving the N-S equations. At the end of each time step, the blade loads are extracted and re-applied to the system. This process is performed repeatedly until the end of the computation, as shown in Figure 3.7(b). The method is efficient since it involves *NASTRAN* only once, but assumes that the modes are unchanged during the unsteady solution.

Chapter 4

Multi-body simulation method

In this work, the wind turbine dynamics is modelled using a multi-body formulation of rigid bodies and frictionless joints. For this reason, a Multi-Body Dynamic Module (MBDM) was developed. This chapter describes the mathematical concept behind the MBDM and explains how the resulting system of differential algebraic equations is solved. The theory presented here is mostly based on the textbooks of Haug ^[73] and Nikravesh ^[153].

4.1 Concept and essential formulation

The basic assumptions employed in MBDM are that bodies under consideration are rigid, and all joints are frictionless.

Each body is assigned a local coordinate system, which is attached to the body and follows its translational and rotational motions. The position and orientation of each body is then described in a global coordinate system by seven quantities: a vector $\mathbf{r} = [x, y, z]^T$ pointing to the local coordinate system of the body, and the Euler parameters $\mathbf{p} = [e_0, e_1, e_2, e_3]^T \equiv [e_0, \mathbf{e}]^T$ indicating orientation of body frame in global coordinate system. According to Euler's theorem^[50], any orientation of body can be achieved by a single rotation from the reference orientation about some axis. Thus, the Euler parameters define an axis of rotation

\mathbf{u} , and an angular displacement χ about the axis as:

$$e_0 = \cos \frac{\chi}{2}, \quad (4.1a)$$

$$e_1 = u_x \sin \frac{\chi}{2}, \quad (4.1b)$$

$$e_2 = u_y \sin \frac{\chi}{2}, \quad (4.1c)$$

$$e_3 = u_z \sin \frac{\chi}{2}. \quad (4.1d)$$

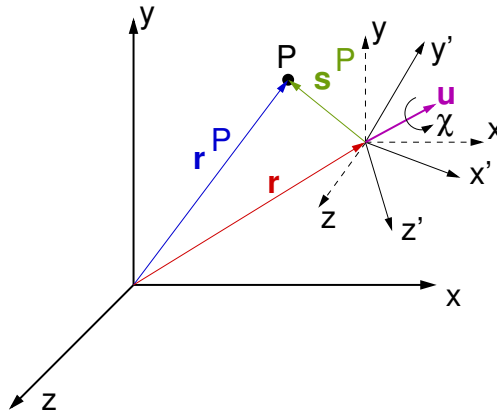


Figure 4.1: Translation and rotation of a reference frame.

Any given vector \mathbf{s}' in the body coordinate system (the superscript " ' " denotes vectors defined in body-fixed reference frame) can be transferred to the global coordinate system vector \mathbf{s} using transformation matrix \mathbf{A} , which is given by:

$$\mathbf{A} = 2 \begin{bmatrix} e_0^2 + e_1^2 - \frac{1}{2} & e_1 e_2 - e_0 e_3 & e_1 e_3 + e_0 e_2 \\ e_1 e_2 + e_0 e_3 & e_0^2 + e_2^2 - \frac{1}{2} & e_2 e_3 - e_0 e_1 \\ e_1 e_3 - e_0 e_2 & e_2 e_3 + e_0 e_1 & e_0^2 + e_3^2 - \frac{1}{2} \end{bmatrix}. \quad (4.2)$$

\mathbf{A} is a rotational matrix, which becomes an identity matrix if both frames of reference coincide. Therefore, if a point P is described by a vector \mathbf{s}'^P in the body local reference frame, the location of this point \mathbf{r}^P in the global coordinate frame can be found by the following expression:

$$\mathbf{r}^P = \mathbf{r} + \mathbf{A} \mathbf{s}'^P, \quad (4.3)$$

where $\mathbf{r} = [x, y, z]^T$ is the vector pointing to the location of body local coordinate system, as defined previously and shown in Figure 4.1. This simple relation forms basis for the constraint equations of motion for

multi-body model. Also, as can be easily shown, the transformation matrix is orthogonal i.e. $\mathbf{A}^{-1} = \mathbf{A}^T$, which simplifies the reverse transformation of a vector from the global to the local reference frame of the body.

4.1.1 Joint definition frames

First, let us consider a body denoted by i and shown in Figure 4.2. Its (x'_i, y'_i, z'_i) body-fixed reference frame

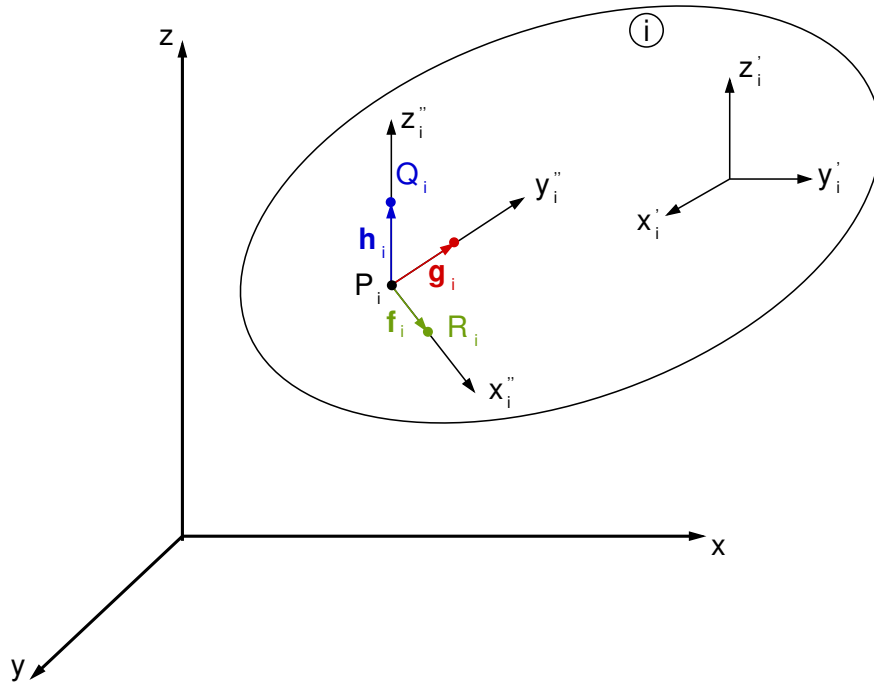


Figure 4.2: Construction of a joint definition frame.

is used to position and orient the body in the global reference frame. A second frame (x''_i, y''_i, z''_i) is attached to the body, with its origin at point P_i and is called *joint definition frame*. To orient the (x''_i, y''_i, z''_i) frame, the unit vectors \mathbf{f}_i , \mathbf{g}_i and \mathbf{h}_i are defined along its coordinate axes. To define \mathbf{h}_i , a point Q_i is defined on the z''_i axis, at unit distance from point P_i . To define \mathbf{f}_i , a point R_i is defined on the x''_i axis, at unit distance from point P_i . Finally, the vector $\mathbf{g}_i = \mathbf{h}_i \times \mathbf{f}_i = \tilde{\mathbf{h}}\mathbf{f}_i$, where $\tilde{\mathbf{h}}$ is a skew-symmetric matrix, associated with an algebraic vector $\mathbf{h} = [h_x, h_y, h_z]^T$ and is defined as:

$$\tilde{\mathbf{h}} = \begin{bmatrix} 0 & -h_z & h_y \\ h_z & 0 & -h_x \\ -h_y & h_x & 0 \end{bmatrix}. \quad (4.4)$$

In terms of the unit vectors \mathbf{f}'_i , \mathbf{g}'_i and \mathbf{h}'_i , represented in the (x'_i, y'_i, z'_i) frame, the transformation matrix from the (x''_i, y''_i, z''_i) frame to the (x'_i, y'_i, z'_i) frame is obtained as

$$\mathbf{C}_i^P = [\mathbf{f}'_i, \mathbf{g}'_i, \mathbf{h}'_i]. \quad (4.5)$$

4.1.2 Basic kinematic constraints

In this subsection, the mathematical expressions of the kinematic constraints on the absolute position and orientation of bodies in space, and on relative position and orientation of a pair of bodies connected by joints, are derived.

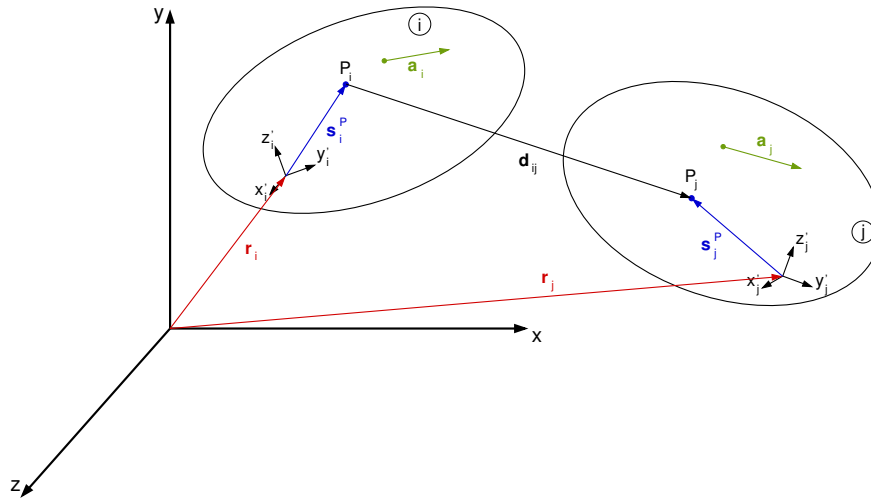


Figure 4.3: Position vectors \mathbf{r}_i and \mathbf{r}_j , vector between bodies \mathbf{d}_{ij} , and body fixed vectors \mathbf{a}_i and \mathbf{a}_j .

There are four basic constraints that relate two vectors or points defined in two different coordinate frames. The first is the orthogonality of two body-fixed, nonzero, vectors \mathbf{a}_i and \mathbf{a}_j on bodies i and j , respectively, as shown in Figure 4.3. The two vectors are orthogonal if their scalar product is zero:

$$\Phi^{d1}(\mathbf{a}_i, \mathbf{a}_j) \equiv \mathbf{a}_i^T \mathbf{a}_j = 0 \quad (4.6)$$

where the superscript "d1" indicated the first form of dot product condition. Writing the vectors \mathbf{a}_i and \mathbf{a}_j in terms of their respective body reference frames using transformation matrices, $\mathbf{a}_i = \mathbf{A}_i \mathbf{a}'_i$ and $\mathbf{a}_j = \mathbf{A}_j \mathbf{a}'_j$, Equation 4.6 may be then written as

$$\Phi^{d1}(\mathbf{a}_i, \mathbf{a}_j) = \mathbf{a}'_i{}^T \mathbf{A}_i^T \mathbf{A}_j \mathbf{a}'_j = 0 \quad (4.7)$$

The dot product condition can also be used to prescribe the orthogonality of a body-fixed vector \mathbf{a}_i and a vector \mathbf{d}_{ij} between bodies, as shown in Figure 4.3, provided $\mathbf{d}_{ij} \neq \mathbf{0}$. This condition is expressed as:

$$\Phi^{d2}(\mathbf{a}_i, \mathbf{d}_{ij}) = \mathbf{a}_i^T \mathbf{d}_{ij} = \mathbf{a}_i'^T \mathbf{A}_i^T (\mathbf{r}_j + \mathbf{A}_j \mathbf{s}_j'^P - \mathbf{r}_i) - \mathbf{a}_i'^T \mathbf{s}_i'^P = 0 \quad (4.8)$$

where transition to the right-hand-side is achieved by writing the vector \mathbf{d}_{ij} as:

$$\mathbf{d}_{ij} = \mathbf{r}_j + \mathbf{A}_j \mathbf{s}_j'^P - \mathbf{r}_i - \mathbf{A}_i \mathbf{s}_i'^P, \quad (4.9)$$

and applying basic mathematical transformations. It is important to recall that the orthogonality condition of Equation 4.8 breaks down if $\mathbf{d}_{ij} = \mathbf{0}$.

It is often required that two points defined on two different bodies coincide. The condition for points P_i and P_j to coincide is that vector $\mathbf{d}_{ij} = \mathbf{0}$, as shown in Figure 4.3. This is mathematically expressed as

$$\Phi^S(P_i, P_j) = \mathbf{r}_j + \mathbf{A}_j \mathbf{s}_j'^P - \mathbf{r}_i - \mathbf{A}_i \mathbf{s}_i'^P = \mathbf{0} \quad (4.10)$$

where the superscript S indicates the use of this equation to define a spherical joint. Note that this vector equation consists of three scalar equations.

Finally, the constraint on the distance between a pair of points on adjacent bodies is derived. A condition that the distance between points P_i and P_j in Figure 4.3 be equal to $C \neq 0$ has a form of

$$\Phi^{SS}(P_i, P_j, C) = \mathbf{d}_{ij}^T \mathbf{d}_{ij} - C^2 = 0 \quad (4.11)$$

Note that if $C = 0$, the Jacobian of this constraint equation has all elements equal to 0 i.e. it does not have full row rank and cannot be used for kinematic analysis. For this reason, use of distance constraint is restricted to the case $C \neq 0$.

The four basic constraint equations derived so far form the foundation for defining a library of kinematic constraints between bodies. Two parallelism conditions are additionally derived.

First, let us consider two bodies with joint definition frames defined, as shown in Figure 4.4. Next, let the z_i'' and z_j'' axes be required to be parallel. It is equivalent to requirement of the vectors \mathbf{h}_i and \mathbf{h}_j to be parallel. The vector \mathbf{h}_j is parallel to \mathbf{h}_i if and only if it is orthogonal to \mathbf{f}_i and \mathbf{g}_i . This condition can be expressed as

$$\Phi^{p1}(\mathbf{h}_i, \mathbf{h}_j) = \begin{bmatrix} \Phi^{d1}(\mathbf{f}_i, \mathbf{h}_j) \\ \Phi^{d1}(\mathbf{g}_i, \mathbf{h}_j) \end{bmatrix} = \mathbf{0} \quad (4.12)$$

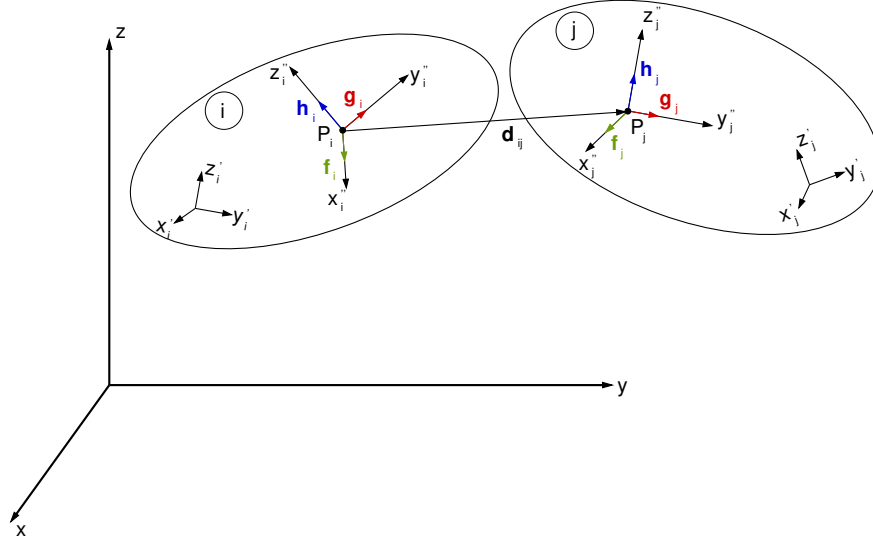


Figure 4.4: Parallel vectors on and between adjacent bodies.

Finally, consider the condition that vector the \mathbf{h}_j is parallel to vector \mathbf{d}_{ij} , in accordance to the schematic in Figure 4.4. The vector $\mathbf{d}_{ij} \neq \mathbf{0}$ is parallel to \mathbf{h}_j if and only if it is perpendicular to \mathbf{f}_i and \mathbf{g}_i :

$$\Phi^{p2}(\mathbf{h}_i, \mathbf{d}_{ij}) = \begin{bmatrix} \Phi^{d2}(\mathbf{f}_i, \mathbf{d}_{ij}) \\ \Phi^{d2}(\mathbf{g}_i, \mathbf{d}_{ij}) \end{bmatrix} = \mathbf{0} \quad (4.13)$$

Note that this constraint breaks down if $\mathbf{d}_{ij} = \mathbf{0}$, since the orthogonality constraint (Equation 4.8) breaks down in this case.

4.1.3 Absolute constraints on a body

Absolute constraints may be placed on the position of the point P_i of body i , and on the orientation of the local coordinate frame of body i . Six such constraint equations on individual generalised coordinates of a body i may be expressed as:

$$\begin{aligned} \Phi^1 &= x_i^P - x_i^0 = 0, \\ \Phi^2 &= y_i^P - y_i^0 = 0, \\ \Phi^3 &= z_i^P - z_i^0 = 0, \\ \Phi^4 &= e_{1i} - e_{1i}^0 = 0, \\ \Phi^5 &= e_{2i} - e_{2i}^0 = 0, \\ \Phi^6 &= e_{3i} - e_{3i}^0 = 0, \end{aligned} \quad (4.14)$$

where the vector $\mathbf{r}_i^P = [x_i^P, y_i^P, z_i^P]^T$ is defined in the global reference frame and depends on vectors \mathbf{r}_i and \mathbf{s}_i^P through Equation 4.3. Therefore, absolute constraints on the position and orientation may be rewritten as

$$\Phi^{123} = \mathbf{r}_i + \mathbf{A}_i \mathbf{s}_i^P - \mathbf{r}_i^0 = 0 \quad (4.15a)$$

$$\Phi^{456} = \mathbf{e} - \mathbf{e}_i^0 = 0 \quad (4.15b)$$

where $\mathbf{e} = [e_1, e_2, e_3]^T$ is a vector part of quaternion \mathbf{p} . Note that only 3 equations are needed to constrain 4 Euler parameters. The reason is that the Euler parameters are not independent, since

$$e_0^2 + [e_1, e_2, e_3]^T [e_1, e_2, e_3] = \cos^2\left(\frac{\chi}{2}\right) + \mathbf{u}^T \mathbf{u} \sin^2\left(\frac{\chi}{2}\right) = 1 \quad (4.16)$$

that is, they must satisfy the Euler parameter normalisation constraint as presented later in Equation 4.28.

4.1.4 Constraints between pairs of bodies

Construction of mechanisms and machines employs a variety of spacial joints between pairs of bodies. The constraint equations that define a library of such joints are derived in this subsection.

Distance constraint

The distance between points P_i and P_j on bodies i and j can be fixed and set equal to $C \neq 0$, as shown in Figure 4.5.

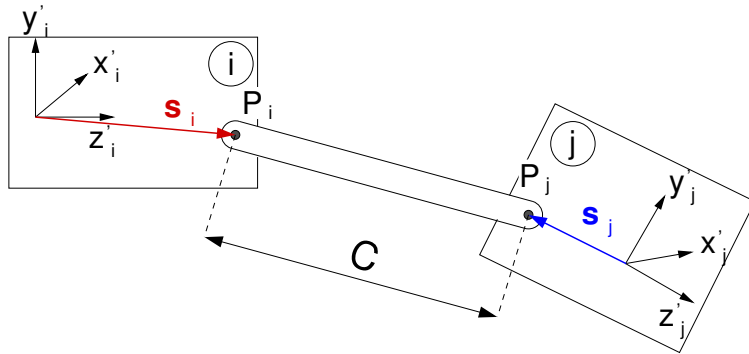


Figure 4.5: Distance constraint.

Equation 4.11 can be directly used for the distance constraint:

$$\Phi^{SS}(P_i, P_j, C) = 0 \quad (4.17)$$

This scalar constraint equation permits five relative degrees of freedom between bodies i and j .

Spherical joint

A spherical joint is defined by the condition that the centre of the ball at point P_i on body i coincides with the centre of the socket at P_j on body j , as shown in Figure 4.6. This condition is the same as spherical constraint of Equation 4.10, that is

$$\Phi^S(P_i, P_j) = \mathbf{0} \quad (4.18)$$

These three scalar constraint equations restrict the relative position of points P_i and P_j , whilst three relative degrees of freedom remain unconstrained.

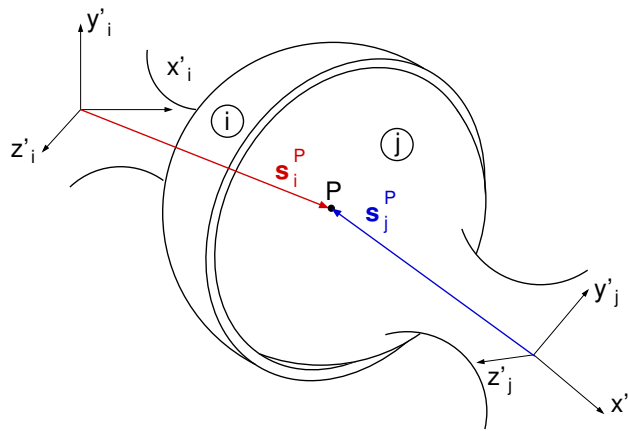


Figure 4.6: Spherical joint.

Revolute joint

A revolute joint between two bodies i and j is constructed with a bearing that allows their relative rotation about a common axis, but precludes relative translation along this axis, as shown in Figure 4.7. To define the joint, the centre of the joint is located on bodies i and j by points P_i and P_j . The axis of the relative rotation is specified in bodies i and j by points Q_i and Q_j i.e. by the unit vectors \mathbf{h}_i and \mathbf{h}_j along the respective z'' axes of the joint definition frames. The mathematical formulation of the revolute joint is that points P_i and P_j coincide, and that the body-fixed vectors \mathbf{h}_i and \mathbf{h}_j are parallel, which leads to the constraint equations:

$$\begin{aligned} \Phi^S(P_i, P_j) &= \mathbf{0}, \\ \Phi^{P1}(\mathbf{h}_i, \mathbf{h}_j) &= \mathbf{0}. \end{aligned} \quad (4.19)$$

These five scalar constraint equation leave only one relative degree of freedom: the rotation about the common axis.

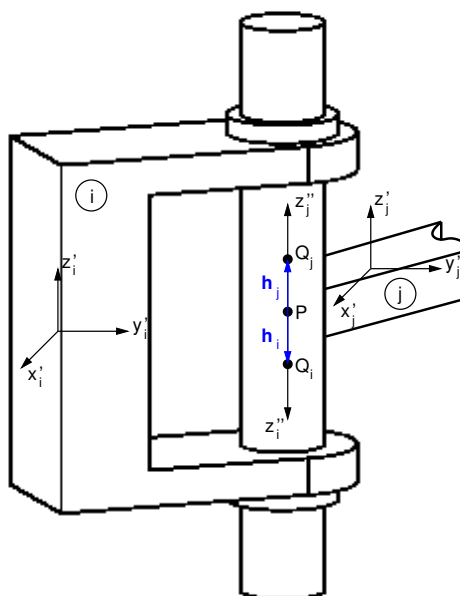


Figure 4.7: Revolute joint.

Revolute-cylindrical composite joint

The revolute cylindrical joint shown in Figure 4.8 consists of a coupler that is constrained to body i by the revolute joint about the \mathbf{h}_i axis on body i and to body j through a cylindrical joint about the \mathbf{h}_j axis. Vectors

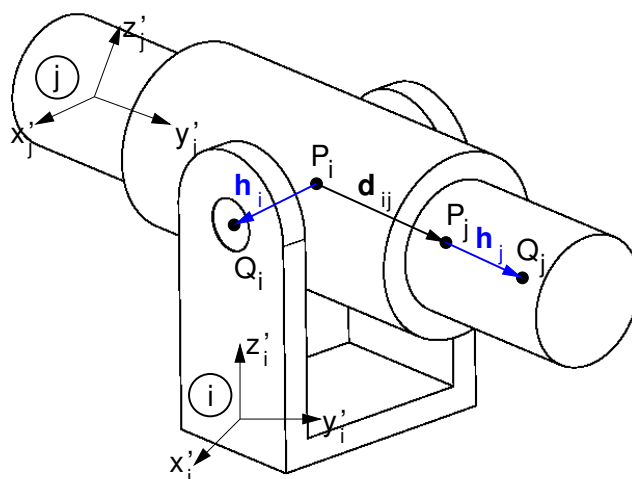


Figure 4.8: Revolute-cylindrical joint.

\mathbf{h}_i and \mathbf{h}_j are required to be orthogonal. Additionally, providing that $\mathbf{d}_{ij} \neq \mathbf{0}$, the vector \mathbf{h}_j must be parallel to \mathbf{d}_{ij} . These conditions may be written as:

$$\begin{aligned}\Phi^{d1}(\mathbf{h}_i, \mathbf{h}_j) &= 0, \\ \Phi^{d2}(\mathbf{h}_i, \mathbf{d}_{ij}) &= 0.\end{aligned}\tag{4.20}$$

Note that even if $\mathbf{d}_{ij} = \mathbf{0}$, then $P_i = P_j$ and the geometric conditions of the joint are satisfied. Since three scalar equations comprise the definition of the revolute-cylindrical joint, there are three relative degrees of freedom between bodies i and j .

Translational joint

The translation joint shown in Figure 4.9 allows for the relative translation along a common axis between two bodies, but precludes the relative rotation about that axis. The joint is defined by points P_i and P_j that are

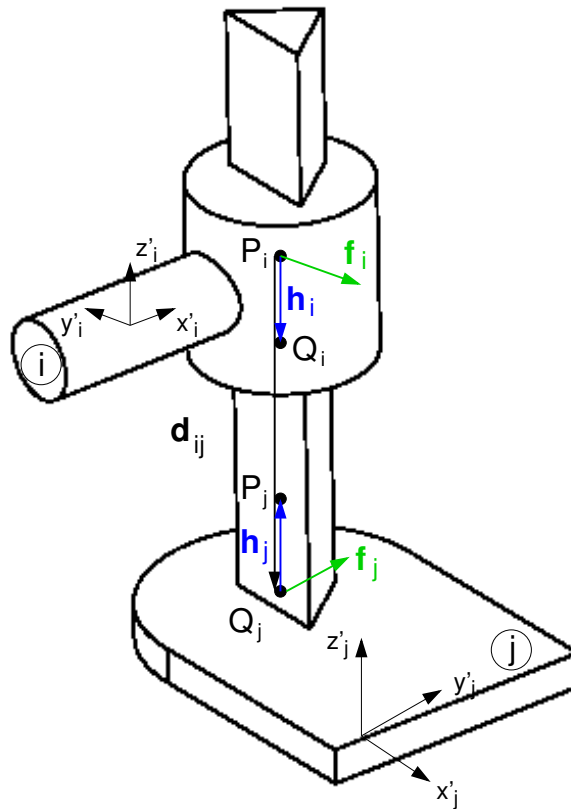


Figure 4.9: Translational joint.

located on the common axis of translation and some additional points Q_i and Q_j on each body are defined along the axis of translation to establish unit vectors \mathbf{h}_i and \mathbf{h}_j along the respective z'' axes of the joint

definition frames. The x'' axes of the joint definition frames on bodies i and j are chosen so that they are perpendicular, and are defined by the vectors \mathbf{f}_i and \mathbf{f}_j , as shown in Figure 4.9.

The analytical definition of the translational joint is that vectors \mathbf{h}_i and \mathbf{h}_j are collinear and vectors \mathbf{f}_i and \mathbf{f}_j are orthogonal. Since the vectors \mathbf{h}_i , \mathbf{h}_j and \mathbf{d}_{ij} have points in common, the collinearity condition is enforced by the condition that \mathbf{h}_i is parallel to both \mathbf{h}_j and \mathbf{d}_{ij} , if $\mathbf{d}_{ij} \neq \mathbf{0}$. Equations of constraints for the translational joints can be expressed as

$$\begin{aligned}\Phi^{p1}(\mathbf{h}_i, \mathbf{h}_j) &= \mathbf{0} \\ \Phi^{p2}(\mathbf{h}_i, \mathbf{d}_{ij}) &= \mathbf{0} \\ \Phi^{d1}(\mathbf{f}_i, \mathbf{f}_j) &= 0\end{aligned}\tag{4.21}$$

Note that if $\mathbf{d}_{ij} = \mathbf{0}$, then $P_i = P_j$ and the geometric conditions of the joint are satisfied.

Relative rotational driving constraint

For a relative rotational driver, the angle between the bodies to be driven in time must be specified. Consider two bodies i and j with corresponding joint definition frames (x_i'', y_i'', z_i'') and (x_j'', y_j'', z_j'') , where the vectors \mathbf{h}_i and \mathbf{h}_j are parallel, as shown in Figure 4.10. The angle of rotation θ is to be calculated, and is positive

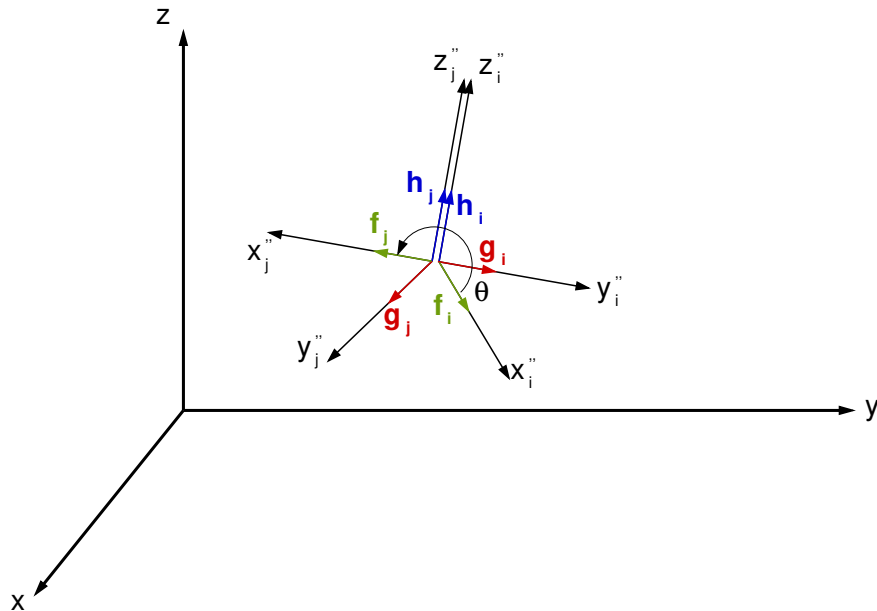


Figure 4.10: Parallel vectors on and between adjacent bodies.

if counterclockwise from \mathbf{f}_i to \mathbf{f}_j . From the definition of the scalar product and the fact that the coordinate

vectors are unit vectors,

$$\mathbf{f}_i^T \mathbf{f}_j = \cos(\theta) \quad (4.22)$$

Similarly, from the definition of a vector product

$$\tilde{\mathbf{f}}_i \mathbf{f}_j = \mathbf{h}_i \sin(\theta) \quad (4.23)$$

Taking the scalar product of both sides of this equation with \mathbf{h}_i and using the fact that $\tilde{\mathbf{f}}_i \mathbf{h}_i = -\mathbf{g}_i$,

$$\sin(\theta) = \mathbf{h}_i^T \tilde{\mathbf{f}}_i \mathbf{f}_j = \mathbf{g}_i^T \mathbf{f}_j \quad (4.24)$$

Writing the unit vectors in terms of the respective body-fixed reference frames, and using the transformation matrices from these frames to the global reference frame, the above equations for $\cos(\theta)$ and $\sin(\theta)$ become

$$\begin{aligned} \cos(\theta) &= \mathbf{f}_i'^T \mathbf{A}_i^T \mathbf{A}_j \mathbf{f}_j' \\ \sin(\theta) &= \mathbf{g}_i'^T \mathbf{A}_i^T \mathbf{A}_j \mathbf{f}_j' \end{aligned} \quad (4.25)$$

If $\cos(\theta)$ and $\sin(\theta)$ are known, the value of θ , $0 \leq \theta < 2\pi$ can be uniquely determined:

$$\theta = \begin{cases} \arcsin(\sin(\theta)), & \text{if } \sin(\theta) \geq 0 \text{ and } \cos(\theta) \geq 0 \\ \pi - \arcsin(\sin(\theta)), & \text{if } \sin(\theta) \geq 0 \text{ and } \cos(\theta) < 0 \\ \pi - \arcsin(\sin(\theta)), & \text{if } \sin(\theta) < 0 \text{ and } \cos(\theta) < 0 \\ 2\pi + \arcsin(\sin(\theta)), & \text{if } \sin(\theta) < 0 \text{ and } \cos(\theta) \geq 0. \end{cases} \quad (4.26)$$

The calculated angle θ is in the range $0 \leq \theta < 2\pi$.

Consider now a situation, where the angle from the body-fixed x_i'' axis to the x_j'' axis (positive counterclockwise), is specified by some function $C(t)$. The analytical definition of the relative rotational driver, using the relative angle θ of rotation of Equation 4.26 is obtained as

$$\Phi^{rot} \equiv \theta + 2n\pi - C(t) = 0 \quad (4.27)$$

where n is the number of revolutions that have occurred. These are taken into account by requiring $0 \leq C(t) - 2n\pi < 2\pi$.

4.1.5 Euler parameter normalisation constraint

In addition to the kinematic and driving constraints derived above, the Euler parameter generalised coordinates of each body must satisfy the normalisation constraint

$$\Phi_i^p = \mathbf{p}_i^T \mathbf{p}_i - 1 = 0, \quad i = 1, \dots, nb \quad (4.28)$$

where i indicates the body index, and nb is the number of all bodies.

4.2 Kinematic analysis

This section derives the equations that determine the position, velocity and acceleration of the system, given that all degrees of freedom are constrained.

First, consider the generalised coordinate vector for a body i in a system

$$\mathbf{q}_i = [\mathbf{r}_i, \mathbf{p}_i]^T \quad (4.29)$$

The composite set of generalised coordinates for the entire system is thus:

$$\mathbf{q} = [\mathbf{q}_1^T, \mathbf{q}_2^T, \dots, \mathbf{q}_{nb}^T]^T, \quad (4.30)$$

where nb is the number of all bodies in the system.

The combined system of kinematic, driving, and Euler parameter normalisation constraint equations, that determines the position and orientation of the system is

$$\Phi(\mathbf{q}, t) \equiv \begin{bmatrix} \Phi^K(\mathbf{q}) \\ \Phi^D(\mathbf{q}, t) \\ \Phi^P(\mathbf{q}) \end{bmatrix} = \mathbf{0} \quad (4.31)$$

where the superscripts "K", "D" and "P" denote a set of kinematic, driving and Euler parameter normalisation constraints, respectively. It is assumed, for the purpose of kinematic analysis, that an adequate number of independent driving constraints has been specified so that Equation 4.31 comprises $7nb$ equations in $7nb$ generalised coordinates.

4.2.1 Position analysis

To solve the nonlinear position equations in form of Equation 4.31, the Jacobian matrix of the system must be calculated. The derivatives of the basic kinematic constraints, the absolute and driving constraints are presented in Table 4.1 at the end of this section. They may be combined to form the Jacobian of the constraint equations as

$$\Phi_{\mathbf{q}} = \begin{bmatrix} \Phi_{\mathbf{q}}^K \\ \Phi_{\mathbf{q}}^D \\ \Phi_{\mathbf{q}}^P \end{bmatrix}. \quad (4.32)$$

If the kinematic, driving and Euler parameter normalisation constraints are independent and if all degrees of freedom are constrained, the Jacobian is nonsingular. Thus, provided that the system can be assembled at a nominal position, there is a unique solution for the position and orientation of the system in a neighbourhood of the assembled configuration.

The kinematic constraint equations are highly nonlinear. Therefore, the iterative Newton-Raphson method is adopted to solve Equation 4.31:

$$\begin{aligned} \Phi_{\mathbf{q}} \Delta \mathbf{q}^i &= -\Phi(\mathbf{q}^i, t) \\ \mathbf{q}^{i+1} &= \mathbf{q}^i + \Delta \mathbf{q}^i \end{aligned} \quad (4.33)$$

with \mathbf{q}^0 an initial estimate of the assembled configuration, improved estimates are obtained by solving the sequence of equations in Equation 4.33, until a prescribed convergence criterion is met.

4.2.2 Velocity analysis

Since Equation 4.31 must hold at all times, both sides may be differentiated with respect to time and rearranged to obtain the velocity equation:

$$\Phi_{\mathbf{q}} \dot{\mathbf{q}} = -\Phi_t \equiv \mathbf{v}. \quad (4.34)$$

Presuming that the Jacobian matrix of Equation 4.32 is nonsingular, this equation uniquely determines the velocity $\dot{\mathbf{q}}$. This computation is efficient and direct, since the Jacobian must have been already assembled to solve the position equations using the Newton-Raphson method. It is also useful to note that time appears explicitly only in the driving constraints, therefore facilitating the computation of Φ_t .

4.2.3 Acceleration analysis

Similarly to the velocity equations, Equation 4.31 must hold at all times, and can be differentiated twice and rearranged to obtain the acceleration equation:

$$\Phi_{\mathbf{q}}\ddot{\mathbf{q}} = -(\Phi_{\mathbf{q}}\dot{\mathbf{q}})_{\mathbf{q}}\dot{\mathbf{q}} - 2\Phi_{\mathbf{q}t}\dot{\mathbf{q}} - \Phi_{tt} \equiv \boldsymbol{\gamma}. \quad (4.35)$$

This determines the acceleration $\ddot{\mathbf{q}}$. Note that the right hand side of the above equation can be evaluated once the solution for velocities is obtained.

4.2.4 Derivatives of basic constraints

For the purposes of kinematic and dynamic analyses the Jacobian $\Phi_{\mathbf{q}}$ of the set of constraint equations (Equation 4.31) must be calculated. Also the vectors \mathbf{v} and $\boldsymbol{\gamma}$ appearing in Equations 4.34 and 4.35 must be obtained. Since all kinematic constraints are represented by the combination of 4 basic constraints, it is sufficient to calculate the partial derivatives and corresponding components of the \mathbf{v} and $\boldsymbol{\gamma}$ vectors only for those 4 constraints. Additionally, partial derivatives of absolute constraints (Equation 4.14), relative rotational driving constraint (Equation 4.27) and Euler parameter normalisation constraint (Equation 4.28) and corresponding elements of \mathbf{v} and $\boldsymbol{\gamma}$ vectors must be evaluated. Table 4.1 gathers the necessary partial derivatives to construct the Jacobian $\Phi_{\mathbf{q}}$, \mathbf{v} and $\boldsymbol{\gamma}$.

The matrix \mathbf{G} presented in the equations of Table 4.1 is constructed using Euler's parameters

$$\mathbf{G} = \begin{bmatrix} -e_1 & e_0 & e_3 & -e_2 \\ -e_2 & -e_3 & e_0 & e_1 \\ -e_3 & e_2 & -e_1 & e_0 \end{bmatrix}, \quad (4.36)$$

and along with the similar matrix \mathbf{E}

$$\mathbf{E} = \begin{bmatrix} -e_1 & e_0 & -e_3 & e_2 \\ -e_2 & e_3 & e_0 & -e_1 \\ -e_3 & -e_2 & e_1 & e_0 \end{bmatrix}, \quad (4.37)$$

are used to relate the time derivative of the rotational matrix \mathbf{A} to the time derivatives of the Euler parameters through:

$$\mathbf{A} = \mathbf{E}\mathbf{G}^T \Rightarrow \dot{\mathbf{A}} = 2\mathbf{E}\dot{\mathbf{G}}^T. \quad (4.38)$$

Table 4.1: Partial derivatives of constraint functions

Constraint function	$\Phi_{\mathbf{r}_i}$	$\Phi_{\mathbf{r}_j}$	$\Phi_{\mathbf{p}_i}$	$\Phi_{\mathbf{p}_j}$	\mathbf{v}	$\boldsymbol{\gamma}$
$\Phi^{d1}(\mathbf{a}_i, \mathbf{a}_j)$	$\mathbf{0}$	$\mathbf{0}$	$-2(\mathbf{a}_i^T \mathbf{A}_j^T \mathbf{A}_i \tilde{\mathbf{a}}_i) \mathbf{G}_i$	$-2(\mathbf{a}_i^T \mathbf{A}_i^T \mathbf{A}_j \tilde{\mathbf{a}}_j) \mathbf{G}_j$	$\mathbf{0}$	$-\mathbf{a}_j^T [\mathbf{A}_j^T \mathbf{A}_i \tilde{\boldsymbol{\omega}}_i + \tilde{\boldsymbol{\omega}}_j \mathbf{A}_j^T \mathbf{A}_i] \mathbf{a}_i + 2\boldsymbol{\omega}_j^T \tilde{\mathbf{a}}_j \mathbf{A}_i^T \mathbf{A}_j \mathbf{a}_i \tilde{\boldsymbol{\omega}}_i$
$\Phi^{d2}(\mathbf{a}_i, \mathbf{d}_{ij})$	$-\mathbf{a}_i^T \mathbf{A}_i^T$	$\mathbf{a}_i^T \mathbf{A}_i^T$	$2(\mathbf{a}_i^T \tilde{\mathbf{s}}_i^P - \mathbf{d}_{ij}^T \mathbf{A}_i \tilde{\mathbf{a}}_i) \mathbf{G}_i$	$-2(\mathbf{a}_i^T \mathbf{A}_i^T \mathbf{A}_j \tilde{\mathbf{s}}_j^P) \mathbf{G}_j$	$\mathbf{0}$	$2\boldsymbol{\omega}_i^T \tilde{\mathbf{a}}_i \mathbf{A}_i^T (\mathbf{r}_i - \mathbf{r}_j) + 2\tilde{\mathbf{s}}_j^P \boldsymbol{\omega}_j^T \mathbf{A}_i^T \mathbf{A}_i \tilde{\boldsymbol{\omega}}_i \mathbf{a}_i - \mathbf{s}_i^T \tilde{\boldsymbol{\omega}}_i \mathbf{a}_i +$ $-\mathbf{s}_j^T \tilde{\boldsymbol{\omega}}_j \mathbf{A}_i^T \mathbf{A}_i \mathbf{a}_i - \mathbf{d}_{ij}^T \mathbf{A}_i \tilde{\boldsymbol{\omega}}_i \mathbf{a}_i$
$\Phi^S(P_i, P_j)$	$-\mathbf{I}$	\mathbf{I}	$2(\mathbf{A}_i \tilde{\mathbf{s}}_i^P) \mathbf{G}_i$	$-2(\mathbf{A}_j \tilde{\mathbf{s}}_j^P) \mathbf{G}_j$	$\mathbf{0}$	$\mathbf{A}_i \tilde{\boldsymbol{\omega}}_i \mathbf{s}_i^P - \mathbf{A}_j \tilde{\boldsymbol{\omega}}_j \mathbf{s}_j^P$
$\Phi^{SS}(P_i, P_j, C)$	$-2\mathbf{d}_{ij}^T$	$2\mathbf{d}_{ij}^T$	$4(\mathbf{d}_{ij}^T \mathbf{A}_i \tilde{\mathbf{s}}_i^P) \mathbf{G}_i$	$-4(\mathbf{d}_{ij}^T \mathbf{A}_j \tilde{\mathbf{s}}_j^P) \mathbf{G}_j$	$\mathbf{0}$	$-2(\mathbf{r}_j - \mathbf{r}_i)^T (\mathbf{r}_j - \mathbf{r}_i) + 2\mathbf{s}_j^T \tilde{\boldsymbol{\omega}}_j \mathbf{s}_j^P + 2\mathbf{s}_i^T \tilde{\boldsymbol{\omega}}_i \mathbf{s}_i^P +$ $-4\mathbf{s}_j^T \tilde{\boldsymbol{\omega}}_j \mathbf{A}_i^T \mathbf{A}_i \tilde{\boldsymbol{\omega}}_i \mathbf{s}_i^P + 4(\mathbf{r}_j - \mathbf{r}_i)^T (\mathbf{A}_i \tilde{\mathbf{s}}_i^P \boldsymbol{\omega}_j - \mathbf{A}_j \tilde{\mathbf{s}}_j^P \boldsymbol{\omega}_i) +$ $-2\mathbf{d}_{ij}^T [\mathbf{A}_i \tilde{\boldsymbol{\omega}}_i \tilde{\mathbf{s}}_i^P \boldsymbol{\omega}_j - \mathbf{A}_j \tilde{\boldsymbol{\omega}}_j \tilde{\mathbf{s}}_j^P \boldsymbol{\omega}_i]$
$\Phi^{123}(P_i)$	\mathbf{I}	$\mathbf{0}$	$-2(\mathbf{A}_i \tilde{\mathbf{s}}_i^P) \mathbf{G}_i$	$\mathbf{0}$	$\mathbf{0}$	$-\mathbf{A}_i \tilde{\boldsymbol{\omega}}_i \mathbf{s}_i^P$
$\Phi^{456}(\mathbf{p}_i)$	$\mathbf{0}$	$\mathbf{0}$	$[\mathbf{0}, \mathbf{I}]$	$\mathbf{0}$	$\mathbf{0}$	$-\frac{1}{2}(\hat{\mathbf{e}}_i + \hat{\mathbf{e}}_{0i}) \boldsymbol{\omega}_i$
$\Phi^{rad}(\boldsymbol{\theta})$	$\mathbf{0}$	$\mathbf{0}$	$-2\mathbf{h}_i^T \mathbf{G}_i$	$2(\mathbf{h}_i^T \mathbf{A}_i^T \mathbf{A}_j) \mathbf{G}_j$	$\dot{\mathbf{C}}(t)$	$-\mathbf{h}_i^T (\mathbf{A}_i^T \mathbf{A}_j \tilde{\boldsymbol{\omega}}_j - \tilde{\boldsymbol{\omega}}_i \mathbf{A}_i^T \mathbf{A}_j) \boldsymbol{\omega}_j + \dot{\mathbf{C}}(t)$
$\Phi^P(\mathbf{p}_i)$	$\mathbf{0}$	$\mathbf{0}$	$2\mathbf{p}_i^T$	$\mathbf{0}$	$\mathbf{0}$	$-2\mathbf{p}_i^T \mathbf{p}_i$

Another useful set of relations employing the matrix \mathbf{G} are the dependencies between the Euler parameter variations and the virtual rotations, and relationships between the Euler parameter derivatives and the angular velocity, and angular acceleration. The former relationship may be expressed as:

$$\delta \mathbf{p} = \frac{1}{2} \mathbf{G}^T \delta \boldsymbol{\pi}' \quad (4.39)$$

while the other two relations are:

$$\begin{aligned} \dot{\mathbf{p}} &= \frac{1}{2} \mathbf{G}^T \boldsymbol{\omega}' \\ \ddot{\mathbf{p}} &= \frac{1}{2} \mathbf{G}^T \dot{\boldsymbol{\omega}}' - \frac{1}{4} \boldsymbol{\omega}'^T \boldsymbol{\omega}' \dot{\mathbf{p}} \end{aligned} \quad (4.40)$$

for the first and second time derivatives, respectively. These relations are important in dynamic analysis, as explained in the next section. Note that matrix \mathbf{G} is orthogonal i.e. $\mathbf{G}^{-1} = \mathbf{G}^T \Rightarrow \mathbf{G}\mathbf{G}^T = \mathbf{I}$, where \mathbf{I} is the identity matrix. This way, the elements of the Jacobian matrix $\Phi_{\mathbf{q}}$ presented in Table 4.1 can be easily expressed in virtual rotations $\Phi_{\boldsymbol{\pi}'}$ instead of Euler parameter variations $\Phi_{\mathbf{p}}$.

4.3 Dynamic analysis

This section provides formulation of spatial equations of motion for multi-body system and presents the way of solving the resulting system of mixed algebraic-differential equations.

4.3.1 Equations of motion of a rigid body

Consider the rigid body shown in Figure 4.11, which is located in space by the vector \mathbf{r} , and a set of Euler parameters, \mathbf{p} , that define the orientation of the (x', y', z') body-fixed reference frame in an inertial (x, y, z) reference frame. A differential mass $dm(P)$ is located in the point P defined on the body by the vector \mathbf{s}^P .

Forces acting on the differential elements of mass at point P include the external forces $\mathbf{F}(P)$ per unit of mass at point P , and the internal force $\mathbf{f}(P, R)$ per unit of masses at points P and R . Newton's equation of motion for a differential mass $dm(P)$ are

$$\ddot{\mathbf{r}}^P dm(P) - \mathbf{F}(P) dm(P) - \left(\int_m \mathbf{f}(P, R) dm(R) \right) dm(P) = \mathbf{0} \quad (4.41)$$

where integration of internal force $\mathbf{f}(P, R)$ is taken over the whole body. Let $\delta \mathbf{r}^P$ be a virtual displacement of a point P i.e. an infinitesimal variation of the location of point P that is consistent with the allowed motion

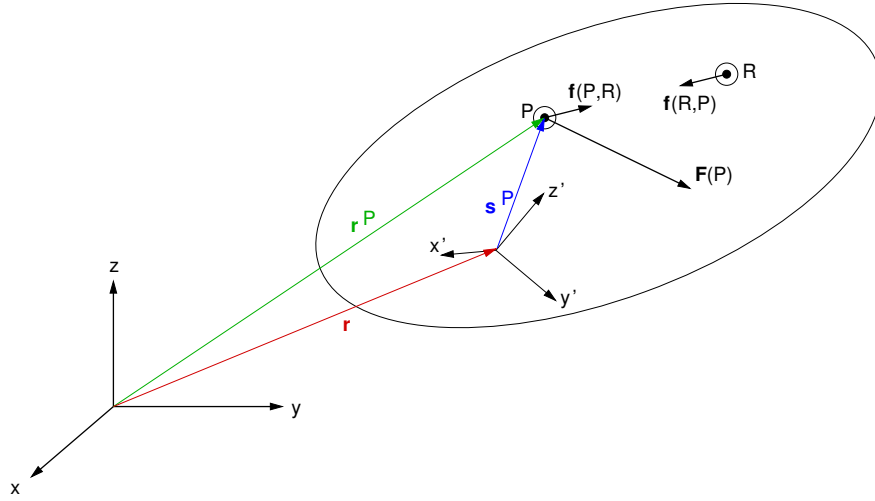


Figure 4.11: Forces acting on a rigid body in space.

of a point P . Premultiplying both sides of Equation 4.41 by $\delta \mathbf{r}^{PT}$ and integrating over the entire mass of the body yields:

$$\int_m \delta \mathbf{r}^{PT} \ddot{\mathbf{r}}^P dm(P) - \int_m \delta \mathbf{r}^{PT} \mathbf{F}(P) dm(P) - \int_m \int_m \delta \mathbf{r}^{PT} \mathbf{f}(P,R) dm(R) dm(P) = 0. \quad (4.42)$$

The double integral that appears in the above equation can be evaluated as:

$$\int_m \int_m \delta \mathbf{r}^{PT} \mathbf{f}(P,R) dm(R) dm(P) = \frac{1}{2} \int_m \int_m (\delta \mathbf{r}^P - \delta \mathbf{r}^R)^T \mathbf{f}(P,R) dm(R) dm(P). \quad (4.43)$$

But, for a rigid body the distance between any two points is constant

$$(\mathbf{r}^P - \mathbf{r}^R)^T (\mathbf{r}^P - \mathbf{r}^R) = C, \quad (4.44)$$

and taking the differential of both sides results in:

$$(\delta \mathbf{r}^P - \delta \mathbf{r}^R)^T (\mathbf{r}^P - \mathbf{r}^R) = 0. \quad (4.45)$$

Since the internal force $\mathbf{f}(P,R)$ in the model of rigid body acts between points P and R i.e.

$$\mathbf{f}(P,R) = k(\mathbf{r}^P - \mathbf{r}^R) \quad (4.46)$$

where k is a constant coefficient, from Equation 4.45, the double integral of Equation 4.43 is equal zero.

Using this result, Equation 4.42 simplifies to

$$\int_m \delta \mathbf{r}^{PT} \ddot{\mathbf{r}}^P dm(P) - \int_m \delta \mathbf{r}^{PT} \mathbf{F}(P) dm(P) = 0 \quad (4.47)$$

The virtual displacement $\delta \mathbf{r}^P$ of a point P can be written in terms of the virtual displacement of the (x', y', z') body frame $\delta \mathbf{r}$ and a virtual rotation of the body $\delta \boldsymbol{\pi}'$ ^[73]

$$\delta \mathbf{r}^P = \delta \mathbf{r} - \mathbf{A} \tilde{\mathbf{s}}'^P \delta \boldsymbol{\pi}' \quad (4.48)$$

Similarly, the acceleration of a point P may be written as:

$$\ddot{\mathbf{r}}^P = \ddot{\mathbf{r}} + \ddot{\mathbf{A}} \tilde{\mathbf{s}}'^P = \ddot{\mathbf{r}} + \mathbf{A} \tilde{\boldsymbol{\omega}}' \tilde{\mathbf{s}}'^P + \mathbf{A} \tilde{\boldsymbol{\omega}}' \tilde{\boldsymbol{\omega}}' \tilde{\mathbf{s}}'^P. \quad (4.49)$$

Substituting Equations 4.48 and 4.49 into the variational equation of Equation 4.47 and expanding the integrals yields:

$$\begin{aligned} \delta \mathbf{r}^T \ddot{\mathbf{r}} \int_m dm(P) + \delta \mathbf{r}^T (\mathbf{A} \tilde{\boldsymbol{\omega}}' + \mathbf{A} \tilde{\boldsymbol{\omega}}' \tilde{\boldsymbol{\omega}}') \int_m \tilde{\mathbf{s}}'^P dm(P) + \delta \boldsymbol{\pi}'^T \int_m \tilde{\mathbf{s}}'^P dm(P) \mathbf{A}^T \ddot{\mathbf{r}} \\ + \delta \boldsymbol{\pi}'^T \int_m \tilde{\mathbf{s}}'^P \tilde{\boldsymbol{\omega}}' \tilde{\mathbf{s}}'^P dm(P) + \delta \boldsymbol{\pi}'^T \int_m \tilde{\mathbf{s}}'^P \tilde{\boldsymbol{\omega}}' \tilde{\boldsymbol{\omega}}' \tilde{\mathbf{s}}'^P dm(P) - \delta \mathbf{r}^T \int_m \mathbf{F}(P) dm(P) \\ - \delta \boldsymbol{\pi}'^T \int_m \tilde{\mathbf{s}}'^P \mathbf{F}'(P) dm(P) = 0. \end{aligned} \quad (4.50)$$

4.3.2 Equations of motion with a centroidal body-fixed reference frame

Equation 4.50 can be significantly simplified if a body-fixed reference frame (x', y', z') is chosen with its origin at the centre of mass (or centroid) of the body. By definition for the centroid:

$$\int_m \tilde{\mathbf{s}}'^P dm(P) = 0 \quad (4.51)$$

Also, the following identities apply for the total mass m , the total external force \mathbf{F} acting on the body and the total moment \mathbf{n}' of the external forces with respect to the origin of the body-fixed frame:

$$m \equiv \int_m dm(P), \quad (4.52a)$$

$$\mathbf{F} \equiv \int_m \mathbf{F}(P) dm(P), \quad (4.52b)$$

$$\mathbf{n}' \equiv \int_m \tilde{\mathbf{s}}'^P \mathbf{F}'(P) dm(P). \quad (4.52c)$$

The fourth integral in Equation 4.50 can be written as

$$\int_m \tilde{\mathbf{s}}'^P \tilde{\boldsymbol{\omega}}' \tilde{\mathbf{s}}'^P dm(P) = - \left(\int_m \tilde{\mathbf{s}}'^P \tilde{\mathbf{s}}'^P dm(P) \right) \boldsymbol{\omega}' \equiv \mathbf{J}' \boldsymbol{\omega}' \quad (4.53)$$

where \mathbf{J}' is a constant inertia matrix with respect to the centroidal body-fixed reference frame (x', y', z') defined as

$$\mathbf{J}' \equiv \int_m \tilde{\mathbf{s}}^P \tilde{\mathbf{s}}^P dm(P) = \int_m \begin{bmatrix} (y'^P)^2 + (z'^P)^2 & -x'^P y'^P & -x'^P z'^P \\ -x'^P y'^P & (x'^P)^2 + (z'^P)^2 & -y'^P z'^P \\ -x'^P z'^P & -y'^P z'^P & (x'^P)^2 + (y'^P)^2 \end{bmatrix} dm(P) \quad (4.54)$$

The fifth integral may be rearranged and evaluated to yield^[73]:

$$\int_m \tilde{\mathbf{s}}^P \tilde{\boldsymbol{\omega}}' \tilde{\boldsymbol{\omega}}' \tilde{\mathbf{s}}^P dm(P) = \tilde{\boldsymbol{\omega}}' \left(- \int_m \tilde{\mathbf{s}}^P \tilde{\mathbf{s}}^P dm(P) \right) \boldsymbol{\omega}' = \tilde{\boldsymbol{\omega}}' \mathbf{J}' \boldsymbol{\omega}'. \quad (4.55)$$

Finally, substituting the above identities into Equation 4.50 results in the variational Newton-Euler equations of motion for a rigid body with a centroidal body-fixed reference frame,

$$\delta \mathbf{r}^T [m\dot{\mathbf{r}} - \mathbf{F}] + \delta \boldsymbol{\pi}' \left[\mathbf{J}' \dot{\boldsymbol{\omega}}' + \tilde{\boldsymbol{\omega}}' \mathbf{J}' \boldsymbol{\omega}' - \mathbf{n}' \right] \quad (4.56)$$

which must hold for all virtual displacements $\delta \mathbf{r}$, and virtual rotations $\delta \boldsymbol{\pi}'$ of the centroidal frame that are consistent with constraints that act on the body.

If no constraints act on a body, then $\delta \mathbf{r}$ and $\delta \boldsymbol{\pi}'$ are arbitrary, and their coefficients in Equation 4.56 must be zero. This yields the Newton-Euler equations of motion for the unconstrained body:

$$\begin{aligned} m\dot{\mathbf{r}} &= \mathbf{F}, \\ \mathbf{J}' \dot{\boldsymbol{\omega}}' &= \mathbf{n}' - \tilde{\boldsymbol{\omega}}' \mathbf{J}' \boldsymbol{\omega}'. \end{aligned} \quad (4.57)$$

4.3.3 Equations of motion for constrained system

Consider nb bodies that form a constrained multi-body system. The system of generalised coordinates for this system are:

$$\begin{aligned} \mathbf{r} &= [\mathbf{r}_1^T, \mathbf{r}_2^T, \dots, \mathbf{r}_{nb}^T]^T, \\ \mathbf{p} &= [\mathbf{p}_1^T, \mathbf{p}_2^T, \dots, \mathbf{p}_{nb}^T]^T. \end{aligned} \quad (4.58)$$

The set $\Phi(\mathbf{r}, \mathbf{p}, t)$ of the kinematic, driving and Euler parameter normalisation constraints, derived in Section 4.1, must hold at all times.

To implement the variational Newton-Euler equations of motion, Equation 4.56 is evaluated for each body in the system and then added together to form a set of variational equations of motion for the whole

system. To simplify the notation, let us define

$$\begin{aligned}
\delta \mathbf{r} &= [\delta \mathbf{r}_1^T, \delta \mathbf{r}_2^T, \dots, \delta \mathbf{r}_{nb}^T]^T \\
\delta \boldsymbol{\pi}' &= [\delta \boldsymbol{\pi}'_1{}^T, \delta \boldsymbol{\pi}'_2{}^T, \dots, \delta \boldsymbol{\pi}'_{nb}{}^T]^T \\
\mathbf{F} &= [\mathbf{F}_1^T, \mathbf{F}_2^T, \dots, \mathbf{F}_{nb}^T]^T \\
\boldsymbol{\omega}' &= [\boldsymbol{\omega}'_1{}^T, \boldsymbol{\omega}'_2{}^T, \dots, \boldsymbol{\omega}'_{nb}{}^T]^T \\
\mathbf{n}' &= [\mathbf{n}'_1{}^T, \mathbf{n}'_2{}^T, \dots, \mathbf{n}'_{nb}{}^T]^T \\
\mathbf{M} &\equiv \begin{bmatrix} m_1 \mathbf{I} & & & \mathbf{0} \\ & m_2 \mathbf{I} & & \\ & & \ddots & \\ \mathbf{0} & & & m_{nb} \mathbf{I} \end{bmatrix} \\
\mathbf{J}' &\equiv \begin{bmatrix} \mathbf{J}'_1 & & & \mathbf{0} \\ & \mathbf{J}'_2 & & \\ & & \ddots & \\ \mathbf{0} & & & \mathbf{J}'_{nb} \end{bmatrix} \\
\tilde{\boldsymbol{\omega}}' &\equiv \begin{bmatrix} \tilde{\boldsymbol{\omega}}'_1 & & & \mathbf{0} \\ & \tilde{\boldsymbol{\omega}}'_2 & & \\ & & \ddots & \\ \mathbf{0} & & & \tilde{\boldsymbol{\omega}}'_{nb} \end{bmatrix}
\end{aligned} \tag{4.59}$$

Using this notation, the sum of Equations 4.56 over all bodies in the system may be written as

$$\delta \mathbf{r}^T [\mathbf{M} \ddot{\mathbf{r}} - \mathbf{F}] + \delta \boldsymbol{\pi}'^T [\mathbf{J}' \dot{\boldsymbol{\omega}}' + \tilde{\boldsymbol{\omega}}' \mathbf{J}' \boldsymbol{\omega}' - \mathbf{n}'] = 0 \tag{4.60}$$

which must hold for all virtual displacements $\delta \mathbf{r}$ and virtual rotations $\delta \boldsymbol{\pi}'$ that are consistent with constraints Φ . Forces and moments that act on the system may be split into applied forces and torques \mathbf{F}^A and \mathbf{n}'^A , and constraint forces and torques \mathbf{F}^C and \mathbf{n}'^C , respectively. For all constraints under consideration, the forces of constraint do not work as long as the virtual displacements and rotations are consistent with constraints, that is

$$\delta \mathbf{r}^T \mathbf{F}^C + \delta \boldsymbol{\pi}'^T \mathbf{n}'^C = 0 \tag{4.61}$$

Thus, the variational equation of motion for the constrained system (Equation 4.60) reduces to:

$$\delta \mathbf{r}^T [\mathbf{M}\ddot{\mathbf{r}} - \mathbf{F}^A] + \delta \boldsymbol{\pi}' \left[\mathbf{J}' \dot{\boldsymbol{\omega}}' + \tilde{\boldsymbol{\omega}}' \mathbf{J}' \dot{\boldsymbol{\omega}}' - \mathbf{n}'^A \right] = 0, \quad (4.62)$$

which must also hold for all allowed virtual displacements and rotations.

Virtual displacements $\delta \mathbf{r}$ and virtual rotations $\delta \boldsymbol{\pi}'$ are kinematically admissible for constraints

$\Phi(\mathbf{r}, \mathbf{p}, t) \equiv \Phi(\mathbf{r}, \boldsymbol{\pi}, t)$ if

$$\Phi_{\mathbf{r}} \delta \mathbf{r} + \Phi_{\boldsymbol{\pi}'} \delta \boldsymbol{\pi}' = 0 \quad (4.63)$$

where $\Phi_{\mathbf{r}}$ and $\Phi_{\boldsymbol{\pi}'}$ can be assembled using the results of Section 4.2.4. Euler parameters normalisation constraints should not be included if virtual rotations $\delta \boldsymbol{\pi}'$ are employed, since they are automatically satisfied, but must be included if the Euler parameter virtual variations $\delta \mathbf{p}$ are used. Since Equation 4.62 must hold for all $\delta \mathbf{r}$ and $\delta \boldsymbol{\pi}'$ that satisfy Equation 4.63, by the Lagrange multiplier theorem, there exists a Lagrange multiplier vector $\boldsymbol{\lambda}$ such that

$$\delta \mathbf{r}^T [\mathbf{M}\ddot{\mathbf{r}} - \mathbf{F}^A + \Phi_{\mathbf{r}}^T \boldsymbol{\lambda}] + \delta \boldsymbol{\pi}' \left[\mathbf{J}' \dot{\boldsymbol{\omega}}' + \tilde{\boldsymbol{\omega}}' \mathbf{J}' \dot{\boldsymbol{\omega}}' - \mathbf{n}'^A + \Phi_{\boldsymbol{\pi}'}^T \boldsymbol{\lambda} \right] = 0 \quad (4.64)$$

for arbitrary $\delta \mathbf{r}$ and $\delta \boldsymbol{\pi}'$. Since variations are now arbitrary, their coefficients must be equal to zero, to satisfy the equation. This yields the constrained Newton-Euler equations of motion:

$$\begin{aligned} \mathbf{M}\ddot{\mathbf{r}} + \Phi_{\mathbf{r}}^T \boldsymbol{\lambda} &= \mathbf{F}^A, \\ \mathbf{J}' \dot{\boldsymbol{\omega}}' + \Phi_{\boldsymbol{\pi}'}^T \boldsymbol{\lambda} &= \mathbf{n}'^A - \tilde{\boldsymbol{\omega}}' \mathbf{J}' \dot{\boldsymbol{\omega}}'. \end{aligned} \quad (4.65)$$

To complete the set of equations of motion, the acceleration equation associated with the kinematic constraints Φ must be taken into account. As derived in Section 4.2.3, the acceleration equation has a form of

$$\Phi_{\mathbf{q}} \ddot{\mathbf{q}} = -(\Phi_{\mathbf{q}} \dot{\mathbf{q}})_{\mathbf{q}} \dot{\mathbf{q}} - 2\Phi_{\mathbf{q}t} \dot{\mathbf{q}} - \Phi_{tt} \equiv \boldsymbol{\gamma} \quad (4.66)$$

where the vector $\boldsymbol{\gamma}$ is defined in Table 4.1 for each of the constraint equations.

Combining Equations 4.65 and 4.66, the system of acceleration equations to be solved is:

$$\begin{bmatrix} \mathbf{M} & \mathbf{0} & \Phi_{\mathbf{r}}^T \\ \mathbf{0} & \mathbf{J}' & \Phi_{\boldsymbol{\pi}'}^T \\ \Phi_{\mathbf{r}} & \Phi_{\boldsymbol{\pi}'} & \mathbf{0} \end{bmatrix} \begin{bmatrix} \ddot{\mathbf{r}} \\ \dot{\boldsymbol{\omega}}' \\ \boldsymbol{\lambda} \end{bmatrix} = \begin{bmatrix} \mathbf{F}^A \\ \mathbf{n}'^A - \tilde{\boldsymbol{\omega}}' \mathbf{J}' \dot{\boldsymbol{\omega}}' \\ \boldsymbol{\gamma} \end{bmatrix}. \quad (4.67)$$

The above equation is a system of mixed first-order differential-algebraic equations for the velocity variables $\dot{\mathbf{r}}$ and $\dot{\boldsymbol{\omega}}$, and the algebraic variables $\boldsymbol{\lambda}$. It is not a second-order differential-algebraic system, since the angular velocity $\boldsymbol{\omega}$ is not integrable in general. Therefore, once the angular velocities or accelerations are obtained, they must be transferred to the derivatives of Euler parameters through Equations 4.40. In addition, the kinematic and Euler parameter normalisation constraints and the constraint velocity equations must be satisfied, that is

$$\begin{aligned}\boldsymbol{\Phi}(\mathbf{r}, \mathbf{p}, t) &= \mathbf{0} \\ \boldsymbol{\Phi}_{\mathbf{r}}\dot{\mathbf{r}} + \boldsymbol{\Phi}_{\mathbf{p}}\dot{\mathbf{p}} &= \mathbf{v}\end{aligned}\tag{4.68}$$

where the Euler parameter normalisation constraints are already included in the $\boldsymbol{\Phi}(\mathbf{r}, \mathbf{p}, t)$. Initial conditions on position, orientation, and velocity must be provided to define the dynamics of a system.

It is possible to derive equivalent of Equation 4.67 using Euler parameters instead of angular velocities. Resulting system of acceleration equations is more complex and computationally more expensive ^[73] since the inertia matrix is not constant in GCS. However, since the angular velocities and accelerations must be transferred to time derivatives of quaternions, the additional computational cost is not pronounced. The Euler parameter system of acceleration equations is obtained as

$$\begin{bmatrix} \mathbf{M} & \mathbf{0} & \boldsymbol{\Phi}_{\mathbf{r}}^T & \mathbf{0} \\ \mathbf{0} & 4\mathbf{G}^T\mathbf{J}'\mathbf{G} & \boldsymbol{\Phi}_{\mathbf{p}}^T & \boldsymbol{\Phi}_{\mathbf{p}}^{pT} \\ \boldsymbol{\Phi}_{\mathbf{r}} & \boldsymbol{\Phi}_{\mathbf{p}} & \mathbf{0} & \mathbf{0} \\ \mathbf{0} & \boldsymbol{\Phi}_{\mathbf{p}} & \mathbf{0} & \mathbf{0} \end{bmatrix} \begin{bmatrix} \ddot{\mathbf{r}} \\ \ddot{\mathbf{p}} \\ \boldsymbol{\lambda} \\ \boldsymbol{\lambda}^p \end{bmatrix} = \begin{bmatrix} \mathbf{F}^A \\ 2\mathbf{G}^T\mathbf{n}'^A + 8\dot{\mathbf{G}}^T\mathbf{J}'\dot{\mathbf{G}}\mathbf{p} \\ \boldsymbol{\gamma} \\ \boldsymbol{\gamma}^p \end{bmatrix}\tag{4.69}$$

where $\mathbf{G} = \text{diag}(\mathbf{G}_1, \mathbf{G}_2, \dots, \mathbf{G}_{nb})$. It is not derived here in detail, although it is truly second-order differential-algebraic system. This, and other possible formulations of the system of acceleration equations are presented in detail in Haug ^[73] and Nikravesh ^[153]. Both dynamic equations 4.67 and 4.69 were implemented in the MBDM solver, and latter was employed in this work.

4.4 Coordinate partitioning method

In this section, coordinate partitioning method of solving mixed differential-algebraic system of equations is described. This method makes use of the fact that the $n = 7 \cdot nb$ generalised coordinates $\mathbf{q} = [\mathbf{r}^T, \mathbf{p}^T]^T$ are

not independent. There are only as many independent coordinates as there are degrees of freedom. The rest of the coordinates are dependent through the constraint equations. Thus, it is sufficient to solve the dynamic equations for independent variables and obtain the dependent variables by solving kinematic equations.

If the n coordinates are partitioned into m dependent coordinates \mathbf{u} and k independent coordinates \mathbf{v} , then the velocity vector $\dot{\mathbf{q}}$ can be partitioned accordingly into $\dot{\mathbf{u}}$ and $\dot{\mathbf{v}}$. The vectors \mathbf{y} and $\dot{\mathbf{y}}$ are going to be integrated in time and are defined in terms of the independent variables:

$$\mathbf{y} = \begin{bmatrix} \mathbf{v} \\ \dot{\mathbf{v}} \end{bmatrix}, \quad \dot{\mathbf{y}} = \begin{bmatrix} \dot{\mathbf{v}} \\ \ddot{\mathbf{v}} \end{bmatrix}, \quad (4.70)$$

where $\ddot{\mathbf{v}}$ is a vector of independent accelerations.

The kinematic constraints and the velocity Equations 4.31 and 4.34 can be expressed as

$$\Phi(\mathbf{u}, \mathbf{v}, t) = \mathbf{0} \quad (4.71a)$$

$$\Phi_{\mathbf{u}} \dot{\mathbf{u}} = -\Phi_{\mathbf{v}} \dot{\mathbf{v}} - \Phi_t \quad (4.71b)$$

Equations 4.71a and 4.71b, each, represent m independent equations in terms of \mathbf{u} and $\dot{\mathbf{u}}$, respectively. Once vectors \mathbf{v} and $\dot{\mathbf{v}}$ are obtained from \mathbf{y} , Equations 4.71 can be solved for \mathbf{u} and $\dot{\mathbf{u}}$, and the vectors \mathbf{q} and $\dot{\mathbf{q}}$ of the generalised coordinates are completely known.

An algorithm for the coordinate partitioning method can be summarised in its simplest form as follows ^[153]:

A) Main routine

1. Specify the initial conditions on \mathbf{q} and $\dot{\mathbf{q}}$.
2. Specify the independent variables \mathbf{v} and $\dot{\mathbf{v}}$.
3. Define vector \mathbf{y} as $\mathbf{y} = [\mathbf{v}^T, \dot{\mathbf{v}}^T]^T$.
4. Enter numerical integration routine.

B) Numerical integration routine

This routine solves an initial-value problem of the form $\dot{\mathbf{y}} = f(\mathbf{y}, t)$ for \mathbf{y} from the

time t^0 to final time t^f . During integration the function $f(\mathbf{y}, t)$ must be evaluated at least once per time step, or more than once for high-order schemes. For this purpose a DIFEQN routine with known time t and vector \mathbf{y} , to determine $f(\mathbf{y}, t)$ is used.

C) DIFEQN routine

1. obtain \mathbf{v} and $\dot{\mathbf{v}}$ from \mathbf{y} .
2. Solve Equation 4.71a using Newton-Raphson method for \mathbf{u} . This way \mathbf{q} is found.
3. Solve Equation 4.71b for $\dot{\mathbf{u}}$. This way $\dot{\mathbf{q}}$ is found.
4. Solve Equation 4.67 or Equation 4.69 for $\ddot{\mathbf{q}}$ and $\boldsymbol{\lambda}$.
5. Transfer $\dot{\mathbf{v}}$ from $\dot{\mathbf{q}}$ and $\ddot{\mathbf{v}}$ from $\ddot{\mathbf{q}}$ to form $\dot{\mathbf{y}} = \begin{bmatrix} \dot{\mathbf{v}} \\ \ddot{\mathbf{v}} \end{bmatrix}$
6. Return $\dot{\mathbf{y}}$.

In step A.2 an automatic process is employed to partition the generalised coordinates into dependent and independent variables. A matrix factorisation technique can be performed on the Jacobian matrix for this purpose ^[153]. For a mechanical system with m constraints and n generalised coordinates, the Jacobian is an $m \times n$ matrix. The order of the columns of the matrix corresponds to the order of the elements in vector \mathbf{q} . After reducing the Jacobian to the row-reduced echelon form, the order of the columns determines the ordering of the elements of \mathbf{q} . The first m elements of the reordered \mathbf{q} can be used as the dependent coordinates \mathbf{u} , and the remaining k elements represent the independent coordinates \mathbf{v} . This way the Jacobian $\Phi_{\mathbf{u}}$ is guaranteed to have a full row rank.

For the MBDM code, the Jacobian matrix is reduced to row-reduced echelon form through Gaussian elimination with full pivoting. It is important to note, that during the time-stepping routine, the need to change the set of independent variables may arise. The reason is that partitioning influences the accumulation of the numerical error, and this must be kept under control (see Section 4.4.1 for the example). In the extreme case, the Jacobian $\Phi_{\mathbf{u}}$ may have insufficient row rank. It is possible to define criteria indicating

whether the independent coordinates must be redefined [73, 153]. In the MBDM code, the generalised coordinates are partitioned at every time step. This is computationally more expensive, but safer approach to bound the numerical errors.

Another part of the coordinate partitioning method requiring attention is step C.2, where the Newton-Raphson algorithm is employed to solve the nonlinear set of equations $\Phi(\mathbf{u}, \mathbf{v}, t) = \mathbf{0}$. The algorithm is similar to the one in the kinematic analysis of Equation 4.33, but is modified, since the Jacobian $\Phi_{\mathbf{q}}$ has insufficient row rank. The Newton-Raphson algorithm for dynamic analysis can be set as follows

$$\begin{bmatrix} \Phi_{\mathbf{u}} & \Phi_{\mathbf{v}} \\ \mathbf{0} & \mathbf{I} \end{bmatrix} \begin{bmatrix} \Delta \mathbf{u}^i \\ \Delta \mathbf{v}^i \end{bmatrix} = \begin{bmatrix} -\Phi(\mathbf{u}^i, \mathbf{v}^i, t) \\ \mathbf{0} \end{bmatrix} \quad (4.72)$$

$$\mathbf{u}^{i+1} = \mathbf{u}^i + \Delta \mathbf{u}^i$$

where \mathbf{u}^0 is initial estimate of dependent variables at time t , and improved estimates are obtained until prescribed convergence criteria are met. \mathbf{I} is the identity matrix, since the independent variables are known and do not need an iterative update.

4.4.1 Example of automatic partitioning

First, lets consider a $m \times n = 2 \times 3$ matrix of general form (left) and the row reduced echelon form (right)

$$\Phi_{\mathbf{q}} = \begin{bmatrix} a_{11} & a_{12} & a_{13} \\ a_{21} & a_{22} & a_{23} \end{bmatrix} = \begin{bmatrix} 1 & 0 & \alpha \\ 0 & 1 & \beta \end{bmatrix} \quad (4.73)$$

where α and β result from reduction. The first $m = 2$ columns represent the dependent variables, the last $k = n - m = 1$ columns represent the independent variables.

To gain a deeper understanding, considering the following example of a 2D pendulum of length $2d$ presented in Figure 4.12. The pendulum is pivoted about the point O , and is allowed to rotate freely under external forces and moments. In this case the system has in total 3 degrees of freedom, and 2 of them are constrained. The vector of generalised coordinates is $\mathbf{q} = [x_1, y_1, \phi_1]^T$ and the constraint equation vector is

$$\Phi(\mathbf{q}, t) = \begin{bmatrix} \Phi_1 \\ \Phi_2 \end{bmatrix} = \begin{bmatrix} x_1 - d \cdot \sin(\phi_1) \\ y_1 + d \cdot \cos(\phi_1) \end{bmatrix} = \mathbf{0} \quad (4.74)$$

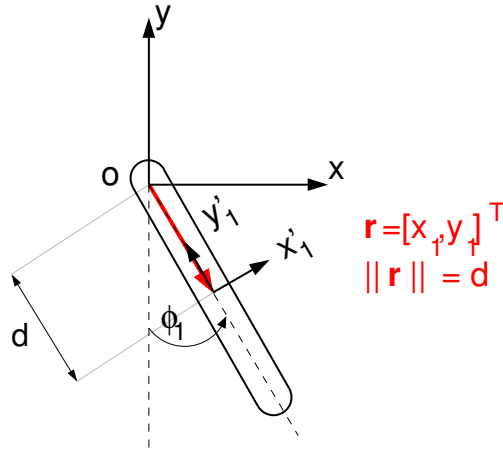


Figure 4.12: Simple pendulum.

The Jacobian of this system is

$$\Phi_{\mathbf{q}} = \begin{bmatrix} \frac{\partial \Phi_1}{\partial x_1} & \frac{\partial \Phi_1}{\partial y_1} & \frac{\partial \Phi_1}{\partial \phi_1} \\ \frac{\partial \Phi_2}{\partial x_1} & \frac{\partial \Phi_2}{\partial y_1} & \frac{\partial \Phi_2}{\partial \phi_1} \end{bmatrix} = \begin{bmatrix} 1 & 0 & -d \cdot \cos(\phi_1) \\ 0 & 1 & -d \cdot \sin(\phi_1) \end{bmatrix} \quad (4.75)$$

and is already in a row reduced echelon form. This indicates that the angle ϕ_1 is a good choice for an independent variable. This is true, because if variable ϕ_1 is known from acceleration analysis, the remaining variables x_1 and y_1 can be readily obtained from Equation 4.74.

This is quite obvious at this stage, but a more rigorous analysis can be performed to show that indeed ϕ_1 is the best choice for independent variable. In the following analysis, the subscript indices are dropped for clarity. If the numerical error in the coordinates is denoted by δx , δy and $\delta \phi$, then

$$\delta x = d \cos(\phi) \delta \phi \quad (4.76a)$$

$$\delta y = d \sin(\phi) \delta \phi \quad (4.76b)$$

In the selection of the independent coordinates, three cases may arise:

1. The independent variable is chosen to be x . An error δx causes errors in y and ϕ , as follows:

$$\delta \phi = \frac{1}{d \cdot \cos(\phi)} \delta x \quad (4.77a)$$

$$\delta y = \frac{\sin(\phi)}{\cos(\phi)} \delta x \quad (4.77b)$$

2. The independent variable is chosen to be y . An error δy causes errors in x and ϕ , as follows:

$$\delta\phi = \frac{1}{d \cdot \sin(\phi)} \delta y \quad (4.78a)$$

$$\delta x = \frac{\cos(\phi)}{\sin(\phi)} \delta y \quad (4.78b)$$

3. The independent variable is chosen to be ϕ . An error $\delta\phi$ causes errors in x and y , as follows:

$$\delta x = d \cos(\phi) \delta\phi \quad (4.79a)$$

$$\delta y = d \sin(\phi) \delta\phi \quad (4.79b)$$

A comparison of the three cases reveals that for $\phi = \pm\pi/2$, case 1, yields large errors in ϕ and y even for a small error δx . Therefore, for these values of ϕ , or any value close to these, the selection of x as the independent variable is the worst choice. Similarly, in the neighbourhood of $\phi = 0$ or $\phi = \pi$, the y coordinate is the worst choice for the independent variable. The third case shows that if ϕ is selected as the independent coordinate, the error remains bounded regardless of the orientation of the pendulum. Therefore, there is no need to switch to another coordinate at any time during computation, and this choice is the best for given problem.

4.5 Translational springs and dampers

The MBDM code takes into account arbitrary number of springs and dampers. The only requirement is that one end of the spring/damper is attached to a body, and the other end is fixed in the global reference frame. This assumption is employed in the derivation below. More general formulation can be found in the book of Haug ^[73]. Also, the rotational spring-damper-actuator is described in the aforementioned publication. Here, the spring-damper system is used to represent the mooring line.

First, consider the body shown in Figure 4.13. The body is connected with one translational spring-damper set to the point \mathbf{r}_i representing anchor, and point P_j represents fairlead. Thus, the vector \mathbf{d}_{ij} pointing from anchor to fairlead is

$$\mathbf{d}_{ij} = \mathbf{r}_j + \mathbf{A}_j \mathbf{s}_j^{\prime P} - \mathbf{r}_i \quad (4.80)$$

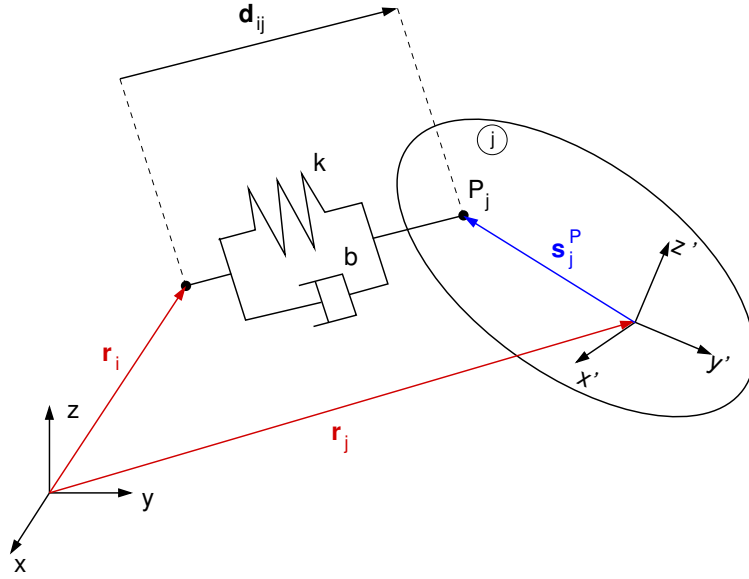


Figure 4.13: Body with translational spring fixed at one point.

The length l of the spring-damper set is given by

$$l^2 = \mathbf{d}_{ij}^T \mathbf{d}_{ij} \quad (4.81)$$

and can be differentiated in time to yield

$$2l\dot{l} = 2\mathbf{d}_{ij}^T \dot{\mathbf{d}}_{ij} \quad (4.82)$$

After some rearrangement, the time rate of the length change becomes:

$$\dot{l} = \left(\frac{\mathbf{d}_{ij}}{l} \right)^T \left(\dot{\mathbf{r}}_j + \mathbf{A}_j \mathbf{s}'_j{}^P - \dot{\mathbf{r}}_i \right) = \left(\frac{\mathbf{d}_{ij}}{l} \right)^T \left(\dot{\mathbf{r}}_j - \mathbf{A}_j \tilde{\mathbf{s}}_j{}^P \boldsymbol{\omega}'_j \right), \quad (4.83)$$

where simplification has been made, since anchor location is fixed in time i.e. $\dot{\mathbf{r}}_i = 0$. Note, that if l approaches zero an indeterminate fraction occurs in Equation 4.83. Although it is not the case for mooring cables, L'Hospital's rule may be used for general case to obtain $\lim_{l \rightarrow 0} \frac{\mathbf{d}_{ij}}{l}$.

The magnitude of the force acting in the spring-damper set is

$$f = k(l - l_0) + b\dot{l}, \quad (4.84)$$

where k is the spring stiffness coefficient, and b is the damping coefficient. The virtual work done by this force is

$$\delta W = -f\delta l \quad (4.85)$$

where the variation in length δl is obtained by taking the differential of Equation 4.81 and dividing by l to obtain:

$$\delta l = \left(\frac{\mathbf{d}_{ij}}{l} \right)^T \left(\delta \mathbf{r}_j - \mathbf{A}_j \tilde{\mathbf{s}}_j^P \delta \boldsymbol{\pi}'_j \right). \quad (4.86)$$

Substituting this result in Equation 4.85, yields

$$\delta W = \frac{-f}{l} \mathbf{d}_{ij}^T \left(\delta \mathbf{r}_j - \mathbf{A}_j \tilde{\mathbf{s}}_j^P \delta \boldsymbol{\pi}'_j \right). \quad (4.87)$$

The coefficients of virtual displacements, and virtual rotations, are the force and moment due to the spring-damper system:

$$\mathbf{F}_m^A = \frac{-f}{l} \mathbf{d}_{ij}, \quad (4.88a)$$

$$\mathbf{n}'_m{}^A = \frac{-f}{l} \tilde{\mathbf{s}}_j^P \mathbf{A}_j^T \mathbf{d}_{ij}, \quad (4.88b)$$

where the expression for the magnitude of force f is given by Equation 4.84.

Chapter 5

Conceptual model of coupling

This chapter is devoted to the employed coupling algorithm, its implementation and validation. Firstly, the importance of strong coupling is assessed for studied system and conditions. This is followed by the description of the communication method between the solvers. The procedure to generate a particular sea-state is investigated at the end of this chapter.

5.1 Importance of strong coupling

The strong coupling may be important if the phenomena occurring in both fluids have similar time scales. Due to frequency similarities, resonances may occur, and the exact response of a system will deviate from what is predicted by a loosely coupled algorithm. On the other hand, if the time scales are largely different, loosely coupled algorithm may be sufficient. The exact bounds when the strong coupling is required for particular FOWT must be carefully assessed. Some indication comes from the waves and rotor frequency analysis. The sea state, wave height, wave frequency, and wind speed are empirically related in terms of range and most probable values *e.g.* in [51, 116], see Section 5.3 for details. On the other hand, every wind turbine is designed to operate at a particular rotational frequency for a given wind speed. This allows to construct a "Campbell"-like diagram for the FOWT investigated in this work (Figure 5.1). It is clear that for sea states between 3 and 4 (or wind speed about $9m/s$) resonances may occur. The rated power production for this 10-MW FOWT corresponds to the wind speed of $11.4m/s$, or sea state 4. This indicates that for

rated conditions, the weakly coupled algorithm may be sufficient.

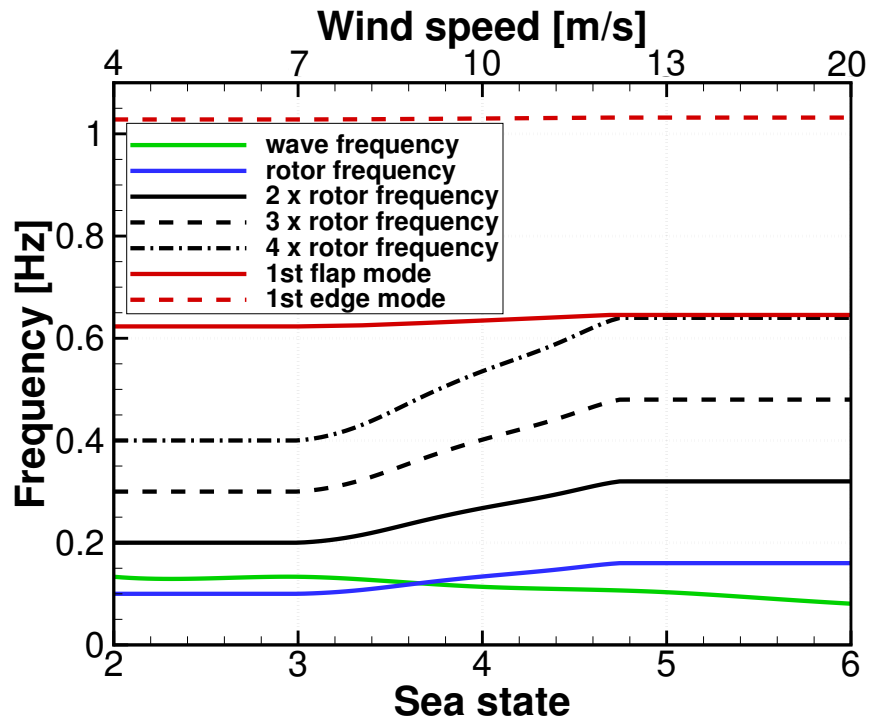


Figure 5.1: "Campbell"-like diagram for the investigated FOWT showing frequencies of the rotor and the waves as function of sea state and wind speed.

5.2 Communication between solvers

As was shown in Chapter 1, many disciplines converge in the coupled model of the FOWT. The current implementation is schematically presented in Figure 5.2, where coupling is between the fluids: air and water. Another option would be to employ a multi-phase solver (e.g. Volume of Fluid as in ^[197]). This approach does not tackle the problem of coupling, but shifts it to the structure-fluid side.

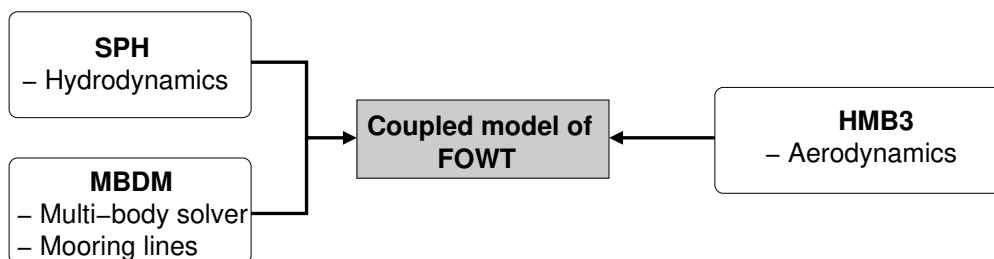


Figure 5.2: Schematic of the solvers employed in the floating off-shore wind turbine model.

In general, the exchange of information without stopping the computations can be implemented in three ways: through files, shared memory or the Message Passing Interface (MPI). Writing a file is the simplest solution. Both solvers can be launched separately and write files whenever exchange of information is required. This approach calls for very minor changes to both codes. The drawback is that writing and reading from a hard drive creates a bottleneck, and slows down the computation especially if information is exchanged often, and large amount of data is to be exchanged.

In the shared memory approach multiple processes have access to the same memory, allowing them to change it and read changes made by other processes. If random access memory (RAM) is to be used, it requires a shared memory machine, which may not be available on a High Performance Computer (HPC), where emphasis is usually placed on distributed memory. The file system can be used instead by mapping the memory on the hard drive. This approach suffers from the same drawback as the case of external storage.

Both employed CFD solvers are parallelised using MPI and the Single Program, Multiple Data (SPMD) paradigm, where each instance of the solver is assigned to perform the same task on different sets of data. Therefore, the easiest way to combine solvers is to employ MPI, but in Multiple Program, Multiple Data (MPMD) approach, where different programs operate on different sets of data. However, direct MPMD implementation of SPMD solvers requires additional effort to split the global communicator, such that each of the solvers is in a separate communicator (*MPI_COMM_WORLD*) with a separate ordering of processes, as detailed in OpenMPI documentation ^[155]. This can be avoided by dedicating one process to execute both solvers using *MPI_Comm_spawn* routine. The dedicated code is referred to as *master program* or *parent*, and spawned processes are referred to as *children*. This approach has a number of advantages briefly summarised as:

1. The spawned program has its own *MPI_COMM_WORLD*, therefore no modifications are required to original code with respect to processes that are going to communicate inside the child group.
2. The ordering of the processes is separate for parent and children. This way no modifications are required to original code with respect to process that is going to be in charge of the computation inside the child group.

3. The child process can easily identify if it was spawned or launched directly with an MPI command. This maintains the original code functionality.

5.2.1 MPI communication

In the present work, the communication between the solvers was established through the Message Passing Interface (MPI), where the MBDM is executed as a single process and is dedicated to start SPH and HMB3 parallel solvers. The data flow diagram of the implementation is presented in Figure 5.3. The communication

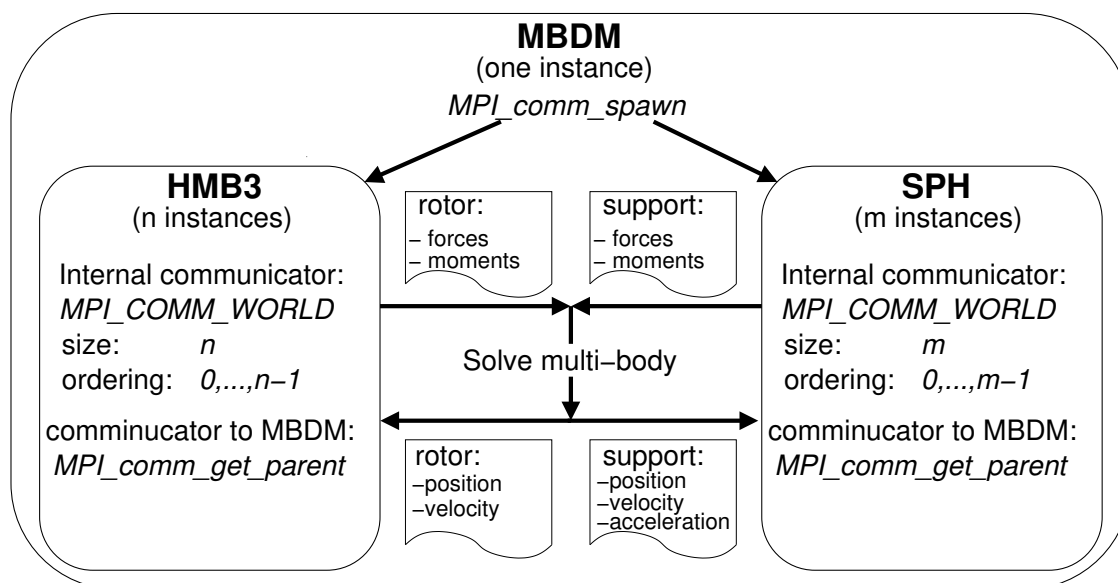


Figure 5.3: Flow chart of the MPI implementation and data exchange for coupled model.

was validated by executing separately SPH or HMB3, and comparing with the results where the body motion was introduced by the MBDM. Due to the Lagrangian nature of the SPH method, the submerged bodies can be represented with particles and do not require specific coupling. Therefore, by utilising MPI, the MBDM substituted the body motion routines of the SPH solver and reduced the number of coupled codes to two - SPH and HMB3. This implies that the MBDM is advancing in time with the same integration scheme as the SPH solver.

MPI communication with HMB

Two tests were performed to validate the communication protocol between the MBDM and HMB3. First, the HMB3 solver was launched as a child process. Mesh velocities were transferred at each time step from the master, redistributed among the HMB3 nodes and applied as mesh motions. This was compared to computation using built-in functions in HMB3 to apply prescribed mesh motions. The test case was 2D unsteady computation of a TL190-82 aerofoil that undergoes sinusoidal pitching motion about the leading edge with amplitude of 10° . The $k-\omega$ turbulence model was employed for this test. The computational parameters are presented in Table 5.1, and the mesh used for this comparison in Figure 5.4. The results

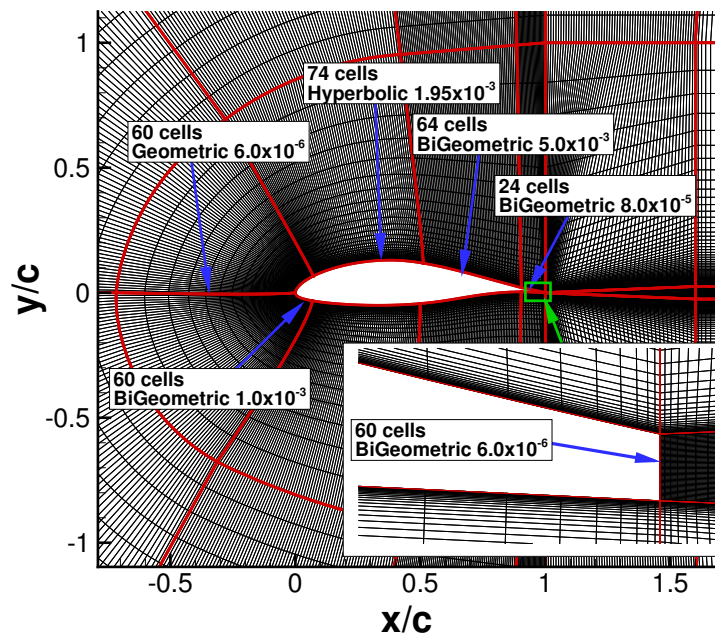


Figure 5.4: Meshes around the TL190-82 aerofoil used in 2D computations to validate communication protocol.

of the test cases in terms of lift, drag and moment coefficients are presented in Figure 5.5. As can be seen, the lift, drag and moment coefficients, over time, become identical for both computations. The positions of the surfaces along with pressure coefficient distribution at time $t = 3s$ are also compared. Results are shown on Figure 5.6, where excellent agreement can be observed. The above results show correctness of the established communication and procedure to apply mesh motion.

Table 5.1: Coupling test case conditions for 2D simulations of TL190-82 aerofoil.

Re	$2.5 \cdot 10^6$
M	0.11
Chord	1m
Grid size	$0.13 \cdot 10^6$ cells
Pitching frequency	1Hz
Pitching amplitude	10°
Pivot point	$[x, y] = [0, 0]m$
Iterations	1110
Steps per iteration	150
L2 convergence criteria per iteration	$1 \cdot 10^{-3}$
Total time	3s
Time step	$2.72 \cdot 10^{-3}s$
Time step in characteristic time scale	0.1

MPI communication with SPH

Four test cases were used to validate the communication between the MBDM and SPH solvers. All test cases had the same initial particle distribution and floating object on the SPH side. The geometry of the test case is shown in Figure 5.7, and the initial distribution of the SPH particles is shown in Figure 5.8. The spacing between the particles was chosen to be $d = 0.01m$, such that the floating body is represented by at least 6 particles in each direction. All test cases were run with the same computational parameters summarised in Table 5.2.

Table 5.2: Computational parameters of SPH communication test cases.

Spacing between particles	$d = 0.01m$
Smoothing length	$1.5d$
Number of particles	157,646
CoG of floating body	$[1.03, 0.31, 0.23]m$
Floating body dimensions	$0.06, 0.06, 0.06m$
Gravity acceleration	$[0, 0, -9.81]m/s^2$
Viscosity treatment	Artificial
Viscosity parameter	$\alpha = 0.01$
CFL number	0.2
Coefficient of speed of sound	20
Density filter	No filter
Boundary Conditions	Repulsive Force
Friction coef. between floating object and wall particles	0.20
Time step	$\Delta t = 1.2 \cdot 10^{-4}s$
Total time	4s

The first test case is the SPH code without any modification. The second test case involves simple

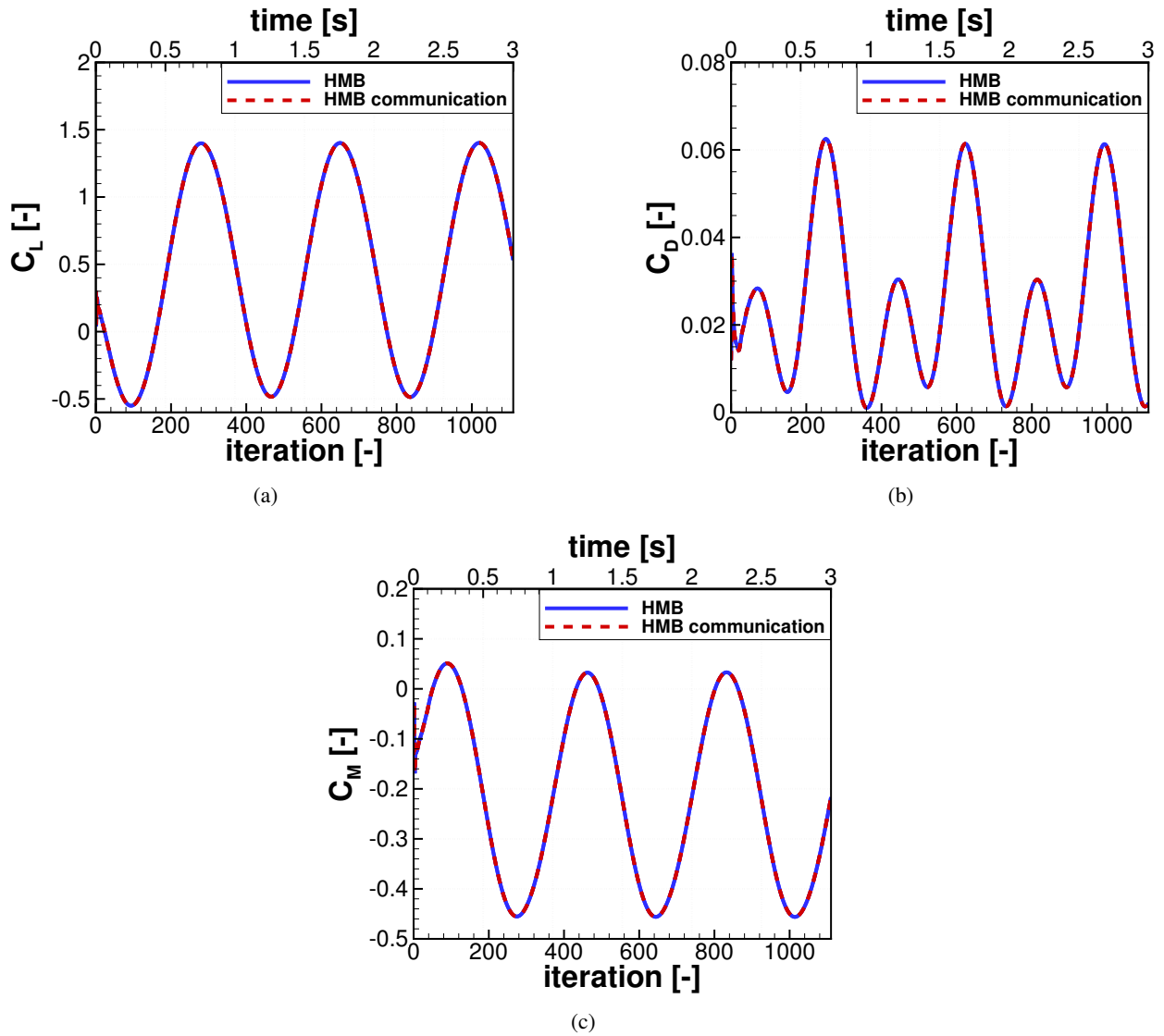


Figure 5.5: Coefficients of lift, drag and moment $c/4$ as functions of time for pure HMB3 and HMB3 with communication, where grid motion is applied at each time step.

communication, where the SPH calculates the new position and the velocity of the floating body, sends this information to the parent process, and receives the position and velocity back from the parent. These variables are then used in the SPH code instead of original variables. This test case should reveal any problems with the MPI communication between different programming languages: *Fortran* for the SPH solver, and *C* for the MBDM solver. The third test case involves computation of the new position and velocity of the floating body outside the SPH code, within the MBDM solver. The computational algorithm was kept the same as it was originally implemented in the SPH code. A more detailed description is presented later in this section. The fourth test case employed the computation of new position and velocity using the MBDM

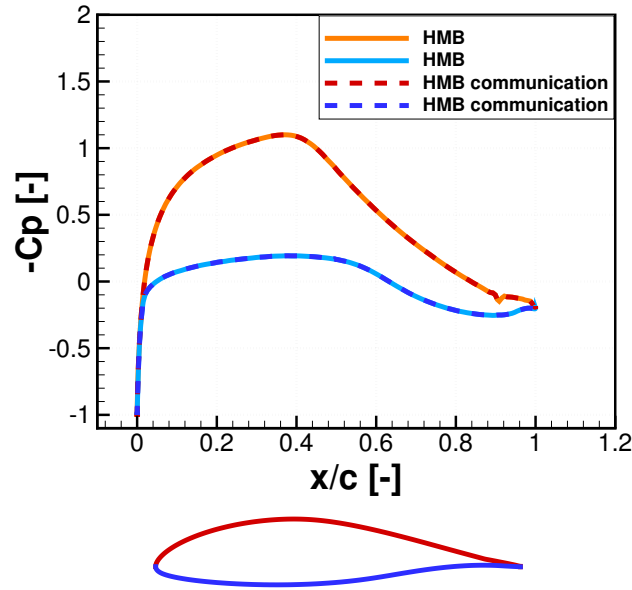


Figure 5.6: Position of the TL190-82 aerofoil and pressure coefficient distribution at time $t = 3s$. Comparison between computations using pure HMB3 and HMB3 with communication.

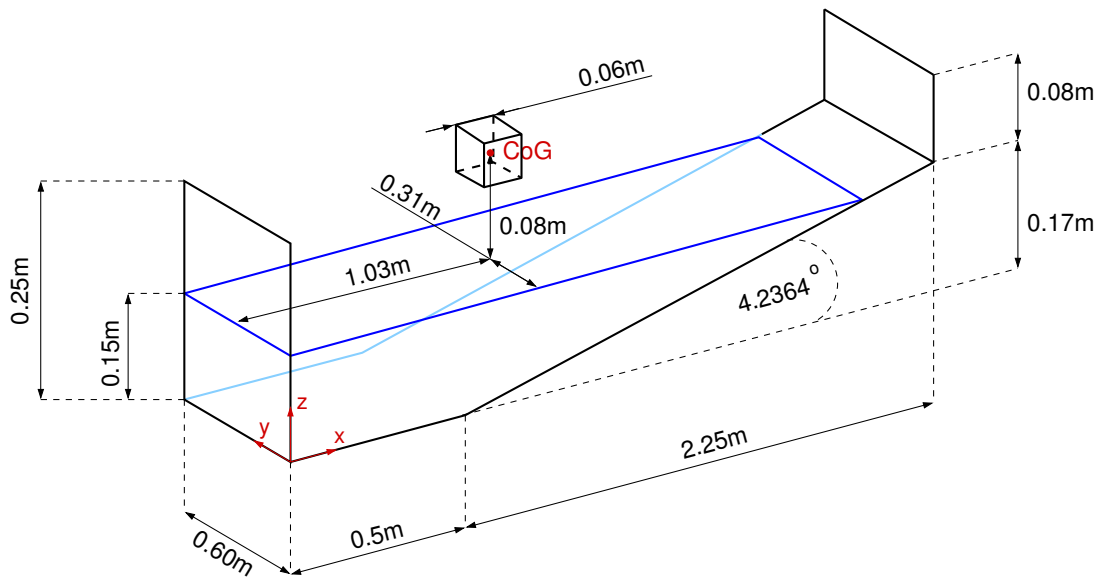


Figure 5.7: Schematic geometry of the test case, not in scale. Floating body is a cube with mass $m = 0.216kg$.

model for 6-DOFs motion. The new position and velocity are then transferred to the SPH and applied. All four cases are summarised in Table 5.3. The results of the computations are presented in Figures 5.9 and 5.10. The position of the floating body is shown in the global reference frame, as presented in Figure 5.7.

The rotational dynamics of the floating body, as was originally implemented in the SPH^[60, 62, 63]

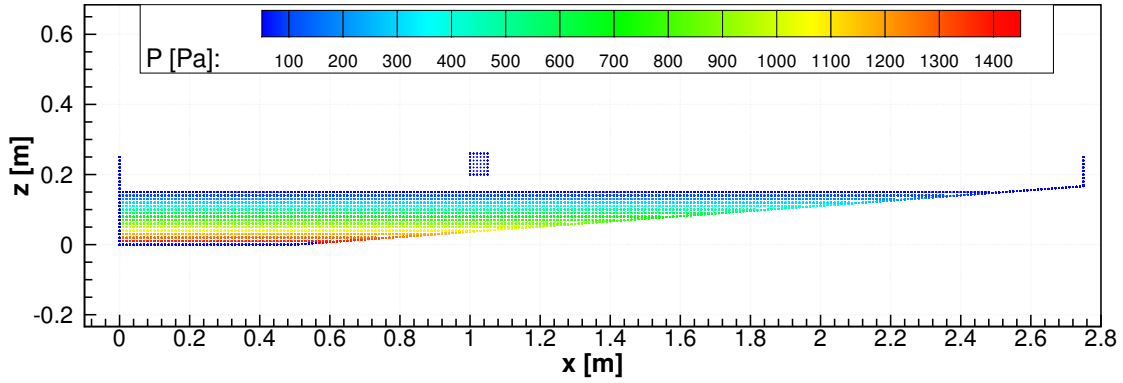


Figure 5.8: Initial particles distribution for all validation test cases. Spacing between particles $d = 0.01m$.

Table 5.3: Test cases to validate communication protocol between SPH and master.

Test case	Description
1. Pure SPH	Pure SPH code without modifications.
2. SPH with simple communication	Position and velocity of floating object are computed with SPH, transferred to MBDM, and returned back to SPH.
3. SPH with calculation	SPH computes the loads and transfers them to the MBDM solver. The MBDM computes new position, velocity and acceleration with the same equations as in the SPH solver and returns position, velocity and acceleration back to SPH.
4. SPH with calc. using MBDM	SPH computes loads and transfers them to the MBDM solver. In return, the MBDM computes new position, velocity and acceleration using multi-body model and returns them to the SPH solver.

code, is the solution to the following equation:

$$\mathbf{J} \frac{\partial \boldsymbol{\omega}}{\partial t} = \sum_k m_k (\mathbf{r}_k - \mathbf{R}) \times \mathbf{f}_k \quad (5.1)$$

where \mathbf{J} is a constant moment of inertia matrix, $\boldsymbol{\omega}$ is rotational velocity, \mathbf{r}_k is the position of the k -th particle in a global reference frame, \mathbf{R} is the position of the centre of mass of the floating body in a global reference frame, \mathbf{f}_k is the force acting on the k -th particle defined in the global reference frame, and summation is over all the floating body particles. As can be seen, the right hand side results in a moment about the centre of mass of the floating body. This moment is defined in the global coordinate system. Equation 5.1 is only valid for a two-dimensional motion, where the rotation is about one of the principal axes i.e. the moment vector has only one non-zero component in the global reference frame. When a body is displaced in such a way that the local body frame does not coincide with the global reference frame, the moment of inertia

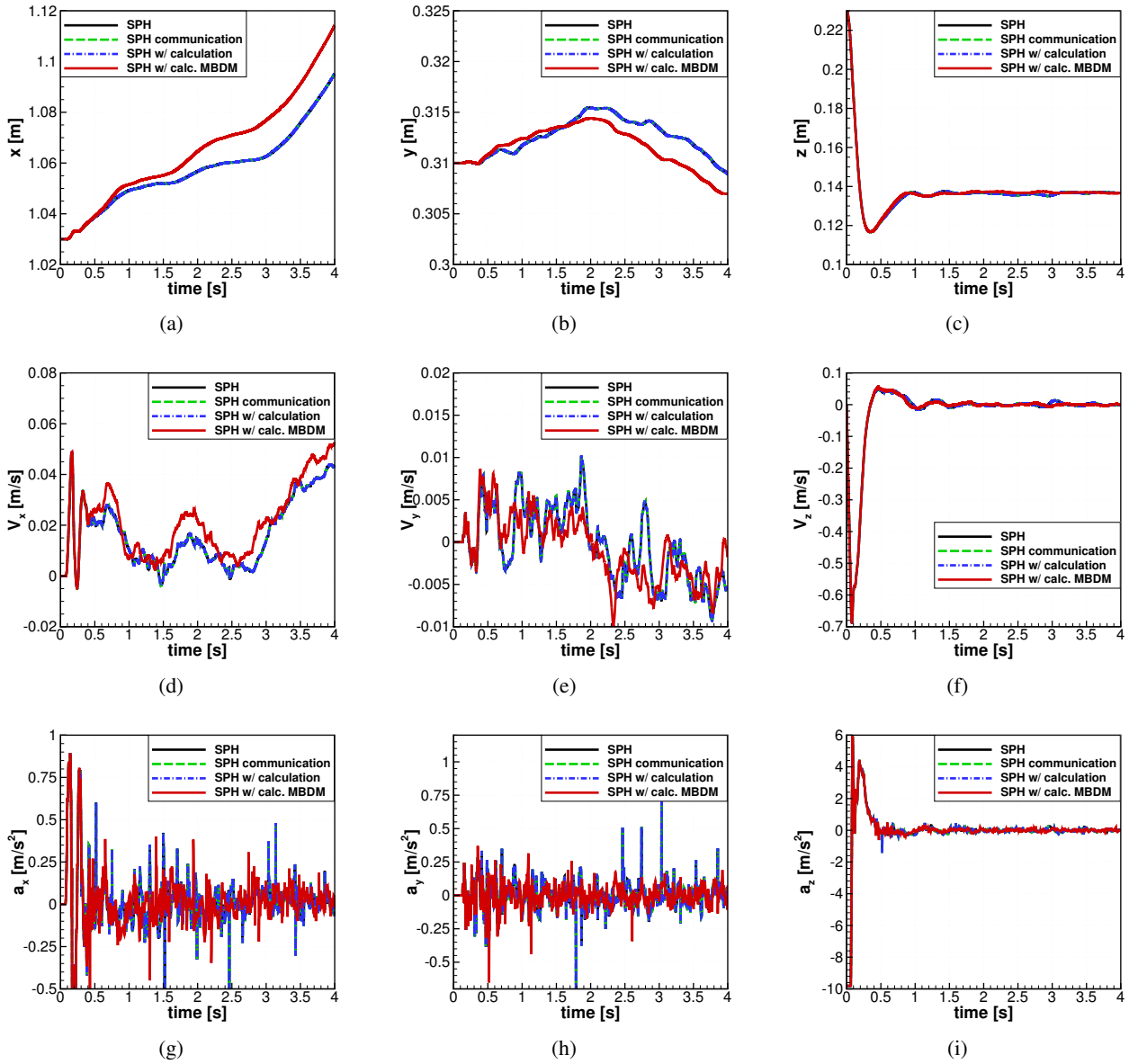


Figure 5.9: Lateral dynamics of the cube during the drop into calm water. Comparison between four test cases - Pure SPH, SPH with simple communication, SPH with calculation and SPH with calculations using MBDM. See Table 5.3 for the description.

matrix is no longer constant, and must incorporate the new body orientation in the global reference frame.

As can be seen in the results, the computation using pure SPH and SPH with the simple communication method produced identical results. This comparison proves the ability of the MPI routines to preserve information while sending messages between the two solvers. Also, the results of the pure SPH and the SPH with calculations are identical. This comparison proves that the same numbers multiplied in *Fortran* (SPH) and *C* (MBDM) codes produced the same results. Differences arise, when the multi-body code is used to

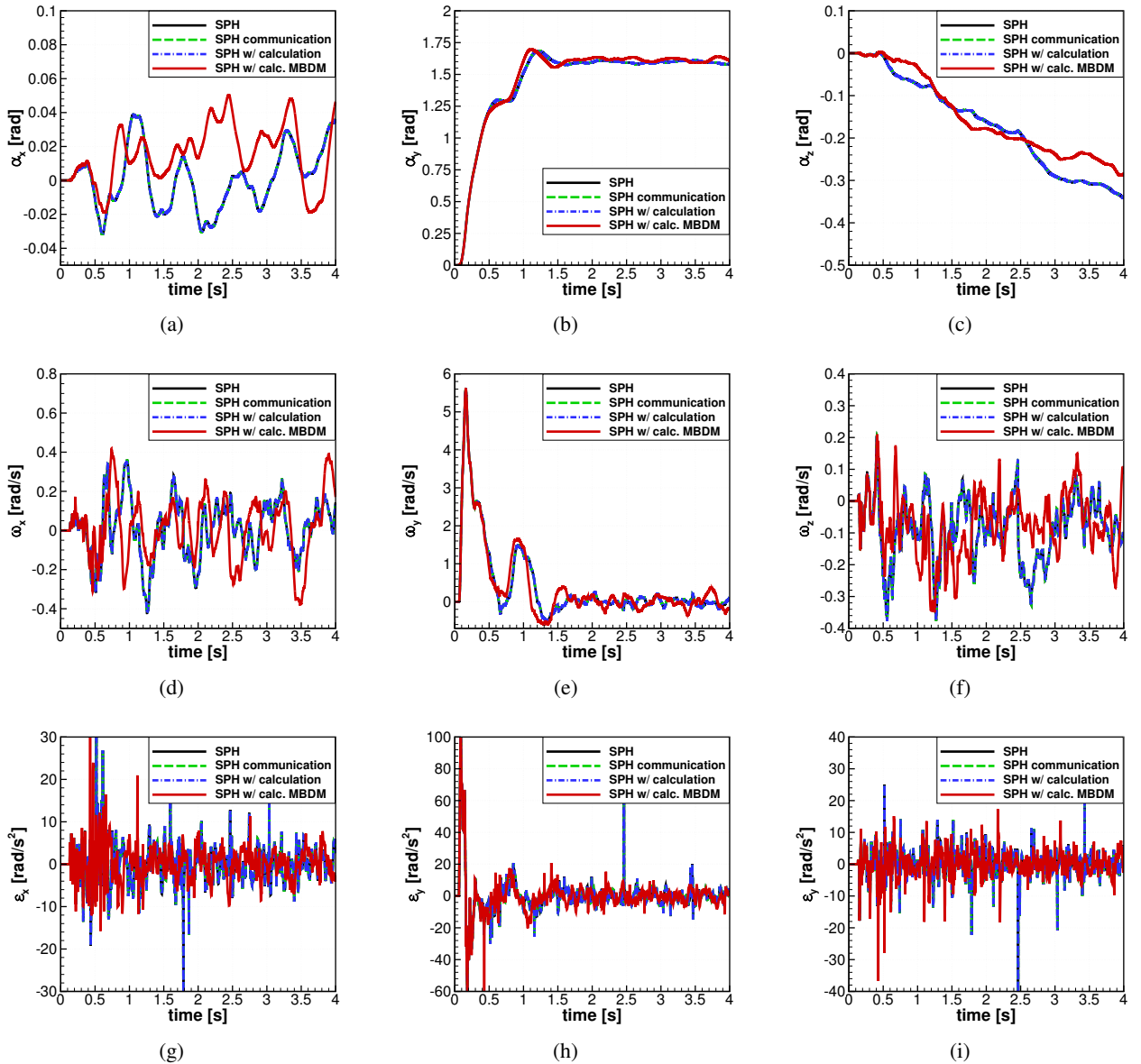


Figure 5.10: Rotational dynamics of the cube during the drop into calm water. Comparison between four test cases - Pure SPH, SPH with simple communication, SPH with calculation and SPH with calculations using MBDM. See Table 5.3 for the description.

compute the dynamics of the floating body. Those differences are due to the different dynamic equations, where Equation 5.1 in the original SPH code is not valid for general three-dimensional motion. Although the difference is only in the rotational equations of motion, the lateral and rotational dynamics are coupled i.e. different orientation of the body results in different lateral forces. The results show that the body flips on the side - rotation about y axis with the angle of $\pi/2$. This is due to the initial particles that were assigned to the body as shown in Figure 5.11. The last layer of particles in the x direction is missing, creating the

moment about the centre of mass. This incorrect representation of the geometry of the floating body was noticed, but was not affecting the validation, since the validation of communication between the solvers was the main objective. However, it indicates that careful attention must be paid to how the floating objects are represented by the particles. Hence, floating objects employed in Chapters 6 and 13 were thoroughly checked for correct particle representation. Also, it is important to note that the results of the SPH with calculations using the MBDM begin to deviate from the SPH solution after approximately $0.5s$. This is because the moment about other axes than y became more pronounced after this time, and the Equation 5.1 was no longer valid.

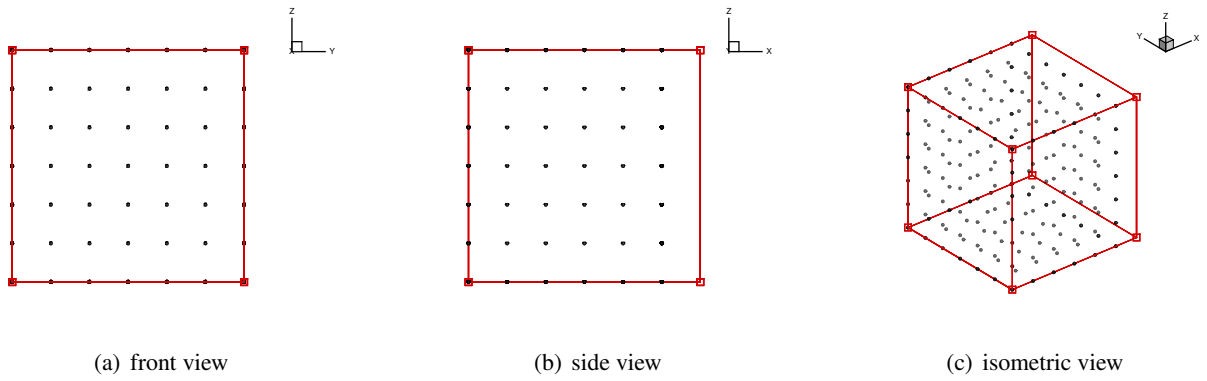


Figure 5.11: Comparison between the real shape of the body (red lines) and the particles used to represent the body. Last layer of particles in x direction is missing.

Another aspect that must be addressed is whether the position of the SPH particles assigned to a floating body correspond to the computed positions in the MBDM solver. This is important because the SPH solver does not send the particles' positions to the MBDM solver, and the MBDM solver does not send the rotational matrix to the SPH solver. Instead, the particles are moved by using the obtained position of the floating body, and the lateral and rotational velocities i.e. the calculated Euler angles are not used. This is obtained by solving the following sequence of equations in the SPH solver:

$$\mathbf{x}_k^{n+1} = \mathbf{x}_k^n + \Delta t \cdot \mathbf{u}_k^n \quad (5.2a)$$

$$\mathbf{r}_k^{n+1} = \mathbf{x}_k^{n+1} - \mathbf{R}^{n+1} \quad (5.2b)$$

$$\mathbf{u}_k^{n+1} = \mathbf{U}^{n+1} + \boldsymbol{\omega}_k^{n+1} \times \mathbf{r}_k^{n+1} \quad (5.2c)$$

where k is a particle that belongs to the floating body, n indicates the time such that $t = n \cdot \Delta t$, \mathbf{x} is the

location of the particle in the global coordinate system (GCS), \mathbf{u} is the velocity of the particle in the GCS, \mathbf{R} is the vector pointing to the centre of mass of the floating object defined in the GCS, \mathbf{r} is a vector pointing from the centre of mass to the particle position in the GCS, \mathbf{U} is the lateral velocity vector of the floating body defined in the GCS, and $\boldsymbol{\omega}$ is the rotational velocity of the floating body defined in the GCS. Quantities \mathbf{R} , \mathbf{U} , and $\boldsymbol{\omega}$ are received from the MBDM solver.

To validate whether the position is identical, the corner particle of the floating body was chosen and traced in time in the SPH and the MBDM solvers separately. The results of the position of this particle are presented in Figure 5.12. As can be seen from the results, the position of the traced particle is the same in

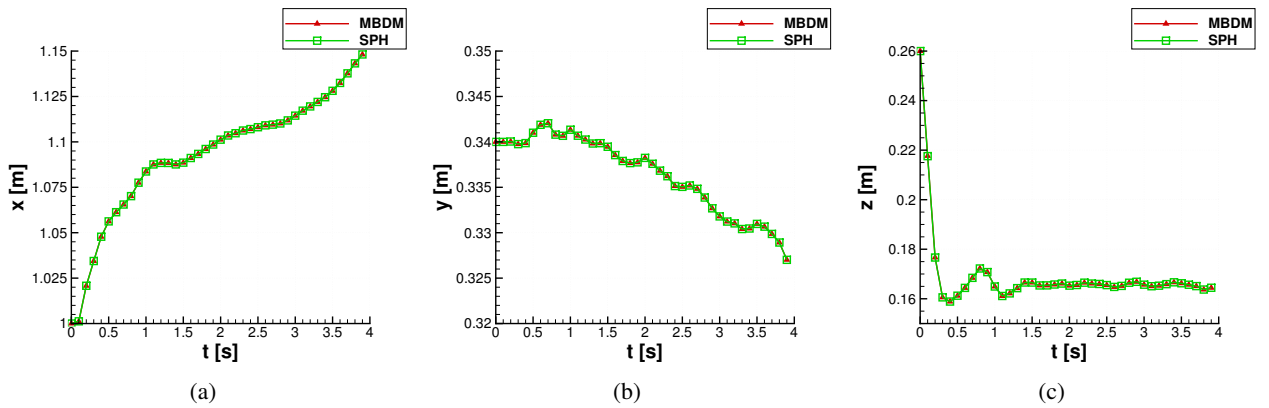


Figure 5.12: Comparison between the position of the corner particle in MBDM and in SPH that is governed by the MBDM dynamic equations. Initial position of the particle was $[1.0, 0.34, 0.26]m$.

the MBDM and SPH codes. This shows the correct position and orientation of the floating body in both solvers as they advance in time.

5.3 Generation of regular waves

This section describes the procedure to generate regular waves using the SPH solver. The sea waves can be described in terms of the sea state, which is represented by the sea state number that is, in return, correlated with the height and frequency of the waves. Table 5.4 shows the annual sea occurrences in the North Atlantic as in^[51]. It must be noted that the most probable modal period presents the modal period corresponding to the centre frequency of the modal period band with the highest probability of occurrence and does not reflect anything about the distribution within that band. Hence, the important aspect for a reproduction of the sea

state is a wave spectrum. Commonly used wave spectra include the Pierson-Moskowitz^[160], and the Joint North Sea Wave Project (JONSWAP)^[72] spectrum. In the following, the simplification is adopted by using a regular wave with characteristic amplitude and frequency of the sea state.

Table 5.4: Annual sea occurrences in the North Atlantic^[51]

Sea State	Significant Wave Height (m)		Modal Period (s)		Substantial wind speed (m/s)	
	Range	Mean	Range	Most probable	Range	Mean
0-1	0-0.1	0.05	0	0	0-3	1.5
2	0.1-0.5	0.3	3.3-12.8	7.5	4-5	4.5
3	0.5-1.25	0.88	5.0-14.8	7.5	6-8	7
4	1.25-2.5	1.88	6.1-15.2	8.8	9-11	10
5	2.5-4.0	3.25	8.3-15.5	9.7	12-14	13
6	4.0-6.0	5	9.8-16.2	12.4	15-24	19.5
7	6.0-9.0	7.5	11.8-18.5	15	25-28	26.5
8	9.0-14.0	11.5	14.2-18.6	16.4	29-32	30.5
>8	>14.0	>14.0	15.7-23.7	20	>32	>32

Two-dimensional computations were performed to find the wave generator parameters required to create characteristic waves for particular sea state. The water tank for this set of test cases was chosen to be 500m long, where the waves are generated by the paddle at one side of the tank, and dissipated by a beach-like slope at the other end of the tank, as shown in Figure 5.13. The tank was filled with water to the level of 20.1m, and the slope of the beach was set to $\beta = 8.5^\circ$.

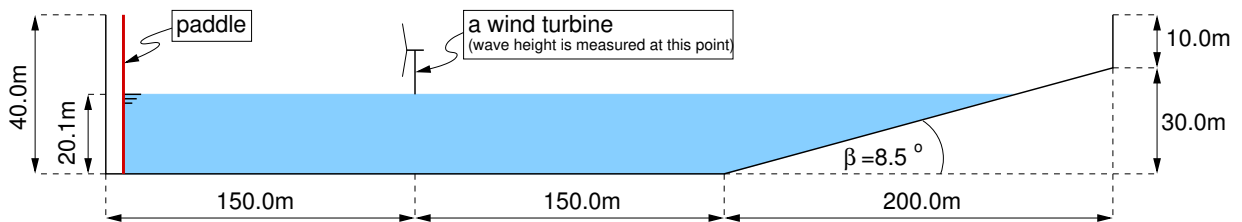


Figure 5.13: Two dimensional water basin for regular waves generation test cases. Not to scale. Wave height is measured around 150m from the paddle.

The flat-bottom part of the domain was 300m long, and the wave height was calculated at a distance of around 150m from the paddle. This was chosen to allow at least one wave length between the paddle and the wind turbine position, although the wind turbine was not considered in this test. The wave height was calculated from crest to trough at given location, as shown in Figure 5.14(a). The trough was measured at some time t , and crest was measured at time $t + T/2$, where T is a period of the waves.

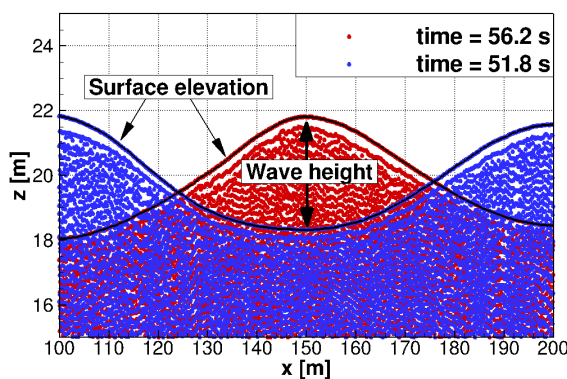
The DTU-10MW^[11] employed in this work is designed to start at 4m/s wind speed, operate at rated

conditions at 11.4m/s , and shut down at wind speed above 25m/s . This corresponds to possible operating sea states ranging from 3 to 6, where rated conditions are obtained for sea state 4, as listed in Table 5.4. Computational parameters employed for the SPH solver are listed in Table 5.5.

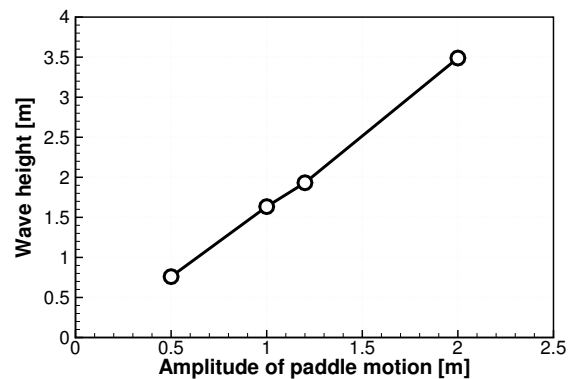
Table 5.5: Computational parameters of SPH for wave generation test cases.

Spacing between particles	$d = 0.3\text{m}$
Smoothing length	$h = 1.5d$
Number of particles	83,033
Viscosity treatment	Artificial
Viscosity parameter	$\alpha = 0.1$
CFL number	0.2
Coefficient of speed of sound	20
Density filter	No filter
Boundary Conditions	Dalrymple
Time step	$\Delta t = 1.2 \cdot 10^{-4}\text{s}$

The wave generator consisted of a paddle that was moving in the x direction in a sinusoidal manner with amplitude A and frequency f . The frequency was kept constant for each sea state, and the amplitude was varied to find the correlation between the amplitude of the paddle and the height of generated waves. The results for characteristic waves for sea state 4 are shown in Figure 5.14(b), where the linear relationship is evident. The best estimate of the sea state 4 was obtained for the paddle amplitude $A = 1.2\text{m}$. Three solutions for different paddle amplitudes are compared in Figure 5.15.



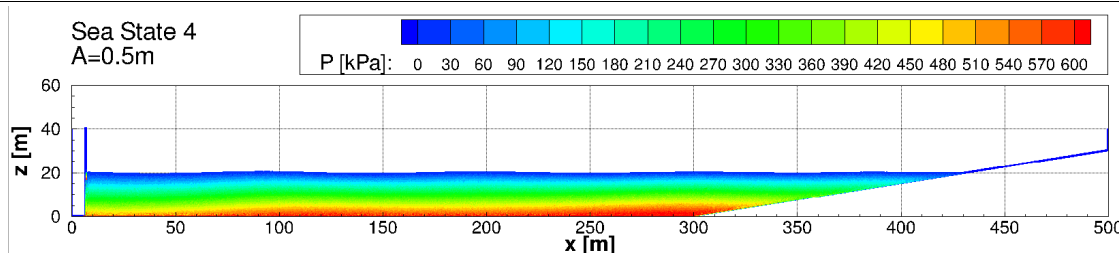
(a) Wave height obtained from two solutions for sea state 4.



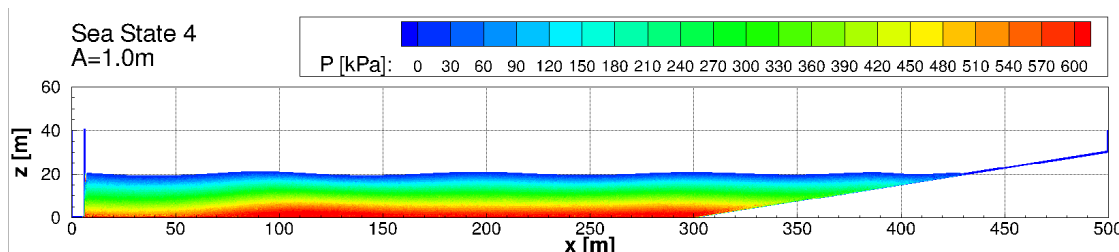
(b) Wave height as function of paddle amplitude for sea state 4.

Figure 5.14: Results for sea state 4 - definition of the wave height (a), and calculated wave height as function of paddle amplitude (b).

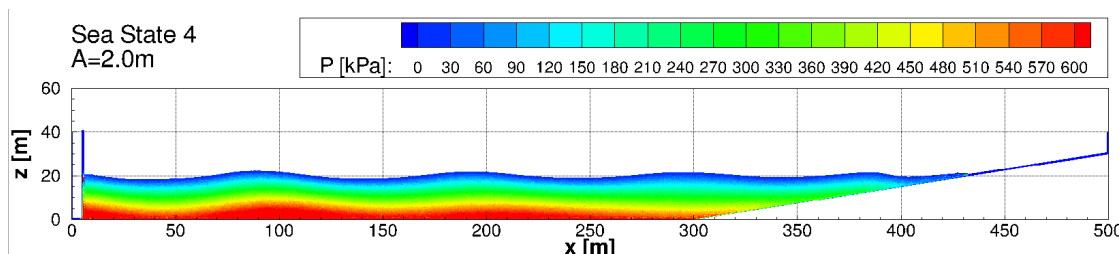
Similar regular wave tests were performed for other sea states, and the results are shown in Figure 5.16



(a) Paddle motion amplitude $A = 0.5m$.



(b) Paddle motion amplitude $A = 1.0m$.



(c) Paddle motion amplitude $A = 2.0m$.

Figure 5.15: Span-shots of the pressure distribution and surface elevation for the sea state 4 for various amplitudes of paddle motion. Period of paddle motion $T = 8.8s$. Time of the solution $t = 60.0s$.

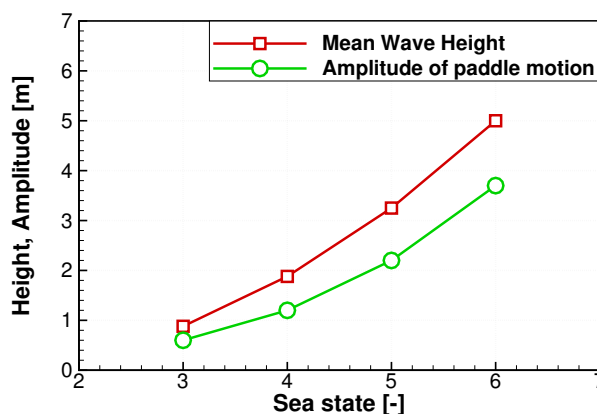


Figure 5.16: Wave height and paddle amplitude as function of sea state.

and Table 5.6. The conclusion can be drawn that amplitude of paddle motion should be around 68% of desired wave height.

Table 5.6: Amplitude and period of paddle motion to generate regular waves corresponding to characteristic waves in sea states from 3 to 6.

Sea state	Wave height [m]	Paddle amplitude [m]	Paddle period [s]
3	0.88	0.60	7.5
4	1.88	1.20	8.8
5	3.25	2.20	9.7
6	5.00	3.70	12.4

Chapter 6

Validation of SPH

The SPH method was validated against experimental results of Greenhow and Lin^[66] for the high speed entry of a half-buoyant solid cylinder into the calm water. Following the experimental setup shown in Figure 6.1, the cylinder of density $500\text{kg}/\text{m}^3$ was allowed to fall freely from the height of 0.8m . The diameter of the cylinder was 0.11m and the length was 0.2m ; the water depth was 0.3m .

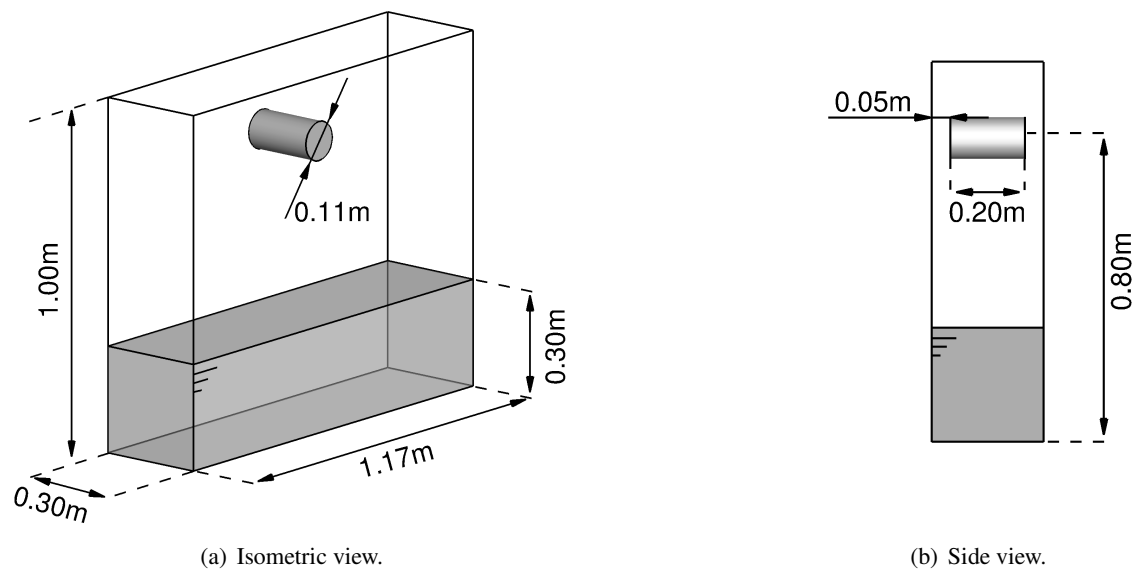


Figure 6.1: Schematic of the SPH validation setup: a) isometric view b) side view.

Simulations were executed with the cubic spline kernel, the artificial viscosity model with viscosity parameter $\alpha = 0.1$, and adiabatic index for the equation of state was set to $\gamma = 7$. The Dalrymple boundary

condition was employed for the cylinder particles, see Section 2.4.3 in Chapter 2 for details. The XSPH parameter (see Section 2.4.1) to move particles with the velocity close to the average in their neighbourhood was $\varepsilon = 0.5$, and sound coefficient to restrict the sound to be c times faster than the maximum fluid velocity was $c = 20$. The density of the cylinder was assigned by defining the relative weight between fluid and cylinder particles to be $w = 0.5$. The viscosity between the cylinder SPH particles and fluid particles was neglected. Finally, the symplectic time integration scheme^[117] was employed for all presented test cases, and the Courant-Friedrichs-Lewy number $CFL = 0.2$ was used. Computational parameters employed for the SPH solver are listed in Table 6.1.

Table 6.1: Computational parameters of SPH for validation test cases.

Smoothing length	$h = 1.5d$
Viscosity treatment	Artificial
Viscosity parameter	$\alpha = 0.1$
CFL number	0.2
Coefficient of speed of sound	20
XSPH parameter	$\varepsilon = 0.5$
Density filter	No filter
Boundary Conditions	Dalrymple
Time step	$\Delta t = 1.0 \cdot 10^{-4} s$

First, the influence of the viscosity parameter α on the depth of penetration was tested for the fixed initial distance between the particles $d = 0.65cm$. The results are presented in Figure 6.2. As can be seen, the reduction of the artificial viscosity below certain value of α does not increase the depth of penetration, where the limiting value appears to be $\alpha \approx 0.1$. For this reason, further validation tests were computed with the viscosity parameter set to $\alpha = 0.1$. Also, it is clear that by tuning artificial viscosity, any slope of the curve below the one calculated for $\alpha = 0.1$ can be achieved.

Next, five test cases were compared with different distance between the particles d , and therefore different amount of particles since the geometry was kept constant. In the first case $d = R/8 \approx 0.69cm$, in the second case $d = R/11 = 0.50cm$, in the third case $d = R/16 \approx 0.34cm$, in the fourth case $d = R/24 \approx 0.23cm$, and in the fifth case $d = R/32 \approx 0.17cm$, where $R = 5.5cm$ is a radius of the cylinder. Table 6.2 presents more information on the number of particles and its mass for the computed test cases.

The penetration depths for those cases are compared to the experimental results in Figure 6.3. It is clear that with increasing number of particles, but up to some limit, the depth of penetration has better agree-

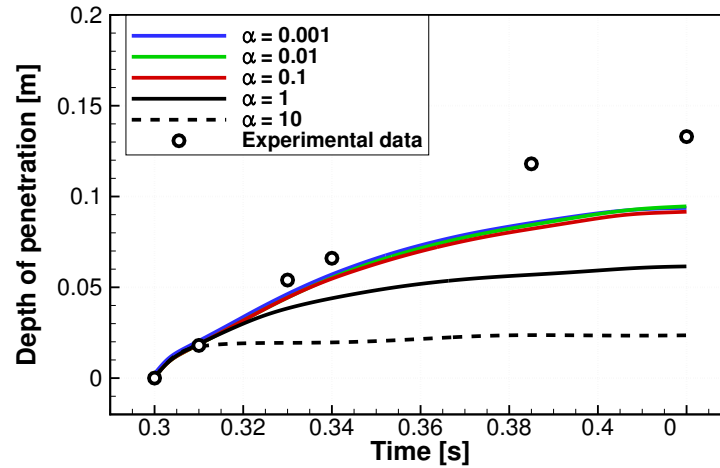


Figure 6.2: Depth of penetration of a cylinder of density 500 kg/m^3 : SPH results for different viscosity parameters α and constant number of particles. Experimental data of Greenhow and Lin^[66] is shown for comparison.

Table 6.2: Validation test cases for the SPH method.

Initial spacing	Property	Cylinder	Fluid	Boundary	Total
$d = 0.69\text{cm}$	Number of particles	5,713	312,481	70,183	388,377
	Mass of one particle [kg]	$1.63 \cdot 10^{-4}$	$3.25 \cdot 10^{-4}$	$3.25 \cdot 10^{-4}$	-
$d = 0.50\text{cm}$	Number of particles	15,000	824,820	132,570	972,390
	Mass of one particle [kg]	$6.25 \cdot 10^{-5}$	$1.25 \cdot 10^{-4}$	$1.25 \cdot 10^{-4}$	-
$d = 0.34\text{cm}$	Number of particles	47,023	2,536,398	279,445	2,862,866
	Mass of one particle [kg]	$2.03 \cdot 10^{-5}$	$4.06 \cdot 10^{-5}$	$4.06 \cdot 10^{-5}$	-
$d = 0.23\text{cm}$	Number of particles	159,221	8,668,270	629,071	9,456,562
	Mass of one particle [kg]	$6.00 \cdot 10^{-6}$	$1.20 \cdot 10^{-5}$	$1.20 \cdot 10^{-5}$	-
$d = 0.17\text{cm}$	Number of particles	381,871	20,556,725	1,116,921	22,055,517
	Mass of one particle [kg]	$2.54 \cdot 10^{-6}$	$5.08 \cdot 10^{-6}$	$5.08 \cdot 10^{-6}$	-

ment with the experimental data. For the finest resolution of the SPH domain, the method predicted deeper penetration as compared to the measurements. As was shown before, this can be improved by increasing the artificial viscosity parameter, but this was not the purpose of this validation. Also, the experiments were conducted in quasi two-dimensional conditions, where top and bottom of the cylinder were close to the walls of the tank. However, during the simulations initial distance of the cylinder from the container walls was introduced, and was set to $7R/8 \approx 5\text{cm}$, as shown in Figure 6.1. This was found to be necessary, as the purpose was to validate three-dimensional SPH method, but proximity of the walls introduced interaction between the falling cylinder and the walls of the tank. The interaction takes place when the cylinder particles fall within the range of the kernel for boundary particles, introducing friction. To avoid this unphysical

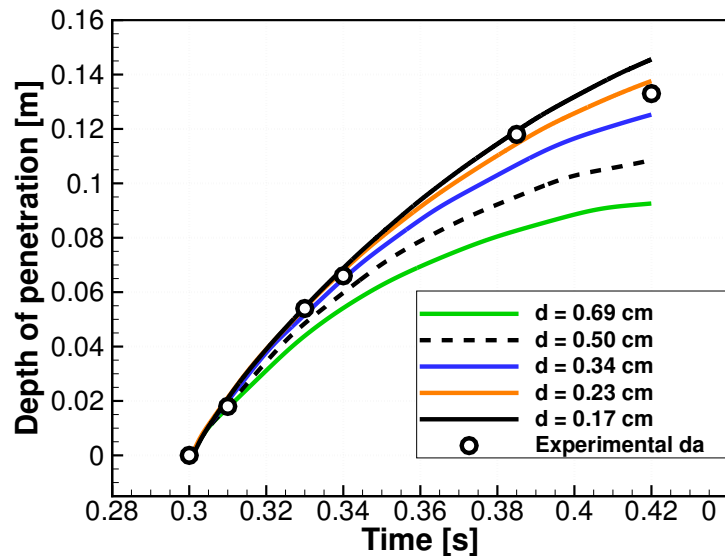


Figure 6.3: Depth of penetration of a cylinder of density 500 kg/m^3 : SPH results for different distance between particles (d) and experimental results of Greenhow and Lin^[66].

friction, the aforementioned gap was introduced, and was chosen large enough to limit interaction for the range of selected d - initial spacing between particles.

Next, the results of the SPH solver for initial particle spacing $d = 0.17 \text{ cm}$ were compared to the results obtained by Vandamme *et al.*^[199] who used weakly compressible SPH (WCSPH) method, and Skillen *et al.*^[185] who used an incompressible SPH (ISPH) method. The comparison is shown in Figure 6.4. First, overall agreement between three methods can be concluded, where current SPH method agrees very

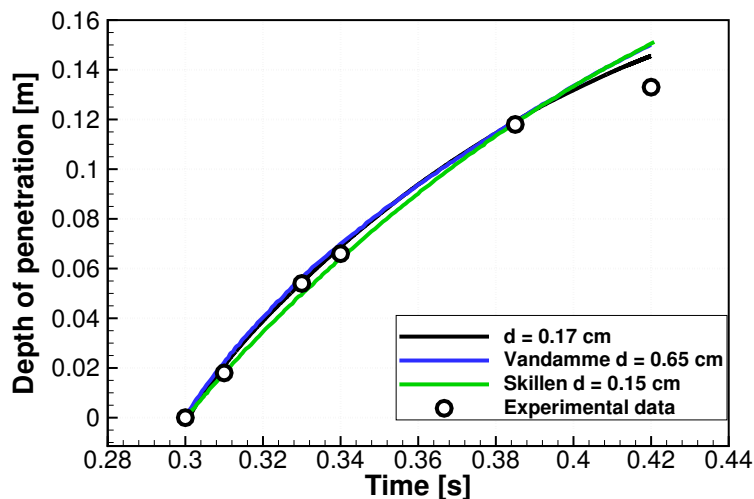


Figure 6.4: Depth of penetration of a cylinder of density 500 kg/m^3 : Comparison between current SPH method and results of Vandamme *et al.*^[199] and Skillen *et al.*^[185], and experimental results of Greenhow and Lin^[66]

well with the WCSPH method of Vandamme^[199] and the experiment up to the time $0.4s$. After this time, the WCSPH and the ISPH methods agree very well, but current SPH method predicts lower penetration depth, which in return agrees better with measurements of Greenhow and Lin^[66].

The free surface deformation is compared to observations of Greenhow and Lin^[66] in Figure 6.5. The slice of particles that fall within range of $y \in < 0.145m, 0.150m >$ are compared to the snapshot taken at time $t = 0.32$ seconds during water entry of a cylinder. The gap between the surface of the water and the surface of the cylinder is caused by the particle interaction. The volume around given particle, where contribution from other particles is taken into account, is directly influenced by the smoothing length h , which in return depends on the initial particle distance d . Therefore, for larger distance d particles have greater range of influence. Hence, larger gap between the water and cylinder.

Finally, velocities and accelerations for all test cases are compared in Figure 6.6. As can be seen, significant oscillations in acceleration are present for all cases and is caused by the particles motion in the fluid, where particles approach and retreat from the boundary surface, and therefore influence their contribution to the acceleration of the cylinder centre of gravity. The width of the acceleration peak is reduced as the spacing between particles decreases. As can be observed in the fluctuations of velocity, the smoothest curve is obtained for the the case with lowest initial particle distance, which indicates the smallest fluctuations in the acceleration for this test case.

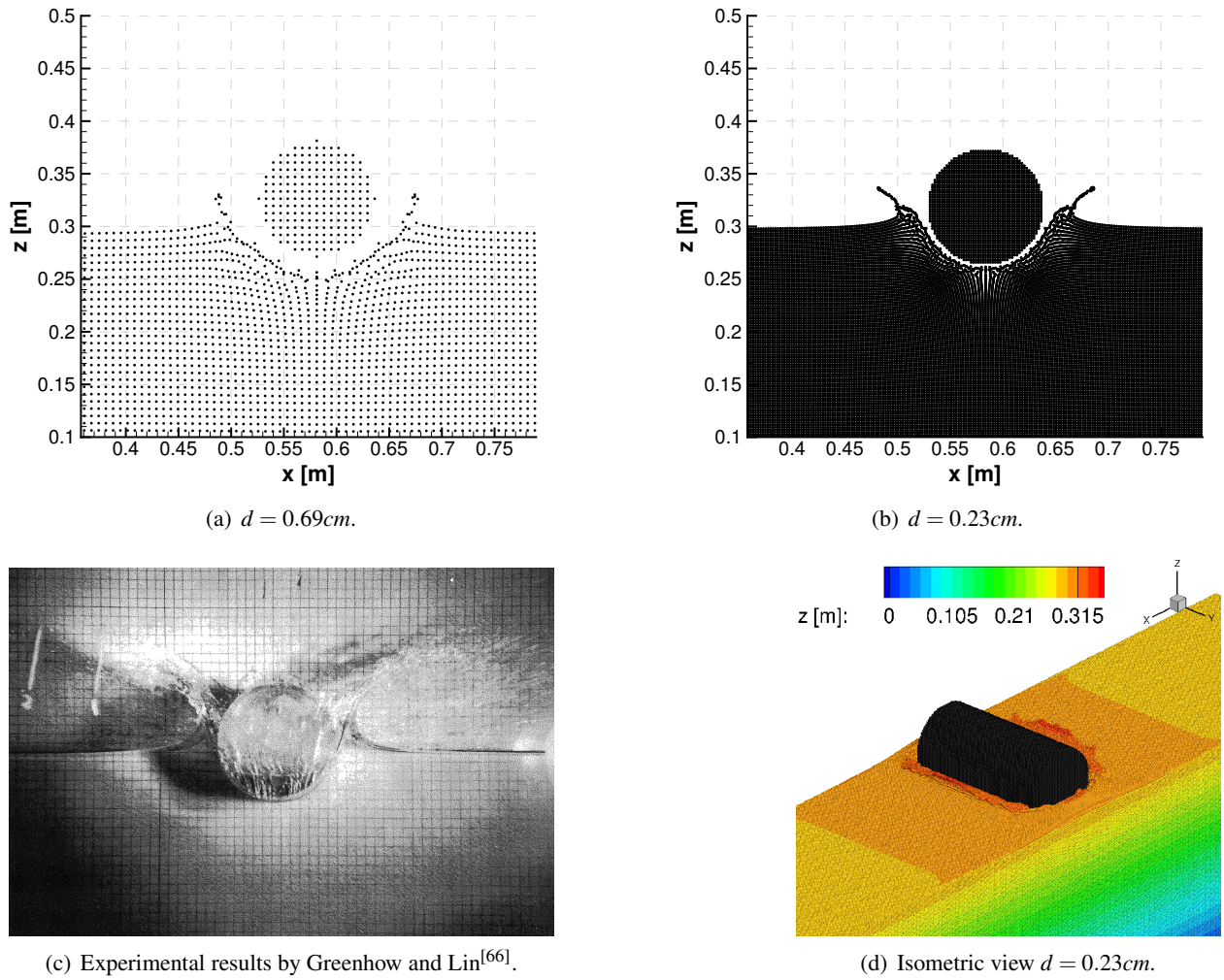


Figure 6.5: Surface deformation during water entry of a cylinder for time $t = 0.32\text{s}$ from the beginning of the fall. Comparison between different distances d and experimental results by Greenhow and Lin^[66].

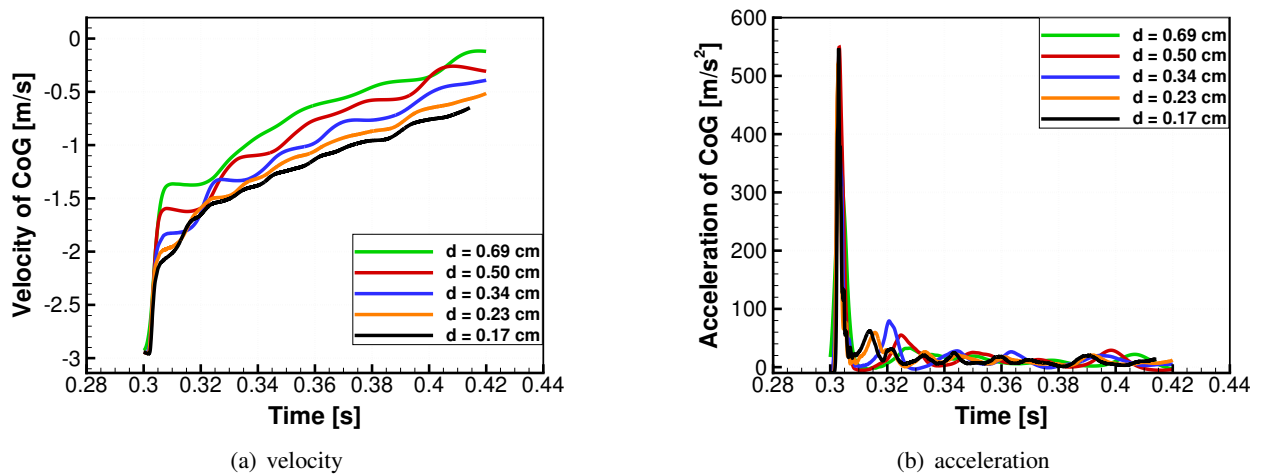


Figure 6.6: Comparison between velocity and acceleration curves over time for different initial particle distance d . CoG - centre of gravity of the cylinder.

Chapter 7

Validation of CFD

The HMB CFD solver has so far been validated for several wind turbine cases, including the NREL Annex XX ^[70] and the MEXICO project ^[176, 177] experiments, where the pressure and PIV data have been used for validation ^[27, 64]. This chapter presents results of those test cases using HMB3.

7.1 NREL Annex XX experiment

The NREL Annex XX experiment employed two-bladed NREL Phase VI rotor in upwind configuration. Each blade consists entirely of a 21-percent thick, laminar flow aerofoil, the S809. The aerofoil is extensively studied in wind tunnels ^[187, 165] and plenty of data is available in the literature. For this reason, NREL used it to design the blade for their Annex XX experiment.

This is a stall-regulated wind turbine and has a power rating of $20kW$. The blade has linear taper, nonlinear twist distribution and uses the S809 aerofoil from root to tip, see Figure 7.1. The span of the blade is 5.029 meters. The blade has a maximum chord of $0.737m$ at 25% of blade span, and chord of $0.457m$ at 80% of the blade span. The pitch is defined at the 75% blade radius and the pitch axis is at 30% of the chord. The wind turbine is designed to operate at a wind speed of $7m/s$ with a rotational speed of $72rpm$ resulting in tip speed ratio $\lambda = 5.61$. Detailed description of the blade design and its characteristics are available in the NREL report ^[61]. Design and experimental results for the S809 aerofoil are presented by Somers ^[187].

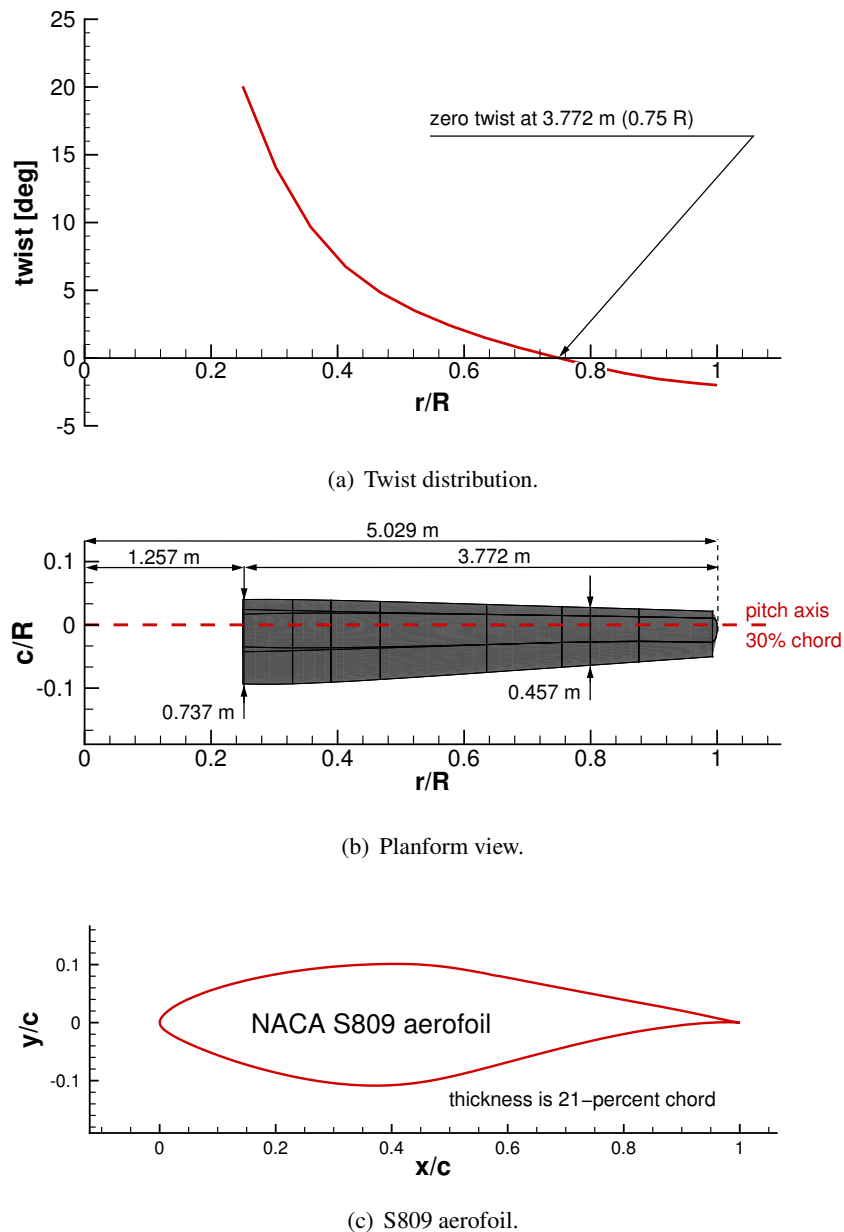


Figure 7.1: NREL Phase VI blade – twist distribution (a), geometry (b), and NACA S809 aerofoil (c).

7.1.1 Grid and computational parameters

The NREL Phase VI rotor was modelled including the hub and the tower, but without tunnel walls and instrumentation boxes^[70]. The grid consisted of $18M$ cells, giving about $9M$ cells per blade. The topology around the aerofoil has a C-H type, as shown in Figure 7.2(a). The normal distance of the first cells in the blocks adjacent to the blade surface was $1 \cdot 10^{-5}c$, where c is a maximum chord of the blade, $0.737m$. Based on the free-stream condition and the size of the first cell, the y^+ parameter was found to be 0.2. The first

layer consisted of 36 cells in the normal direction to the blade surface, and 216 cells were distributed around the aerofoil section. The blade surface was resolved with 124 cells along the span. The tip of the blade was rounded, and represented an approximation to the actual shape since the exact tip shape is not defined in the reports of NREL^[70]. An inflow boundary condition was placed four blade radii upstream of the rotor, and outflow was placed eight blade radii downstream. The far-field was assigned three blade radii from the centre of rotation. In addition, the sliding plane was employed to connect rotor to the nacelle and allow for relative motion. The computational domain with the corresponding boundaries, a slice through the mesh close to the blade surface, and the surface mesh of the blade are shown in Figure 7.2.

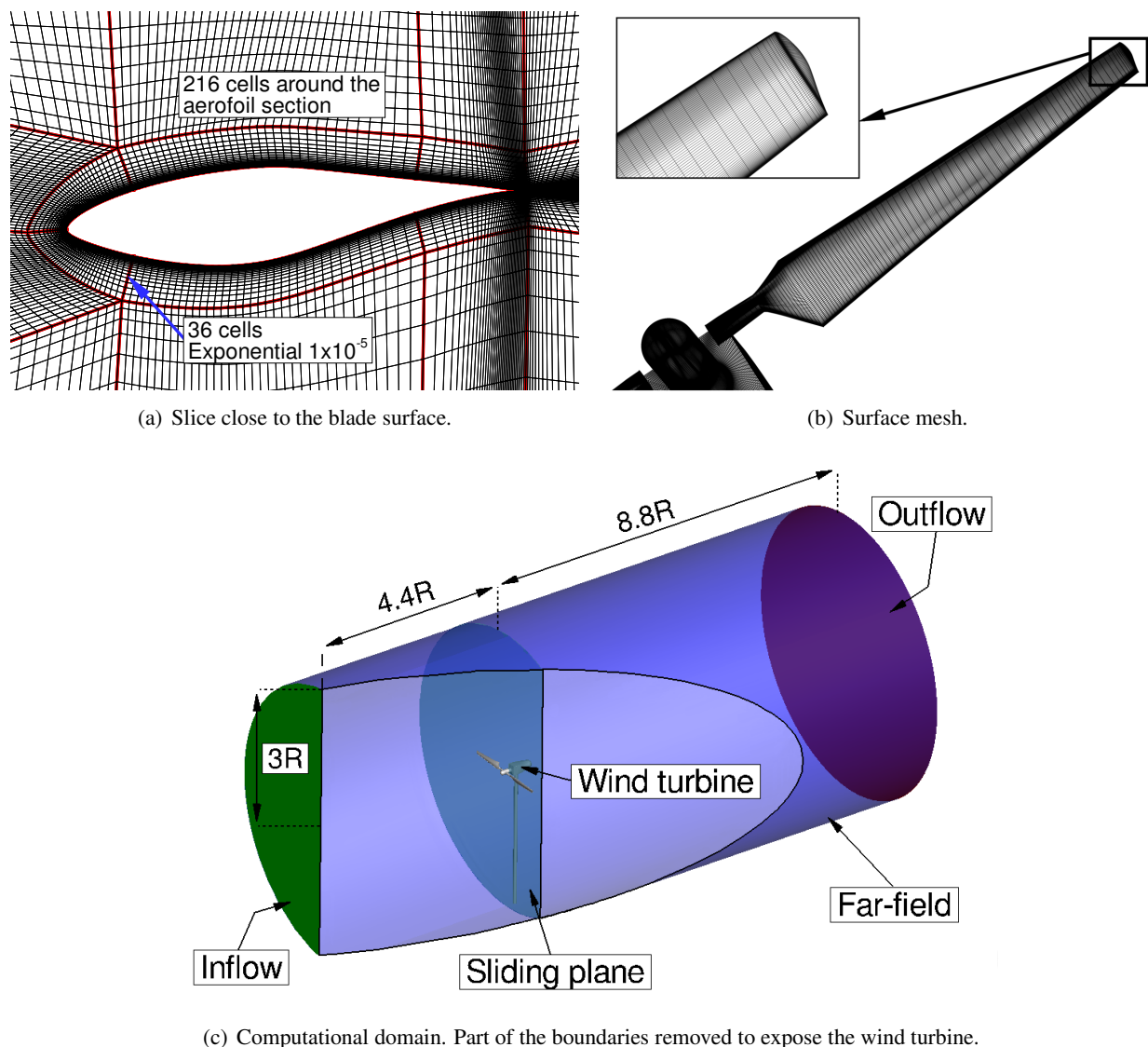


Figure 7.2: Grid employed for the NREL Phase VI wind turbine. Slice through the volume close to the blade surface (a), surface mesh (b), and computational domain (c).

The free-stream was kept to the level of turbulence of 2.6% allowing fully turbulent flow simulations, and the $k - \omega$ shear stress transport (SST) ^[137] turbulence model was employed. The time step employed for the unsteady computations was chosen such that rotor performs one degree of revolution per step, resulting in $\Delta t = 2.3 \cdot 10^{-3} s$. The conditions and computational parameters are presented in Table 7.1.

Table 7.1: Conditions and numerical parameters employed for the validation case against NREL Annex XX experiment.

U_{wind}	7m/s
Rotor speed	72rpm
$\lambda = \frac{U_{tip}}{U_{wind}}$	5.61
Blade radius	5.029m
Number of blades	2
Grid size	18M cells
Turbulence model	$k - \omega$ SST

7.1.2 Results of validation

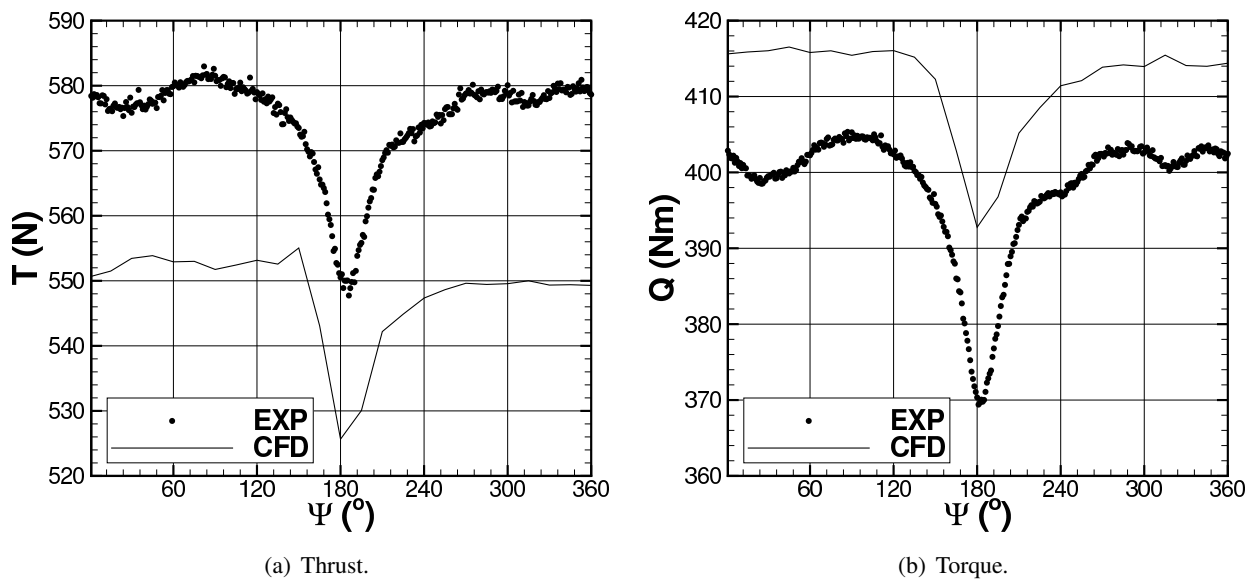


Figure 7.3: Thrust and torque over the fifth revolution for the rigid NREL blade.

Five revolutions were computed assuming rigid blades. Figure 7.3 shows the thrust and torque over the fifth revolution for one blade and compared with the experiments. A deficit in both quantities can be observed as a result of the rotor-tower interaction. This is due to a change in pressure between the blade and the tower and a change in the angle of attack as a consequence of the air deflection when it is hit by the tower.

The under-prediction of thrust and over-prediction of torque of 3% is due to the fact that computations were performed at the nominal conditions for the experiment, and not for the measured pitch. A small change of pitch should account for this difference.

Distribution of pressure coefficient C_p values at different span-wise sections are presented in Figure 7.4. Two blade positions were chosen: 0 and 180 degrees of azimuth, when the blades are normal and parallel to the tower, respectively. Good agreement with measured data can be seen. Additional results and test cases computed for the NREL Phase VI rotor using HMB solver can be found in references [64, 28].

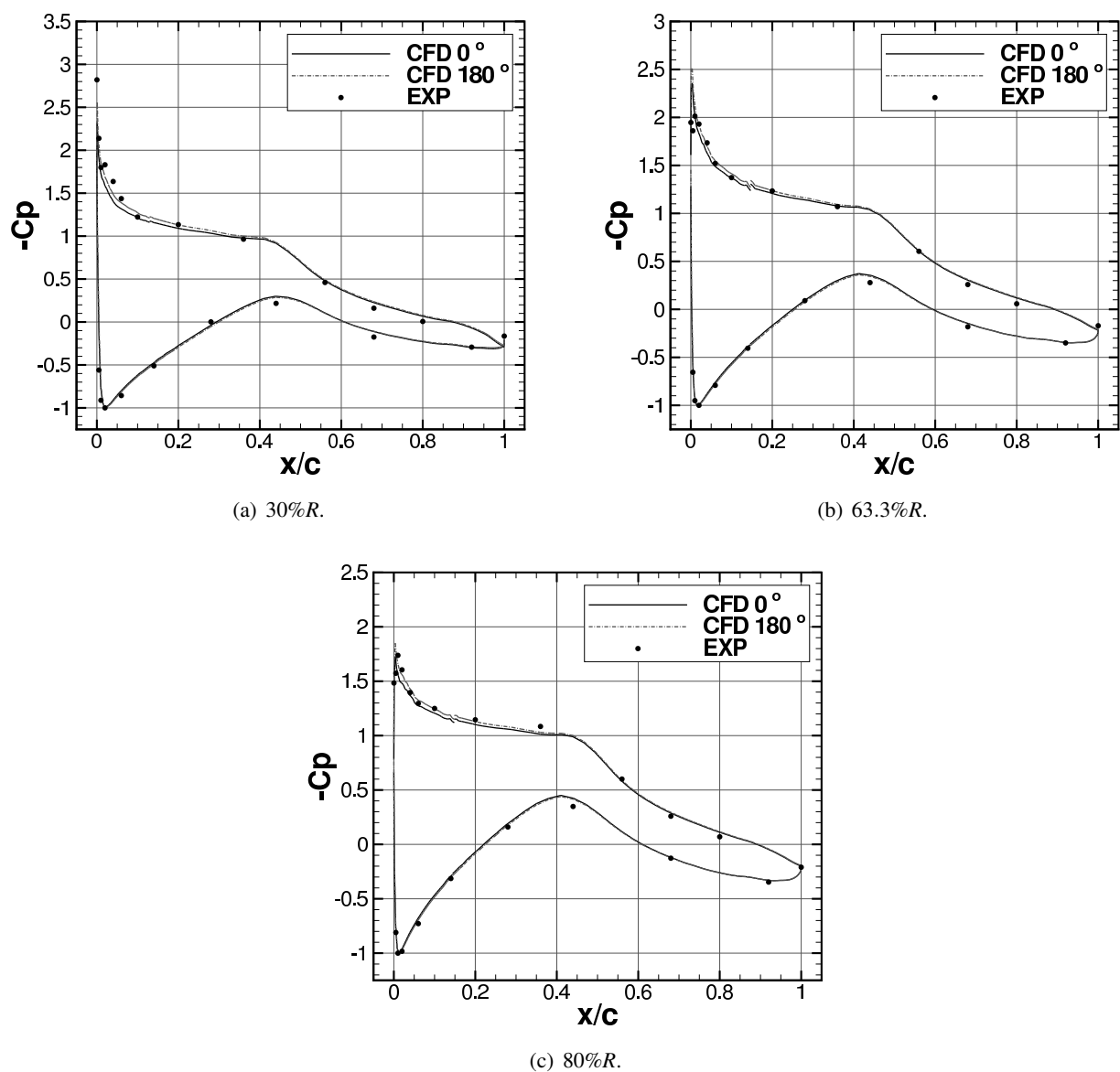


Figure 7.4: Comparison of C_p distribution at three blade stations, for blade azimuth positions of 0 and 180 degrees (rigid blade), at the fifth revolution.

7.2 MEXICO project experiment

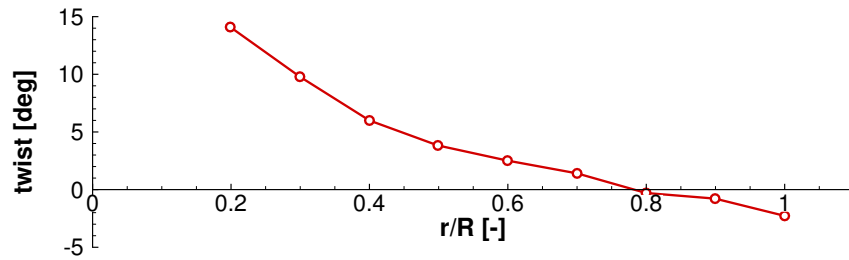
In the MEXICO project^[176, 177], a three-bladed wind turbine of 4.5m diameter was tested in the open section of the German-Dutch Wind tunnel facility. The pressure on the blades was measured at five span-wise sections using 148 Kulite pressure sensors. Flow field mapping of the three velocity components was performed with stereo PIV measurements, employing two cameras focusing on the PIV sheets (which were located horizontally in the symmetry plane of the rotor). The PIV measurements were taken within the rotor plane as radial traverses, as axial traverses from 1 to 1.5 diameters downstream, and the tip vortices were tracked. The PIV samples were rotor-phase locked, and each PIV data point consisted of 30 – 100 samples. Within the MexNext project^[177], averaged results were investigated.

The MEXICO blade consists of three aerofoil families: the DU-W2-250 at the root of the blade (20.0%R to 45.6%R); the RISO A1-21 at mid span (54.4%R to 65.6%R); and NACA 64-418 at the outer part of the blade (outboard of 74.4%R), as shown in Figure 7.5. The blade has nonlinear taper and twist distribution. The span of the blade is $R = 2.25$ meters, and the maximum chord $c = 0.24m$ is located at 20% of the blade span. The wind turbine is designed to operate at a wind speed of 15m/s with a rotational speed of 424.5rpm resulting in tip speed ratio $\lambda = 6.67$. Detailed description of blade design and characteristic is available in references^[176, 177].

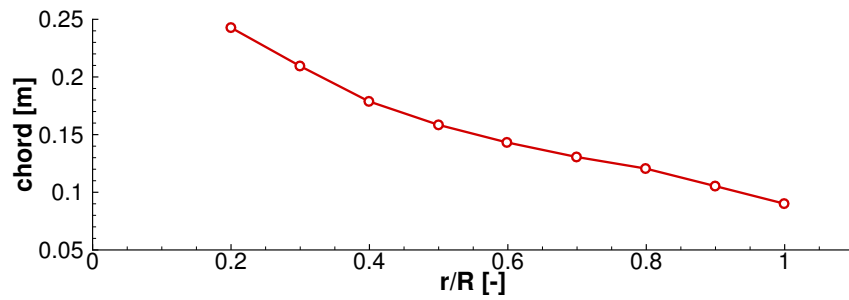
7.2.1 Grid and computational parameters

For the MEXICO rotor, only the blades were modelled, and no nacelle, spinner, or tower were considered in the computations. The overset grid method was employed^[81], which permits localised grid refinement for the wake and the rotor. The grid consisted of 200M cells, giving about 70M cells per blade. The topology around the aerofoil has a C-H type, as shown in Figure 7.6(a). The first grid spacing normal to the blade surface had a size of $1 \cdot 10^{-5}c$, where $c = 0.24m$ is the maximum chord of the blade. This results in y^+ parameter less than 1.0 all over the blade. The first layer consisted of 60 cells in the normal direction to the blade surface, and 344 cells were distributed around the aerofoil section. The blade surface was resolved with 370 cells along the span.

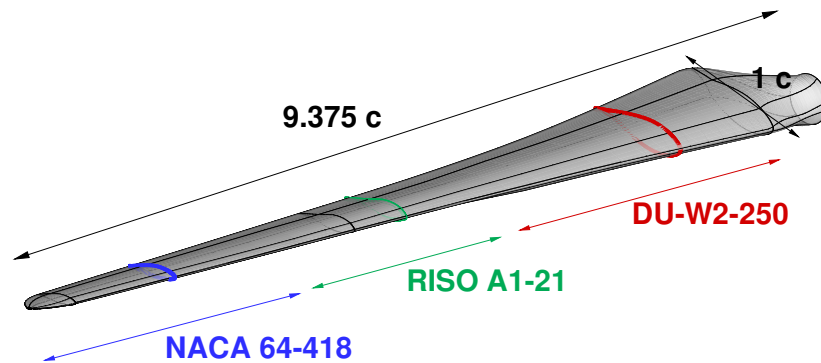
An inflow boundary condition was placed three blade radii upstream of the rotor, and outflow was



(a) Twist distribution.



(b) Chord distribution.



(c) Isometric view and dimensions.

Figure 7.5: MEXICO project blade – twist distribution (a), chord distribution (b), and blade geometry (c).

placed twelve blade radii downstream. The far-field was assigned four blade radii from the centre of rotation. The mesh region for the wake capture extends from the blade's root up to $1.6R$ in the radial direction and $8R$ behind the rotor plane, where R is the radius of the blade. The computational domain with the corresponding boundaries, a slice through the mesh close to the blade surface, and the surface mesh of the blade are shown in Figure 7.6.

The Reynolds-averaged N-S (RANS) computations were performed for these cases, by employing a

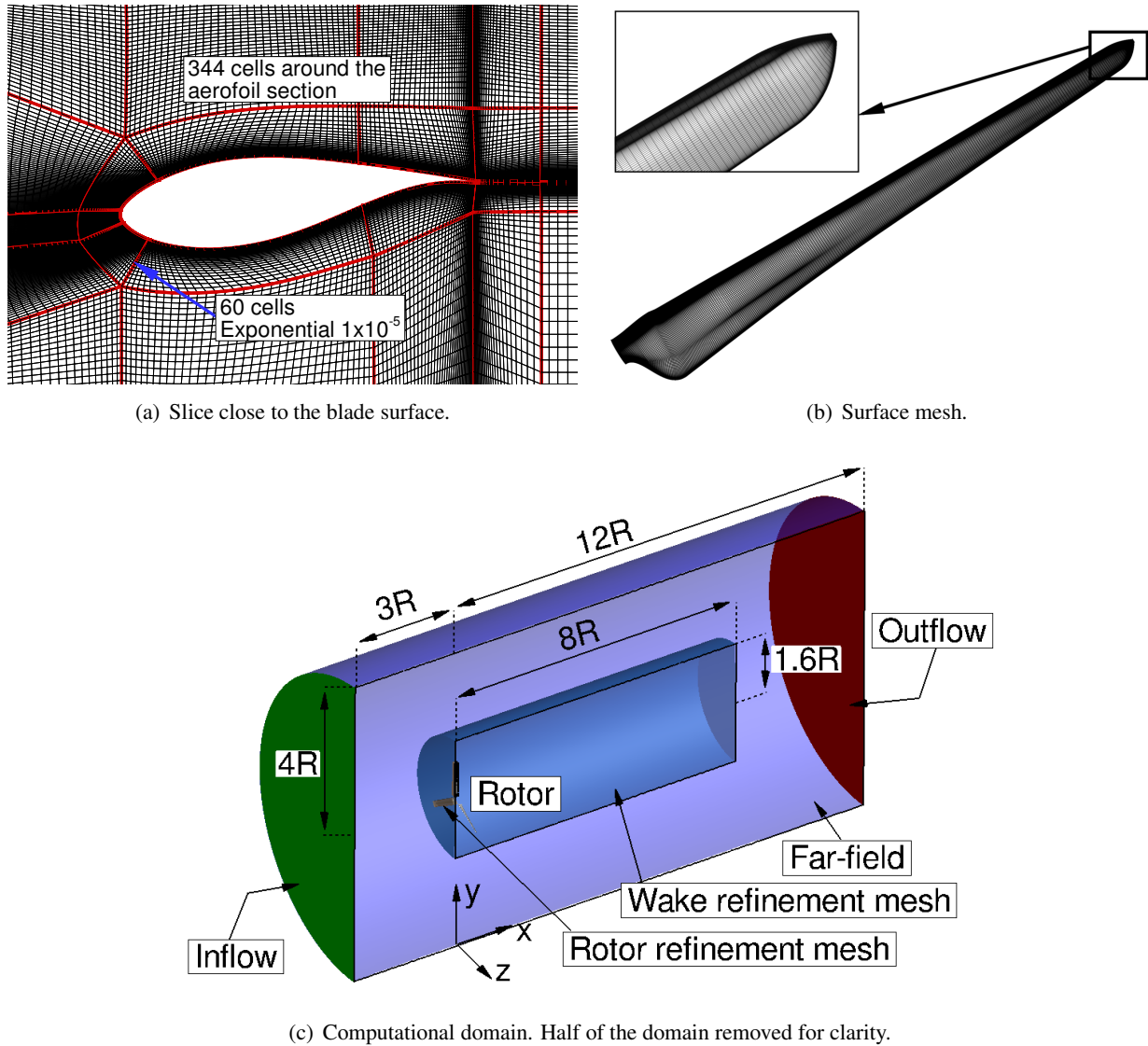


Figure 7.6: Grid employed for the MEXICO wind turbine. Slice through the volume close to the blade surface (a), surface mesh (b), and computational domain (c).

rotating frame of reference. Since they do not march in real time, the results can be obtained faster than with time-accurate simulations. Likewise, the $k - \omega$ turbulence model by Wilcox^[209] was employed. The conditions and computational parameters employed for this test case are presented in Table 7.2.

7.2.2 Results of validation

In this section, a validation against the MEXICO Project experimental data^[177] is presented. Figures 7.7(a-b) show axial and radial velocity profiles extracted at a straight line crossing the first vortex for the wind

Table 7.2: Conditions and numerical parameters employed for the validation case against MEXICO project experiment.

U_{wind}	$15m/s$
Rotor speed	$424.5rpm$
$\lambda = \frac{U_{tip}}{U_{wind}}$	6.67
Blade radius	$2.25m$
Number of blades	3
Grid size	$200M$ cells
Turbulence model	$k - \omega$

speed of $15m/s$. Overall good agreement with the experiments can be seen. Strong oscillations are observed in the region crossing the first vortex, which decay with distance.

Iso-surfaces of λ_2 criterion ^[83] were also generated to visualise the vortical structures and characterise the wake in more detail. Figure 7.7(c) shows the full wake at $15ms$, where the unstable region for $x > 4R$ can be seen.

Finally, a comparison between the measured vortices in the experiments and those computed with CFD is presented in Figure 7.8, where again, good agreement is observed. The first vortices behind the blade at 12 o'clock were chosen for comparison, and were measured at different locations due to different inflow speeds. The vortex was located around $0.28m$ downstream of the blade for $10m/s$ wind speed ($\lambda = 10$), and $0.58m$ downstream for $15m/s$ wind speed. Although the predicted vortices are slightly bigger than in the experiments due to numerical dissipation, the shear spiral generated as the vortex spins, which can be observed in a light colour surrounding the measured vortex core (Figures 7.8(c-d)), is well captured in the CFD (Figures 7.8(a-b)). Additional results and test cases computed for the MEXICO Project rotor using HMB solver can be found in references ^[27, 29].

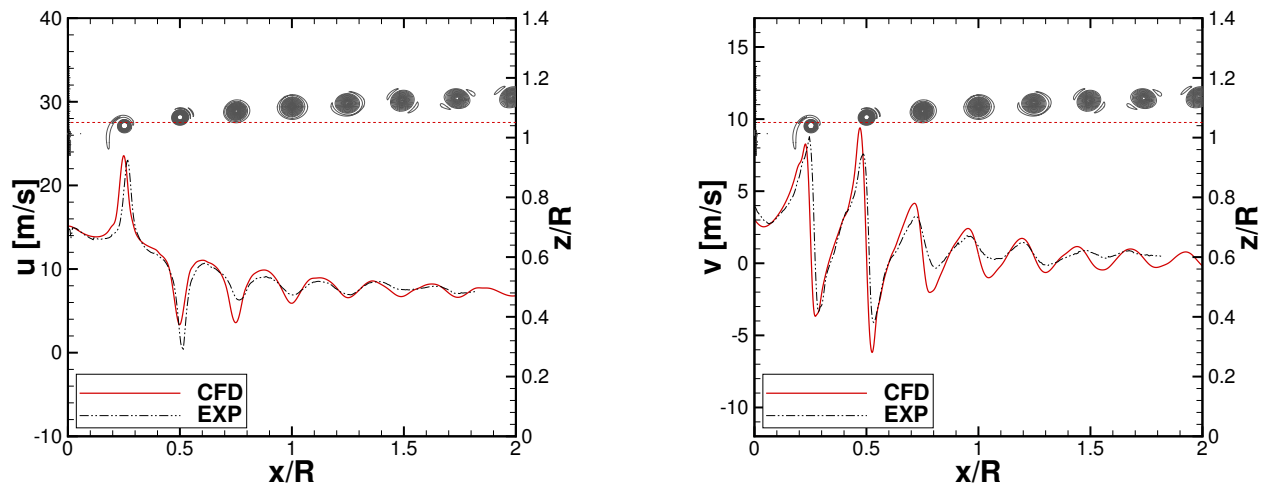
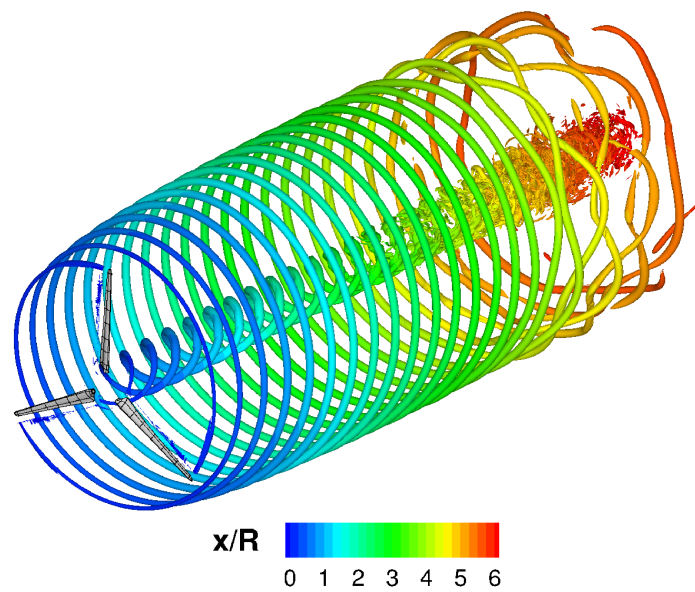
(a) Axial velocity (15m/s).(b) Radial velocity (15m/s).(c) Wake of the rotor (15m/s).

Figure 7.7: Velocity profiles extracted at a straight line crossing the first vortex for wind speed 15m/s : axial velocity (a) and radial velocity (b). Wake behind the MEXICO Project rotor visualised with iso-surfaces of $\lambda_2 = -0.01$ (c). Adapted from ^[29].

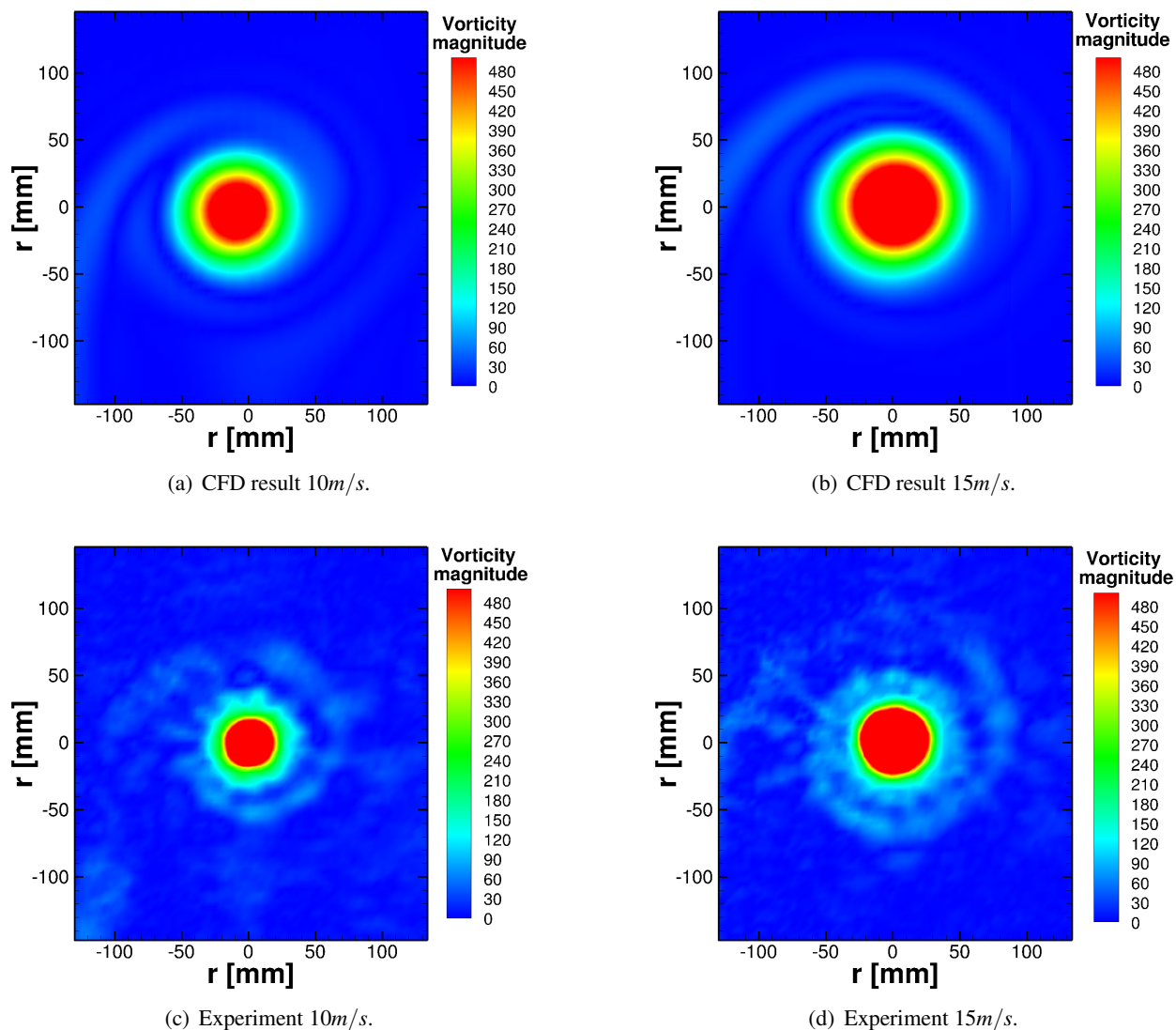


Figure 7.8: Contours of vorticity of the tip vortex for two wind speeds: 10m/s and 15m/s. Comparison between CFD results (a-b), and experimental data (c-d). Adapted from ^[29].

Chapter 8

Validation of the Multi-Body Dynamic

Module

This chapter provides details of cases, run to validate the model. The first test case is a two-dimensional slider-crank mechanism with known kinematic and dynamic solutions. The second test case is a three-dimensional slider-crank mechanism with known kinematic solution. And the last test case is a simple gyroscopic mechanism to validate that the gyroscopic effect is properly accounted for in the multi-body formulation.

8.1 2D slider-crank mechanism

Consider the two-dimensional slider-crank mechanism of Figure 8.1. Although the mechanism is 2D, it is modelled using 3D bodies and joints. The revolute joints are placed at points A and B in Figure 8.1, and the ground constraint is placed on body 4. A revolute driver is imposed on body 1, and a cylindrical joint is placed at point C. At this point body 3 is allowed to move in the x , y and z directions, and rotate about the z axis. To restrict these degrees of freedom, absolute constraints are placed on the motion of body 3 in y and z directions, and a revolute driver about z axis, with 0 angular velocity, is used to link the orientation of bodies 4 and 3. The resulting system has overall $4 \cdot 6 = 24$ degrees of freedom restricted by $2 \cdot 5 + 6 + 1 + 4 + 1 + 1 + 1 = 24$ independent equations. Therefore, kinematic analysis can be performed for

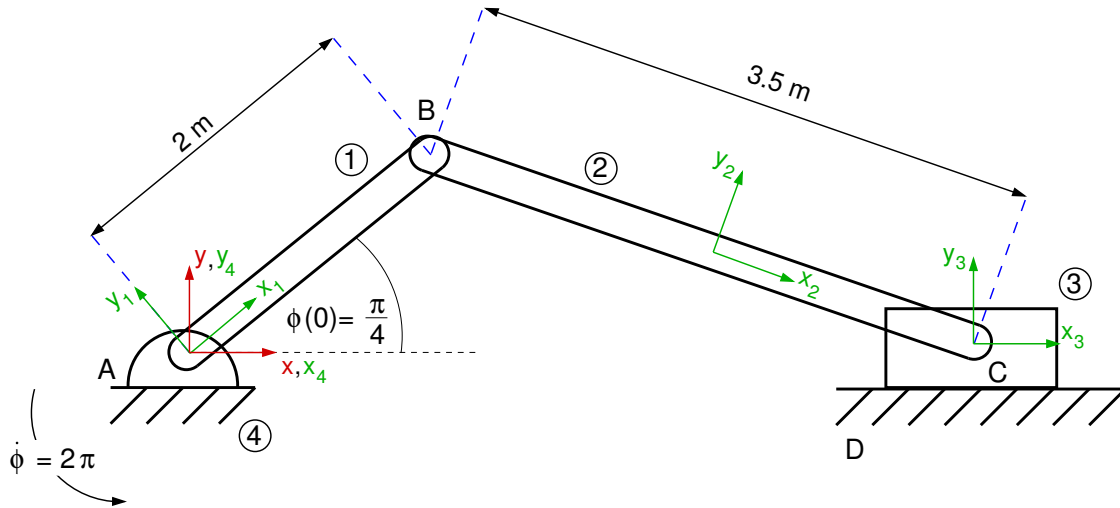


Figure 8.1: Schematic representation of slider-crank mechanism.

the system, see Section 4.2 in Chapter 4 for details. All joints are summarised in Table 8.1.

Table 8.1: Summary of the joints employed to represent the 2D slider-crank mechanism.

Constraints	Body i	Body j	Number of equations
Revolute joint	1	4	5
Revolute joint	1	2	5
Cylindrical joint	2	3	4
Absolute constraint on Y	3	-	1
Absolute constraint on Z	3	-	1
Absolute angular constraint on Z	3	-	1
Ground constraint	4	-	6
Revolute driver	4	1	1
Total number of equations			24

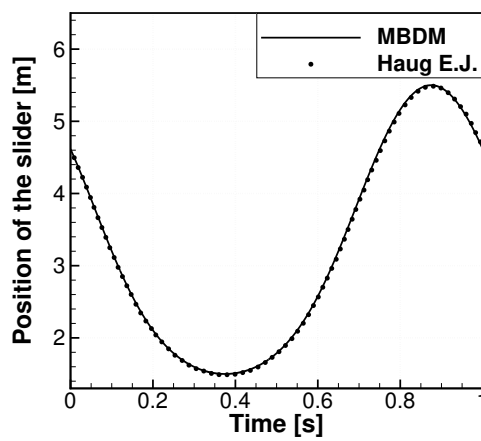
8.1.1 Kinematic analysis of the 2D slider-crank mechanism

The first validation test case was the kinematic analysis of the 2D slider-crank mechanism. Properties of the bodies employed for this test case are summarised in Table 8.2. The crank was placed at angle of $\pi/4$ relative to the global x axis as shown in Figure 8.1. A rotational velocity was imposed at the crank of $\boldsymbol{\omega}_1 = [0, 0, 2\pi]^T$. The solution was compared to the solution obtained by Haug ^[73] for the same mechanism in two dimensions. The results are presented in Figure 8.2, and show good agreement. Note that the results of Haug were extracted from the figures in the reference ^[73], and therefore are prone to errors related to extraction. This is especially visible for the acceleration, but once integrated to velocity and position shows

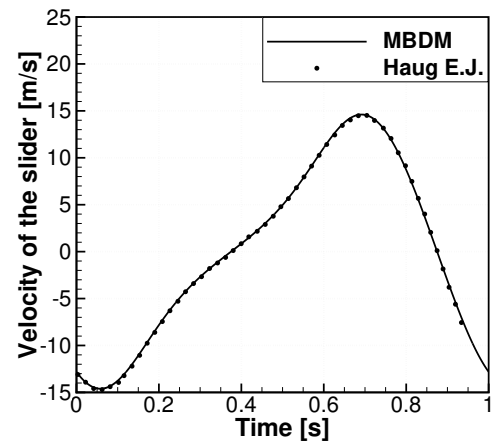
excellent agreement.

Table 8.2: Properties of the bodies employed to represent the 2D slider-crank mechanism for kinematic analysis.

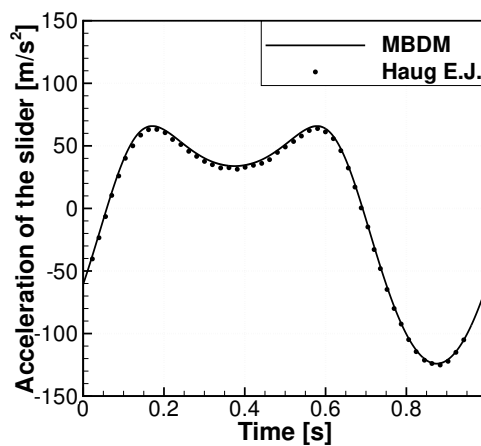
Number	Name	Position [m]	Orientation [rad]	Mass [kg]	Inertia tensor [kg · m ²]
1	Crank	[0, 0, 0]	[0, 0, $\pi/4$]	200	$\begin{bmatrix} 450 & 0 & 0 \\ 0 & 450 & 0 \\ 0 & 0 & 450 \end{bmatrix}$
2	Rod	[3.0152, 0.7066, 0]	[0, 0, -0.4158]	35	$\begin{bmatrix} 35 & 0 & 0 \\ 0 & 35 & 0 \\ 0 & 0 & 35 \end{bmatrix}$
3	Slider	[4.6162, 0, 0]	[0, 0, 0]	25	$\begin{bmatrix} 0.02 & 0 & 0 \\ 0 & 0.02 & 0 \\ 0 & 0 & 0.02 \end{bmatrix}$



(a) Position.



(b) Velocity.



(c) Acceleration.

Figure 8.2: Solution of the kinematic analysis of 2D slider-crank mechanism compared to the results of Haug [73].

8.1.2 Dynamic analysis of the 2D slider-crank mechanism

A second validation test case was the dynamic analysis of the 2D slider-crank mechanism. The same mechanism was employed as for the kinematic analysis. However, different initial conditions were introduced to match the conditions used by ^[73]. Further, the slider-crank was modified to act as a compressor. The slider moves in the compression chamber, as shown in Figure 8.3.

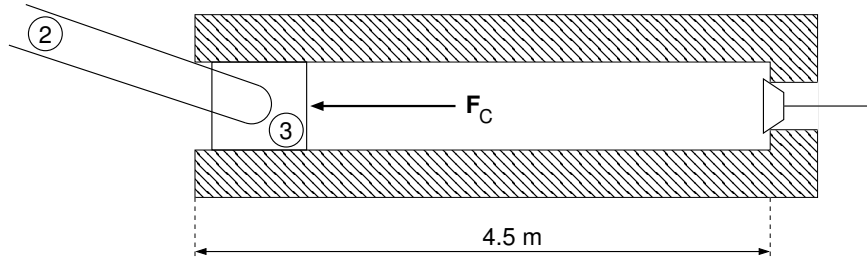


Figure 8.3: Slider in a compression chamber, as used in the dynamic analysis of the 2D slider-crank mechanism.

As the slider moves to the inside of the chamber, a resisting force due to the compression of the gas acts on it. This force increases until the exhaust valve opens. Equation 8.1 defines the gas force F_C on the slider during the compression, that is, when $\dot{x}_3 > 0$. At $x_3 = 5m$, the valve opens. During the intake stroke, no gas force acts on the slider. Figure 8.4 shows the gas force as a function of the position and velocity of the slider.

$$F_C = \begin{cases} 282857/(6 - x_3) + 62857, & 1.5 \leq x_3 \leq 5 \\ -11 \cdot 10^4 [1 - \sin(2\pi(x_3 - 5.25))], & 5 < x_3 \leq 5.5 \end{cases} \quad (8.1)$$

To match the conditions used by ^[73], the gravitational force was acting in the positive x direction. The initial orientation of the crank was set to $\phi(0) = \pi$ and the initial angular velocity of the crank was set to $\dot{\phi}(0) = 30rad/s$. The followed notation is as shown in Figure 8.1. The revolute driver at the crank was removed, and a constant torque of $41,450Nm$ was applied to the crank. The Runge-Kutta fourth order integration scheme was employed, and the time step was chosen to be $\Delta t = 0.001s$. The results are presented in the Figure 8.5. Good overall agreement can be seen. Small discrepancies occur due to errors in reading the published solutions from printed graphs. Also, the numerical integration scheme and time step are not specified in reference ^[73]. This may have introduced some additional differences.

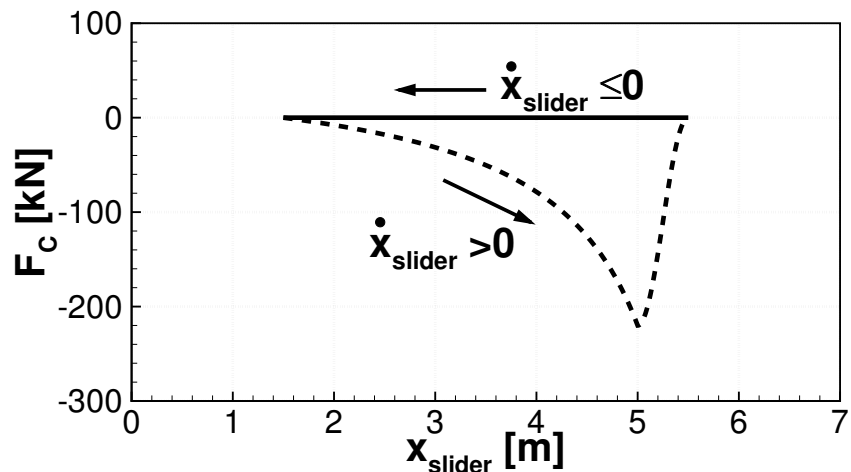


Figure 8.4: Gas force versus slider position.

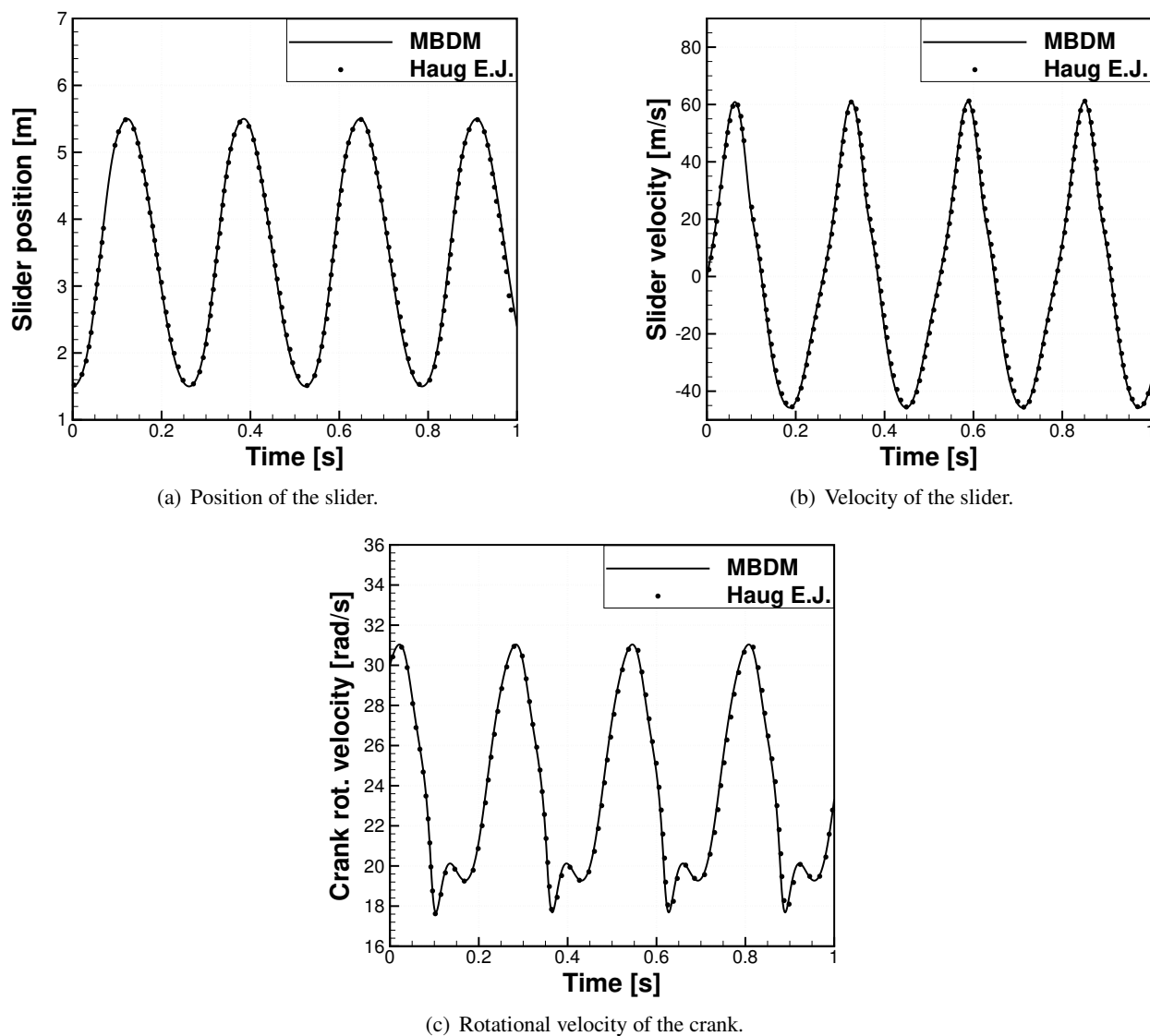


Figure 8.5: Results of the dynamic analysis of 2D slider-crank compression mechanism compared to the results of Haug [73].

8.2 3D slider-crank mechanism

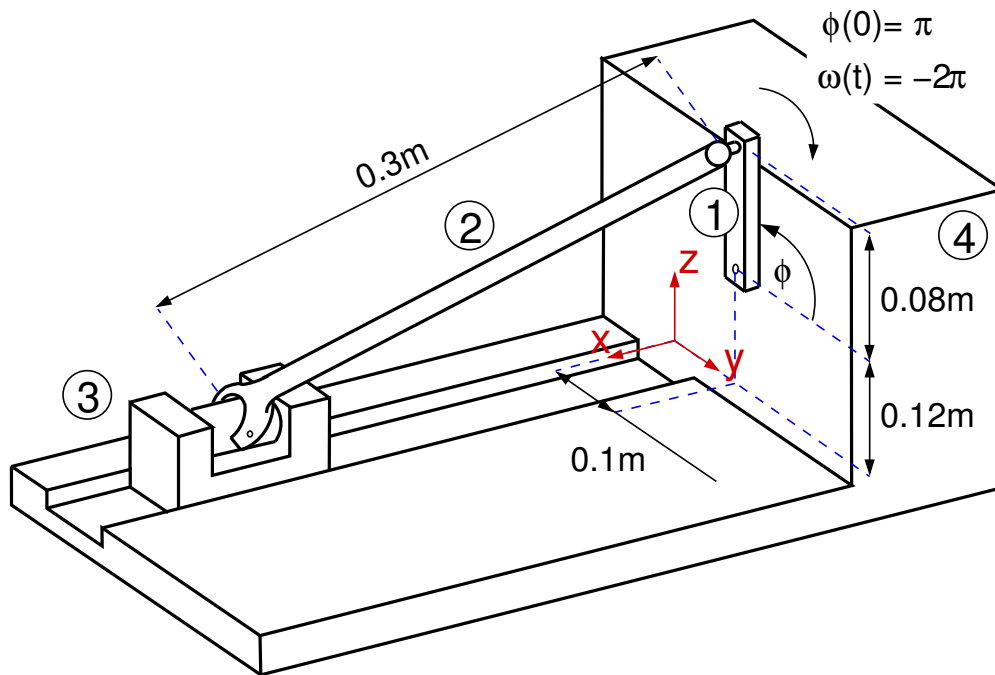


Figure 8.6: Schematic of the 3D slider-crank mechanism.

Table 8.3: Summary of the joints employed to represent the 3D slider-crank mechanism.

Constraints	Body i	Body j	Number of equations
Revolute joint	1	4	5
Spherical joint	1	2	3
Revolute-Cylindrical joint	2	3	3
Translational joint	3	4	5
Distance constraint	2	3	1
Ground constraint	4	-	6
Revolute driver	4	1	1
Total number of equations			24

Consider the tree-dimensional slider-crank mechanism of Figure 8.6. The revolute joint is used to connect the crank (body 1) to the ground body, where the ground constraint is placed on body 4. The spherical joint is used to connect the crank to the rod (body 2), and then the revolute-cylindrical joint is used to connect the rod to the slider (body 3). The translational joint between the slider and the ground is placed to permit only one direction of motion for the slider. Finally, the distance constraint between the rod and the slider is employed to prevent the rod from sliding inside the slider. The revolute driver is imposed on the crank, with a constant rotational velocity of -2π . The notation is indicated in Figure 8.6. The resulting

system has $4 \cdot 6 = 24$ degrees of freedom restricted by $5 + 3 + 3 + 5 + 1 + 6 + 1 = 24$ independent equations.

Therefore, the kinematic analysis is plausible for this system. All joints are summarised in Table 8.3.

Table 8.4: Properties of the bodies employed to represent the 3D slider-crank mechanism for kinematic analysis.

Number	Name	Position [m]	Orientation [rad]	Mass [kg]	Inertia tensor [$kg \cdot m^2$]
1	Crank	[0,0.1,0.12]	$[\pi, 0, 0]$	0.12	$\begin{bmatrix} 1 \cdot 10^{-4} & 0 & 0 \\ 0 & 1 \cdot 10^{-4} & 0 \\ 0 & 0 & 1 \cdot 10^{-4} \end{bmatrix}$
2	Rod	[0.1,0.05,0.1]	$[0, 0, -0.4]$	0.5	$\begin{bmatrix} 4 \cdot 10^{-3} & 0 & 0 \\ 0 & 4 \cdot 10^{-3} & 0 \\ 0 & 0 & 4 \cdot 10^{-3} \end{bmatrix}$
3	Slider	[0.2,0,0]	$[0, 0, 0]$	2.0	$\begin{bmatrix} 1 \cdot 10^{-4} & 0 & 0 \\ 0 & 1 \cdot 10^{-4} & 0 \\ 0 & 0 & 1 \cdot 10^{-4} \end{bmatrix}$

At time $t = 0$, the crank was placed at angle π relative to the global y axis as shown in Figure 8.6. Properties of the bodies employed for this test case are summarised in Table 8.4. The results of kinematic analysis are presented in Figure 8.7, where the solution of the MBDM solver is compared to the solution obtained by ^[73]. Good agreement can be seen.

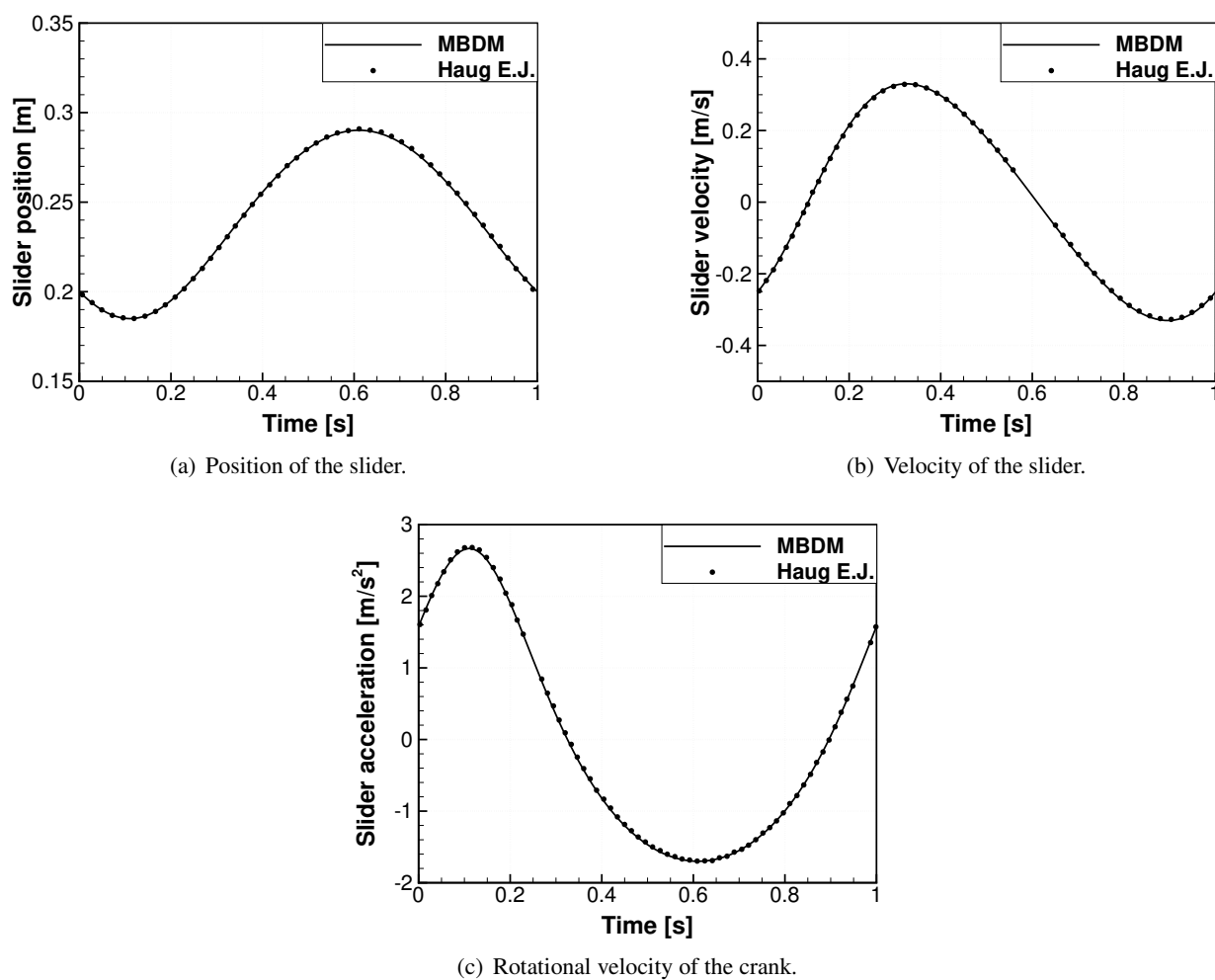


Figure 8.7: Results of the kinematic analysis of 3D slider-crank mechanism compared to the results of Haug ^[73].

8.3 Gyroscopic wheel

In this test case, a simplified system of a gyroscopic wheel is considered to validate that the gyroscopic effect is properly accounted for in the multi-body formulation. The model involves three bodies, as shown in Figure 8.8. The ground body was placed at the origin at the global coordinate system. A short rod of length $0.1m$ was attached to the ground body at height $1.0m$ using an universal joint such that rotation along the rod axis is constrained. The other end of the rod was connected to the centre of mass of the steel wheel with a revolute joint. A constant rotational speed of $60rad/s$ was applied to the wheel by a revolute driver. The system has overall 2 unconstrained degrees of freedom - rotation about the direction of global axes z and y . The gravitational force acting in the negative z direction was applied to all bodies, and at time $t = 0$ the system was assumed to have no precession.

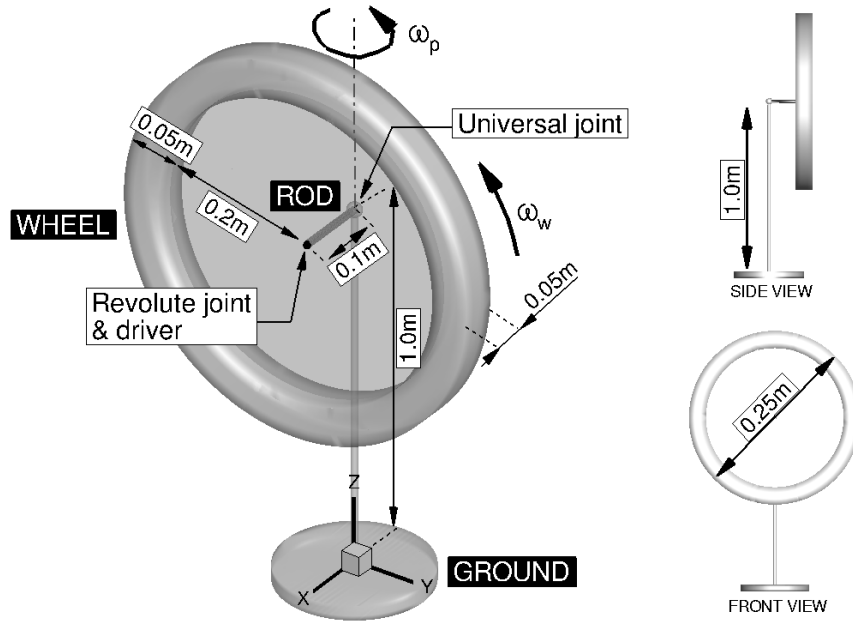


Figure 8.8: Schematic of the MBDM gyroscopic set-up. System shown in the initial condition.

The system is presented in Figure 8.8, while the mechanical properties of all bodies are shown in Table 8.5. The analytical solution was obtained from Equation (8.2) using the gyroscopic approximation, *i.e.* assuming that precession is much slower than rotation of the wheel $\omega_p \ll \omega_w$, so that the magnitude of the angular velocity $|\vec{\omega}| \simeq |\omega_w|$ and that precession and rotation rates are nearly constant.

$$\omega_p = \tau/L = m_w g l / J_{xx} \omega_w \quad (8.2)$$

In the above, ω_p is the angular velocity of precession, τ is the moment due to gravity about the pivot point, and L is the angular momentum of the wheel. The expansion to the right-hand side involves the mass of the wheel m_w , the length of the rod l , the gravitational acceleration g , the mass moment of inertia of the wheel about the axis of rotation J_{xx} , and the rotational velocity of the wheel ω_w . Substitution of values from Table 8.5 into Equation (8.2) yields the rate of precession as $\omega_p \approx 0.319 \text{ rad/s}$.

Table 8.5: Properties of the bodies employed to model the gyroscopic effect.

Name	Mass [kg]	Inertia tensor [$\text{kg} \cdot \text{m}^2$]
Wheel	28.3	$\begin{bmatrix} 1.45 & 0 & 0 \\ 0 & 0.73 & 0 \\ 0 & 0 & 0.73 \end{bmatrix}$
Rod	0.1	$\begin{bmatrix} 10^{-6} & 0 & 0 \\ 0 & 8.3 \cdot 10^{-5} & 0 \\ 0 & 0 & 8.3 \cdot 10^{-5} \end{bmatrix}$

The result of the dynamic computation is presented in Figure 8.9, where the Runge-Kutta integration scheme of fourth order was employed, with a time step $\Delta t = 0.001 \text{ s}$. As can be seen, the rate of precession developed in less than 0.1 s with slight overshoot, and then maintained almost constant value that agreed with the one obtained using the gyroscopic approximation.

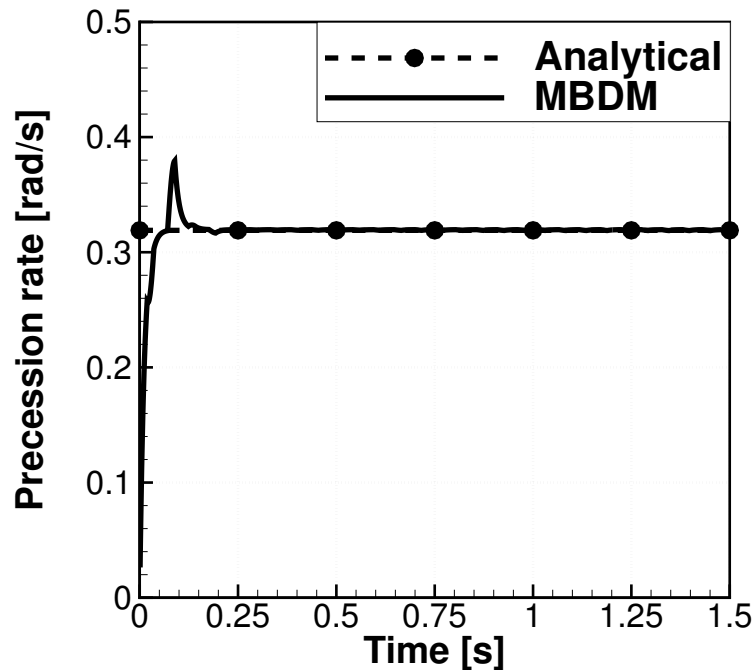


Figure 8.9: Computed rate of precession compared to the analytical value.

Chapter 9

DTU 10-MW Reference Wind Turbine

This chapter starts the aerodynamic analysis of the DTU 10-MW Reference Wind Turbine (DTU 10-MW RWT). Blades are assumed rigid in this chapter, and "clean" i.e. without leading or trailing edge flaps. To begin with, the geometry of the WT is described, along with the employed mesh. The results for the mesh convergence study are also shown. Next, results from steady computations for the DTU 10-MW RWT are presented. The chapter ends with results for the atmospheric boundary layer inflow with and without atmospheric turbulence.

The aerodynamic analysis continues in Chapter 10, where aero-elasticity of the DTU 10-MW RWT is considered. In turn, Chapter 11 considers the effects of employing deformable leading and trailing edge flaps. Floating application of this 10-MW rotor, from aerodynamic perspective, is considered in Chapter 12. Finally, the results for the coupled model are presented in Chapter 13.

9.1 Overview of the design

The DTU 10-MW RWT design^[11] is a result of a joint European effort to up-scale wind turbines (UpWind, InnWind, AVATAR and MARE-WINT projects). The UpWind^[56] project focused on the design tools for the complete range of turbine components. The work continued in the InnWind^[2] project, and resulted in the DTU 10-MW RWT design that, in return, was inspired by the NREL 5-MW baseline wind turbine^[89]. Currently, this 10MW, pitch regulated machine is used for the work within the AVATAR^[1] and MARE-

WINT^[3] projects.

The main objective of the DTU 10-MW RWT design was to optimise the blades, to increase their stiffness and study overall performance of the rotor by taking into account both aerodynamic, and structural considerations. For this reason, aerofoils of the FFA-W3 series^[22] were used. These aerofoils with relative thickness between 24.1% and 36% are presented in Figure 9.1.

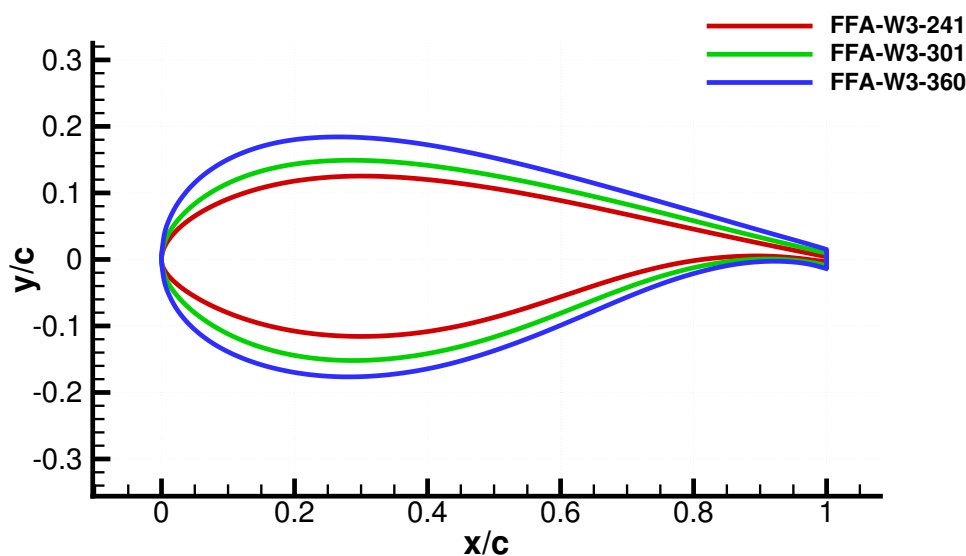
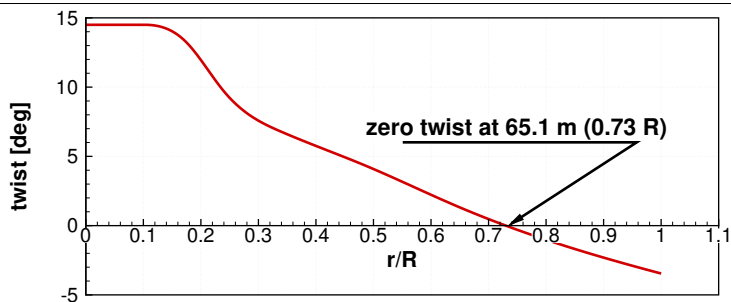


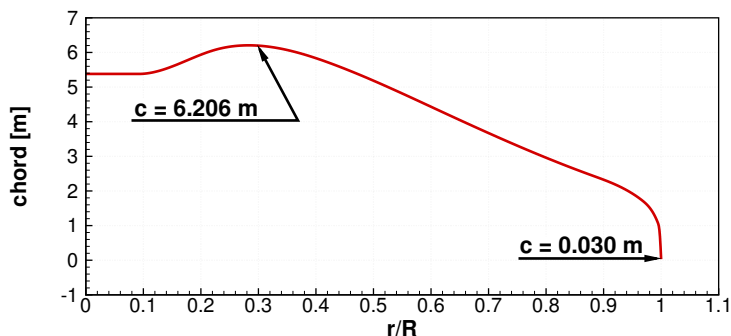
Figure 9.1: FFA-W3 aerofoils with relative thickness between 24.1% and 36%.

The geometry of the DTU 10-MW RWT blade was represented using splines. In this respect, the RWT blade was defined in a piece-wise fashion using a small set of splines, the coefficients of which are given in Tables A.1-A.4 in the appendix A of reference ^[11]. Cubic splines were used to define blade properties as a function of the radial position. Figure 9.2 shows the twist and chord distributions, and the planform of the RWT blade.

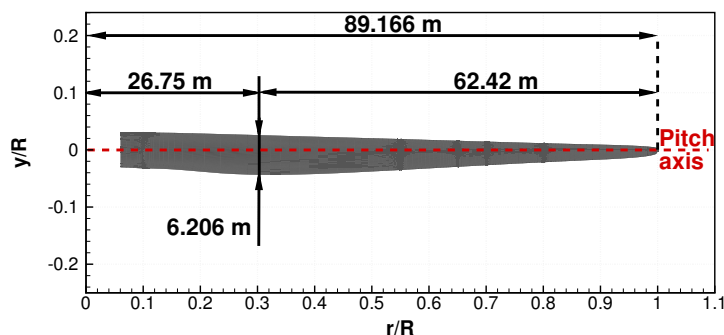
A Gurney flap was added to the root part of the blade using a smooth wedge shape. An example of an aerofoil section with the employed Gurney flap is shown in Figure 9.3(a). The flap was made larger closer to the root of the blade, due to the thick aerofoils and thick boundary layer at this part. Further outboard, the flap height is smaller, and stops after $0.4R$. An isometric view of the blade root showing the Gurney flap is presented in Figure 9.3(b). A more detailed description of the aerodynamic design can be found in Bak *et al.* ^[11].



(a) twist distribution



(b) chord distribution



(c) planform

Figure 9.2: DTU 10MW reference blade.

The complete DTU 10-MW RWT design is shown in Figure 9.5. The integrated mass of the rotor is 227,962kg, and the hub is located 119m above the ground. The rotor is placed 7.1m along the shaft in upwind configuration. The total mass of the nacelle is 446,036kg. The tower design is based on the NREL 5-MW baseline wind turbine^[89], but is scaled to support the rotor. The integrated tower mass is 628,422kg, and the centre of mass is located at 47.6m along the tower centreline and above the ground^[11]. The blades are pre-coned by 2.5°, and pre-bent by 3.3m to increase tower clearance. The shape of pre-bending is based on the static deflection of the blades for the turbine operating at 5m/s wind speed^[11]. Figure 9.4 shows

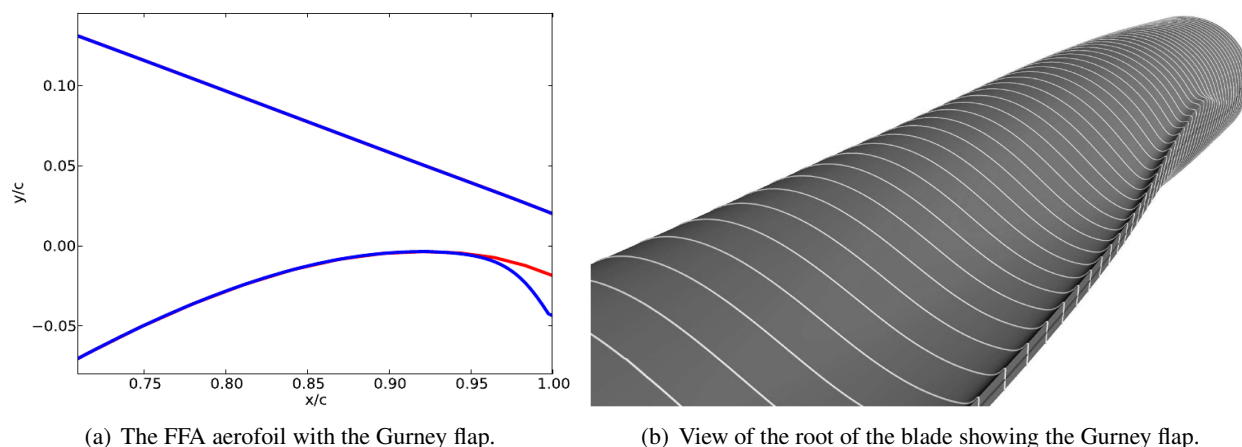


Figure 9.3: The Gurney flap applied to the DTU 10MW RWT blade: aerofoil section with the flap (a), and isometric view of the blade root showing the flap (b). Adapted from ^[11].

the blade axis shape before and after bending. Note that sections of the blade are only shifted to provide deflection i.e. they are not rotated. Also, the pre-bent shape of the blade does not include coning, where coning is a rotation of the blade about the root, as shown in Figure 9.5. The nacelle is tilted by 5° to further increase tower clearance. The resulting tower clearance is $18.26m$, as can be seen in Figure 9.5.

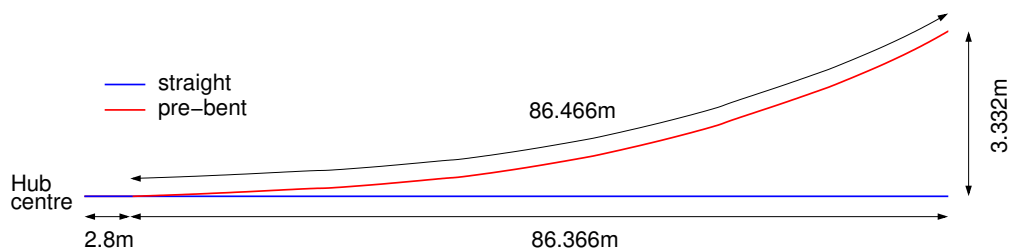


Figure 9.4: The pre-bent shape of the DTU 10MW RWT blade. Not in scale.

9.2 Computational parameters

This section describes the numerical parameters employed in this chapter. For all presented test cases, the air density was assumed to be $\rho = 1.225kg/m^3$, the dynamic viscosity of the air was $\mu = 1.8 \cdot 10^{-5}Ns/m^2$, and the speed of sound was $340m/s$. Further, fully turbulent flow was assumed with a free-stream level of turbulence of 2.6%. Note that the turbulence intensity is required to initiate the small scale turbulence, which in return is modelled with the $k - \omega$ SST^[137] turbulence model, unless otherwise stated. This enables the simulation of cases where turbulence can be assumed to be present from the leading edges and it is

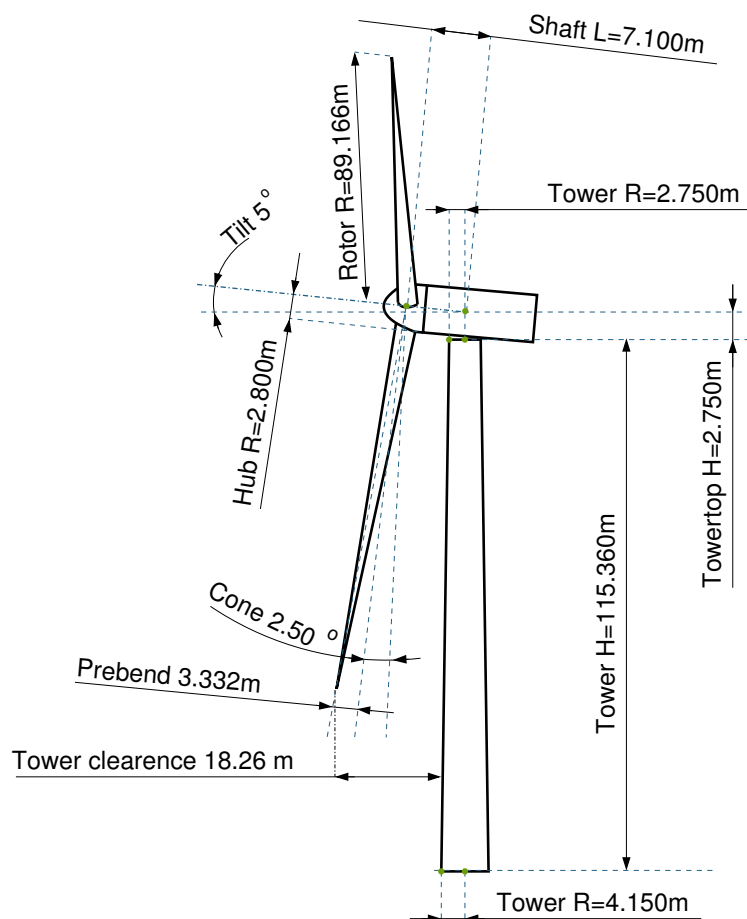


Figure 9.5: DTU 10MW reference wind turbine design. Not in scale.

convenient to avoid the prediction of transition. This 'seeding' turbulence does not imply that small scale turbulence is always present in incident flows, and should be distinguished from atmospheric turbulence obtained by means of Mann's or Sandia models discussed in Section 1.2.9 of Chapter 1, where large and small scale turbulence is indeed present in the flow.

Finally, a uniform inflow velocity distribution was set across the inflow boundary, apart from Section 9.5, where the atmospheric boundary layer inflow was investigated.

9.3 Grid convergence study

The mesh convergence study was performed, before test cases were computed, to find the required density of the mesh and cell distribution in the vicinity to the blade surface. The blade was assumed straight for these cases i.e. without pre-cone or pre-bend. Only 70% of the blade was modelled in this study – from $0.3R$

to $1R$, where R is the radius of the blade. The flow around the blade was considered to be periodic in space and time. This allows the use of the HMB3 "hover" formulation that converts an unsteady flow problem to a steady-state one by using a rotating frame of reference, as described in [192]. The formulation includes a combination of mesh motion and additional source terms in the Navier-Stokes equations. The tower and the complete wind turbine were not modelled. The spinner was approximated as a long cylinder running parallel to the flow and along the computational domain. The conditions selected for the first computations are presented in Table 9.1. These cases should be within the design envelope of the wind turbine and no severe root or tip stall is anticipated.

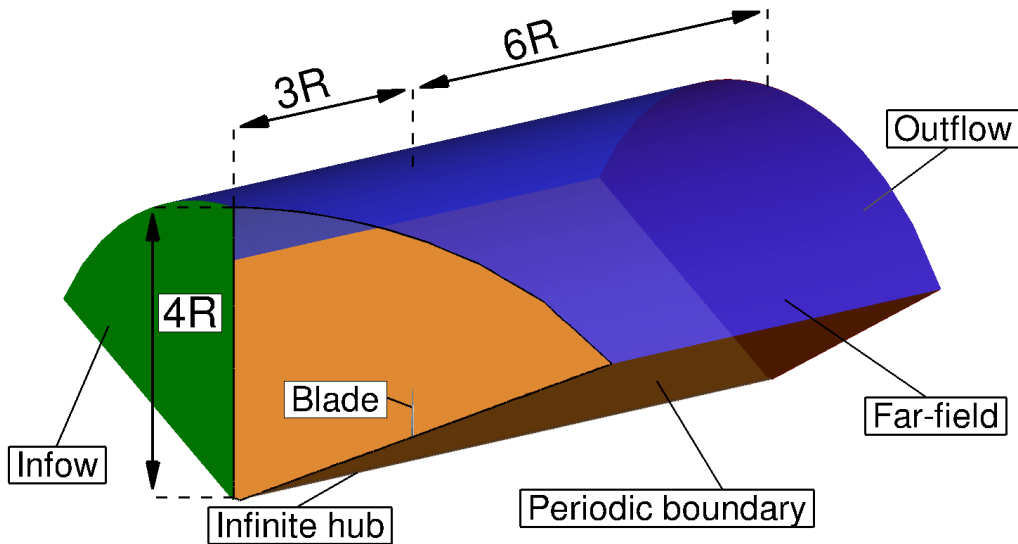


Figure 9.6: Computational domain for mesh convergence study with employed boundary conditions. Part of the domain is removed to expose the blade.

Table 9.1: Conditions for the grid convergence study.

U_{wind}	11m/s
U_{tip}	82.437m/s
Rotor speed	8.836rpm
Re	$34.817 \cdot 10^6$
$M_{tip} = \frac{U_{tip}}{U_{sound}}$	0.243
$\lambda = \frac{U_{tip}}{U_{wind}}$	7.494
Pitch angle	0°

The free-stream was kept to the level of turbulence of 2.6%, and the $k-\omega$ turbulence model of Wilcox^[209] was employed. The normal distance of the first cells in the blocks adjacent to the blade surface was $1 \cdot 10^{-5}c$, where c is a maximum chord of the blade, 6.206m. An inflow boundary condition was

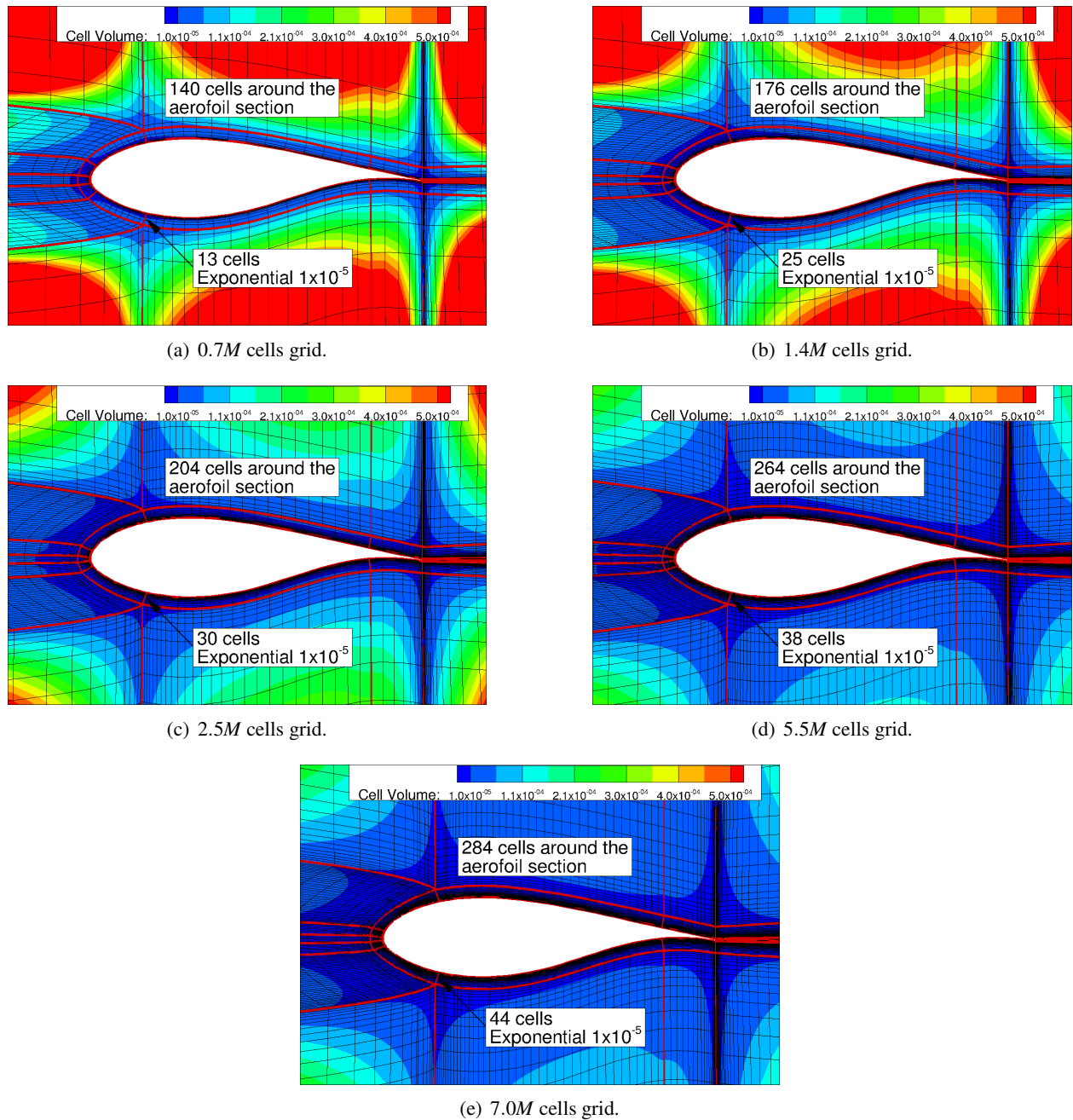


Figure 9.7: Slices through the volume mesh at 75%R and close to the blade surface for various grids employed for the grid convergence study. Colour contours show cell volumes.

placed three blade radii upstream of the rotor, and the outflow was placed six blade radii downstream. The far-field was assigned four blade radii from the centre of rotation. The domain size and boundaries are shown in Figure 9.6.

The study started with a grid of density 0.7M, that was refined up to 7.0M cells. Slices through

the volume at $75\%R$ and close to the blade surface of the employed grids are shown in Figure 9.7. The computations were run using 300 explicit steps at a CFL number of 0.4 and 65,000 implicit steps at a CFL number of 3.0. Figure 9.8 presents the convergence history of thrust and mechanical power for the $7.0M$ cells grid. At the point where the computation ended, the variation between the individual and the averaged blade loads of the last 2000 iterations was less than $4.5 \cdot 10^{-7}N$. The thrust was computed as the aerodynamic force acting along the axis of rotation, and mechanical power was computed as the aerodynamic moment along the shaft multiplied by the rotational velocity of the rotor. The thrust (C_T) and power (C_P) coefficients were computed from the following equations:

$$C_T = \frac{T}{0.5\rho AU^2}, \quad (9.1a)$$

$$C_P = \frac{P}{0.5\rho AU^3}, \quad (9.1b)$$

where T is the thrust force, P is the mechanical power, ρ is the air density, $A = \pi R^2$ is the area of the wind turbine rotor, and U is the wind speed.

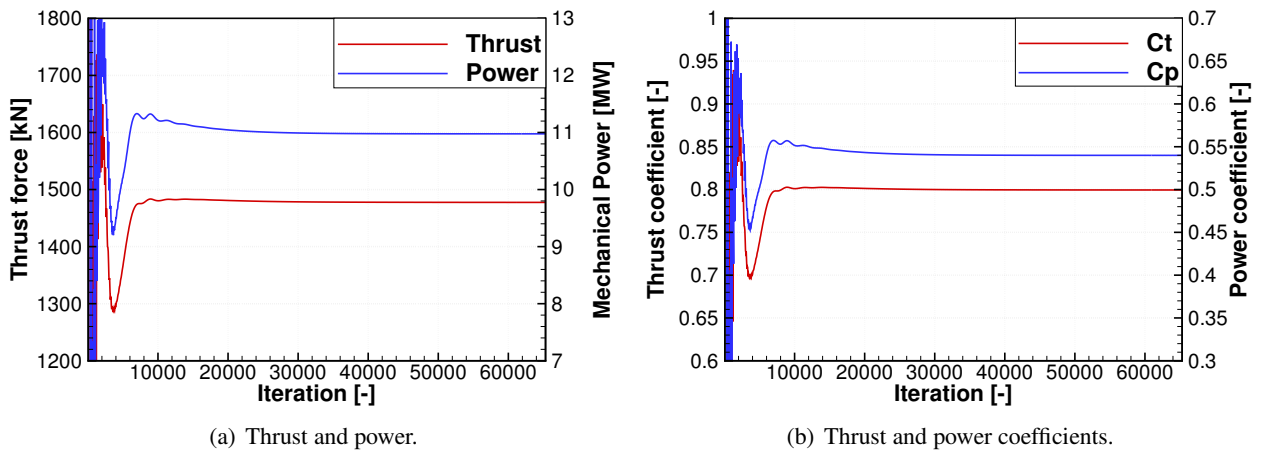


Figure 9.8: Convergence history of thrust and power, and corresponding coefficients for $7.0M$ cells grid.

The results of the mesh convergence study are presented in Figure 9.9, where the thrust force and the mechanical power are shown versus the number of grid cells. This data is also shown in Table 9.2. An additional computation involves the finest grid of $7.0M$ cells and the $k - \omega$ SST turbulence model by Menter^[137]. The pressure was integrated over the surface of the blade to produce the local thrust force and driving forces, and the blade pitching moment as functions of the radial position for employed grids. The driving force is defined as the force acting in the plane of rotation of the rotor. These load distributions are

presented in Figure 9.10. Finally, the distribution of the surface pressure coefficient (C_p) for the 7.0M cells grid is shown in Figure 9.11. The rapid reduction of the pressure coefficient peak can be seen at the tip where the chord is reduced to almost a point, as can be seen in Figure 9.2. Also, the flow is highly three-dimensional at the tip, due to the tip vortex. Integrating the pressure from root to tip it can be concluded that 85% of the loads are generated at the stations between 45 and 98%R.

The grid convergence study showed that a mesh between 3M to 5M cells per blade is sufficient to obtain mesh independent solution. Also, based on the obtained solutions and the size of the first cell, the y^+ parameter was found to be 1.7. This indicates that the spacing close to the wall should be reduced by half an order of magnitude to the value of $5 \cdot 10^{-6}c$, where c is the maximum chord of the blade.

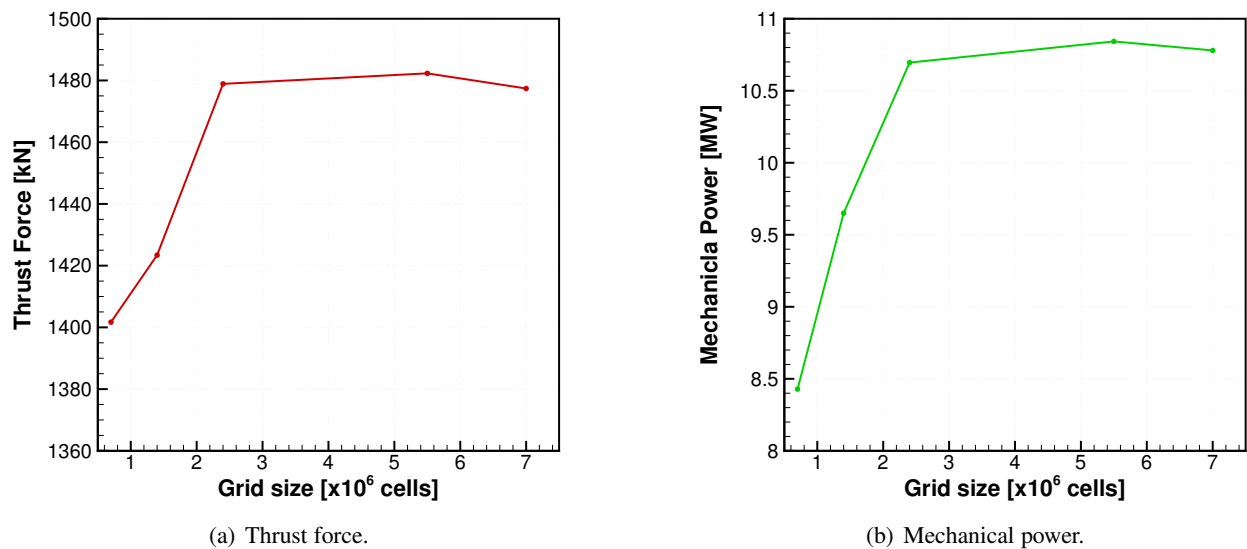


Figure 9.9: Thrust fore and mechanical power as function of computational grid density.

Table 9.2: Comparison between thrust and power coefficients and corresponding thrust and power obtained by present CFD computations and by Bak ^[11].

Turbulence model	CFD computation					results of Bak ^[11]	
	$k - \omega$					SST	SST
Grid size [cells]	$0.7 \cdot 10^6$	$1.4 \cdot 10^6$	$2.4 \cdot 10^6$	$5.5 \cdot 10^6$	$7.0 \cdot 10^6$	$7.0 \cdot 10^6$	$14.1 \cdot 10^6$
C_T	0.758	0.770	0.800	0.802	0.799	0.801	0.840
C_P	0.415	0.475	0.526	0.533	0.530	0.532	0.495
Thrust [kN]	1401.7	1423.4	1478.9	1482.3	1477.4	1478.2	1555.0
Mech. Power [kW]	8428.5	9650.4	10695.5	10842.4	10779.9	10291.8	10088.5

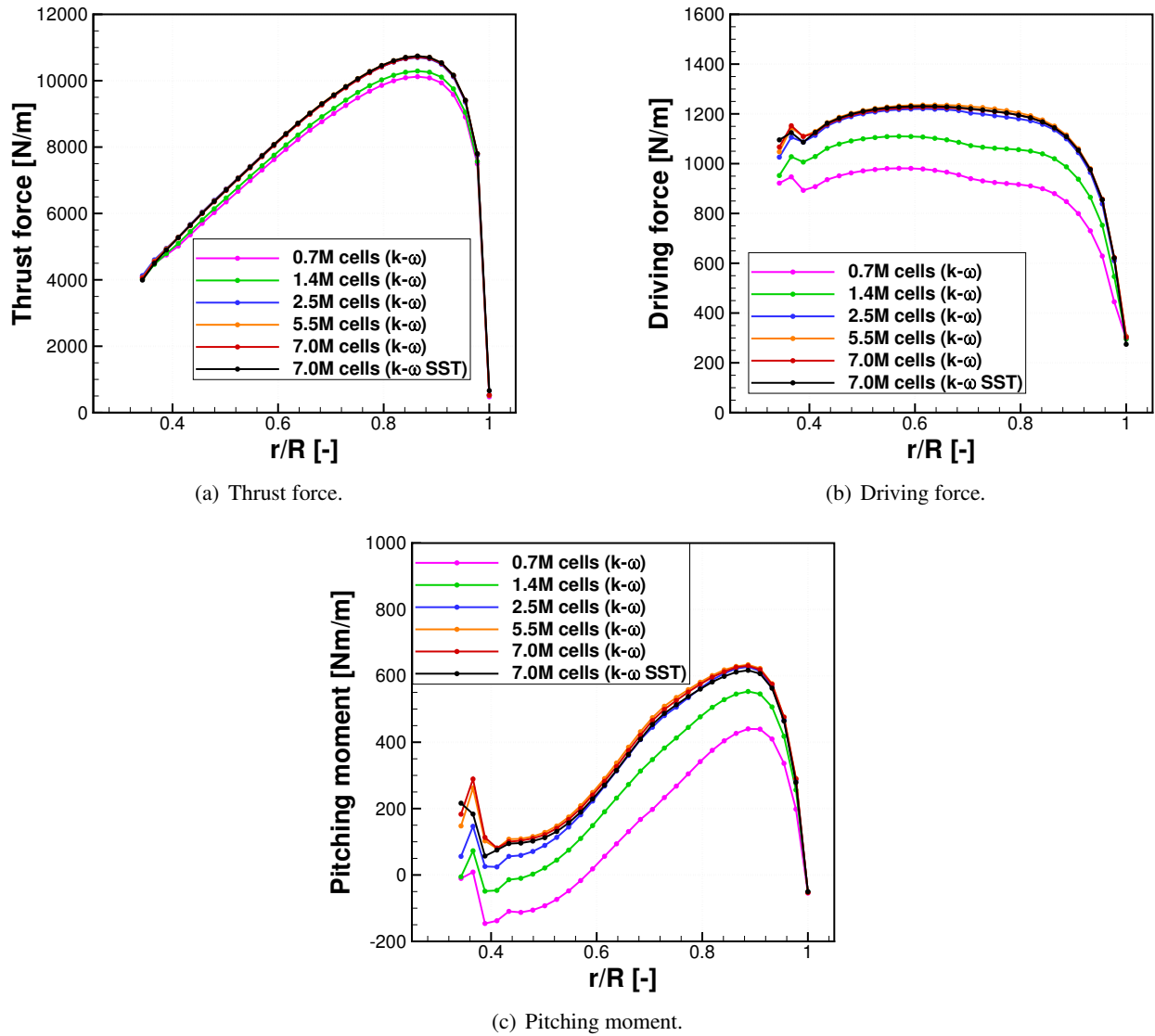


Figure 9.10: Distribution of the thrust and driving forces, and pitching moment along the blade span. Comparison between solutions obtained with grids of different density.

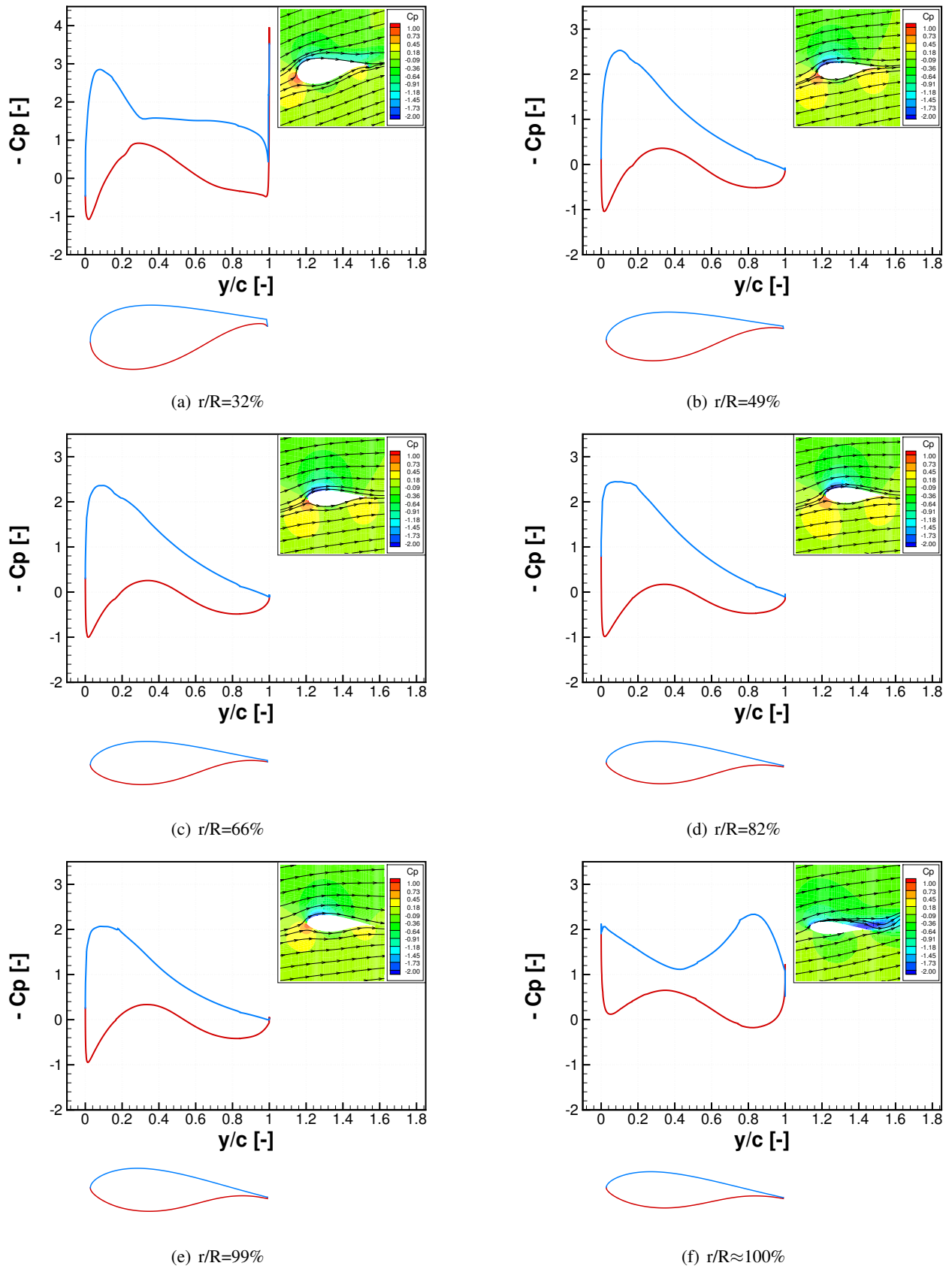


Figure 9.11: Pressure coefficient distribution around the aerofoil section for different radial positions along the blade.

9.4 Rigid blade cases with uniform inflow

9.4.1 Straight blade

For this set of cases, the blades were assumed straight (without pre-cone and pre-bend) and rigid. One blade was included in the computational domain, and periodicity in time and space was assumed with the HMB3 "hover" formulation^[192]. Various wind speeds were computed for the conditions for each case provided in the report of Bak *et al.*^[11] and reproduced here in Table 9.3. The computational domain is the same as for convergence study cases and is shown in Figure 9.6. Two grids were constructed of 7.0M and 9.2M cells as compared in Figure 9.12. The latter grid included the complete DTU 10MW RWT blade in a straight configuration, possessed 0-grid topology, as compared to C-H topology of the 7.0M grid, and the first cell distance from the wall was reduced to $10^{-6}c$, where $c = 6.206m$ is a maximum chord of the blade. This allowed to compute the y^+ parameter for this grid at rated conditions (11.4m/s wind speed) as $y^+ = 0.2$, as compared to $y^+ = 1.7$ for 7.0M cells grid. Another difference is that the nacelle was included in a simplified form in the 9.2M grid. The simplified nacelle shape was obtained by rotating the hub of the rotor by 180° as shown in Figure 9.13.

Table 9.3: Operational parameters for the DTU 10-MW RWT rotor^[11]. The pitch is defined positive nose down.

Wind Speed [m/s]	Pitch [deg]	Rotor speed [rev/min]
5	1.966	6.000
7	0.000	6.000
9	0.000	7.229
11	0.000	8.836
13	7.266	9.600
16	12.499	9.600
20	17.618	9.600
22	19.860	9.600

Results in terms of thrust and mechanical power as functions of the wind speed are presented in Figure 9.14 and Table 9.4. As can be seen, the coarser grid estimated the thrust and power at lower values as compared to the finer grid. This was expected, since only 70% of the blade radius was included in the first mesh. The number of cells in the boundary layer was computed once the solution has been obtained. For the 7.0M grid the boundary layer was resolved with 12 cells at 75% of the radius, while for the 9.2M grid

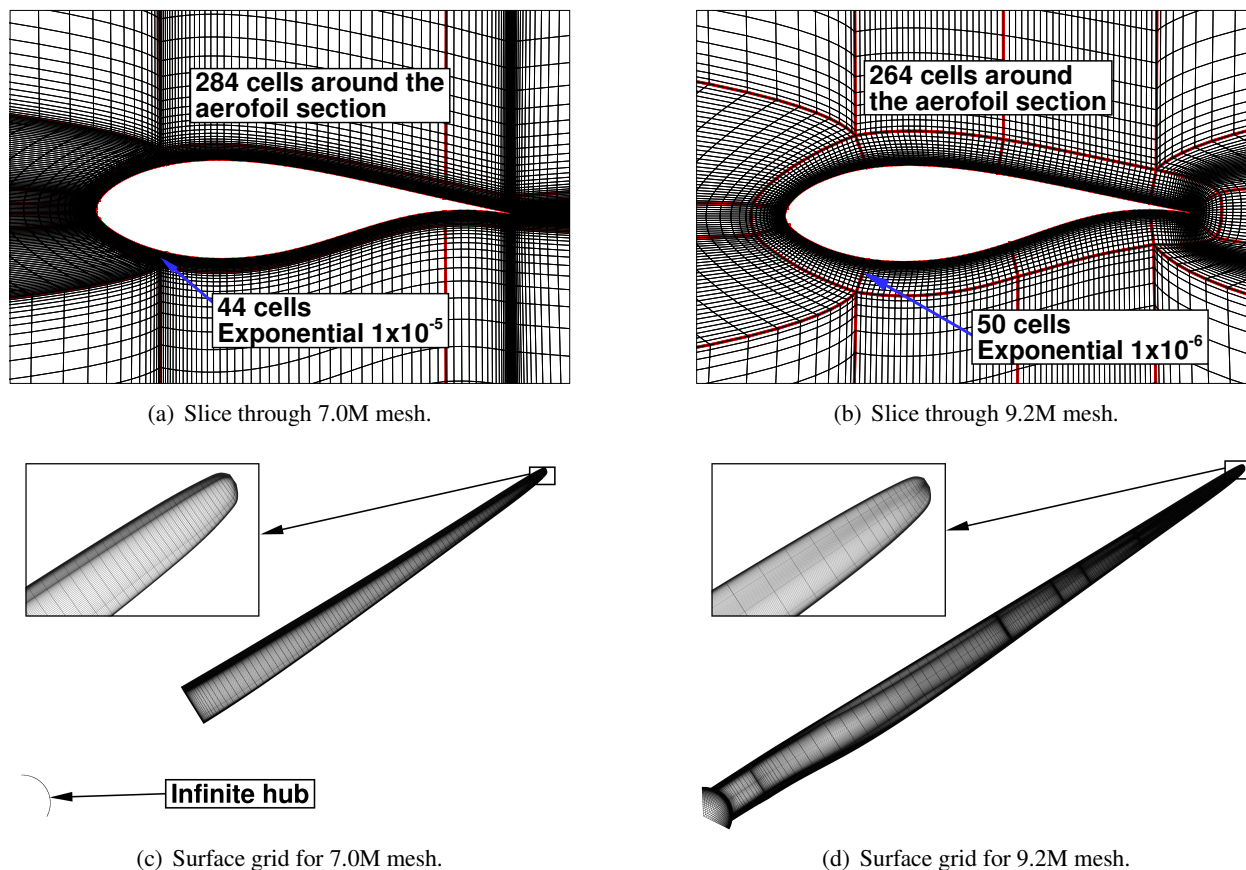


Figure 9.12: Two grids employed for straight and rigid blade cases – 7.0M and 9.2M cells grids. Slices through mesh in the vicinity of the surface of the blade (a-b); and surface grids (c-d). Distances in maximum chords, c .

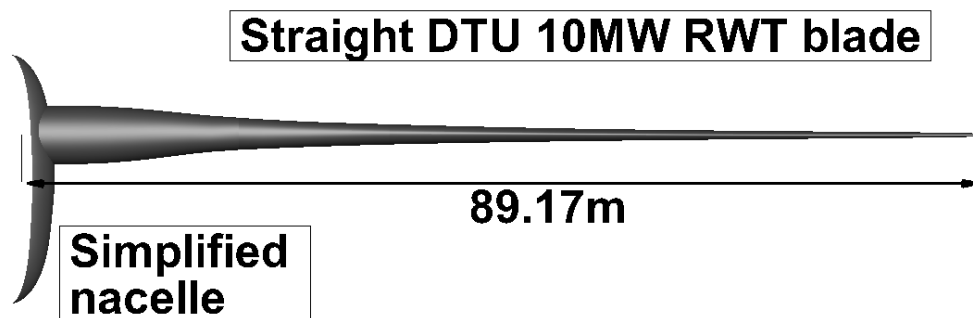


Figure 9.13: Shape of the DTU 10MW RWT blade with simplified nacelle as employed for the 9.2M cells mesh.

from 25 to 30 cells were inside the boundary layer. Results for thrust and power below the rated wind speed agreed fairly well with the results presented by Bak *et al.* ^[11]. Lower values of thrust and power for the first grid were obtained for wind speeds above rated. However, improved results can be seen for the second grid that employs the complete blade, and a lower y^+ parameter, as well as more cells in the boundary layer.

Note that computations involving finer grid and high wind speeds were not conducted, as this was not the main objective of this work and was not required by the MARE-WINT consortium.

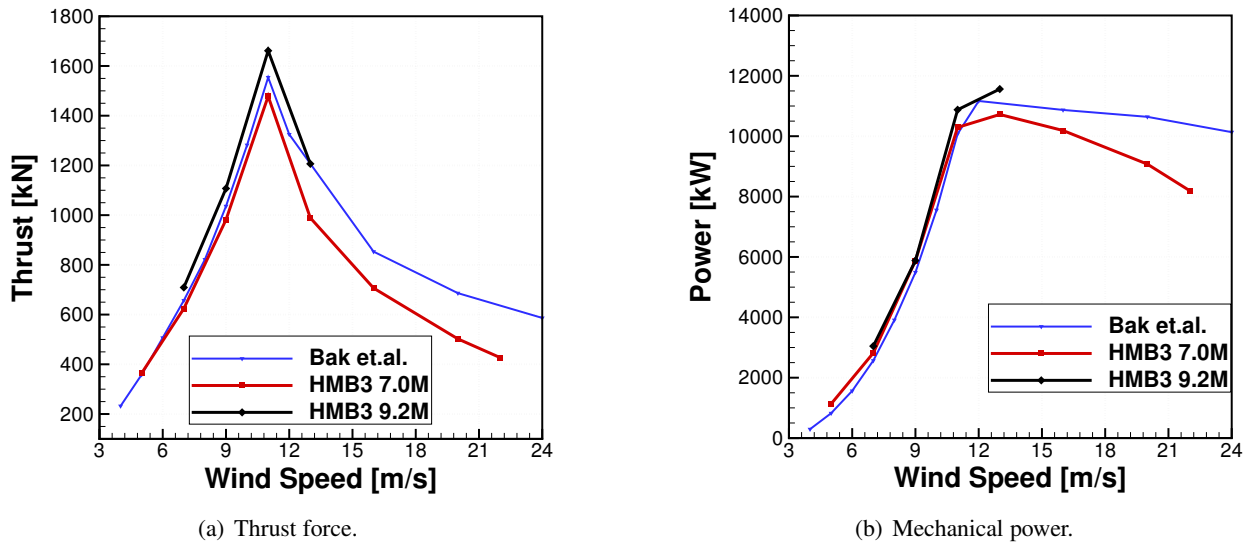


Figure 9.14: Thrust and power as functions of wind speed for straight, rigid blade. Comparison between results obtained by present CFD computations and Bak *et al.* [11].

Table 9.4: Results for straight and rigid blade for two grids in terms of thrust and power.

Grid	Wind Speed [m/s]	Thrust[kN]	Power [kW]	Blade pitch [deg]	Rotor speed [rpm]
7.0M	5	364.35	1132.36	1.966	6.000
	7	624.13	2818.66	0.000	6.000
	9	981.46	5880.54	0.000	7.229
	11	1478.21	10291.75	0.000	8.836
	13	989.15	10720.12	7.266	9.600
	16	706.58	10188.38	12.499	9.600
	20	502.16	9075.03	17.618	9.600
	22	427.01	8198.63	19.860	9.600
9.2M	7	709.08	3045.63	0.000	6.000
	9	1107.35	5880.87	0.000	7.229
	11	1661.31	10876.44	0.000	8.836
	13	1206.43	11562.12	7.266	9.600

The distributions of the thrust force, driving force and pitching moment for various wind speeds for the finer grid are shown in Figure 9.15. As can be seen, the thrust force is increasing with the wind speed below the rated conditions of 11.4m/s . This agrees with the integrated loads shown in Figure 9.14. However, at 13m/s , the thrust force is reduced. In this case, the distribution is similar to the one obtained for 11m/s from the root to $0.3R$, and close to the distribution for 9m/s from around $0.6R$ to the tip. The integrated

thrust over the blade at 13m/s is hence larger, as compared to the 9m/s wind speed case, and lower, as compared to 11m/s case. This shows the asymmetry of the thrust force with respect to the rated wind speed, where the total thrust is higher for 13m/s than for 9m/s . This can be seen in Figure 9.14, where the trend is also confirmed by the results of Bak *et al.* [11]. The stall region was similar for both wind speeds, as will also be shown in the following paragraphs.

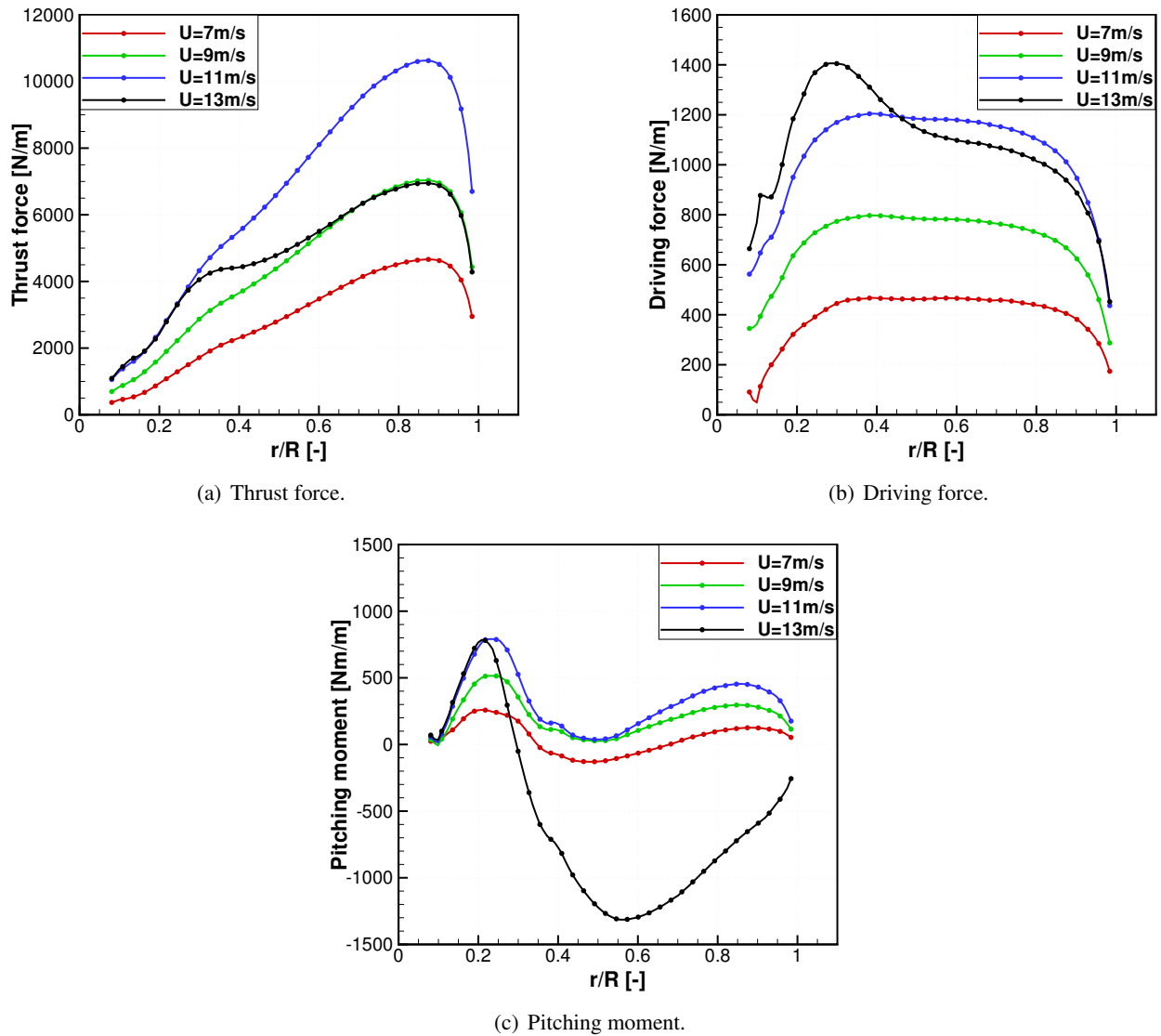


Figure 9.15: Distribution of the thrust and driving forces, and pitching moment along the blade span. Comparison between solutions obtained for different wind speeds using 9.2M cells grid.

The driving force is increasing with the wind speed below the rated conditions. At 13m/s wind speed, a reduction of the driving force can be seen for the outboard part of the blade, with an increase at the inboard

part. The overall driving moment created by this force is lower, as compared to 11m/s ($1.15 \cdot 10^7\text{Nm}$ for 13m/s , and $1.18 \cdot 10^7\text{Nm}$ for 11m/s). However, when converted to mechanical power by multiplying by the rotational velocity, a larger power production is computed for 13m/s , as can be seen in Figure 9.14.

The pitching moment follows similar trends as the thrust and driving forces. The blade is fairly well balanced for the wind speed of 7m/s , where the integrated moment acting along the pitch axis of one blade is 3.8kNm . Positive moment means that the aerodynamic forces tend to increase the angle of attack. Starting from below rated conditions, the pitching moment becomes larger as the wind speed is increased. For 9m/s wind speed, the pitching moment is 19.6kNm , and for 11m/s , it is 23.6kNm . At 13m/s wind

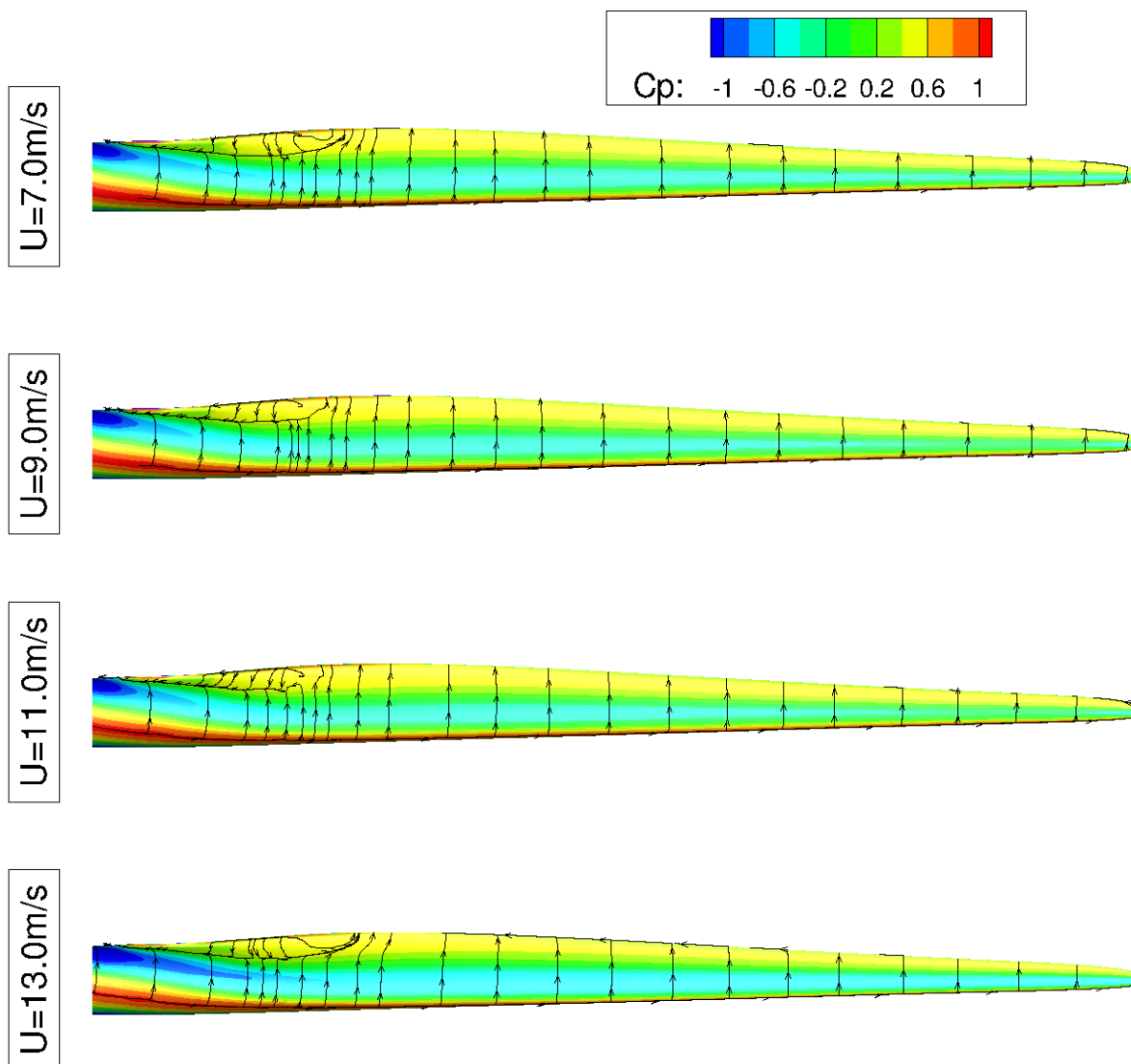


Figure 9.16: Distribution of the surface pressure coefficient (C_p) on the pressure side of the blade for the 9.2M cells grid at various wind speeds.

speed, the pitching moment is $-46.5kNm$, and has a negative sign, meaning that the aerodynamic forces try to decrease the angle of attack. This is a positive effect, since as the wind speed is further increased, the pitch-controlling actuator should work towards the reduction of the angle of attack (pitch to feather).

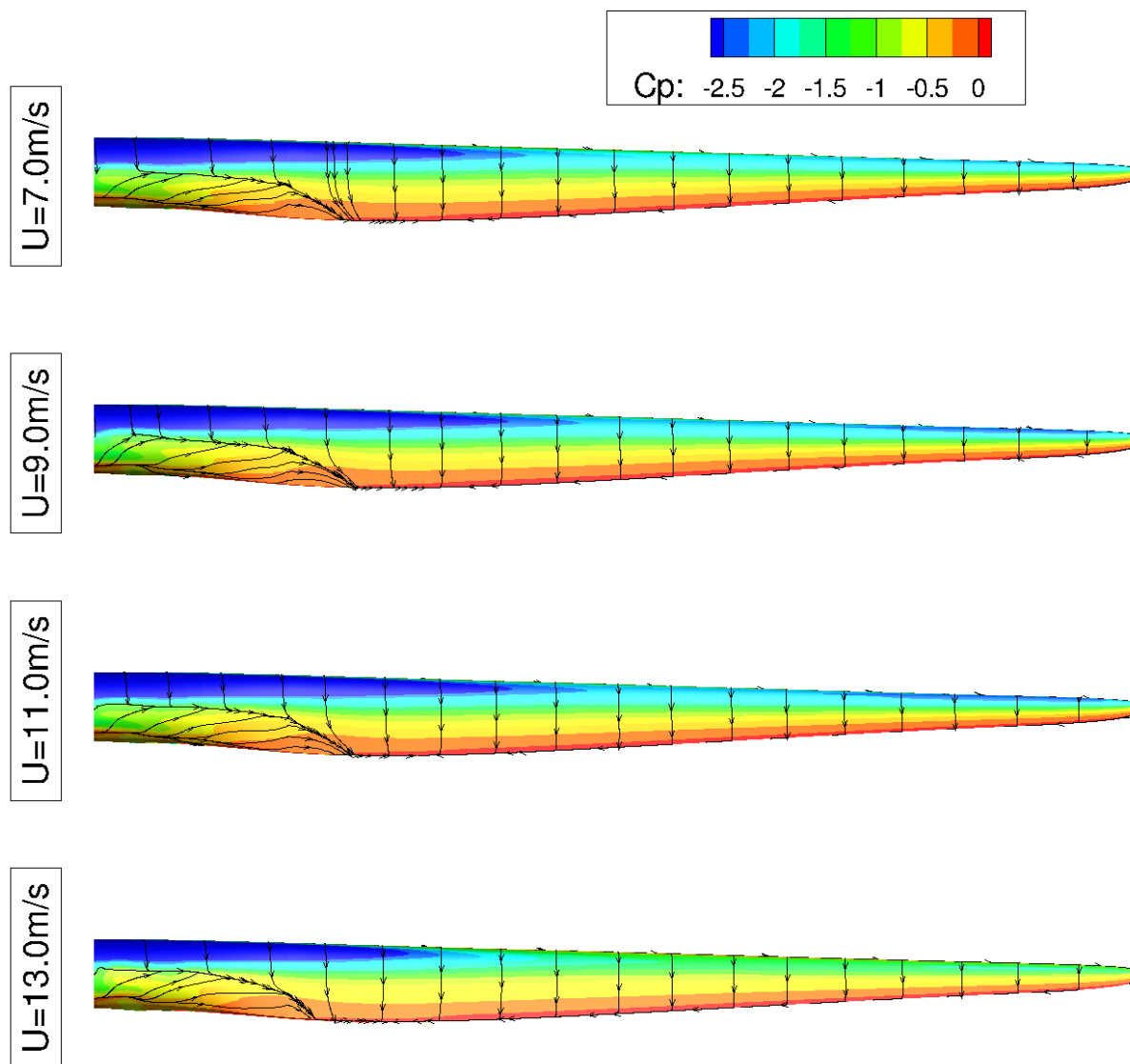


Figure 9.17: Distribution of the surface pressure coefficient (C_p) on the suction side of the blade for the 9.2M cells grid at various wind speeds.

Figures 9.16 and 9.17 present the surface pressure coefficient (C_p) for 9.2M cells grid at various wind speeds. The coefficient was computed using:

$$C_p = 2 \left(\frac{p - p_\infty}{\gamma p_\infty M_\infty^2} \right) = \frac{p - p_\infty}{0.5 \rho_\infty U_\infty^2}, \quad (9.2)$$

where p is the pressure at the point where pressure coefficient is computed, p_∞ is the free-stream pressure,

γ is the adiabatic index, and M_∞ is the free-stream Mach number. The skin friction lines were added to visualise the flow close to the surface. These were obtained by calculating the wall stresses.

The comparison for the pressure side is shown in Figure 9.16. Very little differences can be seen for below the rated conditions. However, for 13m/s the pressure coefficient is lower on the pressure side. The skin friction lines show flow recirculation due to the Gurney flap. The recirculation region spans to around 30% of the blade, and approximately coincides with the location of the flap. This recirculation was observed for all computed wind speeds. The largest recirculation can be seen for 7m/s and 13m/s , whilst for 9m/s and 11m/s the predicted recirculation region is a bit smaller. Introduction of the present Gurney flap did not prevent separation on the suction side, as shown in Figures 9.17 and 9.18. This is also confirmed by the results of Horcas *et al.* [76], where separation was observed for both configurations – with and without the Gurney flap. Also, similar span-wise lengths of pressure and suction side recirculations were reported.

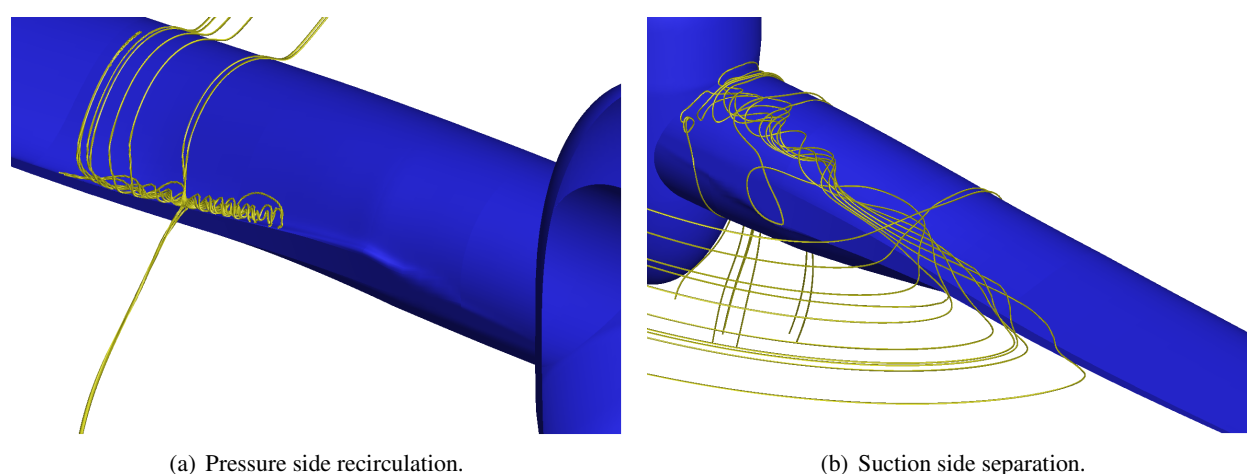


Figure 9.18: Streamlines showing recirculation on the pressure side, and separation on the suction side for DTU 10MW wind turbine at 11m/s wind speed.

The distributions of the pressure coefficient over the suction side are shown in Figure 9.17. Higher coefficients can be seen for 13m/s wind speeds, as compared to other wind speeds. Also, the flow separation at the root can be seen. The separation region spans to around 35%, as also reported in [76].

The comparisons of the pressure coefficient distributions at various radial positions along the blade are shown in Figure 9.19. The largest differences of C_p between both sides of the blade are observed for 9m/s and 11m/s wind speed. On the other hand, the smallest differences can be seen for 13m/s wind,

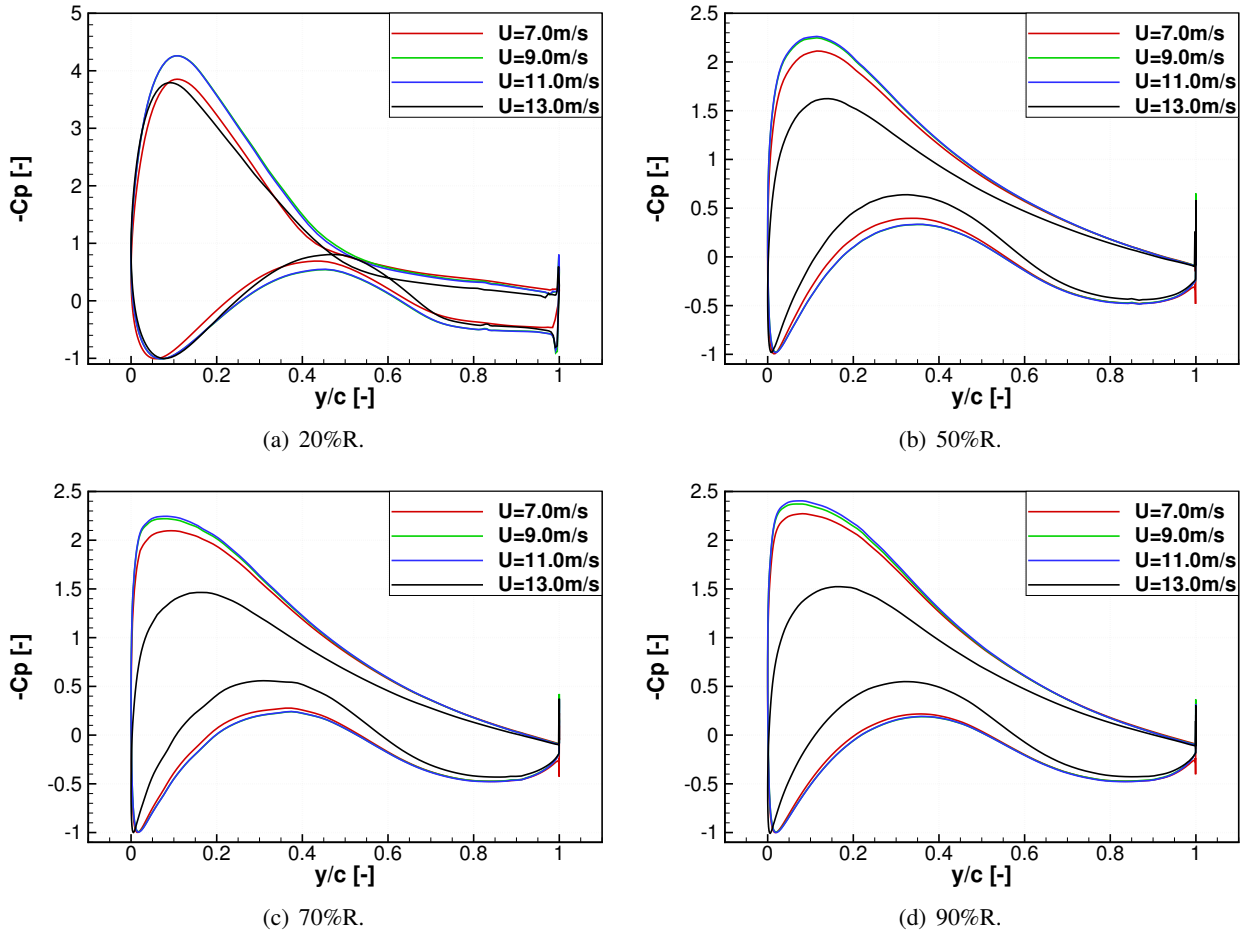


Figure 9.19: Pressure coefficient distribution around the aerofoil section for different radial positions along the blade and for different wind speeds.

which agrees with the observations above. The recirculation regions can also be seen at the section near $0.2R$, where the pressure coefficient is almost constant towards the trailing edge. The results suggest a chord-wise length of suction side separation of 45% of the local chord at this section. Likewise, the pressure side recirculation is affecting 25% of the local chord. Finally, the increase of the pressure difference due to the Gurney flap at the trailing edge of the $0.2R$ station can be observed.

Figures 9.20 and 9.21 present the distribution of the skin friction coefficient (C_f) over the blade surface for 9.2M cells grid at various wind speeds. The coefficient was computed as

$$C_f = \frac{\tau_w}{0.5\rho_\infty U_\infty^2}, \quad (9.3)$$

where τ_w is the wall shear stress at the point where the skin friction coefficient is computed, ρ_∞ is the free-stream density of the fluid, and U_∞ is the free-stream velocity of the fluid. Looking at the pressure side, the

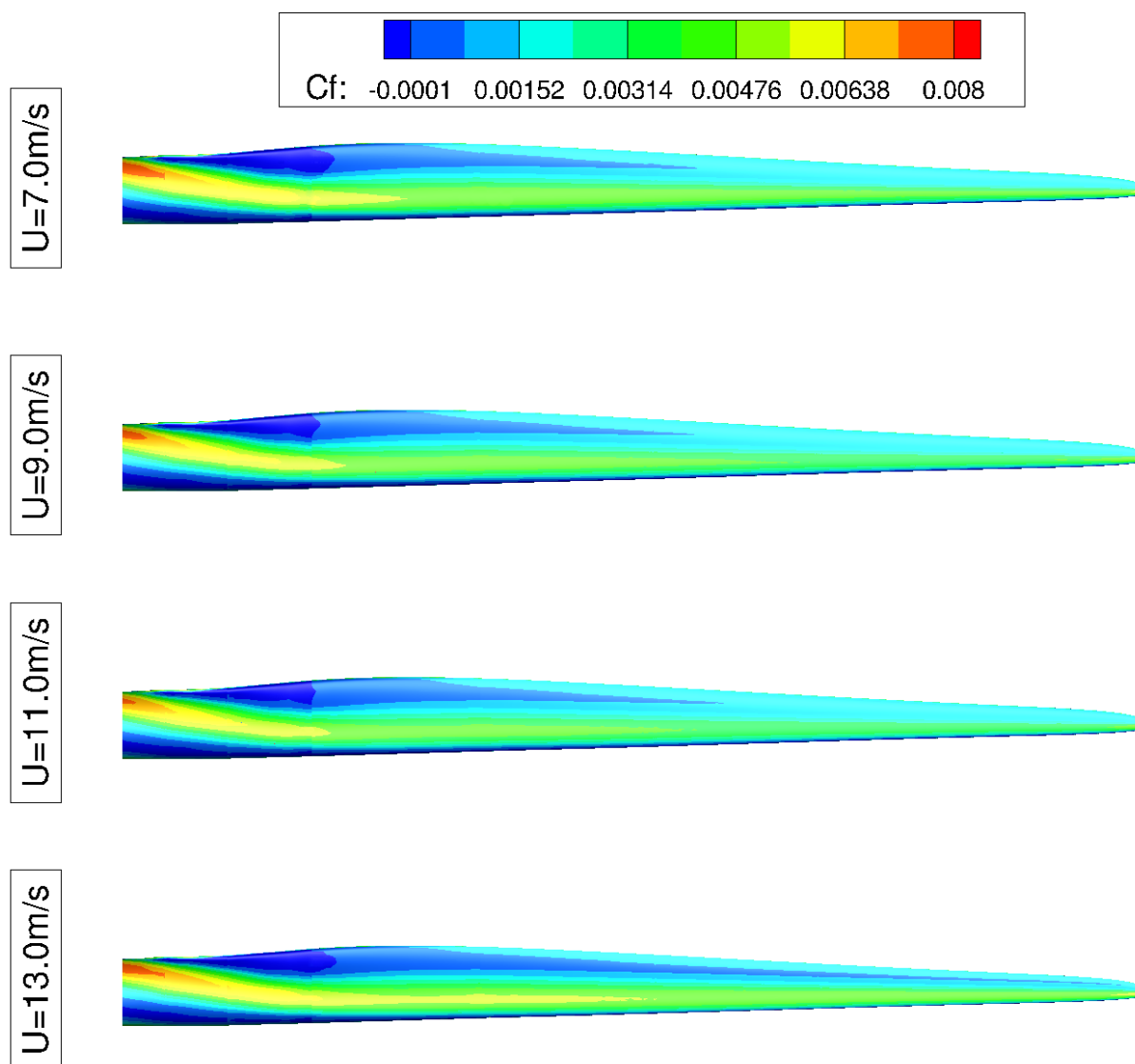


Figure 9.20: Distribution of the skin friction coefficient (C_f) over the pressure side of the blade for the 9.2M cell grid at various wind speeds.

results suggest higher coefficients for 13m/s wind speed, as compared to conditions below the rated speed. The separation region on the suction side can be clearly identified in Figure 9.21. This region is surrounded by low values of C_f , showing the onset of separation, and negative values of C_f can be seen in the separated region.

The comparisons of the skin friction coefficient distributions at various radial positions along the blade are shown in Figure 9.22. The results suggest similar distributions below the rated wind speed. However, at 13m/s wind speed, the differences between skin friction coefficients on both sides of the blade are reduced. The separated regions can also be identified for section near $0.2R$, where the C_f coefficient be-

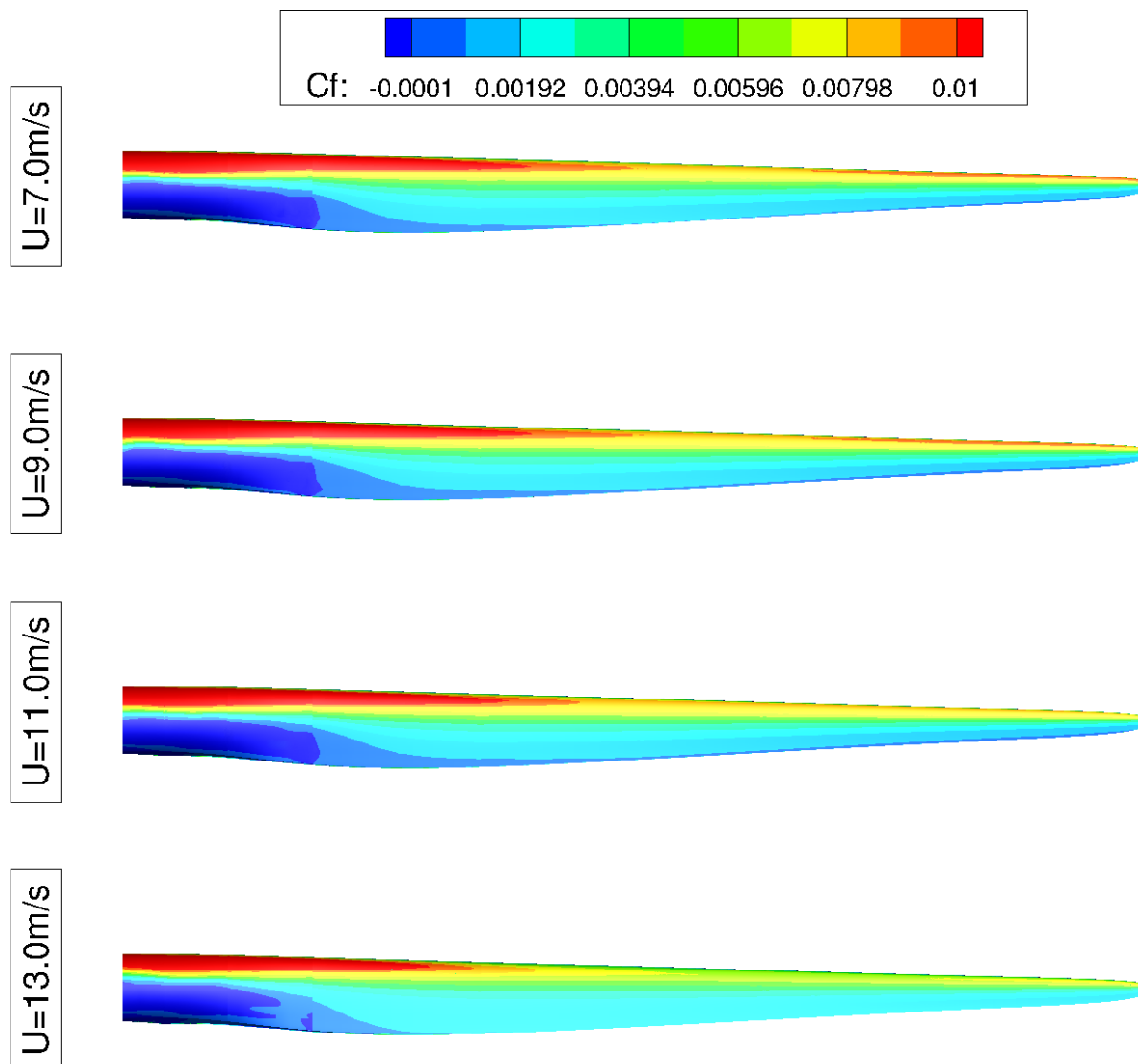


Figure 9.21: Distribution of the skin friction coefficient (C_f) over the suction side of the blade for the 9.2M cell grid at various wind speeds.

comes negative. The recirculation starts at around 55% of the local chord for the suction side, and at 75% for the pressure side. The results also show re-attachment of the flow at the Gurney flap, where C_f changes sign from negative to positive around 95% of the local chord.

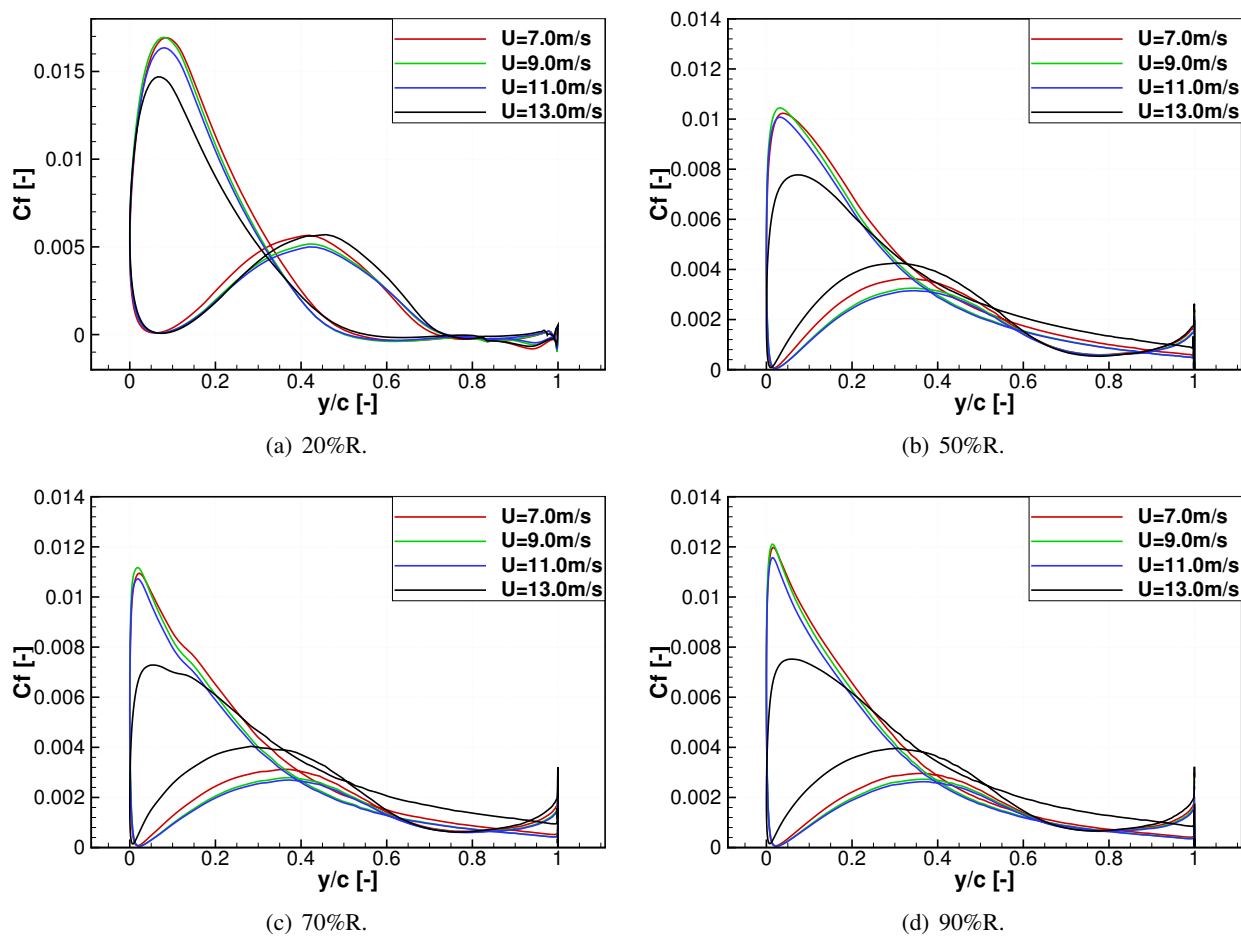


Figure 9.22: Skin friction coefficient distribution around the aerofoil section for different radial positions along the blade and for different wind speeds.

9.4.2 Blade with pre-bend and pre-cone

As described in Section 9.1 of this chapter, the DTU 10MW blade has two design configurations: straight; and with pre-bend and pre-cone. This sections considers the latter configuration at 11 m/s wind speed, and the results are compared to the straight blade.

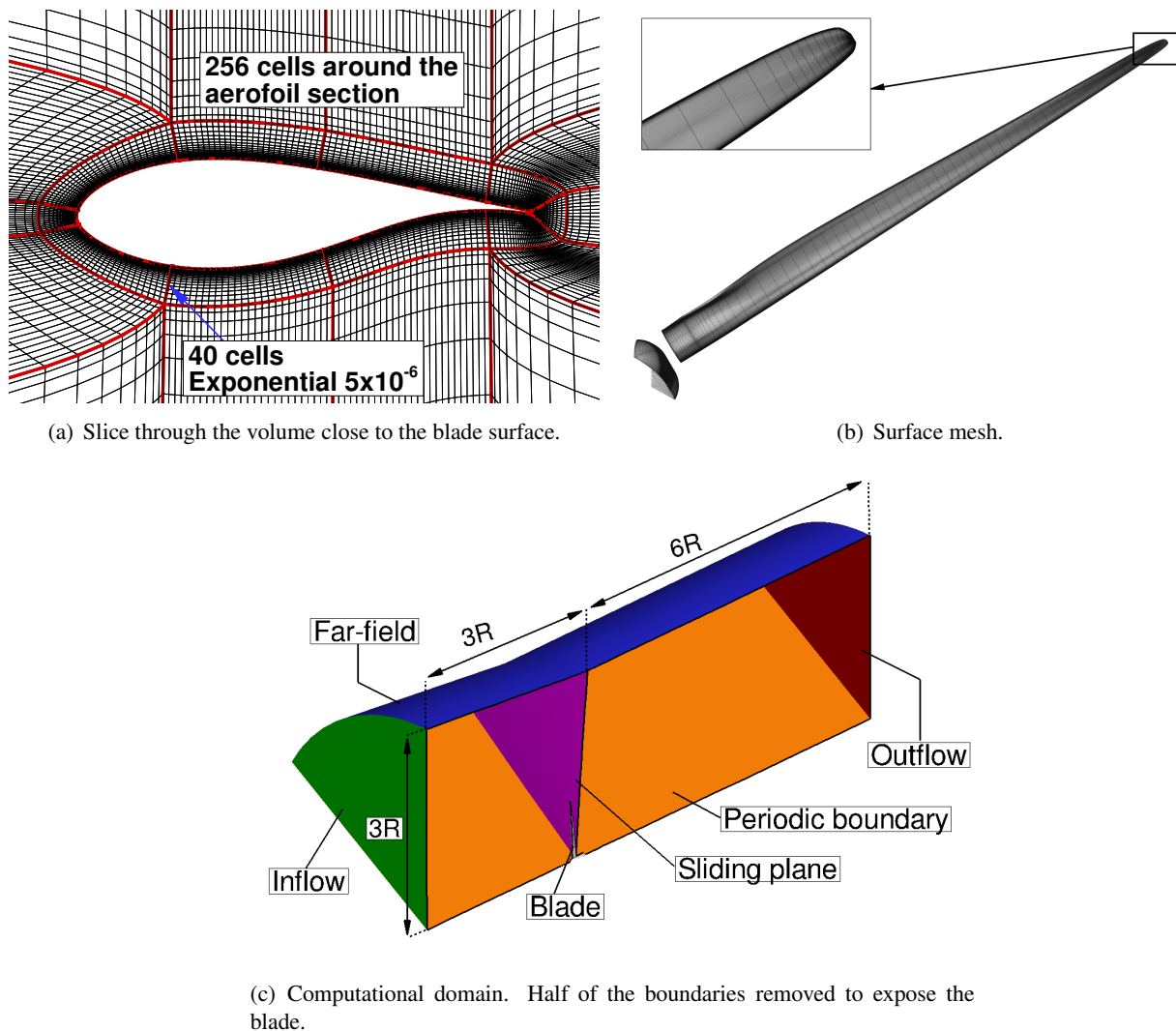


Figure 9.23: Grid employed for the DTU 10MW blade with pre-bend and pre-cone.

Similarly to the previous section, one blade was included in the computational domain, and periodicity in time and space was assumed with the "hover" formulation^[192]. The nacelle was included using sliding planes, and was rigidly attached to the rotor. This allowed to reduce the number of cells, by combining block-to-block unmatched domains, where both grid components are refined in different regions. See Figure 9.24 for domain decomposition methods available in the HMB3 flow solver. The total size of the

grid was $5.4M$ cells. The normal distance for the first cells of the blocks adjacent to the blade surface was $5 \cdot 10^{-6}c$, where c is a maximum chord of the blade, $6.206m$. 40 cells were used within the first layer of the blocks, with 256 cells distributed around the aerofoil section. The blade surface was resolved with 121 cells along the span. Based on experience^[64], an inflow boundary condition was used three blade radii ahead of the rotor, and an outflow was placed six blade radii downstream the rotor. Far-field was assigned three blade radii from the centre of rotation. The computational domain with corresponding boundaries, a slice through the mesh close to the blade surface, and the surface mesh of the blade are presented in Figure 9.23. Note that there is a small gap between the blade and the hub. The wind speed was $11m/s$, and the rotor was rotating at $8.836rpm$. This allowed to compute the y^+ parameter for this grid to be $y^+ = 0.9$.

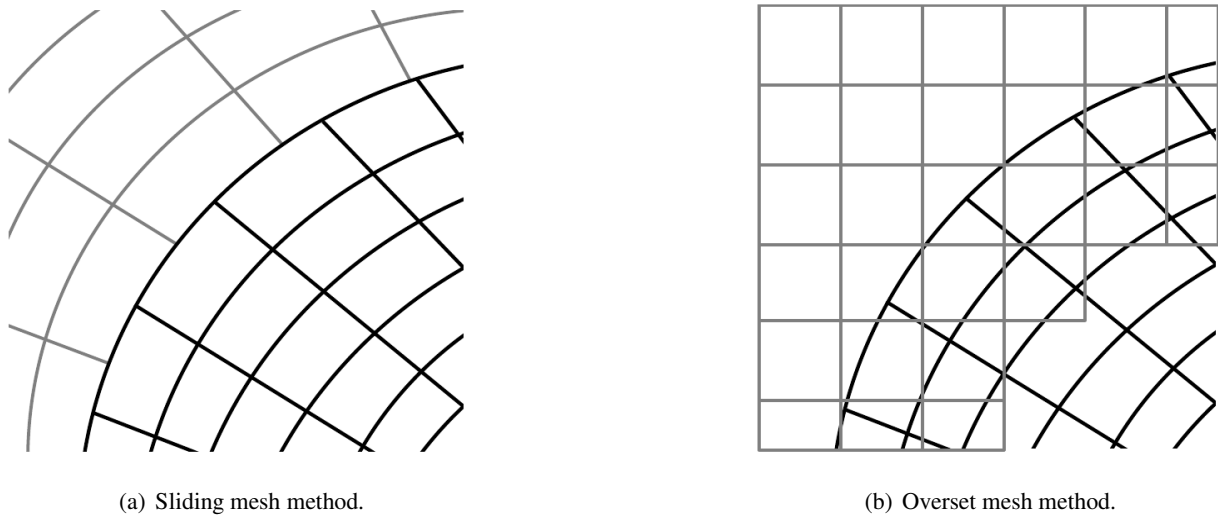


Figure 9.24: Domain decomposition methods: (a) sliding, and (b) overset methods. Adapted from ^[98].

The distributions of the thrust and driving forces, and pitching moment are shown in Figure 9.25, where the results for the straight blade are included for comparison. As can be seen, the straight blade was subjected to higher thrust, especially close to the root. Although, the computed distributions of the thrust are similar for both configurations. The driving force was also higher for the straight blade, as compared to the blade with pre-cone and pre-bend. The distribution of the driving forces coincide close to the tip (around $0.8R - 1R$), but differ closer to the root. The integrated thrust and power over the rotor are compared in Table 9.5, where a reduction of both quantities for the pre-bent blade can be seen.

The distributions of the pressure coefficient C_p for the straight and pre-bent blades are compared in

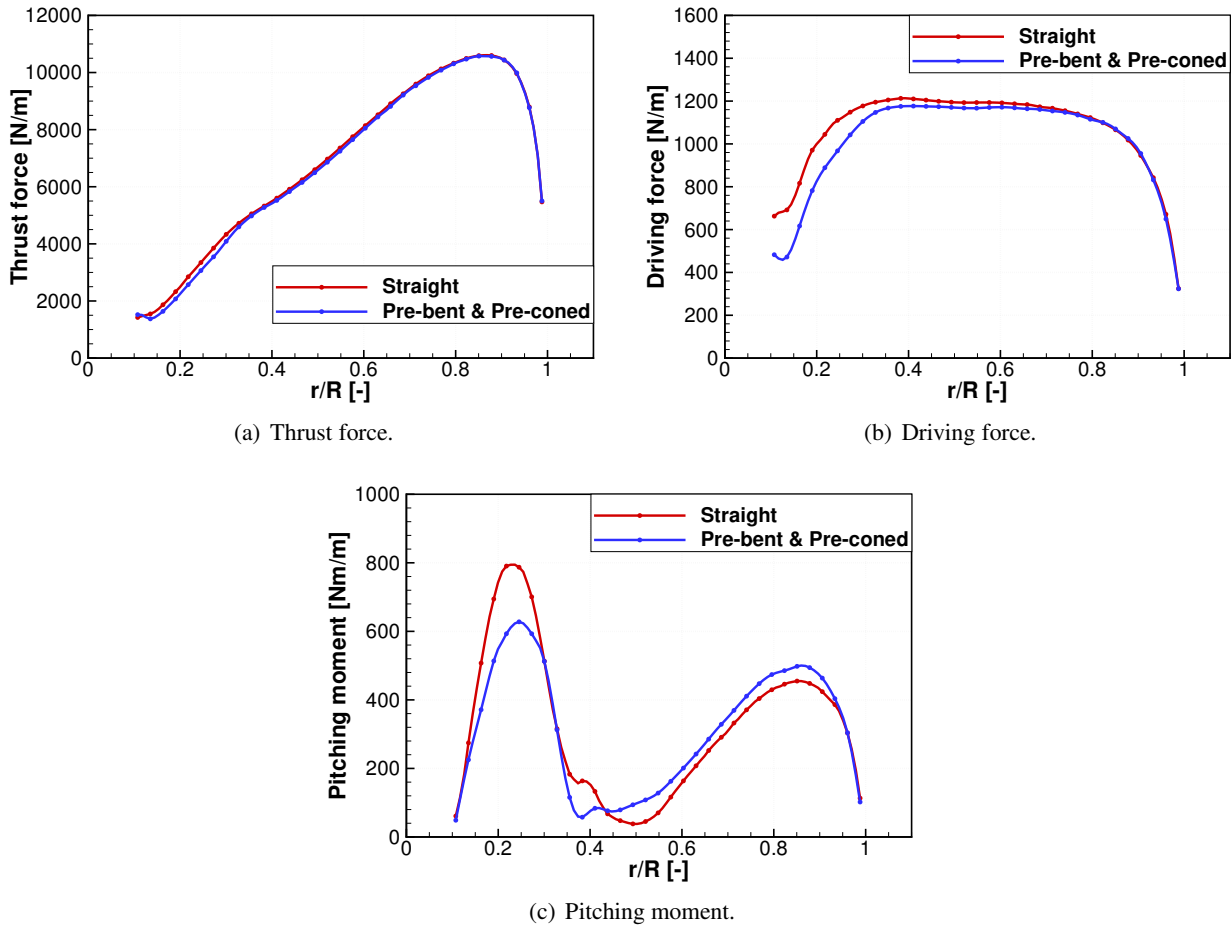


Figure 9.25: Distribution of the loads for straight blade, and with pre-cone and pre-bend.

Table 9.5: Comparison between thrust and power for straight and pre-coned blades.

	Straight blade	Pre-coned blade	Difference
Thrust [kN]	1661.3	1654.1	-7.2 (-0.4%)
Mech. Power [kW]	10876.4	10846.5	-29.9 (-0.3%)

Figure 9.26. The skin friction lines are also included for comparison. Very similar flow patterns can be seen for both configurations of the blade. Differences at the root stem from the fact, that the root part of the blade for the pre-bent configuration was not included. As a result, highly three-dimensional flow occurs at the root for this case, affecting about 10% of the span. Hence, the differences in integrated loads are not caused by this geometrical simplification.

The pressure coefficient distributions at various radial positions along the blade are compared in Figure 9.27. Differences can be seen closer to the root, where a higher suction peak is observed for the straight blade. This agrees with the distributions of loads shown in Figure 9.25.

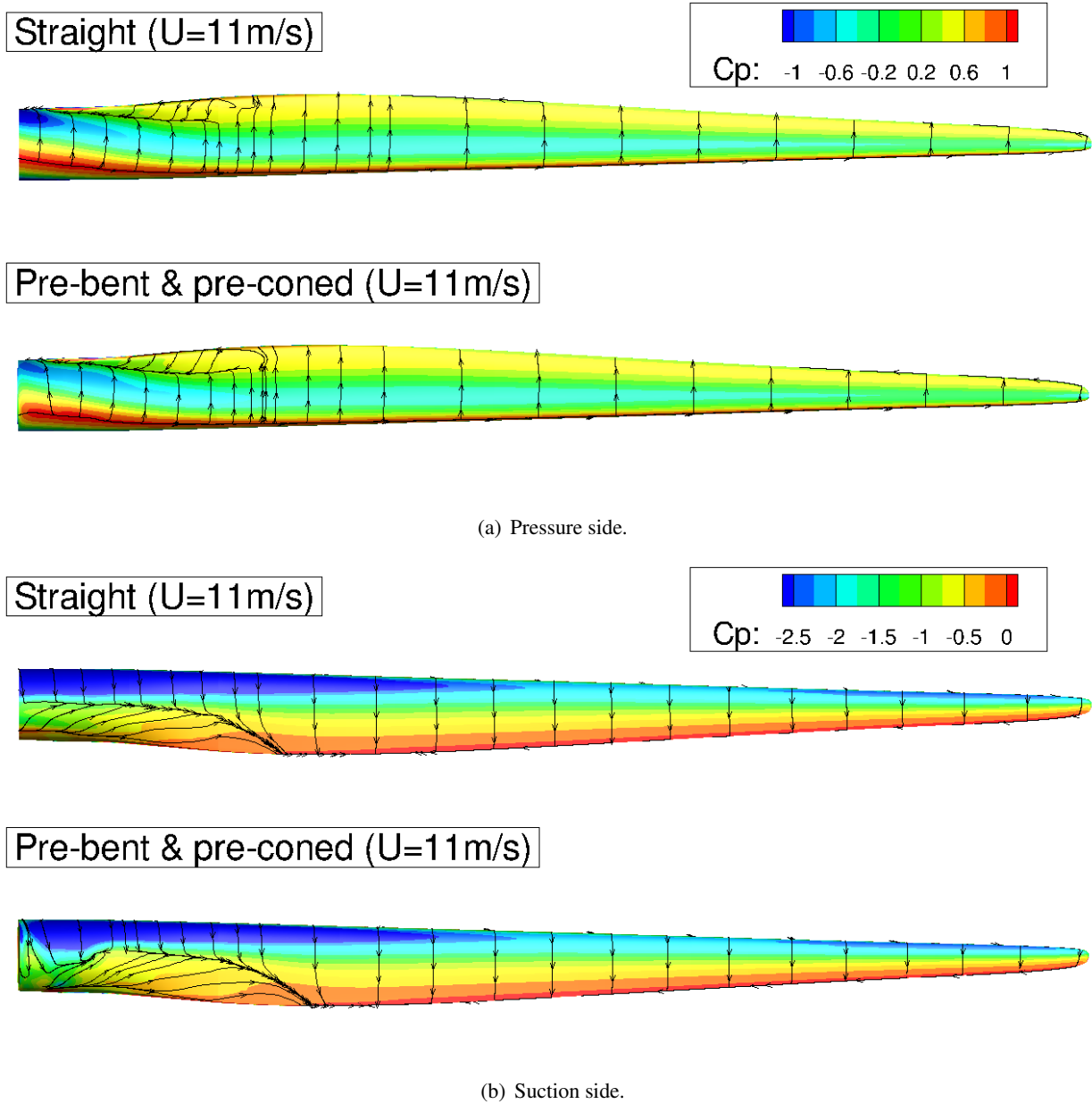


Figure 9.26: Distribution of the surface pressure coefficient (C_p) over the pressure side (a), and suction side (b). Comparison between straight and pre-coned blades.

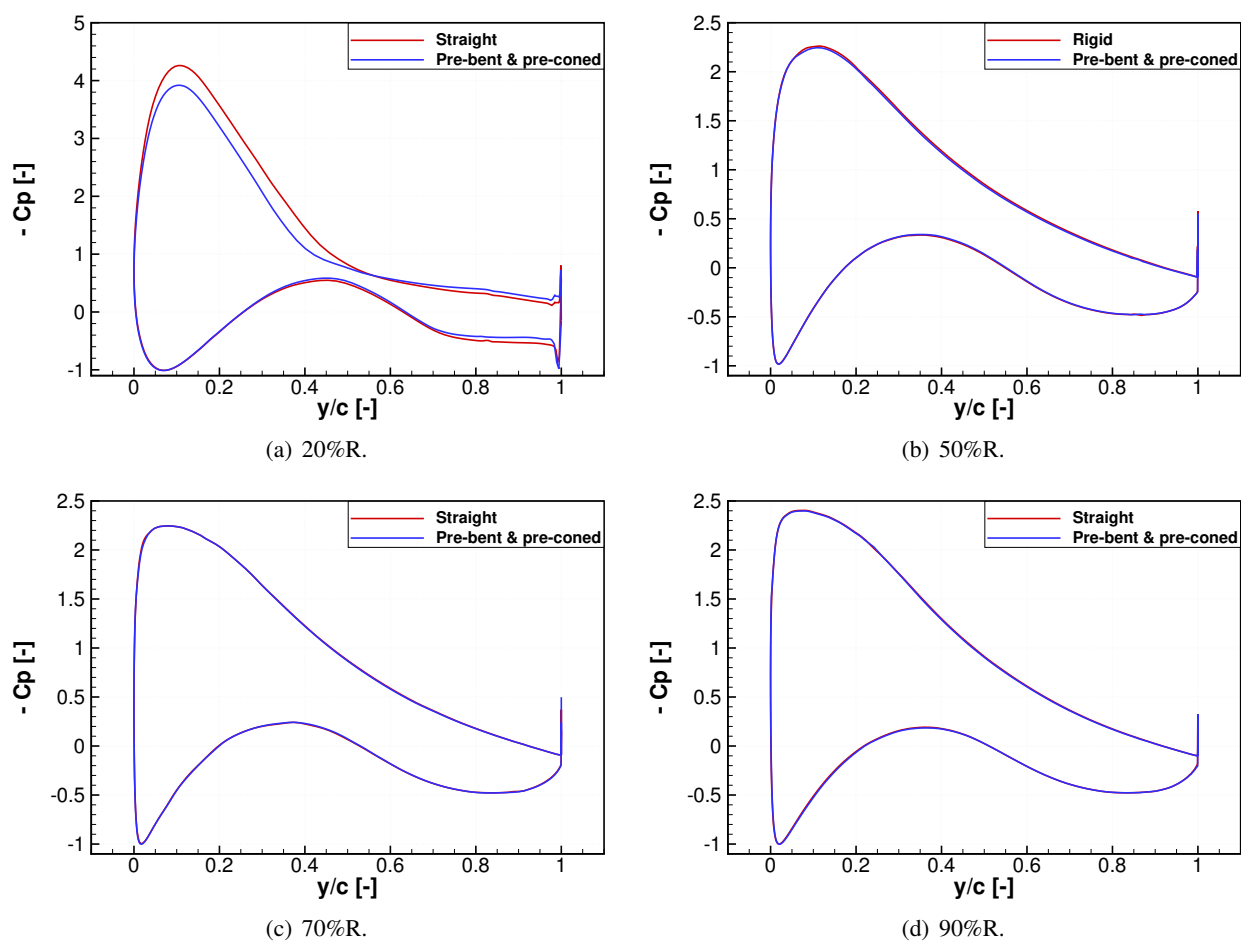


Figure 9.27: Pressure coefficient distributions at different radial positions along the blade.

9.5 Atmospheric boundary inflow and atmospheric turbulence

This section presents results of the DTU 10MW RWT rotor subjected to the atmospheric boundary inflow with and without atmospheric turbulence. A power law profile was used to model the atmospheric boundary layer^[158], and the atmospheric turbulence was included using Mann's turbulence model^[129, 130]. The employed numerical parameters and procedure are also explained in this section.

9.5.1 Atmospheric boundary inflow

The inflow profile was defined using the power law

$$U(z) = U_{hub} \left(\frac{z}{z_{hub}} \right)^{1/\beta}, \quad (9.4)$$

where U_{hub} set to $11m/s$ is the hub-height wind speed, z is the elevation above the ground, $\beta = 7$ is the wind profile power coefficient^[158], and $z_{hub} = 119.0m$ is the height of the hub as specified in Bak *et al.*^[11]. The distribution of pressure and density were computed based on the International Standard Atmosphere (ISA)^[5], assuming sea-level pressure $P_0 = 101325Pa$, temperature $T_0 = 288.16K = 15.0^\circ C$, density $\rho_0 = 1.225kg/m^3$, and the lapse rate $L = -0.0065K/m$. Another possible choice to define the wind profile is the logarithmic law, which is more complex, as the model involves shear velocity, surface roughness, and stability parameters. The logarithmic law model is accurate close to the ground, but above $\sim 100m$ the power law is more accurate in predicting the mean wind speed^[32]. Given the location of the hub ($119.0m$), the power law profile was chosen in this work. The employed distributions of the wind speed, pressure and density are shown in Figure 9.28

9.5.2 Mann turbulence model

The Mann turbulence field generator was provided by the Technical University of Denmark^[215] as part of the MARE-WINT project collaboration^[3]. The model starts from the von Kármán^[207] energy spectrum expressed as

$$E(k) = \alpha \varepsilon^{2/3} L^{5/3} \frac{L^4 k^4}{(1 + L^2 k^2)^{17/6}}, \quad (9.5)$$

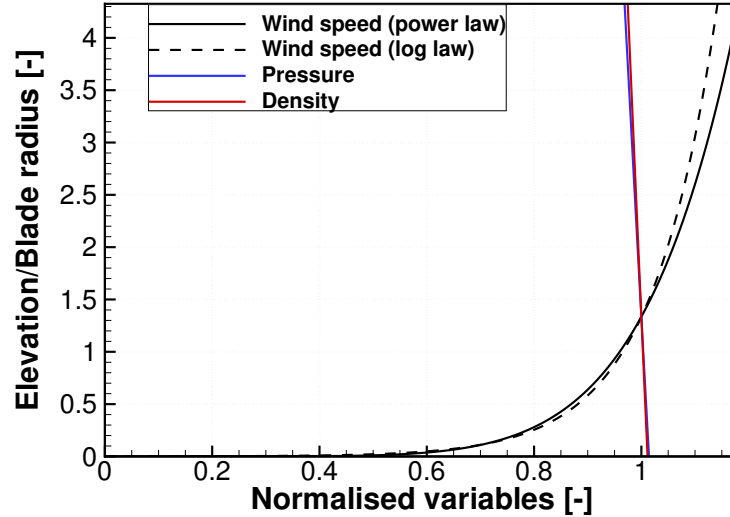


Figure 9.28: Distributions of the wind speed, pressure and density obtained with the power law profile by setting $U_{hub} = 11\text{m/s}$, $z_{hub} = 119.0\text{m}$, and $\beta = 7$. Logarithmic law profile was computed using $U(z) = U_{hub} \ln(\frac{z}{z_0}) / \ln(\frac{z_{hub}}{z_0})$, where $z_0 = 0.03\text{m}$ is the roughness length of a flat terrain. Quantities are normalised to the values at the hub-height.

where α is the Kolmogorov constant, ε is the rate of viscous dissipation of specific turbulence kinetic energy, L is a length scale in meters (often chosen as rotor radius), and k is the wave number. It is postulated in Mann^[130] that eddies are stretched by shear over a time proportional to their lifetime τ . For relatively high frequencies and wave numbers, τ is proportional to $k^{-2/3}$ ^[129, 130]. Denote the dimensionless eddy lifetime by β , then

$$\beta \equiv \frac{dU}{dz} \tau = \Gamma \frac{dU}{dz} (kL)^{-2/3}, \quad (9.6)$$

where U is the wind velocity, z is the height, and Γ is the parameter of the sheared spectral tensor, also known as the stretching parameter. It is assumed in the model that shear is linear such that $\frac{dU}{dz}$ is constant. For $\Gamma = 0$, the tensor is isotropic, and can be used to model the turbulent wind field without shear. In this case $\alpha \varepsilon^{2/3} = \sigma^2 / (0.688 \cdot L^{2/3})$, where $\sigma = Ti \cdot U_{wind}$ is the velocity variance, Ti is the turbulence intensity, and L is the length of the blade. For the atmospheric experiments over water, the parameters are $L/z = 0.87$, $\Gamma = 3.2$; and for flow over flat terrain $L/z = 0.91$, $\Gamma = 2.6$ ^[130], where z is the height above the ground.

The interaction between wind turbines and the turbulent field cannot be predicted using BEM method^[164] i.e. the presence of the rotor has no effect on the turbulent field. Hence, proper value of Γ is important for engineering models. The choice of Γ may be also important for CFD computations, if a precomputed field of turbulence is initiated on the whole CFD domain. In this work, the atmospheric boundary profile is as-

sumed at the inflow, with isotropic turbulence based on Mann's model. Hence, $\Gamma = 0$ at the inflow, and shear in the field of turbulence is allowed to develop due to the imposed ground boundary. Also, the high frequency correction was applied in the Mann's model. As was shown by Mann^[130], without this correction the simulated spectra are typically attenuated at high wave numbers (or frequencies).

Computational procedure

First, the Mann's field of isotropic turbulence was created using the parameters of Table 9.6. The resulting field is a cube (or box, hence *Mann box*) of size $2km \times 2km \times 2km$ with a resolution of $4m$ in each direction. The turbulence intensity is about 5%, assuming that the mean inflow speed is $11m/s$. The obtained Mann box is visualised in Figure 9.29.

Parameter	Value
$\alpha\epsilon^{2/3}$	0.02
L	89m
Γ	0
Number of points in x direction	512
Number of points in y direction	512
Number of points in z direction	512
Spacing in x direction	4.0m
Spacing in y direction	4.0m
Spacing in z direction	4.0m

Table 9.6: Parameters used in the Mann box generator.

The implementation of the Mann turbulence model into the HMB3 solver as a wind turbulence boundary condition is shown in Figure 9.30. The idea is to convect the Mann turbulence to the computational domain through the inflow boundary. By applying Taylor's frozen turbulence hypothesis, the time off-set from the inflow plane of the CFD domain can be converted to a space off-set. Hence, velocity fluctuations are extracted from Mann box in slices i.e. equally spaced planes, with a distance Δx between consecutive planes equal to the Mann box spacial resolution, see Figure 9.30(b) for illustration. These slices are then interpolated onto the inflow plane of the CFD domain, and stored. As depicted in Figure 9.30, at time $t = 0s$ the front face of the Mann box is coincident with the inlet of the computational domain. Interpolated inflow planes, located at $x = -U_{hub} \cdot t$ in the Mann box, are then used to impose turbulent inflow boundary at consecutive times during unsteady computations. This procedure is equivalent to having the Mann box moving

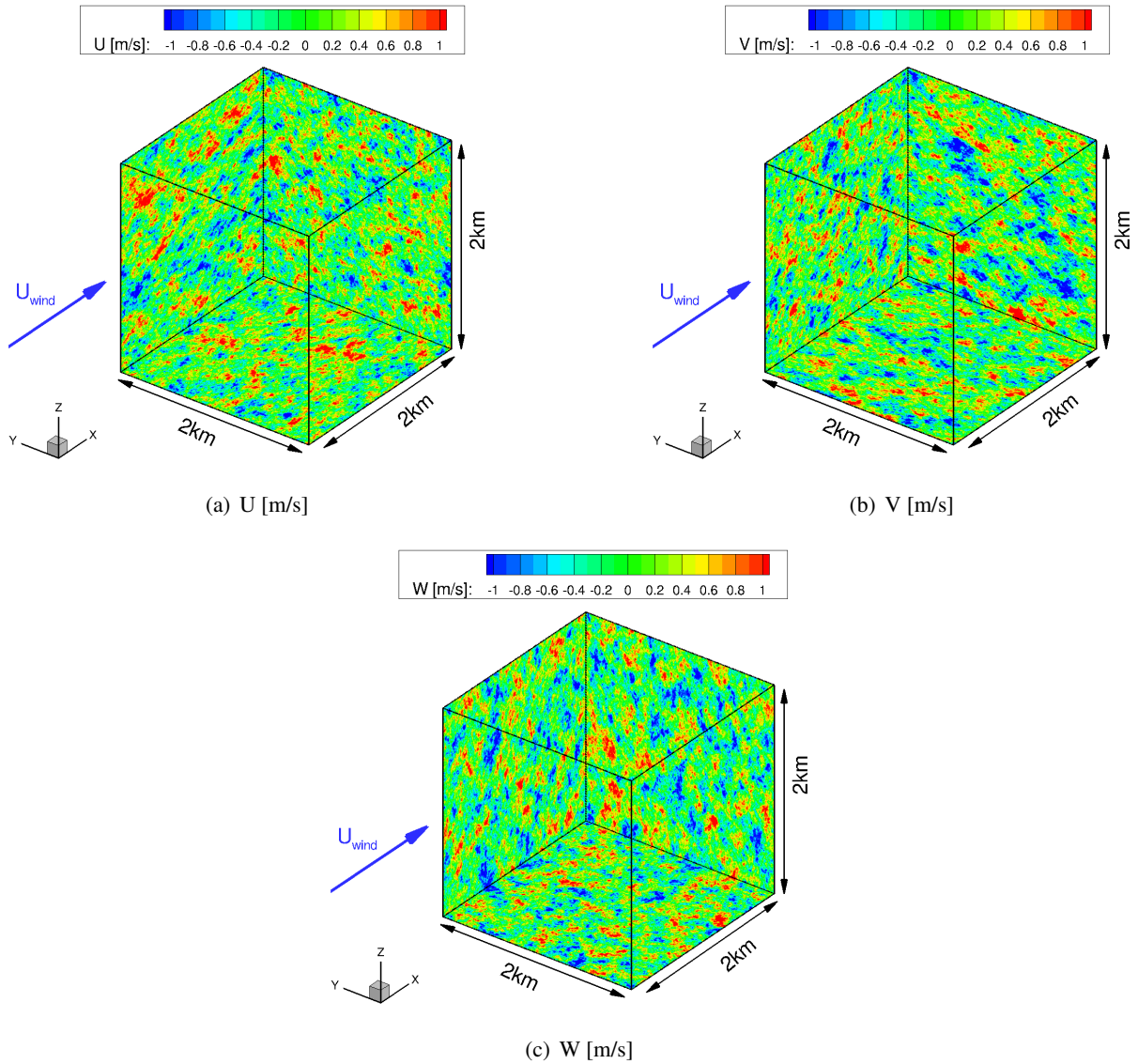


Figure 9.29: The Mann turbulence field obtained with parameters from Table 9.6.

towards the CFD domain, as shown in Figure 9.30(a). Note that the generated turbulence field is periodic due to mathematical construction of the model. This allows to place the same Mann box at the inflow after the previous box was entirely convected to the CFD domain. In practice, this is achieved by applying interpolated inflow boundaries from the start (the one used at time $t = 0$ s). Note that the time resolution during URANS computations is likely to be finer than the Mann box resolution i.e. $\Delta t_{CFD} < \Delta t_{Mann} = \Delta x / U_{hub}$. In this case, the linear interpolation between two inflow planes is employed in the HMB3 solver. The atmospheric boundary inflow profile was included in the computations by superimposing the power-law profile with the Mann's turbulent fluctuations. Note that the CFD domain was placed in the middle of the Mann

box "outflow" plane. This is because the generated turbulence was assumed isotropic by setting $\Gamma = 0$. In another case, the inflow to the computational domain should be placed at the bottom of the Mann box.

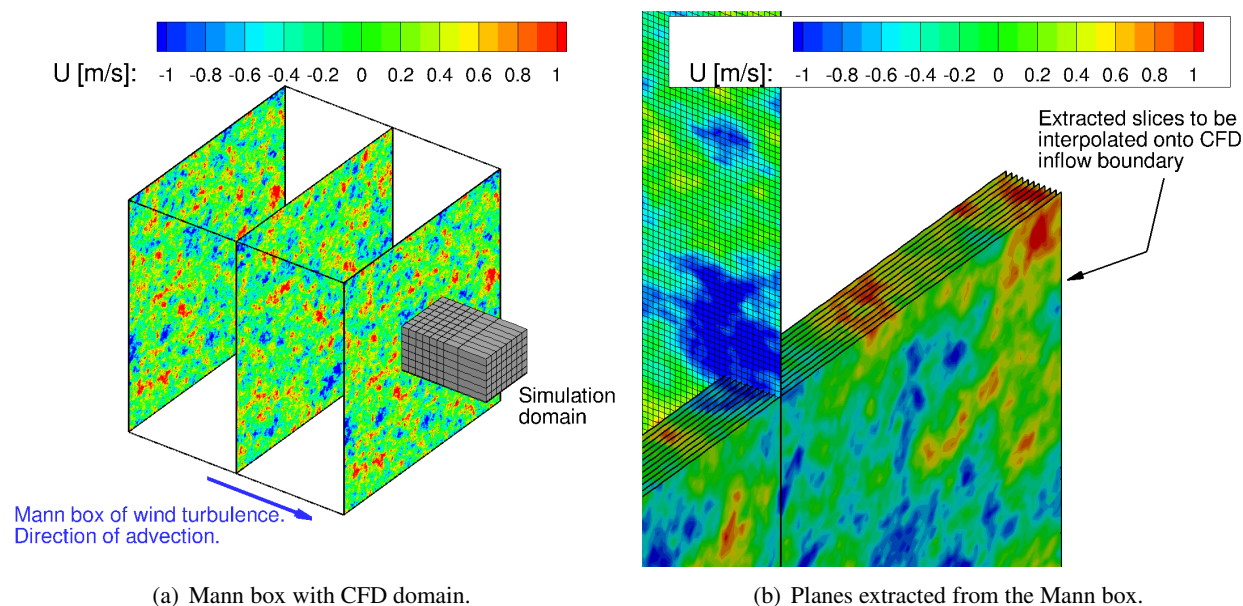


Figure 9.30: The Mann box turbulence field with extracted planes used to interpolate onto the HMB3 inflow plane.

9.5.3 Computational grids and parameters

Two grids were employed in this section, as shown in Figure 9.31. The first grid (G1) was used for the computation with the atmospheric boundary profile, and adopted the sliding plane approach^[193]. The second grid (G2) was employed for the computation with the atmospheric boundary profile and turbulence (based on Mann's model). Grid resolution tests were performed on the Cartesian grids to find the best approach for preserving Mann's turbulence in the CFD domain. The results are presented in Appendix C. Based on this experience, the mesh over-set method^[81] was used for the latter grid.

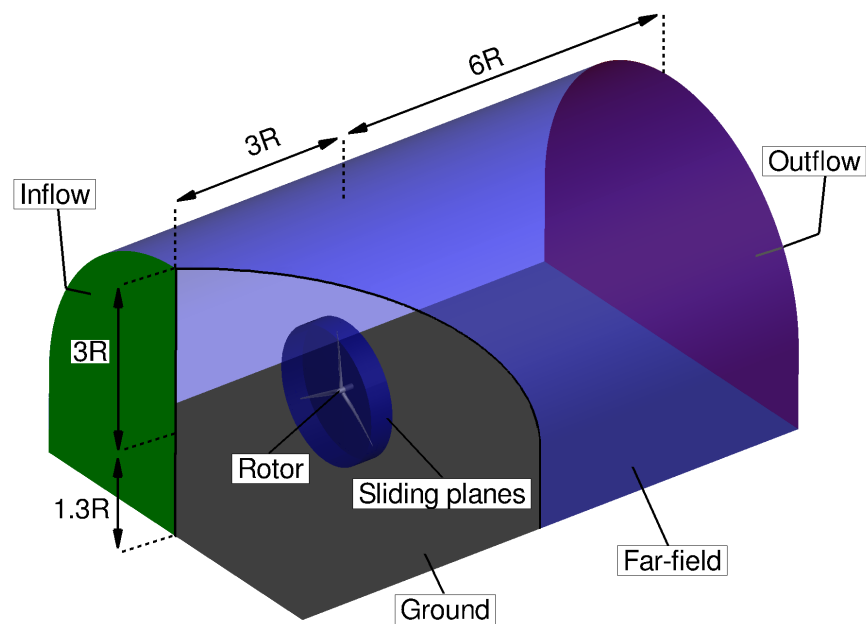
The DTU 10-WM RWT rotor with pre-bend and pre-cone was employed for both cases. The synthetic inflow boundary condition was placed three blade radii upstream of the rotor, and the outflow was placed six blade radii downstream. The far-field was assigned three blade radii from the centre of rotation. The details of those grids are provided in Table 9.7, and the computational domains with the corresponding boundaries are shown in Figure 9.31.

Table 9.7: Details of computational grids employed in this section.

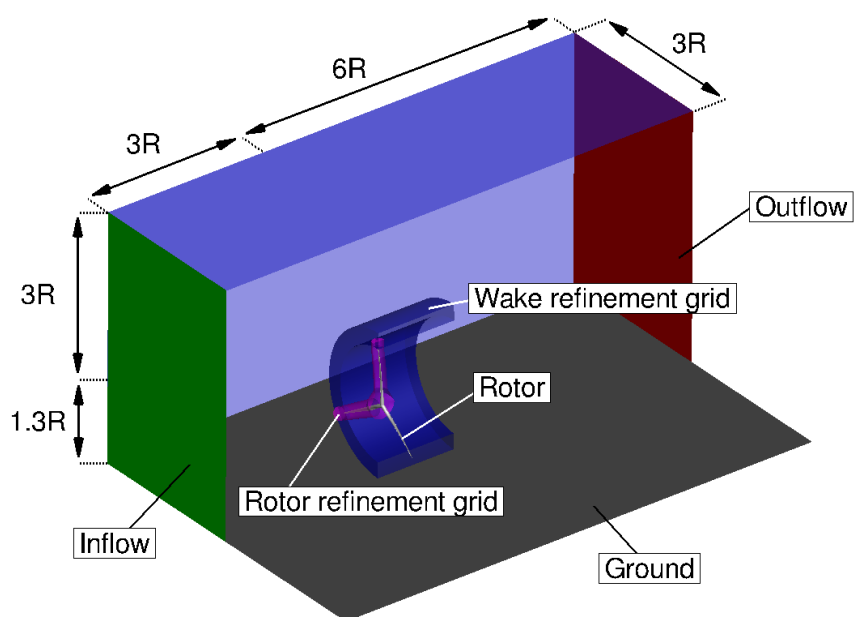
Grid ID	Test case	Number of cells	Number of blocks	Grid assembling
G1	Atmospheric boundary profile	17.3M	2780	Sliding planes
G2	Atmospheric boundary profile and turbulence	27.3M	1468	Over-set method

The DTU 10MW RWT rotor was modelled without the tower. The nacelle was included in the grid G1, but for the second grid the root was extended, such that the blades merged to the rotor without the nacelle, as shown in Figure 9.32(d). Also, note that there was a gap between the blade and the hub for the first grid, as shown in Figure 9.32(c). Apart from those differences, the mesh around the blades was kept as close as possible for both grids. Slices through the volume close to the blade surface are compared in Figures 9.32(a) and 9.32(b). For both grids the normal distance for the first cells of the blocks adjacent to the blade surface was $5 \cdot 10^{-6}c$, where c is the maximum chord of the blade, $6.206m$. Based on the free-stream condition and the size of the first cell, the y^+ parameter was 0.9. The first layer consisted of 40 cells in the normal direction to the blade surface, and 256 cells were distributed around the aerofoil section. The blade surface along the span was resolved with 121 cells for the grid G1, and with 105 cells for the grid G2. The cell spacing next to the ground boundary was set to $10^{-3}c$ for both grids. Note that the second grid had almost twice as many cells as the first grid. This was dictated by the spacial resolution required to better preserve the turbulent structures. The uniform spacing of $4m \times 4m \times 4m$ was employed for most of the background grid in the mesh over-set method used for the second grid. Exception regions were the ground boundary, where the grid was refined, and the outflow boundary, where the grid was coarsened. The comparison of the grids in the middle of the domain is shown in Figure 9.33.

The $k - \omega$ SST turbulence model was used with the grid G1 for the atmospheric boundary profile, and the $k - \omega$ SST-based Scale-Adaptive Simulation (SAS) model^[138] was employed with grid G2 with the atmospheric boundary profile and turbulence. The scale-adaptive model was chosen to resolve the fine turbulent structures present in the generated field of turbulence. The wind speed at the hub was set to $11m/s$ for both cases, and the atmospheric boundary profile was generated using the power-law according to Equation 9.4. Then, the Mann's turbulence field was superimposed on the atmospheric boundary layer for the second case. The rotational speed of the rotor was $8.836rpm$ for both computations.



(a) Grid employed for computation with the atmospheric boundary profile (G1).



(b) Grid employed for computation with the atmospheric boundary profile and Mann's turbulence (G2).

Figure 9.31: Computational grids employed in this section.

9.5.4 Results

The results in terms of thrust and power for each blade are shown in Figures 9.34 and 9.35, respectively. Clear periodicity can be observed in the case of the clean atmospheric boundary layer profile. This is related

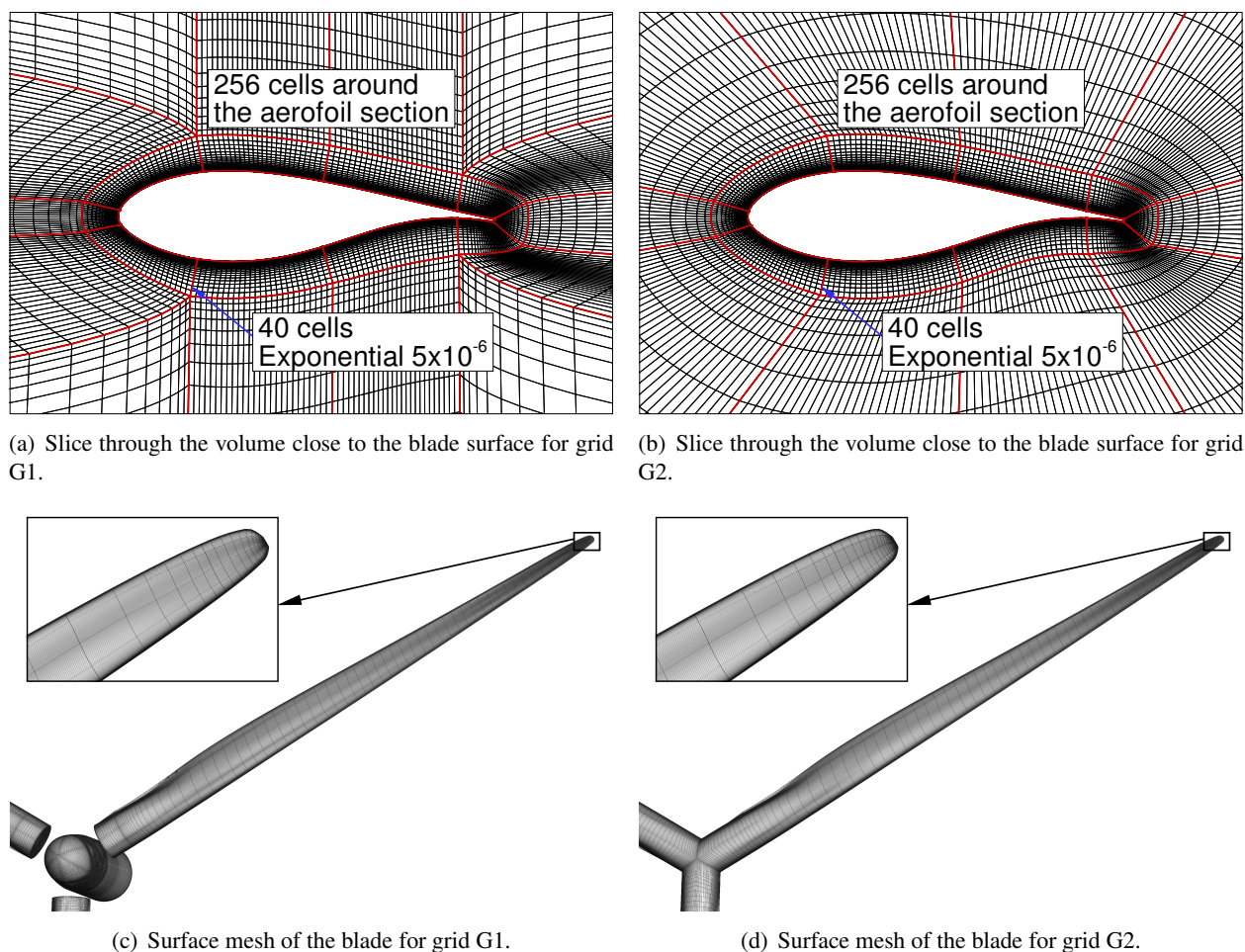
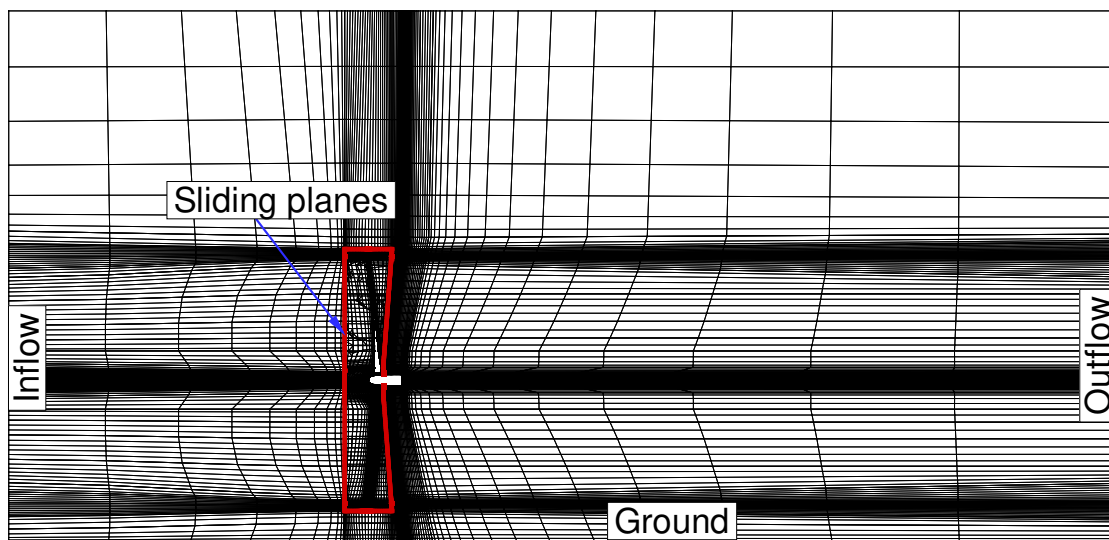


Figure 9.32: Comparison between two employed grids G1 and G2 – (a-b) slice through the rotor grid, (b-c) rotor surface mesh.

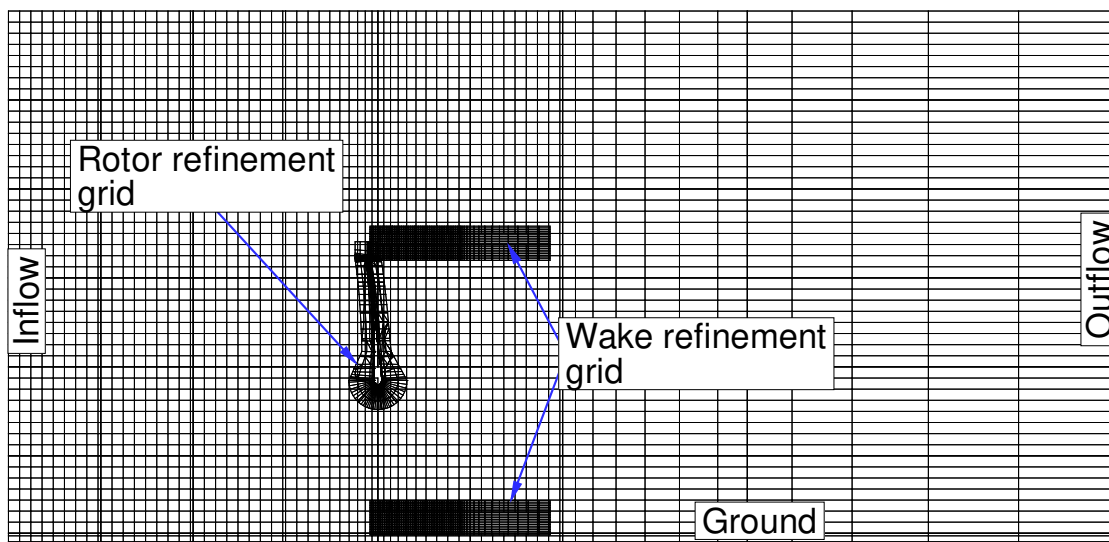
to the blade passing through the low wind speed region closer to the ground, and then through the high wind speed region away from it. Note that the blade number 1 was pointing to 12 o'clock at the beginning of each revolution, and 6 o'clock at half revolution. A phase shift between results for each blade is also visible, and corresponds to the off-set of $1/3$ of revolution, or 120° of azimuth angle.

The results for the atmospheric boundary layer and for the turbulent case show, on average, similar thrust and power for the individual blades. Fluctuations due to the field of turbulence are clearly visible. Those, however, are smaller in magnitude than the fluctuations caused by the blade passing through the low and high wind speed regions. Hence, one per revolution variation of thrust and power are also evident for the case of the atmospheric boundary layer with Mann's turbulence.

Figure 9.36 shows Fast Fourier Transforms (FFTs) of the individual blade thrust and power. The



(a) Slice through the middle of the grid G1.



(b) Slice through the middle of the grid G2.

Figure 9.33: Comparison between employed grids for the atmospheric boundary inflow. Grid points are skipped for clarity (2 for grid G1, and 4 for grid G2).

results for the pure atmospheric boundary profile show a clear peak at the rotational frequency and its multiples. On the other hand, the results for atmospheric turbulence show larger frequency content, where some of the peaks do not coincide with multiples of rotational frequency. However, the largest peak in this case can be seen to correspond to the frequency of rotation.

By adding the contribution from each blade, the total thrust and power were obtained, as shown in Figure 9.37. First, the atmospheric boundary inflow resulted in lower variations of the loads. This is caused

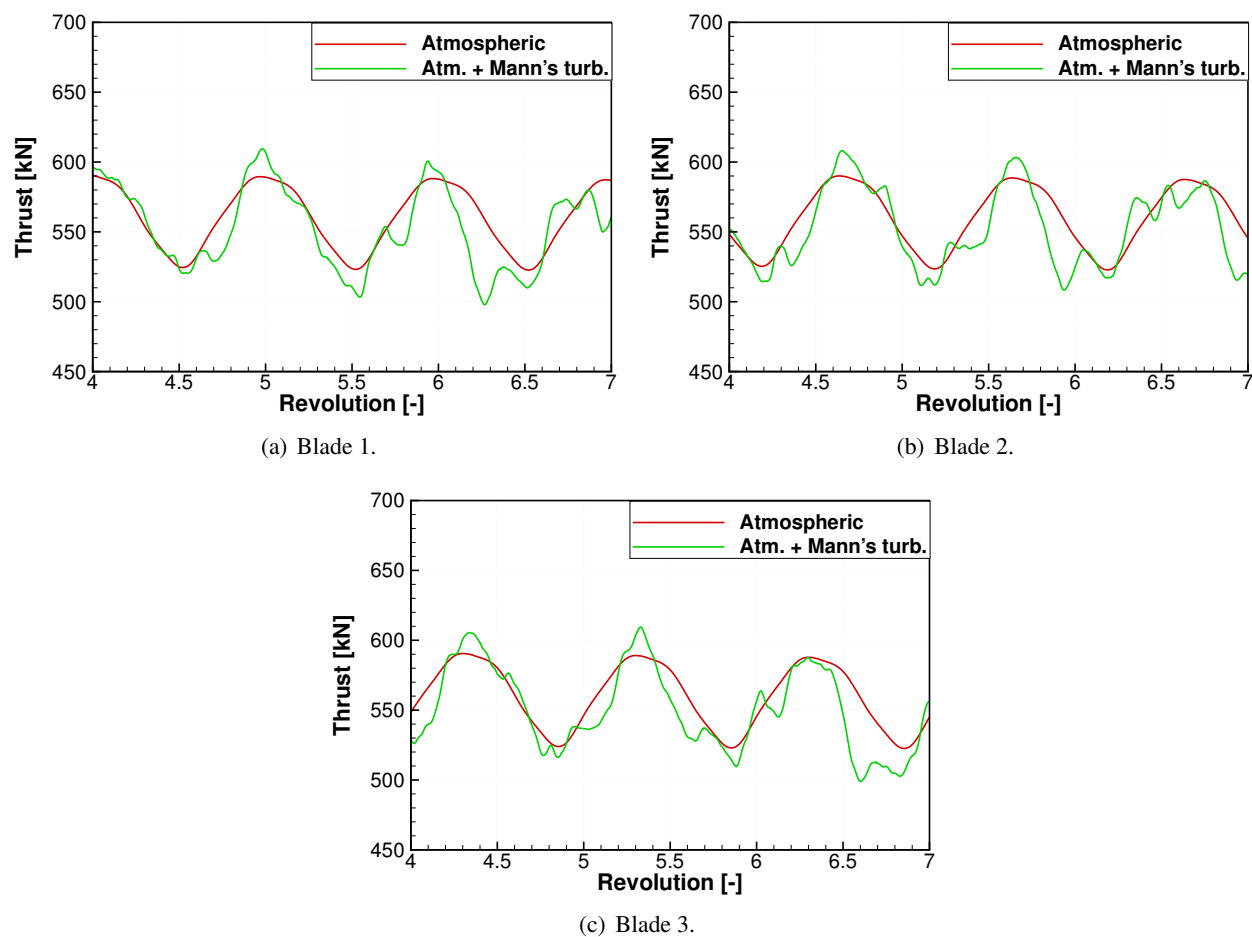


Figure 9.34: Thrust as function of revolution shown for each blade.

by the phase shift in the loads between each blade, and the fact that the variation is very regular. In other words, when one blade is moving from the higher wind speed region to the lower wind speed region, other blades are moving in the opposite direction. For the atmospheric boundary with turbulence, the variation of the loads is considerably increased. This is caused by a rich frequency content in the individual blade loads. In this case, the superposition of loads reduced the total variation, as can be seen by comparing amplitudes of the FFT plots in Figures 9.36 and 9.38. However, the reduction is not as pronounced as for the atmospheric boundary profile only. Finally, the increase of the average loads can be seen for the atmospheric boundary profile, as compared to the uniform inflow case, in contrast to Li *et al.* ^[121], where the reduction was observed. However, several differences in the set-up of test cases should be noted between the present work and the work of Li *et al.* First, the logarithmic law profile was used in ^[121], whereas the power law profile was adopted here. Next, the incompressible solver was used in aforementioned publication,

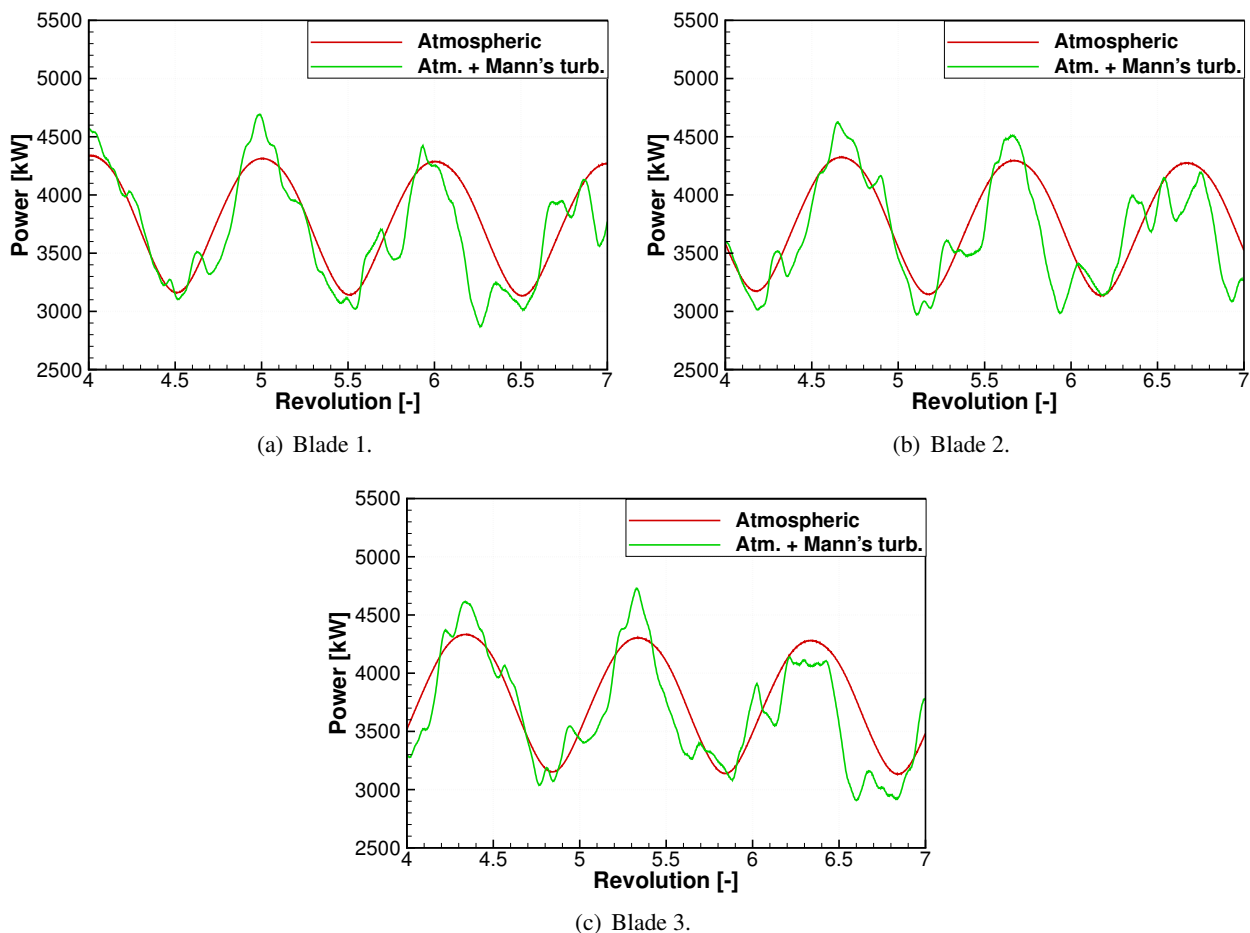


Figure 9.35: Power as function of revolution shown for each blade.

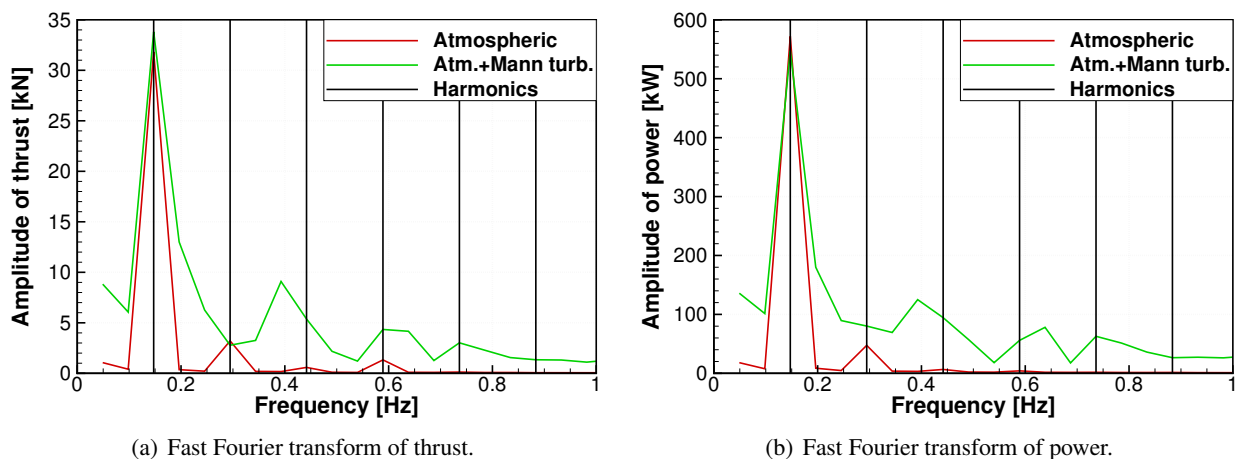


Figure 9.36: Fast Fourier transforms of the thrust and power time series for the blade number 1. The harmonics correspond to multiples of the blade-passing frequency $f_n = n \cdot f_1$, where $f_1 = 0.147Hz$.

and the compressible solver was used in this work. Further, a delayed detached eddy simulation (DDES)

model^[67, 120] was employed in ^[121] to model the turbulence, whereas the $k - \omega$ SST turbulence model^[137] was used in the present work. Also, the comparison between the uniform inflow and the atmospheric profile cases was conducted for below rated conditions in Li *et al.* ($8m/s$ wind speed, $11.4m/s$ rated wind speed), and conditions close to rated were employed in this work ($11m/s$ wind speed, $11.4m/s$ rated wind speed). Other differences include the tower (considered in ^[121] and not included here), and the wind turbine itself ($5MW$ in ^[121] and $10MW$ here). Perhaps one of the above, or combination of them, may explain the differences, but further investigation would be required and is out of scope of this work.

The reduction of average loads can be seen in Figure 9.37 for the atmospheric boundary inflow with turbulence. The results suggest an average thrust of $1628.8kN$ and an average power of $10546.8kW$, which correspond to relative reduction of 1.5% and 2.8% , respectively, with respect to the uniform inflow case.

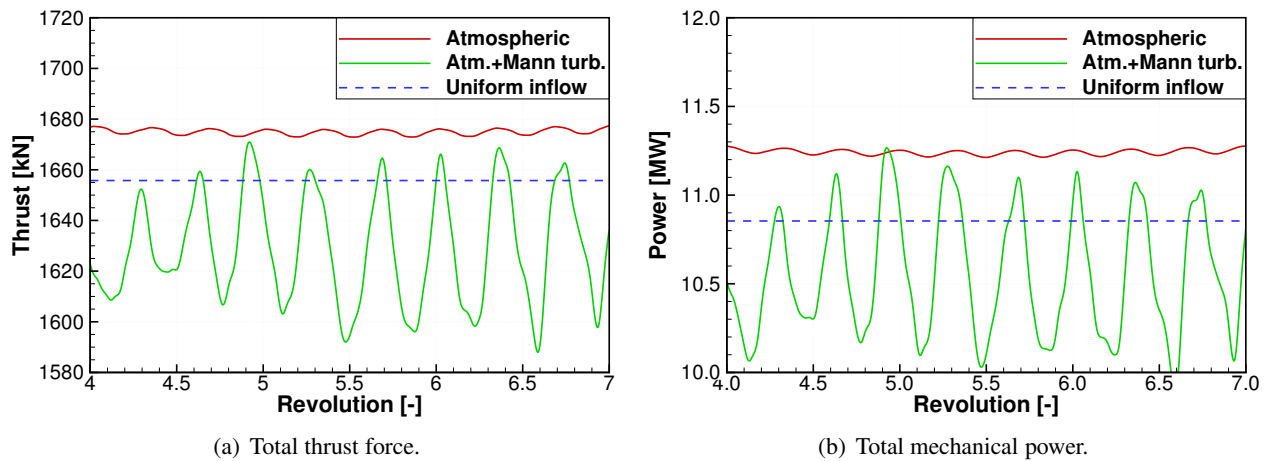


Figure 9.37: Thrust force and mechanical power as function of revolution. Comparison between the cases of atmospheric inflow with and without the turbulence, and uniform inflow of $11m/s$.

The vortical structures visualised with an iso-surface of $Q = 0.01$ are shown in Figure 9.39. Note that for the case with turbulence, the iso-surface of $Q = 0.01$ was used only in the wake refinement mesh to better visualise wake instabilities, while for the rest of the domain, the iso-surface of $Q = 0.001$ was used to expose turbulent structures. Contours shown in Figure 9.39 represent the non-dimensional axial velocity.

The case without wind turbulence had strong tip and root vortices. The tip vortices were following a spiral path, where the vortices located at the high wind speed region were convected faster, as compared to vortices in the low wind speed region close to the ground. Notice that the tip vortices could not be resolved too far downstream for the grid G1 (around 1 rotor radius). Even for the second grid tip vortices resolution

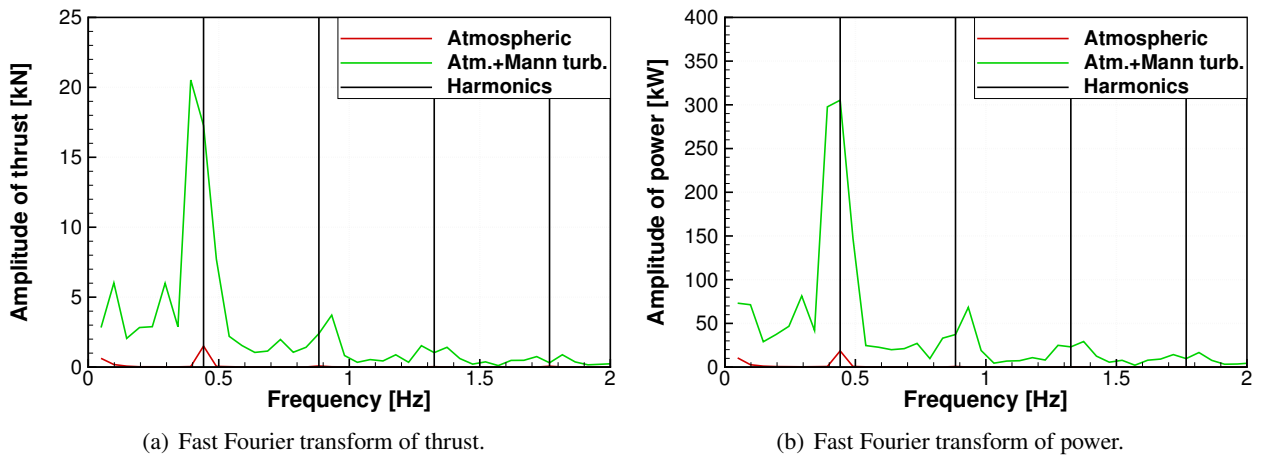


Figure 9.38: Fast Fourier transforms of the total thrust and power. The harmonics correspond to multiples of the blade-passing frequency $f_n = n \cdot f_1$, where $f_1 = 0.441\text{Hz}$.

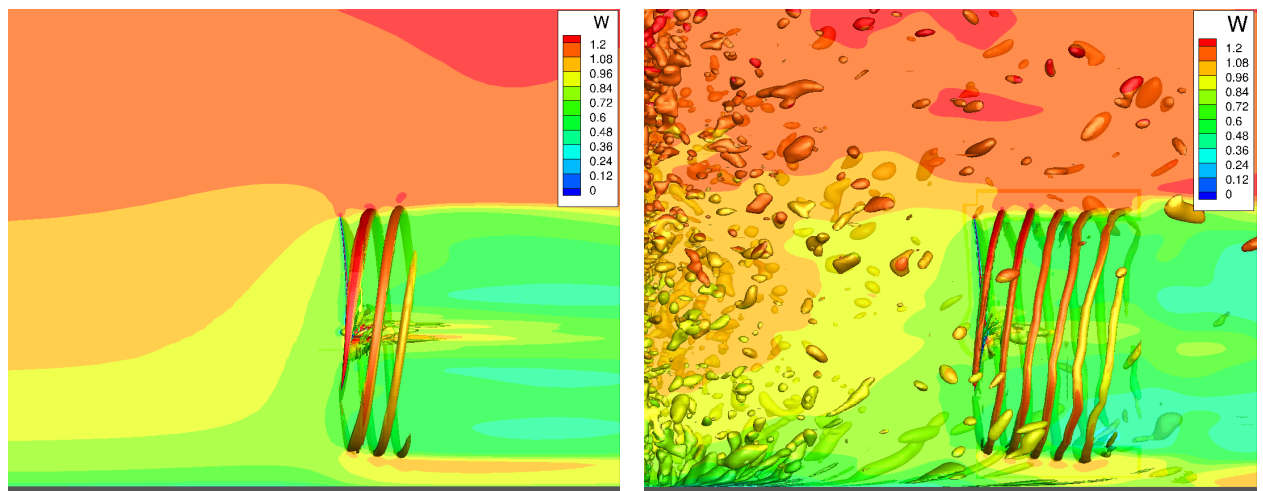


Figure 9.39: Vortical structures represented by iso-surface of Q criterion for cases with and without wind turbulence. Contours of non-dimensional axial velocity W are shown in the middle of domain.

was not possible beyond the region covered by the wake refinement grid.

In the case with turbulence, vortical structures are present in the domain due to imposed atmospheric turbulence. Since the turbulence is introduced as a boundary condition, the decay of turbulence in time can be observed in Figure 9.39(b). This is to be expected in a viscous computation, and has been observed even for inviscid flow due to numerical dissipation, as detailed in Appendix C. A possible remedy is to employ a turbulence scaling factor^[121] in the Mann model, which multiplies (up-scales) all velocity fluctuations.

However, this was not attempted in this work. The development of anisotropic turbulence due to shear can be observed close to the ground surface. The vortical structures there are rather thin and stretched, which agrees with observations made in ^[121].

The turbulent structures present in the domain interact with the rotor, in particular with the tip vortices. Growing instabilities can be observed in the wake, and should lead to a breakdown closer to the rotor, as compared to the case without turbulence. This, however, cannot be concluded from computed cases. The obtained results suggest, that the part of the wake close to the ground surface (in the low wind speed region) is affected more by the turbulent structures. The tip vortices in the high wind speed region are also influenced by the turbulence, but to a lesser extent.

Chapter 10

Elastic computations for DTU 10-MW RWT

This chapter completes the aerodynamic analysis of the DTU 10-MW RWT. It presents results of static and dynamic aero-elastic computations. First, the structural model is described and the results of the elastic eigenvalue analysis are compared to the results of Bak *et al.* ^[11] and Horcas *et al.* ^[77], showing good agreement, especially for the flap-wise modes. Next, static aero-elastic computations are performed for the straight blade, and for the blade with pre-bend and pre-cone. This is followed by the unsteady aero-elastic computations for the DTU 10MW RWT rotor with pre-cone and pre-bend, and the results are compared to the static case. Finally, the complete wind turbine is studied assuming rigid and elastic blades.

10.1 Elastic eigenvalue analysis

The natural frequencies of the DTU 10-MW RWT blade were obtained by employing a similar procedure as Wilkie *et al.* ^[211] for helicopter rotors. The structure of the blade was represented using 50 beam elements. These elements were tapered, non-linear beams using *PBEAM* in *NASTRAN*^[6]. The shear and elastic axes offsets from the centre of the beam were included in the model, where the axis of the beam is defined in ^[11] as the half-cord point of each blade section. At each beam section, rigid bars (*RBAR* elements) without any structural properties were rigidly linked to the beam. The bar elements originate from the centre of the beam towards the leading edge and towards the trailing edge of the blade to assess the displacement of the blade surface. This is shown in Figure 10.1 for the blade with pre-bend and pre-cone. The definitions of

pre-bending and pre-coning are provided in Section 9.1 of Chapter 9. Note that beams and bars create a surface, split into triangular elements as needed for the constant volume tetrahedron (CVT) method, that is used for structure-to-fluid mapping. Details of the employed grid deformation, and aero-elastic methods are presented in Section 3.6.2 of Chapter 3. Since the *PBEAM* element can only represent an isotropic material, the elastic properties of each beam were set to match the flap-wise elastic properties of Bak *et al.* [11]. Figure 10.2 presents the Young's modulus, the shear modulus and the torsional stiffness employed in the *NASTRAN* model. Two models were created – for the straight blade, and for the blade with pre-cone and pre-bend. The *NASTRAN* input files can be found in Appendix A.

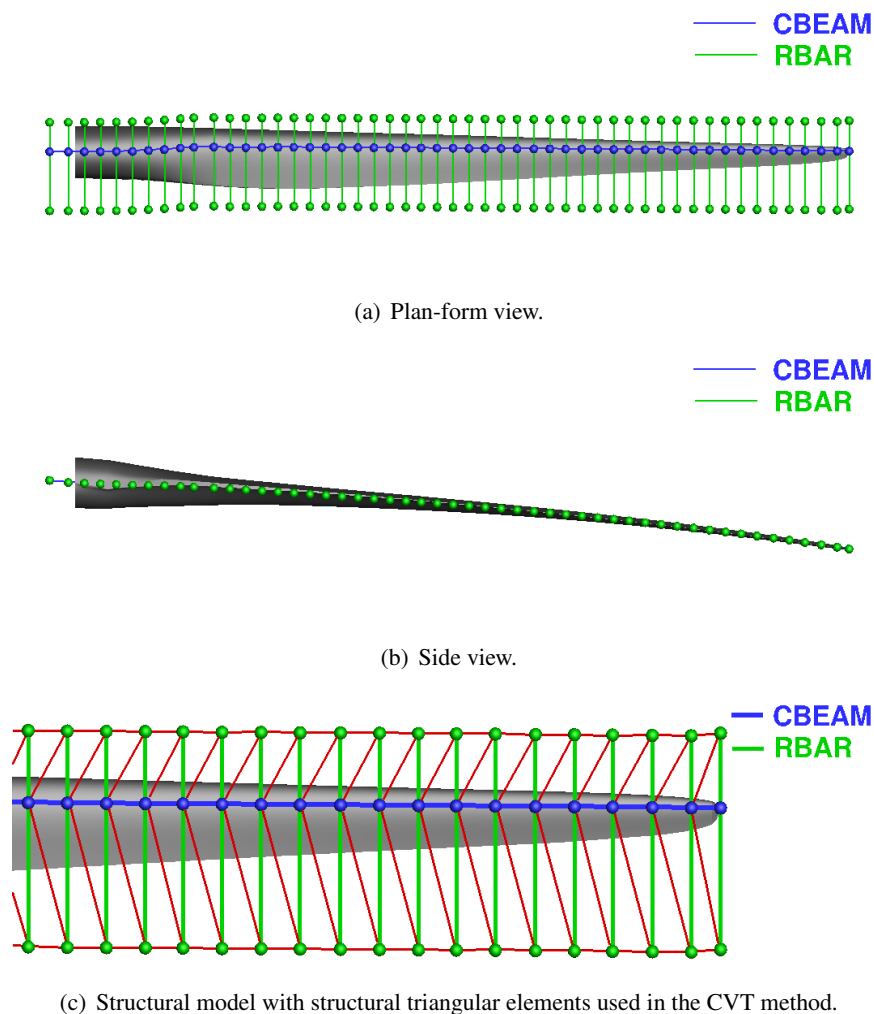


Figure 10.1: The DTU 10MW RWT blade surface with the structural model consisting of beams and bars.

The model frequencies and shapes were obtained by a non-linear static calculation in *NASTRAN* by using the *SOL106* sequence^[6]. The modes were then visualised and identified. Table 10.1 compares

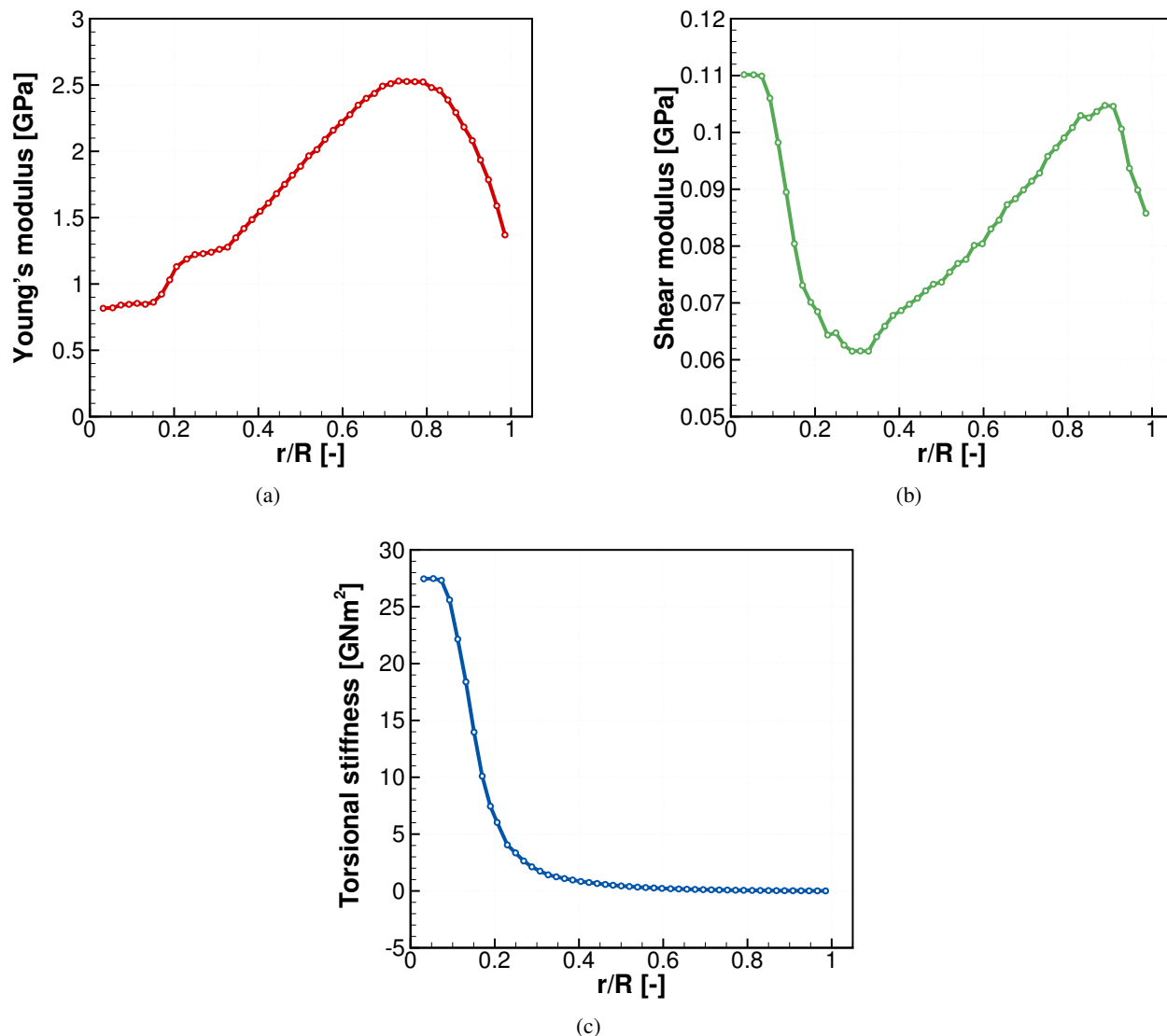


Figure 10.2: DTU 10-MW RWT blade properties along span-wise direction employed in the NASTRAN model.

the natural frequencies for the isolated blade calculated with the present *NASTRAN* model and the values presented in Bak ^[11] and Horcas ^[77]. A very good agreement between the first three flap-wise modes is seen. The differences in the frequency of the edge-wise modes stem from the assumption of material isotropy. Note that the present *NASTRAN* model did not capture the 1st torsional mode reported in ^[11], nor the mixed flap-wise/torsional mode reported in ^[77]. These differences may stem from the fact that for a modal analysis the shell-based Finite Element Method (FEM) was used by Horcas^[77]. On the other hand, anisotropic beams were employed by Bak^[11], in contrast to isotropic beams used in this work. However, only the 1st flap-wise and 1st edge-wise modes are pure, and other modes have some torsional component.

Table 10.1: Comparison between natural frequencies for the isolated blade obtained with NASTRAN and results of Bak^[11] and Horcas^[77].

Present NASTRAN model			Bak ^[11]	Horcas ^[77]
Configuration	Straight blade	Blade with pre-cone and pre-bend	Straight blade	Straight blade
Mode	Natural Frequency [Hz]			
1st flap	0.61	0.61	0.61	0.64
1st edge	1.03	1.03	0.93	0.97
2nd flap	1.74	1.73	1.74	1.79
2nd edge	3.13	3.11	2.76	2.89
3rd flap	3.57	3.55	3.57	3.61
1st torsion	-	-	5.69	5.72
Mixed flap/torsion	-	-	-	5.77
4th flap	5.99	5.98	6.11	6.18
3rd edge	6.48	6.43	6.66	-

Figure 10.4 visualises the first four modes for the straight blade, and Figure 10.5 visualise modes 5 through 8. The modes for the blade with pre-cone and pre-bend are shown in Figures 10.6 and 10.7.

A Campbell diagram (Figure 10.3) was created for the first seven modes showing the natural frequencies of the selected modes as function of the rotational velocity. The rotational speed varied from 0 to 18rpm, which is almost twice the highest designed rotational speed (9.6rpm) the blade is expected to operate at. As can be seen, loads that occur 4 times per revolution and faster, may excite the 1st flapping mode

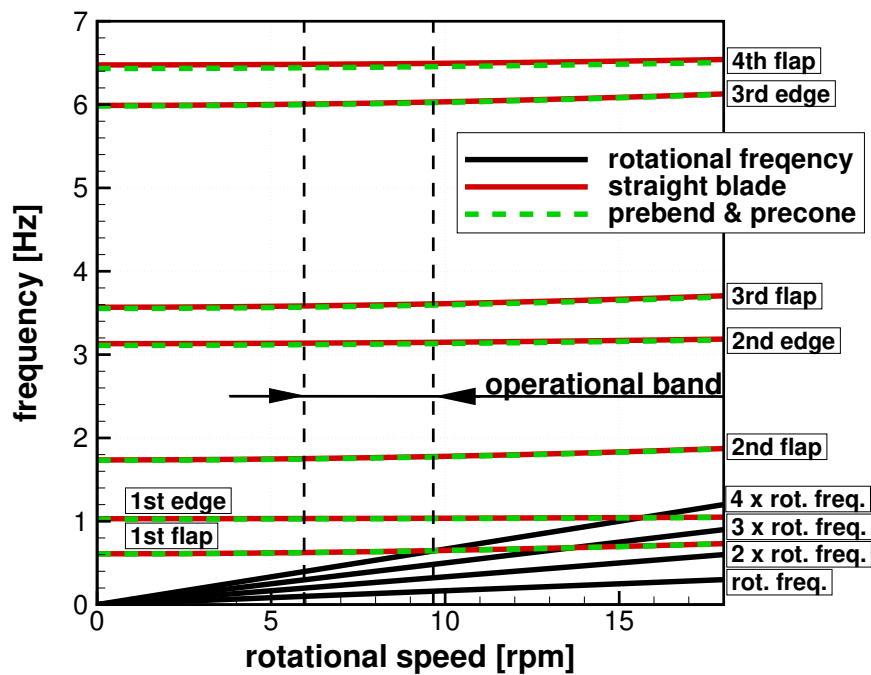


Figure 10.3: Campbell diagram for DTU 10-MW blade.

and possibly other modes in the range of the operating rotational speeds, between $6.0 \leq rpm \leq 9.6$ [11]. Also, the natural frequencies of the modes are very close for both configurations of the blade – straight and pre-bend with pre-cone. The results suggest that the largest difference is 0.64% for the 4th flap-wise mode.

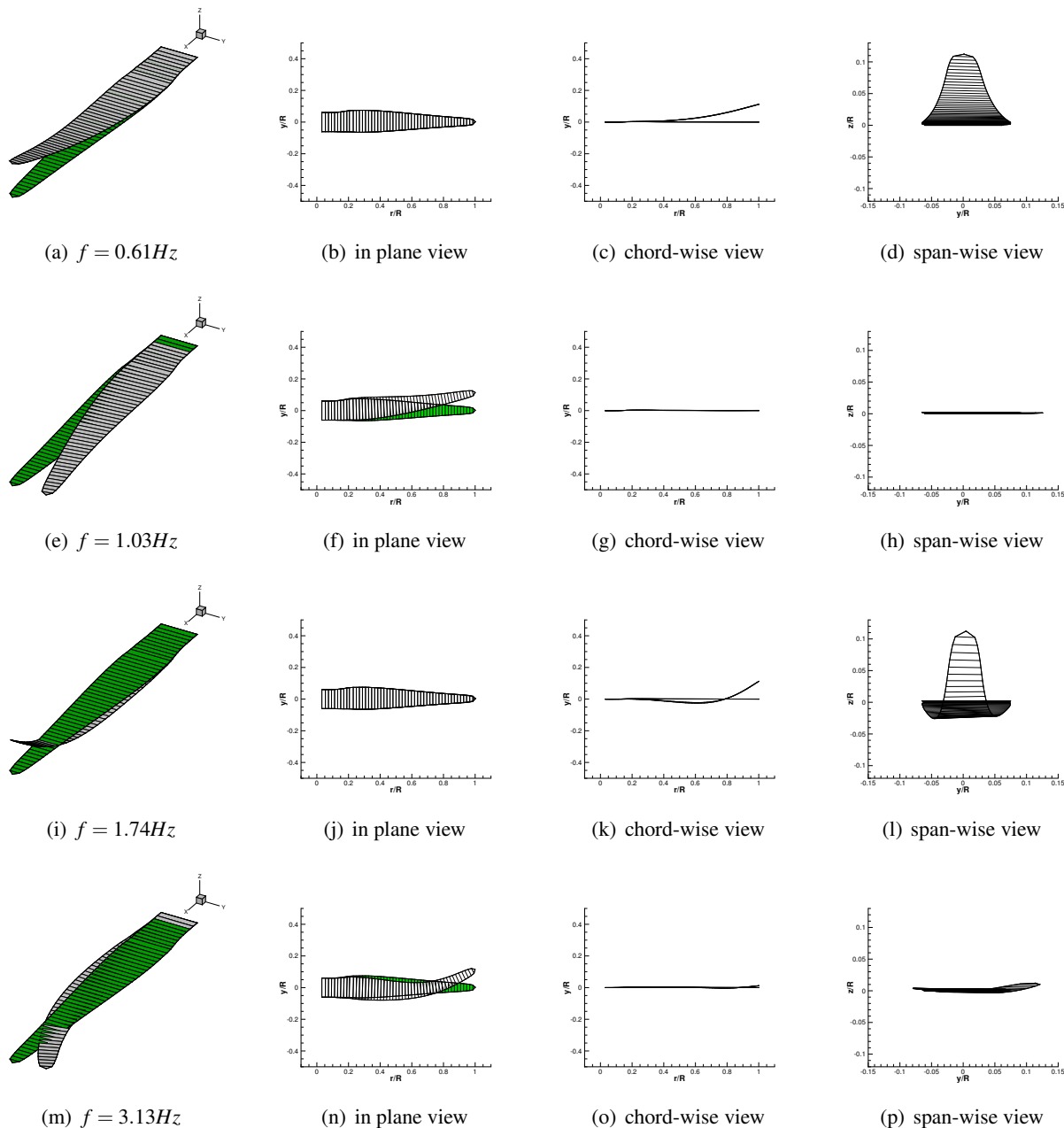


Figure 10.4: Frequencies and corresponding shapes of the first 4 modes for the straight blade.

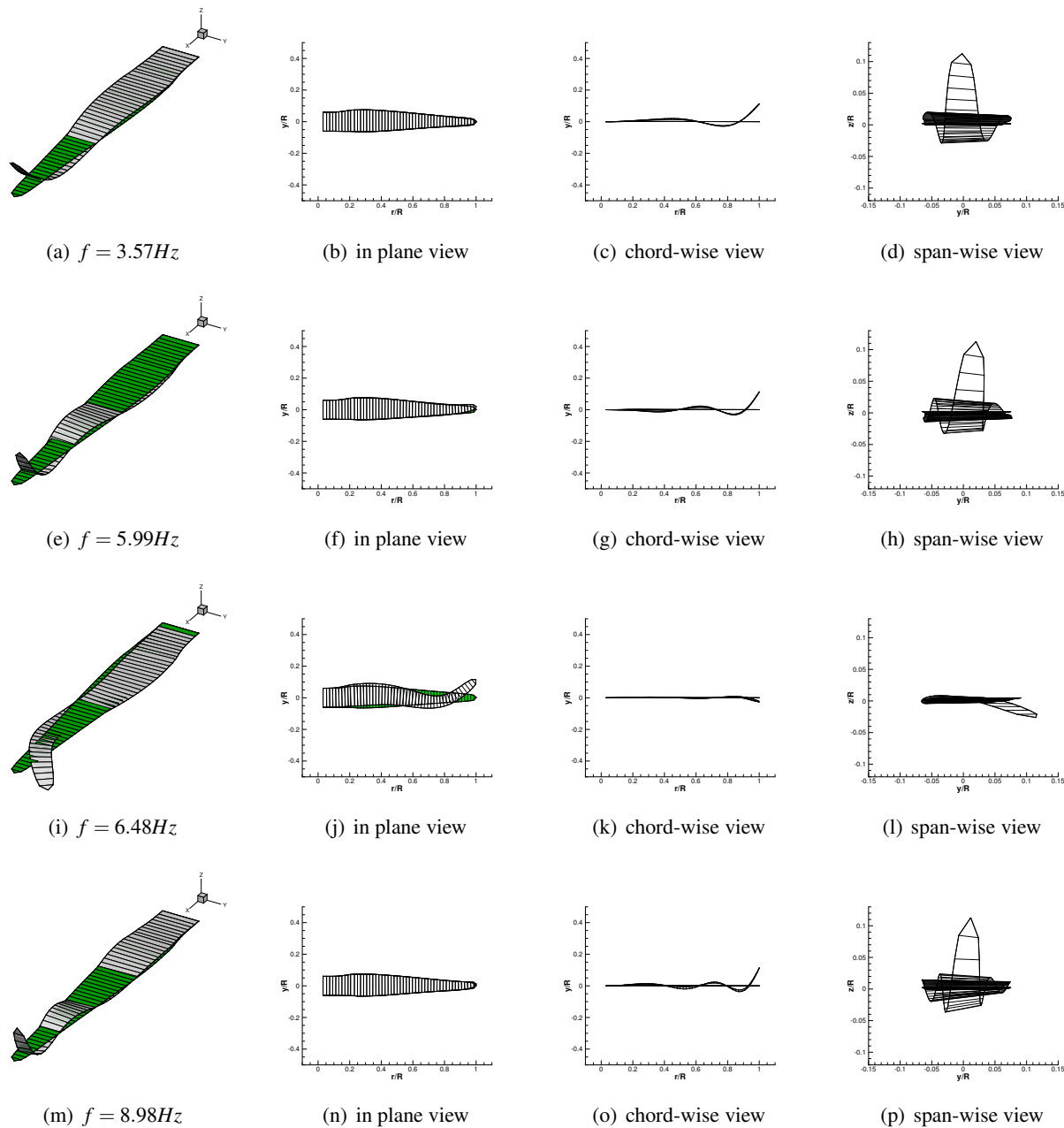


Figure 10.5: Frequencies and corresponding shapes of the modes from 5 through 8 for the straight blade.

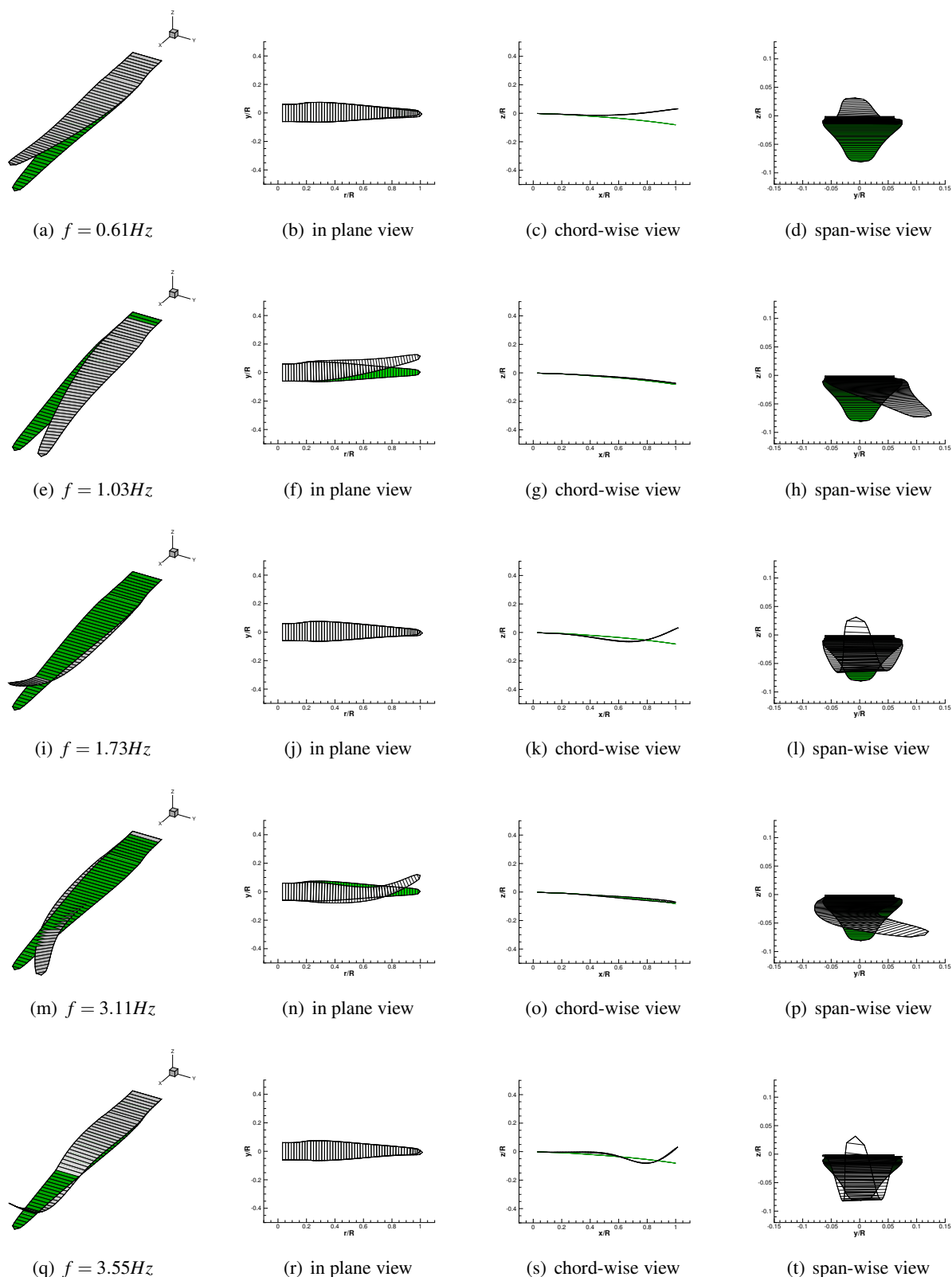


Figure 10.6: Frequencies and corresponding shapes of the first 5 modes for the blade with pre-cone and pre-bend.

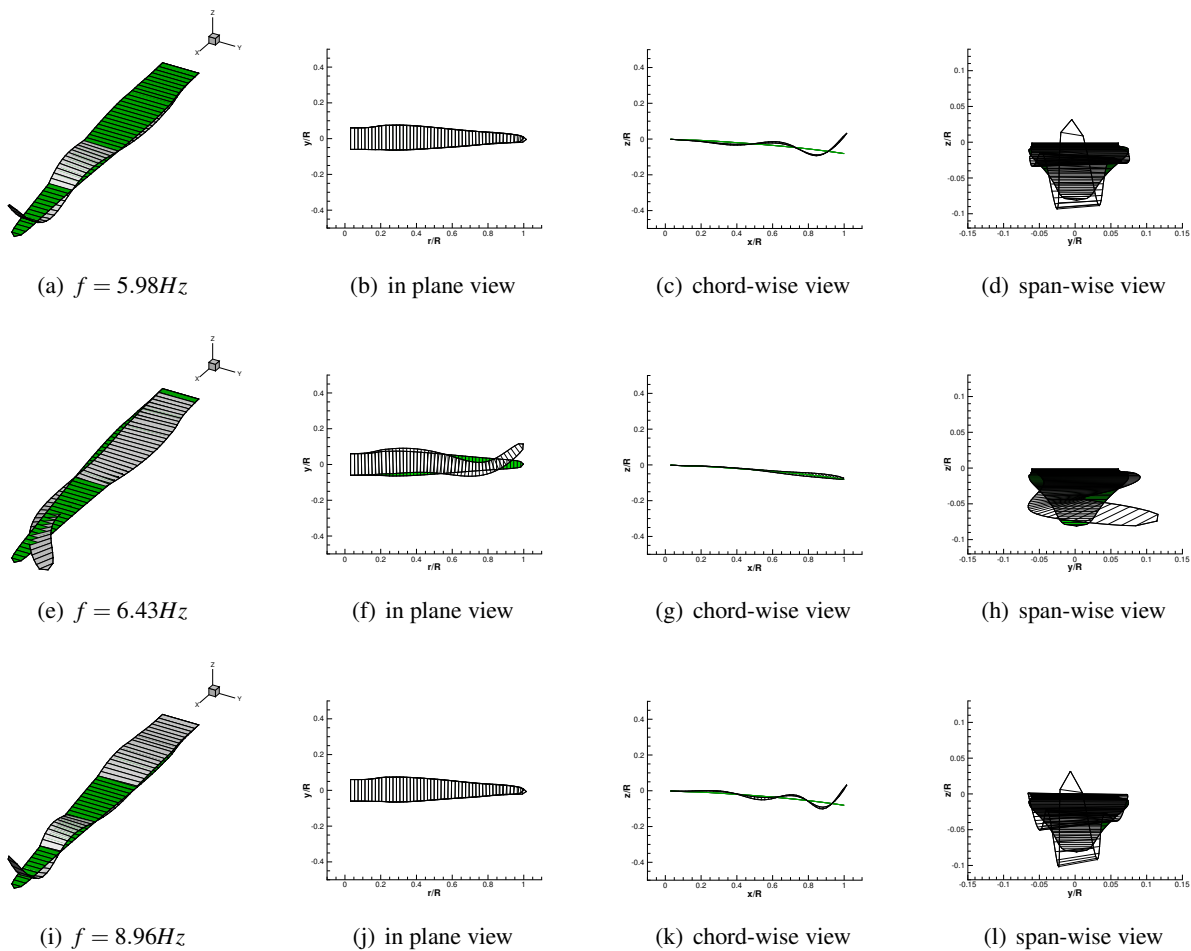
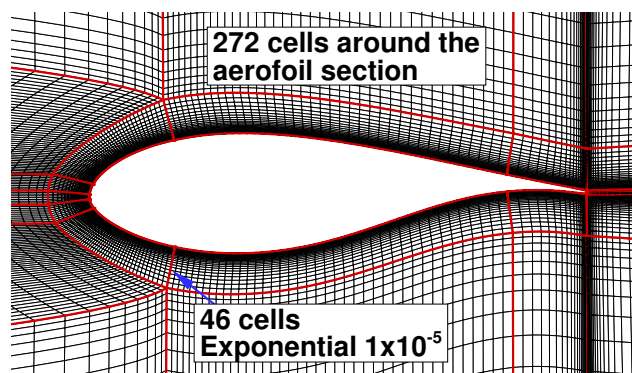


Figure 10.7: Frequencies and corresponding shapes of the modes from 6 through 8 for the blade with pre-cone and pre-bend.

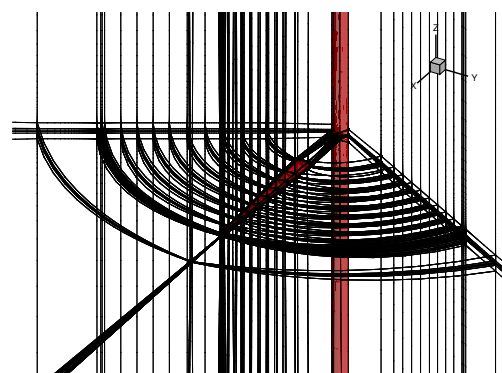
10.2 Static aero-elastic calculations

In this section, the aero-elasticity of the DTU 10MW RWT blade is considered. The static aero-elastic coupling is employed, as explained in Section 3.6.3 of Chapter 3. Two configurations are investigated: the straight blade, and the blade with pre-bend and pre-cone.

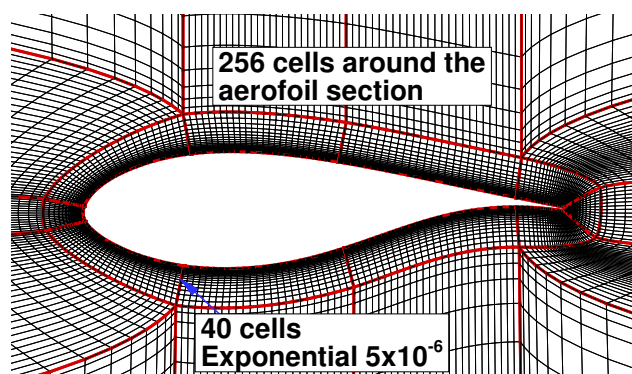
10.2.1 Grids and computational parameters



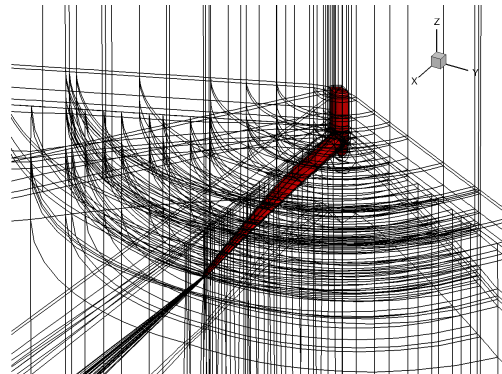
(a) Slice through the mesh around the blade. Grid E1.



(b) Blocking employed for static aero-elastic analysis of the straight blade. Grid E1.



(c) Slice through the mesh around the blade. Grid E2.



(d) Blocking employed for static aero-elastic analysis of the blade with pre-bend and pre-cone. Grid E2.

Figure 10.8: Details of the grids employed for the static aero-elastic analysis of the DTU 10MW RWT. Mesh close to the blade surface (a, c), and blocking (b, d).

Two grids were employed for the steady aero-elastic computations of the DTU 10MW RWT. The first grid (E1) was used for the straight blade, and incorporated the same domain as was used as for the rigid cases in Section 9.4.1. To allow for large block deformations, the domain was split into 444 blocks as shown in Figure 10.8, and the final size of the grid was 8.7M cells. The second grid (E2) was employed for

the blade with pre-bend and pre-cone, the same as in Section 9.4.2. The nacelle was included, using sliding planes, and was rigidly attached to the rotor. The grid was split into 802 blocks, and its total size was 5.4M cells. The details of employed grids are provided in Table 10.2. The slices through the volume close to the blade surface for both grids are shown in Figure 10.8. Note that a reduced spacing at the wall was used for the blade with pre-bend and pre-cone. For both cases, the inflow wind speed was set to 11m/s, the rotational speed of the rotor was 8.836rpm, and the $k - \omega$ SST turbulence model^[137] was employed. The input files for the *NASTRAN*, as used in this chapter, are provided in Appendix A.

Table 10.2: Computational grids employed for static aero-elastic analysis.

Grid ID	Blade configuration	Number of cells	Number of blocks
E1	Straight	8.7M	444
E2	Pre-bend and pre-cone	5.4M	802

The iterative process was used to achieve strong aero-elastic coupling, as explained in Section 3.6.3 of Chapter 3. This can be briefly summarised as follows. The loading is first extracted from the fluid grid, using a sectional pressure integration. The non-linear solution sequence of *NASTRAN* is then used to compute the deformed shape of the blade, with the loads introduced as *PLOAD* elements (linear variation of loading between both ends of the element). This new shape is then applied to the fluid grid. For this, the Constant-Volume Tetrahedron (CVT) method is used to interpolate the deformed shape of the blade surface. Then, the block vertices are moved according to the spring analogy method. Finally, the full mesh is regenerated with the Trans-Finite Interpolation (TFI) method. A new flow solution is obtained on the deformed grid, and loads are extracted. This iterative process is repeated until a load convergence is reached.

10.2.2 Results for the straight blade

The convergence history of the loads of the static aero-elastic calculations for the straight blade are shown in Figure 10.9, where three iterations were performed in total. The final shape of the blade was obtained by applying the aerodynamic loads from the third iteration. This is referred to as the fourth iteration in Figure 10.10, but the flow field solution was not computed after the last grid deformation. Thus, the loads for the fourth iteration are not presented in Figure 10.9.

The results suggest a final displacement at the blade tip of 8.5m in the flap-wise direction, 0.3m in

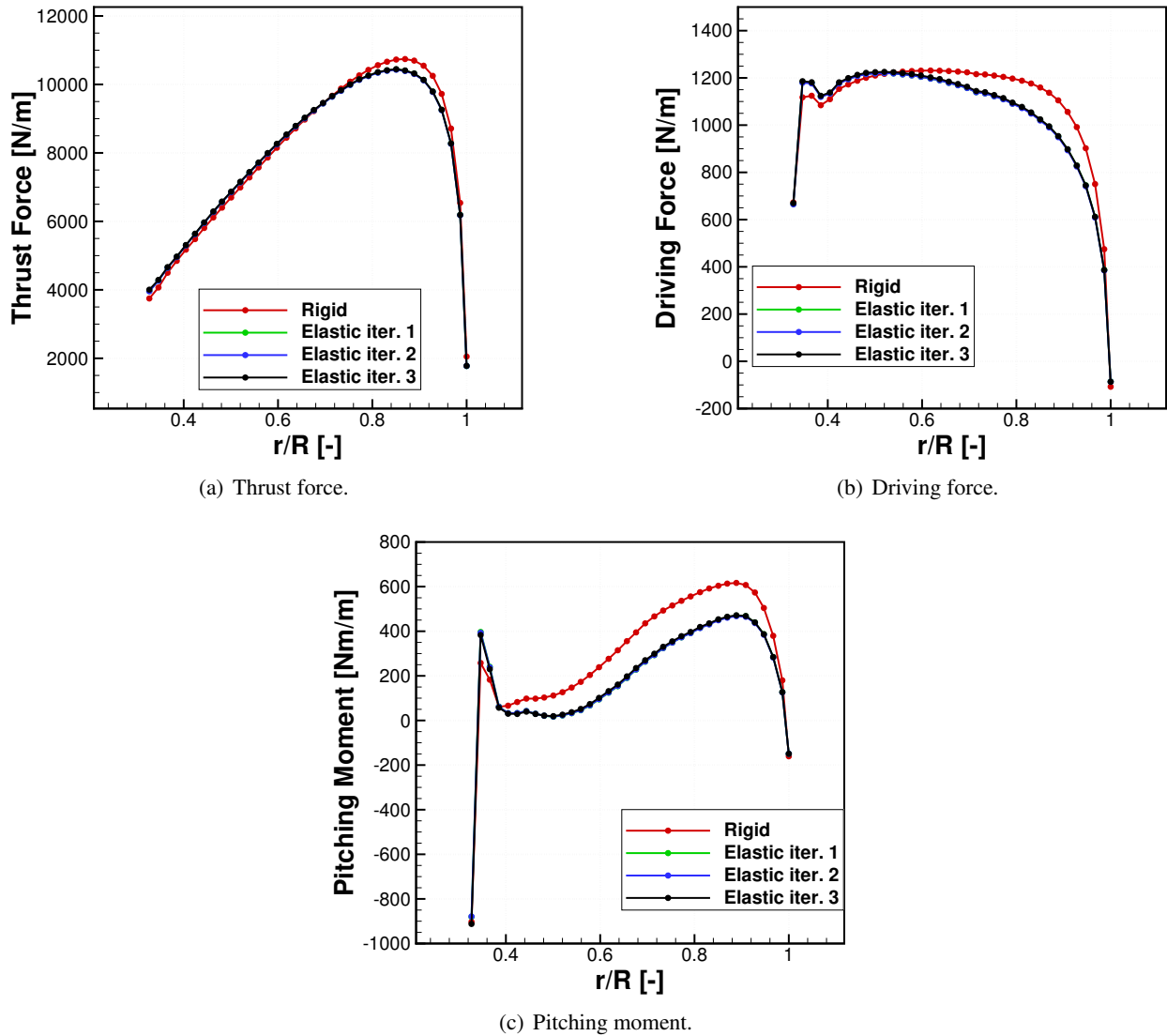
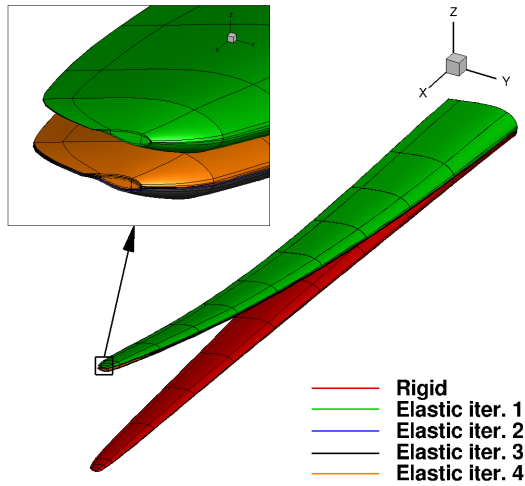
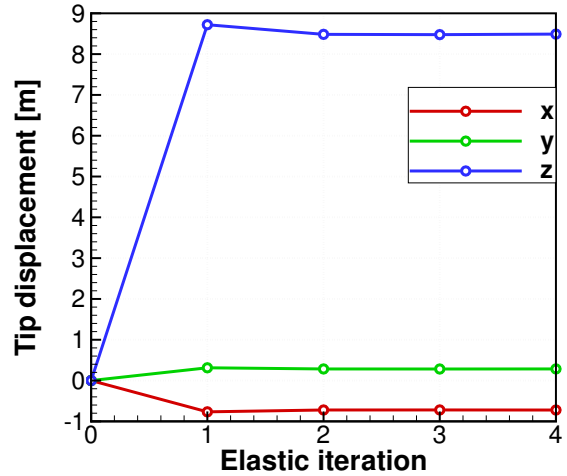


Figure 10.9: Convergence history of the loads for the static aero-elastic computation for straight DTU 10MW RWT blade.

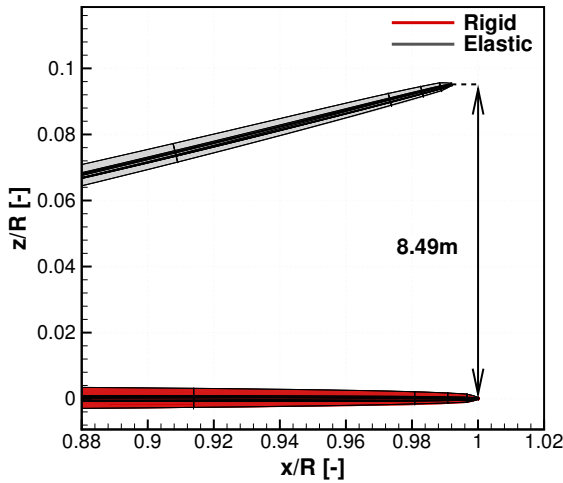
the edge-wise direction, $-0.7m$ in span-wise direction, where negative sign means displacement towards the root. This can be clearly seen in Figure 10.10(c). The tip displacement of $7.8m$ in the flap-wise direction was reported by Horcas *et al.* [77] for the same flow conditions and blade configuration. This indicates a difference in the predicted deformation of 9%. However, a different structural model was employed, where the structure was linearised by means of the reduced-order model (ROM)^[42]. All displacements as functions of the elastic iteration are shown in Figure 10.10(b). The shapes of the blade for consecutive iterations are shown in Figure 10.10(a), where shape convergence is observed.



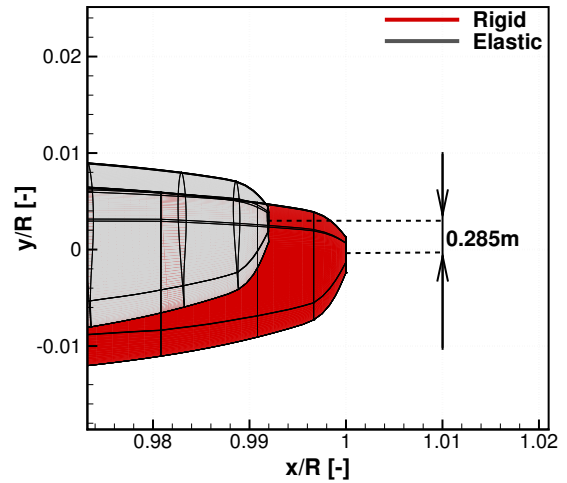
(a) Deformation of the blade for consecutive iteration.



(b) Tip displacement for consecutive iteration.



(c) Final displacement of the tip in flap-wise direction.



(d) Final displacement of the tip in edge-wise direction.

Figure 10.10: Resulting deformations of the initially straight blade from static aero-elastic computations. Shape of the blade for consecutive iteration (a); tip displacement for consecutive iteration (b); and final displacement at the tip in flap-wise (b) and edge-wise (c) directions.

The thrust and power for the rigid and elastic blades are compared in Table 10.3. The obtained results suggest the reduction in both, the thrust force, and mechanical power, due to the elastic deformation. This was expected, since the straight blade was optimal by design, and hence, should represent the best aerodynamic shape for given flow conditions. Distributions of the loads are shown in Figure 10.9 showing a decrease due to deformation. Reductions in thrust of $24kN$, and in power of $305kW$ were computed, which correspond to relative reductions of 1.6%, and 3.0%, respectively. The results presented by Horcas *et al.* [77] seem to suggest a reduction of around $40kN$ in the thrust force, which is almost twice as much, but still less

than 3%. The power reduction was not provided in [77], and a comparison was not possible.

Table 10.3: Comparison between thrust and power for undeformed and deformed blades. Straight blade case.

	Undeformed blade	Deformed blade	Difference
Thrust [kN]	1478.2	1454.2	-24.0 (-1.6%)
Mech. Power [kW]	10291.8	9986.5	-305.3 (-3.0%)

The distributions of the pressure coefficient C_p for the rigid and elastic blades are shown in Figure 10.11. The section at $75\%R$ was chosen as a representative point along the blade span. As can be seen, the deformation reduces the peak of the C_p , and hence, the lift. Also, the pressure side seems to experience slightly lower C_p values, further reducing the lift at this section. This agrees with the distributions of loads presented in Figure 10.9, and the integrated values shown in Table 10.3.

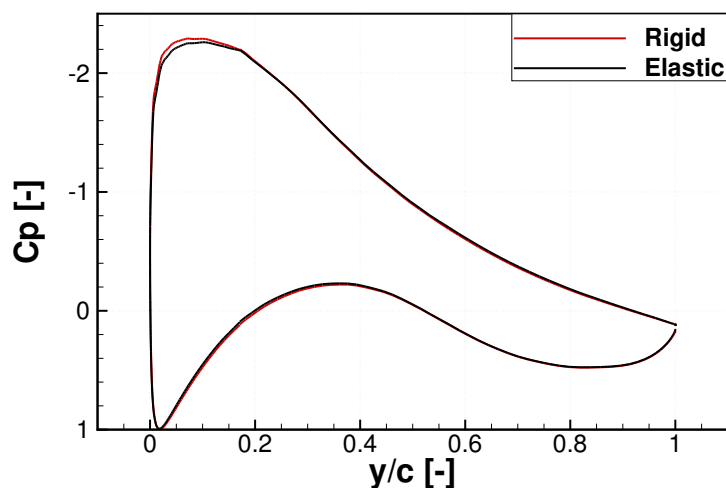


Figure 10.11: Pressure coefficient distribution around the aerofoil section at $0.75R$ for rigid and elastic blade. Straight configuration of the blade.

10.2.3 Results for the blade with pre-bend and pre-cone

The convergence history of the loads for the static aero-elastic calculations for the blade with pre-bend and pre-cone are shown in Figure 10.12. Similarly to the previous case, three iterations were performed in total, and the final shape of the blade was obtained by applying the aerodynamic loads of the third iteration.

The results suggest a final displacement at the blade tip of $8.7m$ in the flap-wise direction, $0.04m$ in the edge-wise direction, $0.18m$ in the span-wise direction. The flap-wise deflection at the tip was comparable

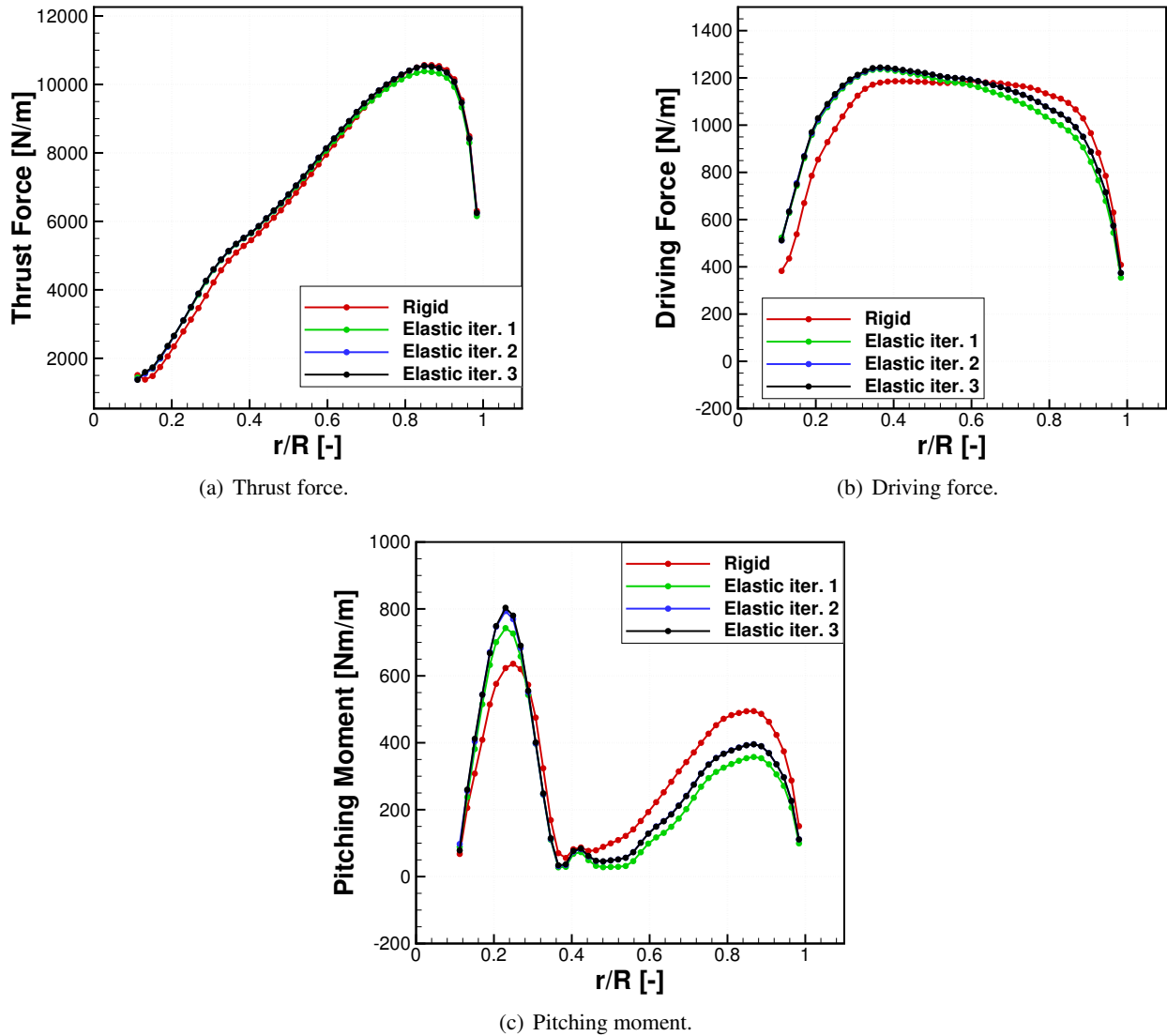
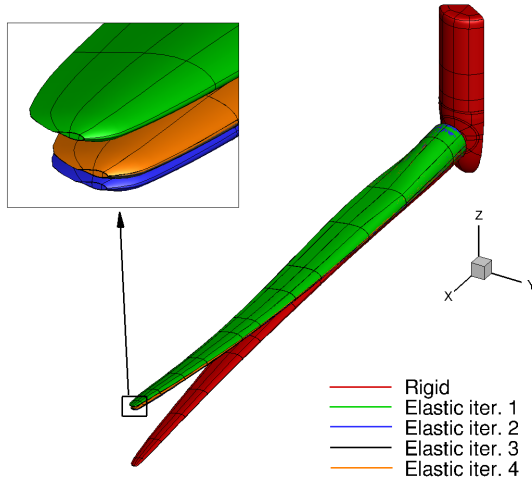
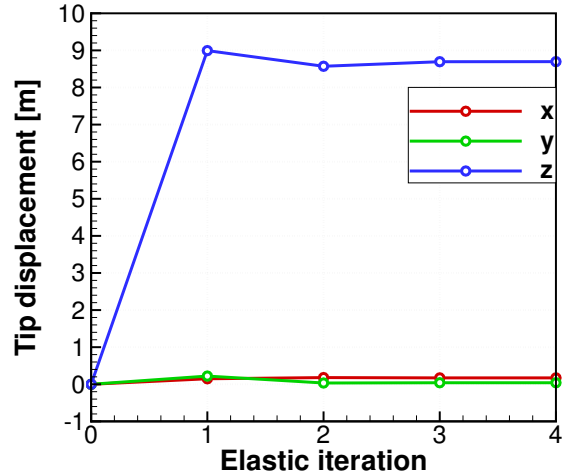


Figure 10.12: Convergence history of the loads for the static aero-elastic computation for the DTU 10MW RWT blade with pre-bend and pre-cone.

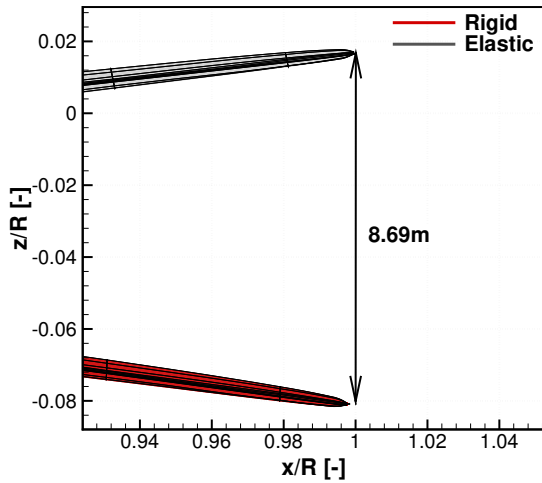
to the one obtained for the straight configuration of the blade, 8.5m. However, the edge-wise deflection was almost 10 times smaller. Also, the displacement in the span-wise direction was positive, as opposed to the previous case, meaning that the blade is slightly elongated due to the deformation. All displacements, as functions of elastic iteration, are shown in Figure 10.13(b). The shapes of the blade for consecutive iterations are shown in Figure 10.13(a), where shape convergence can be observed. The thrust and power for the rigid and elastic blades are compared in Table 10.4. The obtained results suggest an increase in both the thrust force, and mechanical power, due to elastic deformation. This is contrary to the initially straight blade,



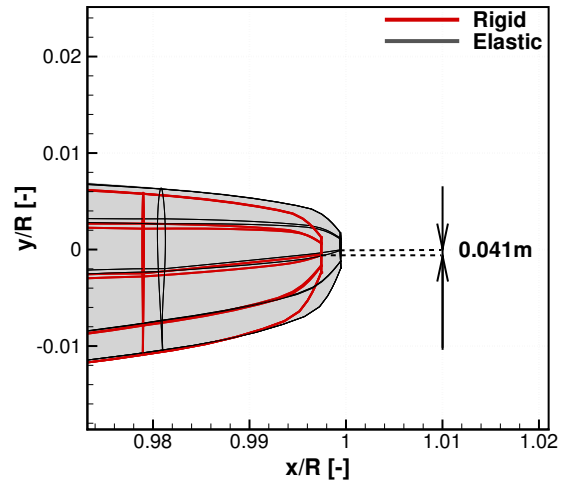
(a) Deformation of the blade for consecutive iteration.



(b) Tip displacement for consecutive iteration.



(c) Final displacement of the tip in flap-wise direction.



(d) Final displacement of the tip in edge-wise direction.

Figure 10.13: Deformations of the blade with pre-bend and pre-cone for static aero-elastic analysis. Shape of the blade for consecutive iteration (a); tip displacement for consecutive iteration (b); and final displacement at the tip in flap-wise (b) and edge-wise (c) directions.

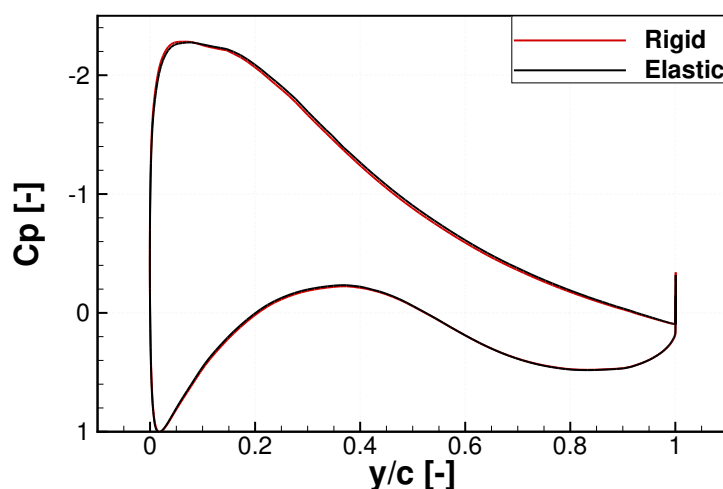
where the reduction was observed. However, this was anticipated, since the deformed blade is closer to the straight configuration than initial shape with pre-bending and pre-coning. The deviation from the straight blade at the tip was $7.2m$ for the rigid, and $1.5m$ for the elastic case. The distributions of loads shown in Figure 10.12 include also the loads due to the deformation. The increase of thrust force of $14.7kN$, and power of $134.5kW$ was computed, corresponding to a relative increase of 0.8% , and 1.2% , respectively.

The distributions of the pressure coefficient C_p at $75\%R$ for the rigid and elastic blades are shown in Figure 10.14. As can be seen, the deformation increased the suction along the whole section, and hence, the

Table 10.4: Comparison between thrust and power for undeformed and deformed blade. Pre-bent and pre-coned configuration of the blade.

	Undeformed blade	Deformed blade	Difference
Thrust [kN]	1654.1	1668.8	14.7 (0.8%)
Mech. Power [kW]	10846.5	10981.0	134.5 (1.2%)

lift. The pressure side seems to experience slightly lower C_p values for elastic blade, but the differences are larger on the suction side, and the total lift is not compensated by this lower pressure. This agrees with the distributions of loads presented in Figure 10.12, and the integrated values from Table 10.4.

Figure 10.14: Pressure coefficient distribution around the aerofoil section at $0.75R$ for rigid and elastic blade. Pre-bent and pre-coned configuration of the blade.

10.3 Dynamic aero-elastic calculations

In this section the dynamic aero-elastic analysis of the DTU 10MW RWT rotor with pre-bend and pre-cone is discussed.

10.3.1 Grids and computational parameters

The complete rotor was modelled for this test case, and the grid was obtained by combining three times the grid E2 used in the previous section. The size of the grid was $16.1M$ cells, and corresponds to $5.4M$ cells per blade. The computational domain with the corresponding boundaries, a slice through the mesh close to the blade surface, and the surface mesh of the blade are presented in Figure 10.15. The structural model

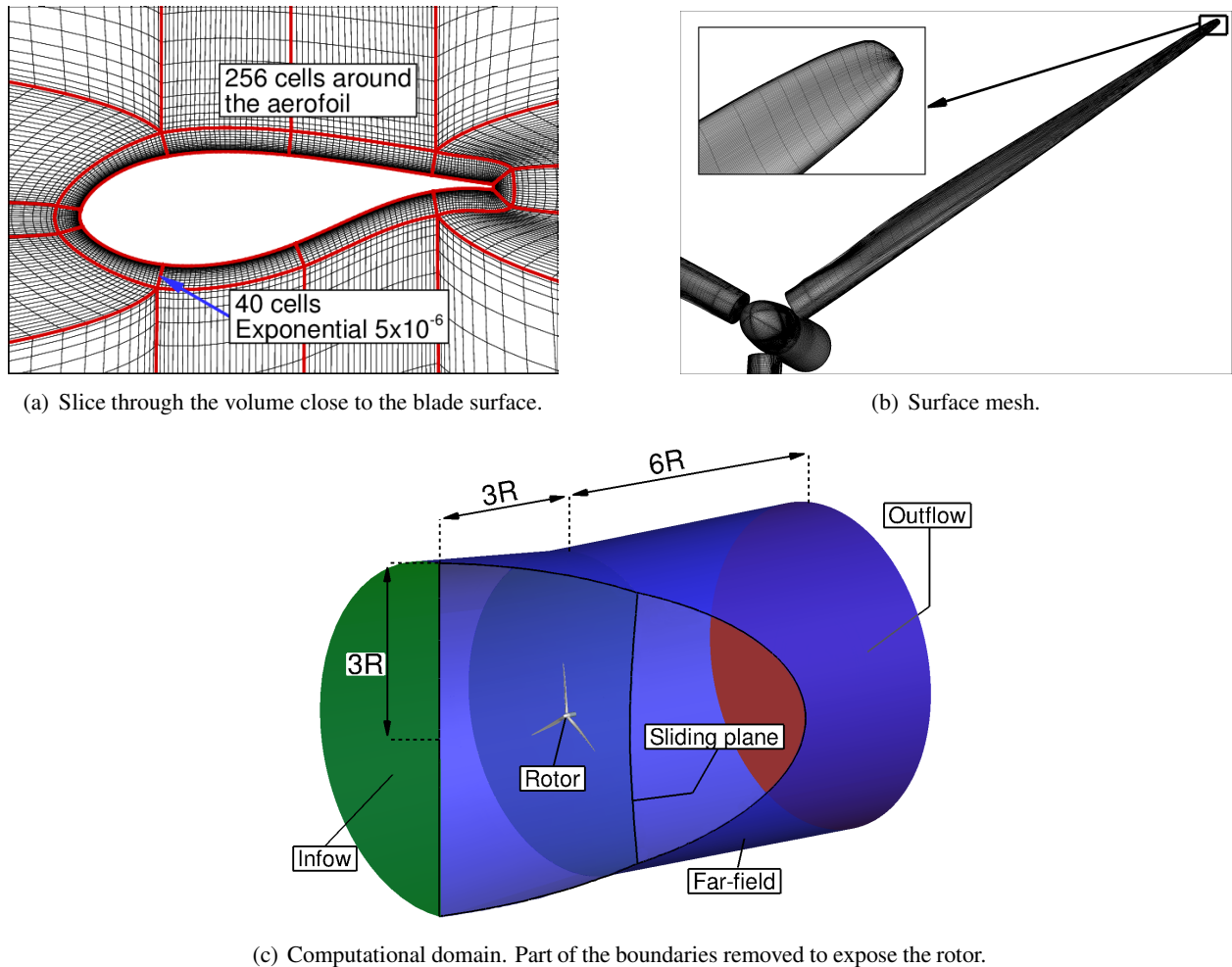


Figure 10.15: Grid employed for the dynamic aero-elastic case of DTU 10MW RWT rotor without the tower - (a) slice through the volume, (b) surface mesh, and (c) computational domain.

was as described in Section 10.1, and the structural damping coefficients were taken from Table 6.4 of Bak *et al.* ^[11]. The modal approach was employed as explained in Section 3.6.4 of Chapter 3, and the first six modes were included in the model.

The unsteady computation was performed with a time step $\Delta t = 4.7 \cdot 10^{-3} s$ corresponding to 0.25° of rotation. The wind speed was set to $11 m/s$, and the rotor was rotating at $8.836 rpm$. This allowed to compute the y^+ parameter for this grid to be $y^+ = 0.9$, and once the solution was obtained, about 20 cells were located inside the boundary layer at the 75% radius station. At the beginning of the computation, the blades were assumed rigid, and the "hover" formulation was first employed. Then, unsteady computations were initiated, and the elasticity was turned on after about 60° of azimuth angle.

10.3.2 Results

The time histories of loads are presented in Figure 10.16(a). The elasticity was engaged at 60° of azimuth angle, and resulted in sudden changes of instantaneous thrust and power. The reduction of loads can be observed first, and then the increase, which is followed by quite periodic variation due to vibration of the blades. Also, the reduction of the thrust force due to elasticity is quite evident, which is opposed to what was observed for the static aero-elastic case. The tip displacements as functions of azimuth angle are shown in Figure 10.16(b). The reference of axes are the same as for previous cases, and can be seen in Figure 10.17, where the shape of the blade after two revolutions is compared to the rigid blade.

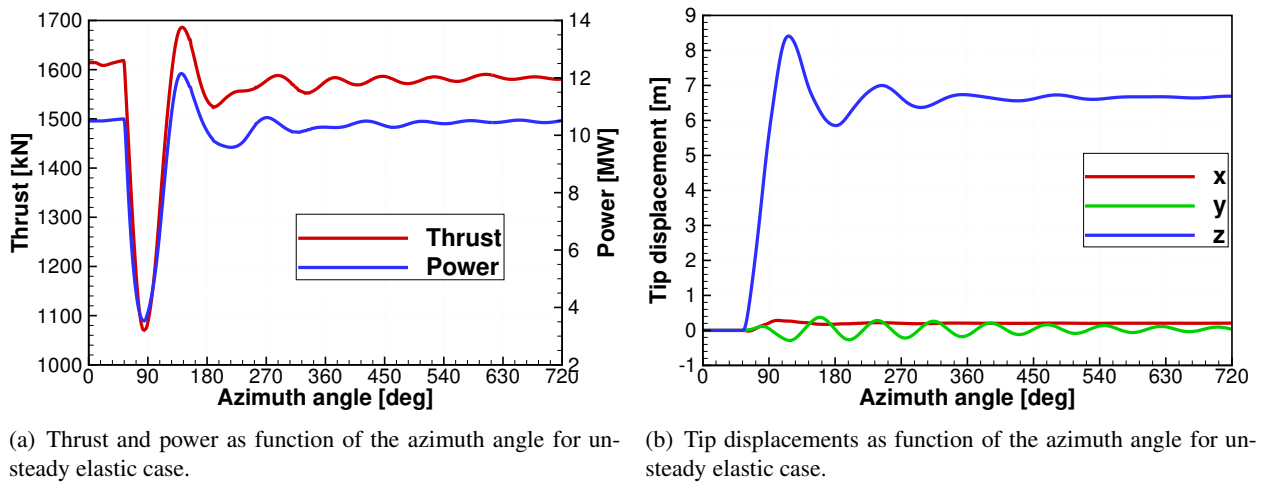


Figure 10.16: Time histories of loads and the tip displacements for unsteady aero-elastic case of DTU 10MW RWT rotor without tower.

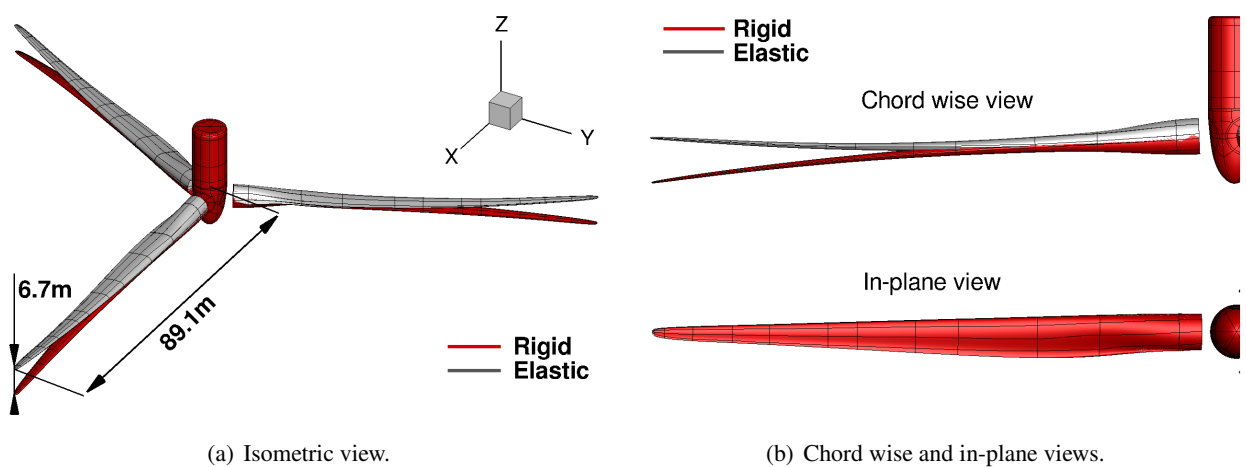


Figure 10.17: Deformation of the DTU 10MW RWT blades after 2 revolutions.

The results suggest that the displacement at the tip reaches an instantaneous value of $8.4m$ in the direction of the wind. This value is close to the displacement obtained for static aero-elastic case presented in Section 10.2.3. However, after the transient phase, the displacement in z direction is damped over half a revolution to $6.7m$. This is about 20% lower, as compared to the result of static aero-elastic analysis, and can be partially attributed to the reduction of the thrust force. The blade straightens and slightly elongates in the x direction by $0.2m$ due to elastic bending. The edge-wise motion is a high frequency oscillation and slowly tends to a displacement of about $0.04m$ towards the leading edge. These two values are in good agreement with the static case results.

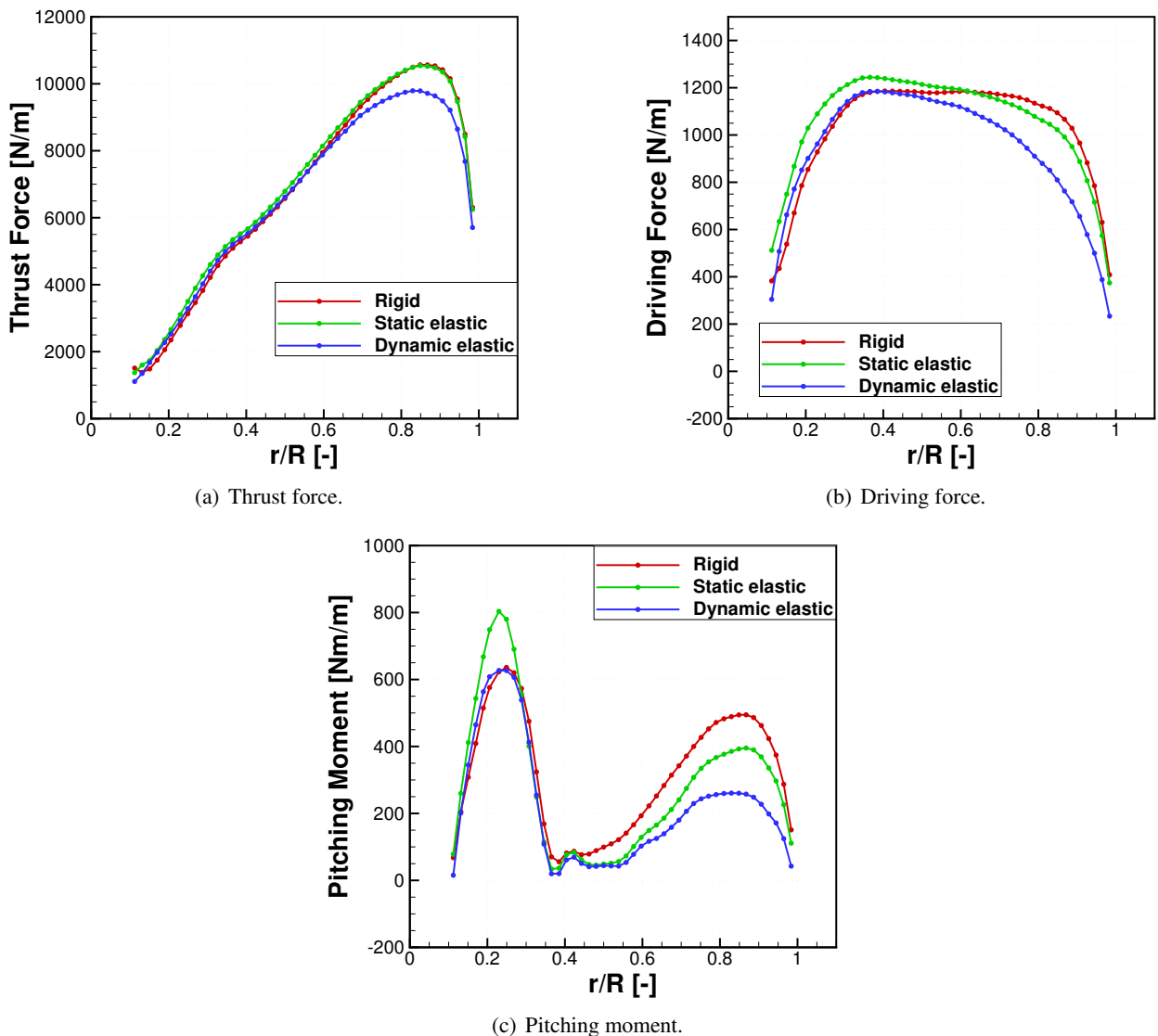


Figure 10.18: Distributions of the loads for the aero-elastic computations for the DTU 10MW RWT blade with pre-bend and pre-cone.

The instantaneous distributions of loads along the blade are shown in Figure 10.18, where they are compared to the loads obtained in the previous section using static aero-elastic analysis. As can be seen, the loads agree with the rigid blade from root up to around $0.5R$, but there is a reduction closer to the tip of the blade. Using these loads, the *NASTRAN* non-linear solution suggests a tip displacement of $8.2m$, which is about 18% larger than what was estimated using the dynamic aero-elastic approach, and is closer to the value obtained from the static aero-elastic analysis ($8.7m$). The shapes of the blade from static and dynamic aero-elastic computations are shown in Figure 10.19.

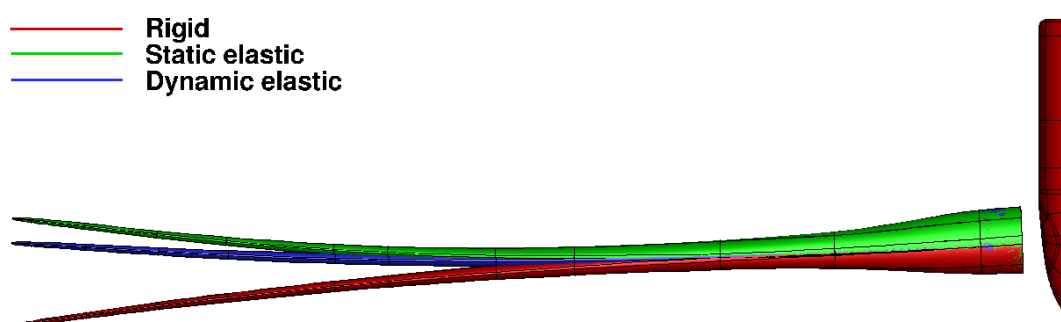


Figure 10.19: Comparison of the blade shapes from static and dynamic aero-elastic computations.

The differences between static and dynamic cases can be attributed to two effects. The first one is related to the predicted aerodynamic loads. Comparing the shapes of the blade in Figure 10.19, it can be seen that the dynamic aero-elastic case predicted a shape closer to the straight configuration. Therefore, higher loadings were anticipated, as compared to the static aero-elastic case. However, this was not observed in Figure 10.18. This indicates that the unsteady motion of the blade resulted in a reduction of the blade loads. The second effect is related to the linearisation of the structural model. The loads from the dynamic aero-elastic case resulted in larger displacements, when applied to the non-linear *NASTRAN* model. This indicates that the modal approach may not completely apply for large rotors with large deformations. This seems to be confirmed by the results presented in Section 10.2.2, where the linearised model of Horcas *et al.* ^[77] predicted smaller flap-wise deflection, as compared to the results of non-linear model employed in this work.

10.4 Complete assembly of DTU 10MW RWT

In this section the complete configuration of the DTU 10MW reference wind turbine is considered with rigid and elastic blades. The wind turbine consists of the tower with nacelle tilted nose-up by 5° , as explained in Section 9.1 of Chapter 9. The blades have pre-cone and pre-bend. The wind speed was 11m/s , and the rotational speed was 8.836rpm .

10.4.1 Grids and computational parameters

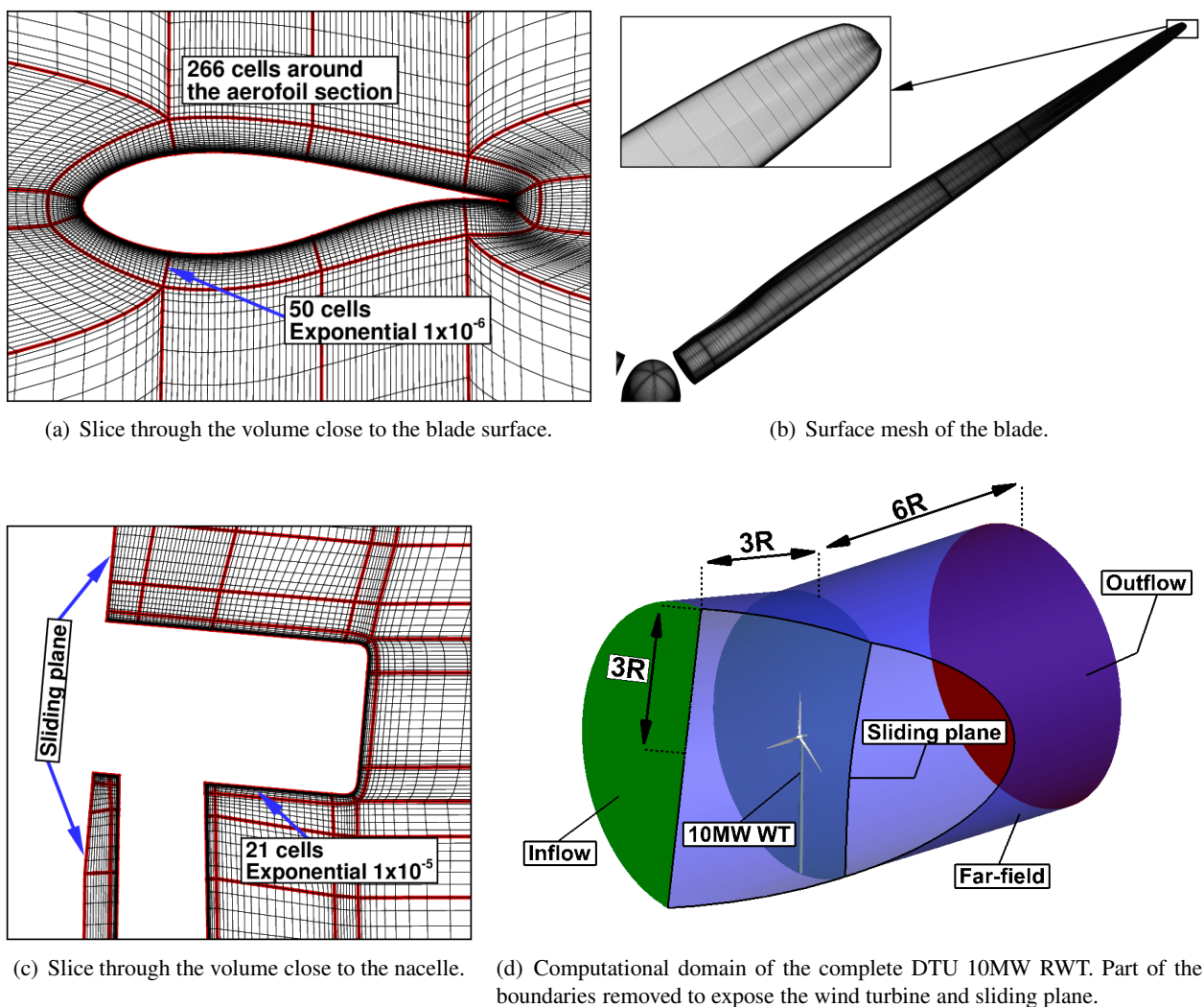


Figure 10.20: Grid employed for the DTU 10MW RWT - (a) slice through the rotor grid, (b) blade surface mesh, (c) slice through the tower grid, and (d) computational domain.

The same computational mesh was employed for both rigid and elastic blades. The grid consisted

of the rotor mesh that was attached to the nacelle and tower grid by means of a sliding plane to allow for relative rotation. The grid size for each of the blades was $8M$ cells, and for the tower with nacelle $1.5M$ cells mesh was employed. The final size of the mesh was $25.5M$ cells. The inflow boundary was placed $3R$ in front of the tower, and the outflow boundary was placed $6R$ behind it, where R is the radius of the rotor. The far-field boundary was assigned three blade radii from the centre of rotation. The computational domain with corresponding boundaries and details of the mesh are presented in Figure 10.20. The tower was extended with a cylinder to the bottom of the domain. The y^+ parameter for this grid at the given conditions, was calculated to be $y^+ = 0.2$, and once the solution was obtained, about 30 cells were located inside the boundary layer at the $75\%R$ station.

The unsteady computations were performed using $k - \omega$ SST turbulence model with a time step $\Delta t = 4.7 \cdot 10^{-3}s$, corresponding to 0.25° of rotation. First, the blades were assumed rigid and three revolutions were performed before aero-elasticity was engaged. To avoid large deformations at the beginning of the aero-elastic computation, the structural damping coefficients present in the modal excitation equation were set to the values shown in Table 10.5. The computation with the rigid blades was continued for another 1.3 revolutions, such that better comparisons to the elastic case can be performed.

Table 10.5: Structural damping coefficients used in the aero-elastic computation for the complete DTU 10MW RWT.

Applied between azimuth angles (revolutions)	1080° – 1260° (3.0-3.5 rev.)	1260° – 1440° (3.5-4.0 rev.)	after 1440° (after 4.0 rev.)
Mode	Damping coefficient [%]		
1st flap	50	10	3
1st edge	50	10	3
2nd flap	50	10	8
2nd edge	50	10	9
3rd flap	50	20	17
4th flap	50	30	26

10.4.2 Results

Time histories of thrust and power for rigid and elastic blades are presented in Figure 10.21. The thrust was computed as the aerodynamic force acting along the axis of rotation, and the mechanical power was computed as the aerodynamic moment along the shaft multiplied by the rotational velocity of the rotor.

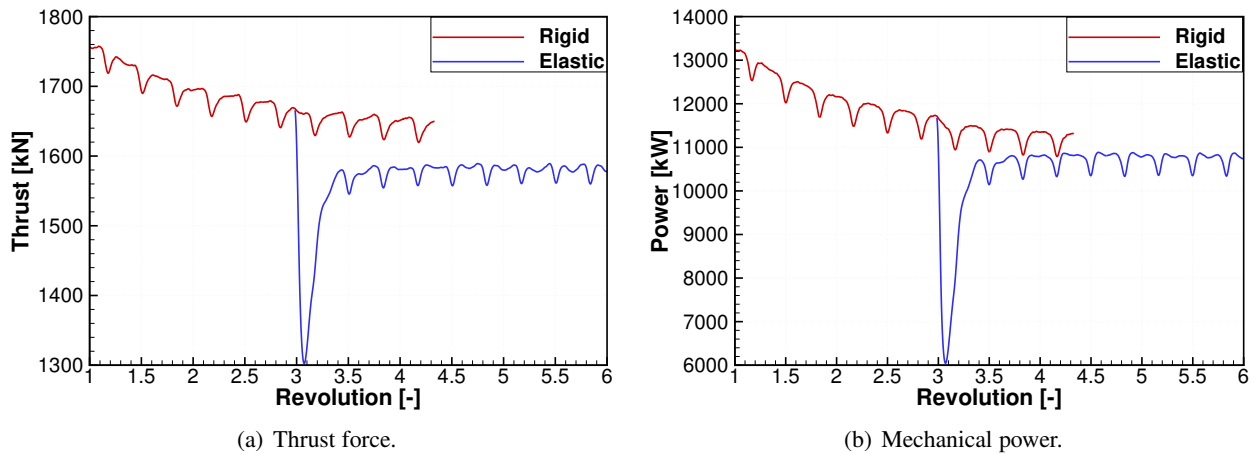


Figure 10.21: Thrust force and mechanical power as functions of revolution for the DTU 10MW RWT. Comparison between the rigid and elastic blades.

A large instantaneous reduction of the thrust and power due to the sudden large deformation of the blades can be observed for the elastic case. This is similar to what was observed for the dynamic elastic case without the tower. However, the large structural damping coefficients at the beginning of the present elastic computation prevented large instantaneous deformations. After the transient phase, the loads stabilised and the blade-tower interaction was clearly visible. The rigid blades case was slower to stabilise. Hence, solving the rigid case for longer would result in better estimates of the relative changes. However, the variations of thrust and power for the last 120° of azimuth angle were quite periodic, as shown in Figure 10.22.

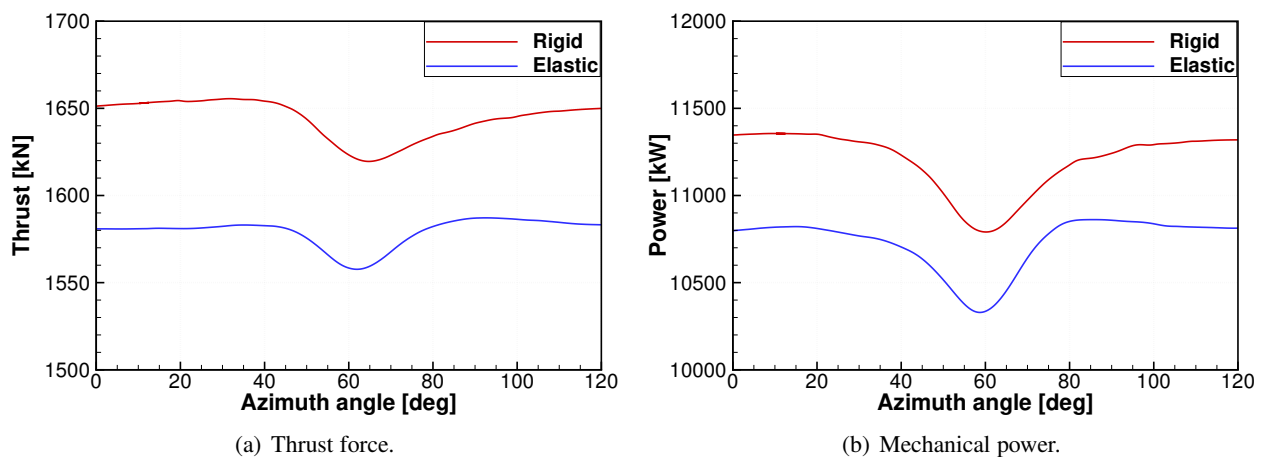


Figure 10.22: Thrust force and mechanical power as functions of azimuth angle for the first 120° of the 4th revolution. Comparison between the rigid and elastic blades.

The results presented in Figure 10.22 suggest a mean reduction in thrust by about 70 kN (4.3%) and

in mechanical power by about 533kW (4.7%) due to the elasticity of the blades. Also, the minima in both quantities for the elastic blades are slightly shifted towards smaller azimuth angles. Similar trends can be observed in the results presented in Carrión *et al.* [28] for a two bladed wind turbine. The instantaneous reduction of thrust by 30kN (1.8%) and power of 561kW (4.9%) due to the blade passing in front of the tower can be concluded, and the variation is similar in both cases. Note that for the rigid blade the minimum in power appears as the blade is passing in front of the tower (at 60° of azimuth angle), whilst the minimum in thrust is delayed by approximately 5°. Also, the overshoot of thrust and power after passing the tower can be seen for elastic blades. This is in contrast with the variations for the rigid blades, where the thrust and power grows gradually and stabilises before the next blade is about to approach the tower.

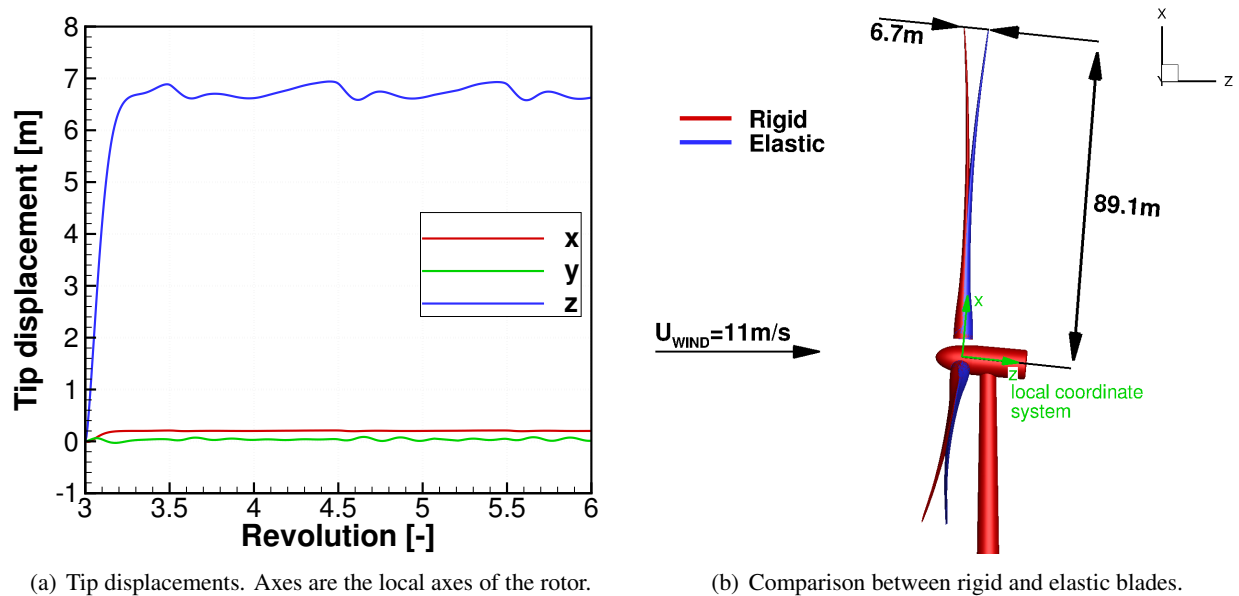


Figure 10.23: Displacement of the tip as function of revolution (a), comparison between the shapes of rigid and elastic blades (b), and shape of the blade for different azimuth angles Ψ (c).

The displacements at the tip, as functions of the rotor revolution, are shown in Figure 10.23(a). Note that displacements are presented for one blade, which points at 12 o'clock at the beginning of each revolution. The obtained results suggest that the flap-wise displacement reached the mean value of $6.7m$, which agrees with the results of the aero-elastic analysis without the tower. Also, span-wise and edge-wise displacements agree very well - $0.2m$ and $0.04m$ respectively. Unlike for the results without the tower, high instantaneous displacements at the tip were not observed due to high structural damping at the beginning of the aero-elastic computation. However, after 4 revolutions, the coefficients were reduced to the same values, according to Table 10.5 and Bak *et al.* [11]. One per revolution excitation can be seen in Figure 10.23(a), especially for the flap-wise and edge-wise motions (in z and y). The span-wise motion is linked to the rotation through the flap-wise deflection, and hence, is less visible. The reduction of the thrust for the blade (due to the tower) in the middle of a revolution delivers an impulse. As a result, the blade reduces its deflection, and vibrates with different frequencies in both directions for about half a revolution. The effect of the tower on the shape of the blade can be seen in Figure 10.23(c). As the blade moves away from the tower, it begins to experience a constant loading. Therefore, the increase of deflection in flap-wise direction can be seen. The motion would stabilise at some point, but then the blade reaches the tower again. The comparison between the shape of the blade for rigid and elastic case is presented in Figure 10.23.

The wakes of the DTU 10MW RWT with rigid and elastic blades were visualised with the iso-surface of $Q = 0.007$ in Figure 10.24. The strong tip and root vortices can be observed. Also, the interaction of the wake generated by the rotor and the Kármán vortex street generated by the cylindrical tower can be identified. Breaking of the vortex sheet behind the blunt trailing edge of the blade can be seen for the blade that just passed the tower. Comparing both solutions, different shape of the blades can be seen, where rigid blades are further away from the tower. This affected the tip vortices, where the rigid case resulted in the tip vortex upstream the tower, whilst for the elastic case, the vortex was interacting with the tower. This is especially clear in Figure 10.25, where contours of velocity in direction of the z axis are shown.

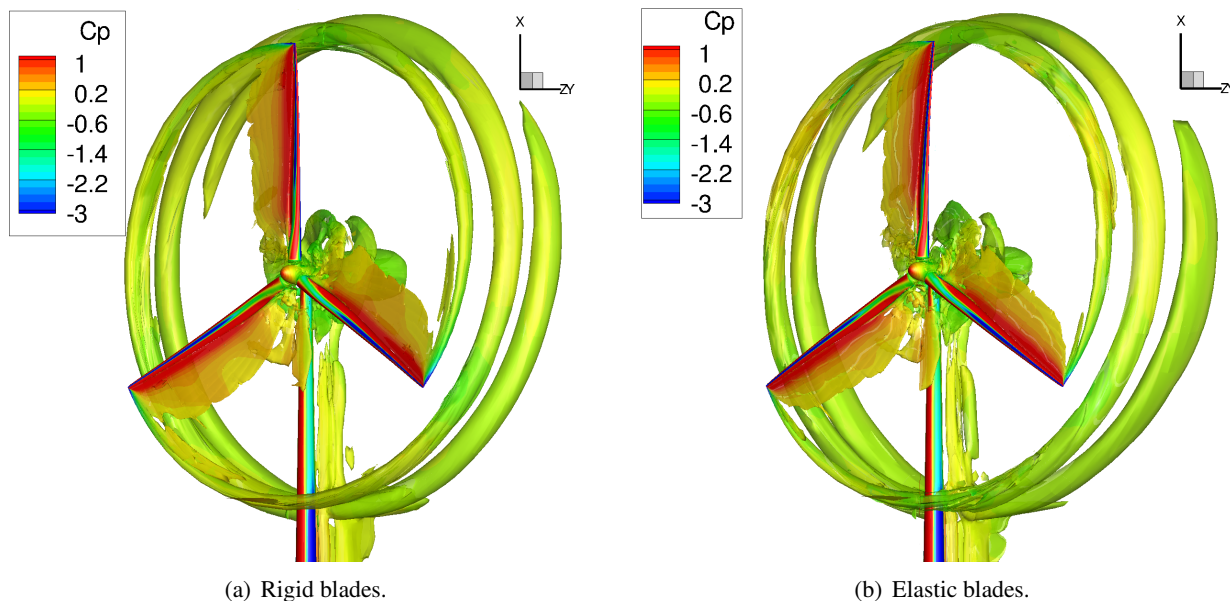


Figure 10.24: The wake of the DTU 10MW RWT visualised with the iso-surface of $Q = 0.007$ criterion: (a) rigid and (b) elastic blades.

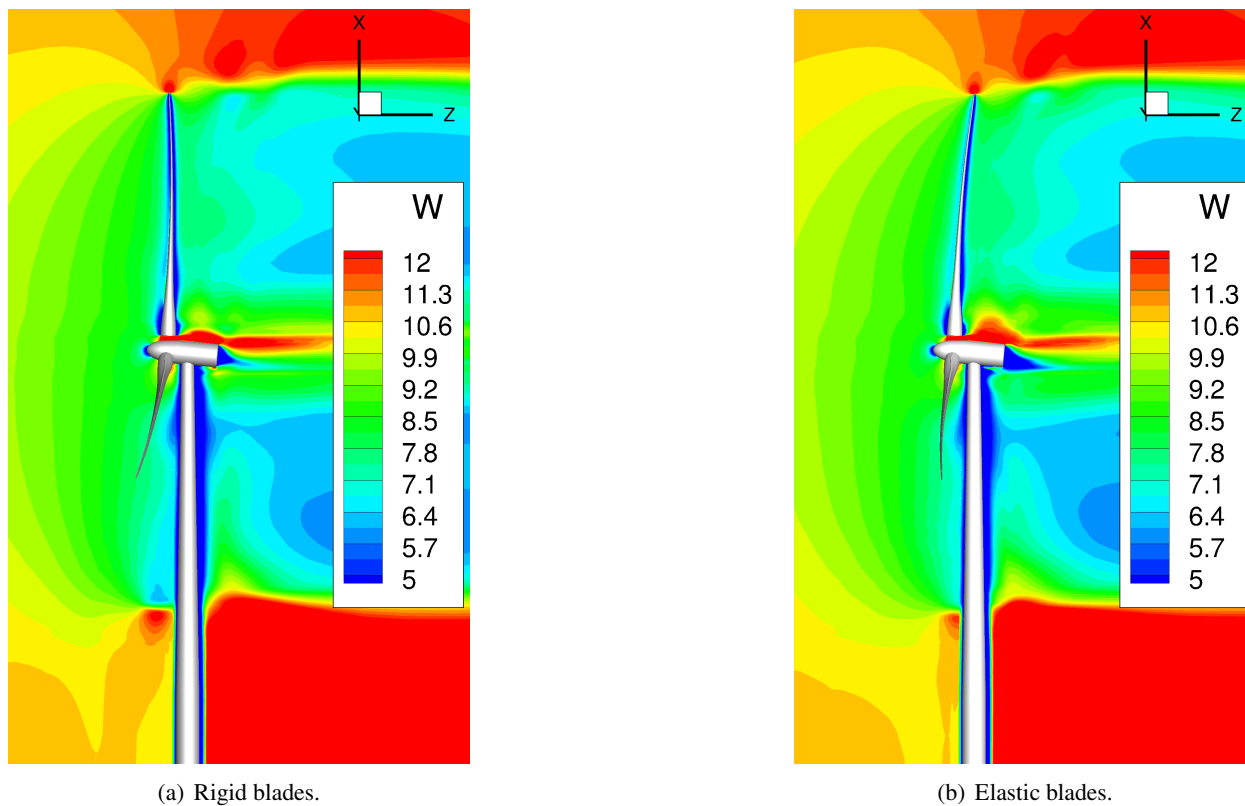


Figure 10.25: Contours of velocity component W in meters per second: (a) rigid and (b) elastic blades.

Chapter 11

Trailing and leading edge flaps for DTU

10-MW RWT¹

In this chapter, the effects of employing deformable trailing and leading edge flaps on a 10-MW wind turbine are investigated. The concept of deformable flaps was introduced in Section 1.2.8 of Chapter 1, and a new flap deflection algorithm was implemented in the HMB3 solver, as explained in Section 11.1. A definition of the employed flaps is given in Section 11.2, and computational results are presented in Section 11.4. The blades are assumed rigid throughout this chapter.

11.1 Flap deflection algorithm

A new flap deflection algorithm was implemented in HMB3 to allow for arbitrary flap shape motion. The algorithm is based on the surface interpolation, where the mean, maximum and minimum flap deflections are defined by separate surfaces. Then, the linear interpolation is employed for each point on the surface between the mean and the deflected shapes of the flap. The motion of the flap in time can be arbitrary, and is described by a Fourier series. Since only mean and maximum surfaces are known to the solver, the interpolation tends to slightly shrink the flap. To understand this behaviour, consider a 2D rod-like flap shown in Figure 11.1. As can be seen, the linear interpolation tends to shrink the flap, but the effect is not

¹ This work was published in Leble and Barakos^[113].

pronounced for relatively small angles of deflection.

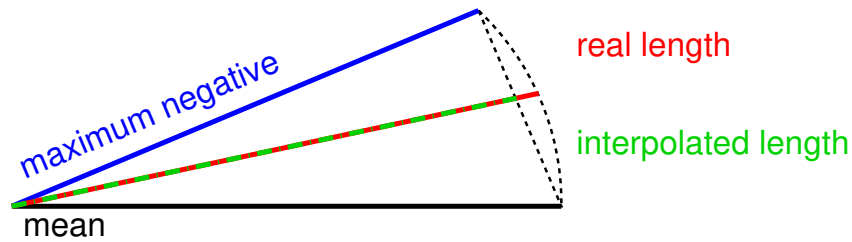


Figure 11.1: Schematic of the trailing edge flap, showing mean and maximum negative deflections, and real and interpolated length of the flap during motion.

The trans-finite interpolation (TFI) method^[49] is employed to regenerate the mesh after the surface deformation. The details of this method are presented in Section 3.6.2 of Chapter 3. Only blocks adjacent to the deformed surface are interpolated for computational efficiency, and so the nearest mesh blocks to the flap must be large enough to accommodate the expected flap deflections. Figure 11.2 shows the changes on the cell volumes and skewness of the grid for the employed leading edge flap deflected towards the pressure side by 10° . Equation 3.46 from Chapter 3 was used to compute the cell volume and skewness ratios.

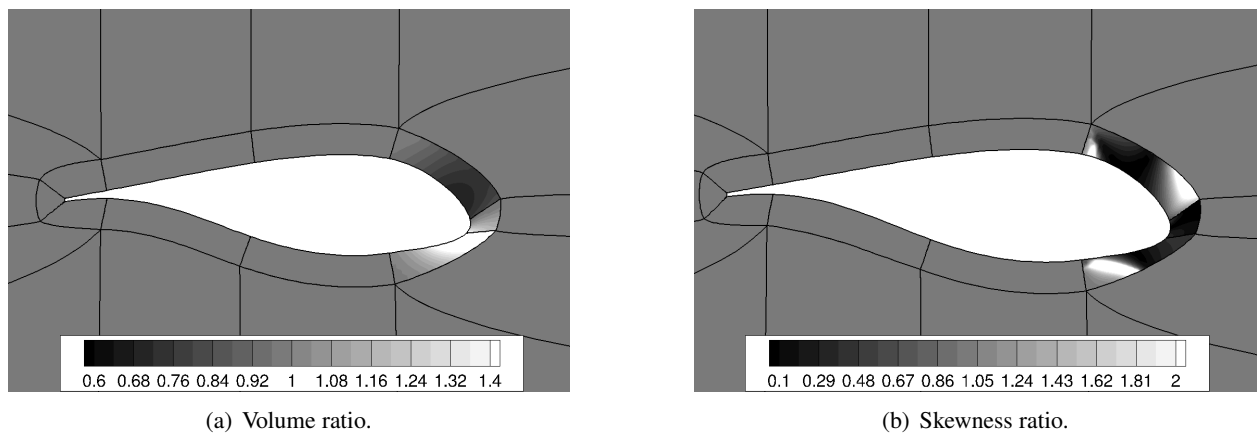


Figure 11.2: Cell volume ratio (a), and skewness ratio (b) between deformed and undeformed grids for the leading edge flap deflected 10° towards the pressure side.

11.2 Definition of the flaps

The DTU 10-MW RWT^[11] blade was equipped with leading and trailing edge flaps. The leading edge (LE) flap was centred at $60\%R$, and the trailing edge (TE) flap was at $75\%R$. The length of each flap was $10\%R$,

but the width of the TE flap was 10% of the local chord, whereas the width of the LE flap was 20% of the local chord, as shown in Figure 11.3. The choice of the TE flap width was made under the understanding that flaps will be used for load control and elevation. For the LE flap, it was assumed that its operation is similar but less efficient to that of the TE flap. The width in this case was increased to 20% to allow for a larger control surface and for smooth transition of the surface slope.

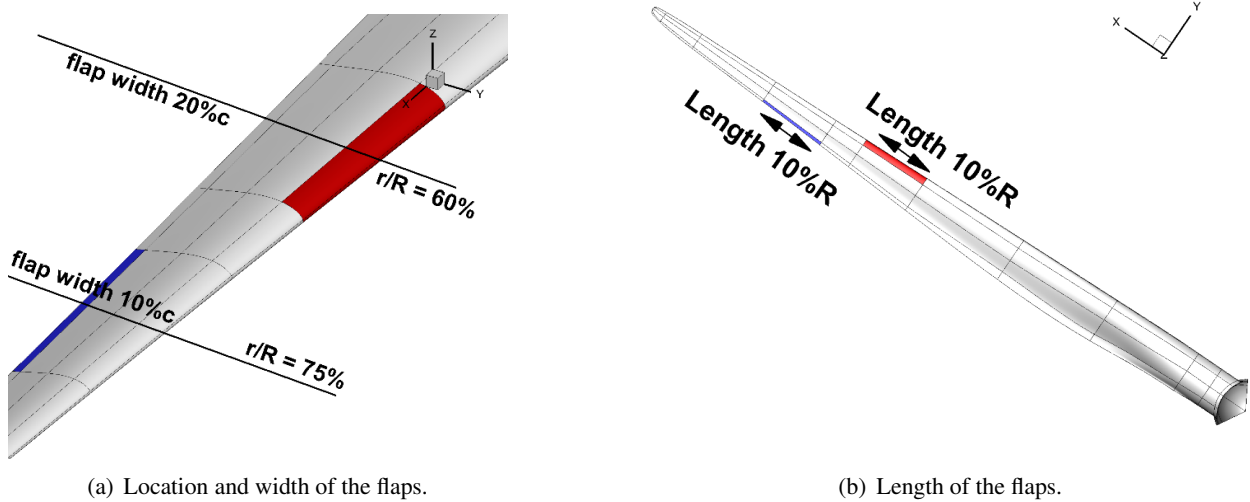


Figure 11.3: The location and dimensions of the trailing and leading edge flaps.

The deformation of the flaps was defined with respect to the mean line of the aerofoils as shown in Figure 11.4. Let \mathbf{X}_m denote the mean line and $h(x)$ denote the thickness distribution. With respect to a curvilinear (ξ, η) system following the mean line, the deformation is defined as $\eta(\xi) = \phi \xi^2(3 - \xi)/2$ where $\xi \in [0, 1]$, and ϕ is providing the deflection. With this definition, the shape of the camber line is C^∞ smooth. The displacement and derivative at the beginning of the flap (at $\xi = 0$) is 0. At the other end of the flap (at $\xi = 1$), the second derivative of the displacement is 0. In this work $\phi \equiv \phi(t) = \phi_m \sin(\omega t)$, where ϕ_m is the maximum value which is determined by the maximum deflection angle β . Then the upper (S+) and lower (S-) sides of the aerofoil are

$$\mathbf{S}^\pm = \mathbf{X}_m + \eta(\xi)\mathbf{N}_m + h(x)\mathbf{N}'_m, \quad (11.1)$$

where \mathbf{N}_m denotes the unit normal to the mean line, and \mathbf{N}'_m denotes the unit normal to the deformed mean line defined by $\mathbf{X}'_m = \mathbf{X}_m + \eta(\xi)\mathbf{N}_m$. By denoting the point at which the flap starts with x_0 , the process to compute flap deflection is as follows:

For each point $x > x_0$

1. Get \mathbf{X}_m , $h(x)$, and \mathbf{N}_m .
2. Define $\xi = \xi(x)$ based on the length along the mean line.
3. Define the deformed mean line $\mathbf{X}'_m(\xi) = \mathbf{X}_m(x) + \eta(\xi)\mathbf{N}_m(x)$, and get $\mathbf{N}'_m(\xi)$.
4. Compute deformed shape from $\mathbf{X}(\pm) = \mathbf{X}_m + \eta(\xi)\mathbf{N}_m + h(x)\mathbf{N}'_m$.

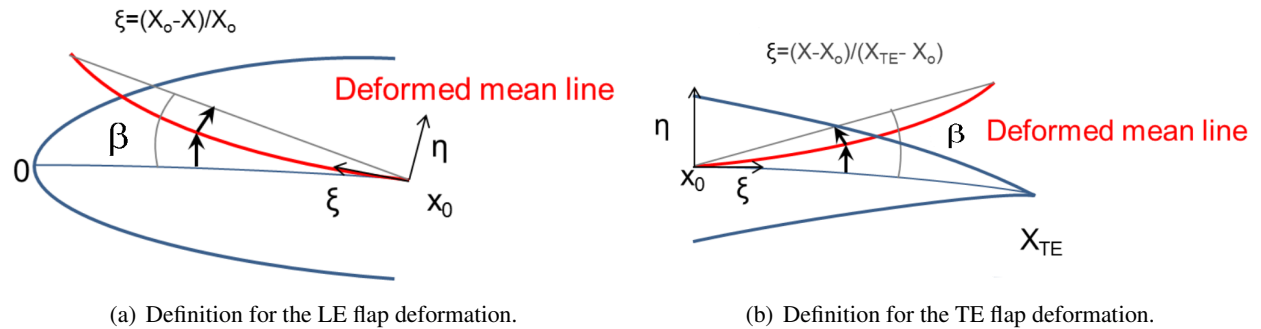


Figure 11.4: Definition conditions for the LE (a) and TE (b) flap deformation.

The FORTRAN code to compute the deflection of the TE and LE flaps is presented in Listing 11.1.

The flaps were deflected from -10° to $+10^\circ$ with the shape and notation presented in Figure 11.5. The frequency of flap motion was set to 0.96Hz , or six times per revolution.

Listing 11.1: FORTRAN pseudo-code to compute the trailing and leading edge flap deflections.

```

! Let X(i), Y(i) denote the coordinates of the nodes on the aerofoil
! Input: Xo (x/c location), amax (max angle), freq (frequency)
! Function: f(x,t)=amax*sin(2.*pi*freq*t)*ksi**2*(3.-ksi)/2.
! N number of points on the aerofoil
! Note: all dimensions are normalised to the chord
! TE Flap motion:
do i=1,N
  Ynew=Y(i); dYnew=0.
  If(X(i).ge.Xo) then
    ksi=(X(i)-Xo)/(XTE-Xo) ! XTE=1.
    dmax=(XTE-Xo)*sin(amax)/cos(amax)
    Ynew=Y(i)+ dmax*sin(2.*pi*freq*t)*ksi**2*(3.-ksi)/2.
    dYnew= 2*pi*freq*dmax*cos(2.*pi*freq*t)*ksi**2*(3.-ksi)/2.
  endif
enddo
! LE Flap motion:
do i=1,N
  Ynew=Y(i); dYnew=0.
  If(X(i).le.Xo) then
    Ksi=(Xo-X(i))/Xo
    dmax=Xo*sin(amax)/cos(amax)
    Ynew=Y(i)+ dmax*sin(2.*pi*freq*t)*ksi**2*(3.-ksi)/2.
    dYnew= 2*pi*freq*dmax*cos(2.*pi*freq*t)*ksi**2*(3.-ksi)/2.
  endif
enddo

```

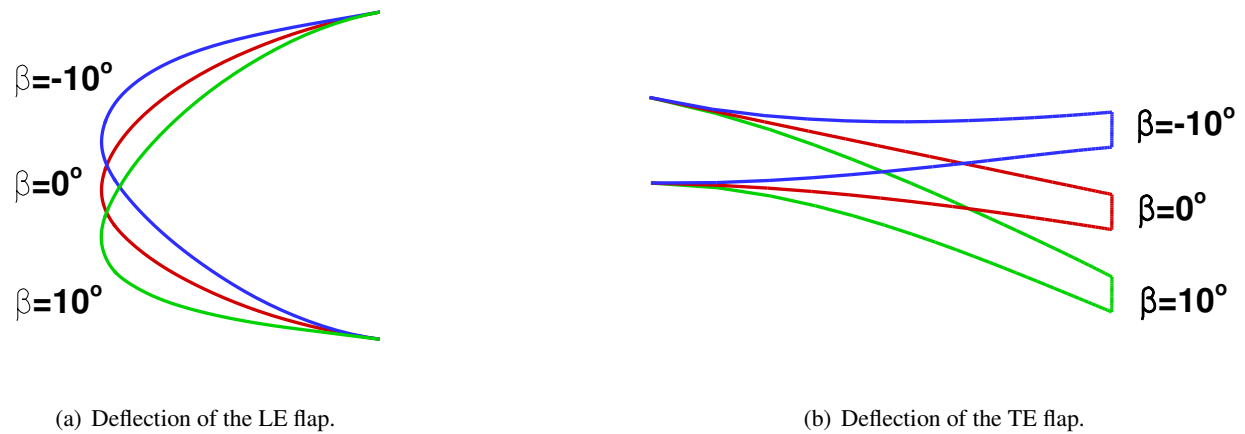


Figure 11.5: Definition of the positive and negative deflection for the LE (a) and TE (b) flap.

11.3 Computational grid and flow conditions

In this chapter, the same $9.2M$ cells grid is employed as in Section 9.4.1 of Chapter 9. This grid included the complete DTU 10MW RWT blade in a straight configuration, and had an 0-grid topology around the aerofoil sections. The first cell distance from the wall was $10^{-6}c$, where $c = 6.206m$ is a maximum chord of the blade. The hub was included based on the simplified nacelle shape, as shown in Figure 9.13.

The $k - \omega$ SST turbulence model by Menter^[137] was employed, and URANS computations were performed using HMB3 solver. The wind speed was set to the rated value of $11.4m/s$, and rotational velocity of the rotor was set to $9.6rpm$. Flap motion frequency was chosen to be six times per revolution, which corresponds to $0.96Hz$. This is close to the frequency of the first edge-wise mode, as shown in Table 10.1. However, no attempt was made to control the flaps to counter particular vibrations. In fact, blades were assumed rigid in this chapter. The results presented here aim to investigate the potential of the TE and LE flaps applied to large rotors.

11.4 Results and discussion

11.4.1 Results for the TE flap

The distributions of the pressure coefficient C_p in the middle of the TE flap, and for different angles of deflection β are shown in Figure 11.6. Significant changes of the pressure at the rear part of the aerofoil can

be observed. However, the whole length of the section is affected by the flap. The change of the maximum value of C_p varies from 2 to about 2.3, and is located near the leading edge of the aerofoil. Interestingly to note, that the C_p distribution crosses at the flap for the maximum negative deflection ($\beta = -10^\circ$). This means that the suction side becomes the pressure side at the trailing edge flap for this angle. Therefore, the lift is reduced, and a larger moment should be applied at the flap to achieve the deflection. As the flap angle β changes towards positive values, the pressure is increasing at the pressure side, and decreasing at the suction side, effectively increasing the lift. The minima and maxima of the C_p distribution are near the beginning of the TE flap. This shows that some surface discontinuity was present. Note that for the angle of deflection $\beta = 0$, computed C_p distribution did not coincide with the one obtained for the case without flaps, referred to as "clean blade" throughout this chapter. This indicates the existence of hysteresis, where the flow cannot adapt instantly to the change of the surface. Indeed, the hysteresis loops were observed in the analysis of non-dimensional coefficients in Section 11.4.3.

The distributions of the pressure coefficient around the whole blade are shown in Figure 11.7. It is quite evident that the flap deflection had only local influence on the pressure distribution, whereas the rest of the blade remained largely unaffected. The change of pressure at the root of the blade is caused by the root vortex shedding. This mostly affected the suction side, from which vortices are shed. This shedding was found to be affecting approximately 10% of the blade span at the root. However, the root section creates very little lift due to mostly cylindrical shape of the blade at this part. The instantaneous vortices were visualised with the iso-surfaces of Q criterion, as shown in Figure 11.8. As can be seen, the tip vortices are much stronger, compared to the TE flap vortices, and hence were preserved for longer, showing the expansion of the wake. The vortex sheet behind the blunt trailing edge of the blade can also be seen. The vortex sheet is stronger, and extends further behind the TE flap due to increased pressure difference at the trailing edge, as was shown in Figure 11.6. Larger loads result in increased momentum deficit and larger shear. Also, the results suggest periodical detachment of the vortex sheet behind the TE flap due to the flap deflection.

The distribution of forces was obtained by integrating the pressure from root to tip of the blade. These are presented in Figure 11.9, where the length of each section in radial direction used in pressure integration is $\Delta r = 2.15m$. Again, the localised effect of the flap deflection on the distribution of the loads can be seen. The variation of $77.4kN$ in the thrust force, and $422.5kW$ in the power with respect to the "clean" blade were

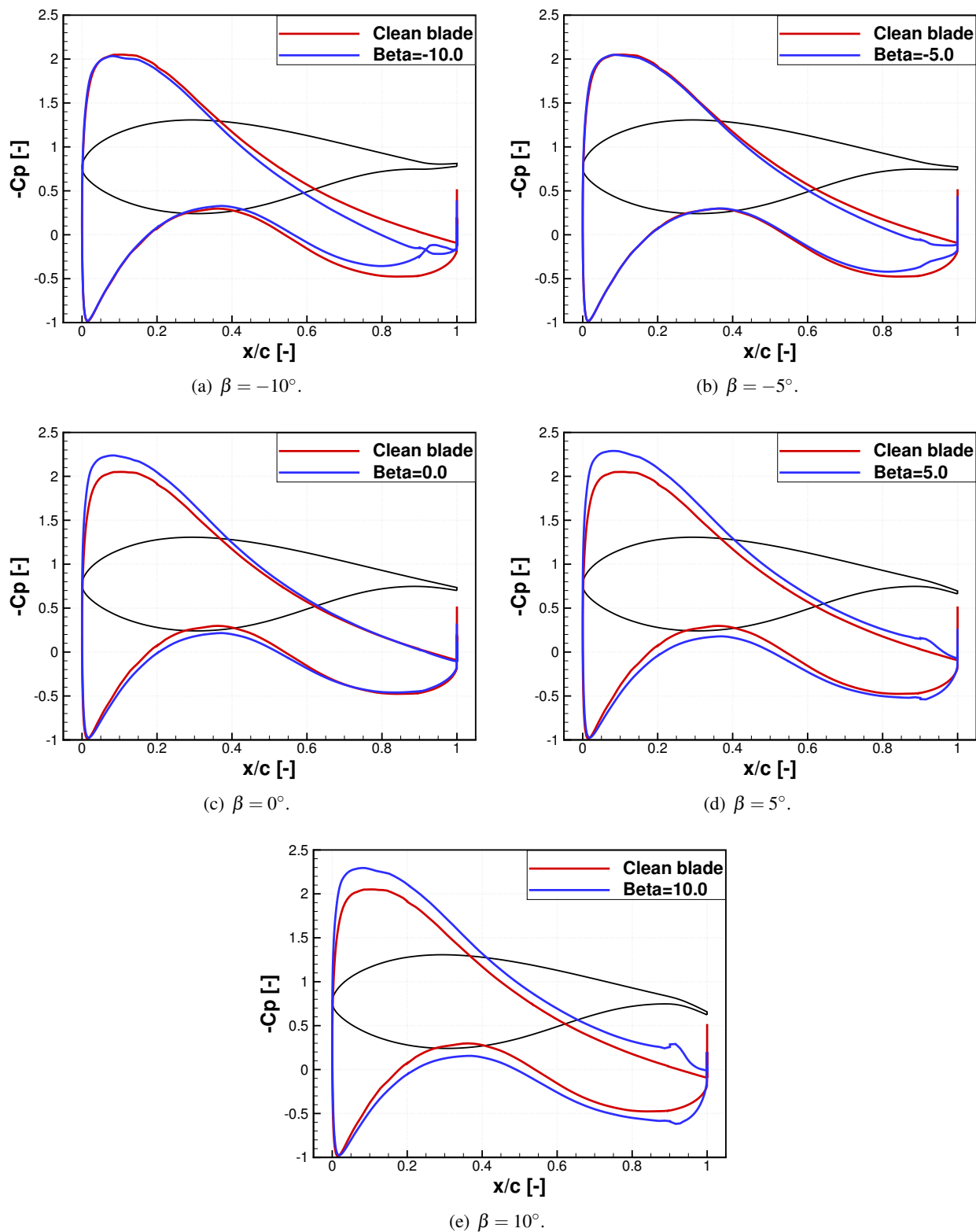
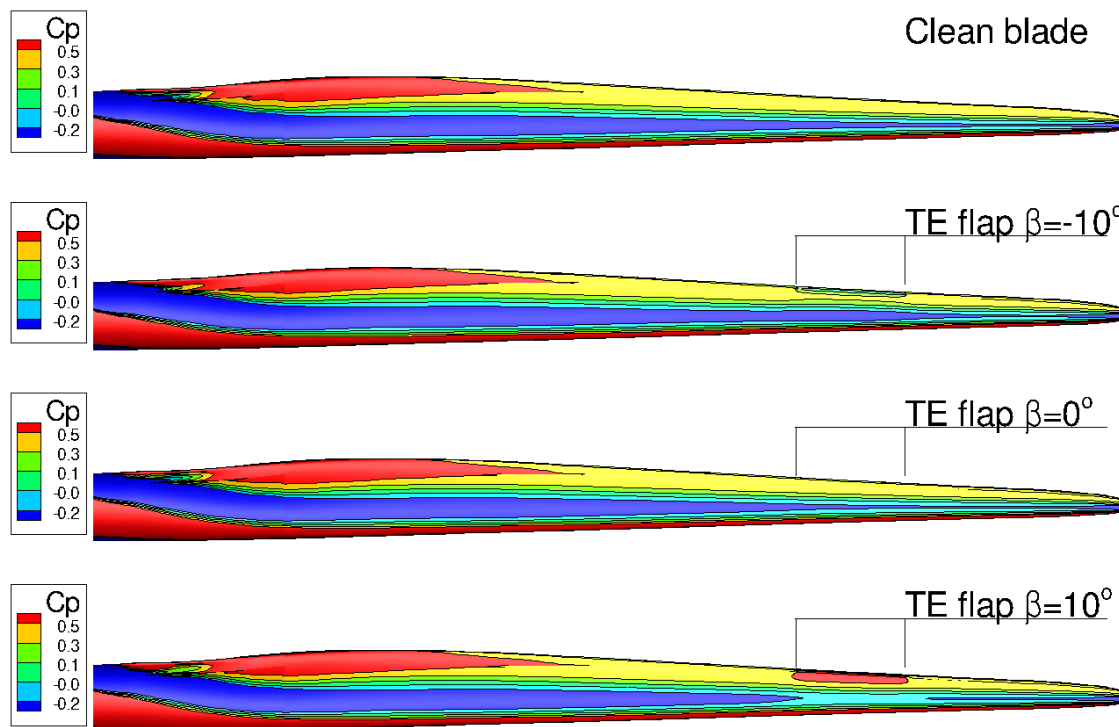
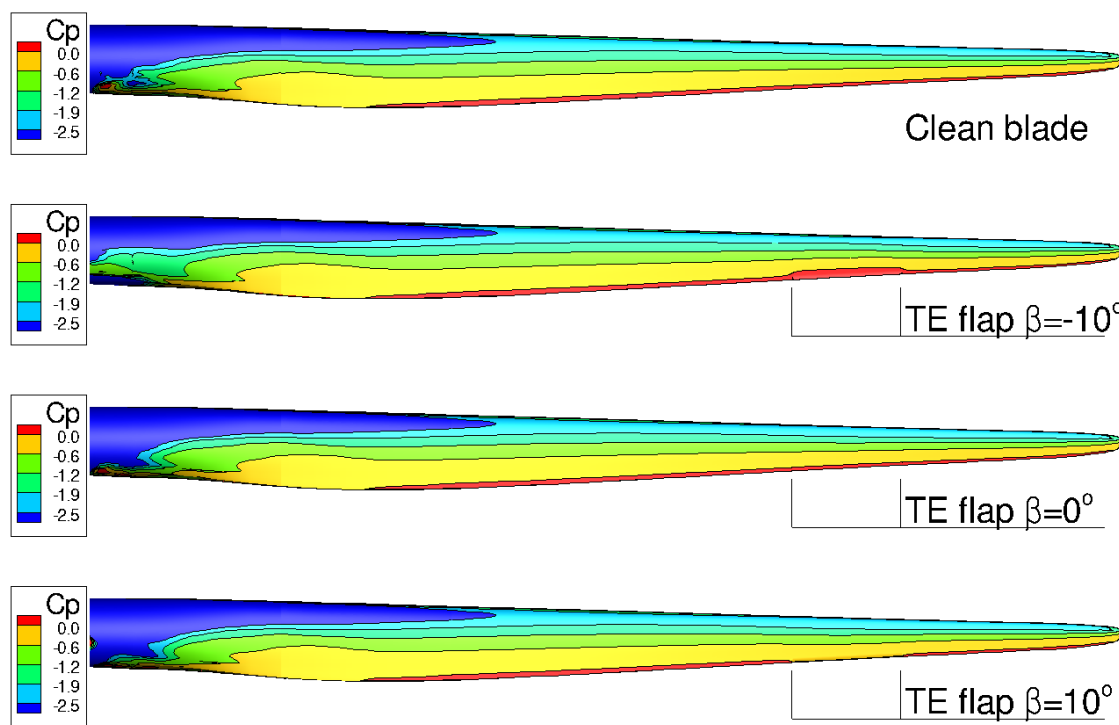


Figure 11.6: Pressure coefficient distribution around the aerofoil section in the middle of the TE flap for different angles of deflection β .



(a) Pressure side.



(b) Suction side.

Figure 11.7: Pressure coefficient distribution around the blade with the TE flap for different angles of deflection β - pressure side (a), and suction side (b).

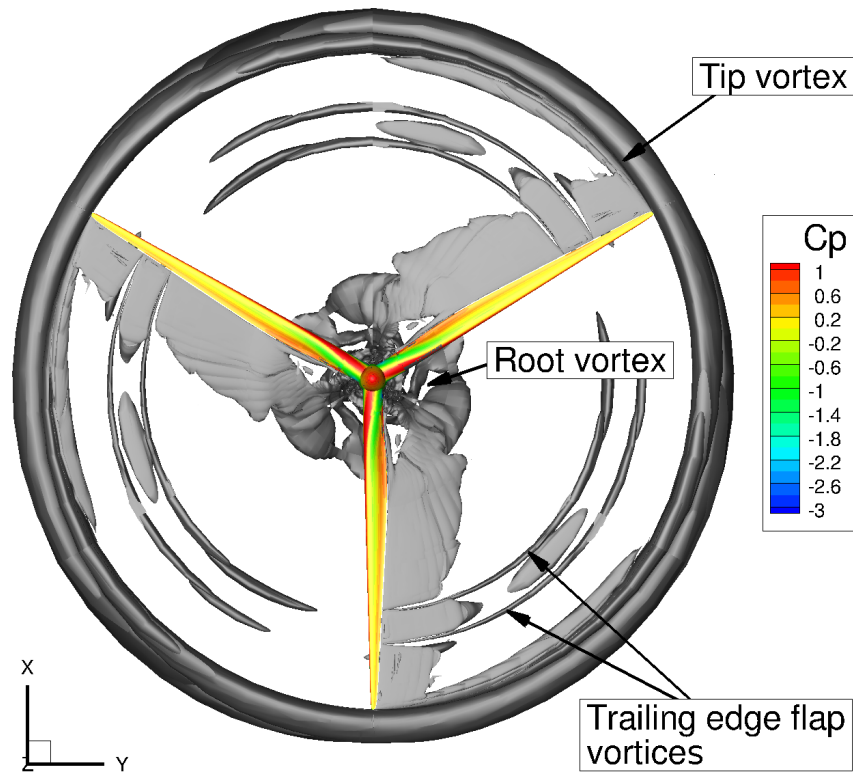
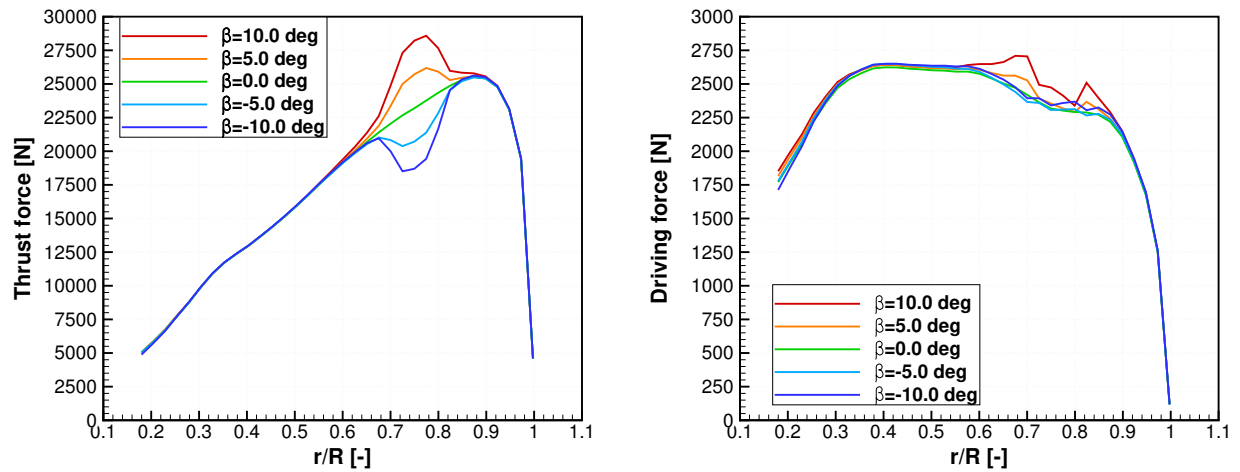


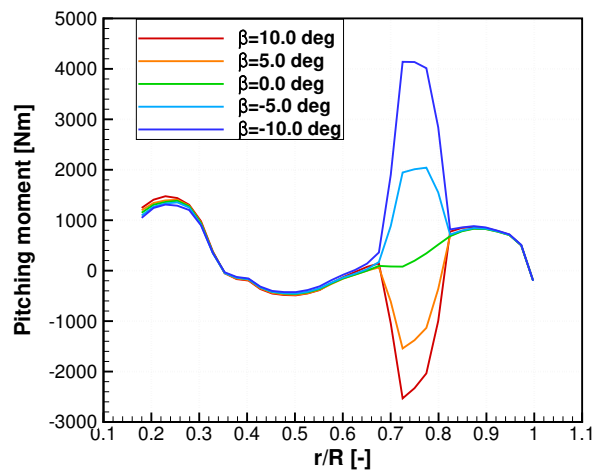
Figure 11.8: Instantaneous vortices visualised with the iso-surfaces of $Q = 0.02$ criterion. The TE flap case with $\beta = 10^\circ$.

observed for the computed test case. Further, the TE flap can modify the thrust force and pitching moment, whereas the driving force is much less affected. This indicates that the positive effect of changing thrust force (for instance to control flap-wise bending, or for elimination of the adverse effect of the blade passing in front of the tower) comes with undesired change in the pitching moment. Hence, stronger pitch bearings, and perhaps also actuators, should be considered, when the TE flaps are employed.



(a) Distribution of thrust force.

(b) Distribution of driving force.



(c) Distribution of pitching moment.

Figure 11.9: Span-wise distribution of thrust force (a), driving force (b) and pitching moment (c) for DTU 10-MW blade equipped with TE flap. Flap motion frequency $f = 0.96\text{Hz}$ (6 times per revolution).

11.4.2 Results for the LE flap

The distributions of the pressure coefficient C_p in the middle of the LE flap, and for different angles of deflection β are shown in Figure 11.10. Significant changes of the pressure at the front of the aerofoil can be observed, with the maximum C_p variation from 2 to almost 3.5. This variation is larger, as compared to the trailing edge flap case. However, the distribution of the C_p at the rear part of the aerofoil (in range between $0.6c - 1.0c$) is almost constant. This is in contrast with the trailing edge flap, where the whole length of the aerofoil section was affected by the flap deflection. Note that the TE flap employed in this work is two times shorter than the LE flap. This indicates that the TE flap is more aerodynamically efficient. A direct comparison of the force coefficients is provided in the next section. The deflection of the LE flap shifts the stagnation point, as can be seen by comparing Figures 11.10(a), 11.10(c) and 11.10(e). The negative deflection shifts the stagnation point towards the trailing edge, and a positive deflection shifts it towards the leading edge. The opposite can be seen for the suction peak, where negative deflection shifts the peak towards the leading edge, whilst positive angles β shift the peak towards the trailing edge of the aerofoil section. However, the suction peak is always increased, regardless of the sign of deflection. This is due to the increase of curvature of the aerofoil at the leading edge in both cases. Interestingly to note here that the flow must pass around the leading edge for $\beta = -10^\circ$, hence, increasing the suction peak even more. This results in increased lift for negative deflections, as opposed to decrease of lift for the same deflection of the TE flap. This observation is confirmed in the following section, where the normal force coefficients are compared. Also, for angle of deflection $\beta = 0$, computed C_p distribution is very close to the one obtained for the case without flaps. This indicates that the flow was able to adapt almost instantly to the change of the surface, which is in contrast to the TE flap case. Indeed, much smaller hysteresis loops were observed in the analysis of non-dimensional coefficients in Section 11.4.3.

The distributions of the pressure coefficient around the whole blade are shown in Figure 11.11. The change of pressure due to the flap deflection is less visible here, as compared to the TE flap case. The change of pressure at the root of the blade is caused by the root vortex, which is similar to what was observed for the previous case. However, vortices created by the leading edge flap deflection are less pronounced and dissipated faster, as compared to the TE flap case. The instantaneous vortices visualised with the iso-surfaces

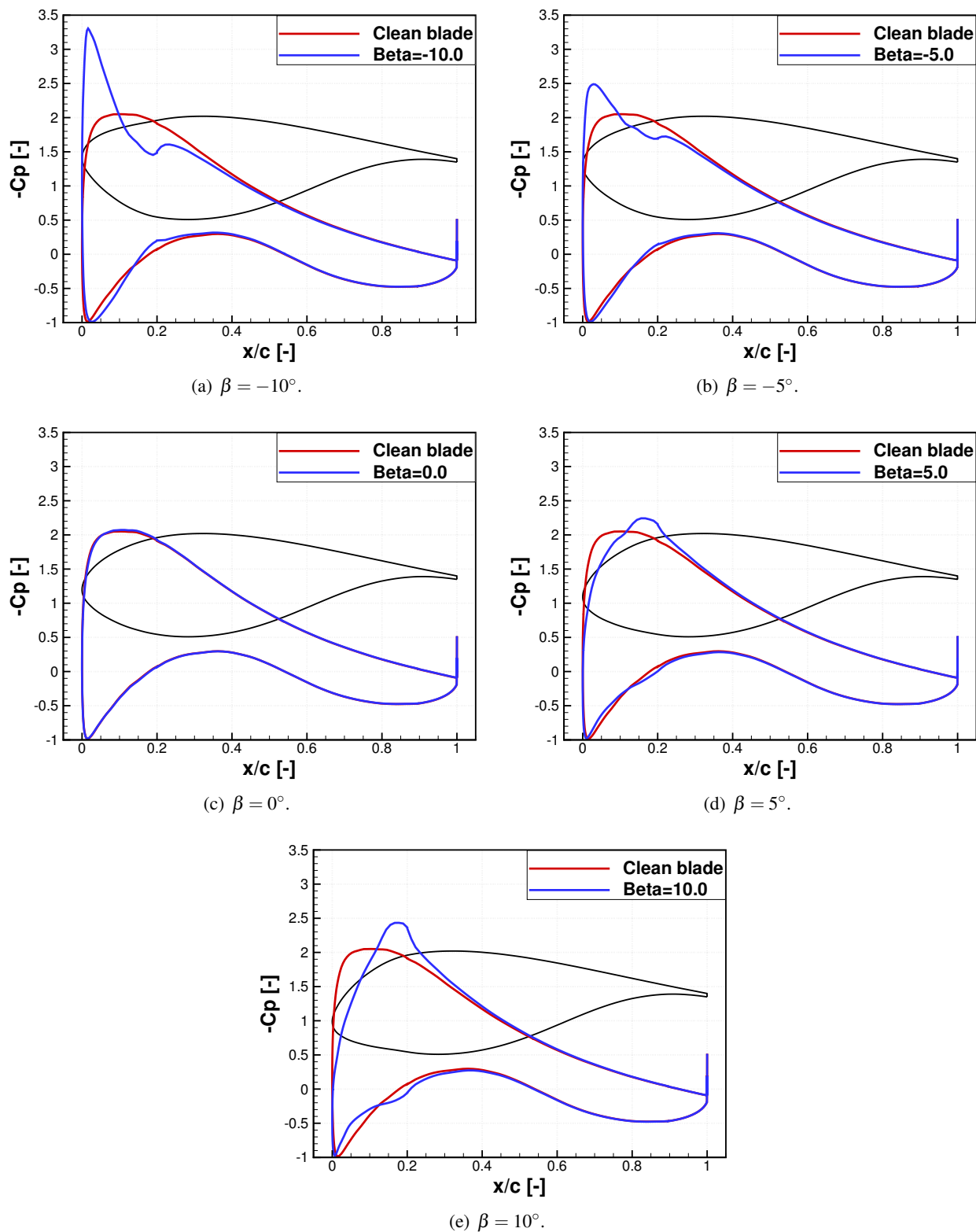
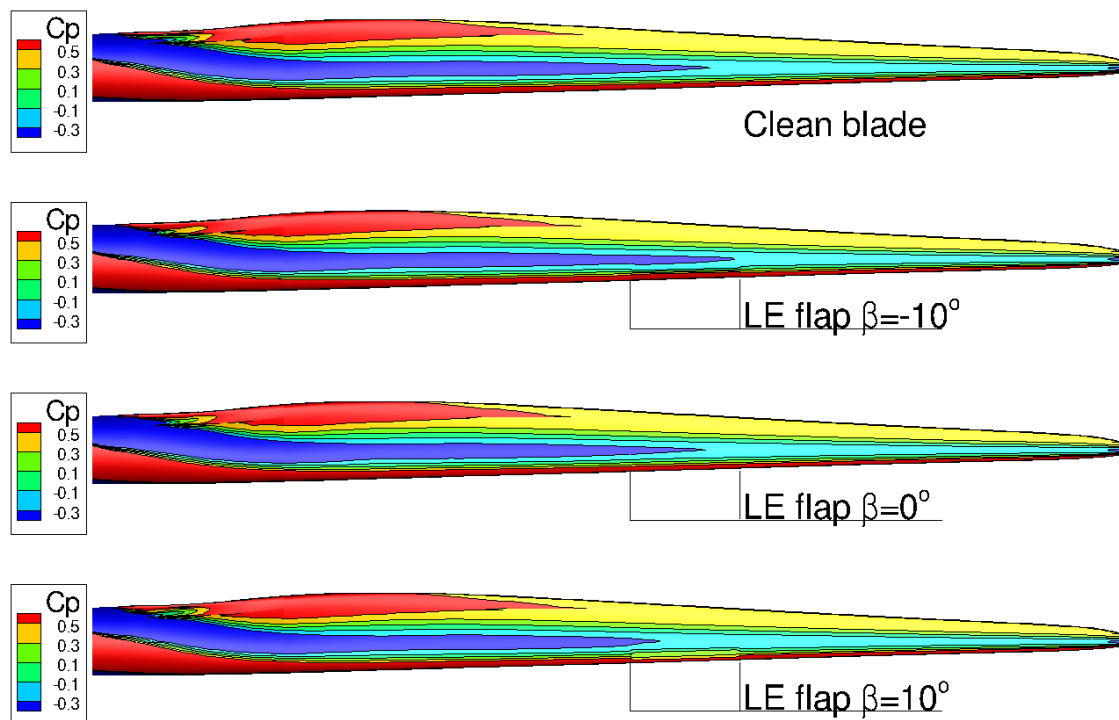
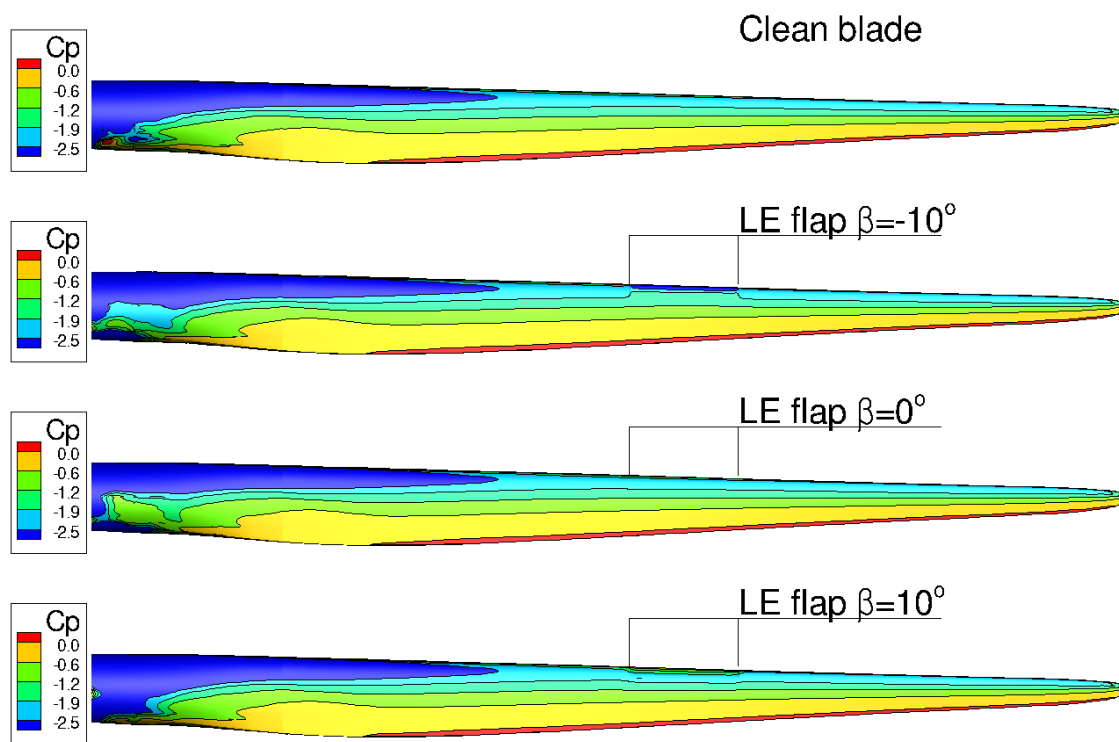


Figure 11.10: Pressure coefficient distribution around the aerofoil section in the middle of the LE flap for different angles of deflection β .



(a) Pressure side.



(b) Suction side.

Figure 11.11: Pressure coefficient distribution around the blade with the LE flap for different angles of deflection β - pressure side (a), and suction side (b).

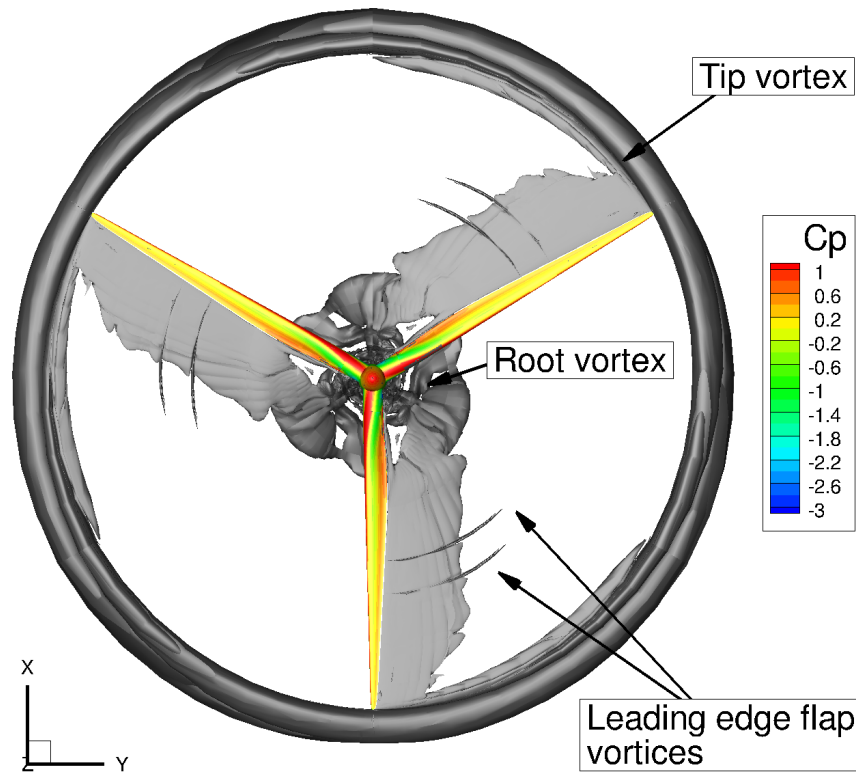
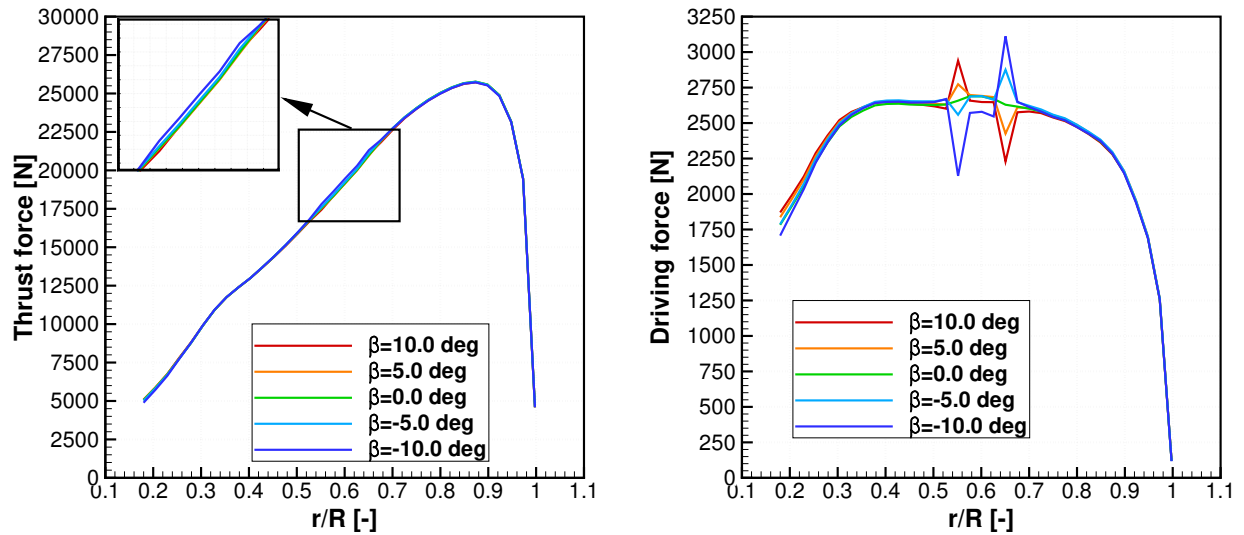


Figure 11.12: Instantaneous vortices visualised with the iso-surfaces of $Q = 0.02$ criterion. The LE flap case with $\beta = 10^\circ$.

of Q criterion are shown in Figure 11.12. As can be seen, the vortex sheet behind the blunt trailing edge of the blade is largely unaffected by the LE flap, which is in contrast to the observations made for the TE flap case.

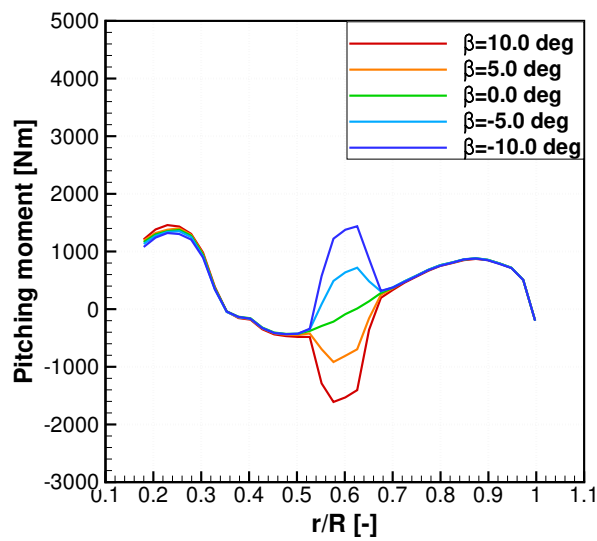
The distribution of forces was obtained by integrating the pressure from root to tip of the blade. These are presented in Figure 11.13, where the length of each section in the radial direction used in pressure integration is $\Delta r = 2.15m$. Similarly to the TE flap case, the LE flap deflection had a localised effect on the distribution of the loads. As can be seen, the thrust force was barely affected by the LE flap deflection. The driving force was influenced by the flap, but the change was towards both sides (negative and positive change at either ends of the flap), resulting in a similar force integral over the blade. Note that this apparent discontinuity stems from the number of points used for integrating the loads in span-wise direction. Further, the most significant change was observed in the pitching moment. This indicates that the LE flap can be used in conjunction with the TE flap to counter the additional pitching moment created by deflection of the trailing edge flap. Finally, the variation of $9.8kN$ in the thrust force, and $90.3kW$ in the power with respect

to the "clean" blade were observed for the LE flap case, which is much less than what was obtained with the TE flap.



(a) Distribution of thrust force.

(b) Distribution of driving force.



(c) Distribution of pitching moment.

Figure 11.13: Span-wise distribution of thrust force (a), driving force (b) and pitching moment (c) for DTU 10-MW blade equipped with LE flap. Flap motion frequency $f = 0.96\text{Hz}$ (6 times per revolution).

11.4.3 Comparison of the performance

To conduct a meaningful comparison of the performance of both flaps, the non-dimensional coefficients were used. This was chosen, since flaps are located at different radial position and exhibit different inflow conditions. For this, the normal force coefficient (C_N), tangential force coefficient (C_T) and pitching moment coefficient (C_M) were computed. First, the thrust and driving forces were projected on the normal and tangential directions using local geometrical pitch angle α as:

$$F_N = T_F \cdot \cos(\alpha) + D_F \cdot \sin(\alpha), \quad (11.2a)$$

$$F_T = D_F \cdot \cos(\alpha) - T_F \cdot \sin(\alpha), \quad (11.2b)$$

where T_F denotes the thrust force, and D_F denotes the driving force. These forces are defined in Fig-

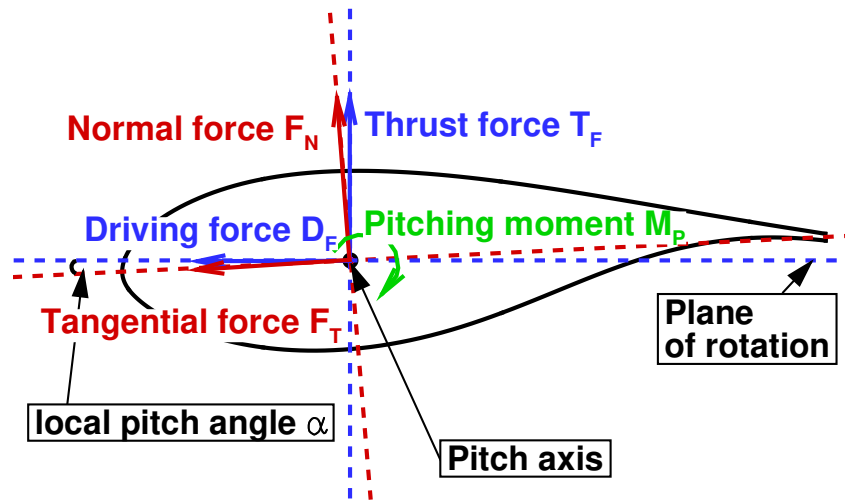


Figure 11.14: Definition of the normal force, tangential force and pitching moment. Quantities shown in the directions defined as positive.

ure 11.14, and were obtained from the surface pressure integration in the middle of the flap with the length of the section in radial direction $\Delta r = 2.15m$. Note that the geometrical pitch angle α is constant i.e. it does not change with the flap angle β . Then, the forces and moment were non-dimensionalised as:

$$C_N = \frac{F_N}{0.5\rho U^2 A}, \quad (11.3a)$$

$$C_T = \frac{F_T}{0.5\rho U^2 A}, \quad (11.3b)$$

$$C_M = \frac{M_P}{0.5\rho U^2 A c}, \quad (11.3c)$$

where U and A are the geometrical local inflow velocity, and the local planform area, respectively. The inflow velocity is defined as $U^2 = (\omega r)^2 + U_{wind}^2$, and the planform area is defined as $A = \Delta r \cdot c$, where c is the local chord in the middle of the flap.

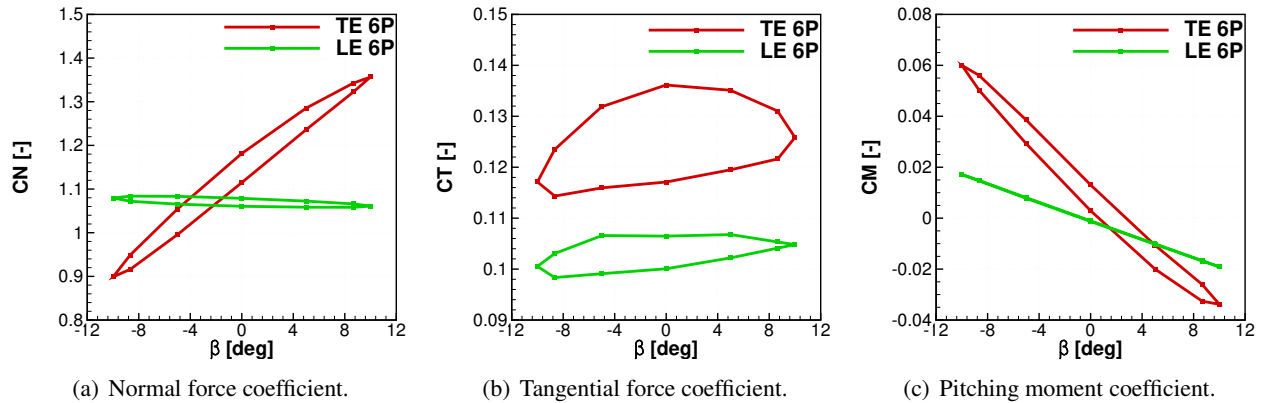


Figure 11.15: Comparison of the performance of TE and LE flaps based on the non-dimensional coefficients as function of flap deflection angle β .

The obtained coefficients for both flaps as functions of the flap angle β are compared in Figure 11.15. As can be seen, the trailing edge flap significantly modifies all three non-dimensional coefficients. On the other hand, the leading edge flap has the most pronounced effect on the pitching moment coefficient, and almost negligible (as compared to the TE flap) influence on the normal force coefficient. Also, the slope of the normal force coefficient has opposite sign for both flaps. This means that for positive angles β the lift is increased for the TE flap, and decreased for the LE flap. This confirms the observations made in previous sections. Further, the relative change and slope of the pitching moment coefficient is higher for the trailing edge flap. This indicates that the LE flap should either be larger in size, or experience larger deflection, such that it can produce similar change in the pitching moment to the TE flap. Finally, both flaps can change the tangential force coefficient, but the TE flap has higher hysteresis loop, as compared to the results for the LE flap. This was also indicated based on the pressure coefficient distributions. Overall, the results are in line with the potential flow theory, where the TE flap is more efficient than the LE flap for all other conditions being equal.

Chapter 12

Forced oscillations of DTU 10-MW

Reference Wind Turbine¹

The possibility of a wind turbine entering vortex ring state during pitching oscillations is investigated in this chapter. Forced yaw and pitch oscillations of the DTU 10MW RWT were computed, suggesting that partial vortex ring state may be encountered during pitching. The results also show the strong effect of the frequency and amplitude of oscillations on the wind turbine performance.

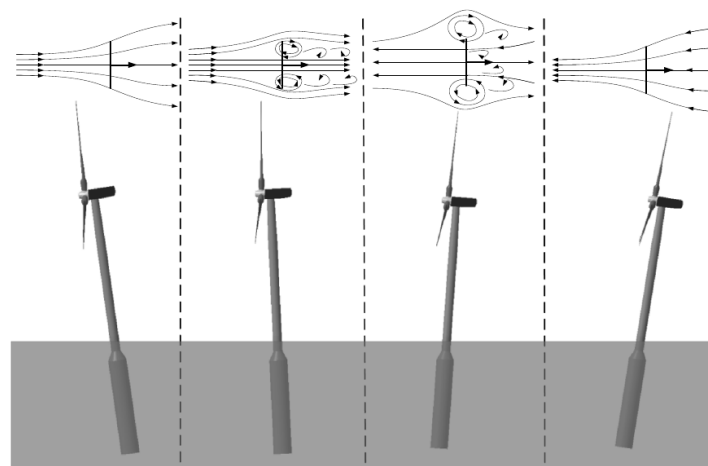


Figure 12.1: Hypothetical flow states of FOWT during pitching motion. From left to right: windmill state, turbulent wake state, vortex ring state and propeller state. Adapted from ^[196].

¹ This work was published in Leble and Barakos^[112].

The motivation for this work is that the FOWT will be subjected to the pitching motion during operation^[91, 97, 111], where the amplitude of motion is dependent on many parameters, including the roughness of the sea, wind speed, support structure, and mooring cables. Hence, the FOWT may operate in various aerodynamic flow states, including windmill, propeller and transient states too. Figure 12.1 shows the hypothetical flow states of the FOWT during a forced pitching motion. Normally, a wind turbine will operate in the windmill state, extracting energy from the flow field. Excessive pitching motion of the FOWT may lead to a rapid change of the effective wind speed and tip speed ratio. In extreme cases, the rotor may also behave like a propeller. This potential cycling between the windmill and propeller states during pitching motion, and the intermediate flow conditions, poses operational and modelling challenges for FOWTs.

The assumptions of the simplified models, which are often used for FOWTs modelling, do not always hold for the complex aerodynamic flow states that can be encountered. For instance the assumptions of BEM and GDW models are violated when the wind turbine undergoes large pitching motion^[179, 195]. Therefore, very recent works employed Navier-Stokes CFD solvers to study pitching wind turbines^[195, 196]. Considerable differences were reported between predictions of BEM, GDW and URANS CFD methods.

Further, contradictory findings were reported in the open literature. For instance, Madsen *et al.*^[128] reported good agreement between the BEM method and URANS CFD computations in terms of power for yawed configuration. The work of Sant and Cuschieri^[172] reported large differences between the power production obtained with BEM, and GDW or FVM aerodynamic models. On the other hand, Tran and Kim^[195] concluded that GDW model agrees better with URANS CFD results than with the BEM model. This shows the need for further research for yawing and pitching wind turbines.

In view of the above, the purpose of this chapter is to present results of numerical computations for a 10-MW wind turbine undergoing prescribed pitching and yawing motions. These results can be used in the future to improve engineering models for FOWTs application.

12.1 Test cases

First, the NREL Phase VI^[70] wind turbine was employed due to available test data at yaw. Three test cases were considered, and the results were compared to experiments^[70].

Next, the DTU 10-MW reference wind turbine (RWT) ^[11] was studied. The test cases presented in this chapter concern the wind turbine with constant yaw misalignment, and with sinusoidal yawing and pitching motions. The inflow was considered uniform for those cases, and the blades were assumed rigid. The list of all test cases is shown in Table 12.1.

Table 12.1: Description of presented test cases.

Name	Wind Turbine	Configuration	Angle/Amplitude	Period	Inflow	Blades
N0	NREL	Aligned	0°	-	Uniform	Rigid
N1	NREL	Fixed Yaw	10°	-	Uniform	Rigid
N2	NREL	Fixed Yaw	30°	-	Uniform	Rigid
Y1	DTU	Fixed Yaw	-3°	-	Uniform	Rigid
Y2	DTU	Fixed Yaw	3°	-	Uniform	Rigid
Y3	DTU	Sinusoidal Yaw	3°	8.8s	Uniform	Rigid
P1	DTU	Sinusoidal Pitch	3°	8.8s	Uniform	Rigid
P2	DTU	Sinusoidal Pitch	5°	8.8s	Uniform	Rigid

12.1.1 NREL Phase VI wind turbine

The HMB3 flow solver was first validated against the experimental data for the NREL Phase VI wind turbine^[70] with yaw misalignments. That wind turbine was stall-regulated and had a power rating of 20 kW. The blade was made entirely of the S809 aerofoil^[187] with relative thickness of 21%. It had non-linear distribution of the twist and linear distribution of the chord. The rotor diameter was 11m, and the wind turbine operated at a wind speed of 7m/s with a rotational speed of 72rpm resulting in tip speed ratio $\lambda = 5.45$. The detailed description of the NREL Phase VI wind turbine can be found in Section 7.1 of Chapter 7.

Grid and computational parameters

The NREL Phase VI rotor was modelled including a hub, but without the tower, tunnel walls and instrumentation boxes^[70]. The grid consisted of 9.3M cells, giving about 4.6M cells per blade. The normal distance of the first cells in the blocks adjacent to the blade surface was $1 \cdot 10^{-5}c$, where c is a maximum chord of the blade, 0.737m. Based on the free-stream condition and the size of the first cell, the y^+ parameter was $y^+ = 0.2$. The first layer consisted of 34 cells in the normal direction to the blade surface, and 204 cells were distributed around the aerofoil section. The blade surface was resolved with 139 cells along the span. The tip

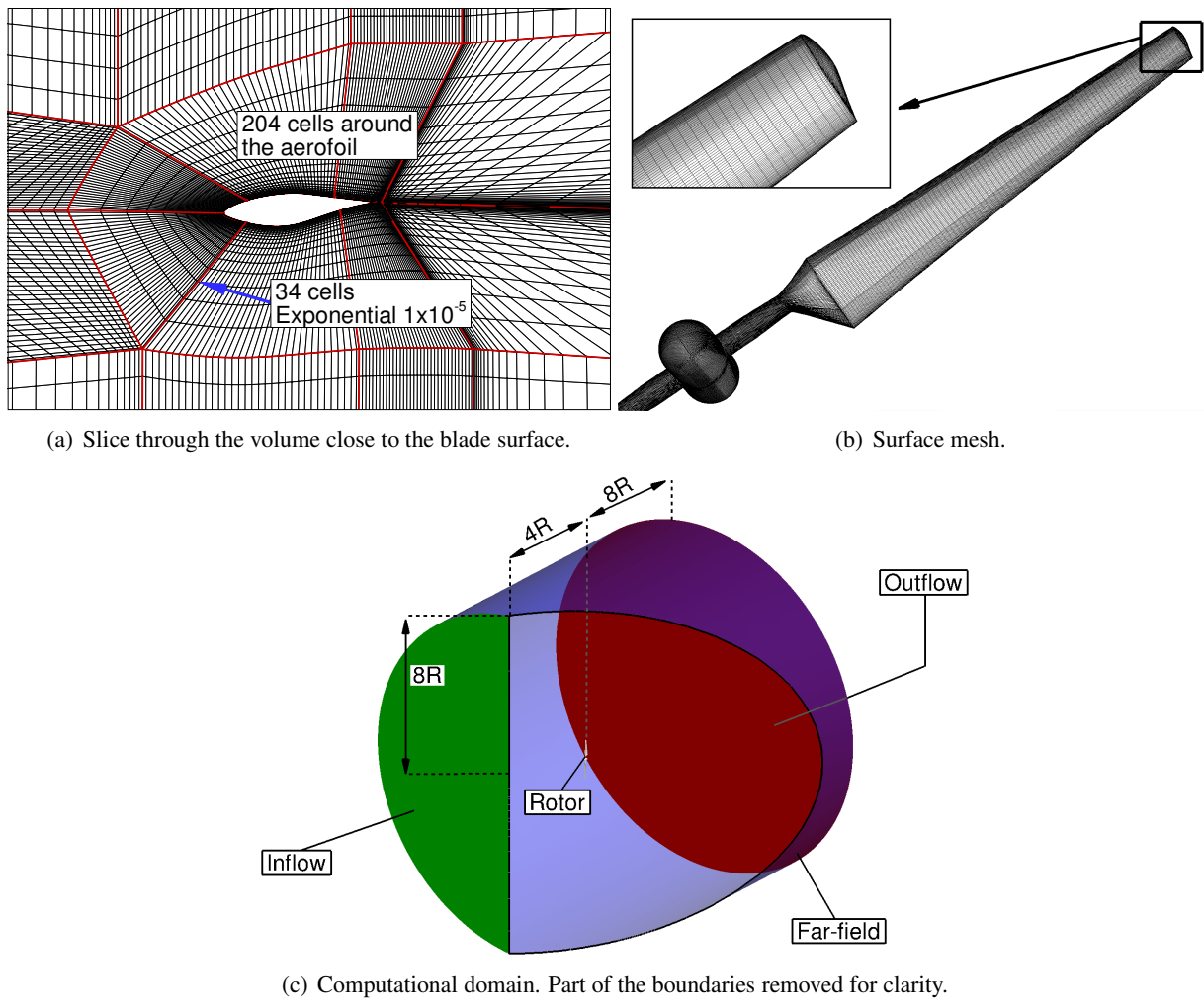


Figure 12.2: Grid employed for the NREL Phase VI rotor without the tower - (a) slice through the volume and (b) surface mesh, and (c) computational domain.

of the blade was rounded, and represented an approximation to the actual shape since the exact tip shape is not defined in the reports of NREL^[70]. An inflow boundary condition was placed four blade radii upstream of the rotor, and the outflow was placed eight blade radii downstream. The far-field was assigned eight blade radii away from the centre of rotation. The computational domain with the corresponding boundaries, a slice through the mesh close to the blade surface, and the surface mesh of the blade are shown in Figure 12.2. The free-stream was kept to the level of turbulence of 2.6% allowing fully turbulent flow simulations, and the $k - \omega$ SST^[137] turbulence model was employed. The time step employed for the unsteady computations was chosen such that rotor performs one degree of revolution per step, resulting in $\Delta t = 2.3 \cdot 10^{-3} s$. The same time step was used for this wind turbine by Li *et al.*^[122].

12.1.2 DTU 10MW reference wind turbine

The DTU 10MW RWT^[11] rotor in the pre-bent and pre-coned configuration was also employed in this chapter. The rotor diameter was $178.3m$, and the wind turbine operates at a wind speed of $11m/s$ with a rotational speed of $8.836rpm$, resulting in the tip speed ratio $\lambda = 7.5$. The blades have a pre-coning of 2.5° and nonlinear pre-bending with $3.3m$ displacement at the blade tip. The detailed description of the DTU 10MW RWT can be found in Section 9.1 of Chapter 9.

Grid and computational parameters

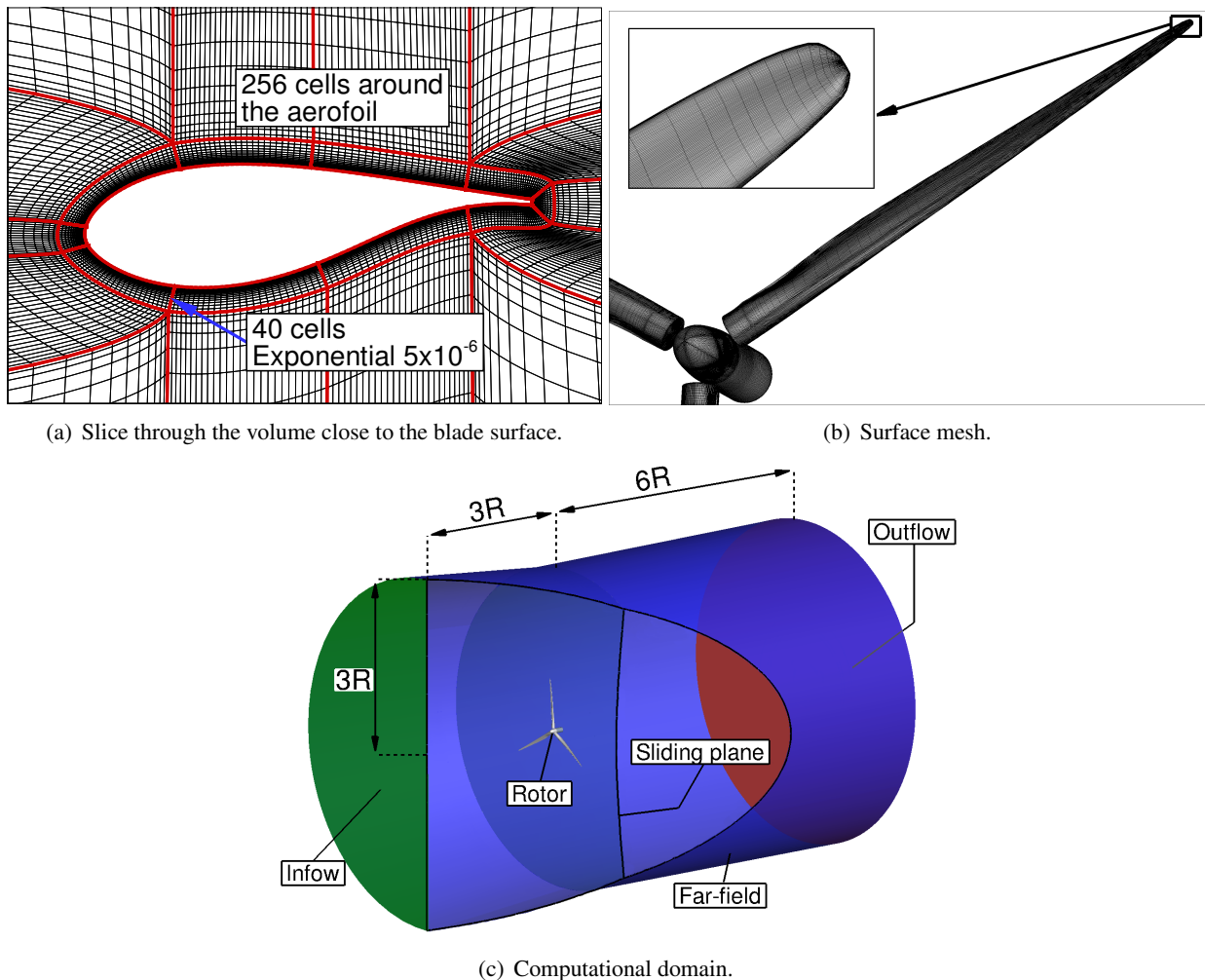


Figure 12.3: Grid employed for the DTU 10MW RWT rotor without the tower - (a) slice through the volume, (b) surface mesh, (c) computational domain.

The DTU 10MW RWT rotor was modelled including the nacelle, but without the tower. As was

shown in Section 10.4 of Chapter 10, the presence of the tower affects the aerodynamic loads. Here, the aim is to reduce the complexity of the flow, and show purely the effects due to the motion in yaw and pitch. Hence, the tower was excluded, and the same grid as in Section 10.3 of Chapter 10 was employed in this chapter. The grid consisted of 16.1M cells, giving 5.4M cells per blade. This grid density is adequate for the studied wind turbine, as was shown in Section 9.3 of Chapter 9. Also, a similar work of Tran and Kim [196] employed 6M cells grid for 5MW wind turbine. The domain consisted of the rotor that was attached to the nacelle through a sliding mesh plane [193]. Based on experience [28], an inflow boundary condition was placed three blade radii upstream of the rotor, and outflow was placed six blade radii downstream. The far-field was assigned three blade radii from the centre of rotation. The computational domain with the corresponding boundaries, a slice through the mesh close to the blade surface, and the surface mesh of the blade are shown in Figure 12.3.

Similarly to the NREL Phase VI wind turbine cases, the free-stream was kept to the level of turbulence of 2.6%, and the $k - \omega$ SST [137] turbulence model was employed. The time step for the unsteady computations was set to $\Delta t = 1.8 \cdot 10^{-2}s$, and corresponds to the time required for rotor to perform one degree of revolution. Work of Tran and Kim [196] employed 2.0 degree increment of azimuth angle, and 3.0 degree increment was used by Sayed *et al.* [174].

12.2 Results and discussion

12.2.1 NREL Phase VI wind turbine

Three yaw angles were investigated for the NREL Phase VI wind turbine, these were 0° , 10° and 30° yaw misalignment cases (N0, N1 and N2 respectively in Table 12.1). The pressure measurements were affected by the wake of the instrumentation [70] as shown in Figure 12.4. This was taken into account by comparing the distributions of the pressure coefficient at azimuth angle of 270° , as indicated in Figure 12.4(b). The experimental data represent the average values as were measured for the same azimuth angle over multiple consecutive revolutions, and the error bars represent the minimum and maximum values. On average, 35 revolutions were measured for each case [70].

The results for 0° yaw misalignment in form of the surface pressure coefficient distributions at var-

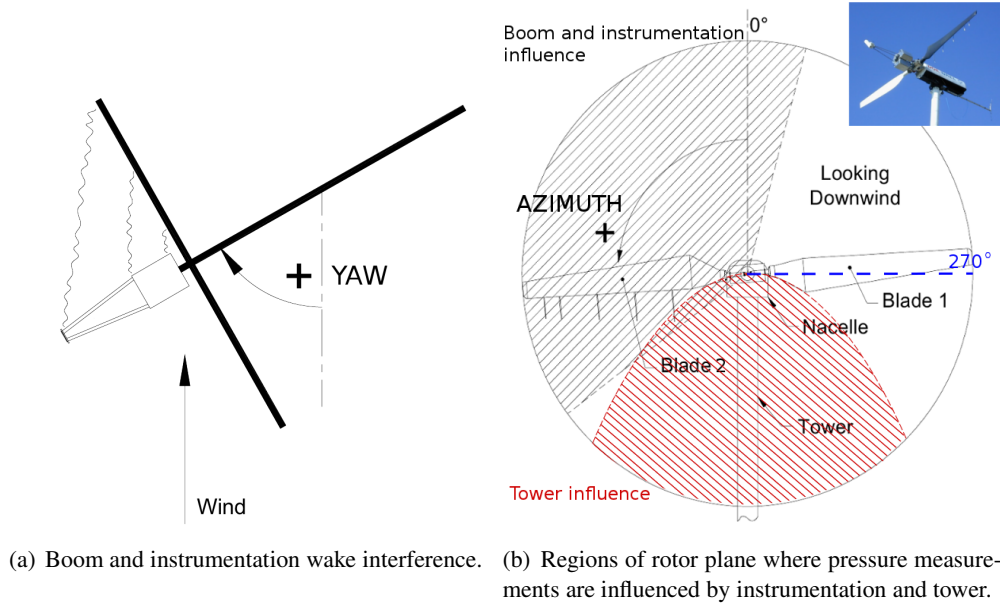


Figure 12.4: Regions of instrumentation and tower influence on measured pressure. Definitions of positive yaw and azimuth angles are also included. Figures adapted from [70].

ious radial stations along the blade are shown in Figure 12.5. Good agreement between the measured and computed pressure can be seen.

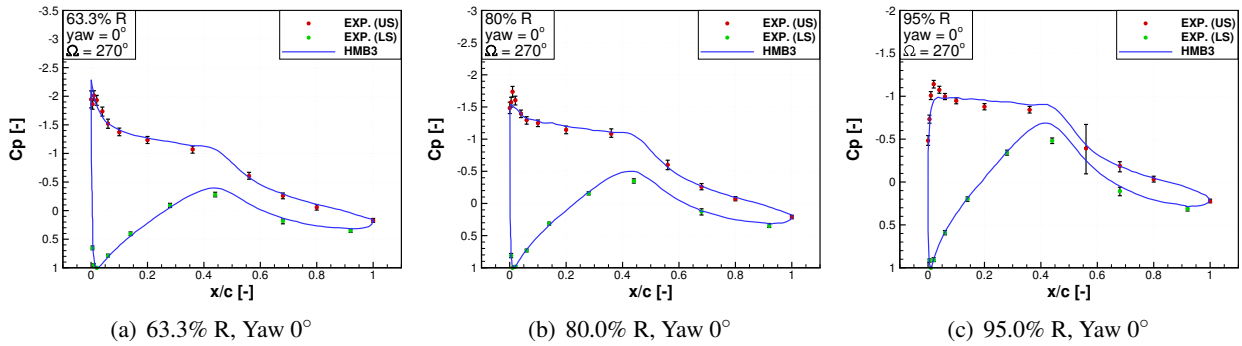


Figure 12.5: Comparison between experimental data and C_p values at various span-wise station for aligned case.

The results for 10° and 30° yaw misalignments are shown in Figure 12.6 and 12.7, respectively. The agreement with the experimental data for those cases is not as good as for the aligned rotor. However, the agreement is not deteriorated as the yaw angle is increased from 10° to 30° . This indicates the source of the discrepancies in yawed flow. The reason can be attributed to the combined effect of the instrumentation, tower and tunnel walls present in the experimental set-up.

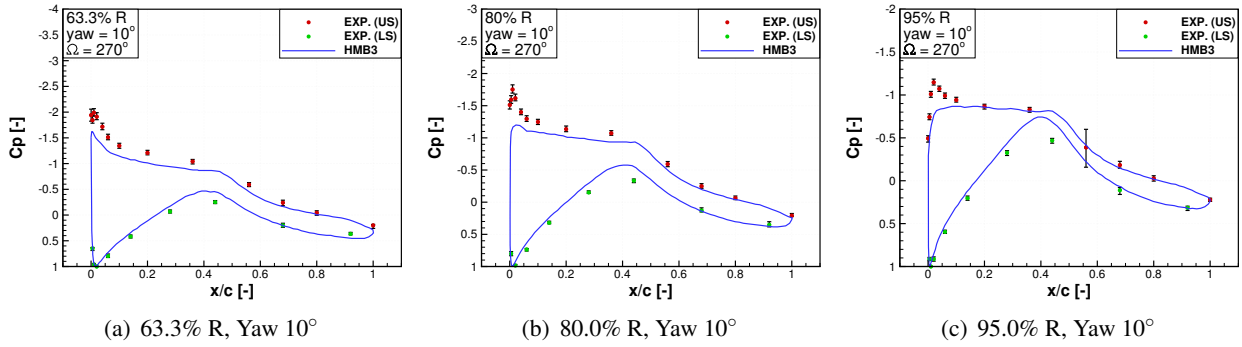


Figure 12.6: Comparison between experimental data and C_p values at various span-wise station for 10° yaw misalignment.

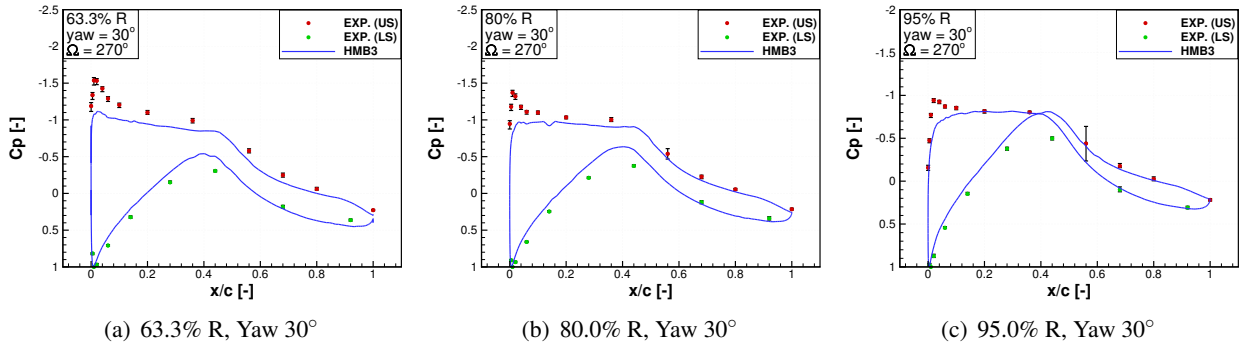


Figure 12.7: Comparison between experimental data and C_p values at various span-wise station for 30° yaw misalignment.

12.2.2 Static and dynamic yawing of DTU 10MW reference wind turbine

This section presents the results obtained for DTU 10MW reference wind turbine with static and dynamic yaw misalignments. First, the comparison of the aligned and static yaw cases is performed in this section. This involves comparison of the aligned case from Section 9.4.2 of Chapter 9, and fixed yaw case of 3° (Y2 in Table 12.1). Next, the sinusoidal yawing case Y3 with yaw amplitude $A = 3^\circ$ and period $T_{yaw} = 8.8s$ is compared to the fixed yaw cases Y1 and Y2. The frequency of motion was chosen based on the most probable frequency of the sea waves for the wind speed of $11m/s$ [116].

The employed notation for yaw angles is shown in Figure 12.8(a). Positive yaw angle corresponds to a reduced inflow angle for the blade at 12 o'clock or 0° of azimuth. Contrary, the blade at 180° of azimuth has increased inflow angle for positive yaw.

The results for the fixed yaw case are shown in Figure 12.8(b). The periodic variation of thrust and power with the blade passing frequency is evident, and is caused by the advancing and retreating blade

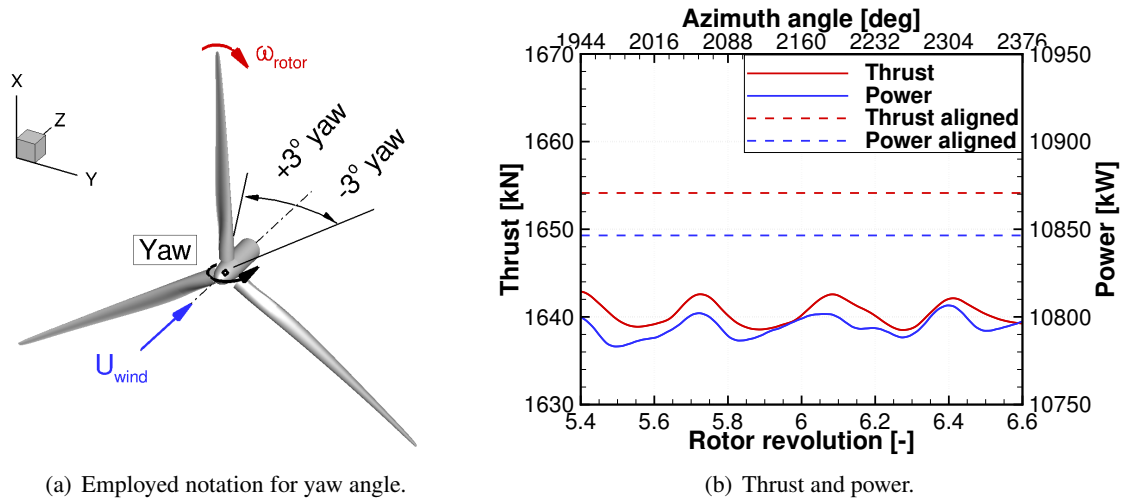


Figure 12.8: Fixed yaw test cases: employed notation for yaw angles (a), and thrust and power as function of the rotor revolution (b).

effect^[175]. To be more specific, the blade is advancing in the upper half plane and retreating in the lower half plane with respect to the in-plane wind component. The results suggest an average reduction of thrust by 0.8% and power by 0.5% due to the yaw misalignment. As was shown in previous chapters, the elasticity and atmospheric boundary layer have much stronger effect on the power production, than static yaw of 3° . This agrees with observation of Krodstat and Adaramola^[103] that the loss in power output is small (less than 3%) when the yaw angle is less than 10° .

Next, the DTU 10-MW RWT was forced to a yawing motion about a mean angle of 0° . The yaw amplitude was set to $A = 3^\circ$, and the period of oscillation was $T_{yaw} = 8.8s$. Power history results are shown in Figure 12.9, where a periodic variation with the frequency of yawing is clearly visible. In this case, the frequency of rotation does not coincide with the frequency of yawing motion. This results in the asymmetries observed in Figure 12.9 due to the advancing and retreating blade effect^[175]. Further, the power obtained for the fixed yaw cases is presented in Figure 12.9(b) for comparison. The power variation with the yaw angle α may be approximated by $P(0^\circ) \cos^x(\alpha)$, given that the yaw angle is fixed for each point^[25]. The exponent x is often thought to be equal to 3. Experimental evidence suggests that the exponent x may vary between 1.8 and 5^[175]. Recent wind tunnel measurements shown that the curve based on $x = 3$ follows well measured data^[103]. In this case, the exponent $x = 3$ shows good agreement with the computed power loss for fixed yaw misalignments, as can be seen in Figure 12.9(b). The error bars indicate the minimum and

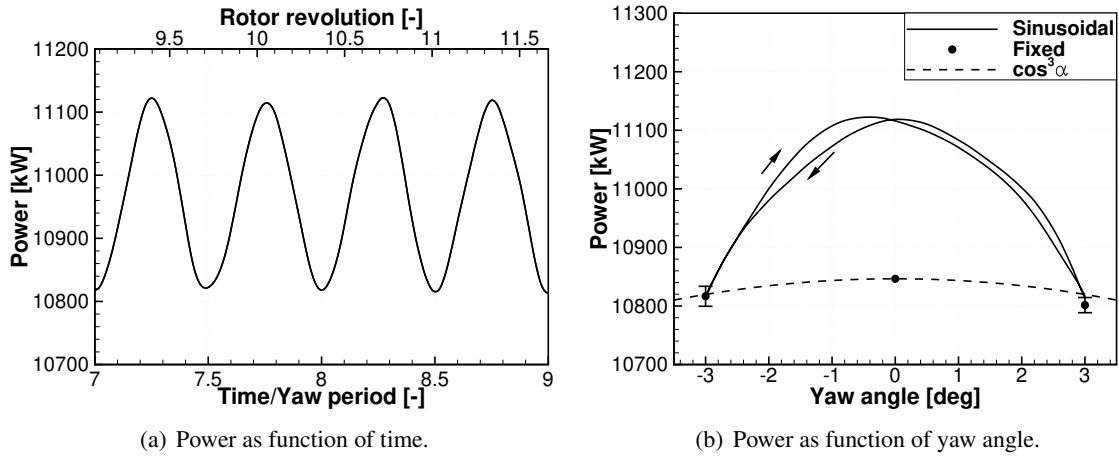


Figure 12.9: Power as function of time (a) and yawing amplitude (b).

maximum value over the revolution.

The power production agrees between static and dynamic yaw cases for the maximum yaw angles. This is expected result, since the rotor has zero yawing velocity at maximum angle. However, the power variation due to the dynamic yaw motion shows larger amplitude, with the maximum value in the middle of the cycle. The increase in power production is about 2.5%, as compared to the aligned rotor case. This dynamic effect is comparable in magnitude to the effect of elasticity (see Section 10.4 of Chapter 10) and atmospheric inflow (see Section 9.5 of Chapter 9).

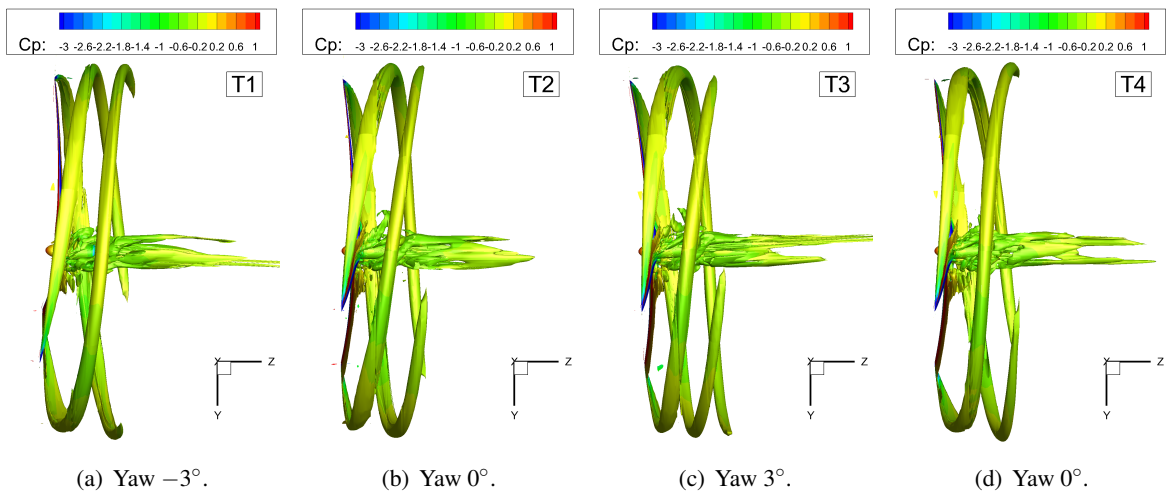


Figure 12.10: Instantaneous vortices visualised with the iso-surfaces of $Q = 0.05$ criterion coloured by the pressure coefficient C_p . Yawing amplitude 3° , and yawing period 8.8s.

Finally, Figure 12.10 shows the wake of the wind turbine at various instances visualised with the iso-surfaces of $Q = 0.05$ criterion. The presented instances correspond to the times shown in Figure 12.11,

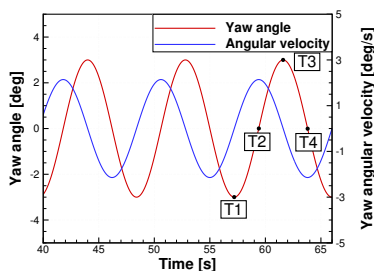


Figure 12.11: Yaw angle and yaw angular velocity as function of time.

where the positive and negative yaw angles are defined in Figure 12.8(a).

12.2.3 Dynamic pitching of DTU 10MW reference wind turbine

In this section, the DTU 10MW RWT rotor was forced to perform a sinusoidal pitching motion about the point located $119m$ below the rotor, what corresponds to the hub height in Bak *et al.*^[11] The pitching amplitude was set to $A = 3^\circ$ for the first test case (Test case P1), and to $A = 5^\circ$ for the second test case (Test case P2). These amplitudes were chosen based on numerical estimates of Jonkman^[91] for 5MW wind turbine. The mean pitch angle was zero degrees, and the period of motion for both cases was set to $T_{pitch} = 8.8s$. The frequency of the pitching motion was chosen based on the most probable frequency of the waves for the wind speed of $11m/s$ ^[116]. The results in terms of thrust and power for both cases are compared in Figure 12.12. They show large variations of the thrust and power. This agrees with the findings presented in ^[195], where a 5MW wind turbine undergoing pitching motion experienced from 0MW to 15MW of instantaneous aerodynamic power. Interestingly, the average thrust for both cases is close to the value obtained without the pitching *i.e.* about $1650kN$ of thrust. However, the mean power is about $12.3MW$ and $14.4MW$ for the pitching amplitudes of 3° and 5° , respectively. This corresponds to an increase of power by 13.4% and 32.8% , as compared to the power output of an aligned rotor not undergoing pitching motion. This variation is significantly larger than the effect of the elastic blades and atmospheric boundary layer inflow. This was anticipated, since energy was delivered to the system through the forced motion.

Figure 12.12(b) shows the thrust and power as functions of the pitch angle, where a hysteresis loop is observed. Figure 12.13 shows the wake of the wind turbine at various instances visualised with iso-surfaces of $Q = 0.05$ criterion. The presented instances correspond to the times shown in Figure 12.14, where

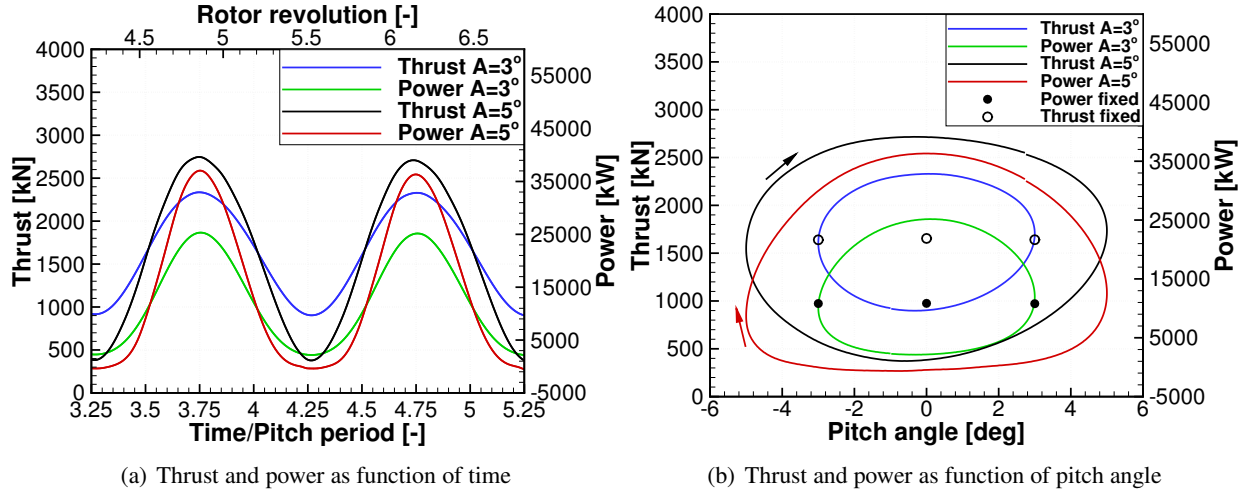


Figure 12.12: Thrust and power as function of time (a) and pitching amplitude (b).

negative pitch angle represents a wind turbine pitching towards the direction of the wind, while positive pitch angle represents the wind turbine pitching away of the wind.

Estimates of the induced velocity v_i were used to show that the wind turbine entered the turbulent wake or the vortex ring states. The induced velocity was estimated from the momentum theory in the applicable range, and the formula of Rand^[166] was used otherwise, leading to the following expression for the rate of induced velocity

$$v_i/v_h = \begin{cases} -\frac{V_c}{2v_h} - \sqrt{\left(\frac{V_c}{2v_h}\right)^2 - v_h^2} & \text{for } V_c/v_h \leq -2 \\ 1 - \frac{V_c}{2v_h} + \frac{25V_c^2}{12v_h^2} + \frac{7V_c^3}{6v_h^3} & \text{for } -2 < V_c/v_h < 0 \end{cases}, \quad (12.1)$$

where v_i is the induced velocity, $v_h = \sqrt{T/2\rho A}$ is the induced velocity in "hover" for the given thrust T and the rotor area A , and V_c is the inflow velocity normal to the rotor plane. The inflow velocity was computed from the wind speed U_{wind} , the linear velocity of the hub in the direction of the wind U_{hub} , and the pitch angle α as:

$$V_c = -(U_{wind} \cos(\alpha) - U_{hub}/\cos(\alpha)), \quad (12.2)$$

where the negative sign of inflow velocity was introduced to agree with the notation used for helicopters^[118, 166]. The results are presented in Figure 12.15. As can be seen, the wind turbine did not encounter a vortex ring state for 3° of amplitude. This agrees with the fluctuations of thrust and power, where variations were almost symmetric with respect to the pitch angle. However, for the second test case ($A = 5^\circ$) the rotor partially entered vortex ring state. The interaction between the blade and tip vortex can be seen in Figure 12.13(h)

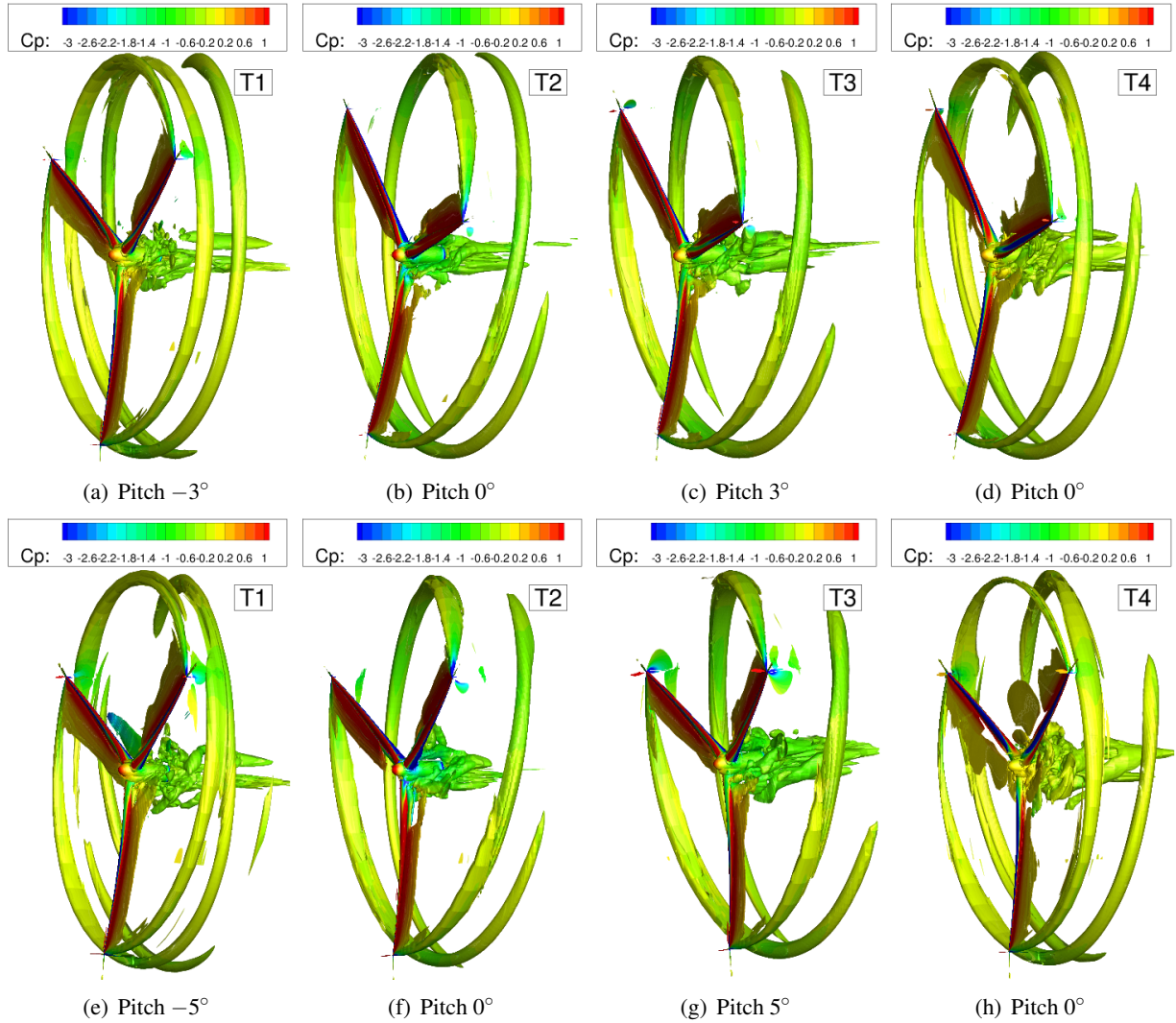


Figure 12.13: Instantaneous vortices visualised with the iso-surfaces of $Q = 0.05$ criterion coloured by the pressure coefficient C_p . Pitching period $8.8s$, pitching amplitude 3° (a-d), and 5° (e-h).

and 12.13(e). A closer look at Figure 12.12(a) shows the asymmetry of the thrust and power for pitch angle of 5° near maximum thrust and minimum power as the pitch velocity changes sign. The comparison of polars in Figure 12.12(b) revealed that the overall shape of the thrust and power with respect to the pitch angle was similar for both cases. The thrust force had a similar expansion towards lower and higher values as the amplitude of motion was increased, therefore maintaining almost the same averaged value (averaged over the cycle). However, the power curves showed a similar low-power part, where the difference in power for both cases was much smaller as compared to the high-power part of the cycle. Although low power output was maintained for a longer part of the pitching cycle, as compared to the high-power part, the power averaged over the cycle increased as the amplitude of motion increased. Finally, the power showed a

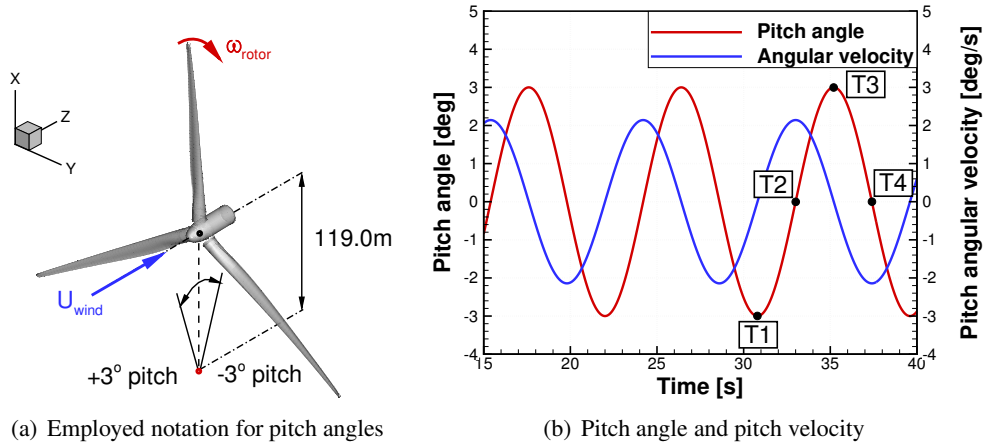


Figure 12.14: Sinusoidal pitch test cases. Definition of the employed notation for pitch angles (a), and (b) the pitch angle and pitch angular velocity as function of time for pitching amplitude 3° .

sharper increase as the turbine transitioned from backward to forward pitching motion. This can be seen in Figure 12.12(b).

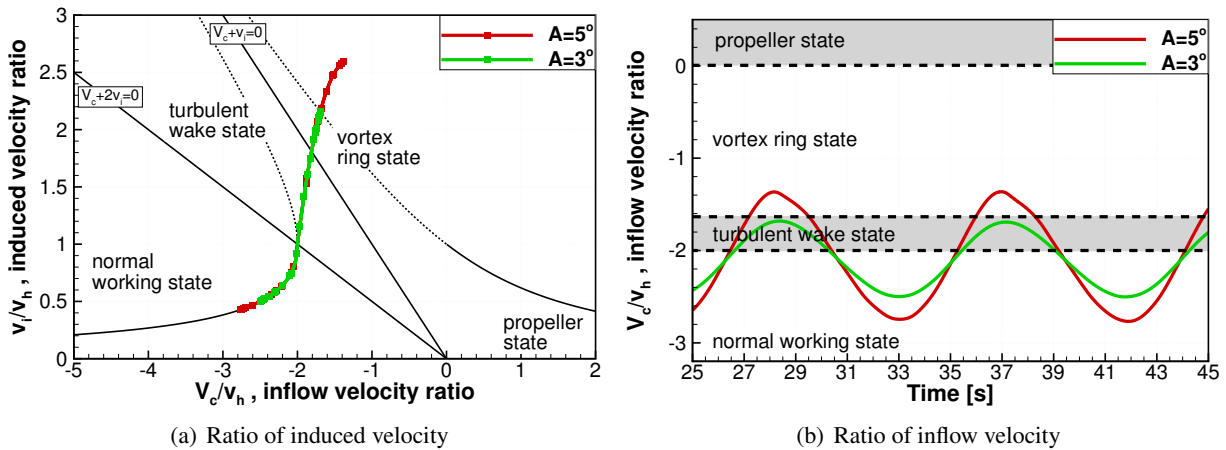


Figure 12.15: Estimated ratio of induced velocity as function of inflow velocity ratio (a), and ratio of inflow velocity as function of time (b) for pitching wind turbines with pitching amplitude of 3° and 5° .

Chapter 13

Coupled computation of floating off-shore wind turbine¹

This chapter presents results of numerical computations for floating off-shore wind turbines. The DTU 10-MW reference wind turbine was employed as an example, and the support platform was introduced to provide sufficient buoyancy. The hydrodynamic loads on the support platform were computed using the Smoothed Particle Hydrodynamics method, details of which are presented in Chapter 2. The aerodynamic loads on the rotor were computed using the Helicopter Multi-Block flow solver introduced in Chapter 3. Further, a Multi-Body Dynamic Model of rigid bodies and frictionless joints was used to compute the motion of the floating offshore wind turbine. Mooring cables were modelled as a set of springs and dampers following the force-displacement approach. As was shown in Chapters 6, 7, and 8, all solvers were validated separately before coupling, and the importance of coupling is assessed in Chapter 5. Here, the employed loosely coupled algorithm is described. The details of the numerical domains and computational parameters are given in this chapter, alongside the obtained results.

¹ This work was published in Leble and Barakos^[111].

13.1 Coupling scheme

In the present work, a weakly coupled approach is employed, namely the parallel, conventional, staggered method of Figure 13.1. Both solvers are advancing with different but constant time steps. The SPH solver employs a time step of $\Delta t_{SPH} = 2 \cdot 10^{-4} s$ with $CFL = 0.2$, whereas HMB3 employs a time step of $\Delta t_{HMB3} = 2 \cdot 10^{-2} s = 100\Delta t_{SPH}$ with implicit $CFL = 5.0$. The small time step for the SPH method is required by the explicit integration scheme. The HMB3 solver employs an implicit dual-time method by Jameson^[80] that is superior for larger time steps. Synchronisation of the solvers is performed at the end of each HMB3 step.

At the beginning of each synchronisation time step, the position and velocities of the rotor are transferred to the HMB3 aerodynamic solver, and forces and moments on the rotor are passed to the SPH. The two solvers are then advanced to a new time level with different methods and different number of steps. SPH performs 100 symplectic steps, while HMB3 performs 350 implicit pseudo-time steps. During the symplectic steps of the SPH code, the aerodynamic loads are kept constant (frozen). In return, the position and velocities of the rotor are kept constant during the implicit steps of HMB3. Once the synchronisation point is reached, the new position and velocities of all bodies, and rotor loads are obtained. Then, the algorithm proceeds to the new time level and information between the solvers is exchanged. Note that in this way the air/water interface was not modelled.

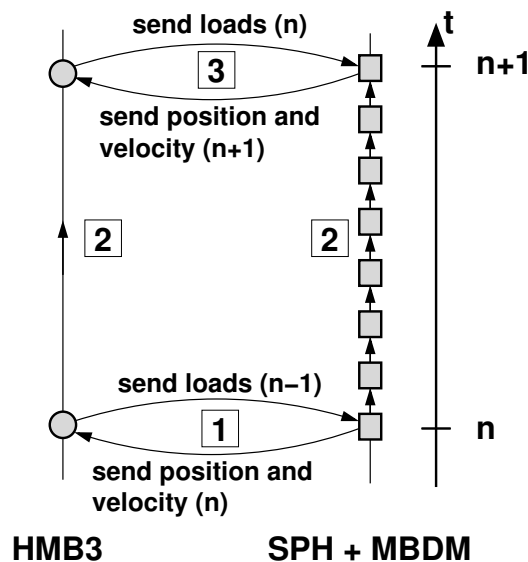


Figure 13.1: The parallel conventional staggered method employed in present work.

13.2 Test case description

A 10-MW wind turbine design by Bak *et al.* [11] was used in this work. The wind turbine is attached to the semi-submersible support which consists of three cylindrical floats that increase the buoyancy and stability of the structure. A similar concept of the support platform was investigated by Roddier [168]. Unlike that design, the present support is simplified to be symmetric with respect to the location of the tower and the floats are connected to the base of the tower with a solid frame. The size of the tower is taken from [11], and the dimensions of the support were calculated to provide sufficient buoyancy. A schematic of the studied FOWT is shown in Figure 13.2.

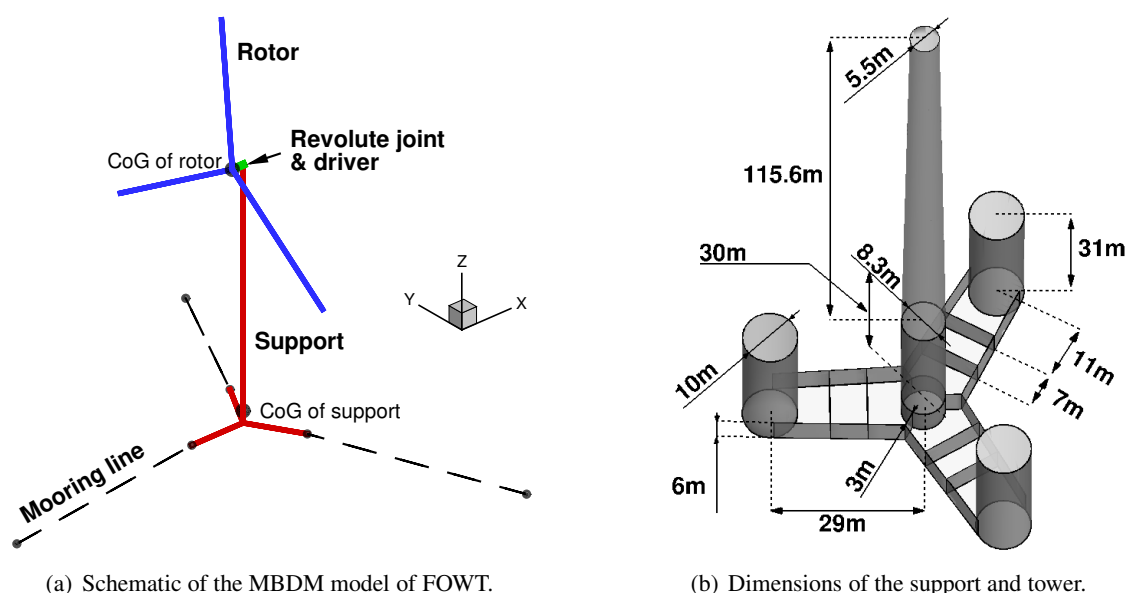


Figure 13.2: Schematic of the employed model of FOWT (a), and dimensions of the semi-submersible support and tower (b). FOWT model consists of three mooring lines and two rigid bodies: the rotor (blue) and combined body representing nacelle, tower and support (red).

In the present model, the FOWT is represented by three mooring lines and two bodies, as shown in Figure 13.2(a). The first body represents the rotor (three blades with the spinner), and the second body represents the combined nacelle, tower and floating support rigidly linked to each other. The two bodies are connected by a revolute joint and a constraint of constant rotational speed is applied to the rotor. The resulting system has 6 unconstrained degrees of freedom. The mechanical properties of the bodies and mooring lines are presented in Table 13.1.

The FOWT is placed in a shallow tank of length 500m, width 150m and height 30m. The tank is filled

Table 13.1: Mechanical properties of the employed bodies and mooring lines.

Rotor	
m [kg]	227,962
J [kg · m ²]	$\begin{bmatrix} 1.56 \cdot 10^8 & 0 & 0 \\ 0 & 7.84 \cdot 10^7 & 0 \\ 0 & 0 & 7.84 \cdot 10^7 \end{bmatrix}$
Nacelle, support and tower	
m [kg]	4,223,938
J [kg · m ²]	$\begin{bmatrix} 2.03 \cdot 10^{10} & 0 & 0 \\ 0 & 2.03 \cdot 10^{10} & 0 \\ 0 & 0 & 2.81 \cdot 10^9 \end{bmatrix}$
Mooring lines	
120.0	Angle between adjacent lines [°]
20.6	Depth of anchors below SWL [m]
7.0	Depth of fairleads below SWL [m]
116.73	Length of the relaxed line [m]
400 · 10 ⁶	Mooring line extensional stiffness [N/m]
40,000	Mooring line damping coefficient [Ns/m]

with water to a depth of 20.6m, and in the initial position of FOWT the hydrodynamic force is equal and opposite to the gravitational force. The waves are generated using a paddle on one side, and dissipated using a beach-like slope on the other side of the tank. The tank is presented in Figure 13.3. Waves are generated to represent the specific sea state corresponding to a given wind speed. Based on the measurements of annual sea state occurrences in the North Atlantic and North Pacific^[116], the wind speed of 11m/s corresponds to a sea state 4 with a mean wave height of 1.88m and a period of 8.8s, as shown in Table 5.4 from Chapter 5. The investigation in Section 5.3 of Chapter 5 showed that the required paddle amplitude is 1.2m, and this value was used in this chapter.

13.2.1 CFD mesh

The aerodynamic grid consists of the rotor and nacelle *i.e.* the tower is not included and the effect of the blade passing on the tower is not investigated. The grid consists of 8M cells, where 24 cells are used in the boundary layer, and 166 cells are distributed around the aerofoil section as presented in Figure 13.4(a). The surface of the blade is resolved with 90 cells along the span, as shown in Figure 13.4(b). The size of the first cell in the direction normal to the surface was $10^{-5}c$, where $c = 6.2m$ is the maximum chord of the blade. Based on the free-stream condition and the size of the first cell, the y^+ parameter was computed

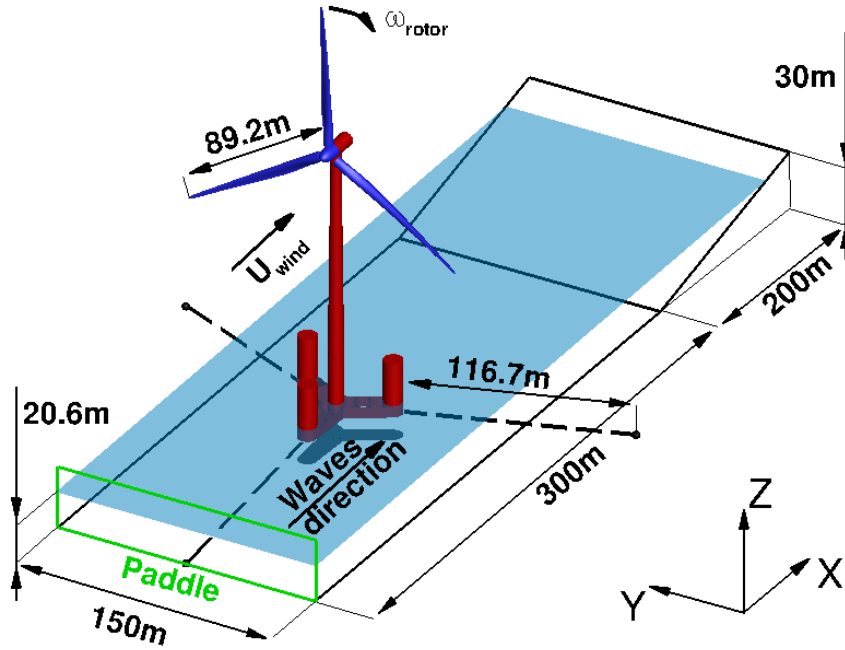


Figure 13.3: The FOWT model placed in a shallow tank. Mooring lines are shown with dashed lines.

to be $y^+ = 1.2$. The grid convergence study presented in Chapter 9 showed that this density is sufficient to produce grid-independent results, but initial spacing may be reduced to improve the y^+ parameter.

The density of the air was assumed to be $\rho = 1.225 \text{ km}/\text{m}^3$, the dynamic viscosity of the air was assumed to be $\mu = 1.8 \cdot 10^{-5} \text{ Ns}/\text{m}^2$, and the speed of sound was assumed to be $340 \text{ m}/\text{s}$. Further, the $k-\omega$ SST turbulence model was employed with the free-stream level of turbulence at 2.6%. The flow was assumed to be fully turbulent, and the atmospheric boundary layer was not modelled. The uniform inflow boundary was set $3R$ upstream of the rotor, and the outflow boundary was set $6R$ downstream of the rotor, where R is the radius of the blade. The far-field boundary was assigned $3R$ from the centre of rotation. In addition, the sliding plane was used to connect rotor to the nacelle and allow relative motion. The computational domain with corresponding boundaries, a slice through the mesh close to the blade surface, and the surface mesh of the blade are presented in Figure 13.4.

13.2.2 SPH setup and resolution

The hydrodynamic domain is resolved using $5M$ particles with initial uniform spacing of $d = 0.625 \text{ m}$, cubic spline kernel, and smoothing length $h = 1.5d$. Note that the best agreement with experimental data was

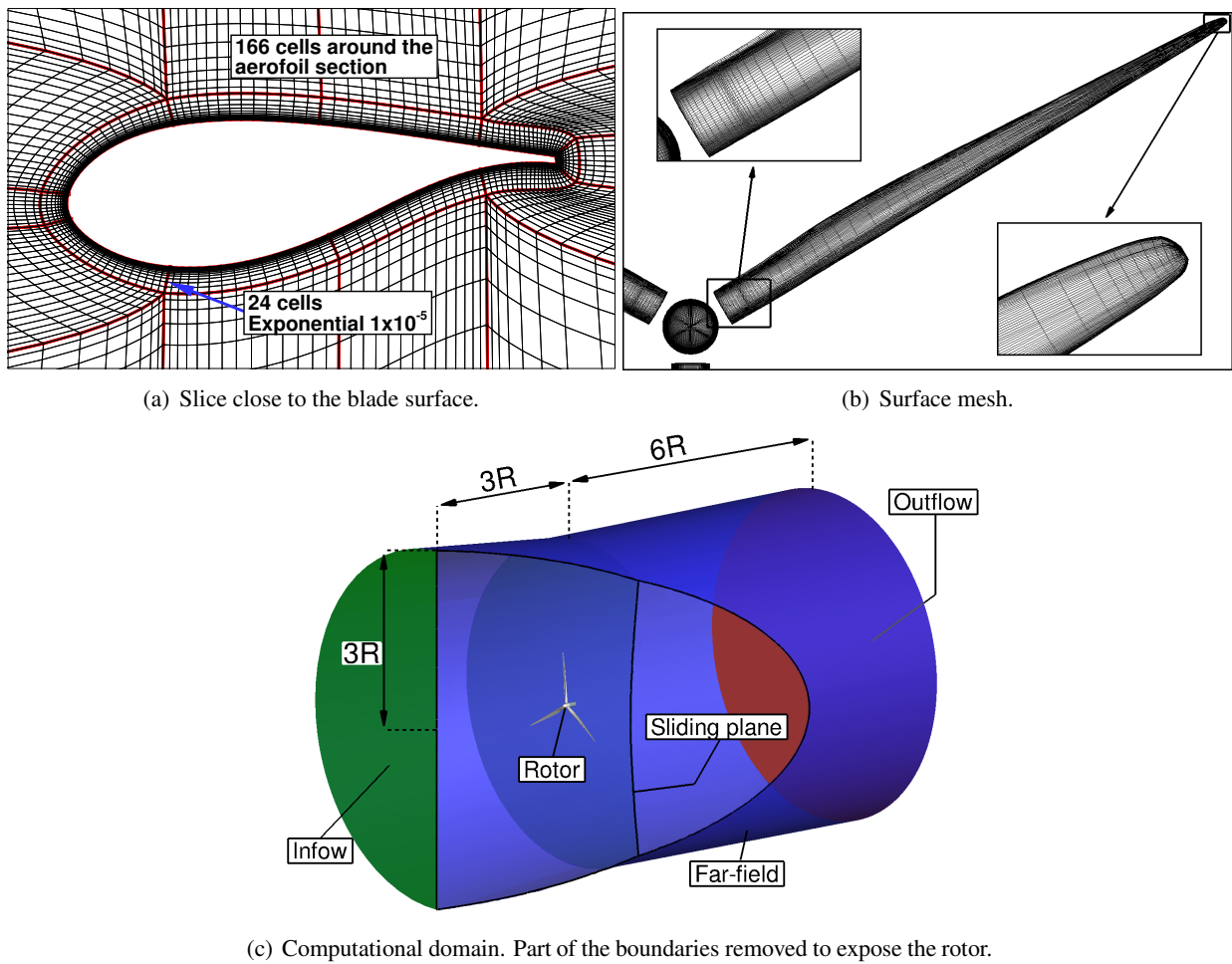


Figure 13.4: $8M$ mesh used to solve for aerodynamic loads. Surface mesh (a), and slice through the volume close to the blade surface (b).

obtained for 25 particles per radius of the cylinder, as shown in Chapter 6. Here, the employed spacing corresponds to 9 particles per radius of the cylindrical leg, or to spacing $d = 0.69\text{cm}$ in Figure 6.3 from Chapter 6. The coarse particle distribution was chosen for economies in CPU time, where coarse domain is obviously solved faster, but tends to under-predict the slamming loads on the structure. Three test were performed to investigate the influence of the domain width and particle spacing on the force acting on the support structure, as presented in Table 13.2. The average hydrodynamic forces acting on the support during 1s of simulation were used for comparison. This time interval was chosen such that it leads to direct comparison of the average loads per unit of time. Percentage difference is computed relative to the size and spacing employed for the coupled computation. As can be seen, the size of the hydrodynamic domain has little effect on the average hydrodynamic force. This is expected if the boundaries are placed far enough

from the support, and indicates that the chosen width of the water basin is adequate for the studied problem. On the other hand, improving the spatial resolution results in about 18% difference in the hydrodynamic force. This agrees with observations made in Chapter 6. A spacing of $d = 0.3125m$ would have been better, but to improve computational performance a spacing of $d = 0.625m$ was employed.

Table 13.2: Test cases investigating the influence of the domain width and particle spacing on the forces acting on the support structure.

Domain size $x \times y[m]$	Spacing $d[m]$	1s averaged hydrodynamic force $[N]$	Difference [%]
500×150	0.6250	$1.070 \cdot 10^7$	–
500×300	0.6250	$1.068 \cdot 10^7$	0.2%
500×150	0.3125	$1.267 \cdot 10^7$	18.4%

13.2.3 Initial conditions

Each of the solvers was executed separately before coupling to obtain a periodic solution of the loads. During this phase of computation the floating support was fixed, and the waves were generated for approximately 30s. The rotor was set to spin about the axis aligned with the direction of the incoming wind, and was first solved using HMB3 "hover" formulation with 20,000 steps during which the L2 norm of the residual vector dropped below 10^{-6} . Then, the unsteady computation was initiated and the flow was solved for an additional 30° of azimuth. The aerodynamic loads were almost constant during unsteady computation. Once the initial conditions were obtained, the coupled computations were initiated.

13.2.4 Demonstration cases

The first demonstration case consisted of the FOWT at the described configuration (see Figure 13.3) with the difference that rotor was not included in multi-body formulation. Instead, the mass of the rotor was concentrated in the centre of gravity of the support to produce correct mass of the floating structure. In this way, the shift of the centre of mass due to rotor over-hang was not considered. Further, the rotor inertia was not included, and the associated gyroscopic effects were not taken into account. The importance of these effects for the system at hand is assessed in the results section. Calm sea was considered, and the constant thrust of $1500kN$ was applied at the location of the rotor. A second demonstration case considered time

varying rotor thrust as shown in Figure 13.5. The thrust variation was estimated from a CFD computations from Chapter 10 of the rotor with the tower included. Five Fourier modes were used to fit the CFD data, and the average thrust over the full revolution was set to $1500kN$. Both test cases were solved for 150 seconds. Note that the demonstration cases are not coupled simulations, since the thrust force is prescribed and independent of the platform motion.

The last test case was a coupled computation, as described in Section 13.1. This case was solved for 60 seconds, and allowed for almost 7 wave passages and about 9 revolutions of the rotor.

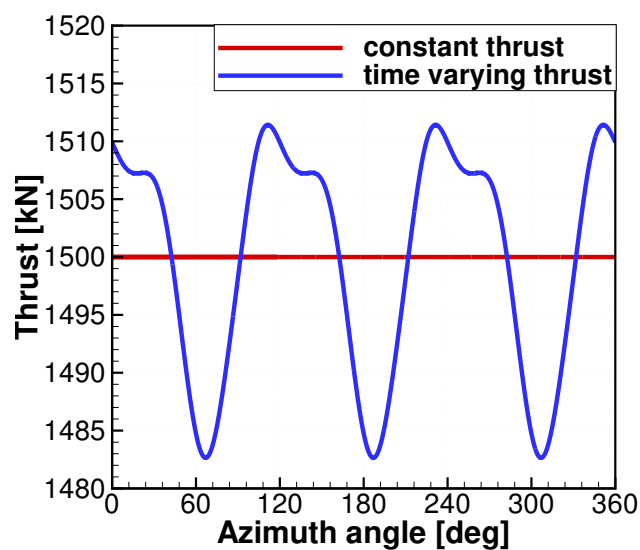
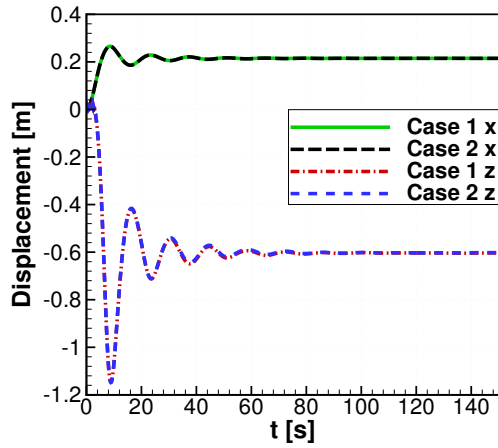


Figure 13.5: Thrust as function of azimuth angle of the rotor. Two test cases are shown: with constant thrust and estimated time varying thrust.

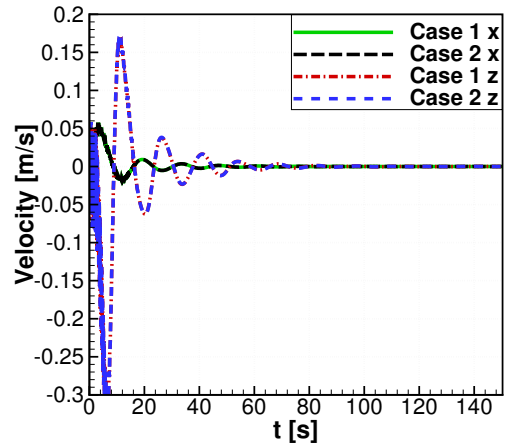
13.3 Results and Discussion

13.3.1 Decoupled cases - constant and time-varying thrust

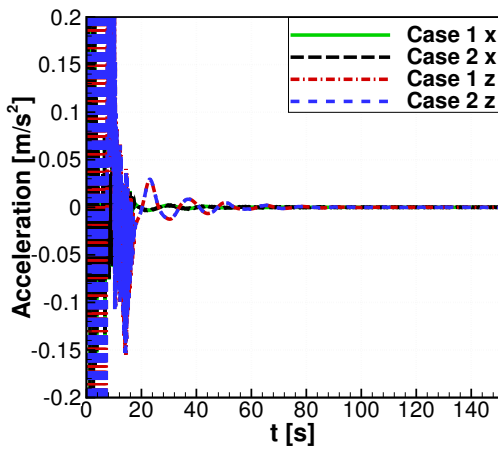
The results of two first cases are presented in Figure 13.6, where rotational dynamics is shown relative to the reference frame attached to the centre of gravity of the support and projected on the direction of global reference axes. As can be seen, the FOWT moves in the direction of the thrust by about $0.215m$ (displacement in x). The FOWT also sinks in the water for about $0.603m$ (displacement in z), and tends to settle at a pitch angle of around $0.09rad$ or 5.2 degrees (rotation about y axis). The SPH particles are settling



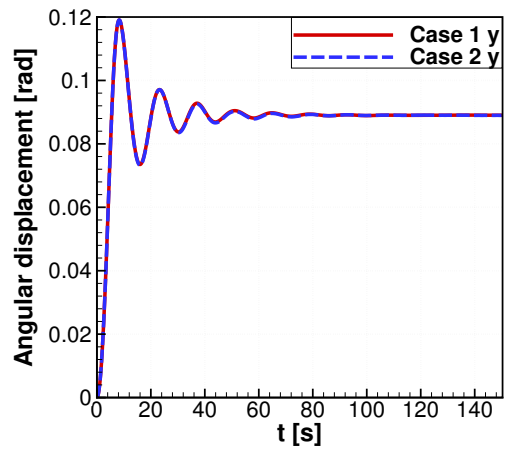
(a) Displacement of centre of gravity.



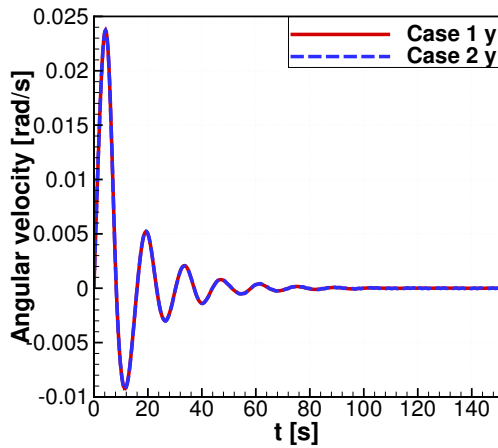
(b) Velocity of centre of gravity.



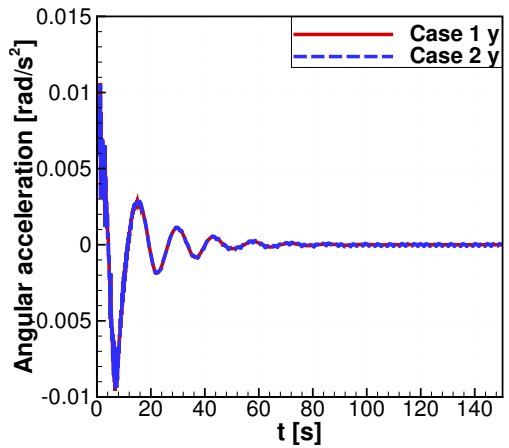
(c) Acceleration of centre of gravity.



(d) Angular displacement.



(e) Rotational velocity.

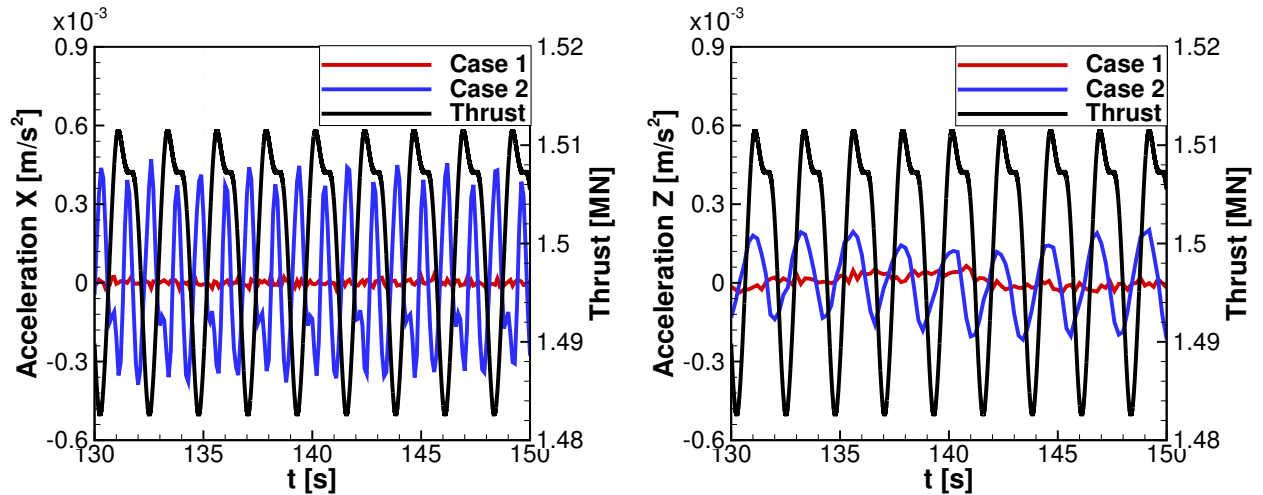


(f) Rotational acceleration.

Figure 13.6: Comparison of lateral and rotational dynamics of the support for two test cases: constant thrust (Case 1) and time varying thrust (Case 2).

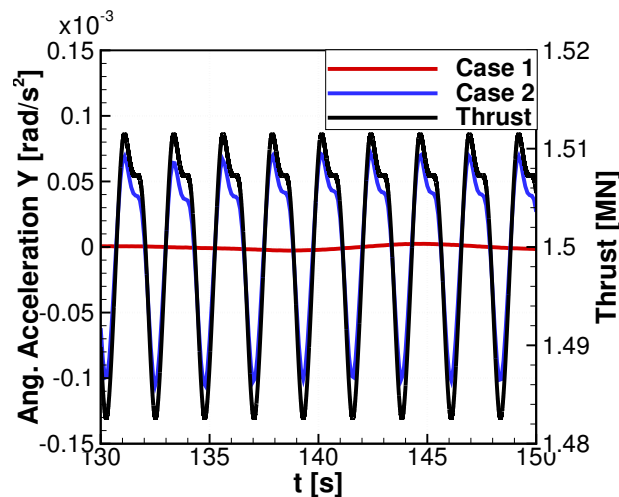
for the first 15 seconds as is visible in the acceleration plot. This can not be avoided even if the floating body is fixed and particles are let to settle. This is because releasing the floating structure is equivalent to a

drop, and therefore does not represent equilibrium. Also, the overall response is dominated by the initial imbalance of the forces, and the differences are barely visible in Figure 13.6.



(a) Acceleration of the centre of gravity in surge.

(b) Acceleration of the centre of gravity in heave.



(c) Pitching acceleration about the centre of gravity.

Figure 13.7: Comparison of last 20 seconds of lateral and rotational accelerations of the support for two test cases: constant thrust (solid line) and time varying thrust (dashed line). Solid line represents time varying thrust, as applied in the second test case.

The last 20s of lateral and rotational accelerations are presented in Figure 13.7. The differences for both cases are now clearly visible. The effect of time varying thrust on the angular acceleration in pitch (about y axis) can be seen in Figure 13.7(c), where the variation for the second test case is overlaid on the response for the first case. The variation in the shape and frequency, corresponds to the applied time dependent thrust.

The effect of time varying thrust on the lateral accelerations can be seen in Figure 13.7. Again, the

acceleration in heave (in z direction) for the second test case (time varying thrust) is overlaid on the response for the first case (constant thrust). Here, the frequency of acceleration corresponds to the frequency of the thrust, but some phase shift is present and the shape of the response does not follow the shape of the thrust. This is because the motion in heave is linked to the applied thrust only through the rotational motion of the support i.e. through the second time integral of the angular acceleration that does follow the shape of the thrust as shown in Figure 13.7(c). The acceleration in the x direction is directly linked to the applied thrust, and the frequency dependence on thrust without the phase shift is clearly visible. However, the shape of the acceleration is not following the shape of applied thrust. This is a result of high stiffness of the mooring lines in this direction, where high frequency response of the mooring system augments the overall response of the support platform.

There are three sources of momentum for the decoupled computations: hydrodynamics, prescribed aerodynamics and mooring lines. Time histories of forces and moments for the test case with constant thrust are presented in Figure 13.8. Note that for clarity, the time starts at 25s. Also, note the differences in magnitude of the computed moments, where moments about y axis are three order of magnitude bigger, as compared to the other moment components.

First, it should be noted that mooring lines are in general opposing the hydrodynamic forces introduced by the SPH solver. This is not true for the pitching moment, where hydrodynamics and mooring lines are acting together to counter the imbalance of the moment due to the thrust. For the mooring lines, moment is created by the displacements of the fairleads, whereas for the hydrodynamics, moment is created by the change of the buoyancy introduced by the rotation of the support. As can be seen, the mooring lines contribute about 30%, whereas buoyancy about 70% of the restoring moment in this system. One would expect similar, cooperative behaviour for the forces in surge (in x direction). The obtained results suggest otherwise, as shown in Figure 13.8(a). As can be seen, only the mooring lines are responsible for balancing the thrust force. Since the water is considered calm for the decoupled cases, the only source of hydrodynamic force acting in x direction is the hydrodynamic damping. Therefore, it is acting in the opposite direction of the motion, and as a result in opposite direction to the mooring force, which is a main source of motion in this direction. Lastly, small spurious moments and forces are noted, e.g. force in sway (y direction), which is normal to the plane of symmetry of the support. This is due to the SPH, where motion of the

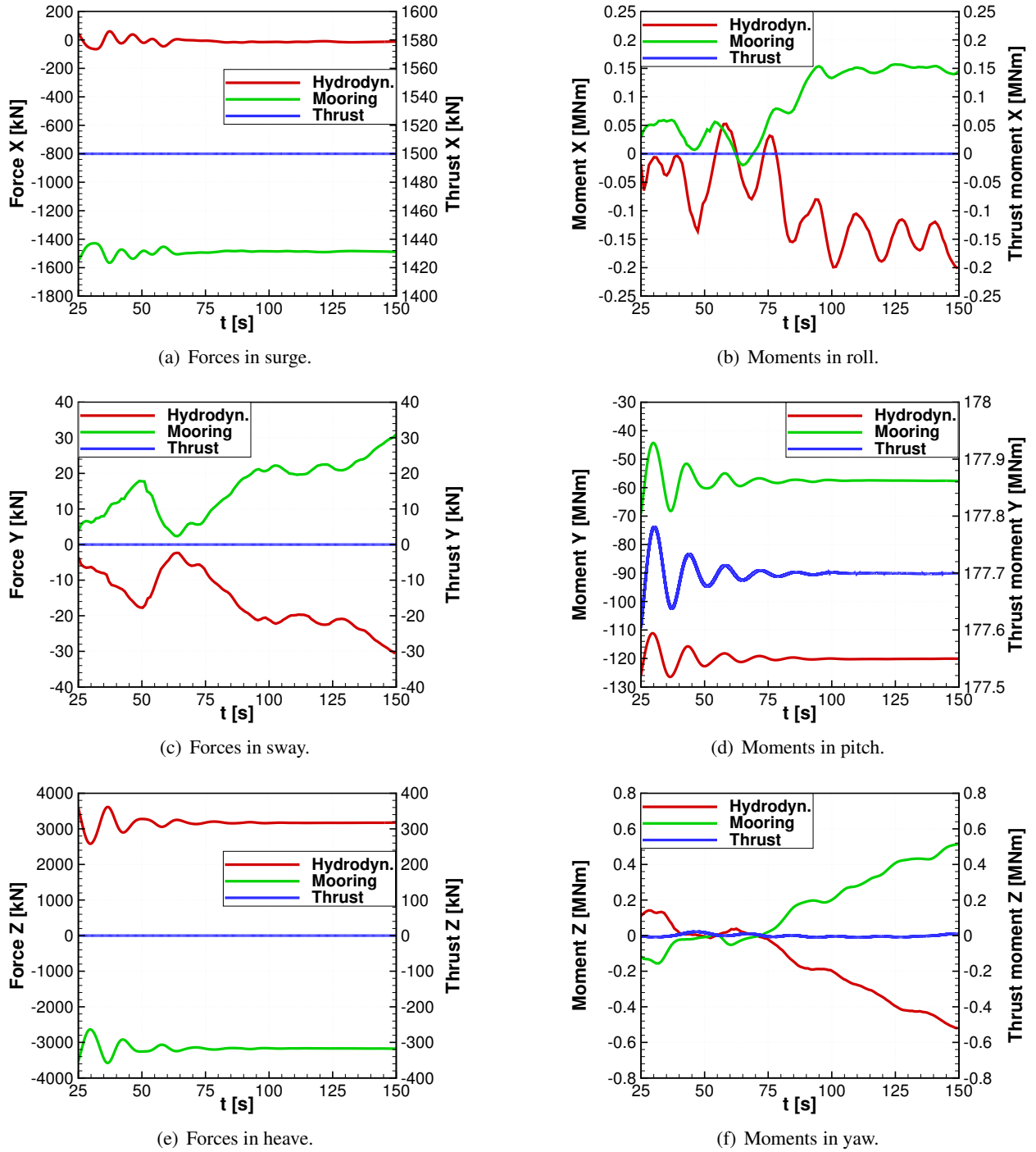


Figure 13.8: Forces and moments acting at CoG of the support for constant thrust case.

particles is never indeed symmetric. However, these discrepancies diminish with the number of particles, as was seen when test cases from Table 13.2 were computed. Further, the SPH method is known for its pressure instabilities, where the pressure field of the particles exhibits large pressure oscillations due to acoustic waves present in compressible fluids. This is commonly tackled with solution smoothing techniques, also

termed particles smoothing. Schemes up to the second order were proposed in the literature e.g. Belytschko *et al.* [18] and Billota *et al.* [21]. In the present work, no particles smoothing was applied, including validation test cases. In fact, stability issues were encountered when a zero-order Shepard density filter was applied to the decoupled test case every 50 and 100 SPH steps. However, smoothing was shown to have a small effect on the overall pressure distribution for the artificial viscosity formulation used in this work^[63].

The time histories of forces and moments for the second test case with time varying thrust are presented in Figure 13.9. Visible trends and relations are analogous to the case with constant thrust, and support the observations made in the previous paragraph. The main difference is the expected variation of the forces in surge and moments in pitch, due to the unsteady aerodynamic forcing. Also, hydrodynamic and mooring forces in the y direction changed sign, although the mooring line forces are still opposing the forces of the SPH solver. The same is observed for the moments about z axis. Those quantities are dependent, and opposite rotation creates opposite mooring line forces.

13.3.2 Coupled case

Coupled computations were also performed, and results are presented in Figure 13.10, where rotational dynamics is shown relative to the reference frame attached to the centre of gravity of the support and projected onto the direction of global reference axes. As was mentioned in Section 13.1, the time step for SPH was set to $\Delta t_{SPH} = 2 \cdot 10^{-4} s$, whereas HMB3 employed a time step of $\Delta t_{HMB3} = 2 \cdot 10^{-2} s = 100 \Delta t_{SPH}$, or 1.06° of revolution per time step. The aerodynamic forces acting on the rotor as functions of time are shown in Figure 13.11(a). The platform motion shows similar trend as for the previous, decoupled test cases. However, the rotor thrust is now dependent on the position and velocity of the rotor. As the wind turbine pitches under the thrust force, the rotor moves in the direction of the wind (velocity in x direction in Figure 13.11(b)). In return, the thrust force decreases due to the smaller inflow speed and the orientation of the rotor disk. As the applied force is reduced, the rotor velocity decreases. The inverse relation between the aerodynamic force and velocity of the hub in x direction is clear in Figure 13.11. Further, due to the pitch angle, a component of the thrust is acting along the z axis. As a result, the FOWT experiences higher displacement in heave: $-0.8m$ as compared to $-0.6m$ for the decoupled solutions.

The initial motion of the FOWT is dominated by the imbalance of the forces due to the applied thrust,

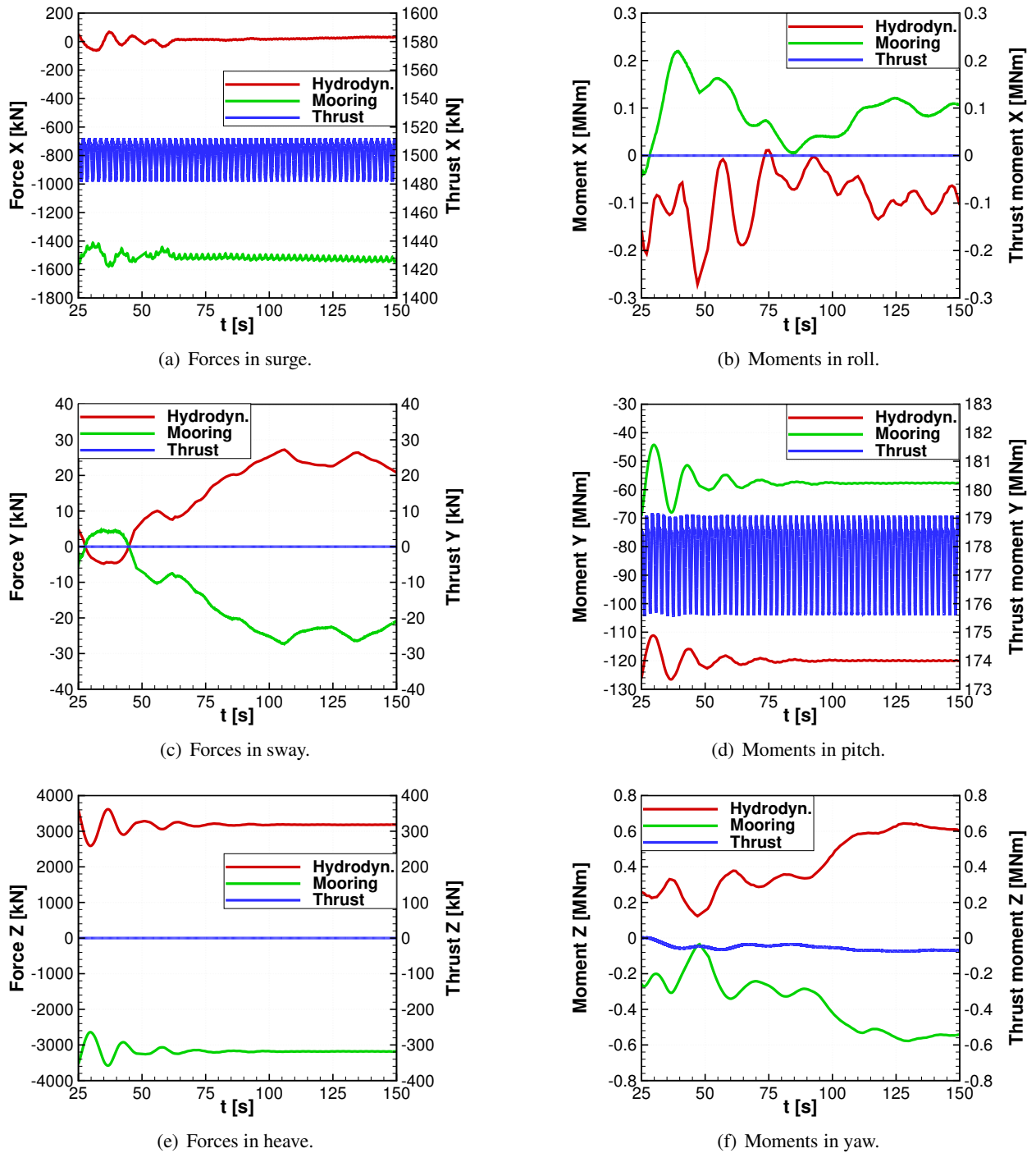


Figure 13.9: Forces and moments acting at CoG of the support for time varying thrust case.

and the effect of the first wave passage is not visible. However, the effect of every consecutive wave is clearly visible in periodic variation of the moment about the y axis, as shown in Figure 13.10(f).

To facilitate the analysis of forces and moments acting on the system, the aerodynamic moments were transferred to the centre of gravity of the support platform. The resulting time histories of forces and

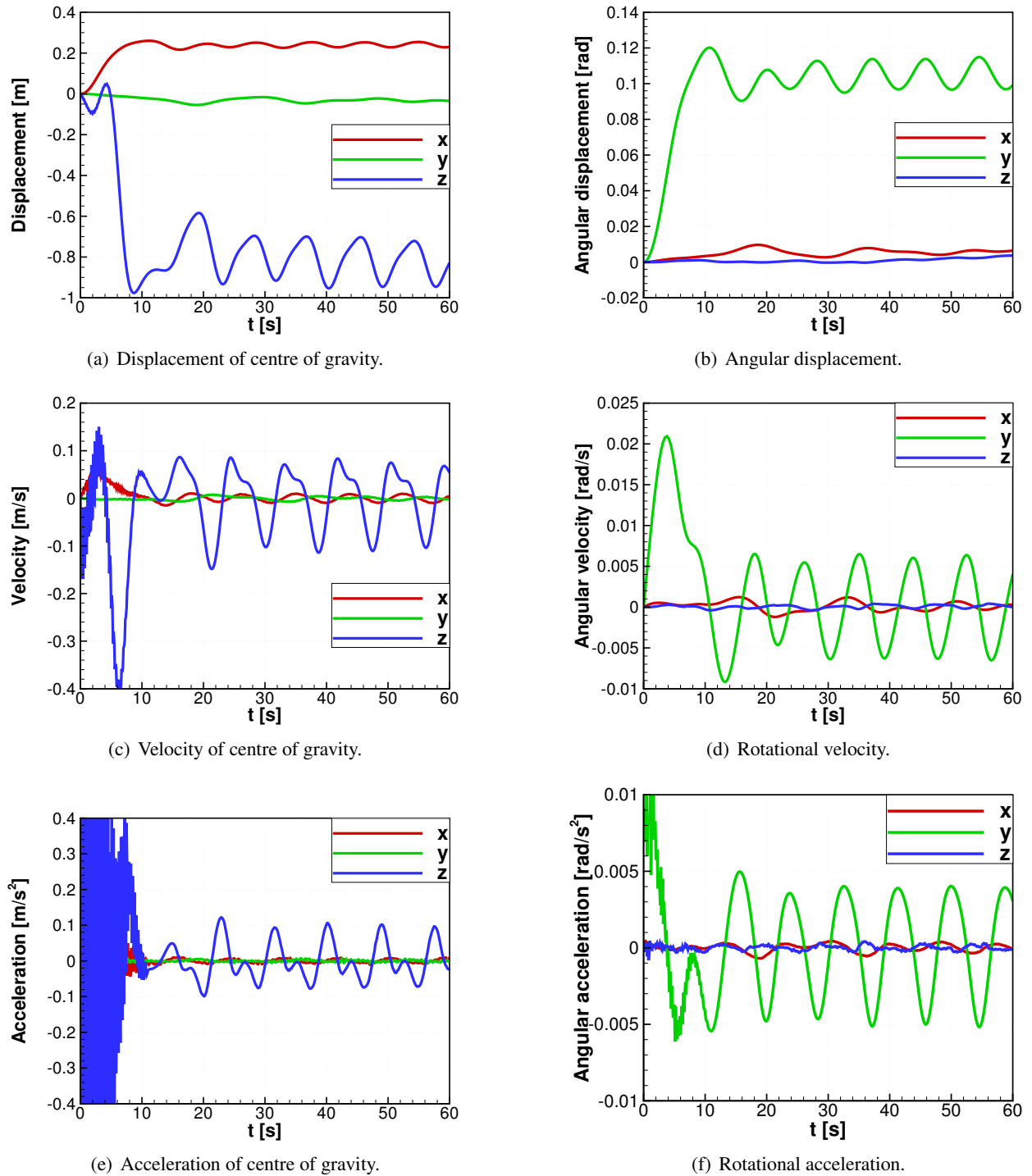


Figure 13.10: Lateral and rotational dynamics of the support platform for coupled test case.

moments for the coupled test case are presented in Figure 13.12. First, we observe lasting for about 10s high frequency hydrodynamic forces and moments due to initial particles settling. Similar was observed for decoupled test cases. After an initial phase, the hydrodynamic forces show periodic variation related to the frequency of the passing waves. Next, the mooring line forces are opposing the SPH forces in all directions.

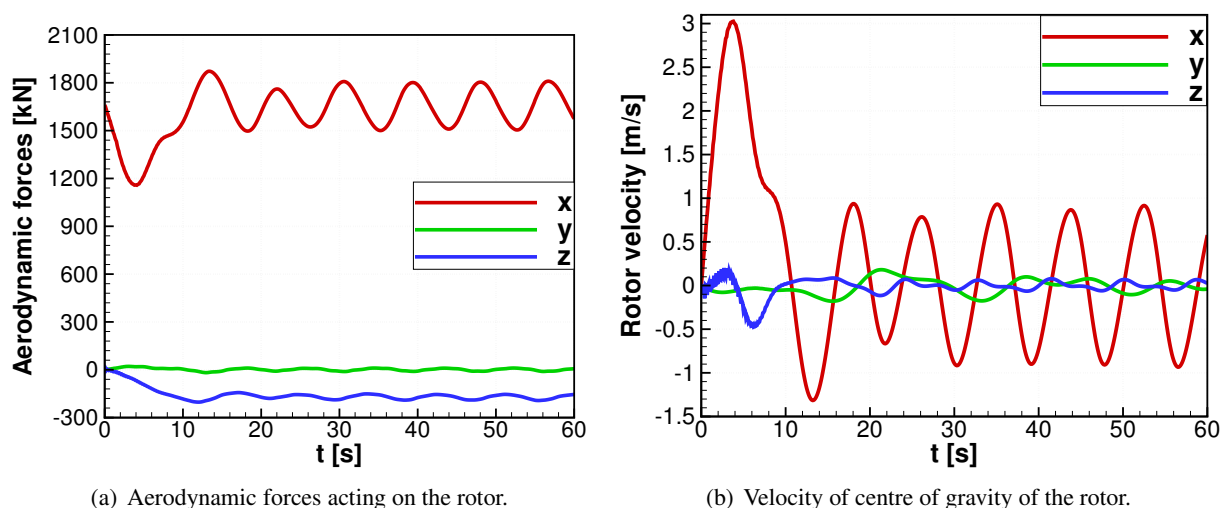


Figure 13.11: Forces acting on the rotor and velocity of centre of gravity of the rotor as function of time for coupled computation.

Finally, periodic variation of the aerodynamic forces with frequency of the waves is noted. A phase shift is present, since the aerodynamic forces are dependent on velocity and position, rather than on forces, as was discussed in previous paragraphs.

For the moments, pitching moment (about y) is dominating and after the initial phase the solvers tend to a periodic solution. The aerodynamic moment follows the inverse relation to the the hydrodynamic pitching moment. The phase shift for the mooring lines moment is present, as it depends on the orientation of the support. The aerodynamic moment about x axis applied at the rotor is a result of a driving force created by the lift and drag. Clearly, the driving force follows the same trend as the thrust force i.e. inverse relation with the velocity of the hub. The aerodynamic moment is transferred to the structure, and hydrodynamic and mooring lines moments are trying to compensate for this moment. Finally, the mooring lines are opposing the hydrodynamic moments for the moment about z axis (yawing).

Note that no significant gyroscopic effect was observed for this FOWT. The value of gyroscopic moment can be estimated using gyroscopic approximation as $\tau = J_{zz}\omega_r\omega_p$. In this case the precession rate ω_p is caused by the waves, and gyroscopic torque τ should develop about body-fixed yaw axis. The pitching angular velocity is shown in Figure 13.10(d) and follows sinusoidal shape with amplitude $\omega_p \approx 0.006\text{rad/s}$. Given that the angular velocity of the rotor $\omega_r = 0.92\text{rad/s} \gg \omega_p$, some of the gyroscopic approximation assumptions are still valid. Substituting the above values and the mass moment of inertia of the rotor

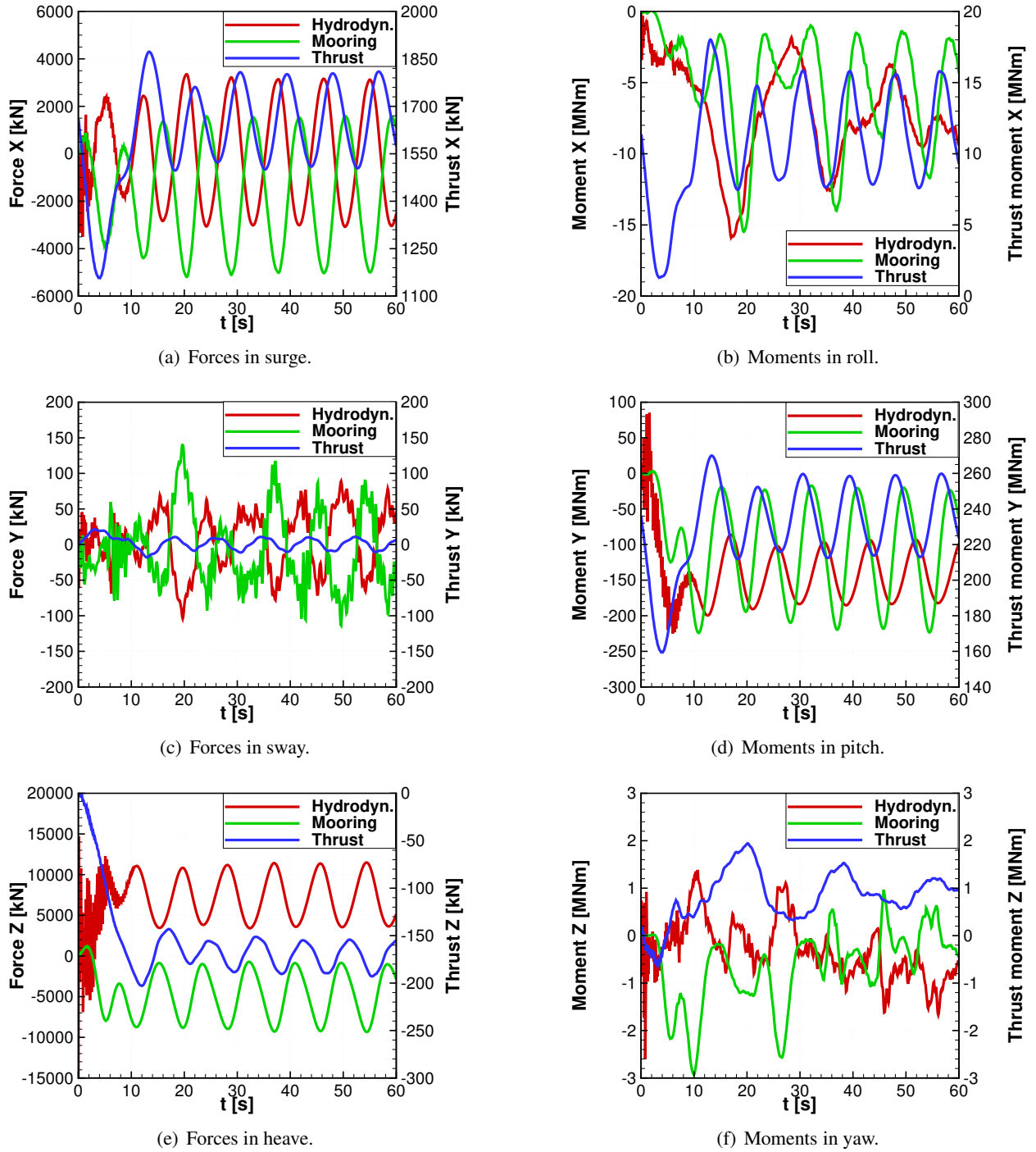


Figure 13.12: Forces and moments acting at CoG of the support for the coupled test case.

from Table 13.1 into the equation of gyroscopic approximation, it follows that the amplitude of gyroscopic torque is $\tau = 0.86MNm$. Since FOWT is oscillating about a mean pitch angle of about $0.11rad$ (6.3°), the gyroscopic torque has two components when projected on the direction of global axes : one about the global z axis, which is equal to $\tau_z = 0.77MNm$, and one about the global x axis, which is equal to

$\tau_x = 0.09MNm$. The magnitude of these estimated values is consistent with that of the computed moments shown in Figure 13.12. As can be seen, the estimated magnitude of the rolling gyroscopic torque is about 0.75% of the mean aerodynamic moment in roll. Therefore, it can be considered negligible. On the other hand, the gyroscopic torque in yaw is comparable to other moments about z axis. However, those small moments did not cause significant rotation of the FOWT about this axis due to large inertia of the floater. Finally, the estimated magnitude of the gyroscopic torque is about 0.35% of the mean aerodynamic moment in pitch. This agrees with the observations made by [201] that gyroscopic effect and resulting moment is small (less than 5%) as compared to the pitching moment for horizontal axis wind turbines with low speed rotors.

Similarly to the previous chapter, estimates of the induced velocity v_i were used to show at which states the FOWT was operating. The induced velocity was estimated based on Equation 12.1 of Chapter 12, and the results are shown in Figure 13.13. As can be seen, the wind turbine did not encounter a vortex ring state. It did, however, enter a turbulent wake state, but only briefly. This is clear in Figure 13.13(b), where the ratio of inflow velocity is shown as function of time. As can be seen, a turbulent wake state was encountered during initial phase, when FOWT was pitching under the thrust force to obtain its mean pitch angle. The angular velocity at this stage was the highest, and so the linear velocity of the hub. Also, the FOWT was periodically approaching a turbulent wake state, but predicted oscillations were not large enough to enter it again.

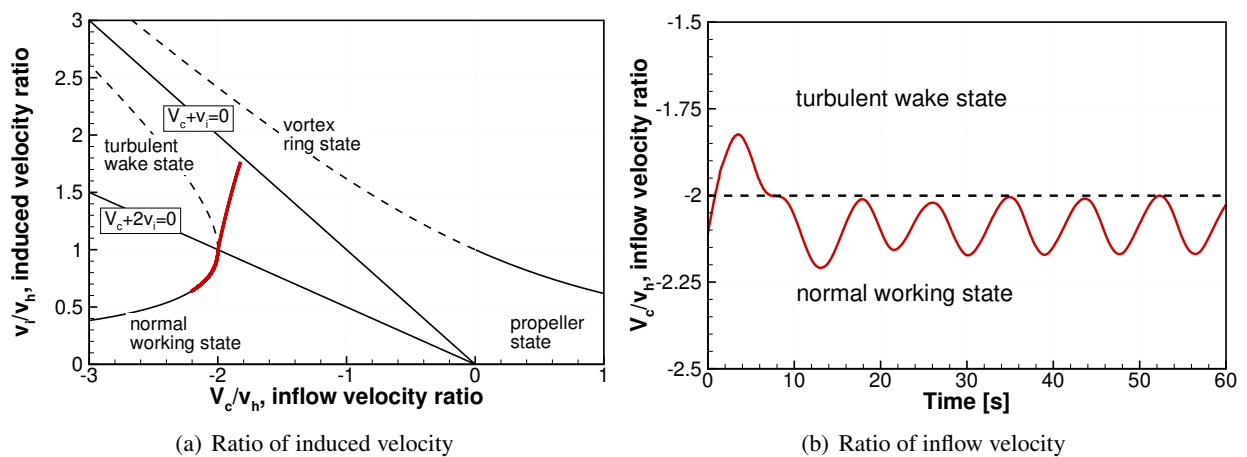


Figure 13.13: Estimated ratio of induced velocity as function of inflow velocity ratio (a), and ratio of inflow velocity as function of time (b) for coupled computation.

Figure 13.14 presents different positions of the FOWT during the computation. The wave breaking effect of the support structure is visible, and the recovery of the waves behind the FOWT can be seen. The change of the pressure on the rotor can also be observed, especially at the tip of the nacelle. Note that the tower was not included in the aerodynamic domain, but it is shown in the figure, as the presence of the tower was accounted for in the multi-body model.

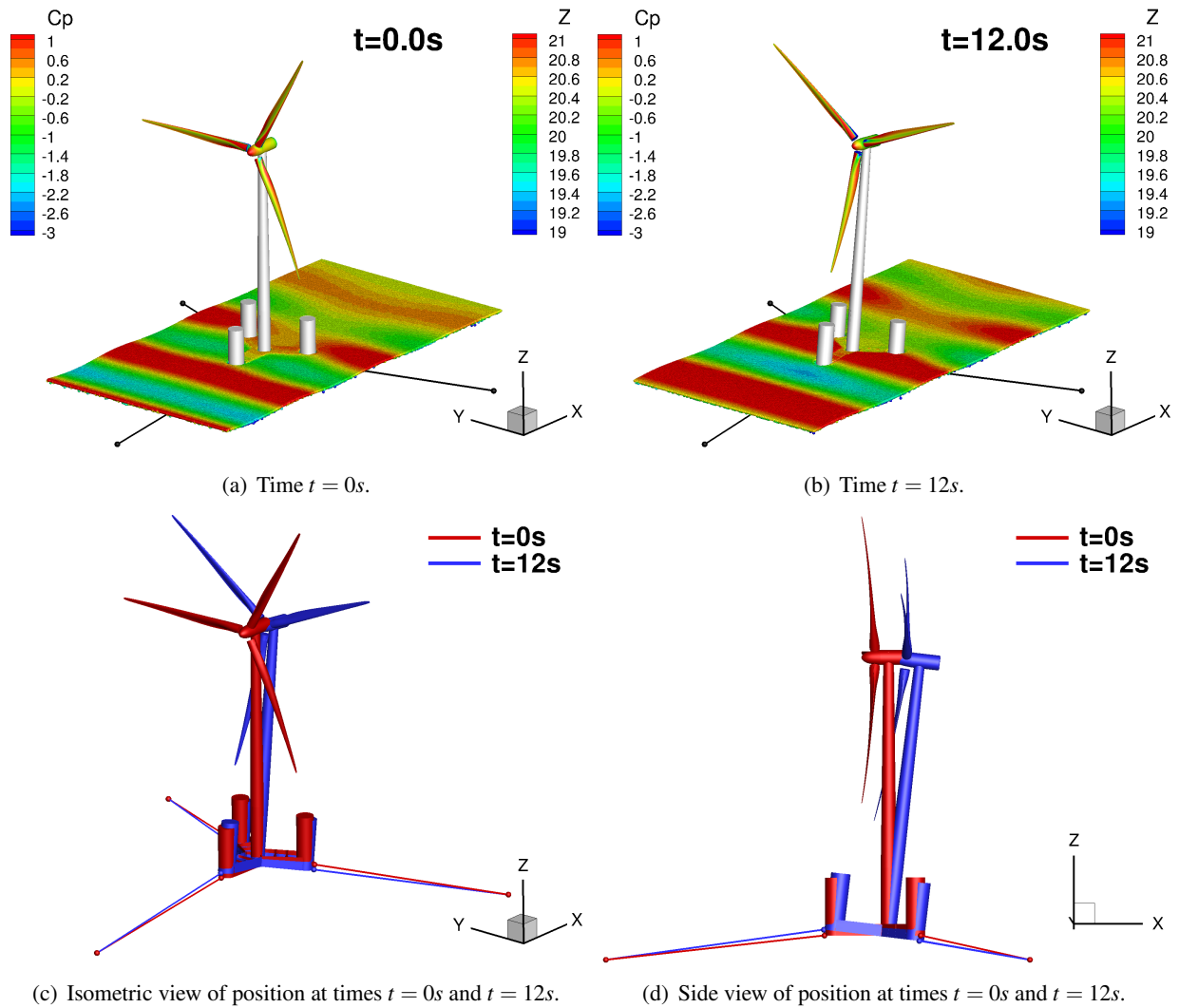


Figure 13.14: Position and orientation of the FOWT at times $t = 0s$ and $t = 12s$ during coupled computation. Contours on the rotor correspond to pressure coefficient C_p , contours on the water surface correspond to surface elevation z in meters.

13.3.3 Computational performance

For all cases, the SPH solver with MBDM were executed on a single 8 cores Intel®Xeon®CPU machine with 16 threads. Each of the CPU cores had a clock rate of $2GHz$, and $6.6GB$ of dedicated memory. As no interconnect switch was involved, the message passing delay between SPH and MBDM solvers was reduced to minimum. For the coupled case, HMB3 was executed on 29 dual-core AMD Opteron™processors with 4 threads, giving in total 116 parallel instances of the solver. Each of the CPU cores had a clock rate of $2.4GHz$, and $4GB$ of random access memory. It should be noted that the SPH method requires only local (limited by the kernel function) weighted average in the vicinity of the given particle, whereas HMB3 solves the complete set of equations involving all the cells in the domain. Hence, more processing units were assigned to the aerodynamic side of the coupled problem.

The average time required to compute a second of the solution for the coupled case is 27.26 hours, where about 27.25 hours were spent to solve aerodynamics, 21.3 hours to solve hydrodynamics, and 0.24 hours to solve multi-body equations. Note that solvers were executed in parallel, as explained in Section 13.1, and were advancing in time concurrently. The average time spent to exchange information for a second of the solution is 0.53 seconds, and was mostly dictated by the communication between the SPH and the MBDM solvers.

It should be noted that time accuracy can be improved, if the coupling step is reduced. In the presented coupled case, the information is exchanged every 100 SPH steps ($\Delta t = 2 \cdot 10^{-2}s$). When information between the solvers is exchanged every 50 SPH steps ($\Delta t = 1 \cdot 10^{-2}s$), the average time required to compute a second of the solution becomes 45.0 hours. If information is exchanged every single SPH step ($\Delta t = 2 \cdot 10^{-4}s$), the average time per one second extends to about 438.9 hours. In the former case, HMB3 requires on average 237 pseudo-time steps to achieve the level of convergence below 10^{-2} , and 45 pseudo-time steps for the later case. The convergence is defined as L2-norm of the residual vector. This suggests that computational cost can be further reduced by employing explicit schemes for both solvers and performing less evaluations (four for Runge-Kutta scheme of 4th order). However, the biggest possible explicit step for HMB3 that would satisfy explicit CFL condition of 0.4 for the smallest cell in the domain is about $3.6 \cdot 10^{-9}$ seconds. Therefore, the aerodynamic time-step becomes the limiting factor for this approach and for the problem at

hand. More information about the computational performance is presented in Table 13.3. Stability issues were encountered for a time step $\Delta t = 2 \cdot 10^{-2} s$ and HMB3 implicit CFL number 10.0, where the residual vector does not converge as fast as for CFL number 5.0. This indicates that CFL number of about 8.0 would be an optimal choice for this time step.

Table 13.3: Computational performance of the coupling algorithm for various coupling time steps.

Coupling Δt [s]	HMB3 CFL number	HMB3 Newton steps	SPH steps	Time per cou- pling step [s]	Time per 1s of solution [s]
$2 \cdot 10^{-2}$	5.0	315	100	$1.95 \cdot 10^3$	$9.81 \cdot 10^4$
$2 \cdot 10^{-2}$	10.0	350	100	$2.29 \cdot 10^3$	$1.15 \cdot 10^5$
$1 \cdot 10^{-2}$	5.0	237	50	$1.61 \cdot 10^3$	$1.62 \cdot 10^5$
$1 \cdot 10^{-2}$	10.0	105	50	$1.04 \cdot 10^3$	$1.06 \cdot 10^5$
$2 \cdot 10^{-4}$	5.0	45	1	$3.13 \cdot 10^2$	$1.58 \cdot 10^6$
$2 \cdot 10^{-4}$	10.0	23	1	$1.59 \cdot 10^2$	$7.97 \cdot 10^5$

Chapter 14

Conclusions and future work

14.1 Conclusions

This study was focused on modelling floating off-shore wind turbines of large diameter. A 10-MW wind turbine was used as an example in this work, since this turbine was designed specifically for off-shore application as part of the InnWind European project. The idea put forward in this work is to employ high fidelity Navier-Stokes solvers for air, and water. For this reason, the Helicopter Multi-Block 3 CFD solver was used to model aerodynamics. Likewise, the Smoothed Particles Hydrodynamic method was used for hydrodynamics. A multi-body solver was implemented to solve for the wind turbine dynamics.

The study started from the aerodynamic analysis of the 10-MW wind turbine. Straight and pre-bent configurations of the blade were investigated under the assumption of uniform inflow. The results showed regions of suction side separation, and pressure side recirculation for all studied wind speeds. This agreed with other results published in the open literature. Also, the pre-bent configuration was found to be slightly less efficient than the straight blade, producing about 0.4% less thrust and mechanical power.

Next, the effects of the atmospheric boundary inflow and atmospheric turbulence were studied. For this, the power law wind speed profile was employed, and the atmospheric turbulence was introduced using Mann's model. An increase of loads variation was seen for the turbulent case, as compared to the case without turbulence. Also, the results for atmospheric inflow suggest a reduction of mean thrust by 1.5%, and power by 2.8% with respect to the uniform inflow case.

The aero-elasticity of the 10-MW rotor was studied next. The structural model was constructed using *NASTRAN*. The natural frequencies and modes were compared to results of other researchers, showing good agreement. This model was then used for steady and unsteady aero-elastic computations. The results suggest the tip displacement of $8.7m$ for static, and $6.7m$ for dynamic cases. Then, the complete assembly of the 10-MW turbine was studied with rigid and elastic blades. The results showed reductions of thrust by 4.3%, and power by 4.7%, due to elastic deformation of the blades.

Next, the effects of employing deformable trailing and leading edge flaps on the 10-MW wind turbine were investigated. It was shown, that the trailing edge flap affects the thrust and driving forces, as well as the pitching moment. The leading edge flap was seen to mostly affect the pitching moment. Hence, the trailing edge flap could be used to control flap-wise bending of the blade, or eliminate the adverse effect of the blade passing in front of the tower. On the other hand, the leading edge flap could be used to counter the additional pitching moment created by the trailing edge flap.

A floating 10-MW wind turbine was considered next, by forcing the rotor to yaw and pitch oscillations. The blades were assumed rigid, and the tower was not included. The results showed larger variations in power for the case of dynamic yaw, as compared to fixed yaw cases. Differences of up to 2.5% were seen for the studied dynamic yaw cases. Hence, the aerodynamic effects due to dynamic yaw were found to be comparable, in magnitude, to the effects due to the blade elasticity and atmospheric boundary layer inflow. The results showed larger variations in thrust and power as the wind turbine pitched about a point located $119m$ below the rotor. Vortex ring state was encountered as the wind turbine was forced to pitch with amplitude of 5° and period of $8.8s$. Also, large changes of thrust and power were obtained for the pitching motion of the rotor. Differences of up to 32.8% were seen for the cases studied.

Finally, a coupling method for the analysis of the dynamics of floating off-shore wind turbines was presented. The results showed that the weak coupling method put forward in this work is adequate for the solution of the studied FOWT. Regardless of the lack of experimental data for a coupled system, validation was carried out for all the components of the model. Data from the MEXICO and NREL Phase VI projects were used for aerodynamics, and good overall agreement has been seen between CFD and test data. For the hydrodynamics solver, experiments related to drops of solid objects in water were used. Again, with a refined set of particles, the SPH method delivered good results. The third component of the method was the

multi-body dynamics and this was validated using simple slider-crank problems. The results showed that the employed FOWT under studied conditions did not enter a vortex ring state. A turbulent wake state was encountered, but only at the initial pitching phase. The gyroscopic effects were also small for the problem studied, and did not cause significant rotations due to large inertia of the floater.

14.2 Future work

The presented results show that FOWT is a highly dynamic system. To obtain a deeper understanding of how rotor thrust and torque vary under dynamic conditions, efforts should be put forward to study aerodynamic flow and loads when wind turbine undergoes prescribed motions in pitch and yaw. This was partially covered in this work, but further research is required, especially comparison with experimental data.

In future, efforts should be directed towards improving the model. First, more sophisticated mooring lines models should be implemented, preferably a dynamic model. For this, the multi-body framework was already developed in this work. Next, the tower should be included in the aerodynamic domain, and the air/water interface should be modelled. This naturally leads to the atmospheric boundary layer and turbulence that can also be included in the model. Then, the deformable flaps may be used to control the FOWT responses. For this, a control algorithm should be developed. Putting all together will lead to a powerful tool for FOWT analysis. The present work is certainly a solid foundation for such a model.

Also, the work should continue with the validation of the method against experimental data, when available, and comparisons with a strong coupling technique. Hence, aspect that should be addressed is the experimental measurements. Clearly, each of the components can be validated separately, but a set of data for a complete FOWT system would be useful. The following measurements would be an asset: forces and moments due to the mooring system, water basin tests with small- or full-scale wind turbine including pressure distributions on support and rotor, and the overall FOWT time response including transient and periodic states.

Bibliography

- [1] AVATAR – Advanced aerodynamic tools for large rotors. <http://www.eera-avatar.eu/>. Accessed: 2016-06-20.
- [2] INNWIND – Innovative wind conversion systems (10-20MW) for offshore applications. <http://www.innwind.eu/>. Accessed: 2016-06-20.
- [3] MARE-WINT – New materials and reliability in offshore wind turbines technology. <http://www.marewint.eu/>. Accessed: 2016-06-20.
- [4] Statoil: Hywind Demo. <http://www.statoil.com/hywind>. Accessed: 2016-07-01.
- [5] *Standard Atmosphere*. International Organization for Standardization, ISO, May 1975. ISO 2533:1975.
- [6] MSC Nastran Quick Reference Guide. <http://www.mscsoftware.com>, 2011.
- [7] Abbott I.H. and von Doenhoff A.E. *Theory of Wing Sections*. Dover Publications Inc., New York, USA, 1960.
- [8] Adam F., Myland T., Dahlhaus F., and Großmann J. Scale tests of the GICON[®]-TLP for wind turbines. In *Proceedings of the ASME 2014 33rd International Conference on Ocean, Offshore and Arctic Engineering*, San Francisco, California, USA, 2014.
- [9] Arapogianni A., Genachte A.B., Manzanas Ochagavia R., Pascual Vergara J., Castell D., Rodriguez Tsouroukdissian A., Korbijn J., Bolleman N.C.F., Huera-Huarte F.J., Schuon F., Ugarte A., Sandberg J., de Laleu V., Maciel J., Tunbjer A., Roth R., de la Gueriviere P., Coulombeau P., Jedrec S., Philippe C., Voutsinas S., Weinstein A., Vita L., Byklum E., Hurley W.L., and Grubel H. Deep water - The next step for offshore wind energy. Report, European Wind Energy Association, EWEA, July 2013.
- [10] Bae, Y.H., Kim M.H., Im S.W., and Chang I.H. Aero-elastic-control-floater-mooring coupled dynamic analysis of floating offshore wind turbines. In *Proceedings of the International Society of Offshore and Polar Engineers*, Maui, Hawaii, USA, June 2011. International Society of Offshore and Polar Engineers.
- [11] Bak C., Zhale F., Bitsche R., Kim T., Yde A., Henriksen L.C., Andersen P.B., Natarajan A., and Hansen M.H. Description of the DTU 10 MW Reference Wind Turbine. DTU Wind Energy Report-I-0092, Technical University of Denmark, June 2013.
- [12] Baker J., Standish K., and van Dam C.P. Two-dimensional wind tunnel and computational investigation of a microtab modified s809 airfoil. In *Proceedings of the 43rd AIAA Aerospace Sciences Meeting and Exhibition*, Reno, Nevada, USA, 2005.

- [13] Barlas T.K., van der Veen G.J., and van Kuik G.A.M. Model predictive control for wind turbines with distributed active flaps: incorporating inflow signals and actuator constraints. *Wind Energy*, 15(5):757–771, 2012.
- [14] Barlas T.K. and van Kuik G.A.M. Review of state of the art in smart rotor control research for wind turbines. *Progress in Aerospace Sciences*, 46(1):1 – 27, 2010.
- [15] Barlas T.K., van Wingerden W., Hulskamp A.W., van Kuik G.A. M., and Bersee H.E. N. Smart dynamic rotor control using active flaps on a small-scale wind turbine: aeroelastic modeling and comparison with wind tunnel measurements. *Wind Energy*, 2012.
- [16] Barltrop N.D.P. *Floating structures: a guide for design and analysis*. Centre for Marine and Petroleum Technology, 1998.
- [17] Bechmann A. *Large-eddy simulation of atmospheric flow over complex terrain*. PhD thesis, August 2007. Risø-PhD-28(EN).
- [18] Belytschko T., Guo Y., Kam Liu W., and Ping Xiao S. A unified stability analysis of meshless particle methods. *International Journal for Numerical Methods in Engineering*, 48(9):1359–1400, 2000.
- [19] Belytschko T., Krongauz Y., Dolbow J., and Gerlach C. On the completeness of meshfree particle methods. *International Journal for Numerical Methods in Engineering*, 43(5):785–819, 1998.
- [20] Benitz M., Schmidt D.P., Lackner M., Stewart G., Jonkman J., and Robertson A. Validation of Hydrodynamic Load Models Using CFD for the OC4 - DeepCwind Semisubmersible. In *Proceedings of the ASME 2015 34th International Conference on Ocean, Offshore and Arctic Engineering*, Saint John's, Canada, June 2015.
- [21] Bilotta G., Russo G., Herault A., and Del Negro C. Moving least-squares corrections for smoothed particle hydrodynamics. *Annals of Geophysics*, 54(5), 2011.
- [22] Björck A. Coordinates and calculations for the FFA-W1-xxx, FFA-W2-xxx and FFA-W3-xxx series of airfoils for horizontal axis wind turbines. Technical Report FFA TN 1990-15, The Aeronautical Research Institute of Sweden, FFA, 1990.
- [23] Blom F.J. Considerations on the spring analogy. *International Journal for Numerical Methods in Fluids*, 32(6):647–668, 2000.
- [24] Borg M., Collu M., and Kolios A. Offshore floating vertical axis wind turbines, dynamics modelling state of the art. Part II: Mooring line and structural dynamics. *Renewable and Sustainable Energy Reviews*, 39:1226 – 1234, 2014.
- [25] Burton T., Sharpe D., Jenkins N., and Bossanyi E. *Wind Energy Handbook*. John Wiley & Sons, Ltd, Chichester, UK, 2002.
- [26] Butterfield S., Musial W., Jonkman J., and Sclavounos P. Engineering Challenges for Floating Off-shore Wind Turbines. Technical Report NREL/CP-500-38776, NREL, September 2007.
- [27] Carrión M., Steijl R., Woodgate M., Barakos G., Munduate X., and Gomez-Iradi S. Computational fluid dynamics analysis of the wake behind the mexico rotor in axial flow conditions. *Wind Energy*, 2014.
- [28] Carrión M., Steijl R., Woodgate M., Barakos G.N., Munduate X., and Gómez-Iradi S. Aeroelastic analysis of wind turbines using a tightly coupled CFD-CSD method. *Journal of Fluids and Structures*, 50:392 – 415, 2014.

- [29] Carrión M., Woodgate M., Steijl R., Barakos G. N., Gomez-Iradi S., and Munduate X. Understanding wind-turbine wake breakdown using computational fluid dynamics. *AIAA Journal*, 53(3):588 – 602, 2015.
- [30] Castaignet D., Barlas T., Buhl T., Poulsen N.K., Wedel-Heinen J.J., Olesen N.A., Bak C., and Kim T. Full-scale test of trailing edge flaps on a Vestas V27 wind turbine: active load reduction and system identification. *Wind Energy*, 2013.
- [31] Cermelli C., Aubault A., Roddier D., and McCoy T. Qualification of a semi-submersible floating foundation for multi-megawatt wind turbines. In *Proceedings of the Offshore Technology Conference*, Houston, Texas, USA, 2010.
- [32] Cook N. *Designers' Guide to EN 1991-1-4 Eurocode 1: Actions on structures, General actions part 1-4: Wind actions*. Thomas Telford Publishing, 2007.
- [33] Corbetta G., Ho A., Mbistrova A., Ho A., Pineda I., and Ruby K. Wind in power: 2015 European statistics. Report, European Wind Energy Association, EWEA, February 2016.
- [34] Corbetta G., Ho A., Pineda I., Ruby K., Van de Velde L., and Bickley J. Wind energy scenarios for 2030. Report, European Wind Energy Association, EWEA, August 2015.
- [35] Corbetta G. and Mbistrova A. The European offshore wind industry - key trends and statistics 2014. Report, European Wind Energy Association, EWEA, January 2015.
- [36] Cordle A. and Jonkman J. State of the art in floating wind turbine design tools. In *Proceedings of the 21st International Offshore and Polar Engineering Conference*, Maui, Hawaii, USA, 2011.
- [37] Cordle A., Kaufer D., Vorpahl F., Fischer T., Sørensen J.D., Schmidt B., Matha D., Lucas J., McCowen D., Pereira R., and Argyriadis K. Final report for WP4.3: Enhancement of design methods and standards. Technical Report of UpWind project, Garrad Hassan and Partners Ltd, 2006.
- [38] Coulling A.J., Goupee A.J., Robertson A.N., Jonkman J.M., and Dagher H.J. Validation of a FAST semi-submersible floating wind turbine numerical model with DeepCwind test data. *Journal of Renewable and Sustainable Energy*, 5(2), 2013.
- [39] Crespo A.J.C. *Application of the Smoothed Particle Hydrodynamics model SPHysics to free-surface hydrodynamics*. PhD thesis, 2008. University of Vigo.
- [40] Cummins W.E. The impulsive response function and ship motions. Report 1661, United States Department of the Navy, 1962.
- [41] Dalrymple R.A and Knio O. SPH Modelling of Water Waves. In *Coastal Dynamics '01*, pages 779–787, Lund, Sweden, 2001.
- [42] Debrabandere F. *Computational methods for industrial Fluid-Structure Interactions*. PhD thesis, University of Mons, Brussels, Belgium, 2014.
- [43] Degroote J., Haelterman R., Annerel S., Bruggeman P., and Vierendeels J. Performance of partitioned procedures in fluid-structure interaction. *Computers & Structures*, 88(7&8):446 – 457, 2010.
- [44] Dehaeze F. *Aeroelastic Analysis of Turbulent Rotor Flows*. PhD thesis, School of Engineering, University of Liverpool, 2012.
- [45] Dehaeze F. and Barakos G. N. Hovering Rotor Computations Using an Aeroelastic Blade Model. *The Aeronautical Journal*, 116(1180):621–649, 2012.

- [46] Dehaeze F. and Barakos G. N. Mesh Deformation Method for Rotor Flows. *Journal of Aircraft*, 49(1):82–92, Jan 2012.
- [47] Dehaeze F. and Barakos G.N. Mesh deformation method for rotor flows. *Journal of Aircraft*, 49(1):82 – 92, 2012.
- [48] Duan F., Hu Z., Liu G., and Wang J. Experimental comparisons of dynamic properties of floating wind turbine systems based on two different rotor concepts. *Applied Ocean Research*, 58:266 – 280, 2016.
- [49] Dubuc L., Cantariti F., Woodgate M., Gribben B., Badcock K.J., and Richards B.E. A grid deformation technique for unsteady flow computations. *International Journal for Numerical Methods in Fluids*, 32(3):285–311, 2000.
- [50] Euler L. Formulae generales pro translatione quacunque corporum rigidorum. *Novi Commentarii academiae scientiarum Petropolitanae*, 20:189 – 207, 1776. English translation by Johan Sten.
- [51] Faltinsen O.M. *Sea loads on ships and offshore structures*. Cambridge University Press., 1990.
- [52] Farhat C., van der Zee K.G., and Geuzaine P. Provably second-order time-accurate loosely-coupled solution algorithms for transient nonlinear computational aeroelasticity. *Computer Methods in Applied Mechanics and Engineering*, 195(17–18):1973 – 2001, 2006. Fluid-Structure Interaction.
- [53] Fellipa C.A., Park K.C., and Farhat C. Partitioned analysis of coupled mechanical systems. Technical Report CU-CAS-99-06, University of Colorado, Boulder, Colorado, USA, March 1999.
- [54] Fernández M.A. and Moubachir M. A newton method using exact jacobians for solving fluid-structure coupling. *Computers & Structure*, 83(2-3):127–142, January 2005.
- [55] Fichaux N., Beurskens J., Jensen P.H., and Wilkes J. Design limits and solutions for very large wind turbines. Technical report, EWEA, March 2011.
- [56] Fichaux N., Beurskens J., Jensen P.H., and Wilkes J. UPWIND: Design limits and solutions for very large wind turbines. Report, European Wind Energy Association, EWEA, March 2011.
- [57] Frederick M., Kerrigan E.C., and Graham J.M.R. Gust alleviation using rapidly deployed trailing-edge flaps. *Journal of Wind Engineering and Industrial Aerodynamics*, 98(12):712–723, 2010.
- [58] Fried L., Qiao L., Sawyer S., Shukla S., and Bitter L. Global wind report 2014: Annual market update. Online, Global Wind Energy Council, GWEC, March 2014.
- [59] Frost W., Long B.H., and Turner R.E. *Engineering handbook on the atmospheric environmental guidelines for use in wind turbine generator development*. NASA technical paper. National Aeronautics and Space Administration, Scientific and Technical Information Office, 1978.
- [60] Gesteira M.G., Rogers B.D., Dalrymple R.A., Crespo A.J.C., and Narayanaswamy M. User Guide for the SPHysics Code. Technical report, September 2010.
- [61] Giguère P. and Selig M.S. Design of a Tapered and Twisted Blade for the NREL Combined Experiment Rotor. Technical report, NREL, April 1999.
- [62] Gomez-Gesteira M., Crespo A.J.C., Rogers B.D., Dalrymple R.A., Dominguez J.M., and Barreiro A. SPHysics – development of a free-surface fluid solver – Part 2: Efficiency and test cases. *Computers & Geosciences*, 48:300 – 307, 2012.

- [63] Gomez-Gesteira M., Rogers B.D., Crespo A.J.C., Dalrymple R.A., Narayanaswamy M., and Dominguez J.M. SPPhysics – development of a free-surface fluid solver – Part 1: Theory and formulations. *Computers & Geosciences*, 48:289 – 299, 2012.
- [64] Gómez-Iradi S., Steijl R., and Barakos G.N. Development and Validation of a CFD Technique for the Aerodynamic Analysis of HAWT. *Journal of Solar Energy Engineering*, 131(3):031009, 2009.
- [65] Goura G.S.L, Badcock K.J., Woodgate M.A., and Richards B.E. Implicit method for the time marching analysis of flutter. *Aeronautical Journal*, 105(1046), April 2001.
- [66] Greenhow M. and Lin W.M. Nonlinear-free surface effects: Experiments and theory. Technical Report 83-19, Massachusetts Institute of Technology, September 1983.
- [67] Gritskevich M.S., Garbaruk A.V., Schütze J., and Menter F.R. Development of DDES and IDDES formulations for the $k-\omega$ shear stress transport model. *Flow, Turbulence and Combustion*, 88(3):431–449, 2012.
- [68] Hall M., Buckham B., and Crawford C. Evaluating the importance of mooring line model fidelity in floating offshore wind turbine simulations. *Wind Energy*, 17(12):1835–1853, 2014.
- [69] Hall M. and Goupee A. Validation of a lumped-mass mooring line model with deepcwind semisubmersible model test data. *Ocean Engineering*, 104:590 – 603, 2015.
- [70] Hand M.M., Simms D.A., Fingersh L.J., Jager D.W., Cotrell J.R., Schreck S., and Larwood S.M. Unsteady Aerodynamics Experiment Phase VI: Wind Tunnel Test Configurations and Available Data Campaigns. Technical Report NREL/TP-500-29955, National Renewable Energy Laboratory, NREL, December 2001.
- [71] Harlow F.H. and Nakayama P.I. Transport of Turbulence Energy Decay Rate. Technical Report LA-3854, "Los Alamos Sci. Lab.", 1968.
- [72] Hasselmann K., Barnett T.P., Bouws E., Carlson H., Cartwright D.E., Enke K., Ewing J.A., Gienapp H., Hasselmann D.E., Kruseman P., et al. Measurements of wind-wave growth and swell decay during the Joint North Sea Wave Project (JONSWAP). *Deutsche Hydrographische Zeitschrift*, 8(12), 1973.
- [73] Haug E.J. *Computer Aided Kinematics and Dynamics of Mechanical Systems. Vol. 1: Basic Methods*. Allyn & Bacon, Inc., Needham Heights, MA, USA, 1989.
- [74] Hauptmann S., Bülk M., Schön L., Erbslöh S., Boorsma K., Grasso F., M Kühn M., and Cheng P.W. Comparison of the lifting-line free vortex wake method and the blade-element-momentum theory regarding the simulated loads of multi-mw wind turbines. *Journal of Physics: Conference Series*, 555(1), 2014.
- [75] Ho A. and Mbistrova A. The European offshore wind industry - key trends and statistics 1st half 2015. Report, European Wind Energy Association, EWEA, July 2015.
- [76] Horcas S.G., Debrabandere F., Tartinville B., Hirsch C., and Coussement G. *CFD Study of DTU 10 MW RWT Aeroelasticity and Rotor-Tower Interactions*, pages 309–334. Springer International Publishing, Cham, 2016.
- [77] Horcas S.G., Debrabandere F., Tartinville B., Hirsch Ch., and Coussement G. Mesh deformation tool for offshore wind turbines fluid-structure interaction. 2014.
- [78] Huang C., Arrigan J., Nagarajaiah S., and Basu B. Semi-active algorithm for edgewise vibration control in floating wind turbine blades. pages 2097–2110, 2010.

- [79] Huijs F., de Ridder E.-J., and Savenije F. Comparison of model tests and coupled simulations for a semi-submersible floating wind turbine. In *Proceedings of the ASME 2014 33rd International Conference on Ocean, Offshore and Arctic Engineering*, San Francisco, California, USA, 2014.
- [80] Jameson A. Time Dependent Calculations Using Multigrid, with Applications to Unsteady Flows Past Airfoils and Wings. In *10th Computational Fluid Dynamics Conference, Honolulu, HI*, June 1991. AIAA-91-1596.
- [81] Jarkowski M., Woodgate M.A., Barakos G.N., and Rokicki J. Towards consistent hybrid overset mesh methods for rotorcraft CFD. *International Journal for Numerical Methods in Fluids*, 74(8):543–576, 2014.
- [82] Jeon S.H., Cho Y.U., Seo M.W., Cho J.R., and Jeong W.B. Dynamic response of floating substructure of spar-type offshore wind turbine with catenary mooring cables. *Ocean Engineering*, 72:356 – 364, 2013.
- [83] Jeong J. and Hussain F. On the identification of a vortex. *Journal of Fluid Mechanics*, 285:69–94, February 1995.
- [84] Jimenez A. High-Order Schemes with HMB3. Technical Report TN16-008, CFD Laboratory, University of Glasgow, 2016.
- [85] Johnson D.A. and King L.S. A mathematically simple turbulence closure model for attached and separated turbulent boundary layers. *AIAA Journal*, 23(11):1684–1692, 1985.
- [86] Johnson S.J., Baker J.P., van Dam C.P., and Berg D. An overview of active load control techniques for wind turbines with an emphasis on microtabs. *Wind Energy*, 13(2-3):239–253, 2010.
- [87] Jones W.P. and Launder B.E. The prediction of laminarization with a two-equation model of turbulence. *Int. J. Heat Mass Transfer*, 15:301–314, 1972.
- [88] Jonkman J. Definition of the Floating System for Phase IV of OC3. Technical Report NREL/TP-500-47535, NREL, May 2010.
- [89] Jonkman J., Butterfield S., Musial W., and Scott G. Definition of a 5 MW Reference Wind Turbine for Offshore System Development. Technical Report NREL/TP-500-38060, NREL, February 2009.
- [90] Jonkman J.M. Dynamics Modeling and Loads Analysis of an Offshore Floating Wind Turbine. Technical Report NREL/TP-500-41958, NREL, November 2007.
- [91] Jonkman J.M. Influence of control on the pitch damping of a floating wind turbine. In *Proceedings of the 2008 ASME Wind Energy Symposium*, January 2008.
- [92] Jonkman J.M. Dynamics of offshore floating wind turbines – model development and verification. *Wind Energy*, 12(5):459–492, 2009.
- [93] Jonkman J.M. and Buhl M.L. FAST User’s Guide. Technical report, NREL, August 2005.
- [94] Journée J.M.J. and Massie W.W. *Offshore Hydromechanics*. Delft University of Technology, first edition, January 2001.
- [95] Kaimal J.C., Wyngaard J.C., Izumi Y., and CotăŃ O.R. Spectral characteristics of surface-layer turbulence. *Quarterly Journal of the Royal Meteorological Society*, 98(417):563–589, 1972.
- [96] Karimirad M. Modelling aspects of a floating wind turbine for coupled wave-wind-induced dynamic analyses. *Renewable Energy*, 53(0):299 – 305, 2013.

- [97] Karimirad M. and Moan T. A simplified method for coupled analysis of floating offshore wind turbines. *Marine Structures*, 27(1):45 – 63, 2012.
- [98] Kennett D. *On the development of a meshless method to study multibody systems using computational fluid dynamics*. PhD thesis, 2013. University of Liverpool.
- [99] Klein M., Sadiki A., and Janicka J. A digital filter based generation of inflow data for spatially developing direct numerical or large eddy simulations. *Journal of Computational Physics*, 186(2):652 – 665, 2003.
- [100] Kolmogorov A.N. Equations of Turbulent Motion of an Incompressible Fluid. *"Izvestiya Akademii Nauk. Seriya Fizicheskaya"*, 6:55–58, 1942.
- [101] Koo B., Goupee A.J., Lambrakos K., and Lim H.J. Model test data correlations with fully coupled hull/mooring analysis for a floating wind turbine on a semi-submersible platform. In *Proceedings of the ASME 2014 33rd International Conference on Ocean, Offshore and Arctic Engineering*, San Francisco, California, USA, June 2014. Offshore and Arctic Engineering.
- [102] Kreuzer E. and Wilke U. Mooring systems - a multibody dynamic approach. *Multibody System Dynamics*, 8(3):279–297, 2002.
- [103] Krogstad P. and Adaramola M. S. Performance and near wake measurements of a model horizontal axis wind turbine. *Wind Energy*, 15(5):743–756, 2012.
- [104] Küttler U and Wall W.A. Fixed-point fluid–structure interaction solvers with dynamic relaxation. *Computational Mechanics*, 43(1):61–72, 2008.
- [105] Kvittem M.I., Bachynski E.E., and Moan T. Effects of hydrodynamic modelling in fully coupled simulations of a semi-submersible wind turbine. *Energy Procedia*, 24:351 – 362, 2012.
- [106] Lackner M.A. and Rotea M.A. Passive structural control of offshore wind turbines. *Wind Energy*, 14(3):373–388, 2011.
- [107] Lackner M.A. and Rotea M.A. Structural control of floating wind turbines. *Mechatronics*, 21(4):704 – 719, 2011.
- [108] Larsen T.J. and Hansen A.M. How to HAWC2, the user's manual. Technical Report Risø-R-1597(ver.4-3) (EN), DTU Wind Energy, April 2012.
- [109] Larsen T.J. and Hanson T.D. A method to avoid negative damped low frequent tower vibrations for a floating, pitch controlled wind turbine. *Journal of Physics: Conference Series*, 75(1):012073, 2007.
- [110] Lavelly A.W., Vijayakumar G., Kinzel M.P., Brasseur J.G., and Paterson E.G. Space-time loadings on wind turbine blades driven by atmospheric boundary layer turbulence. In *Proceedings of the 49th AIAA Aerospace Sciences Meeting*, Orlando, Florida, USA, 2011.
- [111] Leble V. and Barakos G. Demonstration of a coupled floating offshore wind turbine analysis with high-fidelity methods. *Journal of Fluids and Structures*, 62:272 – 293, 2016.
- [112] Leble V. and Barakos G. Forced pitch motion of wind turbines. *Journal of Physics: Conference Series*, 753(2):022042, 2016.
- [113] Leble V. and Barakos G.N. *Trailing and Leading Edge Flaps for Load Alleviation and Structure Control*, pages 103–114. Springer International Publishing, Cham, 2016.

- [114] Lee S., Churchfield M., Moriarty P., and Jonkman J. Atmospheric and wake turbulence impacts on wind turbine fatigue loading. Technical Report NREL/CP-5000-53567, NREL, December 2012.
- [115] Lee T. and Su Y.Y. Unsteady airfoil with a harmonically deflected trailing-edge flap. *Journal of Fluids and Structures*, 27(8):1411 – 1424, 2011.
- [116] Lee W.T., Bales S.L., and Sowby S.E. *Standardized Wind and Wave Environments for North Pacific Ocean Areas*. David W. Taylor Naval Ship Research and Development Center, 1985.
- [117] Leimkuhler B.J., Reich S., and Skeel R.D. *Mathematical Approaches to Biomolecular Structure and Dynamics*. Springer New York, New York, NY, 1996.
- [118] Leishman J.G. *Principles of Helicopter Aerodynamics*. Cambridge University Press, second edition, July 2006.
- [119] Lesoinne M. and Farhat C. Higher-order subiteration-free staggered algorithm for nonlinear transient aeroelastic problems. *AIAA Journal*, 36(9):1754–1757, Sep 1998.
- [120] Li Y. *Coupled computational fluid dynamics/multibody dynamics method with application to wind turbine simulations*. PhD thesis, 2014. University of Iowa.
- [121] Li Y., Castro A.M., Sinokrot T., Prescott W., and Carrica P.M. Coupled multi-body dynamics and CFD for wind turbine simulation including explicit wind turbulence. *Renewable Energy*, 76:338 – 361, 2015.
- [122] Li Y., Paik K.-J., Xing T., and Carrica P.M. Dynamic overset CFD simulations of wind turbine aerodynamics. *Renewable Energy*, 37(1):285 – 298, 2012.
- [123] Liu M.B. and Liu G.R. *Smoothed Particle Hydrodynamics: A Meshfree Particle Method*. World Scientific, 2003.
- [124] Liu M.B., Liu G.R., and Zong Z. An overview on smoothed particle hydrodynamics. *International Journal of Computational Methods*, 5(1):135–188, 2008.
- [125] Lo E.Y.M. and Shao S. Simulation of near-shore solitary wave mechanics by an incompressible sph method. *Applied Ocean Research*, 24(5):275 – 286, 2002.
- [126] Madabhushi G.S.P. and Haiderali A.E. Evaluation of the p-y Method in the Design of Monopiles for Offshore Wind Turbines. In *Proceedings of the Offshore Technology Conference*, Houston, Texas, USA, 2013. Offshore Technology Conference.
- [127] Madsen H.A., Andersen P.B., Andersen L.T., Bak C., Buhl T., and Li N. The potentials of the controllable rubber trailing edge flap (crtef). In *Proceedings of the European Wind Energy Conference 2010*, Warsaw, Poland, 2010.
- [128] Madsen H.A., Sorensen N.N., and Schreck S. Yaw Aerodynamics Analyzed With Three Codes in Comparison With Experiment. In *ASME 2003 Wind Energy Symposium*, pages 94–103. ASME, 2003.
- [129] Mann J. The spatial structure of neutral atmospheric surface-layer turbulence. *Journal of Fluid Mechanics*, 273:141–168, 8 1994.
- [130] Mann J. Wind field simulation. *Probabilistic Engineering Mechanics*, 13(4):269 – 282, 1998.
- [131] Marino E., Borri C., and Peil U. A fully nonlinear wave model to account for breaking wave impact loads on offshore wind turbines. *Journal of Wind Engineering and Industrial Aerodynamics*, 99(4):483 – 490, 2011. The Fifth International Symposium on Computational Wind Engineering.

- [132] Markou H., Andersen P.B., and Larsen G.C. Potential load reductions on megawatt turbines exposed to wakes using individual-pitch wake compensator and trailing-edge flaps. *Wind Energy*, 14(7):841–857, 2011.
- [133] Martin H.R. Development of a scale model wind turbine for testing of offshore floating wind turbine systems. Master’s thesis, The University of Maine, USA, 2011.
- [134] Matha D., Schlipf M., Cordle A., Pereira R., and Jonkman J. Challenges in simulation of aerodynamics, hydrodynamics, and mooring-line dynamics of floating offshore wind turbines. In *21st Offshore and Polar Engineering Conference*, June 2011.
- [135] Matthies H.G., Niekamp R., and Steindorf J. Algorithms for strong coupling procedures. *Computer Methods in Applied Mechanics and Engineering*, 195(17-18):2028–2049, March 2006.
- [136] McTavish S., Feszty D., and Nitzsche F. Evaluating reynolds number effects in small-scale wind turbine experiments. *Journal of Wind Engineering and Industrial Aerodynamics*, 120:81 – 90, 2013.
- [137] Menter F.R. Two-Equation Eddy-Viscosity Turbulence Models for Engineering Applications. *AIAA Journal*, 32(8):1598–1605, 1994.
- [138] Menter F.R. and Egorov Y. The scale-adaptive simulation method for unsteady turbulent flow predictions. part 1: Theory and model description. *Flow, Turbulence and Combustion*, 85(1):113–138, 2010.
- [139] Monaghan J.J. On the problem of penetration in particle methods. *Journal of Computational Physics*, 82(1):1–15, May 1989.
- [140] Monaghan J.J. Smoothed particle hydrodynamics. *Annual review of astronomy and astrophysics*, 30:543–574, 1992.
- [141] Monaghan J.J. Simulating Free Surface Flows with SPH. *Journal of Computational Physics*, 110(2):399 – 406, 1994.
- [142] Monaghan J.J and Kos A. Solitary waves on a cretan beach. *Journal of Waterway, Port, Coastal, and Ocean Engineering*, 125(3):145–155, 1999.
- [143] Monaghan J.J. and Lattanzio J.C. A refined particle method for astrophysical problems. *Astronomy and Astrophysics*, 149:135–143, August 1985.
- [144] Morison J.R., O’Brein M.P, Johnson J.W., and Schaaf S.A. The Force Exerted by Surface Waves on Piles. *Journal of Petroleum Technology*, 2:149 – 154, 1950.
- [145] Morkovin M.V. Effects of Compressibility on Turbulent Flows. In A. Favre, editor, *Mécanique de la Turbulence*, pages 367–380. CNRS, 1962.
- [146] Musial W., Butterfield S., and Boone A. Feasibility of Floating Platform Systems for Wind Turbines. Technical Report NREL/CP-500-34874, NREL, November 2003.
- [147] Nakajima T., Motora S., and Fujino M. On the dynamic analysis of multi-component mooring lines. In *Proceedings of the Offshore Technology Conference*, Houston, Texas, USA, May 1982. Offshore Technology Conference.
- [148] Nayyar P. and Barakos G. A Summary of Turbulence Modelling Approaches in CFD. Aero Report 0206, university of Glasgow, Aerospace Engineering Dept., September 2002.

- [149] Newman J.N. *Marine Hydrodynamics*. MIT Press, 1977.
- [150] Newman J.N. Second-harmonic wave diffraction at large depths. *Journal of Fluid Mechanics*, 213:59–70, 4 1990.
- [151] Newman J.N. The second-order wave force on a vertical cylinder. *Journal of Fluid Mechanics*, 320:417–443, 8 1996.
- [152] Nielsen F.G., Hanson T.D., and Skaare B. Integrated dynamic analysis of floating offshore wind turbines. In *Proceedings of the 25th International Conference on Offshore Mechanics and Arctic Engineering*, Hamburg, Germany, June 2006. ASME.
- [153] Nikravesh P.E. *Computer-aided Analysis of Mechanical Systems*. Prentice-Hall, Inc., Upper Saddle River, NJ, USA, 1988.
- [154] Ogilvie T.F. Recent progress toward the understanding and prediction of ship motions. In *Proceedings of the 5th Symposium on Naval Hydrodynamics*, pages 3–80, Bergen, Norway, 1964.
- [155] Open MPI. Open MPI documentation. URL: <http://www.open-mpi.org/doc/>, 2015.
- [156] Osher S. and Chakravarthy S. Upwind Schemes and Boundary Conditions with Applications to Euler Equations in General Geometries. *Journal of Computational Physics*, 50(3):447–481, June 1983.
- [157] Passon P and Kühn M. State-of-the-art and development needs of simulation codes for offshore wind turbines. In *Proceedings of the Offshore Wind 2005 Conference and Expedition*, Copenhagen, Denmark, October 2005.
- [158] Peterson E.W. and Hennessey J.P. On the Use of Power Laws for Estimates of Wind Power Potential. *Journal of Applied Meteorology*, 17(3):390–394, 1978.
- [159] Philippe M., Babarit A., and Ferrant P. Modes of response of an offshore wind turbine with directional wind and waves. *Renewable Energy*, 49(0):151 – 155, 2013. Selected papers from World Renewable Energy Congress - XI.
- [160] Pierson W.J. and Moskowitz L. A proposed spectral form for fully developed wind seas based on the similarity theory of S. A. Kitaigorodskii. *Journal of Geophysical Research*, 69(24):5181–5190, 1964.
- [161] Piperno S. and Farhat C. Partitioned procedures for the transient solution of coupled aeroelastic problems – part ii: energy transfer analysis and three-dimensional applications. *Computer Methods in Applied Mechanics and Engineering*, 190(24–25):3147 – 3170, 2001. Advances in Computational Methods for Fluid-Structure Interaction.
- [162] Piperno S., Farhat C., and Larrouturou B. Partitioned procedures for the transient solution of coupled aeroelastic problems part i: Model problem, theory and two-dimensional application. *Computer Methods in Applied Mechanics and Engineering*, 124(1–2):79 – 112, 1995.
- [163] D. J. Price. Smoothed particle hydrodynamics and magnetohydrodynamics. *Journal of Computational Physics*, 231:759–794, February 2012.
- [164] Quallen S., Xing T., Carrica P., Li Y., and Xu J. CFD Simulation of a Floating Offshore Wind Turbine System Using a Quasi-Static Crowfoot Mooring-Line Model. *Journal of Ocean and Wind Energy*, 1(3):143–152, 2014.
- [165] Ramsay R.R., Hoffmann M.J., and Gregorek G.M. Effects of Grit Roughness and Pitch Oscillations on the S809 Airfoil. Technical report, NREL, 1995.

- [166] Rand O. A Phenomenological Modification for Glauert's Classical Induced Velocity Equation. *Journal of the American Helicopter Society*, 51(3):279–282, 2006.
- [167] Roald L., Jonkman J., Robertson A., and Chokani N. The effect of second-order hydrodynamics on floating offshore wind turbines. *Energy Procedia*, 35:253 – 264, 2013. DeepWind'2013 – Selected papers from 10th Deep Sea Offshore Wind R&D Conference, Trondheim, Norway, 24 – 25 January 2013.
- [168] Roddier D., Cermelli C., Aubault A., and Weinstein A. Windfloat: A floating foundation for offshore wind turbines. *Journal of Renewable and Sustainable Energy*, 2(3), 2010.
- [169] Roe P.L. Approximate Riemann Solvers, Parameter Vectors, and Difference Schemes. *Journal of Computational Physics*, 43(2):357–372, October 1981.
- [170] Rosswog S. SPH Methods in the Modelling of Compact Objects. *Living Reviews in Computational Astrophysics*, 1, December 2015.
- [171] Sande B., van der Pijl S.P., and Koren B. Review of computational fluid dynamics for wind turbine wake aerodynamics. *Wind Energy*, 14(7):799–819, 2011.
- [172] Sant T. and Cuschieri K. Comparing Three Aerodynamic Models for Predicting the Thrust and Power Characteristics of a Yawed Floating Wind Turbine Rotor. *Journal of Solar Energy Engineering*, 138(3):031004–031004, Feb 2016.
- [173] Savenije L.B., Ashuri T., Bussel G.J.W., and Staerdaal J.W. Dynamic modeling of a spar-type floating offshore wind turbine. In *Scientific Proceedings European Wind Energy Conference & Exhibition*, 2010.
- [174] Sayed M., Lutz T., and Krämer E. 3-D time-accurate CFD simulations of a multi-megawatt slender bladed HAWT under yawed inflow conditions. *Journal of Physics: Conference Series*, 749(1), 2016.
- [175] Schepers J.G. *Engineering models in wind energy aerodynamics: Development, implementation and analysis using dedicated aerodynamic measurements*. PhD thesis, Wind Energy Department, Delft University of Technology, November 2012.
- [176] Schepers J.G. and Snel H. Model Experiments in Controlled Conditions, Final report. Technical Report ECN-E-07-042, Energy Research Center of the Netherlands, ECN, February 2007.
- [177] Schepers J.G. and Snel H. Final report of IEA Task 29, MexNext (Phase I): analysis of Mexico wind tunnel measurements. Technical report, Energy Research Center of the Netherlands, ECN, February 2012.
- [178] Sclavounos P.D. An unsteady lifting-line theory. *Journal of Engineering Mathematics*, 21(3):201–226, 1987.
- [179] Sebastian T. and Lackner M.A. Offshore floating wind turbines - an aerodynamic perspective. In *Aerospace Sciences Meetings*. American Institute of Aeronautics and Astronautics, 2011.
- [180] Sebastian T. and Lackner M.A. Development of a free vortex wake method code for offshore floating wind turbines. *Renewable Energy*, 46:269 – 275, 2012.
- [181] Seyboth K., Matschoss P., Kadner S., Zwickel T., Eickemeier P., Hansen G., Schlömer S., and von Stechow C. Renewable energy sources and climate change mitigation: Summary for policymakers and technical summary. Technical report, Intergovernmental Panel on Climate Change, IPCC, 2012.

- [182] Shun S. and Ahmed N.A. Wind Turbine Performance Improvements using Active Flow Control Techniques. *Procedia Engineering*, 49(0):83 – 91, 2012.
- [183] Sim C., Manuel L., and Basu S. A comparison of wind turbine load statistics for inflow turbulence fields based on conventional spectral methods and large eddy simulation. In *Proceedings of the 48th AIAA Aerospace Sciences Meeting*, Orlando, Florida, USA, 2010.
- [184] Skaare B., Hanson T.D., Nielsen F.G., Yttervik R., and Hansen A.M. Integrated dynamic analysis of floating offshore wind turbines. In *Proceedings of 2007 European Wind Energy Conference and Exhibition*, 2007.
- [185] Skillen A., Lind S., Stansby P.K., and Rogers B.D. Incompressible Smoothed Particle Hydrodynamics (SPH) with reduced temporal noise and generalised Fickian smoothing applied to body-water slam and efficient wave-body interaction. *Computer Methods in Applied Mechanics and Engineering*, (0):-, 2013.
- [186] Smirnov A., Shi S., and Celik I. Random flow generation technique for large eddy simulations and particle-dynamics modeling. *Journal of Fluids Engineering*, 123(2):359–371, Feb 2001.
- [187] Somers D.M. Design and experimental results for the s809 airfoil. Technical report, NREL, January 1997.
- [188] Spalart P., Jou W.H., Strelets M.Kh., and Allmaras S.R. Comments on the Feasibility of LES for Wings, and on a Hybrid RANS/LES Approach. In *Advances in DNS/LES, Columbus*, 1997.
- [189] Spalart P.R. and Allmaras S.R. A One-Equation Turbulence Model for Aerodynamic Flows. *La Recherche Aéronautique*, (1):5–21, 1994.
- [190] Spalding D.B. The Prediction of Two-Dimensional Steady Turbulent Flows. Heat Transfer Section Report EF/TN/A/16, "Imperial College", 1969.
- [191] Speziale C.G., Abid R., and Anderson E.C. Critical evaluation of two-equation models for near-wall turbulence. *AIAA Journal*, 30:324–331, 1992.
- [192] Steijl R., Barakos G., and Badcock K. A framework for cfd analysis of helicopter rotors in hover and forward flight. *International Journal for Numerical Methods in Fluids*, 51(8):819–847, 2006.
- [193] Steijl R. and Barakos G.N. Sliding mesh algorithm for CFD analysis of helicopter rotor-fuselage aerodynamics. *International Journal for Numerical Methods in Fluids*, 58(5):527–549, 2008.
- [194] Tongchitpakdee C., Benjanirat S., and Sankar L.N. Numerical studies of the effects of active and passive circulation enhancement concepts on wind turbine performance. *Journal of Solar Energy Engineering*, 128(4):432–444, Jul 2006.
- [195] Tran T.-T. and Kim D.-H. The aerodynamic interference effects of a floating offshore wind turbine experiencing platform pitching and yawing motions. *Journal of Mechanical Science and Technology*, 29(2):549–561, 2015.
- [196] Tran T.-T. and Kim D.-H. The platform pitching motion of floating offshore wind turbine: A preliminary unsteady aerodynamic analysis. *Journal of Wind Engineering and Industrial Aerodynamics*, 142:65 – 81, 2015.
- [197] Tran T.-T. and Kim D.-H. Fully coupled aero-hydrodynamic analysis of a semi-submersible FOWT using a dynamic fluid body interaction approach. *Renewable Energy*, 92:244 – 261, 2016.

- [198] van Dam C.P., Chow R., Zayas J.R., and Berg D.E. Computational investigations of small deploying tabs and flaps for aerodynamic load control. *Journal of Physics: Conference Series*, 75(1):012027, 2007.
- [199] Vandamme J., Zou Q., and Reeve D.E. Modelling floating object entry and exit using smoothed particle hydrodynamics. *Journal of Waterway, Port, Coastal and Ocean Engineering*, 137(5):213–224, 2011.
- [200] Veers P.S. Three-dimensional wind simulation. Technical Report SAND88–0152 UC–261, Sandia National Laboratories, March 1988.
- [201] Velazquez R. and Swartz R.A. Gyroscopic Effects of Horizontal Axis Wind Turbines Using Stochastic Aeroelasticity via Spinning Finite Elements. In *Proceedings of ASME 2012 Conference on Smart Materials, Adaptive Structures and Intelligent Systems*, pages 823–831, Stone Mountain, Georgia, USA, September 2012.
- [202] Verlet L. Computer "Experiments" on Classical Fluids. I. Thermodynamical Properties of Lennard-Jones Molecules. *Physical Review*, 159:98–103, Jul 1967.
- [203] Verlet L. Computer "Experiments" on Classical Fluids. II. Equilibrium Correlation Functions. *Physical Review*, 165:201–214, Jan 1968.
- [204] Vermeer L.J., Sørensen J.N., and Crespo A. Wind turbine wake aerodynamics. *Progress in Aerospace Sciences*, 39(6-7):467 – 510, 2003.
- [205] Vierendeels J., Lanoye L., Degroote J., and Verdonck P. Implicit coupling of partitioned fluid-structure interaction problems with reduced order models. *Computers & Structures*, 85(11-14):970–976, June 2007.
- [206] Vita L., Ramachandran G.K.V., Krieger A., Kvittem M.I., Merino D., Cross-Whiter J., and Ackers B.B. Comparison of numerical models and verification against experimental data, using Pelastar TLP concept. In *Proceedings of the ASME 2015 34th International Conference on Ocean, Offshore and Arctic Engineering*, St. John's, Newfoundland, Canada, 2015.
- [207] von Kármán T. Progress in the statistical theory of turbulence. *Proc Natl Acad Sci U S A*, 34(11):530–539, Nov 1948.
- [208] Walker S. and Segawa T. Mitigation of flow separation using DBD plasma actuators on airfoils: A tool for more efficient wind turbine operation. *Renewable Energy*, 42(0):105 – 110, 2012.
- [209] Wilcox D.C. Multiscale Model for Turbulent Flows. *AIAA Journal*, 26(11):1311–1320, 1988.
- [210] Wilcox D.C. Simulation of Transition with a Two-Equation Turbulence Model. *AIAA Journal*, 32(2):247–255, 1994.
- [211] Wilkie W.K., Mirick P.H., and Langston C.W. Rotating shake test and modal analysis of a model helicopter rotor blade. Technical report, NASA, 1997.
- [212] Woodgate M., Badcock K., Richards B., and Gatiganti R. A Parallel 3D Fully Implicit Unsteady Multiblock CFD Code Implemented on a Beowulf Cluster. In *Parallel CFD 1999*, Williamsburg, USA, 1999.
- [213] Woodgate M. and Barakos G. Introduction, development, and validation of smoothed particle hydrodynamics methods in NGVLP. Technical report, University of Liverpool, October 2013.

-
- [214] Woodgate M., Barakos G., Scrase N., and Neville T. Simulation of helicopter ditching using smoothed particle hydrodynamics. In *Proceedings of the 39th European Rotorcraft Forum*, Moscow, Russia, September 2013.
- [215] Yde A. Mann 64bit turbulence generator. <http://www.hawc2.dk/Download/Pre-processing-tools>, March 2014. Accessed: 2016-08-01.
- [216] Zhao Y., Yang J., and He Y. Preliminary Design of a Multi-Column TLP Foundation for a 5-MW Offshore Wind Turbine. *Energies*, 5(10):3874, 2012.
- [217] Zienkiewicz O.C., Taylor R.L., and Zhu J.Z. *The Finite Element Method Set (Sixth Edition)*. Butterworth-Heinemann, Oxford, 2005.

Appendix A

Structural models for DTU 10MW RWT blade

This appendix provides the DTU 10MW RWT blade structural model input files for the NASTRAN, as employed in aero-elastic analyses from Chapter 10. First, the structural model for the straight blade is presented. This is followed by the structural model for the blade with pre-bend and pre-cone. Details of the design can be found in Chapter 9.

A.1 Straight DTU 10MW RWT blade

This section considers the DTU 10MW RWT blade in a straight configuration, as employed in Section 10.2.2 of Chapter 10. Input consists of three files: the *DTU.model* file with the structural model, the *nastran-Loads.dat* file with the aerodynamic loads to be applied to the structure, and the *DTU.bdf* file specifying NASTRAN parameters.

Listing A.1: The structural model file (*DTU.model*) for the straight blade.

```
$*****
$ THIS MODEL TAKES INTO ACCOUNT ELASTIC PROPERTIES
$ AND SHEAR AXIS, ELASTIC AXIS AND MASS CENTRE OFFSETS
$ THE STRAIGHT DTU BLADE IS MODELLED
$ BEAMS ARE MODELLED AS ISOTROPIC MATERIAL WITH
$ ELASTIC PROPERTIES TAKEN FROM THE REPORT
$*****
$ Ixx - area moment of inertia about the first elastic axis
$ is computed from the flapwise radius of gyration Rg_xx as
$ Ixx = Rg_xx*Rg_xx*AREA
$ where AREA is the crossection area of the beam taken from the
$ geometry provided along with the report.
$*****
$ Young modulus is computed as
$ E*Ixx/Ixx, where E*Ixx is the flapwise bedning stiffness in the report [Nm^2]
$*****
$ Shear modulus G is computed from the Flapwise shear stiffness [N],
$ assuming it is defined as G*AREA
$*****
$ Polar moment of area J is computed from the Torsional Stiffness [Nm^2]
$ assuming it is defined as G*J, where G is already computed
$*****
$ Grid nodes are located in the shear centre, therefore the shear centre
$ defined in the report was first computed in the Global Referebce Frame of the blade
$*****
$ Neutral axis in NASTRAN is assumed to be the elastic axis in the report,
$ and the off-set from the shear centre to the elastic axis was incorporated
$ in the PBEAM elements
$*****
$ Nonstructural mass off-set in the blade reference frame from shear
$ centre to the mass centre was incorporated in the PBEAM elements
```

```

$*****
$ Structural twist is included in CBEAM elements, and was first
$ transfered to the blade reference frame
$*****
$*****
$ Material properties: ID, Youngs modulus, Shear modulus, Poissons ratio
$*****
$*****
MAT1, 1, 8.167e+08, 1.102e+08,
MAT1, 2, 8.201e+08, 1.101e+08,
MAT1, 3, 8.410e+08, 1.099e+08,
MAT1, 4, 8.462e+08, 1.060e+08,
MAT1, 5, 8.540e+08, 9.821e+07,
MAT1, 6, 8.470e+08, 8.948e+07,
MAT1, 7, 8.623e+08, 8.042e+07,
MAT1, 8, 9.227e+08, 7.309e+07,
MAT1, 9, 1.031e+09, 7.012e+07,
MAT1, 10, 1.130e+09, 6.847e+07,
MAT1, 11, 1.188e+09, 6.434e+07,
MAT1, 12, 1.222e+09, 6.473e+07,
MAT1, 13, 1.228e+09, 6.256e+07,
MAT1, 14, 1.240e+09, 6.151e+07,
MAT1, 15, 1.261e+09, 6.155e+07,
MAT1, 16, 1.277e+09, 6.151e+07,
MAT1, 17, 1.348e+09, 6.403e+07,
MAT1, 18, 1.418e+09, 6.591e+07,
MAT1, 19, 1.485e+09, 6.780e+07,
MAT1, 20, 1.548e+09, 6.865e+07,
MAT1, 21, 1.610e+09, 6.977e+07,
MAT1, 22, 1.681e+09, 7.083e+07,
MAT1, 23, 1.751e+09, 7.213e+07,
MAT1, 24, 1.820e+09, 7.329e+07,
MAT1, 25, 1.887e+09, 7.365e+07,
MAT1, 26, 1.966e+09, 7.542e+07,
MAT1, 27, 2.013e+09, 7.695e+07,
MAT1, 28, 2.090e+09, 7.765e+07,
MAT1, 29, 2.159e+09, 8.012e+07,
MAT1, 30, 2.216e+09, 8.040e+07,
MAT1, 31, 2.277e+09, 8.301e+07,
MAT1, 32, 2.348e+09, 8.457e+07,
MAT1, 33, 2.400e+09, 8.729e+07,
MAT1, 34, 2.437e+09, 8.832e+07,
MAT1, 35, 2.492e+09, 8.989e+07,
MAT1, 36, 2.510e+09, 9.142e+07,
MAT1, 37, 2.530e+09, 9.284e+07,
MAT1, 38, 2.527e+09, 9.579e+07,
MAT1, 39, 2.525e+09, 9.729e+07,
MAT1, 40, 2.523e+09, 9.903e+07,
MAT1, 41, 2.480e+09, 1.008e+08,
MAT1, 42, 2.460e+09, 1.030e+08,
MAT1, 43, 2.387e+09, 1.026e+08,
MAT1, 44, 2.292e+09, 1.037e+08,
MAT1, 45, 2.183e+09, 1.047e+08,
MAT1, 46, 2.081e+09, 1.046e+08,
MAT1, 47, 1.935e+09, 1.006e+08,
MAT1, 48, 1.786e+09, 9.368e+07,
MAT1, 49, 1.589e+09, 8.986e+07,
MAT1, 50, 1.370e+09, 8.577e+07,
MAT1, 51, 1.616e+12, 1.012e+11,
$*****
$ NEW ROOT ATTACHEMENT FOR ROTATION
$ Root starts at 2.8 m
$ First 3 nodes are fixed (from 0.0m to 2.8m)
$ and artificial springs are added, but the nodes are fixed anyway.
$ Springs are added to produce the output understandable
$ by the HMB helicopter routines.
$*****
GRID, 1, , 0.0, 0.0, 0.0,,123456,
GRID, 2, , 2.800, 0.0, 0.0,,123456,
$LeadLag Spring
CELAS2,2,5000.0,1,6,3,6
$Flapping Spring
CELAS2,3,5000.0,1,5,3,5
$ *****
$ BLADE STRUCTURE - grid 3=root, 53=tip
$ *****
GRID, 3, , 2.800, 0.0, 0.0,,123456

```

```
GRID, 4, , 4.815, -0.00108, -0.01020
GRID, 5, , 6.542, 0.00058, -0.00863
GRID, 6, , 8.269, 0.00482, 0.00641
GRID, 7, , 9.996, 0.01839, 0.01621
GRID, 8, , 11.724, 0.03869, 0.04819
GRID, 9, , 13.450, 0.12950, 0.10178
GRID, 10, , 15.176, 0.23001, 0.15779
GRID, 11, , 16.904, 0.37696, 0.17750
GRID, 12, , 18.344, 0.46594, 0.19388
GRID, 13, , 20.498, 0.49932, 0.19549
GRID, 14, , 22.232, 0.42157, 0.19250
GRID, 15, , 23.959, 0.43672, 0.18902
GRID, 16, , 25.686, 0.45379, 0.18188
GRID, 17, , 27.413, 0.46693, 0.17377
GRID, 18, , 29.141, 0.46726, 0.15665
GRID, 19, , 30.868, 0.44684, 0.13719
GRID, 20, , 32.595, 0.45095, 0.12276
GRID, 21, , 34.323, 0.43621, 0.10913
GRID, 22, , 36.050, 0.43031, 0.10234
GRID, 23, , 37.778, 0.42171, 0.09750
GRID, 24, , 39.505, 0.40558, 0.09390
GRID, 25, , 41.233, 0.40227, 0.09232
GRID, 26, , 42.873, 0.38568, 0.08941
GRID, 27, , 44.601, 0.37586, 0.08748
GRID, 28, , 46.328, 0.36633, 0.08513
GRID, 29, , 48.055, 0.35445, 0.08311
GRID, 30, , 49.783, 0.34419, 0.08030
GRID, 31, , 51.510, 0.33313, 0.07767
GRID, 32, , 53.237, 0.32110, 0.07485
GRID, 33, , 55.051, 0.30752, 0.07137
GRID, 34, , 56.779, 0.29670, 0.06776
GRID, 35, , 58.506, 0.28786, 0.06489
GRID, 36, , 60.233, 0.26843, 0.06112
GRID, 37, , 61.961, 0.25695, 0.05710
GRID, 38, , 63.688, 0.24835, 0.05387
GRID, 39, , 65.354, 0.23696, 0.05002
GRID, 40, , 67.081, 0.21636, 0.04653
GRID, 41, , 68.808, 0.20845, 0.04365
GRID, 42, , 70.535, 0.19638, 0.04014
GRID, 43, , 72.324, 0.18664, 0.03729
GRID, 44, , 74.052, 0.17548, 0.03403
GRID, 45, , 75.779, 0.16261, 0.03214
GRID, 46, , 77.459, 0.14850, 0.02973
GRID, 47, , 79.186, 0.14029, 0.02702
GRID, 48, , 80.961, 0.12192, 0.02551
GRID, 49, , 82.688, 0.11157, 0.02330
GRID, 50, , 84.377, 0.09842, 0.02053
GRID, 51, , 86.143, 0.08157, 0.01794
GRID, 52, , 87.871, 0.06403, 0.01364
GRID, 53, , 89.166, 0.17704, 0.00123

GRID, 301, , 2.800, 5.37957, 0.0
GRID, 401, , 4.815, 5.37892, -0.01020
GRID, 501, , 6.542, 5.38058, -0.00863
GRID, 601, , 8.269, 5.38488, 0.00641
GRID, 701, , 9.996, 5.42947, 0.01621
GRID, 801, , 11.724, 5.52816, 0.04819
GRID, 901, , 13.450, 5.73031, 0.10178
GRID, 1001, , 15.176, 5.96094, 0.15779
GRID, 1101, , 16.904, 6.24271, 0.17750
GRID, 1201, , 18.344, 6.43721, 0.19388
GRID, 1301, , 20.498, 6.59796, 0.19549
GRID, 1401, , 22.232, 6.58594, 0.19250
GRID, 1501, , 23.959, 6.63548, 0.18902
GRID, 1601, , 25.686, 6.65889, 0.18188
GRID, 1701, , 27.413, 6.65325, 0.17377
GRID, 1801, , 29.141, 6.61259, 0.15665
GRID, 1901, , 30.868, 6.53166, 0.13719
GRID, 2001, , 32.595, 6.45817, 0.12276
GRID, 2101, , 34.323, 6.35116, 0.10913
GRID, 2201, , 36.050, 6.24086, 0.10234
GRID, 2301, , 37.778, 6.11808, 0.09750
GRID, 2401, , 39.505, 5.98044, 0.09390
GRID, 2501, , 41.233, 5.84948, 0.09232
GRID, 2601, , 42.873, 5.70681, 0.08941
GRID, 2701, , 44.601, 5.55965, 0.08748
GRID, 2801, , 46.328, 5.40901, 0.08513
```

```
GRID, 2901, , 48.055, 5.2529, 0.08311
GRID, 3001, , 49.783, 5.09596, 0.08030
GRID, 3101, , 51.510, 4.9367, 0.07767
GRID, 3201, , 53.237, 4.7756, 0.07485
GRID, 3301, , 55.051, 4.60535, 0.07137
GRID, 3401, , 56.779, 4.44587, 0.06776
GRID, 3501, , 58.506, 4.2894, 0.06489
GRID, 3601, , 60.233, 4.12352, 0.06112
GRID, 3701, , 61.961, 3.96699, 0.05710
GRID, 3801, , 63.688, 3.81515, 0.05387
GRID, 3901, , 65.354, 3.66746, 0.05002
GRID, 4001, , 67.081, 3.50779, 0.04653
GRID, 4101, , 68.808, 3.36334, 0.04365
GRID, 4201, , 70.535, 3.2175, 0.04014
GRID, 4301, , 72.324, 3.07237, 0.03729
GRID, 4401, , 74.052, 2.93365, 0.03403
GRID, 4501, , 75.779, 2.79663, 0.03214
GRID, 4601, , 77.459, 2.66505, 0.02973
GRID, 4701, , 79.186, 2.53916, 0.02702
GRID, 4801, , 80.961, 2.39496, 0.02551
GRID, 4901, , 82.688, 2.24368, 0.02330
GRID, 5001, , 84.377, 2.06192, 0.02053
GRID, 5101, , 86.143, 1.821, 0.01794
GRID, 5201, , 87.871, 1.44912, 0.01364
GRID, 5301, , 89.166, 0.377036, 0.00123

GRID, 302, , 2.800, -10.7604, 0.0
GRID, 402, , 4.815, -10.7611, -0.01020
GRID, 502, , 6.542, -10.7594, -0.00863
GRID, 602, , 8.269, -10.7553, 0.00641
GRID, 702, , 9.996, -10.8038, 0.01621
GRID, 802, , 11.724, -10.9403, 0.04819
GRID, 902, , 13.450, -11.0721, 0.10178
GRID, 1002, , 15.176, -11.2319, 0.15779
GRID, 1102, , 16.904, -11.3545, 0.17750
GRID, 1202, , 18.344, -11.4766, 0.19388
GRID, 1302, , 20.498, -11.6979, 0.19549
GRID, 1402, , 22.232, -11.9072, 0.19250
GRID, 1502, , 23.959, -11.9608, 0.18902
GRID, 1602, , 25.686, -11.9564, 0.18188
GRID, 1702, , 27.413, -11.9057, 0.17377
GRID, 1802, , 29.141, -11.8234, 0.15665
GRID, 1902, , 30.868, -11.7228, 0.13719
GRID, 2002, , 32.595, -11.5635, 0.12276
GRID, 2102, , 34.323, -11.3937, 0.10913
GRID, 2202, , 36.050, -11.1908, 0.10234
GRID, 2302, , 37.778, -10.971, 0.09750
GRID, 2402, , 39.505, -10.7441, 0.09390
GRID, 2502, , 41.233, -10.4922, 0.09232
GRID, 2602, , 42.873, -10.2566, 0.08941
GRID, 2702, , 44.601, -9.99173, 0.08748
GRID, 2802, , 46.328, -9.71902, 0.08513
GRID, 2902, , 48.055, -9.44244, 0.08311
GRID, 3002, , 49.783, -9.15936, 0.08030
GRID, 3102, , 51.510, -8.87401, 0.07767
GRID, 3202, , 53.237, -8.58792, 0.07485
GRID, 3302, , 55.051, -8.28813, 0.07137
GRID, 3402, , 56.779, -8.00164, 0.06776
GRID, 3502, , 58.506, -7.7152, 0.06489
GRID, 3602, , 60.233, -7.44176, 0.06112
GRID, 3702, , 61.961, -7.16312, 0.05710
GRID, 3802, , 63.688, -6.88524, 0.05387
GRID, 3902, , 65.354, -6.62404, 0.05002
GRID, 4002, , 67.081, -6.3665, 0.04653
GRID, 4102, , 68.808, -6.10132, 0.04365
GRID, 4202, , 70.535, -5.84585, 0.04014
GRID, 4302, , 72.324, -5.58481, 0.03729
GRID, 4402, , 74.052, -5.34087, 0.03403
GRID, 4502, , 75.779, -5.10542, 0.03214
GRID, 4602, , 77.459, -4.8846, 0.02973
GRID, 4702, , 79.186, -4.65745, 0.02702
GRID, 4802, , 80.961, -4.42414, 0.02551
GRID, 4902, , 82.688, -4.15265, 0.02330
GRID, 5002, , 84.377, -3.82859, 0.02053
GRID, 5102, , 86.143, -3.39731, 0.01794
GRID, 5202, , 87.871, -2.70615, 0.01364
GRID, 5302, , 89.166, -0.222964, 0.00123
```

```

$*****
$ CBEAMs show the 2 connected grids and the reference pt. location
$ which indicates blade twist by changing the direction of the principle
$ plane of bending
$ cos(twist) and sin(twist)
$ where "twist" is a structural twist from the report defined
$ in the reference frame of the blade
$*****
CBEAM, 1, 1, 3, 4, 0.0, 0.96815, 0.25038
CBEAM, 2, 2, 4, 5, 0.0, 0.96815, 0.25038
CBEAM, 3, 3, 5, 6, 0.0, 0.96815, 0.25038
CBEAM, 4, 4, 6, 7, 0.0, 0.96815, 0.25038
CBEAM, 5, 5, 7, 8, 0.0, 0.96821, 0.25013
CBEAM, 6, 6, 8, 9, 0.0, 0.87916, -0.47652
CBEAM, 7, 7, 9, 10, 0.0, 0.92785, -0.37296
CBEAM, 8, 8, 10, 11, 0.0, 0.97698, -0.21334
CBEAM, 9, 9, 11, 12, 0.0, 0.99377, -0.11144
CBEAM, 10, 10, 12, 13, 0.0, 0.99893, -0.04621
CBEAM, 11, 11, 13, 14, 0.0, 0.99992, -0.01297
CBEAM, 12, 12, 14, 15, 0.0, 0.99998, 0.00674
CBEAM, 13, 13, 15, 16, 0.0, 0.99989, 0.01508
CBEAM, 14, 14, 16, 17, 0.0, 0.99982, 0.01912
CBEAM, 15, 15, 17, 18, 0.0, 0.99973, 0.02303
CBEAM, 16, 16, 18, 19, 0.0, 0.99931, 0.03705
CBEAM, 17, 17, 19, 20, 0.0, 0.99931, 0.03725
CBEAM, 18, 18, 20, 21, 0.0, 0.99934, 0.03625
CBEAM, 19, 19, 21, 22, 0.0, 0.99945, 0.03318
CBEAM, 20, 20, 22, 23, 0.0, 0.99953, 0.03071
CBEAM, 21, 21, 23, 24, 0.0, 0.99955, 0.03001
CBEAM, 22, 22, 24, 25, 0.0, 0.99956, 0.02975
CBEAM, 23, 23, 25, 26, 0.0, 0.99959, 0.02866
CBEAM, 24, 24, 26, 27, 0.0, 0.99964, 0.02681
CBEAM, 25, 25, 27, 28, 0.0, 0.99969, 0.02508
CBEAM, 26, 26, 28, 29, 0.0, 0.99973, 0.02307
CBEAM, 27, 27, 29, 30, 0.0, 0.99981, 0.01955
CBEAM, 28, 28, 30, 31, 0.0, 0.99986, 0.01684
CBEAM, 29, 29, 31, 32, 0.0, 0.99990, 0.01383
CBEAM, 30, 30, 32, 33, 0.0, 0.99995, 0.01025
CBEAM, 31, 31, 33, 34, 0.0, 0.99998, 0.00598
CBEAM, 32, 32, 34, 35, 0.0, 1.00000, 0.00237
CBEAM, 33, 33, 35, 36, 0.0, 1.00000, -0.00138
CBEAM, 34, 34, 36, 37, 0.0, 0.99999, -0.00538
CBEAM, 35, 35, 37, 38, 0.0, 0.99996, -0.00938
CBEAM, 36, 36, 38, 39, 0.0, 0.99991, -0.01306
CBEAM, 37, 37, 39, 40, 0.0, 0.99986, -0.01686
CBEAM, 38, 38, 40, 41, 0.0, 0.99978, -0.02096
CBEAM, 39, 39, 41, 42, 0.0, 0.99970, -0.02446
CBEAM, 40, 40, 42, 43, 0.0, 0.99959, -0.02854
CBEAM, 41, 41, 43, 44, 0.0, 0.99948, -0.03217
CBEAM, 42, 42, 44, 45, 0.0, 0.99934, -0.03629
CBEAM, 43, 43, 45, 46, 0.0, 0.99921, -0.03983
CBEAM, 44, 44, 46, 47, 0.0, 0.99905, -0.04357
CBEAM, 45, 45, 47, 48, 0.0, 0.99889, -0.04715
CBEAM, 46, 46, 48, 49, 0.0, 0.99865, -0.05192
CBEAM, 47, 47, 49, 50, 0.0, 0.99846, -0.05549
CBEAM, 48, 48, 50, 51, 0.0, 0.99819, -0.06012
CBEAM, 49, 49, 51, 52, 0.0, 0.99784, -0.06570
CBEAM, 50, 50, 52, 53, 0.0, 0.99745, -0.07131
$*****
$ Rigid weightless elements showing the torsion
$ Leading Edge
$*****
RBAR, 301, 3, 301, 123456
RBAR, 401, 4, 401, 123456
RBAR, 501, 5, 501, 123456
RBAR, 601, 6, 601, 123456
RBAR, 701, 7, 701, 123456
RBAR, 801, 8, 801, 123456
RBAR, 901, 9, 901, 123456
RBAR, 1001, 10, 1001, 123456
RBAR, 1101, 11, 1101, 123456
RBAR, 1201, 12, 1201, 123456
RBAR, 1301, 13, 1301, 123456
RBAR, 1401, 14, 1401, 123456
RBAR, 1501, 15, 1501, 123456
RBAR, 1601, 16, 1601, 123456
RBAR, 1701, 17, 1701, 123456

```

```

RBAR, 1801, 18, 1801, 123456
RBAR, 1901, 19, 1901, 123456
RBAR, 2001, 20, 2001, 123456
RBAR, 2101, 21, 2101, 123456
RBAR, 2201, 22, 2201, 123456
RBAR, 2301, 23, 2301, 123456
RBAR, 2401, 24, 2401, 123456
RBAR, 2501, 25, 2501, 123456
RBAR, 2601, 26, 2601, 123456
RBAR, 2701, 27, 2701, 123456
RBAR, 2801, 28, 2801, 123456
RBAR, 2901, 29, 2901, 123456
RBAR, 3001, 30, 3001, 123456
RBAR, 3101, 31, 3101, 123456
RBAR, 3201, 32, 3201, 123456
RBAR, 3301, 33, 3301, 123456
RBAR, 3401, 34, 3401, 123456
RBAR, 3501, 35, 3501, 123456
RBAR, 3601, 36, 3601, 123456
RBAR, 3701, 37, 3701, 123456
RBAR, 3801, 38, 3801, 123456
RBAR, 3901, 39, 3901, 123456
RBAR, 4001, 40, 4001, 123456
RBAR, 4101, 41, 4101, 123456
RBAR, 4201, 42, 4201, 123456
RBAR, 4301, 43, 4301, 123456
RBAR, 4401, 44, 4401, 123456
RBAR, 4501, 45, 4501, 123456
RBAR, 4601, 46, 4601, 123456
RBAR, 4701, 47, 4701, 123456
RBAR, 4801, 48, 4801, 123456
RBAR, 4901, 49, 4901, 123456
RBAR, 5001, 50, 5001, 123456
RBAR, 5101, 51, 5101, 123456
RBAR, 5201, 52, 5201, 123456
RBAR, 5301, 53, 5301, 123456
$*****
$ Trailing Edge
$*****
RBAR, 302, 3, 302, 123456
RBAR, 402, 4, 402, 123456
RBAR, 502, 5, 502, 123456
RBAR, 602, 6, 602, 123456
RBAR, 702, 7, 702, 123456
RBAR, 802, 8, 802, 123456
RBAR, 902, 9, 902, 123456
RBAR, 1002, 10, 1002, 123456
RBAR, 1102, 11, 1102, 123456
RBAR, 1202, 12, 1202, 123456
RBAR, 1302, 13, 1302, 123456
RBAR, 1402, 14, 1402, 123456
RBAR, 1502, 15, 1502, 123456
RBAR, 1602, 16, 1602, 123456
RBAR, 1702, 17, 1702, 123456
RBAR, 1802, 18, 1802, 123456
RBAR, 1902, 19, 1902, 123456
RBAR, 2002, 20, 2002, 123456
RBAR, 2102, 21, 2102, 123456
RBAR, 2202, 22, 2202, 123456
RBAR, 2302, 23, 2302, 123456
RBAR, 2402, 24, 2402, 123456
RBAR, 2502, 25, 2502, 123456
RBAR, 2602, 26, 2602, 123456
RBAR, 2702, 27, 2702, 123456
RBAR, 2802, 28, 2802, 123456
RBAR, 2902, 29, 2902, 123456
RBAR, 3002, 30, 3002, 123456
RBAR, 3102, 31, 3102, 123456
RBAR, 3202, 32, 3202, 123456
RBAR, 3302, 33, 3302, 123456
RBAR, 3402, 34, 3402, 123456
RBAR, 3502, 35, 3502, 123456
RBAR, 3602, 36, 3602, 123456
RBAR, 3702, 37, 3702, 123456
RBAR, 3802, 38, 3802, 123456
RBAR, 3902, 39, 3902, 123456
RBAR, 4002, 40, 4002, 123456

```

```

RBAR, 4102, 41, 4102, 123456
RBAR, 4202, 42, 4202, 123456
RBAR, 4302, 43, 4302, 123456
RBAR, 4402, 44, 4402, 123456
RBAR, 4502, 45, 4502, 123456
RBAR, 4602, 46, 4602, 123456
RBAR, 4702, 47, 4702, 123456
RBAR, 4802, 48, 4802, 123456
RBAR, 4902, 49, 4902, 123456
RBAR, 5002, 50, 5002, 123456
RBAR, 5102, 51, 5102, 123456
RBAR, 5202, 52, 5202, 123456
RBAR, 5302, 53, 5302, 123456
$*****
$ PBEAM FORMAT
$ PBEAM, PID MID, A, I1, I2, I12, J, NSM, +P2 (FOR GRID A)
$ +P2, C1, C2, D1, D2, E1, E2, F1, F2, +P3 (NOT USED) . .
$ +P3, SO, X/XB, A, I1, I2, I12, J, NSM, +P4 (FOR GRID B=X/XB)
$ +P4, C1, C2, D1, D2, E1, E2, F1, F2, +P5 (NOT USED)
$ +P5, K1, K2, S1, S2, NSI(A), NSI(B), CW, CW, +P6 (NSI=MASS INERTIA ABOUT CG)
$ +P6, M1, M2, M1, M2, N1, N2, N1, N2 (M1,M2 = Y,Z OFFSET OF CG FROM SHEAR CTR)
$*****
PBEAM,1,1,22.7700,70.9496,75.7551,0.0, 2.4925e+02,1189.51,+103
+103,YESA,1.0, 22.7700,70.9335,75.8133,0.0, 2.4949e+02,1191.64,+105
+105, , , , 0.0, 0.0, , ,+106
+106,-0.00130,0.00600,-0.00180,0.00600,-0.00200,0.00630,-0.00270,0.00630
PBEAM,2,2,22.7700,70.9335,75.8133,0.0, 2.4949e+02,1191.64,+203
+203,YESA,1.0, 22.6236,70.0630,74.9055,0.0, 2.4860e+02,1202.77,+205
+205, , , , 0.0, 0.0, , ,+206
+206,-0.00180,0.00600,-0.01020,0.00280,-0.00270,0.00630,-0.00450,0.00440
PBEAM,3,3,22.6236,70.0630,74.9055,0.0, 2.4860e+02,1202.77,+303
+303,YESA,1.0, 22.1168,67.5472,71.0785,0.0, 2.4143e+02,1171.49,+305
+305, , , , 0.0, 0.0, , ,+306
+306,-0.01020,0.00280,-0.02360,-0.01040,-0.00450,0.00440,-0.02240,-0.00950
PBEAM,4,4,22.1168,67.5472,71.0785,0.0, 2.4143e+02,1171.49,+403
+403,YESA,1.0, 21.2052,62.8430,63.8840,0.0, 2.2545e+02,1113.62,+405
+405, , , , 0.0, 0.0, , ,+406
+406,-0.02360,-0.01040,-0.03880,-0.01930,-0.02240,-0.00950,-0.02390,-0.01630
PBEAM,5,5,21.2052,62.8430,63.8840,0.0, 2.2545e+02,1113.62,+503
+503,YESA,1.0, 19.8717,58.7611,52.0676,0.0, 2.0552e+02,1049.31,+505
+505, , , , 0.0, 0.0, , ,+506
+506,-0.03880,-0.01930,-0.09300,-0.04070,-0.02390,-0.01630,-0.07130,-0.03460
PBEAM,6,6,19.8717,58.7611,52.0676,0.0, 2.0552e+02,1049.31,+603
+603,YESA,1.0, 18.1044,50.2318,41.5099,0.0, 1.7372e+02,974.63,+605
+605, , , , 0.0, 0.0, , ,+606
+606,-0.09300,-0.04070,-0.19280,-0.06340,-0.07130,-0.03460,-0.15440,-0.05930
PBEAM,7,7,18.1044,50.2318,41.5099,0.0, 1.7372e+02,974.63,+703
+703,YESA,1.0, 16.0708,42.7928,30.7696,0.0, 1.3819e+02,908.74,+705
+705, , , , 0.0, 0.0, , ,+706
+706,-0.19280,-0.06340,-0.34310,-0.08770,-0.15440,-0.05930,-0.29520,-0.08910
PBEAM,8,8,16.0708,42.7928,30.7696,0.0, 1.3819e+02,908.74,+803
+803,YESA,1.0, 14.0891,36.4162,22.0072,0.0, 1.0622e+02,868.87,+805
+805, , , , 0.0, 0.0, , ,+806
+806,-0.34310,-0.08770,-0.50000,-0.06940,-0.29520,-0.08910,-0.44390,-0.07510
PBEAM,9,9,14.0891,36.4162,22.0072,0.0, 1.0622e+02,868.87,+903
+903,YESA,1.0, 12.7081,32.5286,16.9177,0.0, 8.8043e+01,845.51,+905
+905, , , , 0.0, 0.0, , ,+906
+906,-0.50000,-0.06940,-0.61290,-0.06550,-0.44390,-0.07510,-0.54870,-0.07330
PBEAM,10,10,12.7081,32.5286,16.9177,0.0, 8.8043e+01,845.51,+1003
+1003,YESA,1.0, 11.2713,28.5702,12.4479,0.0, 6.2972e+01,775.15,+1005
+1005, , , , 0.0, 0.0, , ,+1006
+1006,-0.61290,-0.06550,-0.70430,-0.07180,-0.54870,-0.07330,-0.60580,-0.08200
PBEAM,11,11,11.2713,28.5702,12.4479,0.0, 6.2972e+01,775.15,+1103
+1103,YESA,1.0, 10.5007,26.8347,10.3584,0.0, 5.1766e+01,735.79,+1105
+1105, , , , 0.0, 0.0, , ,+1106
+1106,-0.70430,-0.07180,-0.66680,-0.08410,-0.60580,-0.08200,-0.54190,-0.09350
PBEAM,12,12,10.5007,26.8347,10.3584,0.0, 5.1766e+01,735.79,+1203
+1203,YESA,1.0, 9.8516,24.8214,8.7977,0.0, 4.2163e+01,691.12,+1205
+1205, , , , 0.0, 0.0, , ,+1206
+1206,-0.66680,-0.08410,-0.69000,-0.08110,-0.54190,-0.09350,-0.55030,-0.08910
PBEAM,13,13,9.8516,24.8214,8.7977,0.0, 4.2163e+01,691.12,+1303
+1303,YESA,1.0, 9.2681,22.9148,7.5289,0.0, 3.4452e+01,654.85,+1305
+1305, , , , 0.0, 0.0, , ,+1306
+1306,-0.69000,-0.08110,-0.70100,-0.07580,-0.55030,-0.08910,-0.54140,-0.08250
PBEAM,14,14,9.2681,22.9148,7.5289,0.0, 3.4452e+01,654.85,+1403
+1403,YESA,1.0, 8.7187,21.0144,6.4529,0.0, 2.8330e+01,625.88,+1405
+1405, , , , 0.0, 0.0, , ,+1406

```

+1406,-0.70100,-0.07580,-0.70230,-0.07140,-0.54140,-0.08250,-0.52910,-0.07760
PBEAM,15,15,8.7187,21.0144,6.4529,0.0, 2.8330e+01,625.88,+1503
+1503,YESA,1.0, 8.1566,19.9518,5.3886,0.0, 2.3063e+01,593.32,+1505
+1505, , , , 0.0, 0.0, , , +1506
+1506,-0.70230,-0.07140,-0.73870,-0.06150,-0.52910,-0.07760,-0.57930,-0.06760
PBEAM,16,16,8.1566,19.9518,5.3886,0.0, 2.3063e+01,593.32,+1603
+1603,YESA,1.0, 7.5909,17.8835,4.5194,0.0, 1.9405e+01,580.97,+1605
+1605, , , , 0.0, 0.0, , , +1606
+1606,-0.73870,-0.06150,-0.72080,-0.05460,-0.57930,-0.06760,-0.55550,-0.06090
PBEAM,17,17,7.5909,17.8835,4.5194,0.0, 1.9405e+01,580.97,+1703
+1703,YESA,1.0, 7.0644,15.9438,3.8070,0.0, 1.6531e+01,566.23,+1705
+1705, , , , 0.0, 0.0, , , +1706
+1706,-0.72080,-0.05460,-0.71480,-0.04900,-0.55550,-0.06090,-0.54920,-0.05550
PBEAM,18,18,7.0644,15.9438,3.8070,0.0, 1.6531e+01,566.23,+1803
+1803,YESA,1.0, 6.5743,14.0580,3.2306,0.0, 1.4188e+01,548.24,+1805
+1805, , , , 0.0, 0.0, , , +1806
+1806,-0.71480,-0.04900,-0.69640,-0.04380,-0.54920,-0.05550,-0.51690,-0.05050
PBEAM,19,19,6.5743,14.0580,3.2306,0.0, 1.4188e+01,548.24,+1903
+1903,YESA,1.0, 6.1189,12.3087,2.7525,0.0, 1.2141e+01,529.65,+1905
+1905, , , , 0.0, 0.0, , , +1906
+1906,-0.69640,-0.04380,-0.67030,-0.04170,-0.51690,-0.05050,-0.48750,-0.04860
PBEAM,20,20,6.1189,12.3087,2.7525,0.0, 1.2141e+01,529.65,+2003
+2003,YESA,1.0, 5.7121,10.8750,2.3551,0.0, 1.0672e+01,510.31,+2005
+2005, , , , 0.0, 0.0, , , +2006
+2006,-0.67030,-0.04170,-0.64590,-0.04010,-0.48750,-0.04860,-0.46970,-0.04690
PBEAM,21,21,5.7121,10.8750,2.3551,0.0, 1.0672e+01,510.31,+2103
+2103,YESA,1.0, 5.3162,9.5986,1.9931,0.0, 9.2392e+00,494.68,+2105
+2105, , , , 0.0, 0.0, , , +2106
+2106,-0.64590,-0.04010,-0.62730,-0.03930,-0.46970,-0.04690,-0.45430,-0.04590
PBEAM,22,22,5.3162,9.5986,1.9931,0.0, 9.2392e+00,494.68,+2203
+2203,YESA,1.0, 4.9420,8.3738,1.6878,0.0, 7.9139e+00,477.51,+2205
+2205, , , , 0.0, 0.0, , , +2206
+2206,-0.62730,-0.03930,-0.60890,-0.03900,-0.45430,-0.04590,-0.44250,-0.04560
PBEAM,23,23,4.9420,8.3738,1.6878,0.0, 7.9139e+00,477.51,+2303
+2303,YESA,1.0, 4.6066,7.3879,1.4384,0.0, 6.8618e+00,460.93,+2305
+2305, , , , 0.0, 0.0, , , +2306
+2306,-0.60890,-0.03900,-0.59030,-0.03790,-0.44250,-0.04560,-0.42130,-0.04440
PBEAM,24,24,4.6066,7.3879,1.4384,0.0, 6.8618e+00,460.93,+2403
+2403,YESA,1.0, 4.2736,6.3994,1.2168,0.0, 6.0174e+00,441.78,+2405
+2405, , , , 0.0, 0.0, , , +2406
+2406,-0.59030,-0.03790,-0.57350,-0.03730,-0.42130,-0.04440,-0.40430,-0.04360
PBEAM,25,25,4.2736,6.3994,1.2168,0.0, 6.0174e+00,441.78,+2503
+2503,YESA,1.0, 3.9613,5.6040,1.0247,0.0, 5.1956e+00,425.33,+2505
+2505, , , , 0.0, 0.0, , , +2506
+2506,-0.57350,-0.03730,-0.56100,-0.03610,-0.40430,-0.04360,-0.39260,-0.04220
PBEAM,26,26,3.9613,5.6040,1.0247,0.0, 5.1956e+00,425.33,+2603
+2603,YESA,1.0, 3.6689,4.7206,0.8727,0.0, 4.3906e+00,401.38,+2605
+2605, , , , 0.0, 0.0, , , +2606
+2606,-0.56100,-0.03610,-0.51910,-0.03610,-0.39260,-0.04220,-0.36320,-0.04190
PBEAM,27,27,3.6689,4.7206,0.8727,0.0, 4.3906e+00,401.38,+2703
+2703,YESA,1.0, 3.3956,4.1094,0.7345,0.0, 3.8258e+00,385.14,+2705
+2705, , , , 0.0, 0.0, , , +2706
+2706,-0.51910,-0.03610,-0.50650,-0.03480,-0.36320,-0.04190,-0.35280,-0.04040
PBEAM,28,28,3.3956,4.1094,0.7345,0.0, 3.8258e+00,385.14,+2803
+2803,YESA,1.0, 3.1407,3.5136,0.6233,0.0, 3.2950e+00,365.95,+2805
+2805, , , , 0.0, 0.0, , , +2806
+2806,-0.50650,-0.03480,-0.47970,-0.03420,-0.35280,-0.04040,-0.33810,-0.03940
PBEAM,29,29,3.1407,3.5136,0.6233,0.0, 3.2950e+00,365.95,+2903
+2903,YESA,1.0, 2.9034,3.0147,0.5274,0.0, 2.8004e+00,346.94,+2905
+2905, , , , 0.0, 0.0, , , +2906
+2906,-0.47970,-0.03420,-0.46070,-0.03350,-0.33810,-0.03940,-0.32200,-0.03850
PBEAM,30,30,2.9034,3.0147,0.5274,0.0, 2.8004e+00,346.94,+3003
+3003,YESA,1.0, 2.6720,2.4980,0.4459,0.0, 2.3907e+00,326.32,+3005
+3005, , , , 0.0, 0.0, , , +3006
+3006,-0.46070,-0.03350,-0.42960,-0.03260,-0.32200,-0.03850,-0.29980,-0.03720
PBEAM,31,31,2.6720,2.4980,0.4459,0.0, 2.3907e+00,326.32,+3103
+3103,YESA,1.0, 2.4676,2.1591,0.3771,0.0, 2.0673e+00,310.27,+3105
+3105, , , , 0.0, 0.0, , , +3106
+3106,-0.42960,-0.03260,-0.41860,-0.03110,-0.29980,-0.03720,-0.29020,-0.03560
PBEAM,32,32,2.4676,2.1591,0.3771,0.0, 2.0673e+00,310.27,+3203
+3203,YESA,1.0, 2.2779,1.8189,0.3215,0.0, 1.7455e+00,291.66,+3205
+3205, , , , 0.0, 0.0, , , +3206
+3206,-0.41860,-0.03110,-0.39300,-0.03080,-0.29020,-0.03560,-0.27620,-0.03500
PBEAM,33,33,2.2779,1.8189,0.3215,0.0, 1.7455e+00,291.66,+3303
+3303,YESA,1.0, 2.1013,1.5318,0.2743,0.0, 1.5010e+00,272.43,+3305
+3305, , , , 0.0, 0.0, , , +3306
+3306,-0.39300,-0.03080,-0.36600,-0.02970,-0.27620,-0.03500,-0.25830,-0.03350

```

PBEAM,34,34,2.1013,1.5318,0.2743,0.0, 1.5010e+00,272.43,+3403
+3403,YESA,1.0, 1.9368,1.3112,0.2320,0.0, 1.2962e+00,256.95,+3405
+3405, , , , ,0.0, 0.0, , ,+3406
+3406,-0.36600,-0.02970,-0.35470,-0.02790,-0.25830,-0.03350,-0.24880,-0.03170
PBEAM,35,35,1.9368,1.3112,0.2320,0.0, 1.2962e+00,256.95,+3503
+3503,YESA,1.0, 1.7839,1.0954,0.1990,0.0, 1.1089e+00,237.77,+3505
+3505, , , , ,0.0, 0.0, , ,+3506
+3506,-0.35470,-0.02790,-0.33390,-0.02730,-0.24880,-0.03170,-0.23590,-0.03080
PBEAM,36,36,1.7839,1.0954,0.1990,0.0, 1.1089e+00,237.77,+3603
+3603,YESA,1.0, 1.6494,0.9452,0.1696,0.0, 9.6039e-01,221.77,+3605
+3605, , , , ,0.0, 0.0, , ,+3606
+3606,-0.33390,-0.02730,-0.32590,-0.02550,-0.23590,-0.03080,-0.22940,-0.02900
PBEAM,37,37,1.6494,0.9452,0.1696,0.0, 9.6039e-01,221.77,+3703
+3703,YESA,1.0, 1.5172,0.7916,0.1437,0.0, 8.0393e-01,203.15,+3705
+3705, , , , ,0.0, 0.0, , ,+3706
+3706,-0.32590,-0.02550,-0.30420,-0.02420,-0.22940,-0.02900,-0.21510,-0.02750
PBEAM,38,38,1.5172,0.7916,0.1437,0.0, 8.0393e-01,203.15,+3803
+3803,YESA,1.0, 1.3926,0.6752,0.1207,0.0, 6.7452e-01,186.77,+3805
+3805, , , , ,0.0, 0.0, , ,+3806
+3806,-0.30420,-0.02420,-0.29740,-0.02330,-0.21510,-0.02750,-0.21160,-0.02650
PBEAM,39,39,1.3926,0.6752,0.1207,0.0, 6.7452e-01,186.77,+3903
+3903,YESA,1.0, 1.2755,0.5739,0.1006,0.0, 5.7281e-01,171.66,+3905
+3905, , , , ,0.0, 0.0, , ,+3906
+3906,-0.29740,-0.02330,-0.29000,-0.02140,-0.21160,-0.02650,-0.20570,-0.02450
PBEAM,40,40,1.2755,0.5739,0.1006,0.0, 5.7281e-01,171.66,+4003
+4003,YESA,1.0, 1.1618,0.4737,0.0839,0.0, 4.7588e-01,153.75,+4005
+4005, , , , ,0.0, 0.0, , ,+4006
+4006,-0.29000,-0.02140,-0.27130,-0.02050,-0.20570,-0.02450,-0.19730,-0.02340
PBEAM,41,41,1.1618,0.4737,0.0839,0.0, 4.7588e-01,153.75,+4103
+4103,YESA,1.0, 1.0593,0.4009,0.0695,0.0, 4.0275e-01,140.05,+4105
+4105, , , , ,0.0, 0.0, , ,+4106
+4106,-0.27130,-0.02050,-0.26780,-0.01850,-0.19730,-0.02340,-0.19300,-0.02140
PBEAM,42,42,1.0593,0.4009,0.0695,0.0, 4.0275e-01,140.05,+4203
+4203,YESA,1.0, 0.9637,0.3318,0.0578,0.0, 3.4786e-01,124.35,+4205
+4205, , , , ,0.0, 0.0, , ,+4206
+4206,-0.26780,-0.01850,-0.25330,-0.01780,-0.19300,-0.02140,-0.18650,-0.02050
PBEAM,43,43,0.9637,0.3318,0.0578,0.0, 3.4786e-01,124.35,+4303
+4303,YESA,1.0, 0.8772,0.2879,0.0474,0.0, 2.7961e-01,108.93,+4305
+4305, , , , ,0.0, 0.0, , ,+4306
+4306,-0.25330,-0.01780,-0.25300,-0.01630,-0.18650,-0.02050,-0.18660,-0.01880
PBEAM,44,44,0.8772,0.2879,0.0474,0.0, 2.7961e-01,108.93,+4403
+4403,YESA,1.0, 0.7943,0.2392,0.0384,0.0, 2.2819e-01,95.18,+4405
+4405, , , , ,0.0, 0.0, , ,+4406
+4406,-0.25300,-0.01630,-0.24960,-0.01440,-0.18660,-0.01880,-0.18440,-0.01690
PBEAM,45,45,0.7943,0.2392,0.0384,0.0, 2.2819e-01,95.18,+4503
+4503,YESA,1.0, 0.7107,0.2005,0.0303,0.0, 1.9362e-01,82.34,+4505
+4505, , , , ,0.0, 0.0, , ,+4506
+4506,-0.24960,-0.01440,-0.24550,-0.01290,-0.18440,-0.01690,-0.19090,-0.01520
PBEAM,46,46,0.7107,0.2005,0.0303,0.0, 1.9362e-01,82.34,+4603
+4603,YESA,1.0, 0.6240,0.1613,0.0229,0.0, 1.5443e-01,68.28,+4605
+4605, , , , ,0.0, 0.0, , ,+4606
+4606,-0.24550,-0.01290,-0.24150,-0.01140,-0.19090,-0.01520,-0.18710,-0.01350
PBEAM,47,47,0.6240,0.1613,0.0229,0.0, 1.5443e-01,68.28,+4703
+4703,YESA,1.0, 0.5296,0.1239,0.0159,0.0, 1.2161e-01,54.47,+4705
+4705, , , , ,0.0, 0.0, , ,+4706
+4706,-0.24150,-0.01140,-0.24850,-0.00880,-0.18710,-0.01350,-0.19030,-0.01100
PBEAM,48,48,0.5296,0.1239,0.0159,0.0, 1.2161e-01,54.47,+4803
+4803,YESA,1.0, 0.4182,0.0831,0.0091,0.0, 8.0281e-02,40.65,+4805
+4805, , , , ,0.0, 0.0, , ,+4806
+4806,-0.24850,-0.00880,-0.24000,-0.00690,-0.19030,-0.01100,-0.20380,-0.00850
PBEAM,49,49,0.4182,0.0831,0.0091,0.0, 8.0281e-02,40.65,+4903
+4903,YESA,1.0, 0.2683,0.0378,0.0033,0.0, 3.4228e-02,25.20,+4905
+4905, , , , ,0.0, 0.0, , ,+4906
+4906,-0.24000,-0.00690,-0.22350,-0.00410,-0.20380,-0.00850,-0.20200,-0.00510
PBEAM,50,50,0.2683,0.0378,0.0033,0.0, 3.4228e-02,25.20,+5003
+5003,YESA,1.0, 1.21e-04,8.81e-06,6.36e-07,0.0, 7.8353e-06,15.42,+5005
+5005, , , , ,0.0, 0.0, , ,+5006
+5006,-0.22350,-0.00410,-0.16620,-0.00220,-0.20200,-0.00510,-0.16030,-0.00280

```

Listing A.2: The aerodynamic loads file (*nastranLoads.dat*) for the straight blade.

```

PLOAD1,1,16,FZ,FR,0.,4004.571641,1.,4290.907937
PLOAD1,1,16,FY,FR,0.,669.604764,1.,1185.974568
PLOAD1,1,16,MX,FR,0.,-912.190937,1.,382.946908
PLOAD1,1,17,FZ,FR,0.,4290.907937,1.,4663.807881
PLOAD1,1,17,FY,FR,0.,1185.974568,1.,1181.595288
PLOAD1,1,17,MX,FR,0.,382.946908,1.,229.754201

```

PLOAD1,1,18,FZ,FR,0.,4663.807881,1.,4971.657506
PLOAD1,1,18,FY,FR,0.,1181.595288,1.,1124.224420
PLOAD1,1,18,MX,FR,0.,229.754201,1.,57.107416
PLOAD1,1,19,FZ,FR,0.,4971.657506,1.,5309.540861
PLOAD1,1,19,FY,FR,0.,1124.224420,1.,1138.024722
PLOAD1,1,19,MX,FR,0.,57.107416,1.,30.276422
PLOAD1,1,20,FZ,FR,0.,5309.540861,1.,5640.120297
PLOAD1,1,20,FY,FR,0.,1138.024722,1.,1181.162302
PLOAD1,1,20,MX,FR,0.,30.276422,1.,29.135705
PLOAD1,1,21,FZ,FR,0.,5640.120297,1.,5970.464981
PLOAD1,1,21,FY,FR,0.,1181.162302,1.,1199.132630
PLOAD1,1,21,MX,FR,0.,29.135705,1.,39.576429
PLOAD1,1,22,FZ,FR,0.,5970.464981,1.,6289.130625
PLOAD1,1,22,FY,FR,0.,1199.132630,1.,1212.896487
PLOAD1,1,22,MX,FR,0.,39.576429,1.,29.074141
PLOAD1,1,23,FZ,FR,0.,6289.130625,1.,6579.437330
PLOAD1,1,23,FY,FR,0.,1212.896487,1.,1221.298702
PLOAD1,1,23,MX,FR,0.,29.074141,1.,21.863304
PLOAD1,1,24,FZ,FR,0.,6579.437330,1.,6868.317333
PLOAD1,1,24,FY,FR,0.,1221.298702,1.,1224.249948
PLOAD1,1,24,MX,FR,0.,21.863304,1.,19.366712
PLOAD1,1,25,FZ,FR,0.,6868.317333,1.,7157.131986
PLOAD1,1,25,FY,FR,0.,1224.249948,1.,1225.431314
PLOAD1,1,25,MX,FR,0.,19.366712,1.,25.999115
PLOAD1,1,26,FZ,FR,0.,7157.131986,1.,7440.180591
PLOAD1,1,26,FY,FR,0.,1225.431314,1.,1223.955366
PLOAD1,1,26,MX,FR,0.,25.999115,1.,37.127174
PLOAD1,1,27,FZ,FR,0.,7440.180591,1.,7719.051805
PLOAD1,1,27,FY,FR,0.,1223.955366,1.,1220.117971
PLOAD1,1,27,MX,FR,0.,37.127174,1.,51.593235
PLOAD1,1,28,FZ,FR,0.,7719.051805,1.,7996.439493
PLOAD1,1,28,FY,FR,0.,1220.117971,1.,1215.844637
PLOAD1,1,28,MX,FR,0.,51.593235,1.,73.527718
PLOAD1,1,29,FZ,FR,0.,7996.439493,1.,8265.276214
PLOAD1,1,29,FY,FR,0.,1215.844637,1.,1210.078057
PLOAD1,1,29,MX,FR,0.,73.527718,1.,101.275146
PLOAD1,1,30,FZ,FR,0.,8265.276214,1.,8537.938610
PLOAD1,1,30,FY,FR,0.,1210.078057,1.,1202.174305
PLOAD1,1,30,MX,FR,0.,101.275146,1.,131.510016
PLOAD1,1,31,FZ,FR,0.,8537.938610,1.,8789.141749
PLOAD1,1,31,FY,FR,0.,1202.174305,1.,1195.198343
PLOAD1,1,31,MX,FR,0.,131.510016,1.,160.959802
PLOAD1,1,32,FZ,FR,0.,8789.141749,1.,9028.915227
PLOAD1,1,32,FY,FR,0.,1195.198343,1.,1184.211677
PLOAD1,1,32,MX,FR,0.,160.959802,1.,197.579861
PLOAD1,1,33,FZ,FR,0.,9028.915227,1.,9253.664531
PLOAD1,1,33,FY,FR,0.,1184.211677,1.,1174.228937
PLOAD1,1,33,MX,FR,0.,197.579861,1.,235.126282
PLOAD1,1,34,FZ,FR,0.,9253.664531,1.,9459.693535
PLOAD1,1,34,FY,FR,0.,1174.228937,1.,1162.515414
PLOAD1,1,34,MX,FR,0.,235.126282,1.,270.110166
PLOAD1,1,35,FZ,FR,0.,9459.693535,1.,9658.205599
PLOAD1,1,35,FY,FR,0.,1162.515414,1.,1144.482400
PLOAD1,1,35,MX,FR,0.,270.110166,1.,299.374149
PLOAD1,1,36,FZ,FR,0.,9658.205599,1.,9830.063364
PLOAD1,1,36,FY,FR,0.,1144.482400,1.,1139.547135
PLOAD1,1,36,MX,FR,0.,299.374149,1.,330.359019
PLOAD1,1,37,FZ,FR,0.,9830.063364,1.,10001.408914
PLOAD1,1,37,FY,FR,0.,1139.547135,1.,1127.452990
PLOAD1,1,37,MX,FR,0.,330.359019,1.,354.693407
PLOAD1,1,38,FZ,FR,0.,10001.408914,1.,10150.244375
PLOAD1,1,38,FY,FR,0.,1127.452990,1.,1114.532431
PLOAD1,1,38,MX,FR,0.,354.693407,1.,377.921455
PLOAD1,1,39,FZ,FR,0.,10150.244375,1.,10259.727840
PLOAD1,1,39,FY,FR,0.,1114.532431,1.,1095.480697
PLOAD1,1,39,MX,FR,0.,377.921455,1.,396.695015
PLOAD1,1,40,FZ,FR,0.,10259.727840,1.,10359.017824
PLOAD1,1,40,FY,FR,0.,1095.480697,1.,1077.212392
PLOAD1,1,40,MX,FR,0.,396.695015,1.,419.197009
PLOAD1,1,41,FZ,FR,0.,10359.017824,1.,10414.918752
PLOAD1,1,41,FY,FR,0.,1077.212392,1.,1053.831749
PLOAD1,1,41,MX,FR,0.,419.197009,1.,435.432026
PLOAD1,1,42,FZ,FR,0.,10414.918752,1.,10445.837383
PLOAD1,1,42,FY,FR,0.,1053.831749,1.,1024.372712
PLOAD1,1,42,MX,FR,0.,435.432026,1.,453.449018
PLOAD1,1,43,FZ,FR,0.,10445.837383,1.,10407.780008
PLOAD1,1,43,FY,FR,0.,1024.372712,1.,994.953533

```

PLOAD1,1,43,MX,FR,0.,453.449018,1.,464.859549
PLOAD1,1,44,FZ,FR,0.,10407.780008,1.,10320.522448
PLOAD1,1,44,FY,FR,0.,994.953533,1.,953.574920
PLOAD1,1,44,MX,FR,0.,464.859549,1.,471.482936
PLOAD1,1,45,FZ,FR,0.,10320.522448,1.,10133.922516
PLOAD1,1,45,FY,FR,0.,953.574920,1.,897.942664
PLOAD1,1,45,MX,FR,0.,471.482936,1.,468.233146
PLOAD1,1,46,FZ,FR,0.,10133.922516,1.,9792.697353
PLOAD1,1,46,FY,FR,0.,897.942664,1.,828.820016
PLOAD1,1,46,MX,FR,0.,468.233146,1.,439.694664
PLOAD1,1,47,FZ,FR,0.,9792.697353,1.,9260.542389
PLOAD1,1,47,FY,FR,0.,828.820016,1.,744.887547
PLOAD1,1,47,MX,FR,0.,439.694664,1.,386.712483
PLOAD1,1,48,FZ,FR,0.,9260.542389,1.,8276.231769
PLOAD1,1,48,FY,FR,0.,744.887547,1.,611.645049
PLOAD1,1,48,MX,FR,0.,386.712483,1.,284.292137
PLOAD1,1,49,FZ,FR,0.,8276.231769,1.,6188.951642
PLOAD1,1,49,FY,FR,0.,611.645049,1.,386.614578
PLOAD1,1,49,MX,FR,0.,284.292137,1.,126.954649
PLOAD1,1,50,FZ,FR,0.,6188.951642,1.,1780.671497
PLOAD1,1,50,FY,FR,0.,386.614578,1.,-86.782213
PLOAD1,1,50,MX,FR,0.,126.954649,1.,-149.467491

```

Listing A.3: The NASTRAN instruction file (*DTU.bdf*) for the straight blade.

```

PROJ='DTU BLADE'
ID DTU BLADE
SOL 106
TIME 20
CEND
TITLE=DTU BLADE MODEL
LABEL=ROTATION
SUBTITLE= 8.836RPM
SUPER=ALL
TITLE=DTU TEST
SUBTITLE=STATIC
SEALL=ALL
SUBCASE 1
LOAD=1
NLPARM=100
SET 1=ALL
DISP=ALL
PARAM POST -1
PARAM AUTOSPC YES
PARAM GRDPNT 0
BEGIN BULK
PARAM, TINY, 0.999
PARAM, GRDPNT, 0
PARAM, MAXRATIO, 1.+13
PARAM, COUPMASS, 1
PARAM, AUTOSPC, YES
PARAM, LGDISP, 1
PARAM, NMLoop, 1
NLPARM, 100, 2, , ITER, 1, 150
PARAM, TESTNEG, 1
PARAM, TESTSE, 1.-10
RFORCE, 1, 1, , 0.14727, 0., 0., 1., 2
INCLUDE 'DTU.model'
INCLUDE 'nastranLoads.dat'
ENDDATA

```

A.2 DTU 10MW RWT blade with pre-bend and pre-cone

This section considers the DTU 10MW RWT blade with pre-bend and pre-cone, as employed in Section 10.4 of Chapter 10. Input consists of two files: the *DTU.model* file with the structural model, and the *DTU.bdf* file specifying NASTRAN parameters and instructions. The aerodynamic loads and the blade shape were computed using HMB solver, as explained in Section 3.6.4 of Chapter 3. Note that coning was not included in the structural model, but was taken into account during grid deformation.

Listing A.4: The structural model file (*DTU.model*) for the blade with pre-bend and pre-cone.

```

$*****
$ THIS MODEL TAKES INTO ACCOUNT ELASTIC PROPERTIES
$ AND SHEAR AXIS, ELASTIC AXIS AND MASS CENTRE OFFSETS
$ THE WHOLE DTU BLADE IS MODELLED
$ BEAMS ARE MODELLED AS ISOTROPIC MATERIAL WITH
$ ELASTIC PROPERTIES TAKEN FROM THE REPORT
$*****
$ Prebend is included by offseting the nodes further from the tower
$ the same way it is done for the geometry.
$ Precone is included by rotating the nodes and cross-sections (GRID and CBEAM)
$ entries.
$ PBEAM and MAT1 remain the same as for the straight blade.
$*****
$ Ixx - area moment of inertia about the first elastic axis
$ is computed from the flapwise radius of gyration Rg_xx as
$ Ixx = Rg_xx*Rg_xx*AREA
$ where AREA is the crosssection area of the beam taken from the
$ geometry provided along with the report.
$*****
$ Young modulus is computed as
$ E*Ixx/Ixx, where E*Ixx is the flapwise bedding stiffness in the report [Nm^2]
$*****
$ Shear modulus G is computed from the Flapwise shear stiffness [N],
$ assuming it is defined as G*AREA
$*****
$ Polar moment of area J is computed from the Torsional Stiffness [Nm^2]
$ assuming it is defined as G*J, where G is already computed
$*****
$ Grid nodes are located in the shear centre, therefore the shear centre
$ defined in the report was first computed in the Global Reference Frame of the blade
$*****
$ Neutral axis in NASTRAN is assumed to be the elastic axis in the report,
$ and the off-set from the shear centre to the elastic axis was incorporated
$ in the PBEAM elements
$*****
$ Nonstructural mass off-set in the blade reference frame from shear
$ centre to the mass centre was incorporated in the PBEAM elements
$*****
$ Structural twist is included in CBEAM elements, and was first
$ transferred to the blade reference frame
$*****
$*****
$ Material properties: ID, Youngs modulus, Shear modulus, Poissons ratio
$*****
$*****
MAT1, 1, 8.167e+08, 1.102e+08,
MAT1, 2, 8.201e+08, 1.101e+08,
MAT1, 3, 8.410e+08, 1.099e+08,
MAT1, 4, 8.462e+08, 1.060e+08,
MAT1, 5, 8.540e+08, 9.821e+07,
MAT1, 6, 8.470e+08, 8.948e+07,
MAT1, 7, 8.623e+08, 8.042e+07,
MAT1, 8, 9.227e+08, 7.309e+07,
MAT1, 9, 1.031e+09, 7.012e+07,
MAT1, 10, 1.130e+09, 6.847e+07,
MAT1, 11, 1.188e+09, 6.434e+07,
MAT1, 12, 1.222e+09, 6.473e+07,
MAT1, 13, 1.228e+09, 6.256e+07,
MAT1, 14, 1.240e+09, 6.151e+07,
MAT1, 15, 1.261e+09, 6.155e+07,
MAT1, 16, 1.277e+09, 6.151e+07,
MAT1, 17, 1.348e+09, 6.403e+07,
MAT1, 18, 1.418e+09, 6.591e+07,
MAT1, 19, 1.485e+09, 6.780e+07,
MAT1, 20, 1.548e+09, 6.865e+07,
MAT1, 21, 1.610e+09, 6.977e+07,
MAT1, 22, 1.681e+09, 7.083e+07,
MAT1, 23, 1.751e+09, 7.213e+07,
MAT1, 24, 1.820e+09, 7.329e+07,
MAT1, 25, 1.887e+09, 7.365e+07,
MAT1, 26, 1.966e+09, 7.542e+07,
MAT1, 27, 2.013e+09, 7.695e+07,
MAT1, 28, 2.090e+09, 7.765e+07,
MAT1, 29, 2.159e+09, 8.012e+07,
MAT1, 30, 2.216e+09, 8.040e+07,
MAT1, 31, 2.277e+09, 8.301e+07,

```

```

MAT1, 32, 2.348e+09, 8.457e+07,
MAT1, 33, 2.400e+09, 8.729e+07,
MAT1, 34, 2.437e+09, 8.832e+07,
MAT1, 35, 2.492e+09, 8.989e+07,
MAT1, 36, 2.510e+09, 9.142e+07,
MAT1, 37, 2.530e+09, 9.284e+07,
MAT1, 38, 2.527e+09, 9.579e+07,
MAT1, 39, 2.525e+09, 9.729e+07,
MAT1, 40, 2.523e+09, 9.903e+07,
MAT1, 41, 2.480e+09, 1.008e+08,
MAT1, 42, 2.460e+09, 1.030e+08,
MAT1, 43, 2.387e+09, 1.026e+08,
MAT1, 44, 2.292e+09, 1.037e+08,
MAT1, 45, 2.183e+09, 1.047e+08,
MAT1, 46, 2.081e+09, 1.046e+08,
MAT1, 47, 1.935e+09, 1.006e+08,
MAT1, 48, 1.786e+09, 9.368e+07,
MAT1, 49, 1.589e+09, 8.986e+07,
MAT1, 50, 1.370e+09, 8.577e+07,
MAT1, 51, 1.616e+12, 1.012e+11,
$*****
$ NEW ROOT ATTACHEMENT FOR ROTATION
$ Root starts at 2.8 m
$ First 3 nodes are fixed (from 0.0m to 2.8m)
$ and artificial springs are added, but the nodes are fixed anyway.
$ Springs are added to produce the output understandable
$ by the HMB helicopter routines.
$*****
GRID, 1, , 0.0, 0.0, 0.0,,123456,
GRID, 2, , 2.800, 0.0, 0.0,,123456,
$LeadLag Spring
CELAS2,2,5000.0,1,6,3,6
$Flapping Spring
CELAS2,3,5000.0,1,5,3,5
$ *****
$ BLADE STRUCTURE - grid 3=root, 53=tip
$ *****
GRID, 3, , 2.800, 0.0, 0.0,,123456
GRID, 4, , 4.815, -0.00108, -0.01791
GRID, 5, , 6.542, 0.00058, -0.02439
GRID, 6, , 8.269, 0.00482, -0.01747
GRID, 7, , 9.996, 0.01839, -0.01672
GRID, 8, , 11.724, 0.03869, 0.00516
GRID, 9, , 13.450, 0.12950, 0.04769
GRID, 10, , 15.176, 0.23001, 0.09148
GRID, 11, , 16.904, 0.37696, 0.09766
GRID, 12, , 18.344, 0.46594, 0.10169
GRID, 13, , 20.498, 0.49932, 0.08287
GRID, 14, , 22.232, 0.42157, 0.06158
GRID, 15, , 23.959, 0.43672, 0.03811
GRID, 16, , 25.686, 0.45379, 0.00911
GRID, 17, , 27.413, 0.46693, -0.02287
GRID, 18, , 29.141, 0.46726, -0.06598
GRID, 19, , 30.868, 0.44684, -0.11365
GRID, 20, , 32.595, 0.45095, -0.15864
GRID, 21, , 34.323, 0.43621, -0.20532
GRID, 22, , 36.050, 0.43031, -0.24772
GRID, 23, , 37.778, 0.42171, -0.29089
GRID, 24, , 39.505, 0.40558, -0.33562
GRID, 25, , 41.233, 0.40227, -0.38130
GRID, 26, , 42.873, 0.38568, -0.42888
GRID, 27, , 44.601, 0.37586, -0.48096
GRID, 28, , 46.328, 0.36633, -0.53672
GRID, 29, , 48.055, 0.35445, -0.59555
GRID, 30, , 49.783, 0.34419, -0.65873
GRID, 31, , 51.510, 0.33313, -0.72531
GRID, 32, , 53.237, 0.32110, -0.79582
GRID, 33, , 55.051, 0.30752, -0.87458
GRID, 34, , 56.779, 0.29670, -0.95397
GRID, 35, , 58.506, 0.28786, -1.03668
GRID, 36, , 60.233, 0.26843, -1.12454
GRID, 37, , 61.961, 0.25695, -1.21706
GRID, 38, , 63.688, 0.24835, -1.31321
GRID, 39, , 65.354, 0.23696, -1.41102
GRID, 40, , 67.081, 0.21636, -1.51648
GRID, 41, , 68.808, 0.20845, -1.62613
GRID, 42, , 70.535, 0.19638, -1.74135

```

```
GRID, 43, , 72.324, 0.18664, -1.86527
GRID, 44, , 74.052, 0.17548, -1.99073
GRID, 45, , 75.779, 0.16261, -2.11996
GRID, 46, , 77.459, 0.14850, -2.25146
GRID, 47, , 79.186, 0.14029, -2.39236
GRID, 48, , 80.961, 0.12192, -2.54167
GRID, 49, , 82.688, 0.11157, -2.69359
GRID, 50, , 84.377, 0.09842, -2.84840
GRID, 51, , 86.143, 0.08157, -3.01607
GRID, 52, , 87.871, 0.06403, -3.18811
GRID, 53, , 89.166, 0.17704, -3.33028

GRID, 301, , 2.800, 3.10257, 0.0
GRID, 401, , 4.815, 3.10192, -0.01791
GRID, 501, , 6.542, 3.10358, -0.02439
GRID, 601, , 8.269, 3.10782, -0.01747
GRID, 701, , 9.996, 3.12139, -0.01672
GRID, 801, , 11.724, 3.14169, 0.00516
GRID, 901, , 13.450, 3.2325, 0.04769
GRID, 1001, , 15.176, 3.33301, 0.09148
GRID, 1101, , 16.904, 3.47996, 0.09766
GRID, 1201, , 18.344, 3.56894, 0.10169
GRID, 1301, , 20.498, 3.60232, 0.08287
GRID, 1401, , 22.232, 3.52457, 0.06158
GRID, 1501, , 23.959, 3.53972, 0.03811
GRID, 1601, , 25.686, 3.55679, 0.00911
GRID, 1701, , 27.413, 3.56993, -0.02287
GRID, 1801, , 29.141, 3.57026, -0.06598
GRID, 1901, , 30.868, 3.54984, -0.11365
GRID, 2001, , 32.595, 3.55395, -0.15864
GRID, 2101, , 34.323, 3.53921, -0.20532
GRID, 2201, , 36.050, 3.53331, -0.24772
GRID, 2301, , 37.778, 3.52471, -0.29089
GRID, 2401, , 39.505, 3.50858, -0.33562
GRID, 2501, , 41.233, 3.50527, -0.38130
GRID, 2601, , 42.873, 3.48868, -0.42888
GRID, 2701, , 44.601, 3.47886, -0.48096
GRID, 2801, , 46.328, 3.46933, -0.53672
GRID, 2901, , 48.055, 3.45745, -0.59555
GRID, 3001, , 49.783, 3.44719, -0.65873
GRID, 3101, , 51.510, 3.43613, -0.72531
GRID, 3201, , 53.237, 3.4241, -0.79582
GRID, 3301, , 55.051, 3.41052, -0.87458
GRID, 3401, , 56.779, 3.3997, -0.95397
GRID, 3501, , 58.506, 3.39086, -1.03668
GRID, 3601, , 60.233, 3.37143, -1.12454
GRID, 3701, , 61.961, 3.35995, -1.21706
GRID, 3801, , 63.688, 3.35135, -1.31321
GRID, 3901, , 65.354, 3.33996, -1.41102
GRID, 4001, , 67.081, 3.31936, -1.51648
GRID, 4101, , 68.808, 3.31145, -1.62613
GRID, 4201, , 70.535, 3.29938, -1.74135
GRID, 4301, , 72.324, 3.28964, -1.86527
GRID, 4401, , 74.052, 3.27848, -1.99073
GRID, 4501, , 75.779, 3.26561, -2.11996
GRID, 4601, , 77.459, 3.2515, -2.25146
GRID, 4701, , 79.186, 3.24329, -2.39236
GRID, 4801, , 80.961, 3.22492, -2.54167
GRID, 4901, , 82.688, 3.21457, -2.69359
GRID, 5001, , 84.377, 3.20142, -2.84840
GRID, 5101, , 86.143, 3.18457, -3.01607
GRID, 5201, , 87.871, 3.16703, -3.18811
GRID, 5301, , 89.166, 3.28004, -3.33028

GRID, 302, , 2.800, -6.20643, 0.0
GRID, 402, , 4.815, -6.20708, -0.01791
GRID, 502, , 6.542, -6.20542, -0.02439
GRID, 602, , 8.269, -6.20118, -0.01747
GRID, 702, , 9.996, -6.18761, -0.01672
GRID, 802, , 11.724, -6.16731, 0.00516
GRID, 902, , 13.450, -6.0765, 0.04769
GRID, 1002, , 15.176, -5.97599, 0.09148
GRID, 1102, , 16.904, -5.82904, 0.09766
GRID, 1202, , 18.344, -5.74006, 0.10169
GRID, 1302, , 20.498, -5.70668, 0.08287
GRID, 1402, , 22.232, -5.78443, 0.06158
GRID, 1502, , 23.959, -5.76928, 0.03811
```

```

GRID, 1602, , 25.686, -5.75221, 0.00911
GRID, 1702, , 27.413, -5.73907, -0.02287
GRID, 1802, , 29.141, -5.73874, -0.06598
GRID, 1902, , 30.868, -5.75916, -0.11365
GRID, 2002, , 32.595, -5.75505, -0.15864
GRID, 2102, , 34.323, -5.76979, -0.20532
GRID, 2202, , 36.050, -5.77569, -0.24772
GRID, 2302, , 37.778, -5.78429, -0.29089
GRID, 2402, , 39.505, -5.80042, -0.33562
GRID, 2502, , 41.233, -5.80373, -0.38130
GRID, 2602, , 42.873, -5.82032, -0.42888
GRID, 2702, , 44.601, -5.83014, -0.48096
GRID, 2802, , 46.328, -5.83967, -0.53672
GRID, 2902, , 48.055, -5.85155, -0.59555
GRID, 3002, , 49.783, -5.86181, -0.65873
GRID, 3102, , 51.510, -5.87287, -0.72531
GRID, 3202, , 53.237, -5.8849, -0.79582
GRID, 3302, , 55.051, -5.89848, -0.87458
GRID, 3402, , 56.779, -5.9093, -0.95397
GRID, 3502, , 58.506, -5.91814, -1.03668
GRID, 3602, , 60.233, -5.93757, -1.12454
GRID, 3702, , 61.961, -5.94905, -1.21706
GRID, 3802, , 63.688, -5.95765, -1.31321
GRID, 3902, , 65.354, -5.96904, -1.41102
GRID, 4002, , 67.081, -5.98964, -1.51648
GRID, 4102, , 68.808, -5.99755, -1.62613
GRID, 4202, , 70.535, -6.00962, -1.74135
GRID, 4302, , 72.324, -6.01936, -1.86527
GRID, 4402, , 74.052, -6.03052, -1.99073
GRID, 4502, , 75.779, -6.04339, -2.11996
GRID, 4602, , 77.459, -6.0575, -2.25146
GRID, 4702, , 79.186, -6.06571, -2.39236
GRID, 4802, , 80.961, -6.08408, -2.54167
GRID, 4902, , 82.688, -6.09443, -2.69359
GRID, 5002, , 84.377, -6.10758, -2.84840
GRID, 5102, , 86.143, -6.12443, -3.01607
GRID, 5202, , 87.871, -6.14197, -3.18811
GRID, 5302, , 89.166, -6.02896, -3.33028
$*****
$ CBEAMS show the 2 connected grids and the reference pt. location
$ which indicates blade twist by changing the direction of the principle
$ plane of bending
$ cos(twist) and sin(twist)
$ where "twist" is a structural twist from the report defined
$ in the reference frame of the blade.
$ rotation due to precone is also included
$*****
CBEAM, 1, 1, 3, 4, 0.70711, 0.68458, 0.17705
CBEAM, 2, 2, 4, 5, 0.70711, 0.68458, 0.17705
CBEAM, 3, 3, 5, 6, 0.70711, 0.68458, 0.17705
CBEAM, 4, 4, 6, 7, 0.70711, 0.68458, 0.17705
CBEAM, 5, 5, 7, 8, 0.70711, 0.68463, 0.17687
CBEAM, 6, 6, 8, 9, 0.70711, 0.62166, -0.33695
CBEAM, 7, 7, 9, 10, 0.70711, 0.65609, -0.26373
CBEAM, 8, 8, 10, 11, 0.70711, 0.69083, -0.15085
CBEAM, 9, 9, 11, 12, 0.70711, 0.70270, -0.07880
CBEAM, 10, 10, 12, 13, 0.70711, 0.70635, -0.03268
CBEAM, 11, 11, 13, 14, 0.70711, 0.70705, -0.00917
CBEAM, 12, 12, 14, 15, 0.70711, 0.70709, 0.00476
CBEAM, 13, 13, 15, 16, 0.70711, 0.70703, 0.01067
CBEAM, 14, 14, 16, 17, 0.70711, 0.70698, 0.01352
CBEAM, 15, 15, 17, 18, 0.70711, 0.70692, 0.01628
CBEAM, 16, 16, 18, 19, 0.70711, 0.70662, 0.02620
CBEAM, 17, 17, 19, 20, 0.70711, 0.70662, 0.02634
CBEAM, 18, 18, 20, 21, 0.70711, 0.70664, 0.02563
CBEAM, 19, 19, 21, 22, 0.70711, 0.70672, 0.02346
CBEAM, 20, 20, 22, 23, 0.70711, 0.70677, 0.02172
CBEAM, 21, 21, 23, 24, 0.70711, 0.70679, 0.02122
CBEAM, 22, 22, 24, 25, 0.70711, 0.70679, 0.02103
CBEAM, 23, 23, 25, 26, 0.70711, 0.70682, 0.02026
CBEAM, 24, 24, 26, 27, 0.70711, 0.70685, 0.01896
CBEAM, 25, 25, 27, 28, 0.70711, 0.70688, 0.01773
CBEAM, 26, 26, 28, 29, 0.70711, 0.70692, 0.01632
CBEAM, 27, 27, 29, 30, 0.70711, 0.70697, 0.01382
CBEAM, 28, 28, 30, 31, 0.70711, 0.70701, 0.01191
CBEAM, 29, 29, 31, 32, 0.70711, 0.70704, 0.00978
CBEAM, 30, 30, 32, 33, 0.70711, 0.70707, 0.00725

```

```

CBEAM, 31, 31, 33, 34, 0.70711, 0.70709, 0.00423
CBEAM, 32, 32, 34, 35, 0.70711, 0.70710, 0.00168
CBEAM, 33, 33, 35, 36, 0.70711, 0.70711, -0.00097
CBEAM, 34, 34, 36, 37, 0.70711, 0.70710, -0.00381
CBEAM, 35, 35, 37, 38, 0.70711, 0.70708, -0.00663
CBEAM, 36, 36, 38, 39, 0.70711, 0.70705, -0.00924
CBEAM, 37, 37, 39, 40, 0.70711, 0.70701, -0.01192
CBEAM, 38, 38, 40, 41, 0.70711, 0.70695, -0.01482
CBEAM, 39, 39, 41, 42, 0.70711, 0.70690, -0.01730
CBEAM, 40, 40, 42, 43, 0.70711, 0.70682, -0.02018
CBEAM, 41, 41, 43, 44, 0.70711, 0.70674, -0.02275
CBEAM, 42, 42, 44, 45, 0.70711, 0.70664, -0.02566
CBEAM, 43, 43, 45, 46, 0.70711, 0.70655, -0.02816
CBEAM, 44, 44, 46, 47, 0.70711, 0.70644, -0.03081
CBEAM, 45, 45, 47, 48, 0.70711, 0.70632, -0.03334
CBEAM, 46, 46, 48, 49, 0.70711, 0.70615, -0.03672
CBEAM, 47, 47, 49, 50, 0.70711, 0.70602, -0.03924
CBEAM, 48, 48, 50, 51, 0.70711, 0.70583, -0.04251
CBEAM, 49, 49, 51, 52, 0.70711, 0.70558, -0.04646
CBEAM, 50, 50, 52, 53, 0.70711, 0.70531, -0.05042
$*****
$ Rigid weightless elements showing the torsion
$ Leading Edge
$*****
RBAR, 301, 3, 301, 123456
RBAR, 401, 4, 401, 123456
RBAR, 501, 5, 501, 123456
RBAR, 601, 6, 601, 123456
RBAR, 701, 7, 701, 123456
RBAR, 801, 8, 801, 123456
RBAR, 901, 9, 901, 123456
RBAR, 1001, 10, 1001, 123456
RBAR, 1101, 11, 1101, 123456
RBAR, 1201, 12, 1201, 123456
RBAR, 1301, 13, 1301, 123456
RBAR, 1401, 14, 1401, 123456
RBAR, 1501, 15, 1501, 123456
RBAR, 1601, 16, 1601, 123456
RBAR, 1701, 17, 1701, 123456
RBAR, 1801, 18, 1801, 123456
RBAR, 1901, 19, 1901, 123456
RBAR, 2001, 20, 2001, 123456
RBAR, 2101, 21, 2101, 123456
RBAR, 2201, 22, 2201, 123456
RBAR, 2301, 23, 2301, 123456
RBAR, 2401, 24, 2401, 123456
RBAR, 2501, 25, 2501, 123456
RBAR, 2601, 26, 2601, 123456
RBAR, 2701, 27, 2701, 123456
RBAR, 2801, 28, 2801, 123456
RBAR, 2901, 29, 2901, 123456
RBAR, 3001, 30, 3001, 123456
RBAR, 3101, 31, 3101, 123456
RBAR, 3201, 32, 3201, 123456
RBAR, 3301, 33, 3301, 123456
RBAR, 3401, 34, 3401, 123456
RBAR, 3501, 35, 3501, 123456
RBAR, 3601, 36, 3601, 123456
RBAR, 3701, 37, 3701, 123456
RBAR, 3801, 38, 3801, 123456
RBAR, 3901, 39, 3901, 123456
RBAR, 4001, 40, 4001, 123456
RBAR, 4101, 41, 4101, 123456
RBAR, 4201, 42, 4201, 123456
RBAR, 4301, 43, 4301, 123456
RBAR, 4401, 44, 4401, 123456
RBAR, 4501, 45, 4501, 123456
RBAR, 4601, 46, 4601, 123456
RBAR, 4701, 47, 4701, 123456
RBAR, 4801, 48, 4801, 123456
RBAR, 4901, 49, 4901, 123456
RBAR, 5001, 50, 5001, 123456
RBAR, 5101, 51, 5101, 123456
RBAR, 5201, 52, 5201, 123456
RBAR, 5301, 53, 5301, 123456
$*****
$ Trailing Edge

```

```

$*****
RBAR, 302, 3, 302, 123456
RBAR, 402, 4, 402, 123456
RBAR, 502, 5, 502, 123456
RBAR, 602, 6, 602, 123456
RBAR, 702, 7, 702, 123456
RBAR, 802, 8, 802, 123456
RBAR, 902, 9, 902, 123456
RBAR, 1002, 10, 1002, 123456
RBAR, 1102, 11, 1102, 123456
RBAR, 1202, 12, 1202, 123456
RBAR, 1302, 13, 1302, 123456
RBAR, 1402, 14, 1402, 123456
RBAR, 1502, 15, 1502, 123456
RBAR, 1602, 16, 1602, 123456
RBAR, 1702, 17, 1702, 123456
RBAR, 1802, 18, 1802, 123456
RBAR, 1902, 19, 1902, 123456
RBAR, 2002, 20, 2002, 123456
RBAR, 2102, 21, 2102, 123456
RBAR, 2202, 22, 2202, 123456
RBAR, 2302, 23, 2302, 123456
RBAR, 2402, 24, 2402, 123456
RBAR, 2502, 25, 2502, 123456
RBAR, 2602, 26, 2602, 123456
RBAR, 2702, 27, 2702, 123456
RBAR, 2802, 28, 2802, 123456
RBAR, 2902, 29, 2902, 123456
RBAR, 3002, 30, 3002, 123456
RBAR, 3102, 31, 3102, 123456
RBAR, 3202, 32, 3202, 123456
RBAR, 3302, 33, 3302, 123456
RBAR, 3402, 34, 3402, 123456
RBAR, 3502, 35, 3502, 123456
RBAR, 3602, 36, 3602, 123456
RBAR, 3702, 37, 3702, 123456
RBAR, 3802, 38, 3802, 123456
RBAR, 3902, 39, 3902, 123456
RBAR, 4002, 40, 4002, 123456
RBAR, 4102, 41, 4102, 123456
RBAR, 4202, 42, 4202, 123456
RBAR, 4302, 43, 4302, 123456
RBAR, 4402, 44, 4402, 123456
RBAR, 4502, 45, 4502, 123456
RBAR, 4602, 46, 4602, 123456
RBAR, 4702, 47, 4702, 123456
RBAR, 4802, 48, 4802, 123456
RBAR, 4902, 49, 4902, 123456
RBAR, 5002, 50, 5002, 123456
RBAR, 5102, 51, 5102, 123456
RBAR, 5202, 52, 5202, 123456
RBAR, 5302, 53, 5302, 123456
$*****
$ PBEAM FORMAT
$ PBEAM, PID MID, A, I1, I2, I12, J, NSM, +P2 (FOR GRID A)
$ +P2, C1, C2, D1, D2, E1, E2, F1, F2, +P3 (NOT USED) . .
$ +P3, SO, X/XB, A, I1, I2, I12, J, NSM, +P4 (FOR GRID B=X/XB)
$ +P4, C1, C2, D1, D2, E1, E2, F1, F2, +P5 (NOT USED)
$ +P5, K1, K2, S1, S2, NSI(A), NSI(B), CW, CW, +P6 (NSI=MASS INERTIA ABOUT CG)
$ +P6, M1, M2, M1, M2, N1, N2, N1, N2 (M1,M2 = Y,Z OFFSET OF CG FROM SHEAR CTR)
$*****
PBEAM,1,1,22.7700,70.9496,75.7551,0.0, 2.4925e+02,1189.51,+103
+103,YESA,1.0, 22.7700,70.9335,75.8133,0.0, 2.4949e+02,1191.64,+105
+105, , , , 0.0, 0.0, , , +106
+106,-0.00130,0.00600,-0.00180,0.00600,-0.00200,0.00630,-0.00270,0.00630
PBEAM,2,2,22.7700,70.9335,75.8133,0.0, 2.4949e+02,1191.64,+203
+203,YESA,1.0, 22.6236,70.0630,74.9055,0.0, 2.4860e+02,1202.77,+205
+205, , , , 0.0, 0.0, , , +206
+206,-0.00180,0.00600,-0.01020,0.00280,-0.00270,0.00630,-0.00450,0.00440
PBEAM,3,3,22.6236,70.0630,74.9055,0.0, 2.4860e+02,1202.77,+303
+303,YESA,1.0, 22.1168,67.5472,71.0785,0.0, 2.4143e+02,1171.49,+305
+305, , , , 0.0, 0.0, , , +306
+306,-0.01020,0.00280,-0.02360,-0.01040,-0.00450,0.00440,-0.02240,-0.00950
PBEAM,4,4,22.1168,67.5472,71.0785,0.0, 2.4143e+02,1171.49,+403
+403,YESA,1.0, 21.2052,62.8430,63.8840,0.0, 2.2545e+02,1113.62,+405
+405, , , , 0.0, 0.0, , , +406
+406,-0.02360,-0.01040,-0.03880,-0.01930,-0.02240,-0.00950,-0.02390,-0.01630

```

```

PBEAM,5,5,21.2052,62.8430,63.8840,0.0, 2.2545e+02,1113.62,+503
+503,YESA,1.0, 19.8717,58.7611,52.0676,0.0, 2.0552e+02,1049.31,+505
+505, , , , ,0.0, 0.0, , ,+506
+506,-0.03880,-0.01930,-0.09300,-0.04070,-0.02390,-0.01630,-0.07130,-0.03460
PBEAM,6,6,19.8717,58.7611,52.0676,0.0, 2.0552e+02,1049.31,+603
+603,YESA,1.0, 18.1044,50.2318,41.5099,0.0, 1.7372e+02,974.63,+605
+605, , , , ,0.0, 0.0, , ,+606
+606,-0.09300,-0.04070,-0.19280,-0.06340,-0.07130,-0.03460,-0.15440,-0.05930
PBEAM,7,7,18.1044,50.2318,41.5099,0.0, 1.7372e+02,974.63,+703
+703,YESA,1.0, 16.0708,42.7928,30.7696,0.0, 1.3819e+02,908.74,+705
+705, , , , ,0.0, 0.0, , ,+706
+706,-0.19280,-0.06340,-0.34310,-0.08770,-0.15440,-0.05930,-0.29520,-0.08910
PBEAM,8,8,16.0708,42.7928,30.7696,0.0, 1.3819e+02,908.74,+803
+803,YESA,1.0, 14.0891,36.4162,22.0072,0.0, 1.0622e+02,868.87,+805
+805, , , , ,0.0, 0.0, , ,+806
+806,-0.34310,-0.08770,-0.50000,-0.06940,-0.29520,-0.08910,-0.44390,-0.07510
PBEAM,9,9,14.0891,36.4162,22.0072,0.0, 1.0622e+02,868.87,+903
+903,YESA,1.0, 12.7081,32.5286,16.9177,0.0, 8.8043e+01,845.51,+905
+905, , , , ,0.0, 0.0, , ,+906
+906,-0.50000,-0.06940,-0.61290,-0.06550,-0.44390,-0.07510,-0.54870,-0.07330
PBEAM,10,10,12.7081,32.5286,16.9177,0.0, 8.8043e+01,845.51,+1003
+1003,YESA,1.0, 11.2713,28.5702,12.4479,0.0, 6.2972e+01,775.15,+1005
+1005, , , , ,0.0, 0.0, , ,+1006
+1006,-0.61290,-0.06550,-0.70430,-0.07180,-0.54870,-0.07330,-0.60580,-0.08200
PBEAM,11,11,11.2713,28.5702,12.4479,0.0, 6.2972e+01,775.15,+1103
+1103,YESA,1.0, 10.5007,26.8347,10.3584,0.0, 5.1766e+01,735.79,+1105
+1105, , , , ,0.0, 0.0, , ,+1106
+1106,-0.70430,-0.07180,-0.66680,-0.08410,-0.60580,-0.08200,-0.54190,-0.09350
PBEAM,12,12,10.5007,26.8347,10.3584,0.0, 5.1766e+01,735.79,+1203
+1203,YESA,1.0, 9.8516,24.8214,8.7977,0.0, 4.2163e+01,691.12,+1205
+1205, , , , ,0.0, 0.0, , ,+1206
+1206,-0.66680,-0.08410,-0.69000,-0.08110,-0.54190,-0.09350,-0.55030,-0.08910
PBEAM,13,13,9.8516,24.8214,8.7977,0.0, 4.2163e+01,691.12,+1303
+1303,YESA,1.0, 9.2681,22.9148,7.5289,0.0, 3.4452e+01,654.85,+1305
+1305, , , , ,0.0, 0.0, , ,+1306
+1306,-0.69000,-0.08110,-0.70100,-0.07580,-0.55030,-0.08910,-0.54140,-0.08250
PBEAM,14,14,9.2681,22.9148,7.5289,0.0, 3.4452e+01,654.85,+1403
+1403,YESA,1.0, 8.7187,21.0144,6.4529,0.0, 2.8330e+01,625.88,+1405
+1405, , , , ,0.0, 0.0, , ,+1406
+1406,-0.70100,-0.07580,-0.70230,-0.07140,-0.54140,-0.08250,-0.52910,-0.07760
PBEAM,15,15,8.7187,21.0144,6.4529,0.0, 2.8330e+01,625.88,+1503
+1503,YESA,1.0, 8.1566,19.9518,5.3886,0.0, 2.3063e+01,593.32,+1505
+1505, , , , ,0.0, 0.0, , ,+1506
+1506,-0.70230,-0.07140,-0.73870,-0.06150,-0.52910,-0.07760,-0.57930,-0.06760
PBEAM,16,16,8.1566,19.9518,5.3886,0.0, 2.3063e+01,593.32,+1603
+1603,YESA,1.0, 7.5909,17.8835,4.5194,0.0, 1.9405e+01,580.97,+1605
+1605, , , , ,0.0, 0.0, , ,+1606
+1606,-0.73870,-0.06150,-0.72080,-0.05460,-0.57930,-0.06760,-0.55550,-0.06090
PBEAM,17,17,7.5909,17.8835,4.5194,0.0, 1.9405e+01,580.97,+1703
+1703,YESA,1.0, 7.0644,15.9438,3.8070,0.0, 1.6531e+01,566.23,+1705
+1705, , , , ,0.0, 0.0, , ,+1706
+1706,-0.72080,-0.05460,-0.71480,-0.04900,-0.55550,-0.06090,-0.54920,-0.05550
PBEAM,18,18,7.0644,15.9438,3.8070,0.0, 1.6531e+01,566.23,+1803
+1803,YESA,1.0, 6.5743,14.0580,3.2306,0.0, 1.4188e+01,548.24,+1805
+1805, , , , ,0.0, 0.0, , ,+1806
+1806,-0.71480,-0.04900,-0.69640,-0.04380,-0.54920,-0.05550,-0.51690,-0.05050
PBEAM,19,19,6.5743,14.0580,3.2306,0.0, 1.4188e+01,548.24,+1903
+1903,YESA,1.0, 6.1189,12.3087,2.7525,0.0, 1.2141e+01,529.65,+1905
+1905, , , , ,0.0, 0.0, , ,+1906
+1906,-0.69640,-0.04380,-0.67030,-0.04170,-0.51690,-0.05050,-0.48750,-0.04860
PBEAM,20,20,6.1189,12.3087,2.7525,0.0, 1.2141e+01,529.65,+2003
+2003,YESA,1.0, 5.7121,10.8750,2.3551,0.0, 1.0672e+01,510.31,+2005
+2005, , , , ,0.0, 0.0, , ,+2006
+2006,-0.67030,-0.04170,-0.64590,-0.04010,-0.48750,-0.04860,-0.46970,-0.04690
PBEAM,21,21,5.7121,10.8750,2.3551,0.0, 1.0672e+01,510.31,+2103
+2103,YESA,1.0, 5.3162,9.5986,1.9931,0.0, 9.2392e+00,494.68,+2105
+2105, , , , ,0.0, 0.0, , ,+2106
+2106,-0.64590,-0.04010,-0.62730,-0.03930,-0.46970,-0.04690,-0.45430,-0.04590
PBEAM,22,22,5.3162,9.5986,1.9931,0.0, 9.2392e+00,494.68,+2203
+2203,YESA,1.0, 4.9420,8.3738,1.6878,0.0, 7.9139e+00,477.51,+2205
+2205, , , , ,0.0, 0.0, , ,+2206
+2206,-0.62730,-0.03930,-0.60890,-0.03900,-0.45430,-0.04590,-0.44250,-0.04560
PBEAM,23,23,4.9420,8.3738,1.6878,0.0, 7.9139e+00,477.51,+2303
+2303,YESA,1.0, 4.6066,7.3879,1.4384,0.0, 6.8618e+00,460.93,+2305
+2305, , , , ,0.0, 0.0, , ,+2306
+2306,-0.60890,-0.03900,-0.59030,-0.03790,-0.44250,-0.04560,-0.42130,-0.04440
PBEAM,24,24,4.6066,7.3879,1.4384,0.0, 6.8618e+00,460.93,+2403

```

```

+2403,YESA,1.0, 4.2736,6.3994,1.2168,0.0, 6.0174e+00,441.78,+2405
+2405, , , , 0.0, 0.0, , ,+2406
+2406,-0.59030,-0.03790,-0.57350,-0.03730,-0.42130,-0.04440,-0.40430,-0.04360
PBEAM,25,25,4.2736,6.3994,1.2168,0.0, 6.0174e+00,441.78,+2503
+2503,YESA,1.0, 3.9613,5.6040,1.0247,0.0, 5.1956e+00,425.33,+2505
+2505, , , , 0.0, 0.0, , ,+2506
+2506,-0.57350,-0.03730,-0.56100,-0.03610,-0.40430,-0.04360,-0.39260,-0.04220
PBEAM,26,26,3.9613,5.6040,1.0247,0.0, 5.1956e+00,425.33,+2603
+2603,YESA,1.0, 3.6689,4.7206,0.8727,0.0, 4.3906e+00,401.38,+2605
+2605, , , , 0.0, 0.0, , ,+2606
+2606,-0.56100,-0.03610,-0.51910,-0.03610,-0.39260,-0.04220,-0.36320,-0.04190
PBEAM,27,27,3.6689,4.7206,0.8727,0.0, 4.3906e+00,401.38,+2703
+2703,YESA,1.0, 3.3956,4.1094,0.7345,0.0, 3.8258e+00,385.14,+2705
+2705, , , , 0.0, 0.0, , ,+2706
+2706,-0.51910,-0.03610,-0.50650,-0.03480,-0.36320,-0.04190,-0.35280,-0.04040
PBEAM,28,28,3.3956,4.1094,0.7345,0.0, 3.8258e+00,385.14,+2803
+2803,YESA,1.0, 3.1407,3.5136,0.6233,0.0, 3.2950e+00,365.95,+2805
+2805, , , , 0.0, 0.0, , ,+2806
+2806,-0.50650,-0.03480,-0.47970,-0.03420,-0.35280,-0.04040,-0.33810,-0.03940
PBEAM,29,29,3.1407,3.5136,0.6233,0.0, 3.2950e+00,365.95,+2903
+2903,YESA,1.0, 2.9034,3.0147,0.5274,0.0, 2.8004e+00,346.94,+2905
+2905, , , , 0.0, 0.0, , ,+2906
+2906,-0.47970,-0.03420,-0.46070,-0.03350,-0.33810,-0.03940,-0.32200,-0.03850
PBEAM,30,30,2.9034,3.0147,0.5274,0.0, 2.8004e+00,346.94,+3003
+3003,YESA,1.0, 2.6720,2.4980,0.4459,0.0, 2.3907e+00,326.32,+3005
+3005, , , , 0.0, 0.0, , ,+3006
+3006,-0.46070,-0.03350,-0.42960,-0.03260,-0.32200,-0.03850,-0.29980,-0.03720
PBEAM,31,31,2.6720,2.4980,0.4459,0.0, 2.3907e+00,326.32,+3103
+3103,YESA,1.0, 2.4676,2.1591,0.3771,0.0, 2.0673e+00,310.27,+3105
+3105, , , , 0.0, 0.0, , ,+3106
+3106,-0.42960,-0.03260,-0.41860,-0.03110,-0.29980,-0.03720,-0.29020,-0.03560
PBEAM,32,32,2.4676,2.1591,0.3771,0.0, 2.0673e+00,310.27,+3203
+3203,YESA,1.0, 2.2779,1.8189,0.3215,0.0, 1.7455e+00,291.66,+3205
+3205, , , , 0.0, 0.0, , ,+3206
+3206,-0.41860,-0.03110,-0.39300,-0.03080,-0.29020,-0.03560,-0.27620,-0.03500
PBEAM,33,33,2.2779,1.8189,0.3215,0.0, 1.7455e+00,291.66,+3303
+3303,YESA,1.0, 2.1013,1.5318,0.2743,0.0, 1.5010e+00,272.43,+3305
+3305, , , , 0.0, 0.0, , ,+3306
+3306,-0.39300,-0.03080,-0.36600,-0.02970,-0.27620,-0.03500,-0.25830,-0.03350
PBEAM,34,34,2.1013,1.5318,0.2743,0.0, 1.5010e+00,272.43,+3403
+3403,YESA,1.0, 1.9368,1.3112,0.2320,0.0, 1.2962e+00,256.95,+3405
+3405, , , , 0.0, 0.0, , ,+3406
+3406,-0.36600,-0.02970,-0.35470,-0.02790,-0.25830,-0.03350,-0.24880,-0.03170
PBEAM,35,35,1.9368,1.3112,0.2320,0.0, 1.2962e+00,256.95,+3503
+3503,YESA,1.0, 1.7839,1.0954,0.1990,0.0, 1.1089e+00,237.77,+3505
+3505, , , , 0.0, 0.0, , ,+3506
+3506,-0.35470,-0.02790,-0.33390,-0.02730,-0.24880,-0.03170,-0.23590,-0.03080
PBEAM,36,36,1.7839,1.0954,0.1990,0.0, 1.1089e+00,237.77,+3603
+3603,YESA,1.0, 1.6494,0.9452,0.1696,0.0, 9.6039e-01,221.77,+3605
+3605, , , , 0.0, 0.0, , ,+3606
+3606,-0.33390,-0.02730,-0.32590,-0.02550,-0.23590,-0.03080,-0.22940,-0.02900
PBEAM,37,37,1.6494,0.9452,0.1696,0.0, 9.6039e-01,221.77,+3703
+3703,YESA,1.0, 1.5172,0.7916,0.1437,0.0, 8.0393e-01,203.15,+3705
+3705, , , , 0.0, 0.0, , ,+3706
+3706,-0.32590,-0.02550,-0.30420,-0.02420,-0.22940,-0.02900,-0.21510,-0.02750
PBEAM,38,38,1.5172,0.7916,0.1437,0.0, 8.0393e-01,203.15,+3803
+3803,YESA,1.0, 1.3926,0.6752,0.1207,0.0, 6.7452e-01,186.77,+3805
+3805, , , , 0.0, 0.0, , ,+3806
+3806,-0.30420,-0.02420,-0.29740,-0.02330,-0.21510,-0.02750,-0.21160,-0.02650
PBEAM,39,39,1.3926,0.6752,0.1207,0.0, 6.7452e-01,186.77,+3903
+3903,YESA,1.0, 1.2755,0.5739,0.1006,0.0, 5.7281e-01,171.66,+3905
+3905, , , , 0.0, 0.0, , ,+3906
+3906,-0.29740,-0.02330,-0.29000,-0.02140,-0.21160,-0.02650,-0.20570,-0.02450
PBEAM,40,40,1.2755,0.5739,0.1006,0.0, 5.7281e-01,171.66,+4003
+4003,YESA,1.0, 1.1618,0.4737,0.0839,0.0, 4.7588e-01,153.75,+4005
+4005, , , , 0.0, 0.0, , ,+4006
+4006,-0.29000,-0.02140,-0.27130,-0.02050,-0.20570,-0.02450,-0.19730,-0.02340
PBEAM,41,41,1.1618,0.4737,0.0839,0.0, 4.7588e-01,153.75,+4103
+4103,YESA,1.0, 1.0593,0.4009,0.0695,0.0, 4.0275e-01,140.05,+4105
+4105, , , , 0.0, 0.0, , ,+4106
+4106,-0.27130,-0.02050,-0.26780,-0.01850,-0.19730,-0.02340,-0.19300,-0.02140
PBEAM,42,42,1.0593,0.4009,0.0695,0.0, 4.0275e-01,140.05,+4203
+4203,YESA,1.0, 0.9637,0.3318,0.0578,0.0, 3.4786e-01,124.35,+4205
+4205, , , , 0.0, 0.0, , ,+4206
+4206,-0.26780,-0.01850,-0.25330,-0.01780,-0.19300,-0.02140,-0.18650,-0.02050
PBEAM,43,43,0.9637,0.3318,0.0578,0.0, 3.4786e-01,124.35,+4303
+4303,YESA,1.0, 0.8772,0.2879,0.0474,0.0, 2.7961e-01,108.93,+4305

```

```

+4305, , , , 0.0, 0.0, , , +4306
+4306, -0.25330, -0.01780, -0.25300, -0.01630, -0.18650, -0.02050, -0.18660, -0.01880
PBEAM, 44, 44, 0.8772, 0.2879, 0.0474, 0.0, 2.7961e-01, 108.93, +4403
+4403, YESA, 1.0, 0.7943, 0.2392, 0.0384, 0.0, 2.2819e-01, 95.18, +4405
+4405, , , , 0.0, 0.0, , , +4406
+4406, -0.25300, -0.01630, -0.24960, -0.01440, -0.18660, -0.01880, -0.18440, -0.01690
PBEAM, 45, 45, 0.7943, 0.2392, 0.0384, 0.0, 2.2819e-01, 95.18, +4503
+4503, YESA, 1.0, 0.7107, 0.2005, 0.0303, 0.0, 1.9362e-01, 82.34, +4505
+4505, , , , 0.0, 0.0, , , +4506
+4506, -0.24960, -0.01440, -0.24550, -0.01290, -0.18440, -0.01690, -0.19090, -0.01520
PBEAM, 46, 46, 0.7107, 0.2005, 0.0303, 0.0, 1.9362e-01, 82.34, +4603
+4603, YESA, 1.0, 0.6240, 0.1613, 0.0229, 0.0, 1.5443e-01, 68.28, +4605
+4605, , , , 0.0, 0.0, , , +4606
+4606, -0.24550, -0.01290, -0.24150, -0.01140, -0.19090, -0.01520, -0.18710, -0.01350
PBEAM, 47, 47, 0.6240, 0.1613, 0.0229, 0.0, 1.5443e-01, 68.28, +4703
+4703, YESA, 1.0, 0.5296, 0.1239, 0.0159, 0.0, 1.2161e-01, 54.47, +4705
+4705, , , , 0.0, 0.0, , , +4706
+4706, -0.24150, -0.01140, -0.24850, -0.00880, -0.18710, -0.01350, -0.19030, -0.01100
PBEAM, 48, 48, 0.5296, 0.1239, 0.0159, 0.0, 1.2161e-01, 54.47, +4803
+4803, YESA, 1.0, 0.4182, 0.0831, 0.0091, 0.0, 8.0281e-02, 40.65, +4805
+4805, , , , 0.0, 0.0, , , +4806
+4806, -0.24850, -0.00880, -0.24000, -0.00690, -0.19030, -0.01100, -0.20380, -0.00850
PBEAM, 49, 49, 0.4182, 0.0831, 0.0091, 0.0, 8.0281e-02, 40.65, +4903
+4903, YESA, 1.0, 0.2683, 0.0378, 0.0033, 0.0, 3.4228e-02, 25.20, +4905
+4905, , , , 0.0, 0.0, , , +4906
+4906, -0.24000, -0.00690, -0.22350, -0.00410, -0.20380, -0.00850, -0.20200, -0.00510
PBEAM, 50, 50, 0.2683, 0.0378, 0.0033, 0.0, 3.4228e-02, 25.20, +5003
+5003, YESA, 1.0, 1.21e-04, 8.81e-06, 6.36e-07, 0.0, 7.8353e-06, 15.42, +5005
+5005, , , , 0.0, 0.0, , , +5006
+5006, -0.22350, -0.00410, -0.16620, -0.00220, -0.20200, -0.00510, -0.16030, -0.00280

```

Listing A.5: The NASTRAN instruction file (*DTU.bdf*) for the blade with pre-bend and pre-cone.

```

PROJ='DTU BLADE PRE-BEND PRE-CONE'
ID DTU_BLADE
SOL 106
TIME 20
CEND
TITLE=DTU BLADE MODEL
LABEL=STATIC
SUBTITLE= ORPM
SUPER=ALL
TITLE=DTU TEST
SUBTITLE=STATIC
SEALL=ALL
SUBCASE 1
NLPARM=100
SET 1=ALL
DISP=ALL
METHOD=10
PARAM POST -1
PARAM AUTOSPC YES
PARAM GRDPNT 0
BEGIN BULK
PARAM, TINY, 0.999
PARAM, GRDPNT, 0
PARAM, MAXRATIO, 1.+13
PARAM, COUPMASS, 1
PARAM, AUTOSPC, YES
PARAM, LGDISP, 1
PARAM, NMLOOP, 1
NLPARM, 100, 2, , ITER, 1, 150
PARAM, TESTNEG, 1
PARAM, TESTSE, 1.-10
EIGR, 10, MGIV, 0.1, 50., , , , 1.0E-6, +EIG
+EIG, MAX
INCLUDE 'DTU.model'
ENDDATA

```

Appendix B

Simplified hydrodynamic model in MBDM

In this appendix the hydrodynamic model based on buoyancy is derived assuming a cylindrical support structure. This model was included in the Multi-Body Dynamic Module (MBDM) solver, and validated using a cylinder floating in calm water.

B.1 Cylinder in calm water

The buoyancy force and resulting restoring moments are calculated based on Archimedes' principle, i.e. the total hydrostatic force exerted on a body is equal in magnitude to the weight of the displaced volume of fluid and has opposite orientation to the gravity vector. The resulting buoyancy force is applied to the centre of mass of the displaced fluid, creating a restoring moment about the centre of mass of the submerged body. In this section forces and moments are derived as functions of the cylinders' location and orientation, and the model is verified for simple cases.

B.1.1 Buoyancy force and moment

To calculate buoyancy forces and moments, the submerged volume and centre of mass of the displaced volume of fluid must be calculated. Consider a submerged and rotated cylinder as shown in Figure B.1 with a centroidal body-fixed, reference frame $x' - y' - z'$. If the water surface, location, and orientation in a global reference frame are known, the distance z_w from the body-fixed frame to the water surface and the unit vector \mathbf{u} normal to the water surface defined in the global reference frame are also known. Since it is easier to conduct all computations in the local reference frame $(x' - y' - z')$ of the floater, the unit vector \mathbf{u} is transferred to this frame through relation $\mathbf{u}' \equiv [a, b, c]^T = \mathbf{A}_{cylinder}^T \mathbf{u}$.

The distance k from the centre of mass to the bottom of the cylinder is known and fixed in time. The distance d from centre of mass to the water surface measured along the centreline of the cylinder is time dependent and is a function of z_w and angle ϕ measured between centreline of the cylinder and vector \mathbf{u}' . This relation may be expressed as:

$$d = \frac{z_w}{\cos(\phi)} = \frac{z_w}{c}, \quad (\text{B.1})$$

where c is a third component of unit vector \mathbf{u}' and the transition to the right hand side is done by noting that $\mathbf{v}' \cdot \mathbf{u}' = \cos(\phi) = [0, 0, 1][a, b, c]^T = c$.

The plane for which normal unit vector $[a, b, c]^T$ is known, is described by:

$$ax + by + cz + d = 0, \quad (\text{B.2})$$

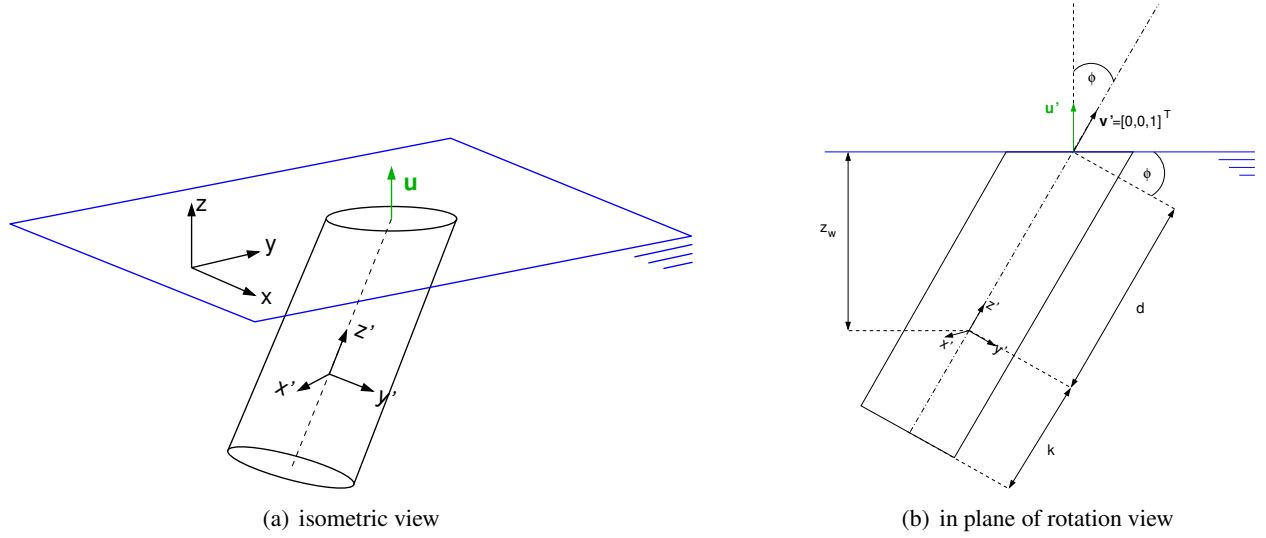


Figure B.1: Configuration of the cylinder in calm water with arbitrary rotation and position.

where a , b and c are components of unit vector, and d is an offset in the direction of the z axis. This definition is consistent with the problem under consideration, and thus the lower and upper boundaries for volume integration are known. Cylindrical coordinates $r - \alpha - z$ are used to integrate the submerged volume of the cylinder in the $x' - y' - z'$ reference frame. The integration is for $0 \leq r \leq R$, $0 \leq \alpha \leq 2\pi$ and $-k \leq z \leq \frac{ax+by+d}{c}$. The submerged volume V is calculated as:

$$V = \int_0^R \int_0^{2\pi} \int_{-k}^{\frac{a r \cos \alpha + b r \sin \alpha + d}{c}} r \, dz d\alpha dr = \left(\frac{d}{c} + k \right) \pi R^2, \quad (\text{B.3})$$

where R is the radius of the cylinder. Once the volume is obtained, the buoyancy force in the global coordinate system calculated from Archimedes' principle yields:

$$\mathbf{F}_b = -V \rho_{water} \mathbf{g} = - \left(\frac{d}{c} + k \right) \pi R^2 \rho_{water} \mathbf{g}, \quad (\text{B.4})$$

where ρ_{water} is density of water and \mathbf{g} is a gravity acceleration vector.

The buoyancy force must be applied at the centre of buoyancy $\mathbf{r}_b \equiv [x_b, y_b, z_b]^T$ i.e. in the centre of mass of the displaced volume. The centre of mass of any body of arbitrary shape is defined as

$$\mathbf{r}_b = \frac{1}{M} \int_V \rho \mathbf{r} dV \quad (\text{B.5})$$

where M is the total mass of the body. Water is a homogeneous fluid with constant density across the displaced volume. Therefore, centre of buoyancy in the body-fixed reference frame is

$$\mathbf{r}'_b = \frac{\rho}{M} \int_V \mathbf{r}' dV = \frac{\rho}{M} \int_V [x'_b, y'_b, z'_b]^T dV, \quad (\text{B.6})$$

where each term of the vector is integrated separately. It is useful to note that $\frac{\rho}{M} = \frac{1}{V}$ and expression for submerged volume V was already obtained in Equation B.3. Integration for each component of the vector

\mathbf{r}'_b yields:

$$x'_b = \frac{1}{V} \int_0^R \int_0^{2\pi} \int_{-k}^{\frac{\arccos \alpha + b r \sin \alpha + d}{c}} (r^2 \cos \alpha) dz d\alpha dr = \frac{a\pi}{4Vc} R^4 \quad (\text{B.7a})$$

$$y'_b = \frac{1}{V} \int_0^R \int_0^{2\pi} \int_{-k}^{\frac{\arccos \alpha + b r \sin \alpha + d}{c}} (r^2 \sin \alpha) dz d\alpha dr = \frac{b\pi}{4Vc} R^4 \quad (\text{B.7b})$$

$$z'_b = \frac{1}{V} \int_0^R \int_0^{2\pi} \int_{-k}^{\frac{\arccos \alpha + b r \sin \alpha + d}{c}} (rz) dz d\alpha dr = \frac{\pi R^2}{V} \left[\frac{a^2 R^2}{8c^2} + \frac{b^2 R^2}{8c^2} + \frac{d^2}{2c^2} - \frac{k^2}{2} \right]. \quad (\text{B.7c})$$

Since in the constrained Newton-Euler equations of motion of Equation 4.67 applied moments \mathbf{n}'^A are defined in the body-fixed reference frame, the resulting buoyancy applied moment \mathbf{n}'^A_b is

$$\mathbf{n}'^A_b = \tilde{\mathbf{r}}'_b \mathbf{F}'_b = \tilde{\mathbf{r}}'_b \mathbf{A}_{cylinder}^T \mathbf{F}_b \quad (\text{B.8})$$

where $\mathbf{r}'_b = [x'_b, y'_b, z'_b]^T$ and \mathbf{F}_b is a buoyancy force from Equation B.4 defined in the global coordinate system.

B.1.2 Validation of the model

The cylinder representing the floating platform is designed to support the NREL 5-MW baseline wind turbine^[88] and is used for validation purposes in this section. The mass and inertia properties of the cylinder are identical to the one derived by Jonkman^[88], but because the tower with the nacelle and the rotor are not considered in the model, the overall draft is smaller. Properties of the floater and mooring cables are gathered in Table B.1. The mooring line damping coefficient was set equal to the stiffness coefficient, and the water density was taken as $\rho_{water} = 1000 \text{ kg/m}^3$ with gravity acceleration of $g = 9.81 \text{ m/s}^2$.

Table B.1: Properties of the cylinder and mooring cables representing moored floating platform.

Properties of the cylinder	
Total draft	107.5874 m
Elevation of platform top above SWL	22.4126 m
Platform diameter	9.4 m
Platform mass	7 466 330 kg
Centre of mass location below SWL	77.5029 m
Platform roll inertia about centre of mass (I_{xx})	4 229 230 000 $\text{kg} \cdot \text{m}^2$
Platform pitch inertia about centre of mass (I_{yy})	4 229 230 000 $\text{kg} \cdot \text{m}^2$
Platform yaw inertia about centre of mass (I_{zz})	164 230 000 $\text{kg} \cdot \text{m}^2$
Properties of the mooring cables	
Number of mooring lines	3
Angle between adjacent lines	120°
Depth of anchors below SWL	320 m
Depth of fairleads below SWL	57.5874 m
Radius of anchors from platform centreline	853.87 m
Radius of fairleads from platform centreline	5.2 m
Mooring line extensional stiffness	384 243 N/m
Mooring line damping coefficient	384 243 Ns/m

The first test case considered the cylinder placed at equilibrium position, therefore the gravity force was opposed by buoyancy and no moments acted on the cylinder. Next, the cylinder was offset from the

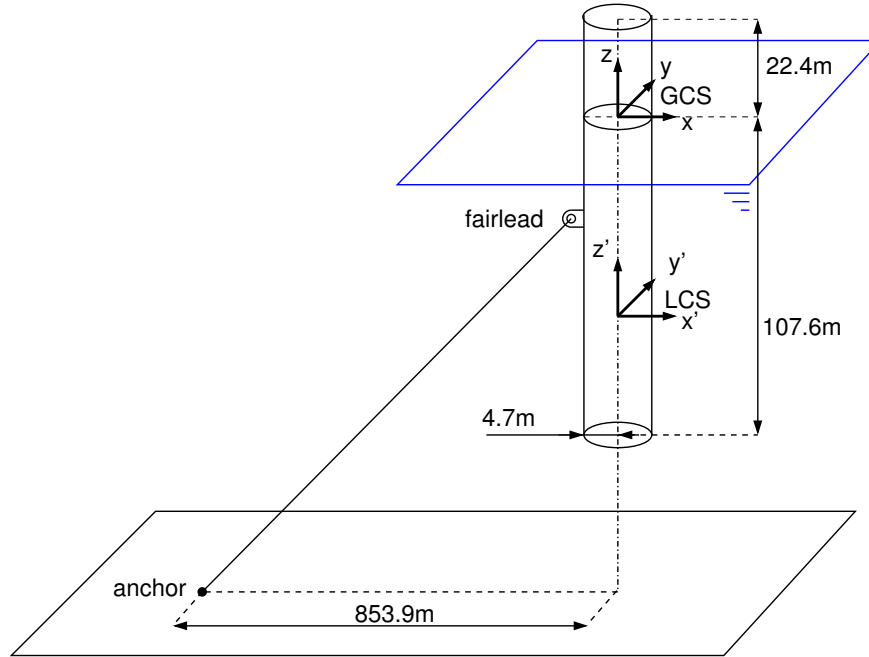


Figure B.2: Schematics of the floating platform. Not in scale. Only one mooring line is presented for simplicity.

equilibrium by rotating it around its centre of gravity by 15° and about the y axis in pitch forward direction, as shown in Figure B.5. This test case has two sub-cases, namely a cylinder without mooring cables, and a cylinder with mooring lines modelled as combinations of springs and dampers. The numerical integration used for all test cases is the Runge-Kutta scheme of fourth order with time step of $\Delta t = 0.1s$. The convergence criterion for the Newton-Raphson algorithm was set to 10^{-6} , meaning that every component of the residual vector is below that value. All cases were computed with the final time of calculation set to $t_{final} = 200s$ to capture all low frequency motions. Results are presented in Figures B.3 and B.4.

Results of the cylinder placed in the equilibrium position show no change in position and orientation of the cylinder over time. This is a trivial and expected behaviour. Consider now the cylinder rotated about its centre of mass that is below the surface of calm water as shown in Figure B.5. The displaced volume of fluid is now bigger than in case of the cylinder placed in a vertical position. Hence, larger buoyancy force is exerted on the body. First of all, this simple consideration shows coupling between rotational and lateral dynamics even for such a simple cases. Second, this means that the centre of gravity of the cylinder should oscillate above the equilibrium position. Third, the cylinder should be excited along z direction due to rotation about y axis. Further, the cylinder should be excited two times per rotation cycle, since there are two angular maxima per period. Fourth, the restoring moment due to buoyancy should be influenced by slower lateral motion of the cylinder. Finally, cylinder has symmetric inertia tensor and no forces acting in other directions than z . Therefore, centre of mass is expected to remain in initial x and y position. All these phenomena can be observed in the results. Note that fast accelerations in z direction due to change in orientation about y axis are overlayed on the slow lateral accelerations due to initial imbalance i.e. buoyancy force is higher than gravity force at time $t = 0$. Also, note slow variation of angular acceleration ε_y that corresponds to slow variation of lateral displacement - approximately 2.5 cycles in 50 seconds.

Damping in the model is introduced only by the mooring lines. Hence, by including mooring cables in the model, it is expected to dampen the motion of the cylinder to the equilibrium position. As can be observed in the results, the mooring lines do not just dampen the motion, but also slightly increase the natural frequencies of the system. Further, mooring lines smoothen high frequency oscillations as in case

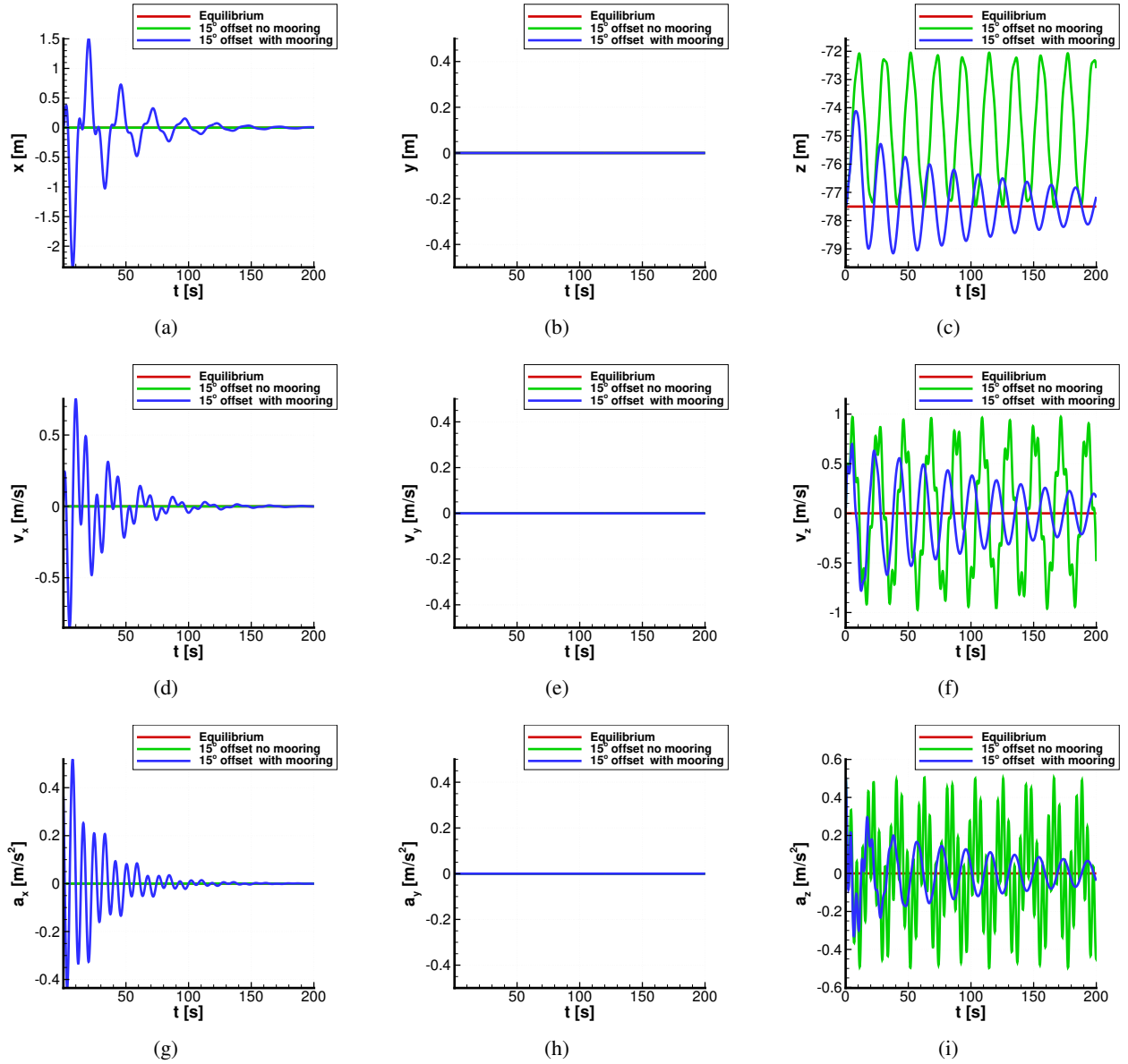


Figure B.3: Lateral dynamics of a cylinder in calm water. Cylinder placed in equilibrium position and cylinder with offset from equilibrium by 15° about y axis. Results with and without mooring lines.

of acceleration in z direction. Also, mooring cables introduce the lateral motion of centre of mass in x direction. This is because the fairleads do not coincide with centre of mass and have initial displacement. Therefore, there is an initial force in x direction coming from springs that try to put the cylinder back in a vertical position.

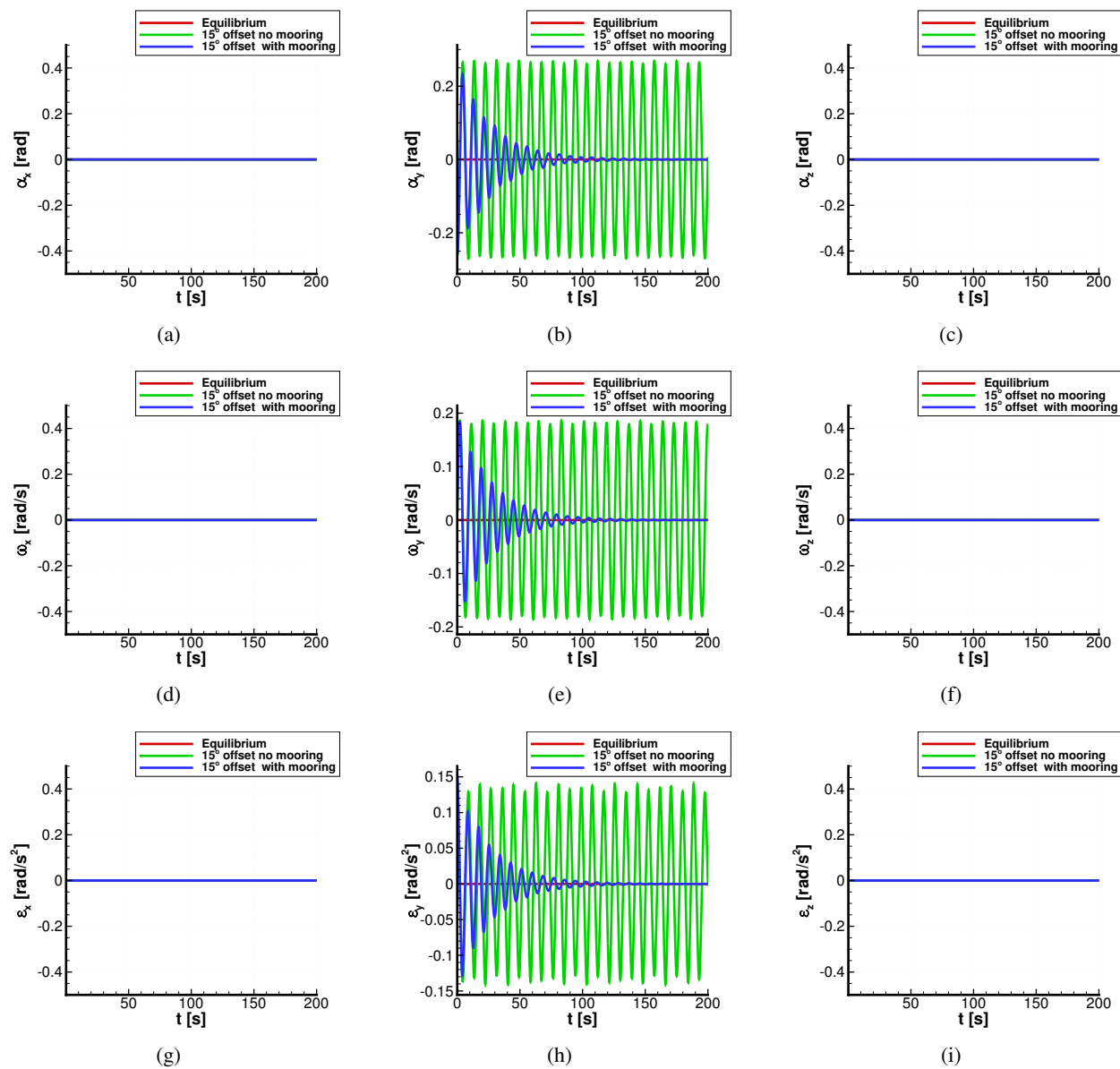


Figure B.4: Rotational dynamics of a cylinder in calm water. Cylinder placed in equilibrium position and cylinder with offset from equilibrium by 15° about y axis. Results with and without mooring lines.

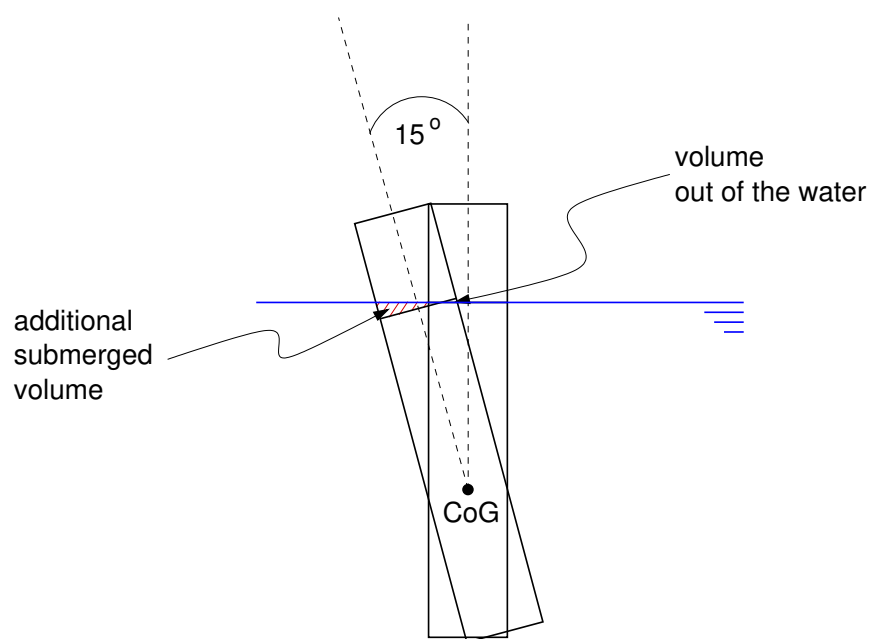


Figure B.5: Schematics of the floating platform rotated by 15°.

Appendix C

Convection of the Mann's turbulence field into Cartesian grids

This appendix is complementary to the results presented in Section 9.5 of Chapter 9 for the 10-WM wind turbine. Here, the effect of grid density on the ability of the HMB3 solver to preserve small turbulent structures present in the generated Mann's field is investigated. The parameters used to generate the field of turbulence are provided in Table 9.6 of Chapter 9. The grids employed in this appendix are Cartesian, and do not contain any solid boundaries, as shown in Table C.1 and Figure C.1. The first grid consists of cells with equal size of $4m \times 4m \times 4m$, what corresponds to the resolution of generated Mann turbulent field. The second grid is twice as fine in all directions, resulting in uniform cells of size $2m \times 2m \times 2m$. Finally, the last grid was constructed by combining the Cartesian grid with cell's size of $2m \times 2m \times 2m$ with the cylindrical grid with size of the DTU 10MW rotor (see Section 9.1 for details). The grid overset method^[81] was employed for the last grid, as shown in Figure C.1.

Grid ID	Cell dimensions [m]	Size [cells]	Grid over-set method
M1	$4m \times 4m \times 4m$	$0.75 \cdot 10^6$	No
M2	$2m \times 2m \times 2m$	$5.97 \cdot 10^6$	No
M3	$2m \times 2m \times 2m$	$6.11 \cdot 10^6$	Yes

Table C.1: Computational grids employed in this chapter.

The computations were solved for 1700 steps with time-step $\Delta t = 0.0198s$, or non-dimensional time-step $\Delta t^* = \Delta t \cdot \frac{U_\infty}{C_{max}} = 0.033$. This corresponds to the final time of computation $t = 33.6$ seconds, where the characteristic length scale was used as $C_{max} = 6.206$, and the mean wind speed was set to $U_\infty = 10.5m/s$. Based on these conditions, the free-stream Mach number was $M = 0.031$, and the Reynolds number was $Re = 4.46 \cdot 10^6$.

First, the coarse grid (Grid M1 in Table C.1) was employed, and the solution was obtained with three different methods: (a) assuming inviscid flow and using second-order MUSCL scheme; (b) assuming inviscid flow and using fourth-order MUSCL scheme^[84]; and (c) assuming viscous flow and using the $k - \omega$ Shear Stress Transport (SST)-based Scale-Adaptive Simulation (SAS)^[138] with second-order MUSCL scheme. The obtained results are compared to the case of pure convection of the Mann Box turbulent field through the domain, see Figures C.2 and C.3. The first observation is that very similar solution is obtained with the $k - \omega$ SST-SAS turbulence model and the inviscid fluid model. The absence of walls, and hence the boundary layer, explains this behaviour. The decay of turbulence is caused by numerical dissipation, and no turbulence is produced to balance the dissipation in the domain. The next observation is that the high-order (4th order) MUSCL scheme preserves the imposed fluctuations better on the same grid, as compared to the

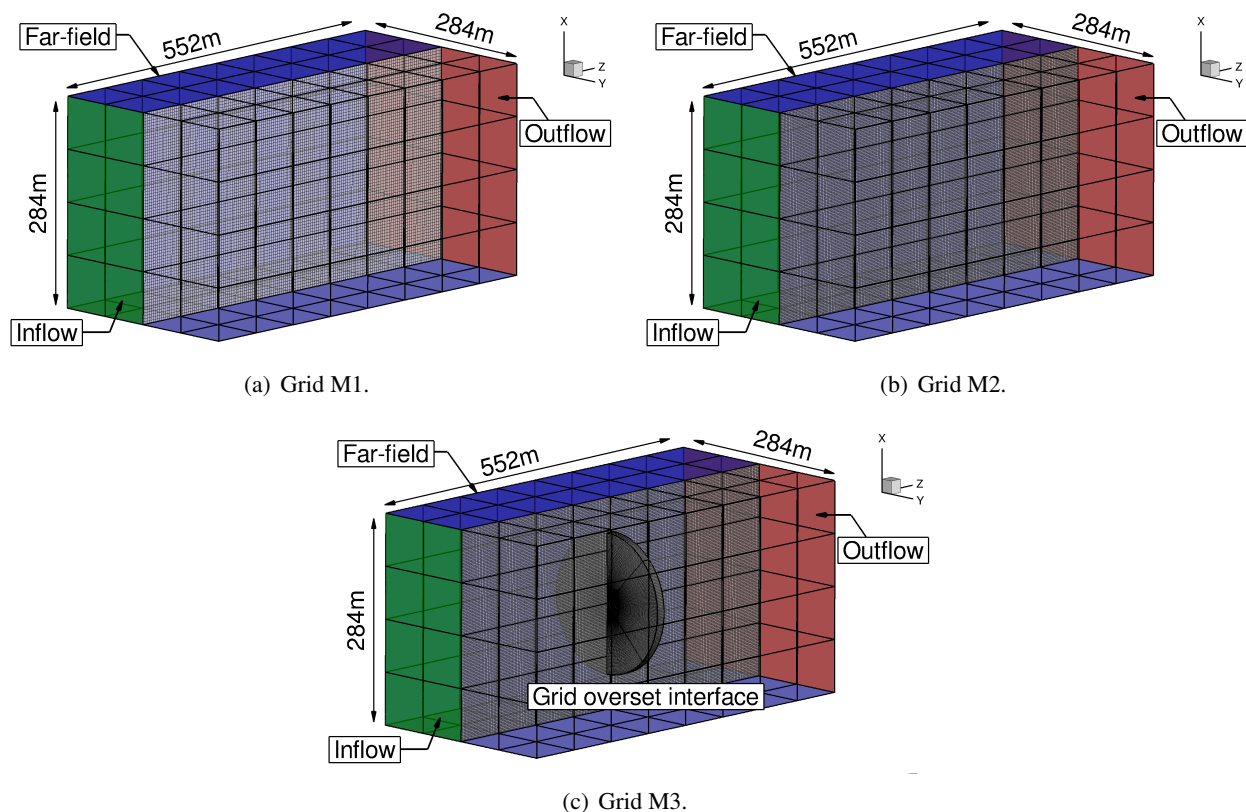
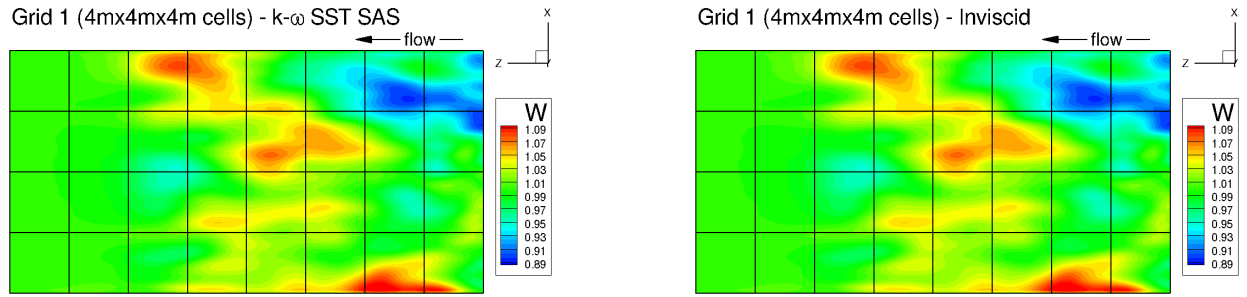


Figure C.1: Comparison of the computational grids employed in this chapter.

$k - \omega$ SST-SAS turbulence model with the 2nd order MUSCL scheme. This is again related to numerical dissipation, where the high-order scheme is less dissipative.

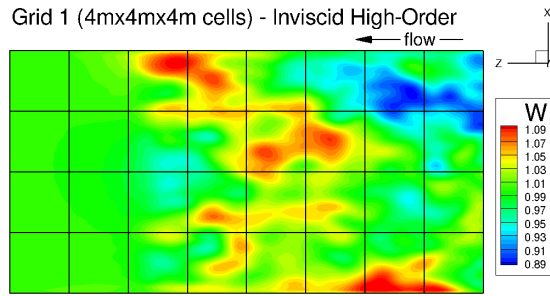
Next, two fine grids were employed (Grid M2 and Grid M3 in Table C.1). First, the $k - \omega$ SST-SAS model with the second-order MUSCL scheme was used for both grids. The fourth-order MUSCL scheme^[84] was also used for the Grid M2, assuming inviscid flow. The comparison is shown in Figures C.4 and C.5. The results suggest that the overset grid interface does not affect the velocity field and turbulent structures in the flow. Further, similarly to the coarse grid tests, the high-order MUSCL scheme preserves the imposed fluctuations better on the same grid, as compared to the $k - \omega$ SST-SAS turbulence model with the second-order MUSCL scheme. Lastly, the 4th order MUSCL scheme is also capable of preserving smaller turbulent structures, as compared to the $k - \omega$ SST-SAS model.

Finally, a comparison between the solutions obtained with the 2nd order MUSCL scheme on the fine grid (Grid M2), and with the 4th order MUSCL scheme^[84] on the coarse grid (Grid M1) is shown in Figure C.6. Similar solutions were obtained in both cases, although Grid M2 seems to preserve smaller structures a bit better. Note that the coarse grid has 8 times less cells than the fine grid. This suggests that the best approach to convect the Mann's turbulent field is to employ the high-order MUSCL scheme on a relatively coarse grid, and possibly employ the grid overset method to include the rotor. Unfortunately, the development of the high-order MUSCL scheme was not complete by the time full rotor computations from Section 9.5 of Chapter 9 were conducted.

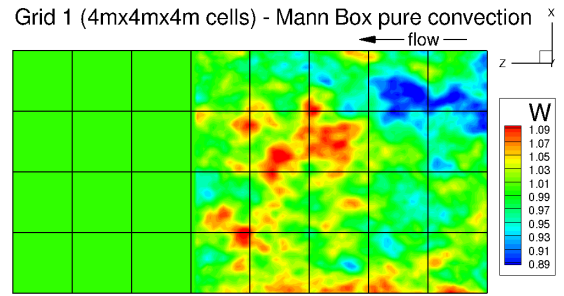


(a) Grid M1 - $k - \omega$ SST-SAS model, 2nd order in space.

(b) Grid M1 - Inviscid flow, 2nd order in space.

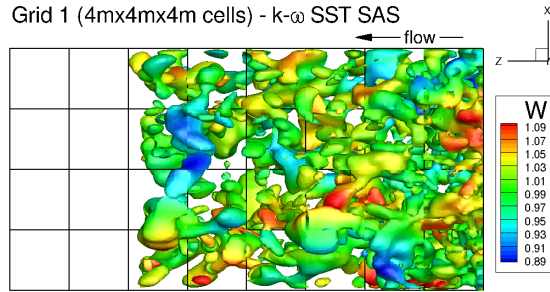


(c) Grid M1 - Inviscid flow, 4th order in space.

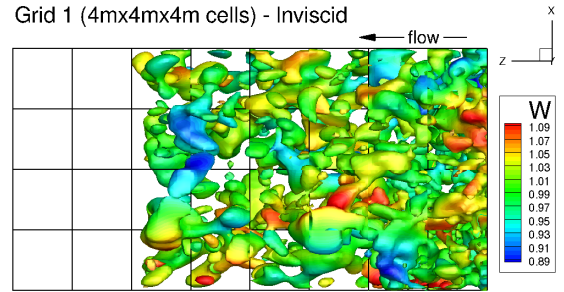


(d) Purely convected turbulent field.

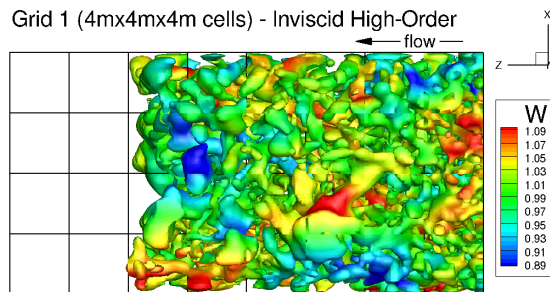
Figure C.2: Comparison of the solutions obtained with different methods for the Grid M1. Contours of the non-dimensional velocity component W in the middle of the domain.



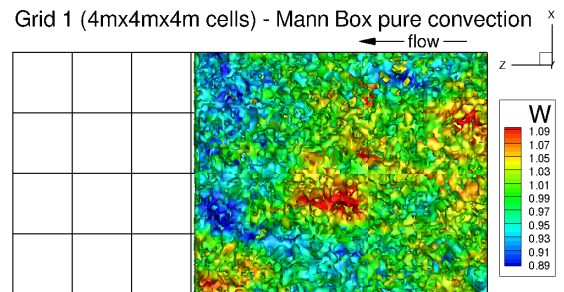
(a) Grid M1 - $k - \omega$ SST-SAS model, 2nd order in space.



(b) Grid M1 - Inviscid flow, 2nd order in space.

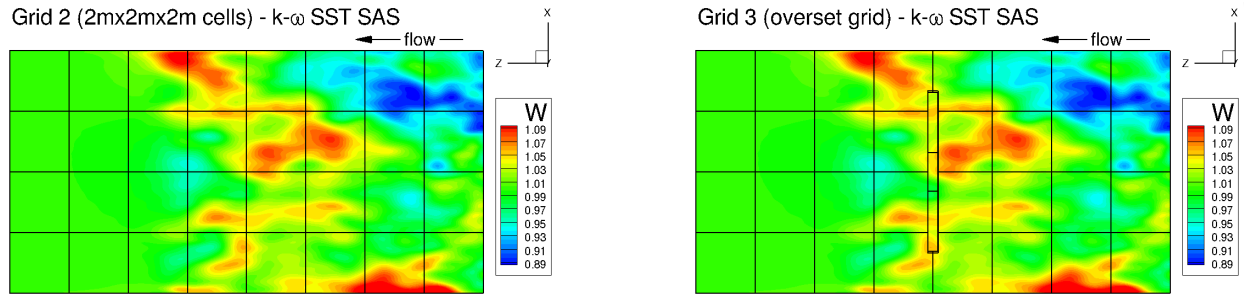


(c) Grid M1 - Inviscid flow, 4th order in space.



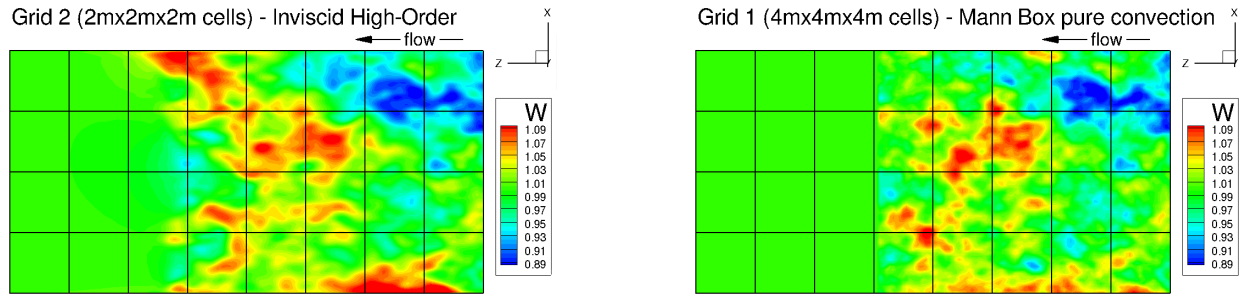
(d) Purely convected turbulent field.

Figure C.3: Comparison of the solutions obtained with different methods for the Grid M1. Iso-surface of non-dimensional $Q = 0.0001$ criterion.



(a) Grid M2 - $k - \omega$ SST-SAS model, 2nd order in space.

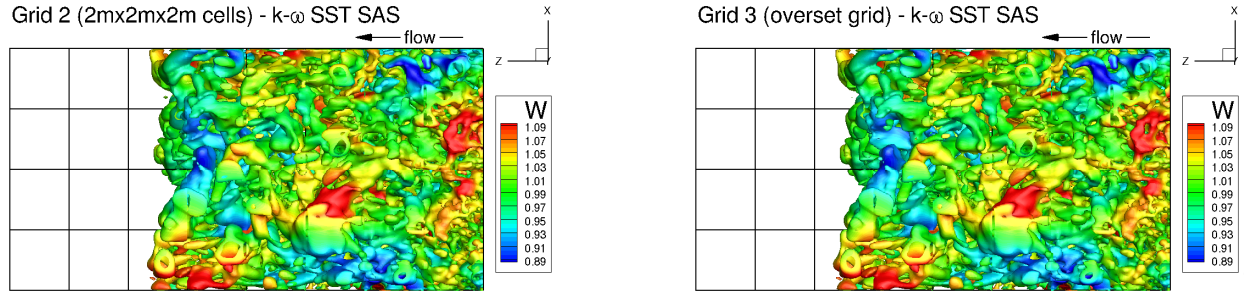
(b) Grid M3 - $k - \omega$ SST-SAS model, 2nd order in space.



(c) Grid M2 - Inviscid flow, 4th order in space.

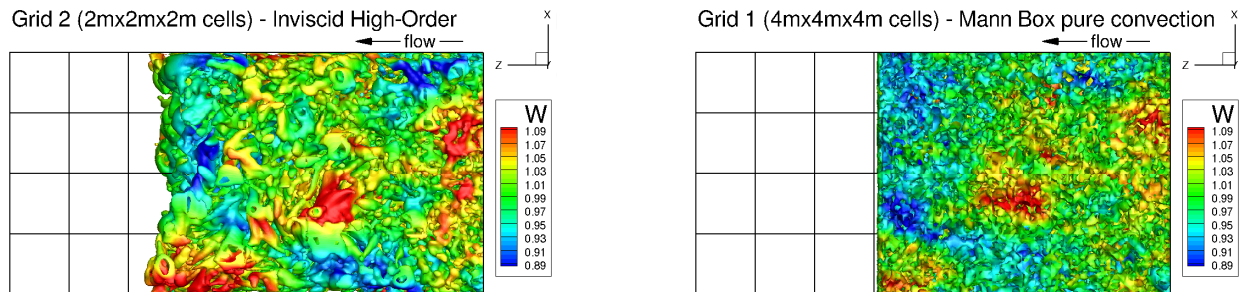
(d) Purely convected turbulent field.

Figure C.4: Comparison of the solutions obtained with different methods for Grids M2 and M3. Contours of the non-dimensional velocity component W in the middle of the domain.



(a) Grid M2 - $k - \omega$ SST-SAS model, 2nd order in space.

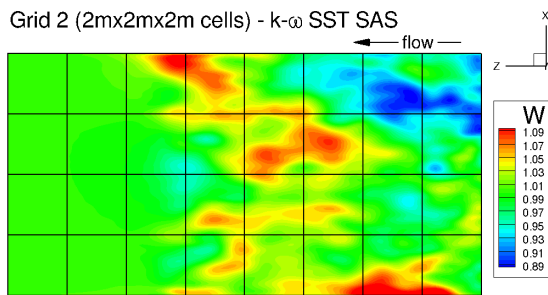
(b) Grid M3 - $k - \omega$ SST-SAS model, 2nd order in space.



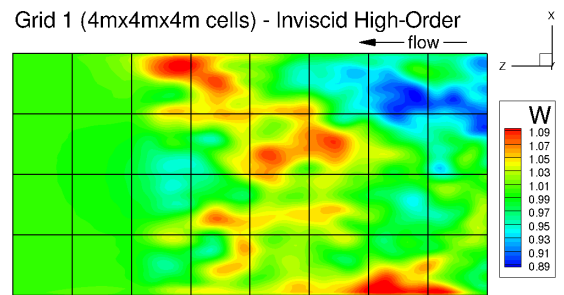
(c) Grid M2 - Inviscid flow, 4th order in space.

(d) Purely convected turbulent field.

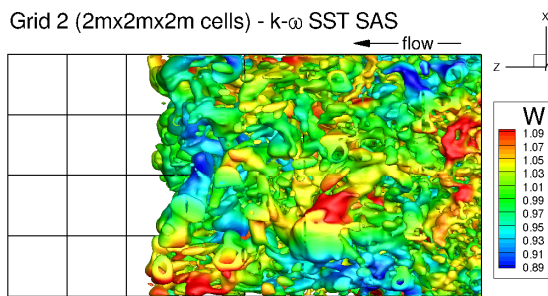
Figure C.5: Comparison of the solutions obtained with different methods for Grid M2 and M3. Iso-surface of non-dimensional $Q = 0.0001$ criterion.



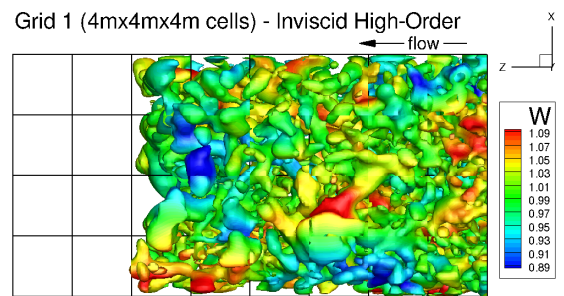
(a) Grid M2 - 2nd order MUSCL scheme.



(b) Grid M1 - 4th order MUSCL scheme.



(c) Grid M2 - 2nd order MUSCL scheme.



(d) Grid M1 - 4th order MUSCL scheme.

Figure C.6: Comparison of the solutions obtained with the 2nd order MUSCL scheme using fine Grid M2, and with the 4th order MUSCL scheme using coarse Grid M1.